MULTIFUNCTIONAL TESTING ARTIFACTS FOR EVALUATION OF 3D PRINTED COMPONENTS BY FUSED DEPOSITION MODELING

A Dissertation
submitted to the faculty of the

Worcester Polytechnic Institute

as a partial fulfillment of the requirements for the
Degree of Doctor of Philosophy
in
Mechanical Engineering

By

Koohyar Pooladvand

19 October 2019

Approved:

Prof. Cosme Furlong, Major Advisor

Prof. John M. Sullivan, Dissertation Committee

Prof. Christopher A. Brown, Dissertation Committee

Prof. Sneha P. Narra, Dissertation Committee

Prof. Pavel Psota, Technical University of Liberec, Czech Republic,
Dissertation Committee

Professor Yihao Zheng, Graduate Committee representative

Abstract:

The need for reliable and cost-effective testing procedures for Additive Manufacturing (AM) is growing. In this Dissertation, the development of a new computational-experimental method based on the realization of specific testing artifacts to address this need is presented. This research is focused on one of the widely utilized AM technologies, Fused Deposition Modeling (FDM), and can be extended to other AM technologies as well. In this method, testing artifacts are designed with simplified boundary conditions and computational domains that minimize uncertainties in the analyses. Testing artifacts are a combination of thin and thick cantilever structures, which allow measurement of natural frequencies, mode shapes, and dimensions as well as distortions, residual stresses, and deformations. We apply Optical Non-Destructive Testing (ONDT) together with computational methods on the testing artifacts to predict their natural frequencies, thermal flow, mechanical properties, and distortions as a function of 3D printing parameters. The complementary application of experiments and simulations on 3D printed testing artifacts allows us to systematically investigate the density, porosity, moduli of elasticity, and Poisson's ratios for both isotropic and orthotropic material properties to better understand relationships between these characteristics and the selected printing parameters. The method can also be adapted for distortions and residual stress analyses. We optimally collect data using a design of experiments technique that is based on regression models, which yields statistically significant data with a reduced number of iterations. Analyses of variance of these data highlight the complexity and multifaceted effects of different process parameters and their influences on 3D printed part performance. We learned that the layer thickness is the most significant parameter that drives both density and elastic moduli. We also observed and defined the interactions among density, elastic moduli, and Poisson's ratios with printing speed, extruder temperature, fan speed, bed temperature, and layer thickness quantitatively. This Dissertation

also shows that by effectively combining ONDT and computational methods, it is possible to achieve greater understanding of the multiphysics that governs FDM. Such understanding can be used to estimate the physical and mechanical properties of 3D printed components, deliver part with improved quality, and minimize distortions and/or residual stresses to help realize functional components.

Acknowledgments

The outstanding guidance and support I have received from Prof. Furlong made this dissertation possible. The wholehearted and continuous support of my wife, Sara, was alongside me during this Ph.D. program and helped me to overcome challenges. I am indebted to Sara's endless encouragement and love. We went through difficult moments together, and her love and devotion elevated my expectations for me.

I also would like to express my gratitude for the members of the committee (Prof. John M. Sullivan, Prof. Christopher A. Brown, Prof. Sneha P. Narra, Prof. Pavel Psota, and Professor Yihao Zheng), whose suggestions and assessments were immeasurable. I also would like to acknowledge the members of the Center for Holographic Studies and Laser micro-mechaTronics (CHSLT) in the Mechanical Engineering Department of Worcester Polytechnic Institute (WPI). I am especially thankful for Dr. Morteza Khaleghi, Dr. Payam Razavi, Mr. Peter Hefti, Mr. Haimi Tang, Mr. Anthony Salerni, Mr. Westly Castro-Carrion, and Mr. Daniel Alberto Ruiz-Cadalso.

I am thankful for my parents (Ozra and Ahmad), my parents-in-law (Zohreh and Ali), my sister (Kiana), and other members of my family for their priceless motivations and encouragement. No words can express the gratitude I feel in my heart for them.

WPI, CHSLT, and the Mechanical Engineering department funded my Ph.D. studies and research, and I am thankful for their support. I also would like to express my gratitude for the support of the Center for Advanced Research in Drying (CARD), SAS Institute Inc., and U.S. Army Natick Soldier Systems Center (NSSC) as well as extend my appreciation to NSF for using the equipment available through the award CMMI-1428921.

I also would like to express my appreciation for Dr. Michael Dedek, Dr. Oluwaseun K. Oyewole, and Mr. Hrachya Kocharyan for their help in this dissertation.

Table of Contents

Table of Figures

List of tables:

Nomenclature

3D	Three Dimensional
ABS	Acrylonitrile Butadiene Styrene
ANSI	American National Standards Institute
ASTM	American Society of Testing and Materials
A_c	Cross-sectional Area
A_h	Perimeter Area for Convection and Radiation,
A_i	Contact Area to Bed or Another Filament,
$A_m, B_m, C_m, and\ D_m$	Constant for Transverse Displacement Definition
AM	Additive Manufacturing
BAAM	Big Area Additive Manufacturing
CAD	Computer-Aided Design
CAM	Computer-Aided Manufacture
CCD	Central Composite Design
CTE	Coefficient of Thermal Expansion
C_{ijkl}	Elasticity Tensor Constants
D	Nozzle Diameter
D_{ij}	Flexural Rigidity
DoE	Design of Experiment
E	Modulus of Elasticity, Young's Modulus
ES	Extruder Speed
ET	Extruder Temperature
FCCCD	Face Centered Central Composite Design
FDM	Fused Deposition Modeling
FGF	Fused Granular Fabrication
FFF	Fused Filament Fabrication
FEA or FEM	Finite Element Analyses or Method
FS	Fan Speed
G	Shear Modulus

G_x, G_y, H_x, H_y, J_x, and J_y	Coefficients for Estimation of Eigenvalues for Modal Analyses
H	Filament's Height
LT	Layer Thickness
HBT	Heated Bed Temperature
I	Moment of Inertia or Flexural Stiffness of The Beam
I_p,	Polar Moment of Inertia
IR	Infrared
L	Length
LENS	Laser Engineered Net Shaping
L_r,	Thickness of The Raft Layer
M	Bending Moment
ONDT	Optical Non-Destructive Testing
Pe_x	Pecklet Number
Pr	Prandtel Number
R_c	Contact Resistance Between Polymer and Bed or Two Adjacent Beads
R_b	Thermal Resistance
Re	Reynolds Numbers
R_n	Beam Curvature
RS	Residual Stress
RSM	Response Surface Methodology
RMS	Root Mean Square
SLS	Selective Laser Sintering
SR	Solidity Ration
STL	Stereolithography
T	Surface or Body Temperature
T_∞	Environment-Wall Temperatures
T_{ave}	Averaged Temperature
T_b	Heated-Bed Temperature
T_e	Enveloped Temperature
T_{ext}	Extruder Temperature

T_g	Glass transition temperature
U	Deposition Velocity
U_∞	Fluid Velocity
W	Filament's Width
$\boldsymbol{W}$	Transverse Displacement
a_k	Constant Relating to The Cross-Section to Define the Stress in a Beam
b	Width of The Specimen
c	Wave Speed
c_p	Specific Heat
c_T	Flexural Wave Speed
c_T	Transversal Wave Propagation Speed
$\boldsymbol{h}$	Enthalpy
h	Thickness
h_c	Contact Equivalent Heat Convection
h_{cov}	Coefficient of Convection Heat Transfer
h_t	Total Heat Transfer Coefficient Including Radiation and Convection
n	Number of Layers
q	With Different Subscribes Indicate Heat Fluxes
q_b	Heat Flux
r, θ, and z	Cylindrical Coordinate
t	Thickness or Time
u	Longitudinal or Flexural Displacement in a Beam
x, y, and z	Cartesian Coordinate
Γ	Transverse Displacement
θ	Angular Displacement
Δh	Layer Thickness
∇^2	Laplace Operator
Δt	Time Increment
ΔT_b	Temperature Difference Between the Last Node and Heated-Bed
α	Coefficient of Thermal Expansion, CTE

α and β	Constant for The Empirical Estimation of Combined Convection-Radiation Heat Transfer
δ	Normal Deformation
δ	Deflection in a Particular Length of The Specimen
ε	Emissivity
κ	Conductivity
κ_r	Conductivity of The Raft Layer
λ_n	Non-dimensional Eigenvalue
μ	Dynamic Viscosity
ν	Kinematic Viscosity
v	Poisson's Ratio
ρ	Density
σ_{ij}	Cartesian Components of the Stress Tensor
u_i	Displacement Vector in The Cartesian System
σ	Stefan-Boltzmann Constant.
σ_m	Mean Stress
σ_k	Gradient Stress
σ_p	Plate area Density, $\rho \times h$
ω_n	Natural Frequency of the nth Mode

Superscripts:

f	Indicates a Thin Layer
l	l-th Time Step

Subscripts:

ave	Average
b	Heated bed
con, conv, neight, and *rad*	Conduction, Convection, Neighbor, and Radiation, Respectively

ext	Extruder
f	Indicates a Thin Layer
i	*i*-th Deposited Layer in *z*-Direction
i,j, and *k*	Indices for Directions, Sequences, Orders, and …
n, and *m*	Indices Sequences, Orders, …
l	*l*-th Time Step
r	Raft Layer
∞	Enveloped Temperature

1. Introduction

A promising Additive Manufacturing (AM) technology, which has been adopted widely, is polymer-based 3D printing. Polymer-based AM can print a wide range of materials from biomaterial like collagen and chitosan to high-performance polymers like nylon, poly-ether-ether-ketone (PEEK), and Ultem (Polyetherimide, PEI). This technology recently has received increased attention for industrial applications; an example of successful application of this technology is Big Area Additive Manufacturing (BAAM), a result of cooperation between industries and Oak Ridge National Laboratory (ORNL) [1]. In addition to pioneering names like STRATASYS [2], other companies, such as Thermwood© [3], Markforged© [4], Strangpresse [5], and Lemantek [6], are advancing these technologies to industry's floor.

In polymer-based additive manufacturing, the complex nature of polymers hinders the development of reliable and efficient computational-experimental approaches. Viscoelasticity, entanglement, wetting, bonding, rheology, and creep hold back a comprehensive understanding of the evolution of parts during and after fabrication [7-9]. Despite its rapid development in recent years, polymer-based AM is still suffering from critical limitations, including rough surface finish, uncertain dimensional accuracy, and precision, as well as low mechanical strength and reliability of the printed components [7, 10-12]. Turning 3D printing into a leading producer of functional components requires addressing these limitations by understanding how build parameters affect the mechanical and structural properties of the printed component and select them efficiently to overcome these shortcomings.

There is a need for a practical approach to efficiently, non-invasively, and cost-effectively evaluate the 3D printing processes and characterize printed components. Such an approach intends to deliver a better and quantitative understanding of the governing physics. Neither

experimental nor numerical studies alone have been able to provide a reliable understanding of the influences of process and manufacturing parameters on part performance. On the one hand, simulations have been used to understand the effects of process parameters on some characteristics of printed components, i.e., layer bonding, mechanical properties, distortions, microstructures, and residual stresses [12-16]; however, effective experimental verifications are still needed. On the other hand, there are well-developed nondestructive testing (NDT) procedures capable of measuring structural properties and health. Methods such as Digital Holographic Interferometry (DHI), Digital Image Correlation (DIC), and Digital Fringe Projection (DFP) enable characterization of mechanical properties, shape and geometrical distortions, as well as porosity and defect identification [17-20]. We applied these NDTs differently from previous studies to understand the effects of process parameters on printed components.

We are proposing to use a designed testing artifact with simplified boundary conditions to tackle challenges in 3D printing using both numerical modeling and experimental approaches concurrently. We design testing artifacts with the objective of simplifying boundary conditions and reducing computational costs while minimizing uncertainties in the extraction of the parameters of interest. Our method consists of simulations that can capture the complex physics of 3D printing and can be tuned based on nondestructive measurements of thermal and structural characteristics. Within our method, we are designing, simulating, printing, and testing artifacts to investigate how some printing and manufacturing parameters—including layer thickness, extruder temperature, heated bed temperature, fan speed, and extruder speed— affect the performance and quality of the artifacts. This allows us to identify mechanical and geometrical

properties as a function of process parameters. In the following sessions, more details about this approach are explained and demonstrated.

1.1 Introduction to additive manufacturing and 3D printing

AM is a revolutionary manufacturing process that fabricates a 3D object directly from a 3D solid file by selective deposition of the material. ASTM Committee F42T agreed to name this category of manufacturing "Additive Manufacturing (AM)" as opposed to subtractive manufacturing [21]. There are several aliases that each refer to AM, i.e., additive fabrication, additive processes, additive techniques, additive layer manufacturing, layer manufacturing, Free Form Fabrication (FFF), solid freeform fabrication, rapid prototyping, and 3D printing, each of which names a process of joining material layer-upon-layer to realize a part consecutively and controllably according to a sliced 3D digital file. The process of manufacturing by AM consists of three main steps: The first step is the preparation of a 3D file utilizing a Computer-Aided Design (CAD) software. In the second step, the file translated into a machine executable code is manufactured layer-by-layer. An AM machine receives the file and reads, runs, and deposits material accordingly to define the object. Finally, the 3D file gradually turns into an object with the same shape and dimension and goes through a set of post-processing processes as needed for final improvement. These three steps converting a 3D file to a real object are shown in Fig. 1.

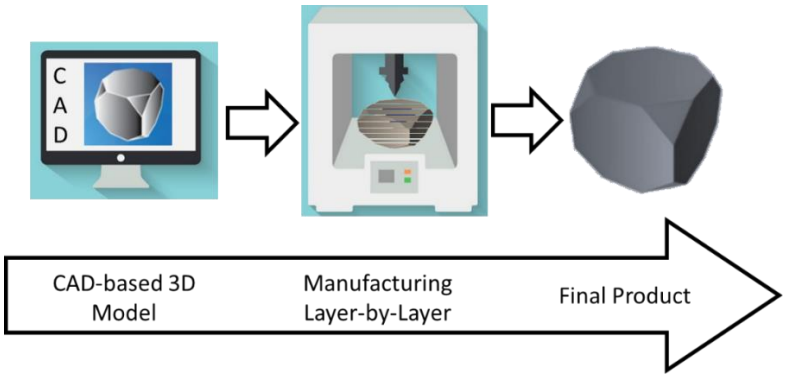

Fig. 1. Overview of the process of additive manufacturing.

In the past few decades, there has been tremendous progress in the promotion of emerging AM technologies as potentially disruptive manufacturing methods [22, 23]. However, AM is not going to supplant subtractive manufacturing in terms of mass production, low material cost, capital investment, speed, and centralized manufacturing, at least in the near future. Still, AM has a few merits that may accelerate its adoption worldwide: customization, optimization, sustainability, design freedom, flexibility, energy efficiency, and limitless creation [24-26]. Additionally, growing interest could reduce costs, energy consumption, and carbon emission sooner than ever.

Design freedom and optimization, alongside the possibility of printing functionally graded material, gives AM advantages over conventional manufacturing in the fabrication of intricate and complex shapes that are accessible with no or little tooling. Components assumed to be made with AM can be designed for manufacturing with fewer concerns about their manufacturability and more focus on customizability and functionality [27].

The classes of materials that are able to be manufactured by AM include metals, ceramics, polymers, composites, and biological substances [24, 25]. Although the technology initially started with polymer-based materials, it sharply shifted toward metallic materials, and soon a wide variety of technologies became available that fabricate parts with high quality and conceivable applications. Advances in computer-aided design (CAD) and manufacturing (CAM), the advent of powerful computational tools, and availability of various 3D printable materials have paved the ground for AM to democratize and globalize manufacturing at the customer level. However, there are lots of challenges to be addressed in these technologies to go beyond the current status quo and deliver reliable functional components.

1.2 Current challenges in AM technologies

Research groups are focusing on different aspects of AM in order to overcome the challenges and uncertainties that hinder AM's growing adoption. Some of these important challenges are summarized in Fig. 2. These challenges include developing novel materials, predicting the performance and properties of printed components, predicting the effects of AM parameters on product specifications, NDT protocols, new advanced sensing and monitoring systems, and intelligent machine control [7, 24, 26, 28-30].

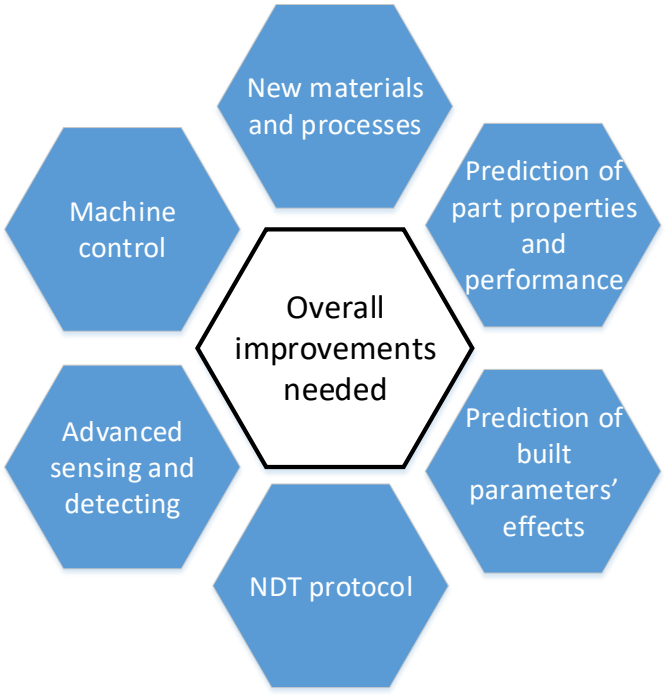

Fig. 2. A list of some of the critical challenges of improving 3D printing technologies.

AM manufactured components may come with different visible and invisible defects either internally or externally, such as rough surface finish, unfused material, swelling, cracks, delamination, deformation, warpage, porosity, and residual stress [7, 31, 32]. The defects and problems associated with the nature of AM technologies can be seen in different scales. In large scale metal or plastics components, cracks, distortions, delamination, warpage, detachment from a bed, effects of residual stresses, and dimensional mismatches are appreciated, as shown in Fig.

3-a through Fig. 3-c. These defects can be addressed with active control and post-processing. However, on a small scale (e.g., micro- and nano-scale), they can be challenging to detect, and their effects would be just as, if not more, harmful than macro ones. Such detrimental defects and imperfections in the micro-scale are illustrated in Fig. 3-d, which shows that the performance of an open optic lens was affected by such defects and that these defects were not visible without the help of Scanning Electron Microscope (SEM) imaging.

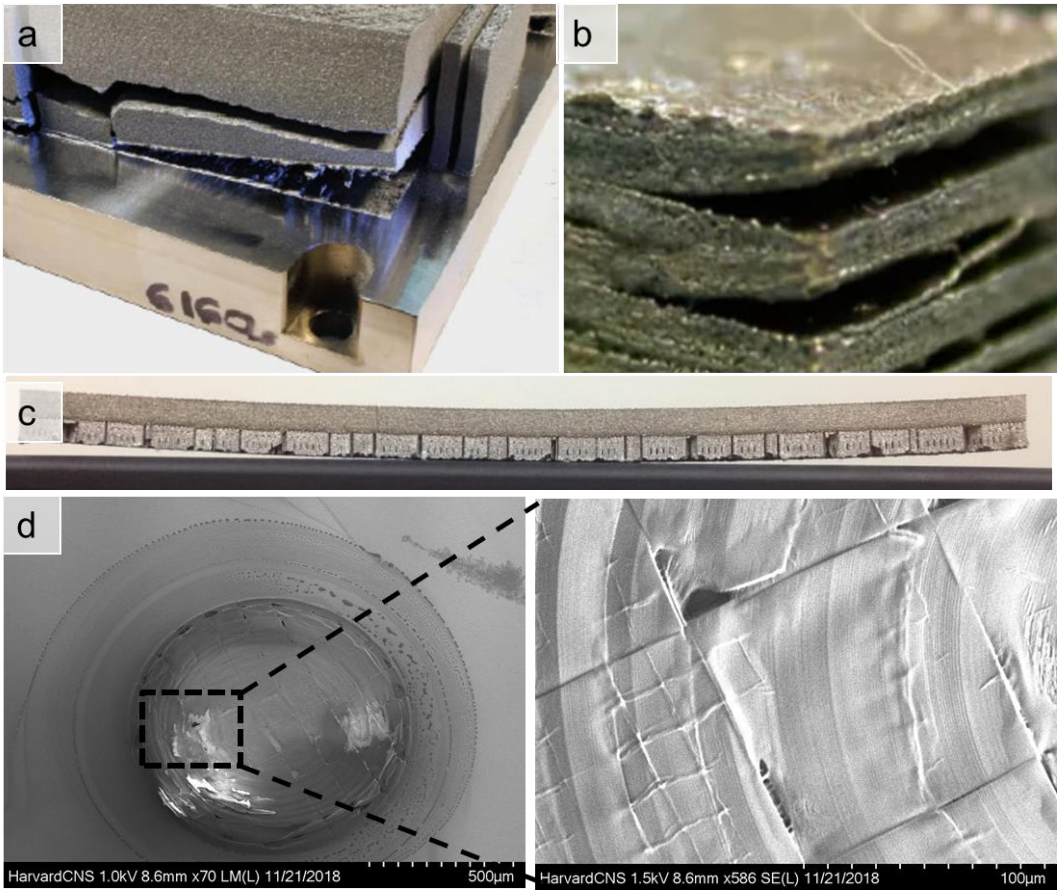

Fig. 3. Challenges and defects associated with 3D printed components in different scales: a) a failed printed part detached from bed due to residual stress (Image courtesy of Penn State CIMP-3D.); b) delamination and separation due to lack of adhesion and bonding in interlayers (Image courtesy of International Materials Reviews.); c) warpage and significant deformation occurred in metal 3D printed components (Image courtesy of the Center for Additive Manufacturing and Logistics at North Carolina State University.); d) delamination, warpage, and wrinkles in a 3D printed open optic polymeric Aspheric singlet lens with 1mm in diameter and 2mm focal length (Image courtesy of CHSLT at WPI).

The performance of printed components can be improved by a better understanding of the physics behind these challenges in meso, micro, and nano scales, and verified simulation can provide such a beneficial understanding to predict issues and suggest solutions to mitigate imperfections.

In FDM, one can easily observe some of these visible defects. In addition, FDM technology is affordable, and the printing is inexpensive compared to other AM technologies. Thus, it can help to combine simulation and experiment on FDM to understand the physics and improve the quality.

Experimental tools and NDTs can be employed to assess the functionality of components in terms of residual stresses, dimensional accuracy, and mechanical characteristics. However, some of these tools are expensive and intricate to operate. Experimental tools such as x-ray diffraction, synchrotron, and Neutron diffraction for measurement of residual stresses are challenging. Other devices, such as hole drilling, slitting method, contour methods, tensile test, Charpy impact test, and flexural test, are destructive, require sample preparation, and in some cases, require operating sophisticated tools as well as procedures. To solve these challenges, we proposed Optical Non-Destructive Testings (ONDTs) to perform our set of measurements because they are inexpensive, full-field-of-view, accurate, and easy to use. Tests such as shape measurement, vibration analyses, density estimation, and dynamic response analyses were examined on devised testing artifacts to envision a conceivable method that leads to optimization and improvement in both component and machine level.

On the other hand, multi-physics simulation is a growing research area for polymeric AM, where attempts have been made to predict microstructure and residual stresses [13, 15, 33-36]. These numerical platforms are usually computationally expensive and require supercomputers

and powerful clusters to model a small volume, e.g., 1.5x1.5x0.5 mm[14, 37-39][14, 37-39][14, 37-39][14, 37-39][14, 37-39][14, 37-39][14, 37-39][14, 37-39]. To overcome this challenge, we developed simplified numerical simulations that were capable of explaining the complexity of the multi-physics problem, avoided computationally extensive simulations, and delivered a 2D thermo-mechanical prediction for FDM.

Manufacturing final functional products with consistent quality and reliability is assumed to be the most prominent and critical challenges, specifically in growing polymer-based technology such as FDM [7, 30]. Real-time closed-loop process control can be a solution to these problems and ensure quality, consistency, and reproducibility in AM machines [24, 40]. Such a closed control system needs to be based on a practical understanding of the effects of printing history and *in-situ* monitoring. Our efforts attempted to evaluate the effect of process parameters on characteristics of 3D printed components and defined them mathematically. In addition, we worked on the *in-situ* temperature measurements using Infrared (IR) imager to contribute to the improvement of thermal monitoring tools.

1.3 Problem statement

New practical methods are necessary for reliably and cost-effectively evaluating procedures of polymeric 3D printing technologies such as FDM that can assess processes' and components' characteristics accurately and efficiently. Several computational and experimental studies have progressed to enable evaluation of the characteristics, performance, and functionality of 3D printed components during and after manufacturing. However, a practical, reliable, and affordable solution still demands extensive attention. This solution ought to deliver a better insight of the multiphysics that governs polymer-based 3D printing (e.g., FDM) to understand the underlying relationships between print parameters and resulting characteristics of printed

specimens as well as their impact on mechanical performance and geometrical accuracy. To reach this solution, a combined computational-experimental approach has to be developed. Such an approach capable of fulfilling the following criteria can advance a reliable and cost-effective procedure:

- testing artifacts with simplified boundary conditions and reduced computational costs must be designed to minimize uncertainties in the extraction of the parameters of interest in FDM;
- testing artifacts must be designed for systematical investigation of distortions and residual stresses as well as structural properties such as a module of elasticity, porosity, and strength by employing both experimental and computational methods;
- testing procedure must be practicable to different AM technologies and able to provide meaningful and concrete knowledge to both professional and lay users to better manage and control their 3D printers;
- testing procedures must be compatible with full-field-of-view ONDT to reveal the effects of process and printing parameters on temperature distribution, distortion, residual stresses, and module of elasticity;
- testing procedures must be capable of collecting data and be versatile and adaptable.

To resolve these problems, our approach relies on numerical simulation to develop a reliable and computationally efficient uncoupled thermo-mechanical model by accounting for the complexity of transient layer-upon-layer deposition. We also employ ONDTs that help to measure the most critical characteristics of the 3D printed components, e.g., distortions, final shapes, moduli of elasticity, and residual stresses in a verifiable way. This study aims to provide an enhanced understanding of the 3D printing processes specifically in FDM and paves the

ground to manufacture a part with improved quality, predicted performance, and customized applications while satisfying the consistency in manufacturing 3D printed components.

1.4 Motivation and research objectives

Among different AM technologies, FDM is fast-growing with diverse applications and significant potential for emerging from a prototype manufacturer to a fabricator of functional products. In addition, we want to develop a new method based on particularly designed testing artifacts to affordably and reliably address the improvement in quality and functionality of printed components by FDM. The objective of this research is defined to develop a combined experimental-numerical framework to systematically investigate relationships between process parameters and mechanical characteristics, geometrical characteristics, residual stresses, density, and bonding quality of 3D printed component by FDM. Through this process, we want to contribute to the promotion of FDM as a solution to 3D printing demands by:

- development of an advanced computational framework to study the thermo-mechanical phenomena,
- application of non-invasive optical methods for verification of numerical models and evaluation of 3D printed components,
- design, characterization, and application of specific testing artifacts to improve our understanding of the complexity of FDM based on the framework.

Fulfillment of the above objectives leads to the following progress in the long term and strengthens the future of FDM as a polymer-based AM technology, which can become a leading technology due to its broad acceptance and flexibility:

- minimization of time and cost of the printing process of FDM technology,
- improvement of the performance and consistency of printed parts,

- promotion of FDM technology as a reliable 3D printing for manufacturing functional and optimized components.

1.5 Significance and contributions

Assessing thermal flow, distortions, and residual stresses concurrently is a distinct contribution of this work. These effects mostly were addressed individually or in a combination of thermal with mechanical strength or thermal with dimensional tolerances [12-15, 33, 41-43]. The critical feature in this research is the procedure by which we developed and applied testing artifacts to study 3D printing processes. These artifacts with specific shape and geometry are designed for structural and thermal investigations with a reduced level of complexity and improved degrees of comprehension. By designing, simulating, printing, and testing the artifacts under different printing settings, we are directly exploring the effects and interconnections of printing and manufacturing parameters such as extruder temperature, extruder speed, heated bed temperature, cooling fan speed, and layer thickness on distortion and thermal distribution, while analyzing structural characteristics such as a module of elasticity, bonding performance, density, and residual stresses.

In addition, we incorporated numerical simulations of thermo-mechanical effects with experimental validations via utilization of the *in-situ* thermal measurements and full-field-of-view non-destructive optical metrology methodologies. From this perspective, this unique approach leads to a reliable understanding of thermo-mechanical effects and offers promising improvements such as reliability, simplicity, verifiability, versatility, and effectiveness.

We developed simplified but practical computational solutions that not only imitated the realistic manufacturing procedure in a layer-by-layer fashion but also improved the limits of available modeling efforts. Developed solutions were realized by tuning and adjusting the

assumptions in simulations in the presence of experimental data. From the computational simulation point of view, all of the following listed essential factors were included in the numerical work, and a few of them were verified experimentally:

- effects of the thermal and structural contact between platforms and heated bed;
- validated coefficient of heat transfer;
- radiation heat transfer;
- temperature dependent material properties such as yield stress, ultimate strength, module of elasticity, convection heat transfer coefficient, and radiation heat transfer;
- phase transmission heat effects;
- bonding and neck growing;
- spatially and temporally varying conductivity;
- plastic thermo-mechanical deformation.

In this dissertation, we used a non-destructive method using full-field optical sensors to understand the effect of printing parameters on components' characteristics. The testing artifacts allow us to examine the effectiveness of experimental non-invasive methods such as holography, digital image correlation, and fringe projection to measure the distortions, natural frequencies, and mode shapes. Knowing the shape and dimension of the testing artifact led to the estimation of the curvature in cantilever beams and subsequently residual stresses via a non-invasive and practical way that significantly reduces the complexity of the expensive and complicated experimental tools. On the other hand, computational simulation provided data on the expected distortion and residual stresses. These complementary effects of experimental and computational results enhance our understanding of the governing physics and effect of process parameters.

Our literature review indicates that although different attempts have been made to achieve reliable experimental-computational methods, there is not a similar approach that incorporates above-listed items to better simulate distortions and residual stresses.

1.6 Organization of the dissertation

This dissertation is organized into nine chapters, including this chapter, the introduction. In the next chapter, Chapter 2, we look into the research on different corresponding areas, including numerical simulations, non-destructive testings, characterization, and combined experimental-numerical approaches. This chapter establishes the challenges and precedents from other research in theory and practice.

Establishing this progress and delving into the issues and solutions provide the background needed to tackle the problem of interest by framing our unique approach, articulated in Chapter 3. We describe our application of a combined analytical, experimental, and computational methodology to fulfill our goals and our rationale behind this methodology. Our methodology is based on our background study, which revealed that independent efforts might not yield satisfactory results. In Chapter 3, we mainly explain our theoretical and experimental steps and measures to a greater extent. The process of developing the testing procedure, along with simplification and the structure of our numerical methods (e.g., finite element and finite difference) are explained. Furthermore, applied boundary conditions and associated assumptions are among the detailed information laid out in this chapter.

Once our strategy and approach are explained in Chapter 3, we proceed, perform experiments, run simulations, gather data, and eventually analyze them in Chapter 4. Following the results chapter, in Chapter 5, we discuss and assess our findings to deliver a better understanding of the effects of build parameters on FDM processes and components'

characteristics. In addition, we examine the applicability and efficiency of the applied methods to evaluate the AM processes and printed components affordably, practically, and cost-effectively.

We conclude and sum up our research in Chapter 6 and list the potential future work for further investigations. Significant accomplishments and impacts of the results in terms of the project goals are noted with the plan and directions for continuing the research. On top of the engineering and scientific contributions, the social and economic influences of this research and its outcomes are mentioned in Chapter 7. We wrap up this dissertation with a bibliography in Chapter 8 and Appendices in Chapter 9. In the very last chapter, the gathered data and results of statistical analyses with other related nuts and bolts are explained for different topics.

2. Literature review and background

In this chapter, we review the literature and state-of-the-art on different areas of this dissertation, including Additive Manufacturing (AM), Fused Depositions Modeling (FDM), computational modeling, experimental investigations using testing artifacts, and the effects of build parameters on 3D printed processes and characteristics of the printed components. We start with the definition of AM and wrap up by addressing the challenges in combined experimental-computational investigations.

2.1 Additive manufacturing and 3D printing technologies

According to American Society for Testing and Materials (ASTM), additive manufacturing is classified into seven main categories: (1) binder jetting, (2) directed energy deposition (DED), (3) material extrusion, (4) material jetting, (5) powder bed fusion, (6) sheet lamination, and (7) vat photopolymerization [26, 44]. All of these technologies share the common steps, as shown in Fig. 4, which starts with a product idea and a digital watertight 3D file. A preparation software slices this file numerically into thousands of layers according to the printer resolutions or selected layer thicknesses, and adds support if needed. Each layer is a cross-section of the part of that specific height. Finally, different sources of energy (e.g., laser, electric beam, plasma, extruder, ultrasonic, heating elements, or electric arc) are used for deposition of the material on each layer sequentially from the very first spot on the build plate to the last spot on the last layer [24, 45]. In the following sections of Chapter 2.1, we briefly describe a few polymer-based 3D printing technologies: polymerization, and material extrusion. Although we only studied FDM in this dissertation, we explained them here to emphasize the other AM technologies which this dissertation could be relevant to. In addition, we look more deeply into FDM using polymeric materials and describe both 3D-printer and material properties and specifications.

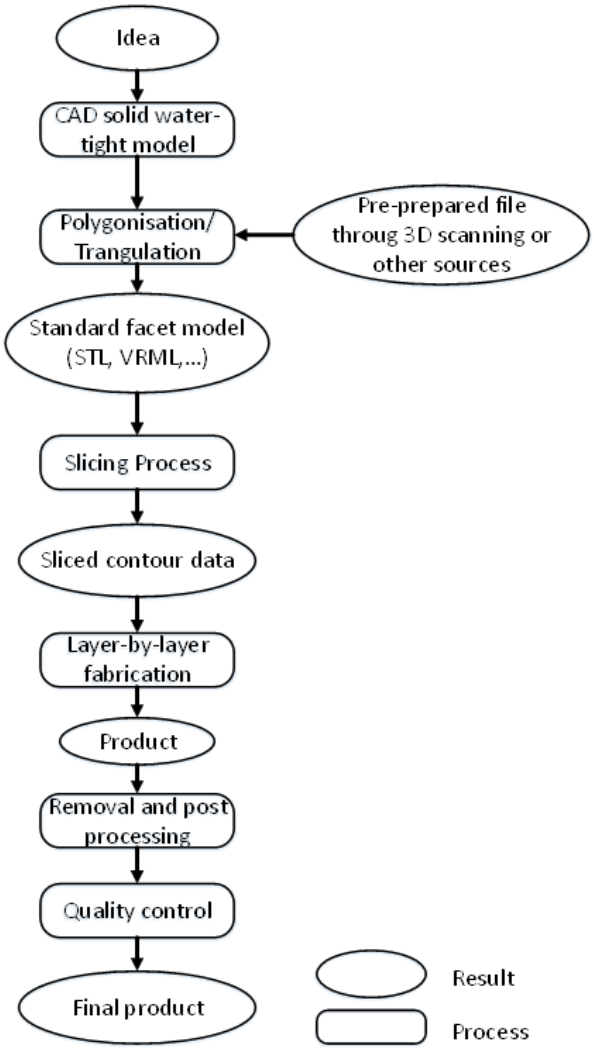

Fig. 4. The flowchart shows the process of converting an idea to actual components based on AM adapted from DIN standard [46]

2.1.1 Photopolymerization

One of the first 3D printing technologies, developed in 1984, was stereolithography (SLA), which works by polymerization of a photosensitive curable resin due to exposure to ultraviolet light [47, 48]. 3D Systems was the first company to introduce a commercialized 3D printer to the world. In this technology, liquid polymer is consecutively solidified by a concentrated ray of UV light. The process is comprised of the layer-upon-layer exposure of the thin layer of the photosensitive polymer while the light scans the cross-section. When it is finished, the platform moves down, new material pours into it, and the process continues as shown in Fig. 5. This

technology also has been used for manufacturing ceramic [49]. However, this newly developed technology bears more resemblance to binder jetting, although it uses UV and polymer sensitive liquid for binding ceramic to fabricate the green part.

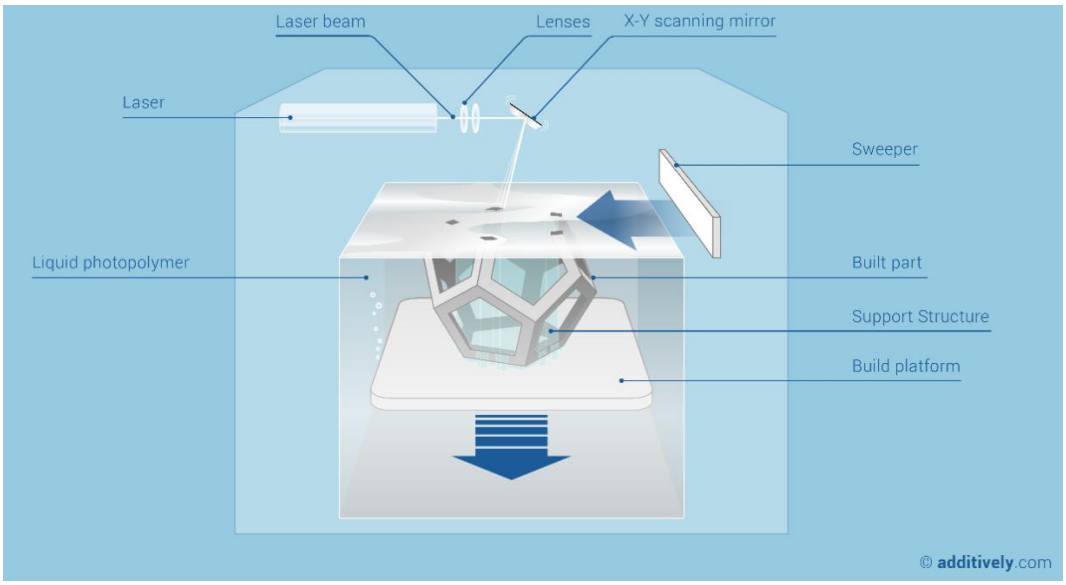

Fig. 5. Stereolithography (SLA) technology for manufacturing Polymeric parts using photosensitive resin. The system consists of Liquid photopolymers, laser, focusing tools, build platform, polymer supply system, and leveling system. [50]

This technology is capable of bottom-up and top-down manufacturing and primarily is limited to photopolymers. However, efforts have been made to introduce nanoceramic particles to the resin and print ceramic parts as well [51].

2.1.2 Material extrusion and polymer-based 3D printing

In 1988 FDM utilizing thermoplastic polymers was commercialized by Scott Crump, a co-founder of Stratasys. This technology now is considered as one the most widely available and adopted 3D printers worldwide [52]. Noticeably, after the expiration of the patent in 2009, a breakthrough took place in this area that popularized 3D printers for office and home applications.

Despite FDM's expansion, its applications for manufacturing functional parts are mostly constrained by a limited choice of available materials, low strength, and inconsistency in final products. Prototyping is the broad industrial application of this technology along with biomedical applications [53-57].

Polymer-based AM has recently received more attention. The reasons for this renaissance include the availability of polymers, flexibility, plasticity, affordability, the large number of companies working with these printers, and advancements in newly improved composite polymers [7, 58-60]. The profitability of the polymer-based AM for complex plastic material in small to medium volumes has been reported with Atzeni et al. [61], and the establishment of companies like Voodoo[1], Shapeways[2], Makelab[3], and Normal[4] in recent years proves the business plan viability for manufacturing polymers with complex geometry in small batches. All these promising features have centered attention on polymer-based 3D printers and have broadened their application to new areas.

Polymers that can be printed with this technology include ABS (acrylonitrile butadiene styrene), investment casting wax, polyamide and methyl- methacrylate acrylonitrile butadiene styrene, polycarbonate (PC), polyphenylsulfone (PPSF / PPSU), polylactic acid (PLA), and several alloys of above-listed polymers [25]. The list has kept growing to include stiff polymers, i.e., PPS and PEEK, and composite polymers with improved material properties capable of fabricating functional parts [47, 58, 60, 62-65].

[1] https://voodoomfg.com/

[2] https://www.shapeways.com/

[3] https://makelab.nyc

[4] http://nrml.com

The availability and flexibility of thermoplastic polymers, ease of operation, affordability, durability, and modulability promote their applications. There are many 3D printers in the market capable of printing various polymers without requiring changes other than settings, nozzles, and hot-end. Considering these merits, polymeric 3D printing is gaining ground and demands more research to discover its potential.

2.1.2.1 Fused Deposition Modeling (FDM)

Desktop 3D printers are salient examples of this type of printer, known as Fused Deposition Modeling (FDM), Fused Filament Fabrication (FFF), or Fused Granular Fabrication (FGF).

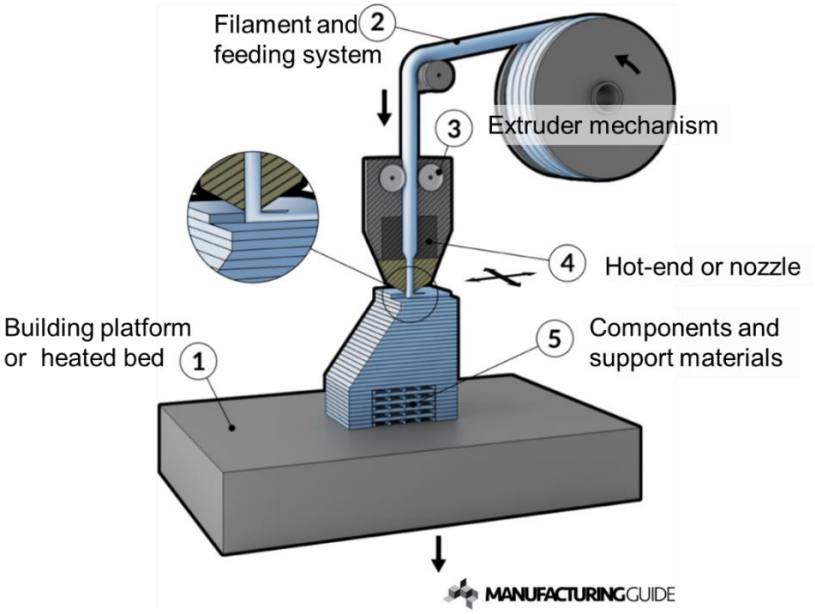

Fig. 6. Fused Deposition Modeling (FDM) technology for manufacturing polymeric parts. The system consists of multiple or single extruders, building platform, firmament feeders, and filament spools or cartridges [66].

Figure 6 shows FDM printers, in which the filament is heated, melted, and extruded through the nozzle that follows the cross-section of the part. The method is similar to other AM technology in terms of the slicing of the part horizontally and depositing sequentially. Its affordability makes it one of the most approachable technologies. FDM has established itself as

an indispensable part of prototyping in various industries, and it can be expected to proceed toward manufacturing functional parts shortly.

FDM 3D printers consist of three main parts. The first one is a set of extruder heads that heat the filament or polymer pellets to melting point and push them through nozzles that can be fixed in z-direction and moves in X-Y like a gantry crane or that can be fixed in the X-Y plane and move in the Z direction. The second part is a platform on which the object is built. Based on the available technologies, the platform also can be at a fixed height with X-Y mobility or be fixed in the X-Y plane and move upward or downward. The last part is the firmware and software that accurately sends commands and controls the movement of the heads, the extrusions, temperatures, platform, the enclosure environments if needed, and almost every aspect of the functionality of the printers [1, 2].

In both fixed and moving platforms, the strategy of the deposition is similar: the cross-section of the components in the X-Y plane is scanned, either by moving the head or platform, while the material is being extruded as needed through the nozzle. These hot and melted polymers join to the previously laid material and coalescence to make solid parts through wetting, welding, healing, and molecular diffusion [38, 67-69]. Before starting the printing processes, a slicing software is used for slicing a solid file, usually STL, into many layers based on printer resolution and rendering the location, motions, feed rate, and other required conditions of the 3D-printed component into readable code for the machine. The most broadly acceptable machine code is G-code. Although some manufacturers have specially developed codes that are designed for their printer, the G-code is accepted widely in the 3D printers community. When the whole section is scanned, and the material is deposited, the platform moves down, or the hot-

end moves up equal to the thickness of the next layer and process repeats until the part is scanned entirely while shaping gradually inside the machine.

The first layer deposited on the heated-bed usually consists of a larger area, which is called a "raft." This first layer is better and more amenable for the subsequent layers than the smooth glass or metal surface of the bed. It gives better confidence in the quality of the adhesion and guarantees the part is kept attached to the heated-bed during manufacturing. In a large FDM machine, instead of relying on the adhesion between the raft and first layer, vacuum or suction is utilized to satisfy the adhesion requirements [1].

To improve quality and to print over-hanged structures, usually a chemically or water-soluble filament is used on a second extruder and is later removed [2]. An effort has been made to manufacture multi-extruder and industrial versions with huge build volumes to manufacture car bodies, boats, or objects of similar size [2, 6].

Additionally, FDM has been used for processing ceramic and metal as well [70-73] and directly or indirectly demonstrated its application in manufacturing final industrial parts. Iftikhar et al. [74], Gill et al. [75], and Wang et al. [76] have researched the applications of FDM in manufacturing turbine blades from the concept of rapid tooling, and rapid casting of certain aluminum parts has shown the potential of FDM for both prototyping and final part production. The technology is flexible, and affordable and keeps increasing its popularity among non-expert consumers. However, several improvements have to be accomplished for FDM 3D printers to become a reliable method of manufacturing final products. These improvements include but not limited to [7, 28, 63, 77]:

- mechanical properties and strength of products;
- surface finish;

- integrity and consistency of products;
- dimensional discrepancy and tolerances;
- toughness and strength of available materials;
- control over the printer parameters to reduce potential defects;
- new materials;
- change in designers' way of thinking.

2.1.2.2 FDM printer's specifications

FDM printers can be categorized into three main groups based on the size of the nozzles and printing volumes: small, medium, and large. The most widely used 3D printers are desktop 3D printers with a common printing volume of 200 × 200 × 200 mm [2, 78], but this volume can significantly increase up to 30 times in Big Area Additive Manufacturing (BAAM) [1]. A large FDM 3D printer has been developed in a collaboration between Oak Ridge National Lab (ORNL) and a few corporations, and the license has been sold to companies like Cincinnati Incorporate [1] and Strangpresse [5]. In addition to printing volume, there are other critical characteristics of the 3D printers, including feed rate, nozzle temperature, enveloped temperature, X-Y speed, and bead width. A few important specifications are listed in Table 1 for three different categories of FDM printers.

Table 1: Some of the typical specifications of the three different categories of FDM 3D printers [1, 2, 78-80]

Specification	Unit	Small	Medium	Large
Gantry deposition velocity, U	mm/min	1000-18000	1000-9000	1000-6000
Envelope temperature, T_∞	°C	40-90	40-90	40-90
Extruder temperature, T_o or T_{ext}	°C	240-450	175-300	175-350
Heated-bed temperature, T_{base}	°C	40-170	40-110	40-110

Nozzle Diameter, *d*	mm	0.25-0.8	1-8	6-14
Feed rate, $\dot{m}$	kg/hr	0.0023-0.23	0.23-35	35-75
Printing volume	mm×mm×mm	200×200×200	1000×1000×1000	6000×2200×1800
Layer thickness range	μm	20-400	50-1000	400-7000
Bead Width range	mm	0.25-1.5	1-14	8-21

Some of these specifications can be considered process parameters, such as temperature, layer thickness, and feed rate, and can vary from one printer to another or within a printer but for different printing settings. The FDM components and process characteristics strongly depend on the set of printing parameters, and changing them alters part characteristics and structural properties in micro-, meso-, and macro-scales [42, 81-86]. These dependencies provide a controllable tuning feature for FDM to alter final product properties by setting the printing parameters to bring about desirable mechanical properties [87]. One example of this application is manufacturing functionally graded material using FDM 3D printers [70, 88]. On the other hand, if these changes and their dependency on printing parameters remain unknown, this technology will not be able to produce the functional components reliably. In both ways, understanding interrelationships between characteristics of 3D printed components and printer specification and parameters is critical to the development and advancement in FDM and other similar polymer-based 3D printing.

2.1.2.3 FDM printable materials and their properties

FDM technologies can print different categories of materials, such as metals, ceramics, polymers, and composites. However, the variety of materials in each category that can be printed is limited; this limitation is one of the foremost obstacles in the way of FDM reaching broader industrial acceptance [53]. Expansion of this limited list of materials would give this technology, considering its wide accessibility, advantages over various other 3D printing. It is

worth noticing that there are two approaches in manufacturing components with FDM, a direct and an indirect way. While polymers and polymeric-composite components are usually manufactured in a direct way, the component purely made of metals and ceramics are fabricated indirectly. In this case, FDM usually creates a raw part called a green part, which the polymer as a binder evaporates during a sintering process in an oven and leaves behind a densified solid part [71-73, 89-91].

In addition, to improve the properties of printed components, various polymeric composites are under development that incorporates metallic particles [68, 97], ceramics particles [60], glass fiber [92, 93], and carbon fiber [52, 94-98] into the polymer matrix. Furthermore, several improvements, notably in mechanical strength (tensile and flexural) and dimensional accuracy, have been reported using these newly developed materials [92].

Despite the progress in introducing new materials, the majority of the commercial FDM 3D printers still use different types of polymers for manufacturing. In this study, we focused on pure polymeric components. However, the framework presented here is not limited intrinsically to pure polymers and can be adapted to other enhanced material by knowing their material properties.

Polymers are organic components that are composed of a repetitive molecular structure, which is called “mere.” Based on their molecular and lattice structures, polymers are divided into three main categories: crystalline, semi-crystalline, and amorphous. In comparison to ceramics and metals, they benefit from low density, low price, and high elongation, but suffer from less strength and stiffness. Polymers are classified into three groups: thermoplastics, thermosets, and elastomers. Only thermoplastics and elastomers can be formed into granules and filament to be used in FDM 3D printers.

Table 2 lists the specifications of the conventional polymers widely used in 3D printing. This research has developed around ABS polymeric parts; however, one may look into the effects of different properties of other polymeric materials in computational models to provide insight into the sensitivity and the effects they have on components made of materials other than ABS.

Table 2: Some specifications of commonly used polymers for FDM 3D printers [99, 100]

Materials	Structure*	Specific heat, CP J/kg-K	Density, ρ kg/m3	Conductivity, κ W/m-K	CTE, α µm/m-°C	Glass transition temperature, T_g, °C	Modulus of elasticity, *E*, GPA	Flexural modulus, *G*, GPa	Yield Strength, MPa	Poisson's ratio
ABS (Acrylonitrile Butadiene Styrene)	A	1390 – 1410	1020 – 1080	0.14-0.21	80 – 234	88-120	2-2.9	1.2-2.8	29.6-44.1	0.39-0.42
ASA (Acrylate styrene acrylonitrile)	A	1680 – 1750	1050 – 1060	0.236 – 0.246	104 – 108	101-116	1.5-2.3	1.5-2.3	35.9-38.6	0.39-0.41
ABS+ PC (Acrylonitrile butadiene styrene + polycarbonate)	A	1400 – 1500	1070 – 1150	0.262 – 0.272	112 – 171	137-145	2.4-2.6	1.99 - 2.58	24.1-51	0.39-0.405
PLA (Polylactic acid)	S	1180 – 1210	1240 – 1270	0.13 – 0.16	126 – 145	52-60	3.3-3.6	3.1-3.6	55-72	0.38-0.4
PC (Polycarbonate)	A	1150 – 1250	1190 – 1210	0.189 – 0.205	66 – 125	142-158	2.32-2.44	2.27 - 2.34	59.1-65.2	0.39-0.41
PEEK (Polyetheretherketone)	S	1340	1300 – 1320	0.24 – 0.26	50 – 108	143-157	3.76-3.95	3.76 - 3.95	87-95	0.39-0.41
PEKK (Polyetherketoneketone)	A	1550 – 1580	1270 – 1290	0.25	75.1 – 78.9	146-163	3.36-3.53	3.29 - 3.46	98-108	0.39-0.41
PEKK (Polyetherketoneketone, semi-crystalline)	S	1510 – 1540	1300 – 13200	0.25	21 – 38	153-170	4.29-4.52	4.46 - 4.69	135-141	0.39-0.41
Nylon 12 (Polyamide (Nylon))	S	1680 – 1720	1030 – 1040	0.218 – 0.306	100 – 180	40-43	0.35-0.42	0.35 - 0.42	22-25	0.4-0.42
PEI (Polyetherimide)	A	1470 – 1530	1260 – 1280	0.123 – 0.25	84.6 – 101	215-217	2.89-3.04	3.22 - 3.38	73.5-81.1	0.38-0.40
PI (Polyimide)	A	1390 – 1450	1330 – 1430	0.0963 – 0.25	40 – 101	240-260	2.07-2.76	2.48 - 3.44	86.2-89.6	0.39-0.41
PPSF aka PPSU (Polyphenylsulfone)	A	1450 – 1510	1290 – 1300	0.269 – 0.35	51 – 61	210-230	2.29-2.4	2.35 -	53-58.5	0.39-0.41

								2.47		
PETG (Polyethylene terephthalate, glycol copolyester)	S	1470 – 1530	1260-1280	0.257 – 0.267	120 – 123	81-91	2.01-2.11	2.01 - 2.11	47.9-52.9	0.39-0.41
PET (Polyethylene Terephthalate)	A	1150-1250	1290-1390	0.138-0.151	115-119	60-84	2.8-3.0	2.41 -3.1	50-55	0.38-0.4
PET (Polyethylene Terephthalate, semi-crystalline)	S	1100-1200	1370-1400	0.138-0.151	75-80	65-70	2.76-3.1	2.99 -3.1	65-70	0.38-0.4
Range of changes	-	1150-1750	1020-1430	0.0963-0.35	21-234	40-260	0.35-4.52	0.35 - 4.69	22-141	0.38-0.42
Average	-	1450	1225	0.22	127.5	150	2.44	2.52	81.5	0.4

***A=Amorphous S=Semi-crystalline C=Crystalline**

2.1.2.4 Acrylonitrile butadiene styrene (ABS) polymer

One broadly used polymer in 3D printing is Acrylonitrile Butadiene Styrene (ABS). ABS is a thermoplastic amorphous polymer with the linear formula of [CH2CH(CN)]x(CH2CH=CHCH2)y[CH2CH(C6H5)]z that is comprised of the polymerization of three monomers: acrylonitrile (C3H3N), butadiene (C4H6), and styrene (C8H8) as shown in Fig. 7 [101]. ABS is made by polymerizing styrene and acrylonitrile in the presence of polybutadiene. The process was patented in 1948 and became commercially available by the Borg-Warner Corporation in 1954 [99, 101].

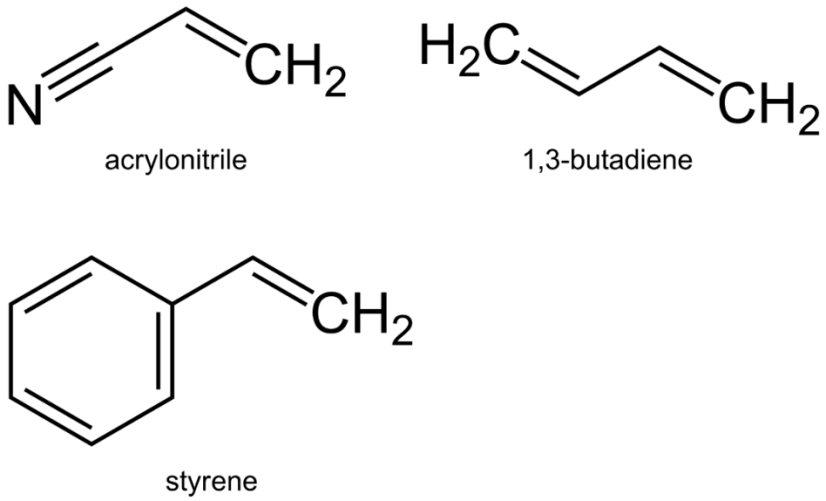

Fig. 7. The three monomers in ABS that compose the amorphous structure of it [102]

Having three monomers in the amorphous structure gives ABS a few specific advantages, it has the rigidity, electrical properties, and stylish glossy feature of styrene while butadiene improves low-temperature toughness and acrylonitrile enhances chemical, weathering, and heat resistance. This polymer is available in both granules and filament forms, making it suitable for small to large 3D printers.

2.2 Numerical simulation for distortions and residual stresses

The process in AM is thermally driven, and temperature gradient, flow, and distribution are crucial to the development of elastic modulus, strength, deformation/warpage, shape, surface finish, residual stresses, and density [71, 92]. Similarly, in the polymer-based 3D printing technology, i.e., FDM, temperature distribution and heat flux dictate surface finish, dimensional accuracy, and precision [12, 13, 33, 103, 104], as well as mechanical strength of printed components [33, 41, 105-109]. The first step toward understanding distortions and residual stresses in the FDM parts is understanding the thermal flow and temperature distribution of highly non-linear and complex phenomena during layer-by-layer deposition of materials. Thermally related phenomena (i.e., convection and radiation heat transfer, phase changes, and deposition advection) are particularly crucial during fabrication and cooling phases [33, 107, 109]. The processes of formation and production in FDM involve all mechanics of heat transfer: radiation, convection, and conduction as well as bonding, melting, diffusion, solidification, phase transformation, and microstructural revolution, as shown in Fig. 8. Radiation plays a significant role in the high-temperature regions, specifically during the first phase of material deposition and bonding [107, 110].

From the heat transfer perspective, modeling conduction, radiation, and convection are crucial, especially when one deals with material properties and boundary conditions that depend

on temperature. A researcher needs to incorporate radiation, transient conditions, and natural or forced convection together with moving boundaries, continually varying conditions, and material properties in order to realize an acceptable computational simulation of FDM processes.

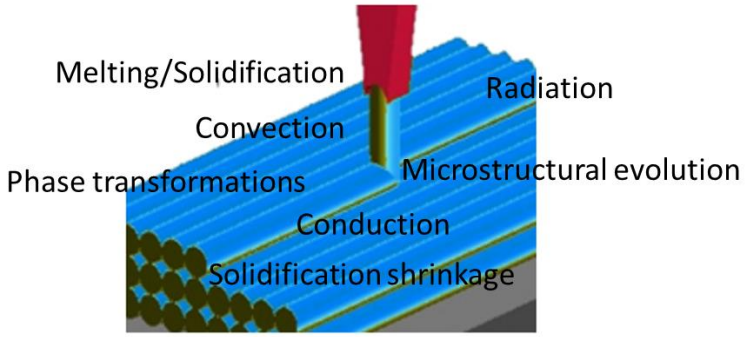

Fig. 8. Representative image of additive manufacturing by layer deposition that includes multiscale and multi-physics investigations [111].

The general platform for numerical modeling of the FDM was described in the pioneering work of Yardimci et al. [109]. Rodriguez et al. [87] suggested a 2D model based on the approach recommended by Yardimci et al. [109] to estimate the thermal flow in a 2D problem. In another semi analytical-computational model, Li et al. [112] developed a lumped model for estimating the temperature by assuming a semi-infinite condition. In recent years Dabiri et al. [113], Costa et al. [107], and Zhou et al. [114] studied the thermal phenomena computationally.

However, although different attempts have been made to ameliorate the numerical models and achieve reliable results, there is still a need for a thorough but effective model that incorporates all of the following listed important factors, and has been experimentally validated:

- effects of resistance between layers;
- the effect of platforms;
- validated coefficient of heat transfer;
- radiation heat transfer;
- temperature-dependent material properties;

- heat effects due to phase change;
- bonding and contact growing;
- spatially and temporally varying conductivity.

There are a few studies focused on estimations and measurements of combined thermo-mechanical effects, precisely distortion and residual stresses. Zhang et al. [12, 13] were one of the first researchers to study distortion in FDM printed parts in a combined experimental-computational approach. Finite Element (FE) software, ANSYS®, modeled the temperature and also estimated the distortion of the sample. They observed similar trends for the effects of bead width and layer thickness on distortion and found that printing speed was the most prominent variable on the state of stresses.

In a recently published in-progress work, Talagani et al. [36] combined FE with an estimation of material properties for anisotropic polymers in both micro- and nano-scale to analyze stresses and deformation evolution in large components for a multi-scale study.

Favaloro et al. [14] and Brenken et al. [15, 92] also reported their progress in a similar approach to Talagani et al. [36] by looking into the microstructure of the composite polymer. They looked into the crystallinity of the polymer structure, in addition to non-crystalline materials, i.e., ABS, and developed a method to predict material properties based on temperature history [16].

Sun et al. [8] experimentally validated and analytically evaluated FDM processes [115]—a simplified 2D analytical solution based on perfect contacts between layers and a vertical stack of filaments — by measuring the temperature on a heated bed for a few different configurations and samples. The sintering phenomena based on the critical sintering temperature were confirmed experimentally to be crucial for the bond establishment in FDM processes specifically for ABS

thermoplastics. They found the current heat transfer models required improvement to capture the creep and molecular diffusion to predict bond strength [8].

Alongside numerical simulations, Kishore et al. [116] recently investigated the interface formation in composite material experimentally. In fiber-reinforced ABS filaments, the effect of preheating on the fracture energy was investigated by using the thermal fusion and polymer interdiffusion at temperatures above the glass transition temperature, T_g.

However, a model has not been achieved yet that effectively and thoroughly captures the complexity and interactions of underlaying material properties and the physics of thermal and mechanical phenomena. This dissertation suggests a way to advance modeling by benefiting from experimental data while avoiding the simulation of complicated and computationally extensive physics, such as wetting, diffusion, crystallization, microstructure, and entanglement.

2.3 Characterization of 3D printed components

Mechanical characterization of 3D printed parts was among the first studies that were carried out when the FDM machine was introduced by STRATASYS. Fodran et al. [117] studied the mechanical properties of the specimens printed by Stratasys 1600 while changing the raster angles, air gaps, and bonding agents. Their studies indicated the effect of orientation and bonding between layers in final mechanical properties of the specimen printed and tested according to ASTM D 638. They showed the expected structural performance of a 3D printed part could significantly vary by modifying a few settings of an FDM machine [117]. Since then many studies on different aspects of involved build parameters have been done. Rodriguez et al. [67, 68, 87, 115, 118], Bertoldi et al. [119], Bellini et al. [120], and recently Tymark et al. [121], Dawoud et al. [122] and Zaldivar et al. [105] investigated the mechanical characteristics and the influences of build parameters on final fabricated specimens.

In addition, optical metrology methodologies and nondestructive testing (NDT) have been utilized for measurement of shapes [17, 123-128], deformations[127, 129, 130], residual stresses [131-138]; impact dynamic analyses [18-20, 127, 129, 139, 140]; mechanical characterization [17-20, 141, 142]; and structural health monitoring [141] for different applications ranging from aerospace and automation to health and energy. They enable the characterization of mechanical properties, shape, and geometrical distortions, as well as porosity and defect [17-20, 128]. For instance, researchers applied dynamic and controlled vibration using non-invasive optical methods to evaluate components' performance [17-20, 34, 139, 140, 143]. These methods are capable of non-invasively and accurately assessing some mechanical and structural properties such as moduli of elasticity, damping coefficient, stiffness, shear moduli, and Poisson's ratio. Additionally, this analysis provides information about inhomogeneity and defects in the structure.

Thermocouples have been conventionally used for accurately measuring the temperature at specific points of interest [8, 144]. On the other hand, thermography offers full-field-of-view, non-contact, and non-invasive measurements. These superior capabilities make thermography one of the most widely used sensors in monitoring and closed-loop control systems in AM technologies [110, 145-147]. However, the thermal measurement can only measure surface temperature and is very sensitive to environmental fluctuations. Another issue is that accurate measurement requires a reliable understanding of the material properties such as emissivity and absorptivity [148-150].

IR camera shows promising potential in FDM processes due to the less harsh environment inside the machine. Seppala et al. [151] and Dinwiddie et al. [146] have already explored its potential and demonstrated how it could be used to study the FDM processes. In recent studies

Costa et al. [69], Pooladvand et al. [110], and Seppala et al. [282] used an IR camera to estimate material and process properties.

In this dissertation, we took advantage of the non-destructive full-field of view optical method to characterize the physical and mechanical properties of 3D printed components and printers. We characterized density, porosity, elastic moduli, and emissivity of ABS specimens and introduced a procedure to find the relationship between these properties and printing parameters.

2.4 Measurement and estimation of residual stresses and distortion

Residual stress is the state of stresses in a component not because of any external load but as a result of the current interactions of the locally distributed stresses in the part as in its present equilibrium condition [152]. The part that has residual stresses may not be distinguishable based on its shape and appearance, but the stresses inside the part have significant effects on its functionality, endurance, fatigue life, and performance. Residual stress can arise from differences in thermal expansion, yield stress, or stiffness [152].

There are three main causes for residual stresses: the mismatch of coefficients of thermal expansion (CTE), the plastically induced misfits, and the phase change or chemical generated misfits [152]. In the nonlinear structural environment, expansion and contraction of the material due to phase change and temperature differences interact with material elastic-plastic behavior to develop stress/strain distribution that may deform components.

There are various techniques to measure residual stresses. These techniques can be categorized into three groups: destructive, semi-destructive, and non-destructive [153]. Measuring elastic strains in the atomic lattice plane of crystalline material is a Non-destructive method to estimate the residual stresses accurately [154]. X-ray diffraction [155], neutron

diffraction [156], and synchrotron X-ray [157, 158] are three well-known non-destructive methods based on atomic lattice plane measurements. Although these methods are accurate, they have some disadvantages, for example, limited penetration depth up to some centimeters in steel, the price and size of the equipment, hazards to operators, and their limited availability to specific and secure areas, i.e., atomic reactors in neutron diffraction. These disadvantages circumscribe the applications and effectiveness of these methods for practical usages.

Destructive methodologies are those that depend on the stress relaxation that happens after removing the material locally. Any changes in the current equilibrium condition cause the part to reach a new equilibrium status, and measuring the changes leads to the estimation of residual stresses. These changes are usually subtle, especially when the material has a high module of elasticity, i.e., steel that requires precise measuring tools. Sectioning [159], and the contour method [160] are two popular destructive methodologies. One of the main difficulties with these methods is the sacrification of the components to estimate residual stresses. This scarification consumes time, energy, and resources and may not be applicable to all cases, specifically in additive manufacturing, when the 3D printed part is expensive.

The most common and well-accepted tools for measurements of residual stresses are semi-destructive methods. In these methods, instead of cutting through the part or removing a portion of the structure, a tiny hole is drilled on the surfaced [131-134, 138, 161, 162] that can be successively continued to measure averages of residual stresses on different depths in the component under investigation [138, 153, 163]. In some other similar techniques, local relaxation due to thermal or laser ablation can be performed instead of hole drilling [164, 165].

The accuracy of these techniques is less than diffraction methods, but the setups are reliable and versatile and can be used for the measurement of different materials, either crystalline or

amorphous, in different conditions. Most of the modern measuring tools, in contrast to old ones using strain rosette, are based on full-field optical measurement using different methodologies such as Holographic Interferometry (HI) [133, 134, 166], Digital Speckle Pattern Interferometry (DSPI) [136, 138, 165], or Digital Image Correlation (DIC) [167, 168]. However, these require a high level of understanding of the physics of the residual stresses, knowledge of the optical techniques, and preparation of the surface or drilling tools. Nonetheless, DIC among the other tools is more user-friendly and less complex, but the sensitivity of the system, specifically in stiff material, limits the application of DIC for residual stress measurements.

A few indirect methods have been developed to estimate the residual stresses, specifically in thin films, MEMS, and NEMS devices [19, 169]. These indirect methods rely on the mechanical properties, shape, and curvature of a specimen that can be measured during fabrication or afterward [158, 170]. In these techniques, distortion is associated with residual stresses; for example, by measuring the curvature of a cantilever beam, one can estimate the level of stresses [169, 171, 172]. We prepared the basis to employ this method because it is easy to use, cost-effective, and accurate, and with the help of simulations, a specific artifact can be implemented for estimation of the residual stresses in FDM components.

2.5 Effects of process and printing parameters on components properties

Manufacturing constraints and build parameters, including process and printing parameters, affect the geometry, surface finish, microstructure, and mechanical properties of the printed components. The very first studies done by Fodran et al. [117], Bertoldi et al. [119], Rodriguez et al. [68, 118], Bellini et al. [120], and Anitha et al. [42] indicated that component properties are significantly affected by parameters such as infill patterns (stacking sequence), air gap, printing

orientation, road width, build layer thickness, extruder temperature, envelope temperature, and speed of deposition.

The fracture strength of extruded beads was studied by Thomas et al. [115], Bellehumeur et al. [38], and Sun et al. [8]. They reported that the initial wetting stage was significant at a slower cooling rate and resulted in strong bonding between layers to improve the component strength [115].

Components printed by FDM exhibit orthotropic material properties in terms of strength and stiffness, i.e., module of elasticity, yield, and ultimate stresses [67, 118, 173-176]. These properties are subjected to different build parameters, including deposition strategy, orientations, void spaces between layers, and the bonding between the road in inter- and intra-layers. These parameters substantially alter the microstructures and govern the mesostructure of the printed components. For example, print orientation significantly alters the mechanical properties of the 3D printed components not only in polymeric base 3D printers [34] but also in metal components [177, 178]. Surface finish is another critical factor affecting the performance, fatigue, and the endurance of AM components [179]. Higher temperatures, lower layer thickness, and slower deposition speed are reported to improve the surface finish in FDM components [11, 180].

In addition, raster orientation, part orientation, layer thickness, and air gap had a substantial effect on tensile strength, whereas other parameters such as raster width, contour width, extruder temperature, and color have no to little influences [176, 181-184]. Maximum mechanical properties have been reported when the applied force and the raster orientation occur in parallel [181].

An analytical solution, such as constitutive modeling, was used to estimate these properties [67, 83, 173, 185]. For example, the theory of laminated composite was applied by taking into

account the bonding and void spaces of the contiguous filament [67, 173, 185]. The non-independent elastic moduli, e.g., three Young's moduli, three shear moduli, and three Poisson's rations, were determined theoretically to define the anisotropicity in the printed components. The critical parameter in this theory, as discussed in Rodrigues at al. [67], is porosity or void, which directly defines the meso-structural properties.

Many other studies investigating the correlation between build parameters and printed components' properties have been accomplished. However, the understanding of the interconnections between parameters that led to selecting the suitable printing configurations has not been achieved yet. Thus, some recent studies such as M. W. M. Cunico [186], Smith et al. [187], Torrado et al. [188], Panda et al. [189], C.A. Griffiths et al. [190], Mohamed et al. [85, 191-193], and A. Lanzotti et al. [81] are focused on investigation and optimization of parameters.

Also, it is becoming increasingly important to look into the effects of build parameters on microstructure, inter- and intra-layer bonding, and the presence of cavities, particularly for new high-performance and high-temperature polymeric materials such as PEEK, PEI, and composite polymers [194, 195]. The microstructure has significant influences on mechanical characteristics, and micro CT helps researchers to investigate these effects. In recent work, S. Berretta et al. [194] utilized micro CT to study the cavities in the samples of interest. Their study indicated that selection of the build parameters, such as raster orientation and air gap, required educated consideration to fulfill the uniform density inside the part, mainly made from new materials, which demand higher temperature for the extruder and actively controlled condition during printing. This extended consideration has to be addressed with further process optimization [194].

Residual stresses and distortion in 3D printed components by FDM have been exhibited on the bottom layer [12, 13, 175], and the increased number of layers imputed to the higher distortion and eventually greater stresses [196]. Increasing the envelope temperature, decreasing the glass transition temperature, or CTE of materials also contributes to decreasing the distortion in 3D printed components [196]. One hypothesis has suggested that high-temperature gradient and heat flux due to rapid cooling and heating cycles contributes to this phenomenon [197]. The dimensional accuracy has also been studied by Sood et al. [198], Zhang et al. [12], Nancharaiah et al. [199], Bansal et al. [103], Sahu et al. [196], Lieneke et al. [200], Mohamed et al. [85], and Chohan et al. [11].

In summary, these studies suggest properties and characteristics of 3D printed components strongly depends on layer thickness, air gap, scan (extruder) speed, build orientation, raster angel, and envelope temperature; other parameters, such as raster width, contour width, number of contours, feed rate, and nozzle temperature, were observed to be less significant. There may be other vital parameters; however, the author was not able to find studies on the effect of nozzle diameter, fan speed (cooling rate), and heated bed temperature on dimensional accuracy. Thus, we included these parameters along with layer thickness, extruder speed, printing orientation, and extruder temperature to be studies studied in this dissertation. More details on these relationships are presented in the method chapter (Chapter 3).

2.6 Combined experimental-computational analyses

In numerical modeling, in order to obtain solutions, several details, boundary conditions, properties, and considerations are assumed. Numerical simulation alone without experimental verification may not be able to capture the reality of the process to provide reliable data that can be incorporated into the design of the FDM printed components. A comprehensive and

dependable solution backed with experiments is needed to be systematically developed to verify and evaluate the assumptions.

Sun et al. [8] developed an experimental thermal evaluation of two analytical methods. The author has indicated that neither a1D lumped capacity model and nor a 2D model was able to capture the temperature distribution in a 3D model, for different courses of manufacturing. The authors, through a comparison with experimental measurements, noted that although the lump capacity model predicted temperature more accurately for higher temperatures from the beginning of the process, the 2D analytical model achieved the better agreement for lower temperatures. There is a need to develop an experimentally validated analytical or computational model that can predict the temperature profile correctly and reliably for different phases of FDM processes. This model could be incorporated into structural, material, and combined simulations to make possible the prediction of structural and material evolutions during manufacturing and cooling—and even possibly during shelf storage and long-term applications.

In general, the currently developed thermo-mechanical simulations and studies lack validation, and a few experimentally validated work such as Zhang et al. [12, 13] indirectly verified models by measuring distortions. Aware of the lack of experimentally validated thermal analyses, new research has been developed recently by X. Zhou et al. [106], Favaloro et al. [14, 16], and Brenken et al. [15, 92] to capture the physics and microstructure better. For example, X. Zhou et al. [106] changed different parameters such as nozzle temperature, heated-bed temperature, printing speed, and filament thickness to cross-validate the correlation between theory and practices. The combined experimental-computational analyses are perplexing and require intensive study for further development. We worked on the development of such a combined approach to deliver a better understanding of the FDM process.

2.7 Non-destructive testing procedures for evaluation of AM processes and components

Development of AM technologies leads to manufacturing components for direct application in industries. Sustainable progress in this direction requires reliable and effective testing procedures to assess both processes and printed components. The non-destructive testing is more appealing for AM technology, where the printed component is expensive, and operation is costly. Developing a standard testing procedure to address the challenges and issues in processes and components can contribute to significant improvement in the acceptance of the AM. In addition, this standard procedure can provide datasets for statistical analyses, machine learning, and data mining that open the door to approach the optimization to AM more strongly.

However, commercially developed non-destructive methods are costly, complex, and time-consuming. Methods such as CT-scan, X-ray, and ultrasonic are able to provide information on internal structural characteristics and defects (i.e., cracks, porosity, and delamination) within a part [141, 142, 201-206], but require professional operators and specialized data analyzers.

There are other testing methodologies that are less sophisticated but practical and can provide valuable information specifically about mechanical characteristics. Some of these methods are based on the measurement of natural frequencies and modal analyses of the object of interest subjected to either impact load [141, 142, 207] or vibrations [18, 128, 208]. Vibration analyses are one of the widely used methods for invasive characterization, and mechanical quality inspection has been applied to additively manufactured components as well [19, 20, 139, 140, 209]: for example, evaluation of the micro-cantilever made by silicon wafer technology [19]. In practice, dynamic non-destructive methods can be applied more naturally to additive manufacturing compared to destructive methods like a tensile test, compressive test, three-point bending, and four-point bedding in the evaluation of mechanical properties. Methods such as bar

resonance can provide more accurate results while exciting the component below elastic limits [142]. Besides, other noninvasive methods like ultrasonic resonance spectroscopy can be used for internal part inspection to find cracks and porosity [204, 210-212]. Recently, SANDIA national lab [141] and D. Plagge [142] developed an applied testing methodology using computational analyses of intricate coupons to be tested for mechanical characterization. In this methodology, a finite element model analyzed folded structures for different dimensional and mechanical characteristics and associated them with the module of elasticity. The same object then can be printed, and an impact analysis reveals the natural frequencies of the sample, which were used for estimation of the moduli of elasticity and other mechanical properties.

2.8 Summary and conclusion

Effects of process parameters on the mechanical, geometrical, and physical properties of 3D printed components are measurable, a method that employs non-destructive tests with numerical analyses can measure the effects and elucidate the physics behind them. Specific structural artifacts have been designed based on numerical and analytical analyses using non-destructive tests to extract mechanical and structural properties. A similar method can be adapted for 3D printing. Thus, we combined computational and experimental methods to define a procedure based on a testing artifact that reveals the properties and characteristics of interest using ONDT. We also worked on a computational model that effectively captures the complexity of underlaying material properties and the physics of thermal and mechanical phenomena. This dissertation suggests a way to advance modeling by benefiting from experimental data while avoiding the simulation of complicated and computationally extensive physics.

3. Methods

The development of a reliable, cost-efficient, and practical approach using testing artifacts requires establishing an effective collaboration between experiments and simulations. Our approach initially started by designing testing artifacts that could be examined by ONDT, i.e., holography, fringe projection, and DIC. It continued by collecting and analyzing the data, and finally constructing meaningful knowledge.

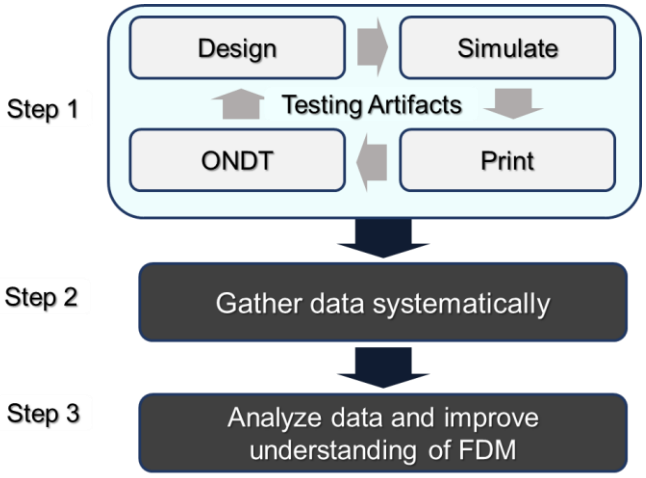

Fig. 9. The simplified flow chart of the three main steps in this dissertation designed for better understanding the physics of FDM 3D printing.

Figure 9 illustrates the three main steps in our work. In step one, we designed testing artifacts, simulated them to find their characteristics, printed them, and tested them to gather data. The process in step one included repetitive tasks, while some process and printing parameters changed systematically from one iteration to another. This step also included some accompanying activities through which we modeled a 1D and 2D thermal flows in 3D printed components and verified them experimentally. We also did 2D thermo-mechanical simulation to estimate the distribution of residual stresses and distortions needed for a better understanding and interpretation of experimental measurements. In the second step, we designed the experiments, performed tests, and collected and analyzed data. This process helps to find the patterns and

relationships between process parameters and characteristics of interest. In the third step, gained knowledge and data were used to better understand the FDM processes and explain the complexity of the physics behind observed patterns and relationships. We hypothesized gathered data could optimize the process and improve the performance by providing quantitative insight on bonding quality, density, distortions, residual stresses, and structural characteristics. The essential feature in all of these steps is the complementary interaction of computational and experimental investigations in a defined framework of known testing artifacts. This key feature leads to less computational cost, reduces uncertainties, and increases confidence in results, which are supported by systematic data analyses and extraction.

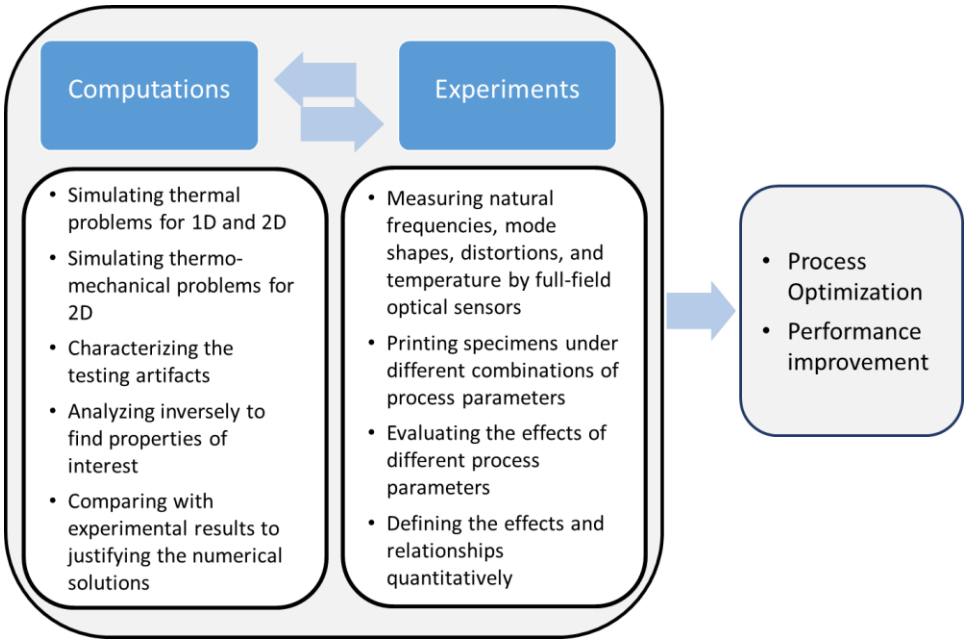

Fig. 10. The framework of the combined computational-experimental methodology to study FDM processes. This methodology will enable research toward understanding process parameters and part performance.

Our approach intends to express mathematically the effects of essential parameters in characteristics such as density, porosity, Young's modulus, shear modulus, and distortion. Experimentally, properties such as density, temperature distributions, shapes, distortions, natural

frequencies, and mode shapes were measured. Figure 10 outlines general activities categorized based on their nature in computational and experimental disciplines.

In computational studies, the temperature evolution in 3D printing by FDM was investigated to understand the development of bonding, moduli of elasticity, distortions, and residual stresses in 3D printed cylinders and cuboids. For this purpose, the transient thermal distributions and flows were initially estimated and experimentally validated. We studied assumptions such as boundary conditions, heat transfer coefficients, and material properties to improve the numerical simulation outcomes. The steps in this process started with thermal 1D models and expanded to 2D thermo-mechanical models, as shown in Fig. 11.

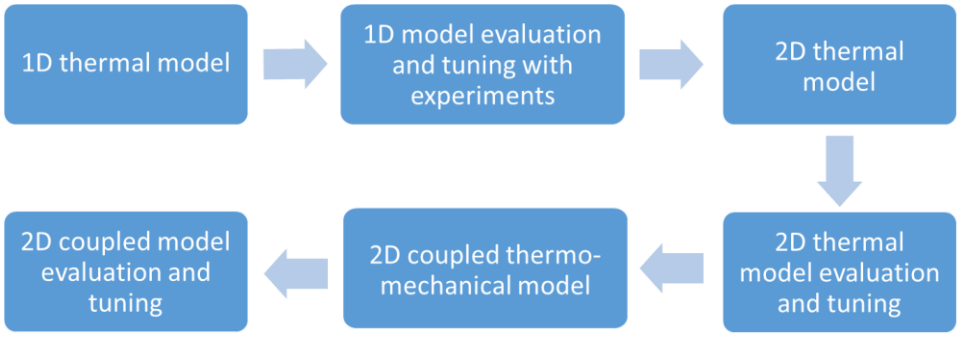

Fig. 11. Different steps in the combined numerical-experimental evaluation of an uncoupled thermo-mechanical problem in 3D printing.

In all numerical simulations, the concept of the layer-upon-layer deposition was considered by customizing the numerical models in order to mimic the deposition process. In this model, an element activation strategy was chosen to activate sets of elements as needed based on the progress of extruder in time and space. The details of the modeling and the assumption are explained in the following chapters. Material nonlinearity and dependency on temperature were assumed in the developed models to improve the simulation outcomes. Notably, emissivity, conductivity, total convection-radiation heat transfer coefficient, yield stress, ultimate stress, and elasticity were assumed as a function of temperature in Finite Element (FE) analyses.

We utilized noninvasive sensors, e.g., thermal imaging, and optical methods, during and after printing, to determine the temperature distributions, distortions, and structural properties of 3D printed components.

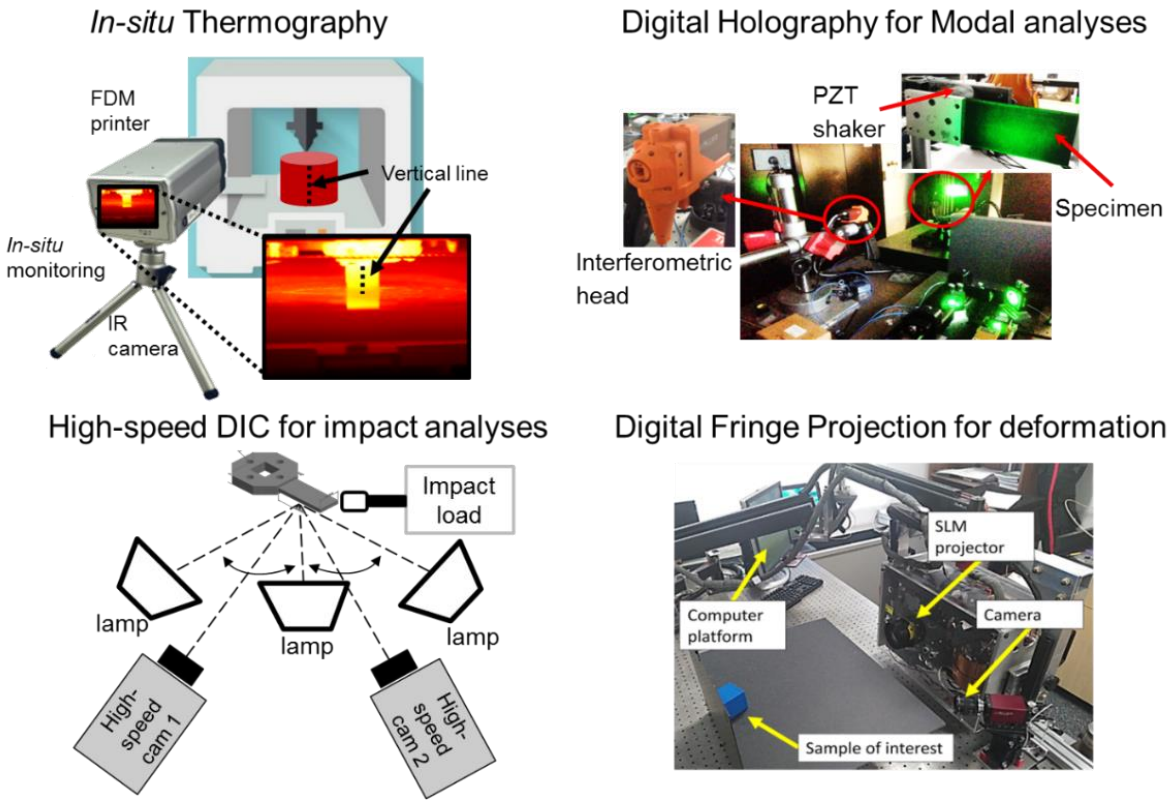

Fig. 12. The representative images of the four main optical non-destructive sensors that were utilized in this study: (a) Thermography to measure the temperature; (b) Digital Holography to measure the natural frequency and mode shape in full-field-of-view; (c) Impact analyses using Digital Image Correlation (DIC); (4) Digital Fringe Projection to measure the shape and curvature of the printed samples.

We performed harmonic and impulse load excitations to carry out modal analysis and transient dynamic measurements, respectively. We conducted modal analyses using Digital Holographic Interferometry (DHI) for recording the natural frequencies and corresponding mode shapes. The transient dynamic measurements were made by applying impulse excitations to the 3D printed cantilever beams and measuring their time-dependent vibrations for further analyses by high-speed DIC. In addition, shapes of the printed components were measured employing Digital Fringe Projection (DFP) to reveal the potential of this method in finding the

interconnections between process parameters with residual stresses and distortions. Thermal imaging using an IR camera was utilized to measure material properties such as emissivity, verify the convective and radiative boundary conditions, and compare computational results with experimental results in terms of temperature distribution and thermal flow. The representation of the four different optical non-destructive testing tools mentioned above is shown in Fig. 12.

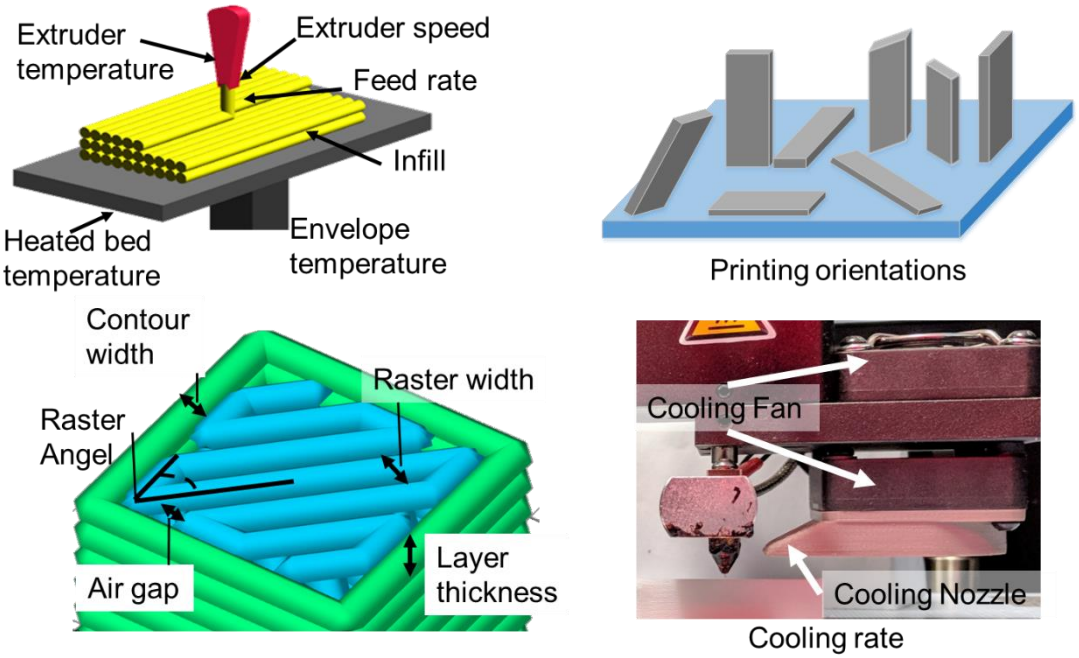

Fig. 13. Demonstration of the different involved printing and process parameters for FDM technology considered in a combined experimental-computational approach.

These analyses enable the determination of structural properties such as elastic moduli, Poisson's ratios, stiffness, and shear moduli, as well as deviations from the typical response that points to microstructural defects [18, 20, 139-141]. These properties are related to different printing and manufacturing parameters; a few of them are shown in Fig. 13.

Our background study confirms among different process parameters, layer thickness, printing orientation, infill, air gap, and extruder speed are among the most significant ones as explained in Chapter 3.5.1. On the other hand, heated bed temperature, fan speed, and the size of the object and extruder have not been studied in the literature. Thus, We selected the parameters of interest

to be extruder speed (ES), extruder temperature (ET), fan speed (FS), heated bed temperature (HBT), layer thickness (LT), and geometries.

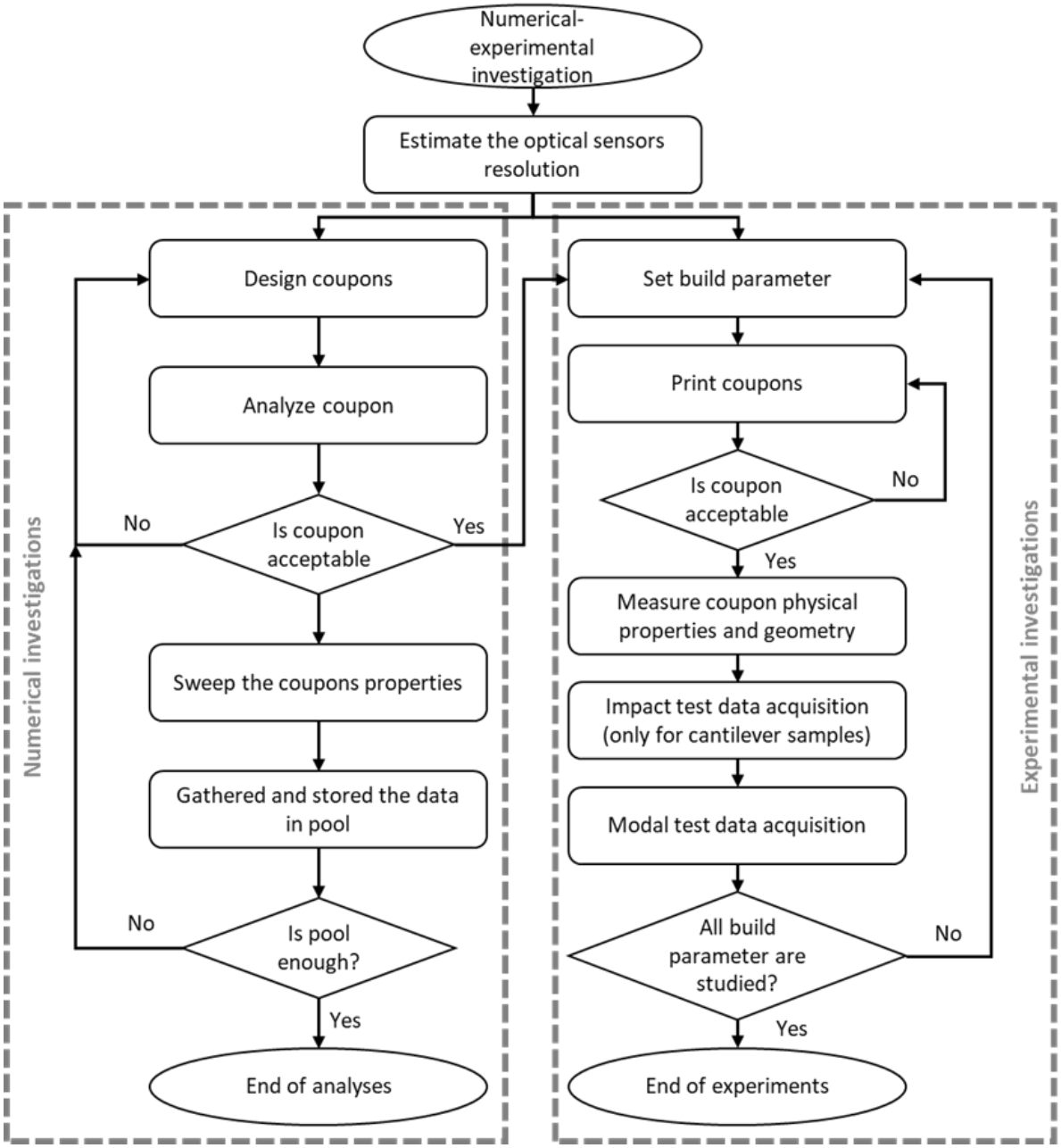

Fig. 14. The schematic flowchart illustrates the flow and steps in a combined numerical-experimental investigation of coupons characterization.

We hope the insight provided through this process along with data collected by ONDTs provides knowledge adequate to improve our understanding of FDM and contribute

quantitatively to the selection of printing parameters for delivering targeted properties within the possible achievable ranges of properties. This gained knowledge leads to process parameters' optimization for a specific shape and geometry.

The general flowchart (Fig. 14) summarizes the explained process. It consists of two main investigation streams, numerical and experimental, and has different steps as shown. The whole process forms a loop that helps to study the effects of build parameters on printed components.

3.1 Designing a testing artifact

This dissertation intended to design testing artifacts to perform multifunctional tests and satisfy different objectives. First and foremost, the testing artifacts had to be versatile for different types of non-destructive testing while being practical for printing and numerical simulations. Furthermore, their geometrical characteristics needed to be quickly and accurately measurable using standard tools such a caliper or full-field optical techniques, i.e., fringe projection or DIC. Moreover, the artifacts needed to be multipurpose to allow measurement of various characteristics such as density, bonding quality, moduli of elasticity, Poisson's ratios, residual stresses, distortion, and geometrical accuracy. We targeted to measure not only isotropic but also orthotropic material properties. We designed them to be compatible and easy to test with non-invasive techniques capable of measuring natural frequency and mode shapes.

Furthermore, we wanted the analyses of the gathered data to be straightforward and simplified with minimal uncertainty in the estimation of the properties of interest. At the same time, the structure of the testing artifact had to allow us to alter process parameters. It needed to have a reasonable size, thickness, and length to enable the effect of the different process parameters to be observed and measured.

Designing a testing artifact satisfying these requirements is challenging. A similar testing artifact was developed and patented by researchers in Sandia National Lab [141] and D. S. Plagge [142] in his dissertation. Isometric views of their developed coupons, along with two as printed specimens are illustrated in Fig. 15. This design is practical and intended for the impact analyses using a hammer test.

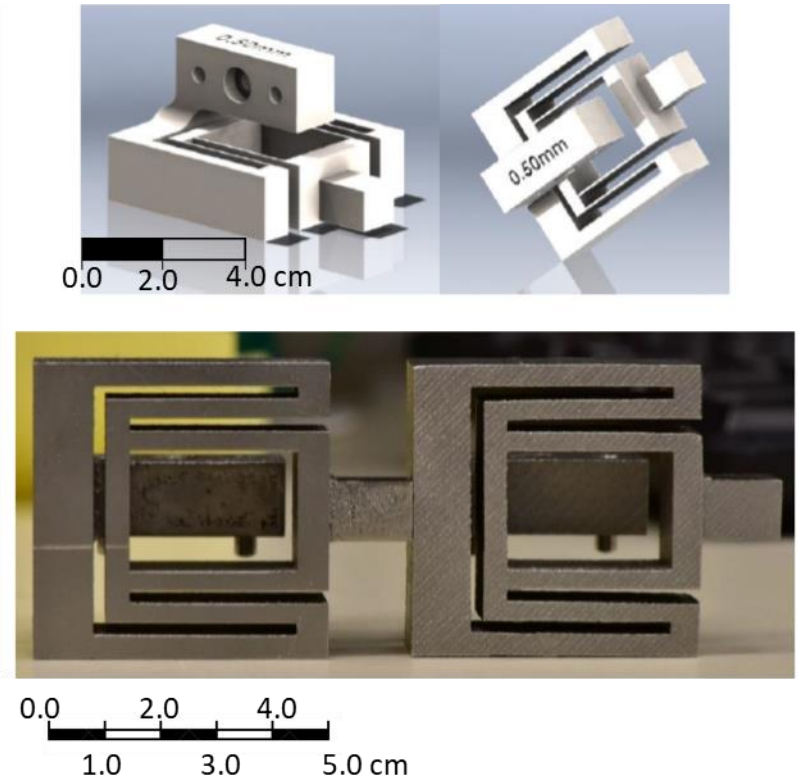

Fig. 15. Examples of the developed coupons for evaluation of the components and processes in AM: (a) a CAD file of the developed coupons in isometric view; (b) two as-printed coupons made of 316L using DMLS AM technology [142] (Copied here with author written consent).

Cantilever and constrained plates and beams also have been employed elsewhere for analyses of the mechanical properties and have proven to be practical for estimating isotropic, orthotropic, and anisotropic elastic properties of different materials [207, 213-216]. The applied approaches also measured the natural frequencies of the vibrating object to evaluate the elastic moduli in complex multi-layer structures, such as composite materials, which lent itself to additively manufactured plates and beams. L. Gaul et al. [217], and Pryputniewicz [208] utilized full-field-

of-view optical sensors to improve the accuracy of moduli estimation and to estimate the Poisson's ratio directly from mode shapes.

Besides, the American Society for Testing and Materials (ASTM) established standard number E-1875 and E-1876 to explain the procedure of evaluation of the dynamic mechanical properties through modal analyses [218, 219]. However, these methods may not be practical to estimate residual stresses, although there have been attempts to estimate the presence of residual stresses in plates using vibrational techniques [220].

The cantilever deflection method has been used to estimate the residual stresses in thin-film specimens; this method draws on beam theory and measures the curvature of the cantilever beam non-invasively [169, 171, 221]. A similar concept was also applied for the estimation of residual stresses in plastic injection-molding specimens with relatively thick plastic bars [222].

Anisotropicity is one of the challenges associated with 3D printed components; this characteristic appears to be directionally and geometrically dependent. We hypothesized that different thicknesses allow orthotropicity to manifest in the vibration analyses. Thus, we examined this theory by designing our testing artifact with two different thicknesses.

With these criteria in mind, we explain below our approach and principles of designing a testing artifact capable of evaluating mechanical properties, distortion, and residual stresses through modal analyses and beam theory.

3.1.1 Design consideration for testing artifacts for residual stress estimation

The curvature of a beam relates to the applied moment and distribution of stresses, which can be explained with the Euler–Bernoulli beam theory. For a beam illustrated in Fig. 16, the following equation defines a mathematical representation of the theory by relating the curvature, structural, and material properties of the beam to applied forces and moments:

$$M = -\frac{EI}{(1-v^2)}\frac{y''}{\left(1+y'^2\right)^{\frac{3}{2}}}, \tag{3-1}$$

where M is bending moment, I is flexural stiffness of the beam, y is the beam normal deflection, v is Poisson's ratio, and E is a module of elasticity. In case of small curvature, the magnitude of y' is negligible compared to 1.0, and this equation becomes analytically solvable. Equation (3-1) also can be rewritten in terms of local curvature as:

$$M = -\frac{EI}{(1-v^2)}\frac{1}{R_n}, \tag{3-2}$$

where, R_n curvature is $\frac{\left(1+y'^2\right)^{\frac{3}{2}}}{y''}$ which can be alternatively defined as $\frac{\left(\delta^2+L^2\right)^{\frac{3}{2}}}{2\delta}$ where δ is the measured deflection in a particular length of the specimen, L. It has to be noted the latter approximation is valid if the deflection is small compared to the length of the beam.

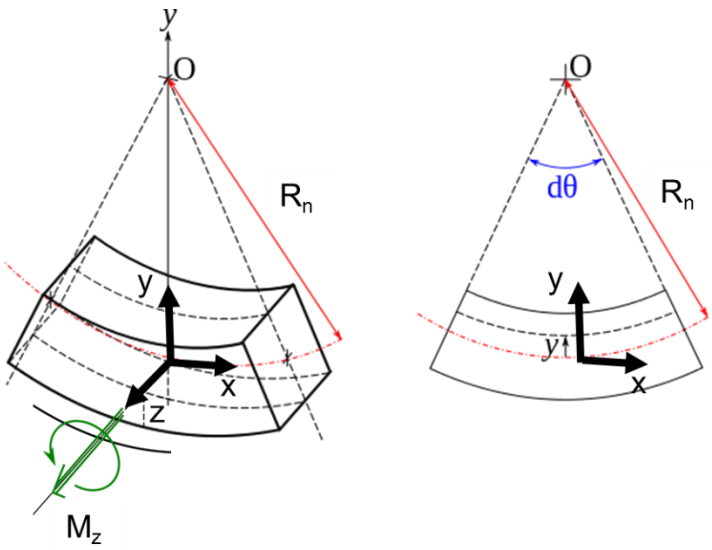

Fig. 16. The representation of the Euler-Belnoli beam with constant cross-section subjected to moment in the z-direction.

To capture the effect of residual stresses by measuring the curvature, it is recommended to have the length of the diagnostic structure 5-10 times larger than the thickness of the areas subjected to residual stresses [169].

Integration of normal stress over the cross-section mathematically defines the applied moment. These normal stresses in the section can be expressed in terms of two stresses, mean and gradient stresses. This definition is constructed as the summation of polynomials as follows:

$$\sigma_{total} = \sigma_m + \sum_{k=1}^{\infty} \sigma_k (a_k y)^k, \tag{3-3}$$

where, σ_m in mean stress, and $\sigma_k$is gradient stress, and a_k is a constant relating to the cross-section; for example, for *k=1* in a rectangular section with height *h*, this is $a_1 = \frac{2}{h}$. *y* is the distance between the fiber and neutral axis.

For nano- and micro-scale components, deposition of a thin layer of dissimilar material causes the substrate to distort [169, 171, 221, 223-226], and if layer thickness satisfies thin-layer criteria, the introduced stresses to the substrate can be estimated according to the following equation, as described elsewhere [223-225]:

$$\sigma = -\frac{E_s}{(1-v_s^2)} \frac{t_s^2}{6t_f} \frac{1}{R_n}, \tag{3-4}$$

where σ is biaxial stress in the film, subscript *s* indicates the substrate, *f* indicates the thin layer, *t* is the thickness, and the rest as defined previously. In case the thickness of the deposited layer does not satisfy the thin-layer approximation, Brenner et al. [227], and K. Roll [228] suggested the following corrected equation:

$$\sigma_c = \sigma \left[1 + 4 \frac{E_f^2 (1-v_s^2) t_f}{E_s \left(1-v_f^2\right)^2 t_s} - \frac{t_f}{t_s} \right], \tag{3-5}$$

where σ_c is the corrected version of the preliminary estimation of σ, and the rest are defined in previous equations. Since the deposition in FDM is conceptually similar to layer deposition, an

analogous approach can be adopted for the estimation of residual stresses, knowing curvature and cross-sections of a 3D printed beam.

3.1.2 Design consideration for testing artifacts for modal analyses

The transverse displacement in an isotropic plate is defined according to the following partial differential equation (PDE) [229]:

$$D\nabla^4 \Gamma + \sigma_p \frac{\partial^2 \Gamma}{\partial t^2} = 0, \tag{3-6}$$

where, t is time, Γ transverse displacement, $\sigma_p = \rho \times h$ plate area density, ∇^2 Laplace operator, and D flexural rigidity is defined as:

$$D = \frac{Eh^3}{12(1-v^2)}, \tag{3-7}$$

where E is Young's modulus, h plate thickness, and v Poisson's ratio. The solution of this PDE is sought in the form of $\Gamma(x,y)e^{i\omega t}$ by finding the ω satisfying the following equation:

$$(D\nabla^4 - \omega^2\sigma)\Gamma = 0. \tag{3-8}$$

The mathematical and numerical approach to solve this differential equation has been elaborated by G.B. Warburton and A. W. Leissa [229, 230] with the general solution for isotropic material in the Cartesian coordinate system found as a Fourier series as:

$$\begin{aligned} \Gamma(x,y) = \sum_{m=1}^{\infty} \Big[& A_m \sin\sqrt{k^2 - L^2}y + B_m \cos\sqrt{k^2 - L^2}y \\ & + C_m \sinh\sqrt{k^2 + L^2}y + D_m \cosh\sqrt{k^2 + L^2}y \Big] \sin Lx \\ & + \sum_{m=0}^{\infty} \Big[A_m^* \sin\sqrt{k^2 - L^2}y + B_m^* \cos\sqrt{k^2 - L^2}y \\ & + C_m^* \sinh\sqrt{k^2 + L^2}y + D_m^* \cosh\sqrt{k^2 + L^2}y \Big] \cos Lx, \end{aligned} \tag{3-9}$$

In the above equation, L is the length of the rectangular plate and $k^4 = \rho\omega^2/D$. In the proposed methodology, the natural frequencies of the cantilever plate are the target of interest and obtained as:

$$\omega^2 = \frac{\pi^4 D}{L^4 \rho h}\left\{G_x^4 + G_y^4\left(\frac{L}{b}\right)^4 + 2\left(\frac{L}{b}\right)^4\left[vH_xH_y + (1-v)J_xJ_y\right]\right\}, \quad (3\text{-}10)$$

G_x, G_y, H_x, H_y, J_x, and J_y are constant coefficients as explained by A. W. Leissa [229] and G. B. Warburton [230]. These series of constants depend on boundary conditions, geometry, mode number, and Poisson's ratio [229].

There are several references dedicated to analytically calculating and experimentally measuring these eigenvalues for different boundary conditions and geometry, specifically for a square or rectangular plate; for example, D. Young [231], W. V. Barton [232], and N. W. Bazely et al. [233] investigated these constants.

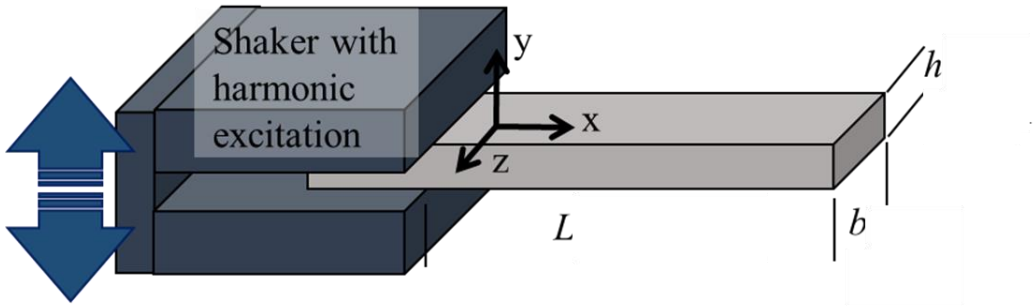

Fig. 17. Representative of the cantilever beam, the boundary condition, dimensions, and the shaker for experimentally determination of the 3D printed testing artifacts.

Rewriting the Eq. (3-10) in the following format indicates that the non-dimensional eigenvalues for each mode and known boundary condition can be represented only as a function of geometrical characteristics and Poisson's ratio.

$$\frac{\omega_n^2 \times L^4 \rho}{\pi^4 D} = \left\{G_x^4 + G_y^4\left(\frac{L}{b}\right)^4 + 2\left(\frac{L}{b}\right)^4\left[vH_xH_y + (1-v)J_xJ_y\right]\right\} = \lambda_n^4(v, L/b), \quad (3\text{-}11)$$

where, λ_n is a non-dimensional eigenvalue of the plate. It also suggests that the ratio between frequencies is equivalent to their corresponding eigenvalues; such a hypothesis was used in a design on the Poisson's test plate (Resonalyser procedure) to estimate the Poisson's ratio directly from two natural frequencies [217, 234]. In addition, the ratio between different natural frequencies can only depend on the Poisson's ratio. Such a dependency was defined as third-order polynomials and was applied to find the isotropic material properties [207, 235].

One can analytically seek a solution of Eq. (3-8) for a simplified geometry, such as a rod or reed with constant cross-section and known geometry, and estimate natural frequencies and mode shapes. For a solid cantilever beam, as shown in Fig. 17, the analytical solution is available in the following terms:

$$\omega_n = \frac{\lambda_n^2}{L^2}\sqrt{\frac{D}{\rho h}}. \tag{3-12}$$

Finding a module of elasticity in a simplified case of a long cantilever thin plate with a large *L/b* ratio and isotropic property can be formulated based on the natural frequency (ω_n), density (ρ), and dimensions as:

$$E = E(\rho, \omega_n, L, h) = \rho \times 12(1 - v^2)\left(\frac{\omega_n \times L^2}{\lambda_n^2 \times h}\right)^2, \tag{3-13}$$

If the sample is a beam with a fixed area, the module of elasticity can be found as:

$$\omega_n = \frac{\lambda_n^2}{L^2}\sqrt{\frac{EI}{\rho A}} \Rightarrow E = E(\rho, \omega_n, L, h) = \rho \times 12\left(\frac{\omega_n \times L^2}{\lambda_n^2 \times h}\right)^2. \tag{3-14}$$

Considering the above definition, the uncertainty in the calculation of the module of elasticity can be found:

$$\delta E = \sqrt{\left(\delta\rho \times \frac{\partial E}{\partial \rho}\right)^2 + \left(\delta\omega_n \times \frac{\partial E}{\partial \omega_n}\right)^2 + \left(\delta L \times \frac{\partial E}{\partial L}\right)^2 + \left(\delta h \times \frac{\partial E}{\partial h}\right)^2}. \quad (3\text{-}15)$$

3.1.2.1 Torsional mode and natural frequencies of testing artifacts with isotropic material

The torsional vibration of a beam with a known and constant cross-section is defined based on the angular displacement along the length of the beam. The following equation defines the governing equations for bar, beam, and rod objects:

$$\frac{\partial^2\theta}{\partial x^2} - \frac{1}{c_T^2}\frac{\partial^2\theta}{\partial t^2} = 0, \quad (3\text{-}16)$$

where θ is angular displacement, and c_T is torsional wave speed. This speed for an isotropic object depends on shear modulus, *G*, density, ρ, polar moment of inertia, I_p, and factor χ as defined in the following equation:

$$c_T = \sqrt{\frac{G\chi}{\rho I_P}}. \text{ And } I_p = \frac{bh}{12}(b^2 + h^2) \quad (3\text{-}17)$$

The factor χ is similar to λ, which depends on the geometry, and for a rectangular cross-section (shown in Fig. 17) can be theoretically found as:

$$\chi = \frac{bh^3}{16}\left[\frac{16}{3} - 3.36\frac{h}{b}\left(1 - \frac{h^4}{12b^4}\right)\right] \quad (3\text{-}18)$$

The frequency and wavenumber for a cantilever torsional vibration are :

$$k_n = \frac{n\pi}{2L} \text{ and } f_n = \frac{nc_T}{4L} \quad (3\text{-}19)$$

3.1.2.2 Testing artifacts with orthotropic materials

If the artifact has orthotropic properties, the transverse differential equation of the motion is defined as :

$$D_x \frac{\partial^4 \Gamma}{\partial x^4} + 2\left(D_1 + 2D_{xy}\right)\frac{\partial^4 \Gamma}{\partial x^2 \partial y^2} + D_y \frac{\partial^4 \Gamma}{\partial y^4} + h\rho \frac{\partial^2 \Gamma}{\partial t^2} = 0, \tag{3-20}$$

where

$$D_x = \frac{E_x h^3}{12\left(1 - v_x v_y\right)}, \tag{3-21-a}$$

$$D_y = \frac{E_y h^3}{12\left(1 - v_x v_y\right)}, \tag{3-21-b}$$

$$D_1 = D_x v_{yx} = \mathrm{D_y} v_{xy}, \tag{3-21-c}$$

$$D_{xy} = \frac{G_{xy} h^3}{12}. \tag{3-21-d}$$

In this case, the natural frequencies can be determined by [213, 214, 229, 236]:

$$\omega_n^2 = \frac{D_x}{L^4 \rho h}\left(\alpha_1^4 + \alpha_2^4 \frac{L^4}{b^4}\, D_y/D_x \, + \alpha_3^4 \frac{L^2}{b^2} D_1/D_x + \alpha_4^4 \frac{L^2}{b^2} D_{xy}/D_x \right). \tag{3-22}$$

For different boundary conditions, it is challenging to determine α_1 , α_2 , α_3 , and α_4 analytically. However, the solution for a specific shape of interest, i.e., beam or plate, can be found computationally or estimated experimentally. It can be shown that the following equations are derivable from the bending stiffness (D_x, D_y, and D_1) and torsional stiffness (D_{xy}) as:

$$E_x = \frac{12}{h^3}\left(D_x - v_x D_y^2\right), \tag{3-23-a}$$

$$E_y = \frac{\mathrm{D_y}}{D_x}\frac{12}{h^3}\left(D_x - v_x D_y^2\right),$$

$$G_{xy} = \frac{6}{h^3}\left(D_1 + 2D_{xy} - v_x D_y\right),$$

$$v_y = v_x D_y \, / D_x.$$

The laminated composite theory was applied to estimate the mesostructure properties of the printed components for FDM technology. Rodriguez et al. [68] theoretically determined the

mechanical properties of a printed part as a function of void and porosity. Authors suggested transversely isotropic material properties and found the 6 independent material constants knowing the fiber elastic modulus and porosity as:

$$E_x = \overline{E_1} = (1 - p_1)E, \tag{3-24-a}$$

$$E_y = \overline{E_2} = \overline{E_3} = \left(1 - p_1^{1/2}\right)E, \tag{3-24-b}$$

$$G_{xy} = \overline{G_{12}} = \overline{G_{13}} = 2 \times G \frac{(1 - p_1)\left(1 - p_1^{\frac{1}{2}}\right)}{(1 - p_1) + \left(1 - p_1^{\frac{1}{2}}\right)}, \tag{3-24-c}$$

$$G_{yx} = \overline{G_{23}} = \left(1 - p_1^{1/2}\right)G, \tag{3-24-d}$$

$$\nu_{xy} = \overline{\nu_{12}} = \overline{\nu_{13}} = (1 - p_1)\nu, \tag{3-24-e}$$

$$\nu_{yx} = \overline{\nu_{23}} = \overline{\nu_{32}} = \overline{\nu_{21}} = \overline{\nu_{31}} = \left(1 - p_1^{1/2}\right)\nu, \tag{3-24-f}$$

where E is the module of elasticity, G is shear moduli, ν is the Poisson's ratio of the pristine bulk filament, and p_1 is the void density of plane *1* with normal along x_1. If the print direction is assumed to be rectilinear along the length of the object, then principle directions *1* and *2* are along the *x* and *y* directions of the specimens, respectively. This approximation was able to predict the material properties with a maximum of 10 percent error compared with experimental measurements [67]. Porosity, p_1, is a critical parameter depending on infill and printing strategy. It can change between minimum theoritical 0, in a perfect bonding with zero void between filaments, to about 90 percent with the lowest possible infill. However, this value in the case of a solid printing option in FDM printers changes between 0 to $1 - \frac{\pi}{4}$.

In addition to the effect of voids, an empirical factor was also introduced to account for the imperfect bonding between two adjacent filaments and known as effective load-carrying potentials of the 3D printed components. This factor, which changes between 0 to 1, with typical

value of 0.85, multiplies to the predicted theoretical values to reflect the imperfect circumstances[237].

3.1.3 Design consideration for testing artifacts for longitudinal and flexural impact load

The effect of the impact load has to be investigated based on the stress wave propagation in materials. The mathematics behind these stress waves can be defined in two frameworks, longitudinal or flexural wave. The following PDE defines the propagation of a stress wave longitudinally inside a slender specimen with a fixed area, such as rods, bars, or beams similar to what is shown in Fig. 18-a and -b:

$$\frac{\partial^2 u}{\partial t^2} = c^2 \nabla^2 u, \tag{3-25}$$

where u can be defined as $u = f_1(x - ct) + f_2(x + ct)$ and c is the longitudinal wave speed that depends on the modulus of elasticity and density:

$$c^2 = \frac{E}{\rho}. \tag{3-26}$$

The PDE for flexural wave propagation in a slender or thin beam with known area and moment of inertia, Fig. 18-b, is written as:

$$\frac{\partial^2 u(x,t)}{\partial t^2} = \frac{EI}{\rho A}\frac{\partial^4 u(x,t)}{\partial x^4}. \tag{3-27}$$

For a flexural wave, the velocity also is a function of frequencies that cause the dispersion of waves propagating in different frequencies:

$$\mathrm{c_B^4} = \frac{\mathrm{EI}}{\rho A(1-\mu^2)}\omega_n^2. \tag{3-28}$$

It is possible to measure the stress wave propagation through the experimental investigation of the impact in high-speed (i.e., 200kHz) by measuring the period required for a specific stress

wave to propagate from one end to another in the direction of the impact. This period and estimated speed can be a basis for the measurement of the module of elasticity and other properties of interest.

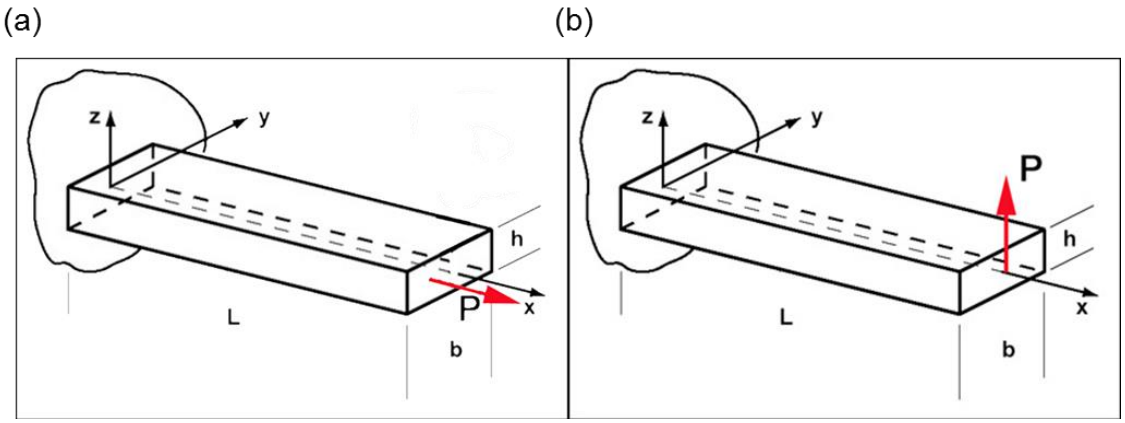

Fig. 18. Representative of a specimen such as a rod, bar, and beam with constant area subjected to impact load: (a) longitudinal load; (b) Flexural load.

The mathematics becomes more perplexing for a three-dimensional wave propagation problem, and a complex system of equations defined in the following form has to be solved:

$$\frac{\partial \sigma_{ij}}{\partial x_j} = \rho \frac{\partial^2 u_i}{\partial t^2}, \tag{3-29}$$

where σ_{ij} is Cartesian components of the stress tensor and u_i is the displacement vector in the Cartesian system, and coordinate x_j, $j=1, 2, 3$ are X, Y, and Z, respectively

In this case, the generalized Hooke's law relates stresses to strain rate:

$$\sigma_{ij} = C_{ijkl} u_{k,l}, \tag{3-30}$$

where C_{ijkl} is elasticity tensor and finally:

$$\frac{\partial}{\partial x_j}\left(C_{ijkl} \frac{\partial u_k}{\partial x_l}\right) = \rho \frac{\partial^2 u_i}{\partial t^2}. \tag{3-31}$$

Assuming the isotropic properties, the longitudinal and transversal wave propagation speeds are found as [238]:

$$c^2 = \frac{E(1-v)}{(1+v)(1-2v)\rho} \; and \; c_T^2 = c_L^2 \frac{(1-2v)}{2(1-v)}. \tag{3-32}$$

3.1.4 Principles of the design of testing artifacts

Considering all of these constraints, we decided to design a testing artifact similar to the cantilever beams shown in Fig. 19. The concept of the cantilever object, such as plate or beam, has been examined for vibration and impact analyses before [207, 229, 232, 233, 239]. This concept also was implemented for the estimation of residual stresses and mechanical properties [169, 171, 172, 207, 213, 220]. The cantilever beam and plate are easy to print and capable of revealing structural and mechanical properties. We went through a few design iterations similar to those are shown in Fig. 19 and examined the potential of a beam with two cantilever structures, one inside another.

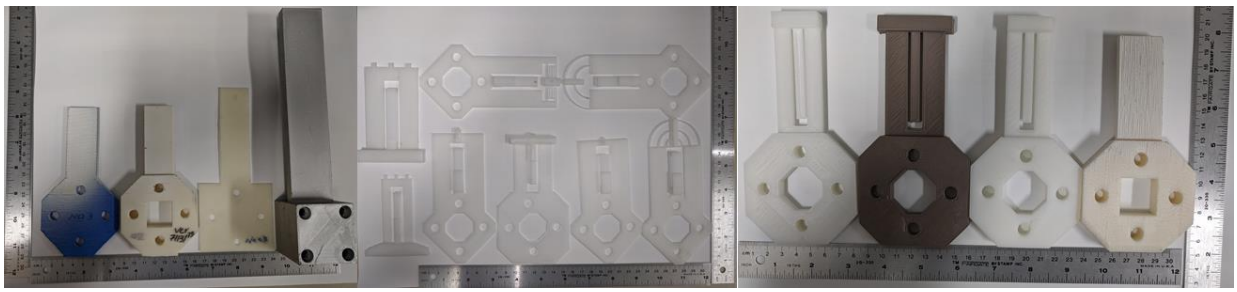

Fig. 19. Different iterations of the designed testing artifact for performing a systematic study on FDM processes

Some of the critical and recommended criteria of the testing artifacts being utilized for similar non-invasive characterization gleaned from the various reference are listed here [215, 218, 219, 240]:

- artifact has to be large enough to examine the performance of the machine near the extremes of the platform as well as near the center;
- artifact should not take too long to build and require no post-treatment or manual intervention;

- artifact should be easy to measure the properties of interest,
- artifact should allow measuring the repeatability;
- the plate and beam have to be rectangular;
- plate and beam should have homogeneous or near-homogeneous in-plane mass distribution;
- a slender ratio of length to cross-section should be preferably as large as 25 but must not be less than 5;
- width-to-thickness ratio must be 5 for shear modulus measurements of rectangular bars (for the central thin section of the testing artifacts);
- the testing artifact for the fundamental flexural frequencies must range between 100 to 10,000 Hz, and a fundamental torsional resonant frequency must be in the range from 200 to 30,000 Hz;
- the mass of the specimen must be a minimum of 5g to avoid coupling effects;
- all surfaces on the rectangular specimen must be flat. Opposite surfaces across the length, thickness, and width must be parallel to within 0.1 %;
- for the plate section, the length-to-thickness and width-to-thickness ratios should be higher than 20 to satisfy the thin plate theory;
- the ratio between Young's modulus and shear modulus should be lower than 50;
- the length-to-width ratio must not equal $(E_1/E_2)^{1/4}$.

There are also some criteria gathered from experimental perspectives and the capability of the tools in the lab:

- shaker frequency should range between 20 Hz to 15KHz;
- achievable resolution for out-of-plane distortion is 50μm;

- thickness is one of the most critical and influential parameters and has to be measured precisely when it is less than 3 mm [218, 219] ;
- the thickness deviation measured for three different locations must be within 0.1% for the calculation error to be less than 0.3% [218, 219];
- the length and width of the specimens must be measured with 0.1% resolution to warranted the measurements with an error of less than 0.3% [218, 219].

We tested several iterations of the design interrogating the thickness, width, and length and expanded the combined design of two sectioned thin-thick beams. This combo structure allowed us to simultaneously capture the effects of residual stresses in the middle section resembling a cantilever beam while measuring the natural frequencies based on the full-field-of-view measurement of both wide wings (plate) and slender section (beam).

Additionally, this particular design allowed us to test artifacts under impact excitation. With this design, one can compare the way stress wave propagates in both thin and thick sections to obtain more data regarding the non-homogeneity of the testing artifacts.

The nature of a cantilever beam simplified the computational thermo-mechanical model in both 2D and 3D. Besides, dealing with flat surfaces relaxes the complexity of applying thermal boundary conditions, specifically convection.

Several geometrical properties of such an artifact were measurable using a caliper and other shape measuring tools, including full-field-of-view optical sensors. We also studied testing artifact parametrically using finite element analyses (FEA) to demonstrate the effects of geometry and mechanical characteristics on the natural frequencies and mode shapes. In this sense, we parameterized our designs such that it was possible to alter their geometrical, structural, and physical properties and obtained their corresponding natural frequencies and

mode shapes. Through this approach, we related the different geometry and structural properties, such as elastic moduli, density, and Poisson's ratio, to natural frequencies.

The available FDM printers are XYZ Dou da Vinci and Zortrax M200 with the maximum build volume of 150×200×200 (W×H×D) mm and 200×200×180 mm, respectively. These printers allowed us to print a sample with a length between 100.0 to 200.0 mm with a resolution of 50 micrometers. The total width of the beam was selected to be between 50 to 70 mm, and the thickness between 1.0 to 4.0 mm. The maximum layer thickness was 0.29 mm, and assuming at least 5 layers; the minimum thickness was rounded up to 1.5 mm. Since the recommend width-to-thickness ratio for shear measurement has to be 5, thus the width of the center part obtained 7.0 mm. Finally, the length-to-thickness ratio of 20 suggested the length of at least 30mm. The thickness of the wing is calculated to have the same magnitude of the first natural bending frequencies for center sections. The length of the center part was found to be equal to the length of a single filament to reach room temperature. Thus, the thickness was estimated around 2 mm, and to satisfy the thin-plate theory, the width of each beam was assumed to be 14 mm. Another criterion to consider is satisfying the resonalyzer plate, Poisson's test plate, requirement. Accordingly, the L-to-W ratio ranges from 1.0 to 1.4 for a free plate with Young's moduli ratio of the principal directions E_1/E_2 between 1.0 to 4.0. Since our design is a cantilever, this ratio changes between 0.5 and 0.7, which translates to a length-to-width ratio of 1.4 to 2. We chose the total width between 30 to 50 mm and designed the final artifact accordingly.

3.2 Analytical and computational analyses of FDM processes

3.2.1 Thermal analysis framework

To create a realistic model of the FDM process that includes mechanical and thermal effects, one has to consider solving a highly nonlinear multiphysics problem that faithfully incorporates

all influential physics, adequately captures the details of the process, and successfully exemplifies a highly dynamic environment [241, 242].

Right after the filament leaves the extruder(s), thermal and structural phenomena start affecting the process. The first thermal encounters are radiation and convection on the surface of the filament. The filament also experiences a substantial shear rate inside the nozzle, and when rotates 90^{o} from a vertical to a horizontal direction (see Fig. 20) [14, 15]. This shear rate continues to exert force longitudinally when the extruder follows the tool-path as it scans the cross-section. These changes in direction, shears inside the nozzle, and shears during deposition cause the orientation of the added nano- and micro-fiber be affected significantly[16, 92, 98]. Nozzles used in FDM 3D printers have circular cross-sections; however, the cross-section of the filament when it is laid on the surface or to the contagious filament is semi-ellipsoidal due to the change in direction and pressure. Thus, there are always cavities similar to one shown in Fig. 20 in the body of the printed components.

Different modes of heat transfer, conduction, convection, and radiation, are noticeable in the FDM process [37, 107, 109]. It is also recommended to account for the effect of latent heat around glass transition and softening temperature. The heat dissipation, diffusion, healing, and neck growth affect material properties of 3D printed components locally in the contact zone [8, 38, 39, 41, 67, 243]. These occurring effects eventually define the structural and geometrical characteristics of a 3D printed component.

Costa et al. [107] listed several thermal phenomena involved in an FDM process. These included convection and radiation with surroundings, conduction with support material and between adjacent filaments, conduction with a heated bed, and radiation and convection in the encapsulated enclosed areas among beads. In addition to those listed in their work, there are

several other influential phenomena to consider too, such as changes in conductivity due to temperature, phase change, spatially varying conductivity, thermal resistance between adjacent filament-to -filament, -support material, or -platform, the shape of the filament, and changes in contact areas.

Aside from these factors, there are several other parameters involved known as process and printing parameters such as the position of the component inside the machine, machine environments, air gap, layer thickness, counter thickness, raster angle, orientation, speed, and rate of the deposition.

In addition to process and printing parameters, there are other parameters that relate to manufacturing constraints, for example, fixing mechanism (using vacuum, jig and fixture, or glue), type of the heated bed (metal, glass, or composite), the diameter of the nozzle, stock materials (filament or pellet), type of feeding mechanism, and cooling mechanism.

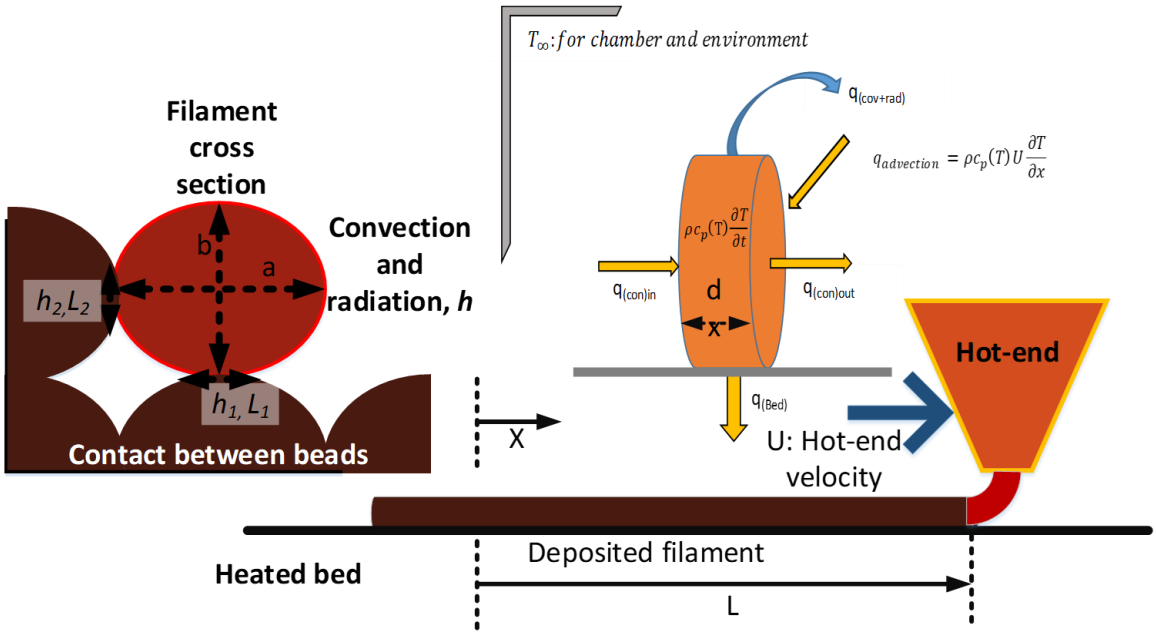

Fig. 20. Schematic of a heat transfer model for 1D single-layer deposition of the filament.

Each of these parameters has to be considered when the model is developed to make sure the results are reliable and can predict the process correctly.

The computational simulation requires reasonable assumptions. Some of the critical and widely accepted assumptions, have appeared in several proposed numerical approaches, are listed hereunder [16, 39, 69, 106, 107, 113, 244-247]:

- material is deposited discontinuously at each time step, Δt. The process, in reality, is continuous, but for modeling the deposition is assumed to take place sequentially at time step Δt; thus, the volume of the deposited material will be equal to the feed rate multiplied by this time step,
- material leaves the extruder in equilibrium thermal condition with its temperature equals to extruder temperature. If the nozzle is large and heating is unstable, this assumption is not valid, and experimental measurement is required to find the relationship between the set temperature and the leaving temperature,
- the relevant boundary conditions are updated as the part proceeds according to the latest local circumstances,
- material properties are updated as the simulation continues based on the local conditions,
- enthalpy formulation is used to model the effect of phase changes.

In an attempt to produce a reliable simulation, this dissertation incorporated assumptions mentioned above and also applied other considerations explained in the following section.

3.2.1.1 The general scheme of the thermal model

Radiation, advection, and convection are the three primary sources of heat loss on the boundaries of the thermal domains. Radiation is ignored in several studies of FDM, arguing its effect is not comparable to the convection and conduction heat transfer [12, 13, 33, 106, 109, 115]. We suggest that, although the effect of radiation for small diameters is negligible compared to the effect of convection, in large diameters, it must be included in the model.

Convection is a significant source of heat loss, and its dependency on temperature and size pertains to accurate thermal flow estimation. Although, in several studies, the constant value of the coefficient of heat convection, h_{cov}, was used [12, 13, 106], we suggest incorporating the experimental correlation for this thermal coefficient. We describe our approach dealing with these challenging and dynamic boundary conditions in the following section (3.2.1.3). In summary, we incorporated the predicted coefficients of heat transfer obtained from empirical correlations and redefined them through mathematical formulas. These formulas depend on size and temperature and are used for applying corresponding boundary conditions on each node and surface. We also combined radiation and convection and introduced the total heat transfer coefficient (THTC).

3.2.1.2 Governing equations

Conservation of mass, momentum, and energy define the framework of the governing equations; however, it also required to contemplate hydrodynamics and rheology of materials to encompass the thermo-fluid-mechanical effects accurately [13, 106, 109, 115, 248]. The first set of equations is the conservation of mass:

$$\begin{aligned} \frac{D\rho}{Dt} &= \frac{\partial \rho}{\partial t} + V_x \frac{\partial \rho}{\partial x} + V_y \frac{\partial \rho}{\partial y} + V_z \frac{\partial \rho}{\partial z} = 0, \text{Cartesian coordinate} \\ \frac{D\rho}{Dt} &= \frac{\partial \rho}{\partial t} + \frac{V_r}{r}\frac{\partial (r\rho)}{\partial x} + \frac{V_\theta}{r}\frac{\partial \rho}{\partial \theta} + V_z \frac{\partial \rho}{\partial z} = 0, \text{cylindrical cordinate} \end{aligned} \tag{3-33}$$

where V is velocity, ρ is density, and subscripts *x*, *y*, and *z* refer to three axes in the Cartesian system and $r, \theta,$ and z are three directions in the cylindrical coordinate. Equation (3-34) defines the general form of the conservation of energy:

$$\begin{aligned} \dot{E}_{advection,in} - \dot{E}_{advection,out} + \dot{E}_{condunction,in} - \dot{E}_{conduction,out} \\ + \dot{W}_{net,on\ CV} + \dot{E}_{Energy\ Generation} = \dot{E}_{internal}\,, \end{aligned} \tag{3-34}$$

where E is energy, W work, and CV control volume. Equation (3-35) is used to develop the governing equation for transient heat transfer with phase transition and enthalpy formulation, as described in [109, 110, 115].

$$\frac{\partial \rho u}{\partial t} + V.\nabla \rho \boldsymbol{h} = \nabla.(\kappa \nabla T) + \dot{q}, \tag{3-35}$$

where t is time, u internal energy, ρ mass density, V velocity vector, $\boldsymbol{h}$ enthalpy, κ conductivity, T temperature, and $\dot{q}$ the volumetric heat generation.

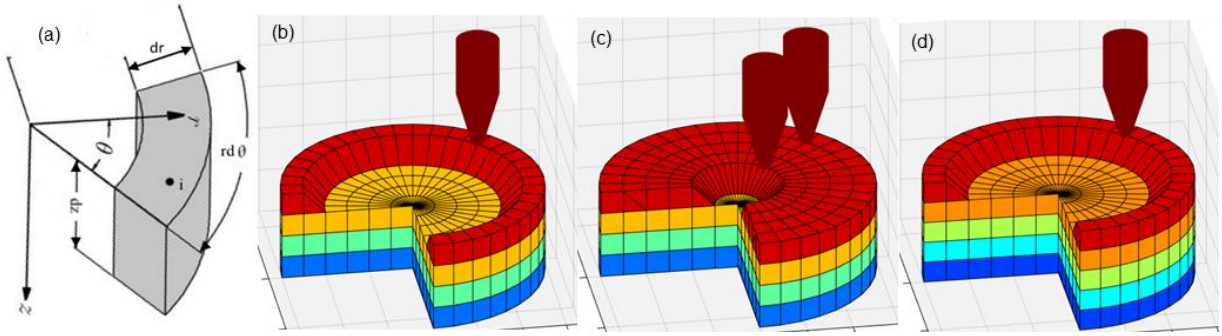

Fig. 21. 3D elements and schematic representing a 2D cylindrical fabrication model with symmetry in θ direction: (a) cylindrical element at node i, j; (b) first radial ring is being deposited from perimeter toward center; (c) last radial ring is being deposited on the same layer at the center, and (d) first radial ring is being deposited on the next layer.

Furthermore, by realizing $du = d\boldsymbol{h} = c_p dT$, and $c_p$is specific heat capacity, the governing equation (3-35) reads as:

$$\frac{\partial \rho c_p T}{\partial t} + V.\nabla \rho c_p T = \nabla.(\kappa \nabla T) + \dot{q}. \tag{3-36}$$

The thermal problem, in general, is complex and 3-dimensional and requires high-performance computing (HPC) to capture a transient thermal problem with high fidelity [37].

It is possible to simplify the 3D problem to 2D without sacrificing the governing physics. For example, the governing equation can be analyzed with symmetry about the θ axis in a cylindrical coordinate for a cylinder manufactured in z-direction continuously, as shown in Fig.

21. In such a 3D problem, we used the following PDE derived from Eq. (3-36) to solve for temperature distributions [34, 110, 249, 250]:

$$\rho c_p \frac{\partial T}{\partial t} + \rho c_p U_z \frac{\partial T}{\partial z} + \rho c_p U_r \frac{\partial T}{\partial r} = \frac{\partial}{\partial z}\left(\kappa \frac{\partial T}{\partial z}\right) + \frac{1}{r}\frac{\partial}{\partial r}\left(\kappa r \frac{\partial T}{\partial r}\right) + \dot{q}. \quad (3\text{-}37)$$

3.2.1.2.1 The 1D model analytical framework

Yardimchi et al. [109], Li et al. [88], Sun et al. [8], and Gkartzou et al. [251] developed a simplified 1-D model to analyze heat transfer in FDM. Their model was achieved by assuming a lumped-capacity criterion. This assumption was made because the heat convection coefficient was large enough in the presence of a small diameter (e.g., 500μ) and low conductivity (e.g., 0.17 W/mK) to lower the Biot number to less than 0.1 [68, 87, 89, 252, 253]. Such a low Biot number suggests the temperature distribution along the cross-section is uniform and relaxes the demand for a 2D and 3D simulation. In Li et al.'s work [112, 237], the temperature of the hot-end, heated-bed, and the environment was assumed constant, and the extruder moved with a fixed velocity equal to *U*. For this problem, the partial differential equation can be obtained as described here [110, 112] and illustrated in the following:

$$\dot{E}_{internal} = q_{con,in} - q_{con,out} - \sum q, \quad (3\text{-}38\text{-a})$$

$$\dot{E}_{internal} = A_c \times \mathrm{dx} \times \rho c_p(\mathrm{T}) \frac{\partial T}{\partial t}, \quad (3\text{-}38\text{-b})$$

$$q_{con,in} - q_{con,out} = +\frac{\partial}{\partial x}\left(\kappa \frac{\partial T}{\partial x}\right) \times A_c \times \mathrm{dx}, \quad (3\text{-}38\text{-c})$$

$$\sum q = q_{con+rad} + \sum q_{neigh}, \quad (3\text{-}38\text{-d})$$

$$q_{con+rad} = A_h\left(\varepsilon\sigma(T^4 - T_\infty^4) + h_{conv}(\mathrm{T} - T_\infty)\right), \quad (3\text{-}38\text{-e})$$

$$\sum q_{neigh} = \sum A_i h_{n,i}(\mathrm{T} - T_{neigh}), \quad (3\text{-}38\text{-f})$$

here q with different subscripts indicates heat fluxes, with *con*, *conv*, *neight*, and *rad* being conduction, convection, neighbor, and radiation, respectively. A_c is the cross-sectional area, A_h is the perimeter area for convection and radiation, A_i is the contact area to bed or another filament, ε is the emissivity, and σ is the Stefan-Boltzmann constant. Also, T and T_∞ are the surface and environment-wall temperatures. h_n is heat transfer coefficients, and subscripts *i* indicates the different neighbors, i.e., heated-bed or other filaments. The filament can be placed on the bed or the previously deposited material; thus, T_{neigh} is either heated bed temperature or the corresponding temperature of the surrounding filament.

In a simplified condition, Li et al. [112] introduced a case of the semi-infinite condition of continuous filament depositing on the heated bed. The authors assumed a large heat convection coefficient for air and large volume for bed. They introduced a total h_T and neglected the effect of the deposited filament on a heated bed. Figure 20 illustrates the assumed condition. Finally, Eq. (3-36) can be simplified to:

$$\rho c_p A_c \frac{\partial T}{\partial t} = \frac{\partial}{\partial x}\left(\kappa \frac{\partial T}{\partial x}\right) \times A_c - A_p h_T (T - T_\infty), \tag{3-39}$$

where, A_c and A_p are cross-section and perimeter of the filament, respectively.

Knowing that $\frac{\partial T}{\partial t} = \frac{\partial T}{\partial x}\frac{\partial x}{\partial t}$, and assuming the constant velocity for hot-end equal to $\frac{\partial x}{\partial t} = U$, Eq. (3-39) can be rewritten as:

$$\rho c_p A_c U \frac{\partial T}{\partial x} = \frac{\partial}{\partial x}\left(\kappa \frac{\partial T}{\partial x}\right) \times A_c - A_p h_T (\mathrm{T} - T_\infty). \tag{3-40}$$

h_T is defined as a total convection-contact-radiation heat transfer coefficient. In other words, the heat transfer due to the contact to the heated bed also was added to convection and radiation:

$$h_T = \left[r_{eff} h_b \frac{(T - T_b)}{(T - T_\infty)} + \left(1 - r_{eff}\right) \frac{\varepsilon \sigma (T^4 - T_\infty^4)}{(T - T_\infty)} + h \right], \tag{3-41}$$

r_{eff} is the ratio of the heated bed contact area of the filament perimeter. The Eq. (3-40) can be solved analytically as follow:

$$T(x) = T_{\infty} + (T_{ext} - T_{\infty})e^{-mx}, \tag{3-42}$$

with $m = \frac{\sqrt{1+4\alpha\beta}-1}{2\alpha}$, where $\alpha = \frac{\kappa}{\rho c_p}$, and $\beta = \frac{h_T A_p}{\rho C_p A_c U}$, and T_{ext} is extruder temperature.

3.2.1.2.2 1D modeling of a slender cylinder satisfies lumped-capacity criterion

We extended the 1D model for studying the case where a cylindrical part was manufactured in a 3D printer. This case was analogous to filament deposition, but the whole cross-section of the cylinder was assumed to be laid continually with a known temperature at a selected time increment commensurate with the layer thickness. It means we supposed the whole cross-section was deposited with the velocity equal to the deposition velocity of the whole layer. The developed 1D model is illustrated in Fig. 22-a.

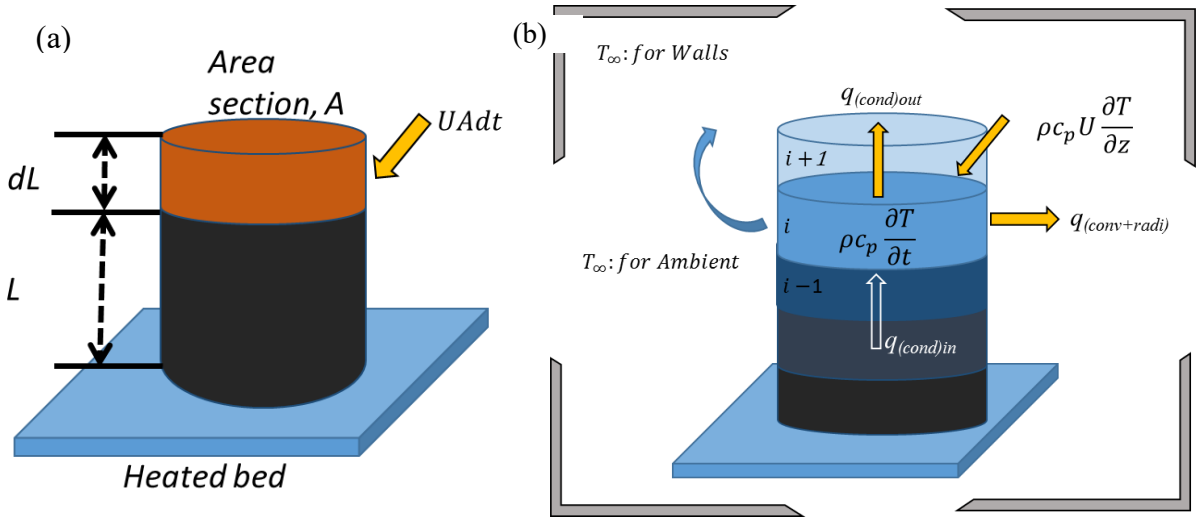

Fig. 22. Schematics of the proposed 1D model for numerical analyses: (a) The addition material simplification as an advent deposition of the whole layer with the velocity of *U* at time increment *dt=dL/U*; and (b)representative schematic of energy balance for a 1D model in a cylindrical coordinate system for deposition of the *i*-th layer.

In order to assure the lumped-capacity criterion was still valid, the diameter had to be chosen to satisfy the Biot number less than 0.1 knowing martial properties (conductivity and density) and environmental constraints (specifically coefficient of convection heat transfer).

Energy balance for such a cylindrical specimen with depicted boundary conditions in Fig. 22-b is obtained as:

$$A \cdot dz \cdot \rho c_p \frac{\partial T}{\partial t} + A \cdot dz \cdot \rho c_p U_z \frac{\partial T}{\partial z} = q_{(cond)in} - q_{(cond)out} - q_{(conv+rad)}, \quad (3\text{-}43\text{-a})$$

$$q_{(cond)in} - q_{(con)out} = \frac{\partial}{\partial z}\left(\kappa \frac{\partial T}{\partial z}\right) \cdot A, \quad (3\text{-}43\text{-b})$$

$$q_{(conv+rad)} = 2\pi r \cdot dz[h_{conv}(T - T_\infty) + \varepsilon\sigma(T^4 - T_\infty^4)], \quad (3\text{-}43\text{-c})$$

where all the parameters are defined before. By substituting Eqs (3-43-a) and (3-43-c) into Eq. (3-43-a), we reached:

$$\rho c_p \frac{\partial T}{\partial t} + \rho c_p U_z \frac{\partial T}{\partial z} = \kappa\left(\frac{\partial^2 T}{\partial z^2}\right) - \frac{4h_{conv}}{d}(T - T_\infty) - \frac{4h_{rad}}{d}(\mathrm{T} - T_\infty), \quad (3\text{-}44)$$

where T and T_∞ are surface and environment-wall temperatures, respectively, d is the diameter, and h_{rad} is the radiation heat transfer coefficient described by [254, 255]:

$$h_{rad} = \varepsilon\sigma(T^2 + T_\infty^2)(T + T_\infty), \quad (3\text{-}45)$$

This radiation heat transfer coefficient was added to the convection heat transfer, h_{conv}, to define the total heat transfer coefficient, h_t, as follows

$$h_t = h_{rad} + h_{conv} = \varepsilon\sigma(T^2 + T_\infty^2)(T + T_\infty) + h_{conv}. \quad (3\text{-}46)$$

Determination of h_t values is crucial for accurate simulations. This total heat transfer coefficient was approximated empirically by exponential functions, such as those proposed in [256, 257] as:

$$h_t = \alpha \varepsilon T^{\beta}, \tag{3-47}$$

where α and β are determined by experimental investigations and procedures. We also estimated h_t for FDM by combining radiation and convection heat transfer through a combined experimental-computational approximation using a 1D model [110].

3.2.1.2.3 A 2D model analytical framework

The physics in FDM deposition is complex, and adding the nonlinearity of the material properties and boundary condition to the problem makes the analytical solution hardly possible. However, by applying several simplifications, Rodiguez et al. [87] introduced an analytical solution. They assumed a rectangular cross-section, seamless contact between layers, constant heat transfer coefficient, constant material properties, and deposited material temperature equal to the extruder temperature. In a vertical stacking assumed in *x*-direction, they reached the following analytical solution:

$$T_{ave}(x,y,t) = T_E\left[1 + \sum_{m=1}^{\infty}\sum_{n=1}^{\infty}(a_{mn}\sin(\lambda_m y)\cos(\beta_n X))e^{-\alpha^2(\lambda_m^2+\beta_m^2)t}\right], \tag{3-48}$$

moreover,

$$a_{mn} = \frac{4T_L^*}{E_m^2 F_n^2 \lambda_m \beta_n}\sin\left(\frac{9\lambda_m H}{2}\right)\sin\left(\frac{\lambda_m H}{2}\right)\sin\left(\frac{\beta_n W}{2}\right), \tag{3-49-a}$$

$$E_{\mathrm{m}}^2 = \frac{1}{2}\left(5\mathrm{H} - \frac{-\sin(10\lambda_m H)}{2\lambda_m}\right), \tag{3-49-b}$$

$$F_{\mathrm{n}}^2 = \frac{1}{2}\left(\mathrm{w} - \frac{-\sin(10\lambda_n \beta_n W)}{\beta_n}\right), \tag{3-49-c}$$

where T_{ave}, is averaged temperature between the envelope temperature, T_{∞}, and the liquefier temperature, T_{ext}. H and W are the filament's height and width. The eigenvalues ζ_m and β_n are the roots of the following transcendental equations:

$$\zeta_n \cot(5\zeta_m H) = -\frac{h}{\kappa} \text{ and } b_n \tan\left(\frac{\beta_n W}{2}\right) = \frac{h}{\kappa}. \quad (3\text{-}50)$$

3.2.1.3 Boundary conditions

3.2.1.3.1 Convective heat transfer boundary conditions

Costa et al. [107] found out that the convection between filament and environment was among the most critical parameters. They determined an increase from 5 W/m^2K to 150 W/m^2K in the magnitude of the convection heat transfer coefficient could exponentially reduce the cooling time to glass transition more than 44 times for a newly deposited filament [107]. Thus the correct value for the convection was crucial for our investigation. We approached this issue by looking into the effect of size and machine characteristics and tried to propose a tenable approximation for a variety of small to large machines.

Table 3: The different classes of FDM printers based on filament and nozzle diameters.

Scale	Nozzle diameter range, mm	Common nozzle diameter, mm
Micro	0.2-0.6	0.4
Meso	0.6-2	1.0
Medium	2-8	6
Large	8-14	10

There are different sizes of FDM and FFF machines available in the market. The effects of the size of the machine have to be considered since it significantly alters the nature of thermal energy deposition and dissipation. We, in the following sub-chapters, looked into the effect of size on convection and radiation boundary conditions and showed large and small 3D printer has

to be treated differently. Considering the availability of the different printers, one can categorize printers according to size and nozzle diameter, as listed in Table 3.

We introduced empirical correlations to estimate the convection heat transfer coefficients for different scales. Also, there were several criteria for the estimation of these coefficients, including the regime of the flow, size, and shape of the surface. The printer heads usually have fans to dissipate the heat of the extruder and cool down the recently deposited material. These fans can be controlled at different levels from off to fully loaded. In addition, the machine can have chamber temperature control based on convection heating or rely only on the natural convection. Thus, we assumed four different flow regimes: natural convection and three intensities of forced convection. In natural convection, the cooling system (e.g., fans) is off. For forced convection, we assumed three levels of flow intensity pertaining to the operational condition of the cooling fans installed in a machine or hot fluid flow inside a chamber. We estimated the velocity as 0.3, 0.8, and 1.7 m/s based on the size of the fan and the dimension of the cooling nozzle of the in-house printers and extended this analogy to other printers as well.

The detail of the calculation associated with the convection heat transfer coefficient is explained in Appendix 9.1. This dissertation looked into this matter systematically by dividing the process to filament level and part level. We also considered the nature of the surfaces to be flat or cylindrical and the nature of the heat convection as forced or free. Temperature ranges and sizes were considered to find the coefficient of convection heat transfer using empirical correlations.

In chapter 9.1.1, the general concept is explained, and in chapter 9.1.2, the estimation for the cylindrical part for different sizes of cylinders ranging from 1 to 500 mm in three groups small,

medium, and large have expatiated. The flat surfaces of different sizes also calculated and presented in chapter 9.1.3. In chapter 9.1.4, we looked into the free convection.

We curve fitted data to find mathematical representations of the effects of size, flow regime, velocity, and temperature to be defined in the numerical solution. The numerical solutions based on this mathematical framework are accurate and cost-effective. This approach helped us to decrease the computational cost of the numerical simulation and assure the correctness of the estimated heat coefficients on the fast-changing boundaries of the numerical model.

3.2.1.3.2 Polymer interface boundary conditions

The resistance between the adjacent material (i.e., bead-to-bead or bead-to-bed) is as essential as the convection heat transfer coefficient. This resistance is defined based on the contact quality, material properties, and geometrical characteristics [258-260]:

$$h_i = \frac{1}{R_c A_i}, \tag{3-51}$$

where, R_c is the contact resistance between polymer and bed or two adjacent polymeric beads, and A_i is the contact area. The values of contact resistance have been measured experimentally for polycarbonate under different conditions in ref. [258]. J. Gibbins found that resistances of polycarbonate-stainless steel (P-SS) and polycarbonate-polycarbonate (P-P) changes between 1.0-9.0 K/W and 0.8-6.0 K/W, respectively. The average of these values can be used to estimate the thermal contact conductance as:

$$h_{P-SS} = \frac{1}{5 \times A_i} \text{ or } h_{P-P} = \frac{1}{3.4 \times A_i}. \tag{3-52}$$

If one assumes half to one-sixth of the perimeter to be a polymer-to-polymer interface, the estimated values of h_i can change between 1,500 to 4,500 W/m^2K for the typical nozzle of 0.4

with bead size of 0.5x0.25 mm. In similar cases, the thermal contact conductance between polymer-to-stainless steel can change between 1,030 to 3100 W/m^2K.

3.2.1.3.3 Radiation heat transfer boundary conditions

Each object emits to and reflects and receives radiation from the surrounding. Radiation heat flux depends on directions, wavelength, and temperature. For most engineering materials, one can assume the directional variation is negligible; thus, radiative heat flux can be defined in terms of wavelength and temperature as described with Planck's law[254, 255, 261]:

$$w_{b\lambda} = \frac{2\pi h_p c^2}{\lambda^5}\left(\frac{1}{e^{\frac{hc}{\lambda kT}} - 1}\right), \tag{3-53}$$

where h_p in Planck's constant, c is the speed of light in vacuum, λ is wavelength, and T is temperature. By integration of Eq. (3-53), Planck determined the maximum energy flux emitted from a perfect object as [254, 262]:

$$\mathrm{q} = \int_0^\infty \frac{2\pi hc^2}{\lambda^5}\left(\frac{1}{e^{\frac{hc}{\lambda kT}} - 1}\right) d\lambda = \sigma T^4. \tag{3-54}$$

Such a perfect object is known as a blackbody, and its maximum radiative energy merely depends on temperature. To avoid the complexity of radiation heat transfer, it helps to treat radiation as convection. This simplification leads to incorporate radiation and convection heat transfers into a single coefficient to apply in a numerical model.

The majority of surfaces cannot satisfy the blackbody assumption. These surfaces are known as opaque and gray, where the radiation from them is less than the maximum emitted from the blackbody. Thus, a coefficient called emissivity, ε, is defined that indicates the ratio of the total energy given off that particular surface to the maximum possible value of heat flux from a

blackbody. The following equation defines the equivalent convection heat transfer coefficient of such a grey body:

$$h_{rad} = \frac{\sigma\left(\varepsilon T^4 - \varepsilon_\infty T_\infty^4\right)}{T - T_\infty}. \tag{3-55}$$

Assuming the emissivity of the environment is equivalent to the surface, which for a polymer with emissivity above 0.75 is rational speculation, the above equation is simplified to:

$$h_{rad} = \sigma\varepsilon\left(T^2 + T_\infty^2\right)(\mathrm{T} + T_\infty). \tag{3-56}$$

Assuming the environment temperature is about 20°C, Fig. 23 shows the equivalent of radiation to the coefficient of heat convection for the range of the temperature of interest for three different emissivities 0.7, 0.8, and 0.9. These values exponentially ascend when the surface temperatures increase and in temperature above 150°C are above 7.5 w/m^{2,} thus comparable to the estimated values of cylindrical and flat surface above 30mm.

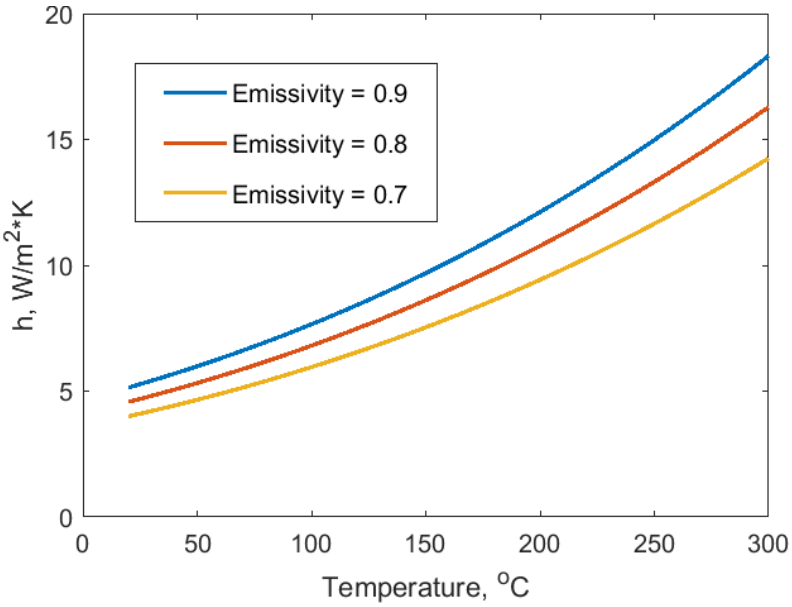

Fig. 23. Equivalent coefficient of convection heat transfer for radiation based on the equation (3-56) for the temperature ranges from 20 to 300 °C, assuming three different emissivities of the surface as 0.7, 0.8, and 0.9.

3.2.2 Thermo-mechanical analysis framework

There are several numerical approaches for this kind of multiphysics problem, with finite element (FE) and finite difference (FD) analyses being the most widely used [37, 263, 264]. In thermo-mechanical analyses, there are two approaches to set up the simulation, coupled and uncoupled. The coupled solution simultaneously solves the thermal and mechanical problem taking into account the different physics, while in uncoupled approach, the thermal solution is solved firstly and then applied as loads to the mechanical domain to estimate the distortion and residual stresses [12, 13, 106].

The coupled solution is computationally extensive and susceptible to instability, but the details of the physics and interconnections among them can be captured accurately. On the other hand, the uncoupled approach deals with thermal and mechanical problems separately. It allows one to allocate resources economically, for example, by ascribing a small time step in the thermal problem to capture the detail while assigning a larger one for the mechanical problem. In other words, the uncoupled approach avoids the complexity of solving the highly extensive mechanical non-linear physics in small time steps and saves time and resources. However, in an uncoupled approach, choosing the right time steps and mapping the thermal distribution to the mechanical domain become challenging.

In this dissertation, we applied the uncoupled thermo-mechanical approach with fine thermal detail and mapping strategy. We defined the problem to be solved in a different domain that allows us to refine the thermal and mechanical model where it is needed. This method helps to solve the convergence issues in the non-linear mechanical domain and allows refinement in the thermal solution without interfering with the integrity of the mechanical simulation.

The 3D printing processes are thermally driven, and analyses start first with thermal simulation. Although the nature of estimation of the temperature distribution and heat flux in

laser deposition technologies, i.e., DED, EBM, and LENS are extensively complex, in material deposition technology like FDM, it can be managed with fewer complications. In our approach, we looked into a practical scheme that captured the transient complexity of the thermal flow and yielded an acceptable level of accuracy in predicting deformation and residual stresses. We did this by simplifying the boundary conditions based on experimental-computational investigation and incorporating them in numerical simulation.

Accurate models that can capture the transient phenomena also needed to account for the dependency of material and boundary conditions on temperature. As temperature changes, polymer properties vary dramatically. These properties include conductivity, enthalpy, specific heat, and elastic-plastic behavior.

In the following chapters, we explained different aspects of the developed thermo-mechanical model and elaborated our particular approach dealing with FE meshes, heat source model, material model, boundary conditions, element activation, and adding material.

3.2.2.1 Governing equations

The total displacement vector at each infinitesimal point is the sum of elastic, plastic, and thermal displacement vectors, as shown in Eq. (3-57).

$$u^{tot} = u^{e} + u^{th} + u^{p}, \tag{3-57}$$

u is the displacement vector, the superscript *e* indicates elastic displacement, *p* plastic, *th* thermal, and *tot* total. The total incremental strain field is a result of their superposition, as formulated in Eq. (3-58) moreover, its integral over time yields the final deformed shape [265]:

$$\Delta\varepsilon^{tot} = \Delta\varepsilon^{e} + \Delta\varepsilon^{th} + \Delta\varepsilon^{p}, \tag{3-58}$$

where Δ indicates the incremental change in each component of strain fields, ε. Among these three, elastic strain follows the generalized Hooke's law, and the stress tensor variation is

obtained according to Eq. (3-59), the final stress tensor is obtained by accumulating the contribution of these changes [265]:

$$\Delta\sigma = \boldsymbol{D} \cdot \Delta\varepsilon^{e} = \boldsymbol{D} \cdot \left(\Delta\varepsilon^{tot} - \Delta\varepsilon^{th} - \Delta\varepsilon^{p}\right). \tag{3-59}$$

It is worth mentioning that the effect of incremental thermal strain only applies to the strain in the principal directions. Equation (3-60) shows the components of thermal strains:

$$\Delta\varepsilon^{th} = \alpha\Delta T \begin{bmatrix} 1 \\ 1 \\ 1 \\ 0 \\ 0 \\ 0 \end{bmatrix}, \tag{3-60}$$

where α is the thermal expansion coefficient (CTE), and ΔT is the temperature difference. Solving Equation (3-59) gives the distribution of stresses throughout the manufacturing period in parts that include residual stresses.

3.2.2.2 Constrained boundary conditions for thermo-mechanical simulations

The structural boundary conditions can be more sophisticated than the thermal boundary conditions, precisely when the intention of the modeling is estimating the distortions and residual stresses. Constrained conditions and fixed displacements are the prevailing boundary conditions for AM modeling. In some cases, applying springs contact elements leads to better estimation and helps to resemble the relaxation after removal from the bed [16, 45]. However, we decided to model the contact between the dissimilar materials of a polymer and heated bed via the Cohesion Zone Model (CZM) [266] to estimate the distortion and residual stresses more reliably.

3.2.3 Fundamental, concepts, and scheme of finite difference

3.2.3.1 1D formulation

In a developed 1D model, we assumed the entire cross-section was laid at once with the velocity *U* representing the average of material deposition at each particular layer with the

selected resolution (layer thickness). Figure 24 illustrates the general process of layer-by-layer deposition in this fashion for a cylindrical and cubical specimen. The modeling was carried out bottom-up with a constant deposition velocity, and the part was attached to the heated bed with a known temperature. At each time step, layer *i* is deposited with its temperature to be found through the satisfaction of energy conservation among advection of extruder, conduction between the layers, and total convection with the environment (includes both radiation and convection). Thus, the total heat transfer in 1D can be simplified to:

$$\rho c_p \frac{\partial T}{\partial t} + \rho c_p U_z \frac{\partial T}{\partial z} = k\left(\frac{\partial^2 T}{\partial z^2}\right) - \frac{4h_t}{d}(\mathrm{T} - T_\infty), \tag{3-61}$$

where *A* is cross-sectional area, $h_t$is the Total Heat Transfer Coefficient (THTC), and *d* is the cylinder diameter or square side, and the rest are defined before.

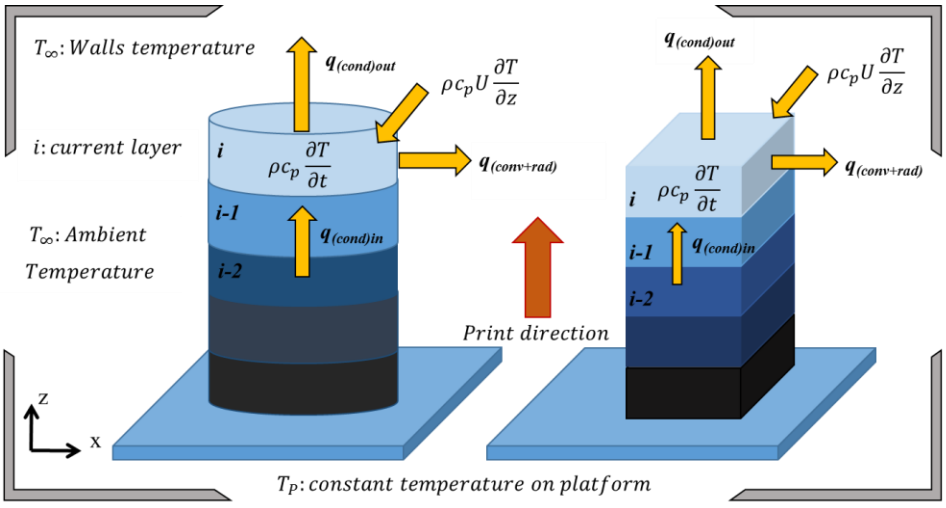

Fig. 24. Representative schematic of energy balance for a 1D cylindrical coordinates system of FDM of the *i*-th layer.

To numerically solve the transient heat transfer governing equation in 1D, Eq. (3-61), forward finite differences were used for the first-order derivative in the direction of deposition, whereas central differences were used for the second-order differential:

$$\delta c_p \frac{T_i^{l+1} - T_i^l}{\Delta t} + \rho c_p U \frac{T_{i+1}^{l+1} - T_i^{l+1}}{\Delta z} = +k\left(\frac{T_{i+1}^{l+1} - 2T_i^{l+1} + T_{i-1}^{l+1}}{(\Delta z)^2}\right) - \frac{4h_t}{d}\left(T_i^{l+1} - T_\infty\right), \quad (3\text{-}62)$$

where Δt is time increment, i indicates i-th deposited layer in z-direction, and l indicates l-th time step. In addition, to assemble the complete set of equations for the entire domain at each Δt increment, the boundary conditions at the top and bottom of the domain were applied with the combined convection-radiation condition at the top layer and contact polymer-metal resistance with the fixed temperature of the heated-bed at the bottom, respectively. The contact resistance included the resistance of the raft too if it exists between the part and the heated-bed as:

$$q_b = \frac{\Delta T_b}{R_b}, \qquad R_b = \frac{1}{h_c} + \frac{L_r}{\kappa_r}, \quad (3\text{-}63)$$

where q_b is heat flux, $\Delta T_b$is the temperature difference between the last node and the heated-bed temperature, T_b, and R_b is resistance. In addition, h_c is contact equivalent heat convection as described in chapter 3.2.1.3.2 Polymer interface boundary conditions, and L_r, and κ_r are the thickness and the conductivity of the raft layer, respectively.

3.2.3.2 Symmetrical 2D finite-difference formulation

We simulated the layer-by-layer deposition in radial, i.e., r, and axial, i.e., z, directions simultaneously to predict thermal distribution in a 3D cylindrical coordinate system. In our model, we could control the deposition rate in radial and axial directions as well as in each deposition and time increment [110]. During all steps of deposition, the estimated total heat transfer coefficient (THTC) was used at the boundaries to model local heat dissipation. We employed Matlab to carry out the entire 3D simulation.

3.2.3.2.1 Finite-difference discretization for symmetrical 2D

The deposition was modeled by defining discrete elements in the same cylindrical coordinate system as in 1D but without lumped model simplifications. Modeling was performed layer-by-

layer with each layer deposited in the *z*-direction. At each layer, the domain was discretized in (*r*, θ, and *z*) with elements having finite dimensions of (*dr*, *rdθ*, *dz*), as shown in Fig. 21-a, with symmetry in the θ direction. We volumetrically integrated Eq. (3-37) at the nodal positions, *i*, *j*, located at the centroid of each element in the (*r*, *z*) plane for each time increment Δt to define the discretization as:

$$\begin{aligned} &\int_{i-\frac{1}{2}}^{i+\frac{1}{2}}\int_{j-\frac{1}{2}}^{j+\frac{1}{2}}\int_{t}^{t+\Delta t}\rho c_p\frac{\partial T}{\partial t}drdzdt = \\ &\int_{t}^{t+\Delta t}\int_{i-\frac{1}{2}}^{i+\frac{1}{2}}\int_{j-\frac{1}{2}}^{j+\frac{1}{2}}\frac{\partial}{\partial z}\left(k\frac{\partial T}{\partial z}\right)drdzdt + \\ &\int_{t}^{t+\Delta t}\int_{i-\frac{1}{2}}^{i+\frac{1}{2}}\int_{j-\frac{1}{2}}^{j+\frac{1}{2}}\left[\frac{1}{r}\frac{\partial}{\partial r}\left(kr\frac{\partial T}{\partial r}\right)\right]drdzdt, \end{aligned} \tag{3-64}$$

where *i* and *j* are node number in *z*, and *r* direction. In Eq. (3-37), $\dot{q}$, U_z, and U_r are zero except in the last deposited ring where advection effects needed to be considered. After integration, we obtained the following:

$$\begin{aligned} \Delta r\Delta z\rho c_{p,i}^{l+1}\int_{t}^{t+\Delta t}\frac{\partial T}{\partial t}dt = k\frac{\partial T}{\partial z}\Big)_{i+\frac{1}{2}}\Delta r\Delta t - k\frac{\partial T}{\partial z}\Big)_{i-\frac{1}{2}}\Delta r\Delta t + \\ kr\frac{\partial T}{\partial r}\Big)_{j+\frac{1}{2}}\frac{\Delta z\Delta t}{r_{j+\frac{1}{2}}} - kr\frac{\partial T}{\partial r}\Big)_{j-\frac{1}{2}}\frac{\Delta z\Delta t}{r_{j-\frac{1}{2}}}. \end{aligned} \tag{3-65}$$

Figure 21 shows intermediate steps of deposition, which started by depositing rings of material from the perimeter to the center of the cylinder. When the center was reached, a layer was defined, and radial deposition was started again at a new node on the perimeter or center. This process was repeated until the final layer was deposited after which the model continued in order to simulate the cooling process. The assembled system of equations at each deposition step was solved by alternating direction implicit (ADI) methods rather than fully implicit to define tridiagonal matrices that could efficiently be solved to reduce the total computational time [248].

3.2.4 Fundamental, concepts, and scheme of finite element

It is recommended to use higher-order elements, i.e., quadratic elements, instead of linear elements with more than two nodes on each edge to get better results [45, 266]. Although a 3D model is required to study additive manufacturing processes, we investigated 2D model using a mapped quadrilateral mesh.

The crucial step in the uncoupled thermo-mechanical model is an accurate and reliable estimation of thermal flow and temperature distributions. Thus, we took into account the dependency of material properties on temperature, specifically conductivity, specific heat capacity, and convection-radiation heat dissipation. Due to the presence of porosity and cavity in 3D printed components as a result of spatially varying bonding and welding, conductivity can change from fully welded locations to places with less and undeveloped bonding between filaments. One has to account for both temporal and spatial changes in conductivity and other material properties to be able to capture the thermal complexity of FDM realistically. This complexity is caused by counter effects between, on the one hand, temperature and printing history and, on the other, time and development of bonding.

Since the deformation is expected to be large compared to the size of the component, large-deformation analyses were active, for which, instead of engineering stress-strain constitutive equations, the Cauchy stress-strain constitutive model was used.

3.2.4.1 Material and contact modeling in ANSYS

There are various models available in ANSYS ADPL for different attributes in materials. Models such as linear elasticity, multiyear elasticity, nonlinear elasticity, large deformation elasticity (hyperelastic), small deformation plasticity (Elasto-plastic), pressure-dependent plasticity (Drucker Prager/ Extended Drucker Prager), rate-dependent plasticity (viscoplasticity),

Bergstrom Boyce, viscoelastic, and creep can be defined in ANSYS. Furthermore, the material response to applied loads can be defined through different material constitutive models such as isotropic, orthotropic, and anisotropic considering behaviors such as elastic, elasto-plastic, isotropic hardening, kinematic hardening, generalized Hill, Drucker-Prager, and Gurson. These models and material properties are integrated into FEA material libraries of ANSYS APDL [266].

Assuming an elastic material model as applied in ref. [106], one can capture the thermo-mechanical complexity in FDM, but plasticity has to be added to accurately estimate stresses and preclude the presence of the exaggerated residual stresses beyond the yield point. S. F. Costa et al. [107] modeled viscoelastic material based on Prony series by curve fitting the available experimental data in an attempt to evaluate the effect of weight and gravity due to stacking on the lower layer of polymeric 3D printed components [267]. They did not report significant deformation due to weight using this viscoelastic model.

We suggested a temperature dependent elasto-plastic behavior to represent the material properties in our FE analyses. We assumed a monotonical increase in stress-strain behavior, although, some polymers (e.g., ABS) exhibit softening after yield stresses before retaining hardening [87, 118]. However, this softening has not been reported for printed components with ABS and PEEK elsewhere [268], and we did not observe it in our micro tensile-test. Kinematic hardening or a combination of kinematic and isotropic hardening has been recommended for material models [45, 244, 269, 270]. Isotropic hardening was selected for plastic deformation considering the dearth of the experimental data and the possibility of reversal plastic deformation [266]. Polymeric materials usually have a nonlinear stress-strain behavior [87, 118] that fits a multilinear stress-strain curve; although it was possible to model the material using the

multilinear stress-strain curve, we avoided that complexity and assumed bilinear plasticity by applying Bilinear Isotropic Hardening (BISO) model as shown in Fig. 25.

Temperature is a critical parameter in transient thermo-mechanical phenomena, affecting properties such as conductivity, thermal heat capacity, and density. The effects of temperature on conductivity and density have been ignored in several studies [12, 13, 68, 69, 107, 115]. Whereas, it is recommended to account for the changes in thermal heat capacity and associated variation in latent heat close to T_g [13, 87]. Enthalpy formulation, as described in Eq. (3-66) was used for modeling the latent heat in this dissertation:

$$\boldsymbol{h}_p = \int_{T_1}^{T_2} c_p(T)dT, \tag{3-66}$$

where $\boldsymbol{h}_p$ is enthalpy, c_p is specific heat, and T is temperature. Parameter c_p is defined as a function of temperature; and its value changes sharply around glass transition temperature and reduces after passing this point [13, 266, 271, 272].

In addition to the model properties for the polymers, setting up the specification of the layer connecting the components to the build-plate is challenging too. Some researchers have applied a fixed boundary condition that could potentially result in physically unjustified stresses and distortion [12, 13, 16, 106]. The fixed boundary condition is rarely applied to constrain the object during printing in FDM, and the contact between polymer and the build-plate is always a location of the interaction of two dissimilar materials. We decided to simulate this contact as an adhesion contact layer. ANSYS APDL offered a variety of different material models and contacts element technologies to do so. These models and technologies mathematically define and evaluate the interaction of dissimilar or similar materials. In our model, we used the cohesion model by defining surface-to-surface contact between the polymer and the heated bed. In particular, the Cohesive Zone Material (CZM) model was defined to predict the interface

mechanics. The CZM model showed a bilinear behavior and allowed two ways to specify material data with tractions and separation distances [266].

3.2.4.1.1 Specification of the Bilinear Isotropic Hardening model

In order to model the distortion and residual stresses in the components, it was crucial to incorporate yield stresses accurately [45, 273]. In our model, we took into account the dependency of yield stresses to temperature. We hypothesize that Young's modulus was linearly related to a combination of dynamic material properties, i.e., storage and loss modulus. The data reported by Nikzad et al. [59] on virgin Acrylonitrile Butadiene Styrene (ABS), as shown in Fig. 25-a, was used to model this dependency.

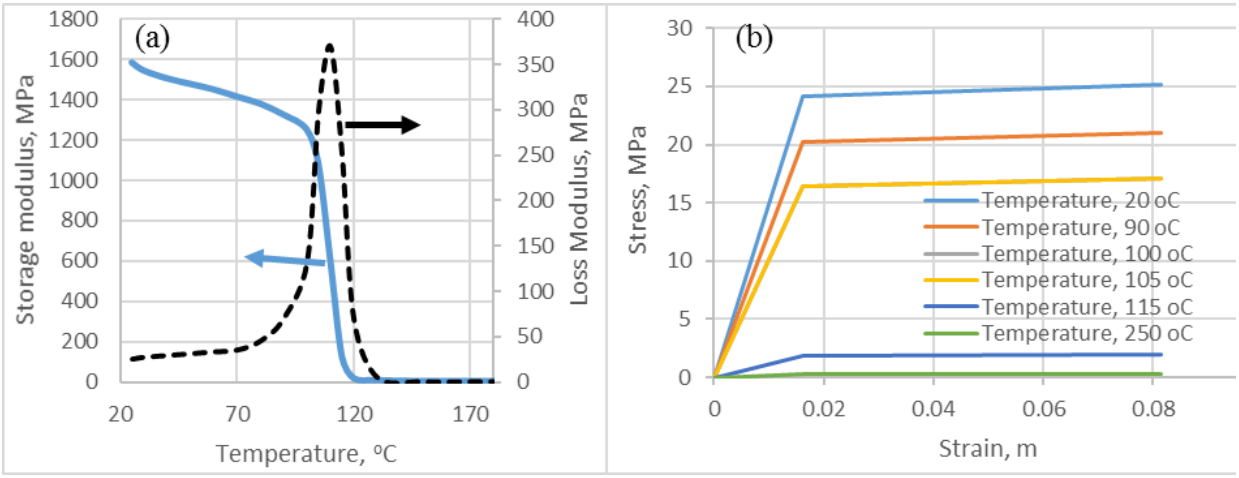

Fig. 25. Dependency of the mechanical property of ABS to temperature: (a) dynamic mechanical properties of virgin ABS [59]; (b) Bilinear Isotropic Hardening (BISO) stress/strain curve adjusted for different temperature.

Figure 25-b exhibits the hypothetically adjusted Young's modulus for different temperatures. In practice, the material above the glass transition temperature did not have a significant module of elasticity and changed plastically as long as the stresses were present.

3.2.5 Summary of simulating thermal and thermo-mechanical

Modeling of the process was complicated and multidisciplinary, and the following conceptual assumptions were made in the FEM model to carry out the simulations:

- the process, in general, was considered thermally driven, and in order to estimate the distortion and residual stresses, an uncoupled thermo-mechanical model was developed where the thermal problem was solved first and then applied as loads to thermo-mechanical model,
- the higher-order quadratic element was used for both thermal and thermo-mechanical models,
- some essential material properties such as a module of elasticity, yield stress, and specific heat were considered temperature dependence,
- radiation was incorporated as a total heat transfer coefficient in the thermal model,
- boundary conditions such as convection and radiation heat transfer were considered temperature dependent,
- the current deposited layer was deemed to be at the same temperature assigned to the extruder head,
- 2D thermo-mechanical simulation was simulated assuming plane strain condition by introducing the depth of the element,
- the manufacturing process was continuous; however, it was simulated step-wise such that at each step deposition of the new bead was modeled by activation of those elements that composed deposited volume; this process was known as element activation or birth/death strategy and applied to both thermal and thermo-mechanical models,
- contact element was introduced between the polymer and heated bed to replicate the cohesion interfaces,

- time step was assumed based on the equivalent time for the deposition of the whole width of the sample in the 2D thermal model,
- the deposited volume was commensurate to deposition length reached with average machine linear velocity (U) in the given time step,
- the new elements that belonged to the newly deposited volume were activated entirely at the beginning of time step,
- the layers were defined by incrementally adding a batch of elements to reach the final set of elements,
- the effect of gaps and voids was applied as a correction factor to density, for connectivity. the procedure explained in chapter 4.2.5 was applied.

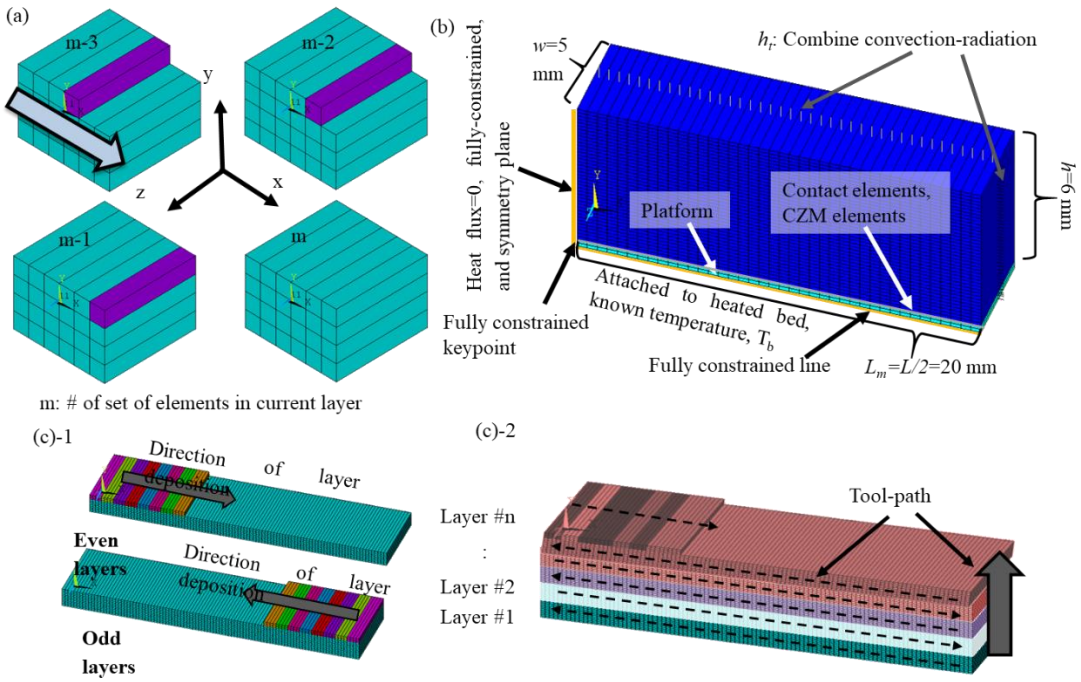

Fig. 26. 3D finite element and schematic representation of the layer-by-layer deposition strategy: (a) sequential deposition of sets of elements within a current layer, with each active set (in purple) laid in time increment *dt*; (b) boundary conditions for thermal and structural analysis and the solid model consists of 6000 elements; and (c) sequences of bottom-up deposited layers simulated as built up in a 3D printer with different layer deposition sequences for odd and even layers assumed in this model.

The model consisted of two different physics with the same geometry but corresponding material properties and element types. The chosen elements were higher-order solid 8-node quadrilaterals with PLANE77 and PLANE183 being used for thermal and structural analysis, respectively. The half-length of the sample is modeled by assuming the symmetry condition on the centerline. The geometry with the applied boundary conditions is shown in Fig. 26-b.

In order to model the nature of the continuous adding material, the birth/death feature in ANSYS was utilized. Figure 26-a illustrates our approach for the simulation of the deposition in Cartesian coordinates. On the current layer, deposition was simulated by progressively activating a set of elements, the purple set, in the direction of the extruder movement, as shown in Fig. 26-a; the tool-path defined the deposition strategy. For example, Fig. 26-c shows deposition as the extruder moves from right to left on the first layer and reversely on the next layer above. This process was repeated until the final layer was deposited after which the simulation continued in order to evaluate the cooling process and the removal of the part from the heated-bed.

3.3 Experimental measurement and optical NDT

3.3.1 Optical Non-destructive for structural analyses

3.3.1.1 Shape and distortion measurements

We chose the following three methods to carry out further investigations on printed components by FDM processes: Digital Holographic Interferometry (DHI), Digital Image Correlation (DIC), and Digital Fringe Projection (DFP). These methods have several merits in comparison to other available methods such as ease of use, rapid full-field-of-view measurement, modular design, high accuracy, and flexibility. These methods can also characterize mechanical properties, shape, geometrical distortions, and porosity and identify defects [17-20].

DIC is a non-contact method that by tracking the random pattern on the surface of an object, measures the displacement of the Area Of Interest (AOI). The patterns must have enough contrast to be registered by the camera's sensor and may be printed, painted, or already existing as natural features of the AOI [130, 274-279]. DFP, broadly categorized under structural light modulation, relies on trigonometry by measuring the deformed shape of a binary or sinusoidal intensity profile that is projected on the area of interest. Out-of-plane information of the object is encoded into images recorded by the acquisition sensor [125, 271, 280-285].

Time-average DHI was used for measurement of the vibration modes and natural frequencies of specimens[17, 208, 286]. A coherent light source is divided into two beams: (1) the intact beam (called the “reference beam”) directly impinges a light-sensitive sensor; and (2) the second beam (called the “object beam”), covers the object of interest and produces a reflection that reunites with the reference beam on the sensor. These two beams interfere and form bands of bright and dark intensity showing the constructive and destructive interferences of the two beams called fringes. In time-average techniques, the imaging tool captures the interference during a window larger than the vibration period, and the fringes that form on the sensor illustrates the amplitude of vibration [208, 286, 287].

3.3.1.2 Modal analyses and mechanical characteristics setups

The employed setup for time-average DHI, optical head, and the schematic labeling the components are illustrated in Fig. 27. The setup consists of a solid-state electrically pumped diode laser, model BWN-532-20E, with a wavelength of 532nm.

The laser beam divided into two beams, one of which, object beam, is reflected by mirrors to illuminate the AOI in the XY plane with a 40x beam expander. This expander diverges the object beam to cover the sample thoroughly. The object beam also passes through a spatial filter

to provide a smooth Gaussian distribution to enhance fringes' quality. The second beam called the reference beam is coupled into a fiber and goes to the optical head where it meets the collected reflected object beam off the surface of the object of interest. These two beams interfere on the sensor of the CCD camera.

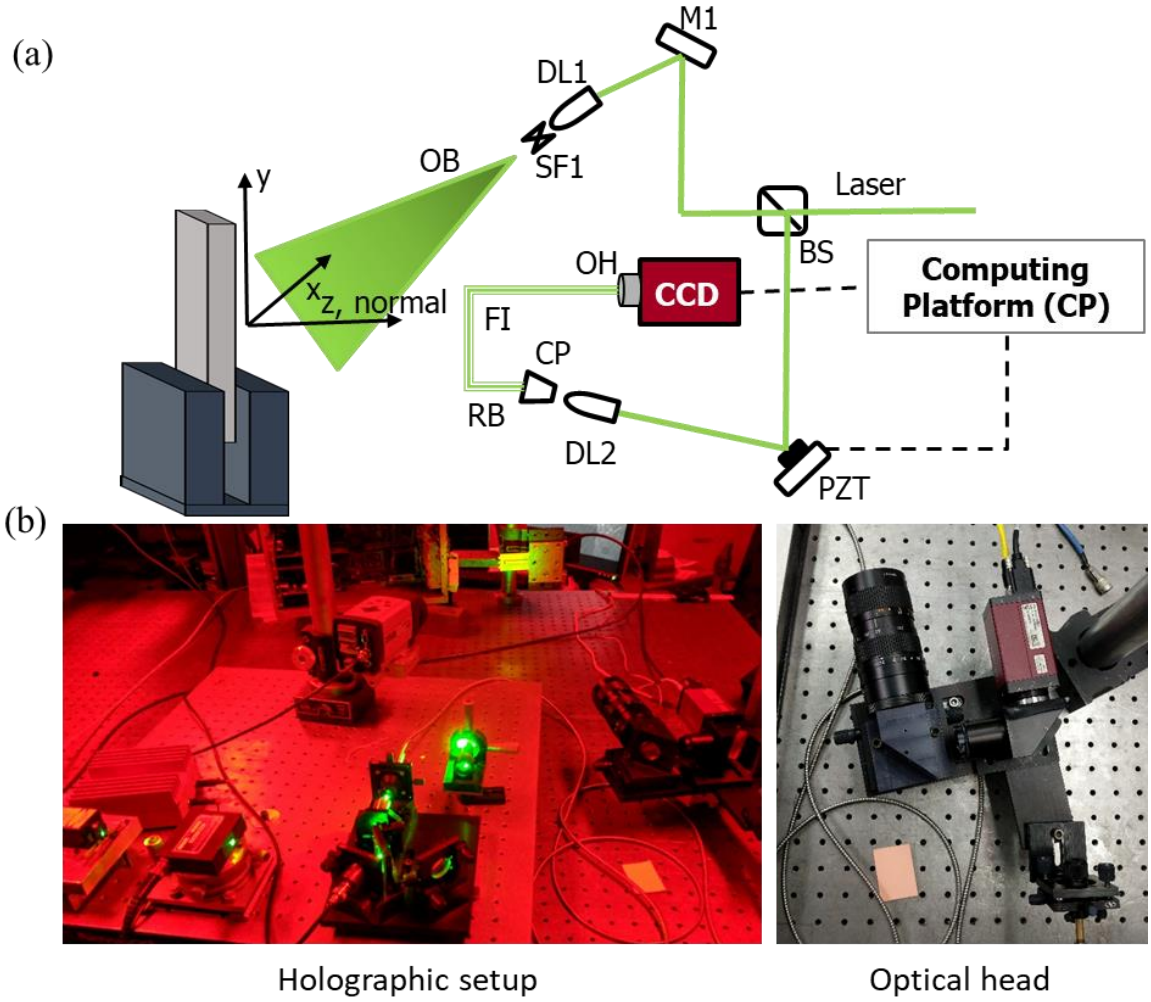

Fig. 27. Digital holographic interferometric setup sensitive to out-of-plane displacement: (a) DHI setup: BS represents beam splitter; M1, mirror; PZT, piezo for phase stepping; DL1 and DL2, beam expanders; SF1, spatial filter; OB and RF, object beam and reference beam; FI, fiber; CP, fiber coupler; and CCD, video camera; and (b) The setup in operation with a close view of the optical head.

Cameras and the PZT were connected to a DAQ and computer platform for synchronization required for the 4-phase stepping algorithm. The digital CCD camera recording images is a Pike F-100 with a resolution of 1024 x 1024 pixel.

In addition to the holographic setup, we employed DIC using high-speed cameras. The setup was designed for impact analyses. We first used a pendulum mechanism for impacting the specimens and then tested the potential of a drop mechanism for impact tests. In both of these configurations, the transient responses of the specimens were measured using Phothron SAZ cameras with the temporal resolution of a maximum of 2 million frames per second. The schematic and the picture of the setups are shown in Fig. 28.

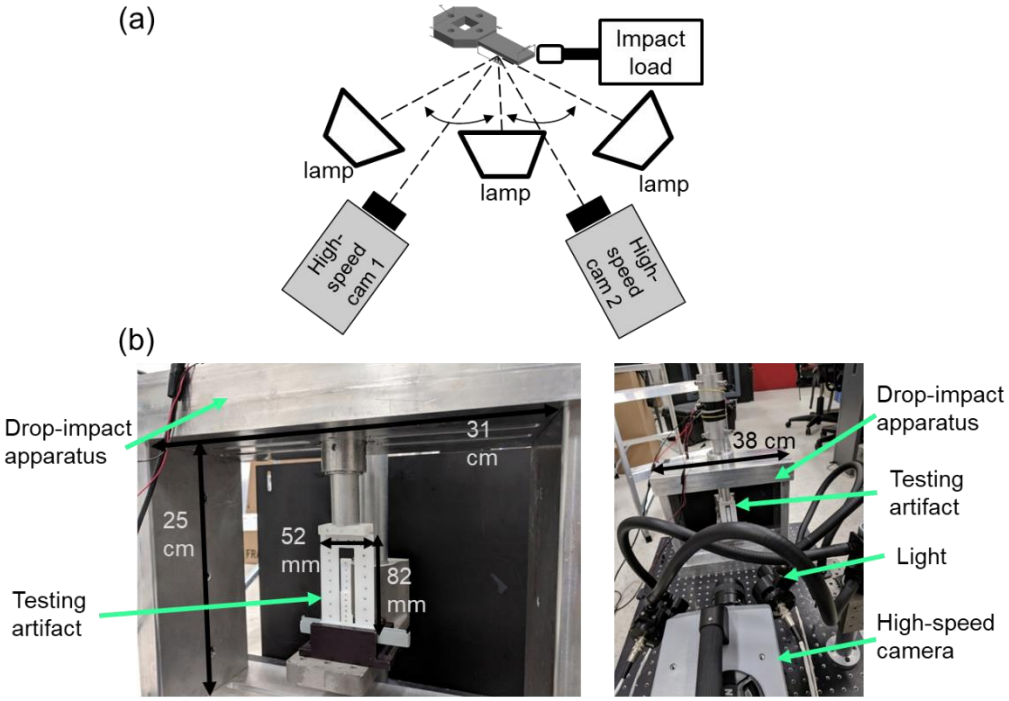

Fig. 28. Digital image correlation for impact analyses on the printed specimens: (a) Schematic of the stereo 3D DIC; and (b) the drop-impact setup for transient analyses on the printed artifacts 2D DIC.

3.3.2 Thermal flow effects and thermography

Temperature and cooling rate, as reported in several studies play crucial roles in the additive manufacturing processes, and measuring them can provide substantial information for predicting the material and part characteristics[8, 33, 38, 69, 107, 145, 151, 288, 289]. AM processes are vigorous, and dynamics, which conventional accurate measuring techniques such as

thermometer, thermocouple, and thermistor are not practical solutions. Thus, the non-contact methods, i.e., Infrared (IR) imager, pyrometer, laser absorption spectroscopy, and photodiodes are better choices [145, 146, 148, 290, 291]. Non-contact methods usually rely on quantifying the received radiative energy to predict the source temperature and require accurate knowledge of the transmissivity, emissivity, and absorptivity of a surface of the source and the participating media, if any. These characteristics vary depending on temperature and color.

In this dissertation, we employed IR imager, calibrated it, and measured material characteristics to deliver reliable full-field-of-view thermograms. Thermal imaging needs to account for emissivity and absorptivity of materials at high temperatures. Although these values for the variety of materials are available at room temperature, including polymeric materials used in FDM, the magnitude and changes in elevated temperature require further investigation specifically for one of the widely used polymers known as ABS.

We estimated the emissivity of three differently colored ABS polymers between 40 to 200^{o}C. This range of temperatures is critical to the bond formation and welding of the polymer, which eventually defines the mechanical strength of the printed components. Using a calibrated IR imager and thermocouples, we measured the emissivity of different ABS polymeric rings at various temperatures. These measurements are based on the comparison between equivalent emissive power at measured temperatures and the measured emissions from a calibrated blackbody. This allows for the determination of subtle changes in emissivity of the ABS polymer. The estimated emissivity is mapped to correct the full-field temperature readout of the IR imager, *in-situ*, and help to monitor the thermal flow accurately. Verification was carried out based on numerical simulations as well as experimental measurements of several cylindrical and cubical specimens (e.g., 3, 5, 7, 10, 11 mm).

3.3.2.1 Principle of thermography by Infrared camera

IR cameras are devices that receive emitted energy from an object of interest and convert them into images. The color and contrast in these images are based on the amount of energy received. The sum of the absorption, reflection, and transmission of radiative energy from each surface is equal to the total incident radiative flux. The IR cameras' detectors measure radiosity, which is a sum of reflection and emission from a particular surface. In addition, the emissivity and transitivity of the media between the source and the detector affect the temperature measurements. In theory, the total received energy contains emission from the object, reflections of other sources, losses due to transmission through, and emission of the participating media [150]. For an object located in the atmosphere, the total energy received by the camera detector is defined as:

$$E_{tot} = \varepsilon_{obj} \cdot \tau_{atm} \cdot E_{obj} + \rho_{obj} \cdot \tau_{atm} \cdot E_{sur} + \varepsilon_{atm} \cdot E_{atm}, \tag{3-67}$$

where E is radiation flux, τ transitivity, ρ reflectivity, and ε emissivity and subscripts tot, obj, atm, and sur denote total, object, atmosphere, and surrounding, respectively. Kirchhoff theory states for each surface the absorptivity, α, is equal to emissivity, ε, in its equilibrium condition [254, 255]. In addition, one can conclude $\rho_{obj} = 1 - \alpha_{obj}$ for opaque surfaces. The atmosphere also is a transparent medium thus, $\varepsilon_{atm} = 1 - \tau_{atm}$. Finally, Eq. (3-67) is rewritten as:

$$\begin{aligned} E_{tot} = {} & \varepsilon_{obj} \cdot \tau_{atm} \cdot E_{obj} + \left(1 - \varepsilon_{obj}\right) \cdot \tau_{atm} \cdot E_{sur} \\ & + (1 - \tau_{atm}) \cdot E_{atm}. \end{aligned} \tag{3-68}$$

When the distance between detector and source is less than a meter, the effect of media can be ignored [150], and therefore τ_{atm} is equal to 1.0 and Eq. (3-68) is simplified to:

$$E_{tot} = \varepsilon_{obj} \cdot E_{obj} + \left(1 - \varepsilon_{obj}\right) \cdot E_{sur.} \tag{3-69}$$

The camera detector receives E_{tot} and uses the integrated lookup table to determine the temperature by knowing the emissivity, humidity, and distance. However, if these parameters are not defined correctly, the IR imager generally assumes the case of a blackbody object and estimates the temperature accordingly. This process leads to an incorrect estimation of the temperature and undervalues the readouts [149, 150]. By knowing the ε, these inaccurate readouts can be corrected either during or after recording the measurements.

3.3.2.2 Experimental setup and equipment

In our experimental measurements, we wanted to achieve three main goals: calibrating the IR camera, measuring the emissivity of three differently colored ABS polymer, and finally implementing gained knowledge to approximate the surface temperature *in-situ*. We designed our setup using an IR camera, type-T thermocouple, aluminum block, hot plate, calibrated blackbody, manual thermometer, aluminum tape, computer platform, high-efficiency thermal paste, and home-made cooling accessories as shown in Fig. 29.

The IR camera was situated above the hot plate facing the center of the aluminum block on the hot plate (Fig. 29-a). In addition, a cooling apparatus consisting of a PVC pipe and a computer fan was utilized above the aluminum block to minimize the effects of the medium. This configuration is shown in Fig. 29-b. The type-T thermocouple was installed between the aluminum block and the aluminum adhesive tape, as shown in Fig. 29-c, and it was connected to the DAQ using LabView to record the temperature continuously. The calibrated blackbody and the computer platform was used to determine the sensitivity of the IR camera (Fig. 29-d). A representative thermogram captured by the IR camera of the blackbody is shown in Fig. 29-g. The image shows a constant distribution of temperature on the surface of the blackbody and the defined AOIs for estimating the radiosity.

In order to provide a stable condition, a block of aluminum (76.03×121.68×37.70 mm) as shown in Fig. 29-a and b was located on the hot plate. The surface of the block was covered with adhesive reflective aluminum tape, where the washers were positioned (Fig. 29-c).

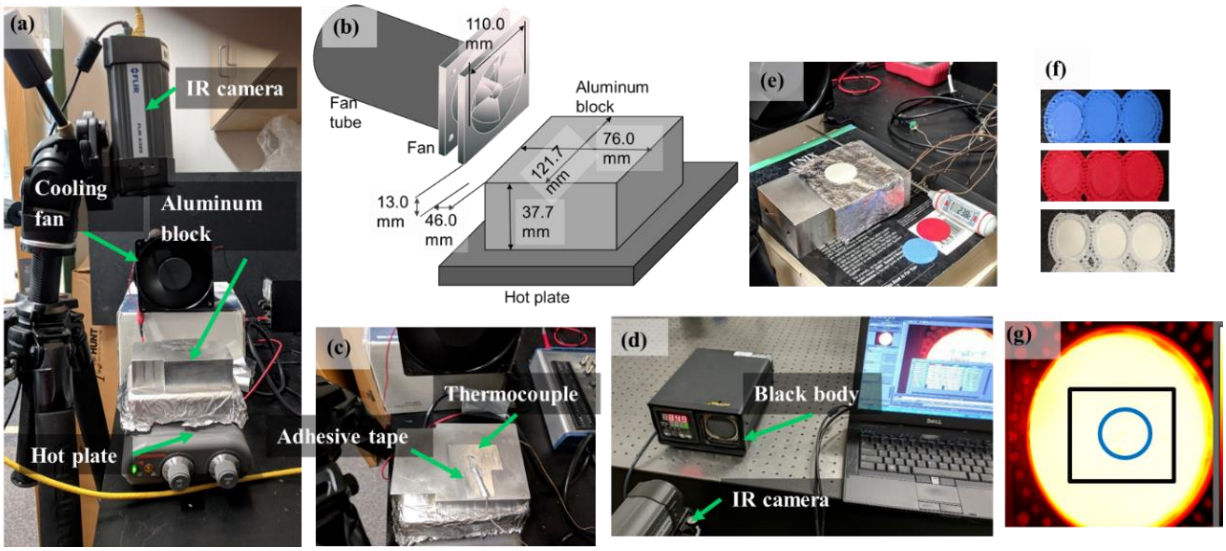

Fig. 29. The configuration of the setup and equipment were used for camera calibration, emissivity estimation, and temperature measurements: (a) IR camera, hot plate, and aluminum block; (b) cooling apparatus; (c) thermocouple installed between the aluminum block and the aluminum adhesive tape; (d) calibrated blackbody and the computer platform; (e) thermometer and the ABS washers; (f) the 3D printed washers consist of three sets of differently colored ABS polymers; and (g) a snapshot of the blackbody captured by the IR camera showing the Area Of Interests.

Between the adhesive tape and aluminum block, a thermocouple was fixed and situated at the center of the block. A highly conductive thermal paste also covered the distance between the aluminum tape and the washer to guarantee a steady and constant thermal flux between two dissimilar materials and fill all the possible void areas between them. A manual thermometer and humidimeter also were used to monitor the room temperature and humidity (Fig. 29-e).

3.3.3 Estimation of heat transfer and temperature distribution in FDM

Cylinders of specific dimensions satisfying the lumped-capacity model were fabricated while thermograms were recorded during the consolidation and cooling phases. These recorded

thermographic data were utilized to estimate the combined convection-radiation heat transfer coefficient, i.e., the total heat transfer coefficient (THTC), which we assumed could be described by a mathematical function as described in section 3.2.1.2.2. To determine the parameters of this function, the following iterative procedure based on the least-squares error minimization algorithm was employed

1. assume a mathematical model to describe the THTC (incorporating radiation and convection heat transfer coefficients),
2. set up an initial 1D transient numerical model with assumed boundary conditions and thermal parameters,
3. record thermograms *in-situ* while a part is fabricated with specific manufacturing parameters,
4. run the numerical simulation,
5. quantitatively compare numerical and experimental results,
6. adjust the total heat transfer coefficient following the assumed mathematical function and using least square error minimization to find the coefficients,
7. run steps 4 to 6 until to achieve a good agreement between numerical results and experimental measurements.

With the estimated THTC in 1D, the model is expanded to 2D in a similar cylindrical coordinate system by modeling the layer-by-layer deposition in radial, r, and axial, z, directions simultaneously. During all steps of deposition, the estimated THTC from the 1D analysis is used at the boundaries to model local heat dissipation. The transient simulations were based on the hypothesis that the estimated THTC from 1D was able to predict realistic heat transfer effects in 3D. Such a hypothesis was tested by fabricating, modeling, and experimenting with a cylindrical

specimen of different diameters, i.e., 10, 20, and 30 mm, and the same height, i.e., 50mm±0.3mm.

3.4 Designed testing artifacts

3.4.1 Concept and fundamental of the designed testing artifacts

We used the concept of a cantilever beam to design testing artifacts with geometries similar to those shown in Fig. 30.

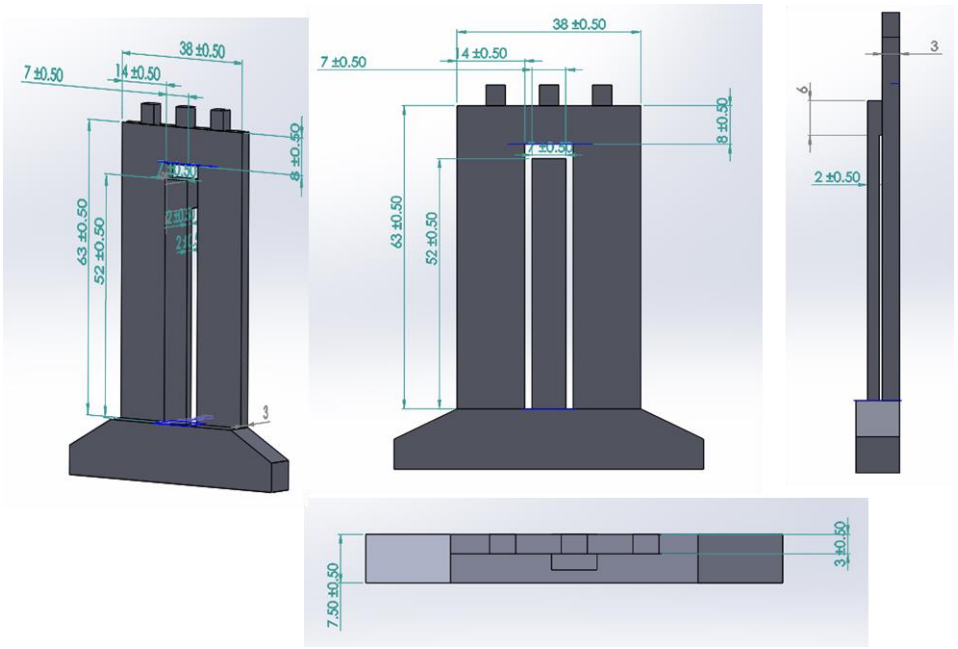

Fig. 30. The isometric, front, side, and top view of the designed testing artifact taken from Solidworks ®.

We parameterized our designs such that it was possible to alter their geometrical, structural, and physical properties from one to another. For each of them, we utilized finite element analysis to obtain their corresponding natural frequencies and mode shapes.

We related the geometry and shape to structural characteristics and subsequently studied the effects of specific process parameters through experimental investigations by modal analyses. Testing artifacts similar to the one shown in Fig. 30, were used to characterize the mechanical and structural properties of components printed with different process parameters using DHI.

3.4.1.1 Analytical modal and sensitivity analyses of a beam shape specimen

It was necessary to understand the sensitivity of the beam part of the testing artifact to geometrical and structural properties. This knowledge is required for both computational and experimental analyses to help understand the acceptable margin of the calculated values and know which parameters may affect the result more severely.

We examined the sensetivity of a simplified structure analytically and then moved to computational sensitivity analyses by changing the parameters. As presented in section 3.1.3 Eq. (3-13) for a fixed area cantilever plate the module of elasticity can be formulated based on the natural frequency (ω_n), density (ρ), and dimensions as:

$$E = E(\rho, \omega_n, L, h) = \rho \times 12(1 - v^2)\left(\frac{\omega_n \times L^2}{\lambda_n^2 \times h}\right)^2.$$

The λ_n is found analytically to be the root of the following equation as listed in Table 4:

$$\cosh \lambda_n L \times \cos \lambda_n L + 1 = 0. \tag{3-70}$$

Where the first eight roots are :

Table 4: roots of the Eq. (3-70) for the first seven bending modes and first torsion mode of a cantilever beam

Mode	Eigenvalue
1st	$\lambda_1 = 1.8751$
2nd	$\lambda_2 = 4.6941$
3rd	$\lambda_3 = 7.8548$
4th	$\lambda_4 = 10.9955$
5th	$\lambda_5 = 14.1372$
6th	$\lambda_6 = 17.2788$
7th	$\lambda_7 = 20.4204$

1st Torsion mode*	$\lambda_{1T}^2 = 2.3327$

* The eigenvalue for the torsion mode was found according to $\omega_n = \lambda_n^2\sqrt{\frac{G}{\rho\times 12}}\frac{h}{L\times b}$ and $\lambda_n^2 = n\pi\sqrt{3}$, for $\frac{b}{h} \gg 1$.

We did sensitivity analyses on the natural frequency for each variable, and Table 5 lists the analytical estimated sensitivity of the module of elasticity to the mentioned parameters.

Table 5: Analytical sensitivity analyses of the isotropic module of elasticity of a cantilever beam.

Variable	Derivative
$\frac{\partial E}{\partial \rho}/E$	$1/\rho$
$\frac{\partial E}{\partial \nu}/E$	$-\frac{2\nu}{1-\nu^2}$
$\frac{\partial E}{\partial \omega}/E$	$2/\omega$
$\frac{\partial E}{\partial L}/E$	$4/l$
$\frac{\partial E}{\partial h}/E$	$-2/h$
$\frac{\partial E}{\partial \lambda}/E$	$-4/\lambda$

Because among variables *h*, thickness, is the smallest value, estimated elasticity is more sensitive to *h*, and one should especially pay attention to measure it [218, 219]. The effect of these parameters on the computational and experimental estimation based on the selected size of the testing artifacts are presented quantitatively in result chapters.

3.4.2 Effect of porosity and solidity ratio on modal analyses

Filament leaves the nozzle in an almost perfect circular shape, but it becomes semi-oval as a result of a 90 degrees turn right after and forces initiated with clearance less than the diameter of the nozzle between the extruder and previously deposited materials, as shown in Fig. 20. This

shape can be defined as a rounded rectangle with an end radius equal to the layer-thickness (clearance between the nozzle and the heated bed or previous layer). The total width of this oval-shaped deposited bead can be larger than the diameter of the nozzle, but it is usually not assumed more than 1.7 times larger. Increasing the flow rate allows the bead to be larger than the diameter of the nozzle. Deposited beads with this shape leave behind porosity.

The solidity ratio (SR) is defined as a ratio between the area of the filament to the rectangular area that the filament fits inside. The height of the bead plays a critical role in this ratio, and the higher the height is, the lower the ratio. The higher SR ratio has been attributed to better strength and improved mechanical properties, which can be credited to the stronger and longer weld between contiguous beads [8, 237, 292].

Various studies show that FDM printed parts have the highest tensile strength when printing orientation aligned with test orientation; in other words, when the raster angle is 0^o. The measured strength for rater angel 0^o is about 90-97% of the injected molded part that decreases to 70-75 % in raster angle of 90^o in a part with solid infill [293].

The effects of the SR can be observed noticeably in the 90^o orientation because the welding is the crucial point in the strength of the part, in this case. The lowest theoretical SR, which is equal to $1-\pi/4$, occurs when the two ellipsoidal beads just touched each other. Increasing SR means approaching a solid part, in which the strength significantly increases, as reported by Koch et al. [293]. The composite laminate theory also has been developed to study the effect of porosity and SR on the strength of the printed components [68, 173].

3.5 Design of Experiments (DoE) and statistical analyses

The goal of our study was to understand how build parameters affect distortion, moduli of elasticity, density, and bonding performance in 3D printed components by FDM technology. We

aimed to reach an empirical approximation of the outputs as a function of build parameters using the Design of Experiments (DoE) approach. DoE is a well-known method and more information can be found in Appendix 9.2.

Among different methods in DoE, we chose to apply a response surface method (RSM) to design our experiments in order to understand the interrelationships. Our literature review indicates several implementations of RSM for FDM and other AM technologies. This method has been used to reveal the relationships between process parameters and different properties with the minimum possible experiment [81, 103, 193, 294-299] and has a potential for optimization and customization [192, 193, 299-302]. During this process, we also did the screening design to make sure to select the essential parameters contributing to our goals, e.g., density, porosity, moduli of elasticity, and distortion.

3.5.1 Selecting the factors and variables for DoE

There are several printing parameters involve in FDM to be considered for analyses. However, some have been reported more influential than others, such as layer thickness, air gap, raster angel, and printing orientation. Besides, some parameters have not been studied adequately yet: for example, heated bed temperature, extruder temperature, cooling rate, and printing speed. The following table, Table 6, lists the different factors involved in 3D printing with FDM and the studies that investigated their effects. These factors can be categorized into three main areas, process parameters, manufacturing parameters, and printing parameters [14]. Also, some other parameters can be included which relate to material properties, humidity, colors, and slicer characteristics [16, 92, 176, 184]. The effects of material properties on mechanical and structural characteristics is a trivial conclusion; however, it is complex to quantitatively relate thermal and physical properties (e.g., CTE, density, module of elasticity,

specific heat capacity, and thermal conduction) to the existence and severity of defects such as distortion, delamination, and warpage [107].

Table 6: The list of the factors affecting 3D printing by FDM.

Description	Type	Category	Range	Studied by others
Nozzle size, D	Continues/Categorical	Manufacturing	0.2-11 mm	-
Heated bed	Categorical	Manufacturing	With/without	-
Heated bed temperature	Continuous	Printing	20-130 ºC	[303]
Layer thickness	Continuous	Process	0.1xD - D	[42, 81, 82, 85, 94, 104, 183, 190, 192, 193, 198, 199, 268, 285, 294, 302, 304-311]
Contour width	Continuous	Process	D-1.7D	[306]
Road (raster) width	Continuous	Process	D-1.7D	[42, 104, 183, 198, 199, 285, 300, 302, 306, 307, 309, 312, 313]
Feed rate	Continuous	Process	0.002-0.37 kg/s	[42, 186, 285, 294, 302]
Printing speed	Continuous	Printing	2000-18000 mm/min	[82, 94, 186, 285, 302, 308, 310, 311]
Printer size	Categorical	Manufacturing	Small, medium, large	
Headed bed material	Categorical	Manufacturing	Glass, Aluminum, Copper, PEI, …	
Extruder working temperature	Continuous	Printing	220-400 oC	[94, 186, 308, 311, 313]
Infill	Continuous	Process	10-95 %	[190, 304, 311, 314]
Raster angle	Continuous	Process	0-90 degree	[81, 85, 86, 94, 104, 183, 192, 193, 198, 199, 268, 300, 305-307, 311, 312, 315, 316]
Printing orientation	Categorical	Process	X, Y, Z, up-right, flat, on-edge, …	[86, 183, 190, 192, 193, 198, 294, 300, 303, 305, 308, 309, 312, 315]
Part position on the bed	Categorical	Process	Center, north, south, east, west, SW, …	

Filament diameter	Categorical	Manufacturing	1.75 mm, 3.0 mm	
Feeder type	Categorical	Manufacturing	Filament, pellet	
Stock material type	Categorical	Manufacturing	Pellet, filament	
Machine style	Categorical	Manufacturing		
Enclosure	Categorical	Manufacturing	Enclosed, Open	
Environment Control	Categorical	Manufacturing	Convection hot air, heated bed	
Enveloped temperature	Continuous	Printing	40-80 ^{o}C	
Component size	Continuous	Printing	2 to 15000 mm	
Air gaps	Continuous	Process	D-1.7D	[85, 86, 104, 183, 191, 193, 198, 199, 300, 305-307, 310]
Infill patterns	Categorical	Process	Line, Rectilinear, grid, honeycomb, hexagonal,	[314]
Number of contours	Categorical	Process	1, 2, 3, …	[81, 104, 190]
Cooling rate	Continuous	Printing	0 to 100 %	
Cooling mechanism	Categorical	Manufacturing	No, fan-cooled,	

The above table is not inclusive, and there may be other parameters to consider as well. Most studies targeted the effect of listed parameters (factors) on the critical characteristics (variables) associated with quality, mechanical properties, dimensional characteristics, and aesthetics of the printed components. Those characteristics include, for example, flexural strength, hardness, tensile strength, compressive strength, dimensional accuracy, surface roughness, production time, yield strength, and ductility. It has been shown there is a definite interrelationship between factors and variables which justifies the development of optimized experimentation based on the concept of DoE to not only find the optimum configuration but also seek the potential mathematical framework to define these variables as functions of factors.

We explained in Chapter 1.4 that our primary goal is to study the crucial characteristics of distortion, residual stresses, and mechanical properties as a function of build parameters. Considering the list of variables and the number of studies on parameters like an air gap, raster

thickness, raster angle, and printing orientation, we ruled out these parameters. Also, there are different parameters in the list—such as feeding mechanism, cooling mechanism, feeder type, stock material, under manufacturing categories—that required access to a variety of different printers. In addition, there are parameters for which there are a few or no investigations, including cooling rate, heated bed temperature, and enveloped temperature.

Finally, considering our goals, background study, preliminary thermal analyses, and numerical modeling, we decided to develop studies in four levels and at each one, examine the selected set of factors. Table 7 lists these four levels along with the associated factors to be investigated. In this table, "Yes" and "No" indicates whether, under each category, the particular factor is considered for analyses or not.

It also should be noted that in this dissertation, only the experimental and 1D modeling are studied, and 2D and 3D simulation will be part of the continuation of this research.

Table 7: The list of the selected factors studied in this dissertation and the four different case studies.

Row	Variables	units	Abbreviation	Values	1, Modeling 1D	2, Modeling 2D	3, Modeling 3D	4, Experiments
A	Extruder temperature	°C	ET	240	yes	yes	Yes	yes
				265				
				290				
B	Heated bed temperature	°C	HBT	40	yes	yes	Yes	yes
				70				
				100				
C	Layer thickness	mm	LT	0.2*D	yes	yes	Yes	yes
				0.55*D				
				0.9*D				
D	Extruder	mm/mi	ES	-50, slow	yes, it	yes	yes	yes

	speed	n		0, normal 50, fast	represents the feed rate in 1D			
E	Fan speed	%	FS	0 50 100	yes	yes	yes	yes
F	Envelope temperature	°C	TE	40 65 90	yes	yes	Yes	No
G	Contour width	mm	CW	D 1.35*D 1.7*D	No	yes	yes	No

3.5.1.1 Selecting the factors and variables for DoE of 1D thermal analyses

We also considered another attempt to verify the effect of temperature and speed and add size consideration to our analyses because size is a critical parameter affecting the average deposition velocity. The larger the cross-section, the longer the time for depositing material.

This analysis also was designed to be used for thermal investigation. The square or circular cross-sections allowed us to investigate the validity of a 1D thermal analysis for the evaluation of the performance of 3D printing. Through this investigation, one is able to explore the effectiveness of simplified numerical analyses for estimating bonding performance in 3D objects. The fixed cross-sections relaxed dimensional complexity. In addition, combining numerical simulations with *in-situ* experimental investigation set the ground for prediction and measuring factors such as bonding potential and bond quality. These factors exclusively evaluate bonding efficiency and contact performance based on thermal flow and temperature history.

The defined DoE table and the critical parameters are listed in Table 8. In this analysis, we assumed layer thickness, heated bed temperature, fan speed, and enveloped temperature were fixed and changed diameter, printing speed, and extruder temperature.

Table 8: The list of the selected factors studied for 1D thermal numerical-experimental comparison and contact performance.

Row	Variables	units	Abbreviation	case	Values
1	Extruder Temperature, A	°C	ET	-1	240
				0	265
				1	290
2	Extruder Speed, D	mm/min	ES	-1	-50, slow ,2000
				0	0, normal, 4000
				1	50, fast, 6000
3	Block side size, H	mm	BS	-1	3
				0	7
				1	11

3.5.2 Application of DoE for analyzing the effect of process parameters

The primary purpose of a DoE is to efficiently assist in understanding the relationships between factors and variables and determine the factors' significance in a given experimental setting [317]. There were assumptions involved before the design and execution of experimental investigation using DoE. First, we assumed there were non-linear relationships between factors themselves and variables, which could be captured by RSM. Also, we assumed these relationships between factors and variables could be defined in a continuous output. We selected seven sets of variables listed in Table 7 and different goals for 1D modeling, 2D modeling, 3D modeling, experimental investigation, and the special case of testing cubes, as listed in Table 8. For each set of goals, we used DoE to run the experiments efficiently. Second, we studied the

residuals carefully to ensure our models were reliable. Our residuals were checked against normal distributed and independently distributed with a mean of 0 [317]. We also assumed the confidence interval level of 95% for all of the analyses. Finally, the standard studies such as analyses of variance (ANOVA), t-test, and P-values were performed for validations.

Assuming five variables, we used a method known as face-centered central composite design (FCCCD) with three levels for each factor to reduce the iteration to 28 (Appendix 9.2). The following table shows one of the designed tables for columns "4, Experiments" in Table 7 sorted left to right. The minimum, medium, and maximum of all values representing the range of permissible magnitude for the analyses of the factors as listed in Table 9. The entire 28 runs are listed in the table, including two center point runs.

Table 9: Experimental plan for FCCCD design of a response surface consisting of five essential factors.

Run	Pattern	Extruder Temperature, ET	Heated Bed Temperature, HBT	Layer thickness, LT	Extruder Speed, ES	Fan speed, FS
1	−−−−−	240	40	0.09	-50	0
2	−−−++	240	40	0.09	50	100
3	−−+−+	240	40	0.29	-50	100
4	−−++−	240	40	0.29	50	0
5	a0000	240	70	0.19	0	50
6	−+−−+	240	100	0.09	-50	100
7	−+−+−	240	100	0.09	50	0
8	−++−−	240	100	0.29	-50	0
9	−++++	240	100	0.29	50	100
10	0a000	265	40	0.19	0	50
11	00a00	265	70	0.09	0	50
12	000a0	265	70	0.19	-50	50
13	0000a	265	70	0.19	0	0

14	00000	265	70	0.19	0	50
15	00000	265	70	0.19	0	50
16	0000A	265	70	0.19	0	100
17	000A0	265	70	0.19	50	50
18	00A00	265	70	0.29	0	50
19	0A000	265	100	0.19	0	50
20	+−−−+	290	40	0.09	-50	100
21	+−−+−	290	40	0.09	50	0
22	+−+−−	290	40	0.29	-50	0
23	+−+++	290	40	0.29	50	100
24	A0000	290	70	0.19	0	50
25	++−−−	290	100	0.09	-50	0
26	++−++	290	100	0.09	50	100
27	+++−+	290	100	0.29	-50	100
28	++++−	290	100	0.29	50	0

3.5.2.1 Application of DoE for analyzing 1D thermal flow

We selected different sizes of the cuboids and studied the effect of extruder speed, and extruder temperature, to analyze the thermal flow, density, and contact quality. The parameters and their limits are shown in Table 10. We carried out the design using the same assumption, this time on only three factors. Table 10 listed the 16 iterations, including two center iterations for this analysis.

Table 10: Experimental plan for FCCCD design of a response surface consisting of three essential factors analyzing 1D thermal flow.

Run	Pattern	Block Size, BS	Extruder Temperature, ET	Extruder Speed, ES
1	−−−	3	240	-50
2	−−+	3	240	50
3	a00	3	265	0

4	−+−	3	290	-50
5	−++	3	290	50
6	0a0	7	240	0
7	00a	7	265	-50
8	000	7	265	0
9	000	7	265	0
10	00A	7	265	50
11	0A0	7	290	0
12	+−−	11	240	-50
13	+−+	11	240	50
14	A00	11	265	0
15	++−	11	290	-50
16	+++	11	290	50

3.5.3 Data acquisition and analytics

The designed DoE helped us to collect experimental data systematically and efficiently where the accuracy and the effectiveness of the methodology were warranted with statistics. The different sets of experiments were carried out in the lab, and the results were collected for further analyses using statistical software such as JMP and Matlab. Specimens were printed using a Zortrax M200 FDM printer. The Simplified 3D software was used to change the parameters as listed for each experiment, and the G-code was translated to the machine code for fabrications.

The collected data was used to predict equations defining the response of the variable to the assigned factors based on a full quadratic model. Residual analysis and effect tests were run to validate the models. Using response surface methodology led to obtaining the empirical relationships between factors (process parameters) and variables (density, distortion, contact quality, and thermal flow). The successful development of the DoE provided the data required for understanding the complex relationships between parameters that helped to investigate the

optimum printing configuration for desirable variables or estimating some properties of the printed parts with better confidence.

In our analyses general numerical statistical indicators such as R^2, R^2 adjusted, Lack of Fit tests, ANOVA tables, p-values, and LogWorth ($-log_{10}(\mathrm{p-value})$) were evaluated.

4. Results

We have explained our methods, theories behind them, and the details of the combined numerical-experimental work. In this chapter, we focus on analyzing gathered data, comprehending the complexity of polymeric 3D printing, and constructing a better understanding of the relationship among some process parameters and mechanical and geometrical properties of 3D printed components.

We start with emissivity measurement and IR Imager calibration. Then we discuss the numerical thermal analyses in 1D and 2D and apply them to evaluate total heat transfer coefficient, density, and conductivity. We also present the Thermo-mechanical analyses in 2D and illustrate how the proposed considerations could deliver a better numerical model capable of simulating distortion and residual stresses.

We then report on our modal analyses and perform sensitivity studies on the designed testing artifact. These efforts help us to estimate the eigenvalues and find their dependency on Poisson's ratios. These eigenvalues are needed for accurate estimation of structural properties for both isotropic and orthotropic materials in the experimental section of this dissertation.

Next, we switch gears to the experimental outcome of this work by characterizing ABS filaments. We continue with the density evaluation of cubes and estimation of isotropic and orthotropic structural properties of several 3D printed artifacts under changing process parameters, from one iteration to another. To conceive the underlay relationships among selected process parameters and some physical and structural characteristics of polymeric 3D printed components, we carried out ANOVA and statistical analyses. We also illustrate the positive effects of calibration of IR imager and emissivity on *in-situ* thermography using an IR camera.

4.1 Estimation of the emissivity

4.1.1 IR camera calibration and analysis

We calibrated an IR camera to first establish a reliable measurement reflecting the correct temperature, and second, used the calibrated camera to measure the emissivity of different colored washers of ABS.

The energy received by a detector of a thermal imager can be merely representative of blackbody radiation if one can assume the emissivity of the object of interest is 1.0, and the effect of participating media is negligible. We employed a calibrated blackbody and keep the distance between the thermal imager and the blackbody about 200mm, to satisfy both criteria. Therefore, the total energy received by the detector is equal to:

$$E_{tot} = E_{obj} = E_{blackbody.} \tag{4-1}$$

The employed thermal imager is an IR camera with a broad spectrum sensitivity in mid-infrared regions (7-18 μm) [150]. The relationship between a camera's readout and temperature can be defined mathematically as a power function explained in Eq. (4-2). This function has been chosen knowing that the blackbody total emissive flux follows a power function in a wide spectral range:

$$readout(T) = \mathrm{a}T^{b} + c. \tag{4-2}$$

We started with the calibration of the thermal imager under an environment similar to a normal camera's working conditions. Figure 29-d shows such a setup used for this study. The set up consisted of an IR camera, computer platform, and calibrated blackbody. The temperature of the blackbody changed from 45 to 345^{o}C in 13 steps, both ascending and descending, and we recorded the room temperatures regularly. The measurement of thermograms was repeated three

times in the laboratory while the room temperature and humidity fluctuated between 20-25^{o}C and 30-45 %, respectively.

At each step, the camera recorded thermograms similar to the one shown in Fig. 29-g and the data associated with the Area Of Interests (AOI) were stored for further analysis and curve fitting using MATLAB®. The curve fitting results show a strong correlation with the coefficient of determination (R^2) being above 0.99. Figure 31 shows the fitted lines, and Table 11 lists the results of curve fitting. We did the curve fitting for three different cases, assuming the temperature in Kelvin and degrees centigrade. Comparing the fitted curve with the camera's readout at low temperature, particularly close to room temperature, showed the accuracy of the degree ^{o}C fitted curve was more than the Kelvin fitted curve.

Table 11: The derived coefficient and a few statistical information of curve fitting for estimating the response curves to blackbody radiation.

Description	Based on Kelvin	Based on Kelvin assuming c=0	Based on Degree C
Coefficients, a	0.008596	0.02272	5.869
Coefficients, b	2.432	2.286	1.527
Coefficients, c	1899.697	0	10464.94
R-squared	0.9997	0.9998	0.9999
Root-mean-square error (RMSE)	240.0865	184.8451	61.1491

After measuring the camera's response curves, we then estimated the emissivity of the 3D printed ABS washers similar to those shown in Fig. 29-f. We printed nine washers with a thickness of 0.8 ±0.1 mm and a diameter of 30.0 ±0.5 mm in three different colors and tested them with the setup explained in chapter 3.3.2.2. The aluminum block, shown in Fig. 29, was heated up until its top surface reached 240^{o}C, after which the washers were carefully situated at its center, where they made contact with the thermocouple. Thermal paste was carefully spread

across the contact area between the washers and the surface of the aluminum block, and a small metallic roller was used to ensure the washers were firmly attached to the surface.

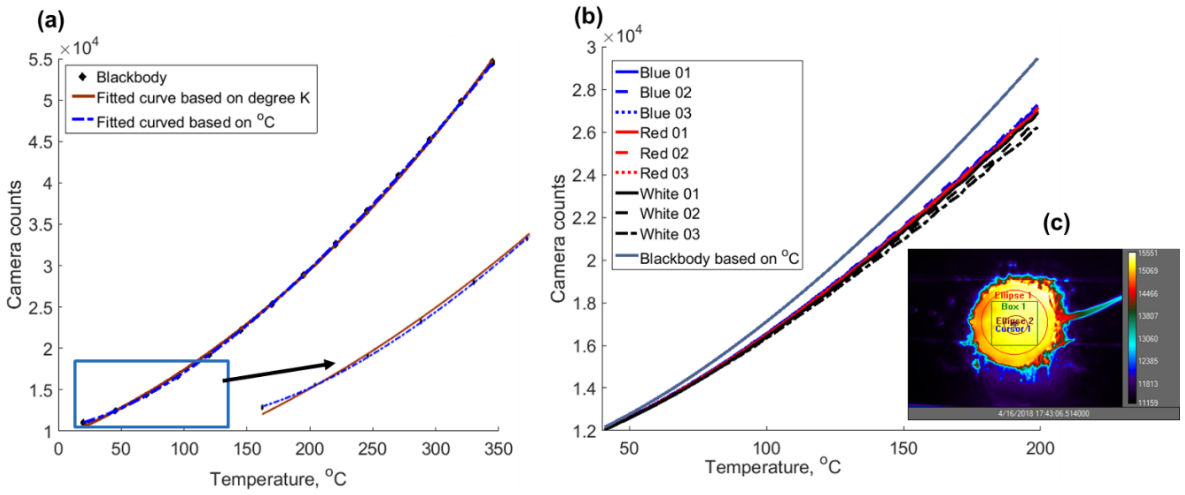

Fig. 31. The acquired data for blackbody and washers and snapshot of the IR camera: (a) three measurements of the blackbody with temperature ranging between 25 to 345 °C with the curved fitting based on K and °C; (b) the response curve of the blackbody juxtaposed with the nine measurements on the washers with temperatures ranging between 45 to 200°C; and (c) a representative snapshot of the IR camera showing the different AOIs used for analyses.

After about five minutes, the system reached a steady-state, at which point the hot plate turned off, and measurements started. The DAQ and the LabView® program acquired the temperatures of the contact point between washer and aluminum block with the data acquisition rate of 1MBs. An interface was designed to calculate the average and standard deviation of the 10,000 subsequent acquired temperatures and store them as a text file. Also, the IR camera located right above the hot plate at a distance of about 200mm captured the thermograms as well. The Cold Junction (CJ) was set based on the room temperature, which was monitored continuously using a thermometer and the required changes were applied to CJ as needed. The room temperature fluctuated between 18 to 21°C during different measurements. The humidity also monitored, which was always less than 40% during all measurements. Humidity caused no

significant effect on the total measurements due to the short distance between the camera and the target surface.

Images and temperatures were stored and later used in Matlab for data analysis and curve fitting. The clock of the DAQ and the camera was used for matching the temporally stored data. We estimated the emissivity at various temperatures using Eq. (3-69) by knowing E_{tot} from the IR camera's readout and E_{obj} from the blackbody response at the specific temperature. In this equation E_{sur} was plugged in based on the room temperature measurements.

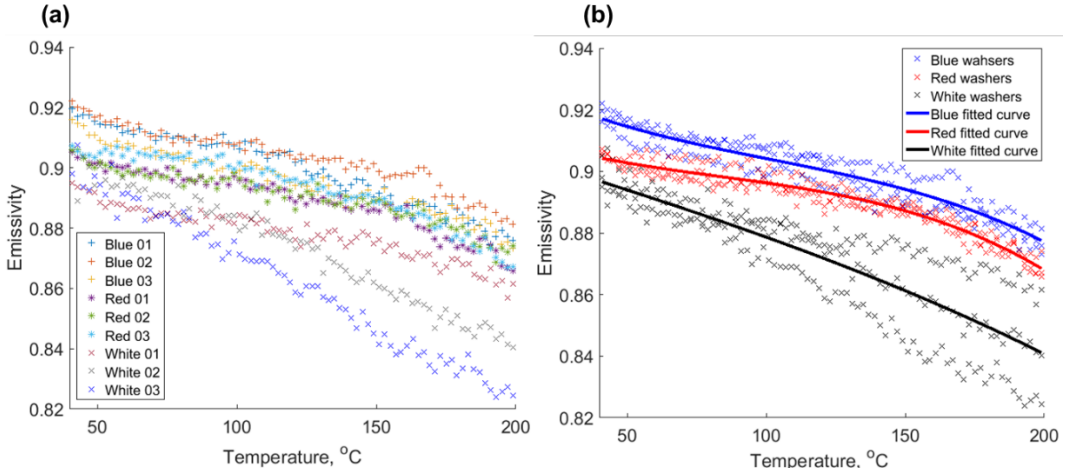

Fig. 32. The estimated emissivity based on the gathered data and fitted curves: (a) scatter plot shows the determined emissivity values of the nine different washers indicating a similarity in trends and effects of the colors; and (b) the entire pool of data for all measurements and the polynomial fitted curve showing the trends and the estimated values.

As shown in Fig. 31-c, a few different AOIs were defined on the washer. The curve fitting and analysis were based on the data within the area of "Ellipse 2", which consisted of 732 pixels, and the comparisons among different AOIs did not show any significant differences in average reported radiosity. The total irradiances off the surface of the washers were measured in camera counts within the 16-bit bandwidth. Figure 31-a illustrates the total readout counts of the IR camera, while Fig. 31-b shows the fitted curves for a blackbody and three sets of measurements for white, blue, and red ABS washers. The difference between a blackbody and the ABS

washers readout increases as the temperature increases, which indicates that at higher temperatures, the emissivity of the ABS decreases. In general, all three different colors show relatively similar trends. Although white ABS is less emissive compared to that of blue and red, the difference between the latter two is negligible.

Table 12: Curve fitting coefficient and statistical information on curve fitting for the entire obtained points for three different colored washers based on Kelvin.

Description	Blue washers	Red washers	White washers
Coefficient, a	-9.916×10^{-9}	-1.022×10^{-8}	-1.487×10^{-9}
Coefficient, b	1.118×10^{-5}	1.093×10^{-5}	1.252×10^{-6}
Coefficient, c	-0.00438	-0.004019	-0.0006367
Coefficient, d	1.497	1.405	1.019
R-square	0.8642	0.9199	0.7145
Root-mean-square error (RMSE)	0.0042	0.0028	0.100

The emissivity is determined and shown in Fig. 32-a. The emissivity, in general, follows a decreasing trend as temperature increases. The measured emissivity in room temperature was approximately 0.89 to 0.92, which is within the expected value for non-conductive materials (0.90 to 0.97)[318], and matches the value of 0.917 measured by the Gier-Dunkle reflectometer for red ABS [318]. The emissivity drops to 0.82 as temperature ascends to 200^{o}C for white ABS.

Figure 32-b also illustrates all the measured points of the samples for each color, and the solid line is the fitted curve based on the entire poll of data for the same colors. A polynomial of degree three ($a \times x^3 + b \times x^2 + c \times x + d$) was used for the curve fitting.

Table 12 lists the coefficients of the polynomial along with some statistical values. The coefficient of determination is above 0.71 for white washers and above 0.86 for red and blue,

which indicates a reasonable correlation between temperature and emissivity. These curves indicate that the difference between blue and red washers decreases as temperature increases.

Gathered data also shows that the emissivity of white washers is lower and decreases more dramatically compared to two others. The curve fitting also exhibits a slowing slope in temperatures between 110 to 130°C, which is attributed to the T_g of the ABS polymer.

4.2 Numerical results discussions

4.2.1 1D numerical modeling

4.2.1.1 Non-dimensionalization of the partial differential equations for 1D

We analytically studied the sensitivity of the filament temperature to some of the main variables in the list of selected process parameters, Table 7. Non-dimensionalization can provide an extendable understanding of the effects of some of the parameters. Thus we revisited the 1D ODE from chapter 3.2.1.2.2, Eq. (3-44) as shown here:

$$c_p U \frac{\partial T}{\partial z} = k\left(\frac{\partial^2 T}{\partial z^2}\right) - \frac{4}{d} h_T (T - T_\infty), \tag{4-3}$$

and we introduced the following none-dimensionalized terms to define a new ODE:

$$\tau = \frac{t \times \alpha}{d^2}, t = \frac{z}{U}, z = \zeta d, \alpha = \frac{\kappa}{\rho c_p}, Bi = \frac{h_t \times d}{4 \times \kappa}, \theta = \frac{T - T_\infty}{T_{Ext} - T_\infty}, \tag{4-4}$$

ζ is non-dimensionalized length, and the rest are previously defined. It is worth noting that z, which can be defined based on extruder motion or a slender part deposition direction, indicates the axis of 1D analyses.

One can rewrite the Eq. (4-3) in the following non-dimensionalized form:

$$\frac{U}{d}\frac{\partial \theta}{\partial \zeta} = \frac{\alpha}{d^2}\frac{\partial^2 \theta}{\partial \zeta^2} - \frac{16}{d^2} Bi \times \alpha\theta. \tag{4-5}$$

We solved Eq. (4-5) for a filament leaving an extruder with the area equal to the area of a nominal size of the extruder. In this case, z-axis is along the relative direction of the extruder

with *U* indicating the speed. We assume the coordinates are attached to the extruder and move with it. We also speculate that the filament leaves the extruder in temperature equal to the extruder temperature. *L* is the deposited length at time *t*, and by applying the following boundary conditions, one can obtain non-dimensional temperature distribution, θ, as:

With $\theta_1 = 1$ at $\zeta = 0$ and $0 \leq t \leq \frac{L}{U}$

And $\theta_0 = 0$, at $\zeta = \infty$ and $0 \leq t \leq \frac{L}{U}$

$$\theta = e^{-\varphi\zeta}, \tag{4-6}$$

where $\varphi = \frac{\sqrt{1+64\left(\frac{\sqrt{Bi}\alpha}{dU}\right)^2}-1}{2\times\frac{\alpha}{dU}}$, and $\zeta = \frac{Ut}{d}$.

We define a critical length, L_c, the length which the temperature of the filaments falls under the glass transition temperature, T_g,

$$L_c = d \times \zeta_c, \tag{4-7}$$

where, $\theta_c = \frac{T_g - T_\infty}{T_{Ext} - T_\infty}$, and T_g is glass transition temperature. We found L_c as:

$$\mathrm{Ln}\,\theta_c = -\varphi\zeta_c = -\frac{\sqrt{1+64\left(\frac{\sqrt{Bi}\alpha}{dU}\right)^2}-1}{2\times\frac{\alpha}{dU}}\zeta_c, \tag{4-8}$$

$$\zeta_c = \frac{-\mathrm{Ln}\,\theta_c \times 2\times\frac{\alpha}{dU}}{\sqrt{1+64\left(\frac{\sqrt{Bi}\alpha}{dU}\right)^2}-1}, \tag{4-9}$$

$$L_c = d \times \frac{-\mathrm{Ln}\,\theta_c \times 2\times\frac{\alpha}{dU}}{\sqrt{1+64\left(\frac{\sqrt{Bi}\alpha}{dU}\right)^2}-1}. \tag{4-10}$$

Equation (4-8) gives the non-dimensional critical length, ζ_c, from which the critical length, L_c, is obtained. We estimated the critical length and critical time for different configurations.

Before, we first estimated the coefficient of convection heat transfer, h_{conv}., and Biot number, as listed in Table 13.

Table 13: The Biot number calculated for different diameter for medium velocity 1.7 m/s for a cylindrical shape resembling the filament

Scale	Nozzle diameter range, mm	Common nozzle diameter, mm	Estimated coefficient of convection, W/m^{2}K	Biot No	Estimated coefficient of convection for common size, W/m^{2}K	Biot No.
Micro	0.2-0.6	0.4	339.69-184.80	0.077-0.126	230.59	0.105
Meso	0.6-2	1.0	184.80-97.39	0.126-0.221	140.44	0.16
Medium	2-8	6	97.39-47.53	0.221-0.432	55.10	0.376
Large	8-14	10	47.53-35.72	0.432-0.568	42.421	0.482

The range of the Biot number indicates that the assumption of lumped-capacity may marginally apply to "Micro" and "Small" cases but not to "Medium" and "Large" cases because Biot No. is more than 0.1. Nonetheless, the lumped-capacity assumption is extended to the latter two cases as well.

In theory, the period a filament stays above the glass transition temperature defines the bonding potential and bonding quality [69, 109, 243]. Thus, we find the period that filament is kept above the critical temperature:

$$\delta_c = \frac{L_c}{U} = \frac{d}{U} \times \frac{-\operatorname{Ln}\theta_c \times 2 \times \frac{\alpha}{dU}}{\sqrt{1 + 64\left(\frac{\sqrt{Bi}\alpha}{dU}\right)^2} - 1}. \tag{4-11}$$

Looking into the critical time, δ_c, and substituting approximate values for the inside of the square root indicates that the values for $\frac{64 \times Bi \times \alpha^2}{d^2 \times U^2}$ are small in comparison to 1. So based on Taylor series, the square root can be approximated by the first order in the following fashion:

If assume $\varepsilon = \frac{64 \times Bi \times \alpha^2}{d^2 \times U^2} \ll 1.0$, then:

$$\sqrt{1 + \frac{64 \times Bi \times \alpha^2}{d^2 \times U^2}} = \sqrt{1 + \varepsilon} \sim 1 + \frac{\varepsilon}{2} + O(\varepsilon^2), \tag{4-12}$$

thus,

$$\delta_c = \frac{L_c}{U} \sim \frac{d}{U} \times \frac{\mathrm{Ln}\,\theta_c \times 2 \times \frac{\alpha}{dU}}{32\left(\frac{\sqrt{Bi}\alpha}{dU}\right)^2} + O(\varepsilon^2) \sim \frac{-\mathrm{Ln}\,\theta_c \times d^2}{16 \times Bi \times \alpha} + O(\varepsilon^2). \tag{4-13}$$

The final equation indicates that the speed of printing does not have a significant effect on the critical time, which is more affected by the size, the coefficient of thermal convection, and material properties. Looking more closely at the equation and substituting Bi and α reveals that there is a linear relationship between density and diameter and a reverse relation to the coefficient of thermal convection.

$$\delta_c = \frac{-\mathrm{Ln}\,\theta_c \times \mathrm{d} \times \rho \times c_P}{4h} = -\mathrm{Ln}\,\theta_c \frac{A \times \rho \times c_P}{\pi h \times d}. \tag{4-14}$$

This observation can be physically interpreted as the energy added to the material due to the volumetric flow over the energy being dissipated by convection. It can be noted that conduction does not play a role in the critical time, and one may attribute this independency to its small magnitude in the polymers; thus, temperature distribution relates to the size of the nozzle and the heat transfer coefficient. Other variables—including deposition velocity, raster angle, and air gap—seem less capable of affecting temperature distribution; therefore, the bonding in intra- or inter-layers depends on material properties, diameter, enveloped temperature, and cooling rate.

The effect of diameter and layer thickness is more pronounced in large 3D printers than smaller ones because the size of the nozzles significantly affects the coefficient of thermal

convection. For example, when the nozzle size increases from 0.4 mm to 10 mm, h_{conv} becomes five times smaller (decreases from 230.59 to 42.42 W/m^{2}K).

Table 14 shows the calculated sensitivity of the critical time based on Eq. (4-14) for nominal values associated with the average of common polymeric material properties listed in Table 2. The diameter is based on the nominal diameter of each category, and the convection heat coefficient corresponds to that nominal size as itemized in Table 13.

Table 14: The sensitivity analyses of the 1D analytical approximation of critical time for the different diameter filaments to reach the glass transition temperature.

Description	unit	Micro	Meso	Medium	Large
$\frac{\partial \delta_c}{\partial h_{conv}}$	m^2.K.s/W	-3.41×10^{-3}	-23.03×10^{-3}	-0.89772	-2.52438
$\frac{\partial \delta_c}{\partial \rho}$	m^3.s/kg	0.643×10^{-3}	2.640×10^{-3}	40.379x10^{-3}	87.416×10^{-3}
$\frac{\partial \delta_c}{\partial d}$	s/m	1969.952	3234.487	8244.127	10708.426
$\frac{\partial \delta_c}{\partial c_P}$	K.s^3/m^2	0.546×10^{-3}	2.243×10^{-3}	34.303×10^{-3}	74.261×10^{-3}

Further analyses on the sensitivity of the critical time to these four variables (d, ρ, c_P, and h_{conv}) shows that, among these variables, the sensitivity to diameter is by far the most pronounced and intensifies as the size of the printer increases. Furthermore, the sensitivity to heat convection is more important for critical time than density and specific heat capacity. The two later are almost equally unimportant, and their effect may be ignored at the critical time. From this perspective, it can be concluded that the most critical parameters in terms of defining the quality of bonding between layers are nozzle diameter, part size, and cooling rate. Since the nozzle diameter directly defines the thickness and the dimension of the bead, these two factors inherently influence the bonding in inter- and intra-layers and subsequently strength and

mechanical properties. In summary, critically important variables are nozzle diameter, enveloped temperature, cooling rate, and the diameter and size of the bead and part.

The changes in the critical time for four cases of different diameters, as explained in Table 13, are shown in Fig. 33 for changes in density, specific heat capacity, and dimensionless temperature.

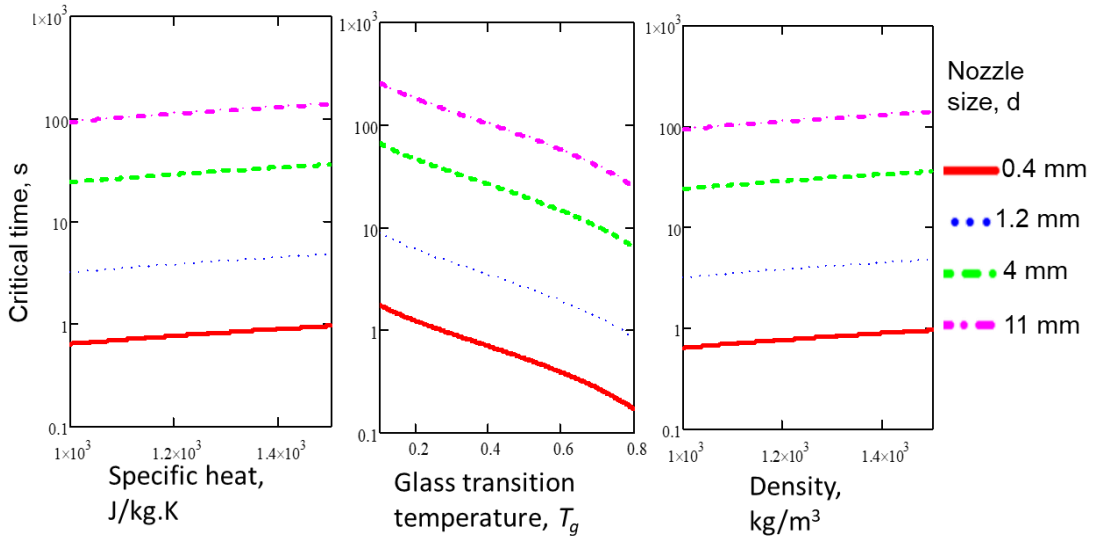

Fig. 33. The critical time changes for different nozzle sizes and associated convection heat transfer coefficient as tabulated in Table 13 for density, specific heat capacity, and dimensionless glass transition temperature.

It also has to be taken into consideration that increasing the diameter from 0.4 mm, which is a standard size for the majority of the desktop 3D printers, to 1 mm increased the critical time up to 4 times from 0.78 s to 3.21 s for the average properties of polymers as shown in Table 2.

It is also worth noticing that the Biot number is not below 0.1 for the third and fourth rows, and the perimeter of the filament decreases in temperature faster than the middle. This temperature distribution from the perimeter toward the center affects the reliability of this approximation for the nozzle with diameters larger than 2 mm. However, this uneven distribution is not detrimental, as explained in the following chapter.

As illustrated in Fig. 34, critical time is nearly flat for different sizes of the filament as the extrusion deposition speed changes from 1000 mm/min to 18,000 mm/min. These graphs are obtained using the original formulation, as expressed in Eq. (4-7) before applying simplification.

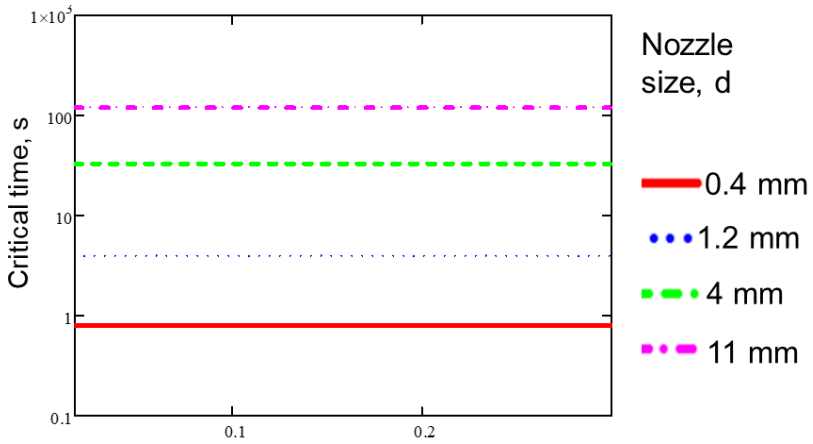

Fig. 34. The critical time changes for different standard nozzle sizes and associated convection heat transfer coefficients as tabulated in Table 13 for different deposition linear velocities range from 1000 mm/min to 18,000 mm/min (0.017 to 0.3 m/s).

4.2.1.2 3D simulation of a filament with Biot number larger than 0.1

In order to study the 3D cases when the Biot number is larger than 0.1 for filaments above 2 millimeters, we developed finite element analyses to compare the 1D model estimation with 3D numerical analyses.

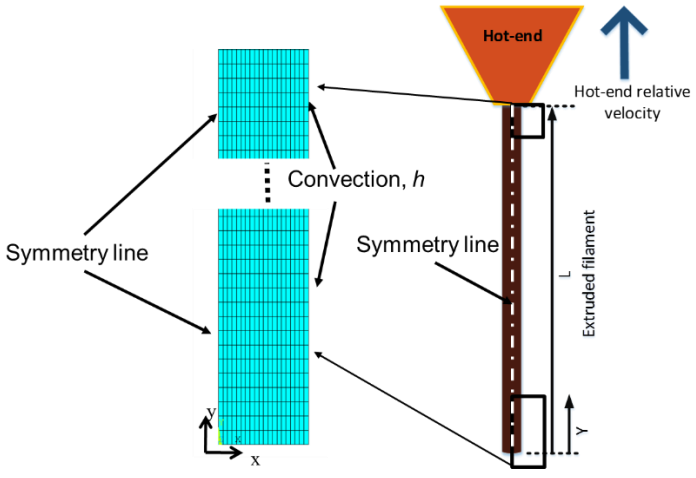

Fig. 35. A schematic of the element deposition and the model developed in Ansys with applied boundary conditions for filament larger than 2 mm.

In this analysis, a straight filament continuously extruded from a nuzzle of a particular diameter was modeled using the axisymmetric condition in the ANSYS–APDL. The geometry of the model is shown in Fig. 35 with the boundary conditions.

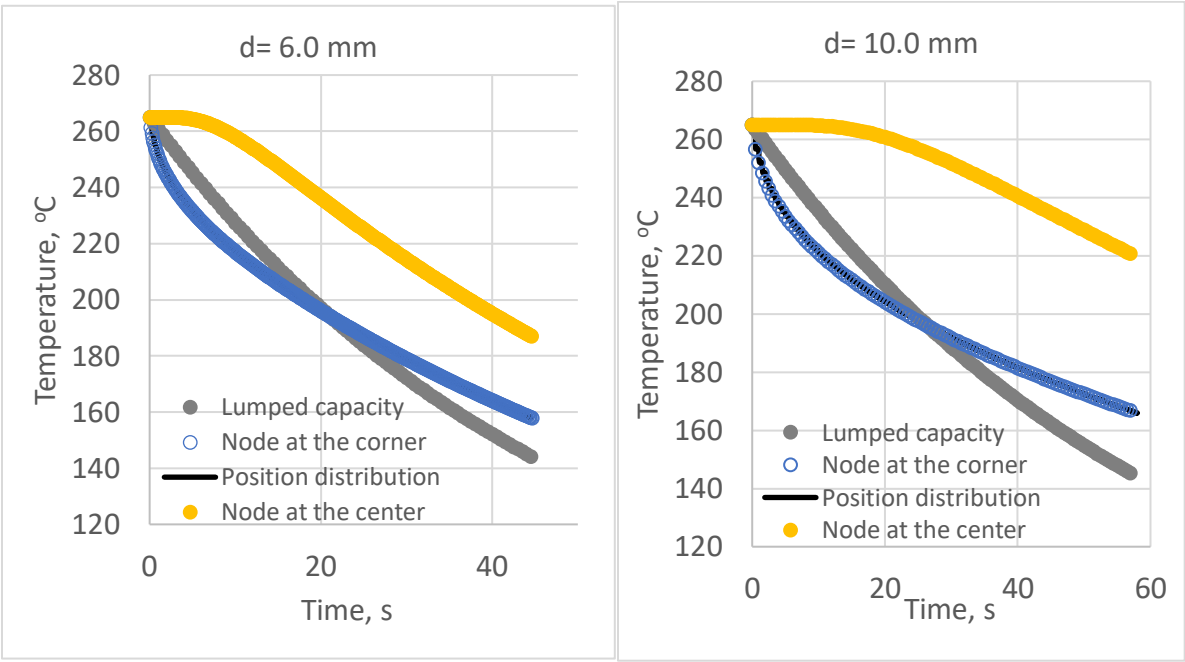

Fig. 36. Comparison between lumped capacity estimation and FEA analyses for 6 mm and 10 mm extruder diameter for 3,000 mm and 8,000 mm long extruder deposition with 4,000 mm/min deposition velocity corrected for the effect of size on convection coefficients.

Two simulations were run for diameters of 6 mm and 10 mm with 3,000 and 8,000 mm lengths, respectively, with the average deposition velocity of 4,000 mm/min.

A comparison was made between the lumped capacity estimation and axis-symmetric FEA model, and Fig. 36 shows how the temperature changes on the notes located on the center and edge of the cross-section over time. Compared to FEA, the lumped-capacity model predicts the temperature higher at the beginning but lower at the ends for the edge node. As expected, the error for 6 mm was less compared with 10 mm.

As shown in Fig. 36, the relative error of the FEA estimation and lumped capacity estimation increases as the solution approached T_g, and the lumped-capacity model is more conservative for

a large FDM machine than FEA because it predicts lower critical time and critical length. The number of activated layers and the position of the extruder follows the $Z=U\times t$ with t being the time and U the deposition velocity. Thus, it is expected that the temperature location distribution matches the time history of the corner nodes, and these distributions based on time and location match exactly as one can see in Fig. 36. Considering the situation and noting that usually the smaller diameter extruder is used, it seems reasonable to use the lumped-capacity estimation to predict the quality of bonding between layers [69].

4.2.2 The coefficient of convection heat transfer and combined radiation-convection

Convection heat transfer plays a vital role in thermal flow in FDM, and the basis is explained in chapter 3.2.1.3 Boundary conditions. The coefficient of convection heat transfer is a function of Reynolds number, material properties, and the average temperature of envelope and surface temperature. The size and velocity play an essential role in the Reynolds number, and it has to be taken into account when dealing with a different scale. As explained in chapter 2.1.2.2 FDM printer's specifications, we are dealing with the different sizes of FDM printers.

On the other hand, looking closely at the nature of the heat transfer also indicates the process has to be studied on two levels: filament and part levels. While in the filament level, the size of the nozzles changes from 0.2 to 14 mm; in part level, the size changes from 1 to 1,000 mm.

4.2.2.1 Required adjustment for the coefficient of heat transfer in different levels

Based on the study of the different cases of heat transfer coefficient ranging from micro to large scale and free to forced convection as explained in chapter 3.2.1.3, one may suggest the applied boundary conditions have to be adjusted based on specific criteria such as size, velocity,

location, and temperature. We suggested the following procedure to be applied to the convection heat transfer coefficient:

- **The filament level**

For analyzing the filament and its associated heat transfer, we suggest the correlation proposed in the third row of Table 48 with the air velocity of 1.7 m/s. The reason is that almost all of the small to large extruder heads are equipped with a fan(s) and cooling apparatus capable of blowing air to the extruder and the filament with a substantial flow rate. The suggested correlation considers the effects of diameters, and it is obtained with a high level of confidence with R^2= 0.998.

- **Top layers or machine with enclosed heating system**

We suggest the filament approximation be used only for the newly deposited filament and not for the previously deposited ones that become a part of the top layers.

We also recommend to estimate the average velocity on the top surface and assume the area of the top surface to estimate the convection heat transfer coefficient. For this purpose, we recommend using the correlation proposed in Table 50 and Table 52, considering the estimated velocity and the shape of the surface. Although the linear interpolation based on velocity is not recommended, it could be an option for those who do not want to repeat the calculation on their own. However, generally, we recommend using the empirical correlation with approximated velocity to estimate the heat convection coefficient.

The estimations based on these criteria suggest that the values were chosen in other studies [12, 13, 33, 69, 106, 107] have to be used more cautiously for estimation of the total heat transfer coefficient. We concluded that those suggested values might not be applicable to estimate

thermal flow in large part where neither velocity nor size met the assumption used for estimation of the heat transfer coefficients.

- **Other layers and open 3D printers**

Desktop or industrial 3D printers are available in both open or closed chambers. Some of the more advanced FDM machines have closed chamber with continuous hot air recirculation. Whereas in the closed chamber 3D printers with hot air recirculation, the difference of heat transfer coefficient may not be found significantly among different surfaces in those without recirculating air it changes meaningfully for the surfaces not experiencing forced air flows, for instances vertical walls or curves far from the location of extruders. This is because the cooling fan installed on the extruder affects the top layer and, more specifically the areas close to the current filament deposition but not other surfaces. Therefore, we recommend to either assign free convection or forced convection with low velocity, for example, 0.3 m/s to those surfaces not influenced by extruder cooling fan. In this case, the first row of Table 50 and Table 52 or the values listed in Table 63 can be used.

- **The effect of radiation heat transfer coefficient**

We estimated the effect of radiation for different emissivity at different temperatures, as shown in Fig. 23. The equivalent convection heat transfer coefficient intensifies from 4 to above 12 W/m^2K as temperature increases from room temperature (20^oC) to 300^oC. Comparing these values with the estimated coefficient of heat transfer in Fig. 110, Fig. 113, and Fig. 115, confirms the significance of the radiation specifically for large diameter or length (above 50 mm) when the medium velocity is less than 0.8 m/s. Thus, it is crucial to take into account the radiation influences in parts that have a size larger than 50 mm and that are fabricated with a machine without an enclosed cooling feature, for example, BAAM machines.

We argue that, although for filament level and top layer, the effect of radiation is negligible, for other layers, the effects of radiation have to be considered. Finally, we suggest including the equivalent coefficient radiation and define a term total heat transfer coefficient (THTC) in our numerical analyses.

4.2.3 Investigation of the effects of a few selected process parameters on sintering time

Bonding is a complicated process that starts with wetting due to interfacial molecular contacts and continues with molecular diffusion and randomization as the materials reach their equilibrium conditions [38, 243]. Diffusion theory [38, 69, 319] has been used for defining the bonding performance between adjacent layers and beads. One can define the following integration to determine the bonding performance for layers and beads as long as their temperatures are above the glass transition temperature [69, 319].

$$D_h = \left[\int_0^t \left(if\ T(\tau) > T_g\right) \times \frac{1}{t_w(T)}\, d\tau\right]^{1/4}, \tag{4-15}$$

where D_h defines the bonding performance with its values above 1.0 indicating a fully developed contact between two contiguous beads, and where $t_w(T)$ is the welding time. This integration has to be calculated for the temperature above glass transition, T_g.

$t_w(T)$ is introduced by Costa et al. [69] based on the experimentally obtained data as:

$$t_w(T) = 1.080 \times 10^{-47}\ exp\left(\frac{Q_d}{RT}\right), \tag{4-16}$$

where, Q_d= 388.7 kJ/mol, and R is the universal gas constant.

In addition to this method, we also calculated two more criteria in order to evaluate the bonding quality between layers. We measured the average time a layer remained above its glass transition temperature:

$$t_b(t) = \int_0^t \left(if\ T(\tau) > T_g\right) d\tau. \quad (4\text{-}17)$$

The bonding potential as defined by Yardamci et al. [109] also calculated for each layer assuming the critical bonding temperature be equal to T_g as:

$$\emptyset(t) = \int_0^t \left(if\ T(\tau) > T_g\right) \times \left(T(\tau) - T_g\right) d\tau. \quad (4\text{-}18)$$

These criteria can be used for comparing the quality of bonding between layers based on the experimentally and numerically gathered data. We calculated these values for cubical specimens printed in an FDM machine to evaluate the validity of the 1D numerical approximation for prediction of the bonding quality. We also looked into the connection between density and bonding quality to explore the success of each of these criteria in addressing the prediction of bonding quality.

4.2.3.1 1D model investigation

The same table developed for the experimental investigation based on the concept of Central Composite Design (CCD), as listed in Table 8, was applied to the 1D numerical model. These five parameters change accordingly, while the boundary conditions are modeled following the criteria explained in Chapter 4.2.2. We also listed all relevant parameters in Table 15, including the material properties, dimension, and process parameters.

Table 15: Part physical, geometries, and printing parameters considered for 1D thermal study.

Length, *L*	15 ±0.19 mm	**Stacking Orientation**	Rectilinear, Longitudinal (0°)
Width, *w*	15 ±0.5 mm	**Average ideal time**	0.25 s
Material	ABS	**Layer thickness**	Low (0.09), Medium (0.19), and high (0.29) mm
Color	White	**Air gap**	0
Specific heat, c_p	1300 J/kg-K	**Average bulk temperature T_∞^a**	35 °C

Density, ρ	Theoretical density based on RS equation (4-20) as explained in chapter 4.2.5	**Raft**	Yes
Conductivity, κ	0.16-0.15 W/m-K	**Heated-bed temperature T_b**	Low (40), Medium (70), and High (100) ^oC
Polymer-Heated bed thermal contact coefficient	4800 W/m^2K	**Bead width**	0.40 mm
h_{conv} for the top layer[b]	Based on Table 59 and Table 60	**Linear deposition velocity for 3D**	Low (2000), Medium (4000), and High (6000) mm/min
h_{conv} for other layers[b]	Based on Table 59 and Table 60	**Extruder temperature T_{Exd}**	Low (240), Medium (265), and High (290) ^oC
Printing Orientation	Vertical	**Cooling**	Fan speed Low (0), Medium (500, High (100) %

[a] The bulk or envelope temperature was monitored using an analog thermometer and its average calculated accordingly.
[b] The correlation proposed by Churchill [23] is used to estimate the convection coefficient by assuming the velocities of 0.3 and 1.7 m/s for other and top layers, respectively.

One of the critical parameters in 1D model is the average deposition velocity. This value represents the deposition in the *z* direction perpendicular to the extruder motion plane and differs from the printing speed. Although printing speed directly affects this value, the layer thickness, contour thickness, and the area of the cross-section are as equally important as speed. Thus, this velocity has to be estimated based on the mentioned variable. To do so, we defined an excel sheet to obtain this average velocity. We determined the number of the path required for a cross-section knowing the stacking orientation and estimated the total length of the deposited roads. This length divided by the extruder velocity to estimate the time for depositing a particular layer. Finally, the average velocity is obtained by dividing layer thickness over this time.

Table 16 lists the determined velocity for all 28 rows. It also should be noted that for finding the correct length, some modifications had to be applied, including rounding the roads numbers, considering the thickness of the contours, and correcting the dimensions accordingly. The object of interest was a cube with 15.0×15.0×15.0 mm×mm×mm.

Table 16: Estimation of the average deposition velocity for 1D simulation based on the designed set of experiments.

Run	Layer thickness, mm	Extruder Speed, mm/min	Total Extruder run, mm	Layer deposition time, s	Idle time, s	Average velocity, mm/min	Correction factors	Corrected velocity, mm/min
1	0.09	2,000	93,240	16.65	0.64	0.31	1.07	0.33
2	0.09	6,000	93,240	5.55	0.21	0.94	0.80	0.75
3	0.29	2,000	29,415	16.65	0.64	1.01	1.07	1.08
4	0.29	6,000	29,415	5.55	0.21	3.02	0.80	2.42
5	0.19	4,000	44,400	8.33	0.32	1.32	0.90	1.19
6	0.09	2,000	93,240	16.65	0.64	0.31	1.07	0.33
7	0.09	6,000	93,240	5.55	0.21	0.94	0.80	0.75
8	0.29	2,000	29,415	16.65	0.64	1.01	1.07	1.08
9	0.29	6,000	29,415	5.55	0.21	3.02	0.80	2.42
10	0.19	4,000	44,400	8.33	0.32	1.32	0.90	1.19
11	0.09	4,000	93,240	8.33	0.32	0.62	0.90	0.56
12	0.19	2,000	44,400	16.65	0.64	0.66	1.07	0.71
13	0.19	4,000	44,400	8.33	0.32	1.32	0.90	1.19
14	0.19	4,000	44,400	8.33	0.32	1.32	0.90	1.19
15	0.19	4,000	44,400	8.33	0.32	1.32	0.90	1.19
16	0.19	4,000	44,400	8.33	0.32	1.32	0.90	1.19
17	0.19	6,000	44,400	5.55	0.21	1.98	0.80	1.58
18	0.29	4,000	29,415	8.33	0.32	2.01	0.90	1.81
19	0.19	4,000	44,400	8.33	0.32	1.32	0.90	1.19
20	0.09	2,000	93,240	16.65	0.64	0.31	1.07	0.33
21	0.09	6,000	93,240	5.55	0.21	0.94	0.80	0.75
22	0.29	2,000	29,415	16.65	0.64	1.01	1.07	1.08
23	0.29	6,000	29,415	5.55	0.21	3.02	0.80	2.42
24	0.19	4,000	44,400	8.33	0.32	1.32	0.90	1.19
25	0.09	2,000	93,240	16.65	0.64	0.31	1.07	0.33
26	0.09	6,000	93,240	5.55	0.21	0.94	0.80	0.75
27	0.29	2,000	29,415	16.65	0.64	1.01	1.07	1.08
28	0.29	6,000	29,415	5.55	0.21	3.02	0.80	2.42

Moreover, the assumed linear velocity does not include the time needed to reach the maximum velocity. In other words, the assumed velocity does not reflect the actual velocity because the extruder accelerates from zero to the maximum speed when it starts and reversely decelerates to lower velocity when it stops or reverses direction. So the actual velocity is less than the estimated one. This effect is more significant when the size of the part is small; however, as the size increase, these effects become less significant. We also used the *in-situ* IR camera to record the thermal flow and temperature distribution of the selected specimen for verification and evaluation. These videos were used to correct an actual velocity. In Table 16, the correction factors are defined to account for these influences, such as acceleration/deceleration and justify the final values for simulation. The correction applied to the estimated velocity and the last row of the table manifests these corrected values.

We also developed a 1D model for the cuboids with three different cross-sections of 3×3, 7×7, and 11×11 millimeters and a length of 30 mm. This study was projected to illustrate the effects of size, extruder temperature, and speed on the thermal flow and through that on the development of bonding and density in the 3D printed parts. In this particular study, the layer thickness, heated bed temperature, and cooling rate were kept constant as 0.19 mm, 70^{o}C, and 100%, respectively. Table 17 lists the specifications for these cases corresponding to the rows of DoE Table 10.

Table 17: Estimation of the average deposition velocity for 1D simulation based on the designed set of experiments for three different sizes of cuboids.

Run	Size, mm	Extruder Speed, mm/min	Total Extruder run, mm	Layer deposition time, s	Idle time, s	Average velocity, mm/min	Correction factors	Corrected velocity, mm/min
1	3	2000	3339	0.63	0.13	15.05	1.07	16.05
2	3	6000	3339	0.21	0.04	45.16	0.39	17.79
3	3	4000	3339	0.315	0.06	30.11	0.59	17.72

4	3	2000	3339	0.63	0.13	15.05	1.07	16.05
5	3	6000	3339	0.21	0.04	45.16	0.39	17.78
6	7	4000	18921	1.785	0.15	5.90	0.79	4.68
7	7	2000	18921	3.57	0.30	2.95	1.10	3.24
8	7	4000	18921	1.785	0.15	5.90	0.79	4.69
9	7	4000	18921	1.785	0.15	5.90	0.79	4.69
10	7	6000	18921	1.19	0.10	8.84	0.58	5.12
11	7	4000	18921	1.785	0.15	5.90	0.79	4.69
12	11	2000	47223	8.91	0.47	1.22	1.06	1.29
13	11	6000	47223	2.97	0.16	3.65	0.67	2.44
14	11	4000	47223	4.455	0.23	2.43	0.85	2.06
15	11	2000	47223	8.91	0.47	1.22	1.06	1.29
16	11	6000	47223	2.97	0.16	3.65	0.67	2.44

4.2.3.2 The 1D numerical simulation results and discussions

The simulation was run for 28 cases as listed in Table 16, and selected parameters were changed according to Table 9, Table 10, Table 15, and Table 16. The simulations were carried out using the home-written code based on the finite-difference, as described in Chapter 3.2.3, and MATLAB used as a programming language. The solutions ran on a laptop with two cores of 2.3 GHz and 8 GB memory and took less than 3 minutes for the longest one to be executed. The average values for the three factors bonding quality, bonding potential, and time above the glass transition temperature calculated for each layer. Table 18 lists the average of these factors for all layers, as well as the maximum and minimum of the entire layers.

Table 18: Results for the 1D simulation showing the average of three selected factors associated with the bonding performance in layers.

Run	Bonding performance, D_h^*			Bonding potential, ∅			Time above Glass transition		
	Average	max	min	Average	max	min	Average	max	min
1	0.000	0.000	0.000	0.0	0.0	0.0	0.0	0.0	0.0

2	0.224	0.290	0.153	779.7	1346.0	435.1	71.3	132.0	45.6
3	0.463	0.575	0.336	1168.0	2028.5	764.4	77.0	155.7	48.3
4	4.516	1.0*	1.0*	2578.2	6000.0	1255.7	81.1	179.8	36.0
5	0.894	1.0*	0.708	2195.5	4083.6	1391.1	123.5	249.1	70.3
6	0.072	0.080	0.042	145.4	215.7	18.8	63.5	81.8	5.5
7	0.547	0.596	0.443	2628.4	3588.4	1975.9	177.1	278.4	139.2
8	0.894	0.970	0.804	2771.5	4311.5	2119.2	177.0	300.7	118.1
9	1.0*	1.0*	1.0*	4558.1	7774.9	2387.7	139.4	215.7	74.3
10	1.0*	1.0*	0.955	2244.2	4511.9	1322.8	107.8	236.3	57.5
11	0.223	0.257	0.183	1093.2	1527.7	621.4	108.2	167.1	80.4
12	0.368	0.423	0.302	1516.7	2206.7	1049.4	116.2	192.7	91.0
13	1.0*	1.0*	1.0*	3439.7	6226.5	2116.4	142.1	271.4	83.0
14	1.0*	1.0*	1.0*	3274.2	5908.8	2023.4	141.6	268.2	83.0
15	1.0*	1.0*	1.0*	3274.2	5908.8	2023.4	141.6	268.2	83.0
16	1.0*	1.0*	1.0*	3760.3	6641.4	2302.6	150.0	277.8	86.2
17	1.0*	1.0*	1.0*	3773.0	6969.7	2142.3	121.1	223.7	67.3
18	1.0*	1.0*	1.0*	3937.3	7745.6	2100.7	131.5	253.1	64.1
19	1.0*	1.0*	1.0*	4873.0	7388.5	3264.1	202.2	316.1	137.3
20	0.024	0.055	0.000	9.5	41.7	0.0	8.1	27.3	0.0
21	0.827	1.084	0.552	2192.9	3775.3	1371.2	115.3	223.2	76.8
22	1.0*	1.0*	1.0*	2653.4	4840.0	1714.4	119.3	247.0	69.8
23	1.0*	1.0*	1.0*	4530.5	9569.4	2177.9	95.0	189.3	43.1
24	1.0*	1.0*	1.0*	4405.3	7692.8	2693.7	155.5	281.0	92.6
25	0.147	0.151	0.099	949.8	1031.8	185.6	143.7	158.2	38.2
26	1.0*	1.0*	1.0*	5842.6	7232.7	4236.9	241.6	357.6	139.2
27	1.0*	1.0*	1.0*	6317.6	9661.2	4261.7	283.9	435.0	166.5
28	1.0*	1.0*	1.0*	6431.0	10857.8	3323.4	145.5	220.5	79.1

*: The values were found above 1.0 were ascribed 1.0 and marked by *

Bonding performance was supposed to be between 0 to 1.0, but several rows had averages of more than 1.0, which assigned to 1.0 and marked by asterisks.

The results, which were obtained by a simplified numerical model, showed that layer thicknesses, extruder temperature, and extruder speed played a significant role in bonding

quality. The effect of layer thickness was found crucial; however, in lower layer thickness, for example, the thickness of 0.09 mm, the effect of other parameters such as extruder temperature and extruder speed became more important. On the other hand, almost all specimens with a layer thickness of 0.29 mm revealed the bonding performance above 0.5 no matter what the speed and temperature were. For the thickness of 0.19, extruder speed was critical and defined the bonding quality. The effect of Bonding potential and time above glass transition temperature is difficult to interpret individually.

According to our observation, one can expect to see a higher potential for improved bonding between layers in a layer thickness of 0.29 mm compared to 0.19 mm. This means that the bonding quality, which is defined in this dissertation and found based on the density, can be assumed for the bonding in higher thickness. However, in lower thickness, the estimated bonding quality based on density should be used with caution and would not be an indication of intra-layer bonding. Thus, with lower thickness, we can expect to have higher interlayer bonding and thus higher shear modulus and E_y; with higher layer thickness, we can expect a little effect of extruder temperature and speed on bonding quality.

4.2.3.3 The 1D numerical simulation results and discussion for long cuboids

We evaluated the significance of layer thickness for thermal and structural characteristics. In order to exclude this effect from our analyses and examine the effects of other important parameters such as extruder temperature and printing speed, we designed an experiment mentioned in chapter 3.5.2.1. We solved the sixteen cases changing the parameters according to the designed circumstances. The results listed in Table 19 contain the three selected factors and their averages, maximums, and minimums.

Table 19: Results for the 1D simulation showing the average, max, and min of three selected factors affecting the bonding performance.

Run	bonding performance, D_h			Bonding potential, Ø			Time above Glass transition		
	Average	max	min	Average	max	min	Average	max	min
1	1.0*	1.0*	1.0*	427.0	1031.2	334.4	10.0	21.3	7.3
2	1.0*	1.0*	1.0*	442.8	1002.1	343.1	9.7	19.9	7.1
3	1.0*	1.0*	1.0*	572.4	1227.6	440.0	10.5	20.8	7.7
4	1.0*	1.0*	1.0*	690.8	1503.1	533.6	11.5	22.7	8.5
5	1.0*	1.0*	1.0*	704.4	1447.5	538.3	11.0	21.2	7.9
6	1.0*	1.0*	1.0*	722.1	1804.5	574.5	27.5	68.1	20.3
7	1.0*	1.0*	0.914	612.2	1457.7	534.9	28.2	83.3	22.3
8	1.0*	1.0*	1.0*	1026.4	2366.5	811.6	30.9	69.7	23.5
9	1.0*	1.0*	1.0*	1026.5	2366.6	811.6	30.9	69.7	23.5
10	1.0*	1.0*	1.0*	1108.3	2465.0	863.8	30.8	66.1	23.0
11	1.0*	1.0*	1.0*	1351.4	2967.6	1059.9	34.1	72.2	25.9
12	0.031	0.032	0.031	5.2	5.3	5.0	2.9	2.9	2.9
13	0.428	0.444	0.369	598.3	1265.3	522.4	38.1	106.0	29.6
14	0.496	0.509	0.430	689.6	1329.3	621.8	41.3	106.8	35.0
15	0.135	0.135	0.116	237.6	266.2	91.8	26.6	38.2	11.8
16	1.0*	1.0*	1.0*	1466.8	3134.0	1197.8	56.0	129.4	42.1

As we concluded in the previous section, the effect of speed and extruder temperature for the layer thickness of 0.19 became important in forming the intra-layer bonding. For specimens of size 7 mm and above, only the highest speed with average to high temperature can result in bonding performance above 0.5.

Besides, small cross-sections, no matter what the range of temperature and speed were, showed durable bonding quality. Thus, the strategies such as using small cross-section, sectioning large components to smaller areas, printing the area along its shortest length, and scanning strategy follows the minimum cross-section length can be used for forming strong bonding where it is needed.

The effect of extruder temperature also became relevant in this case and could define the bonding and improve the inter-layer attachments. Subsequently, in order to have a high level of bonding performance, one must set the printing speed above average with an extruder temperature higher than 265^{o}C. It also became evident that extruder temperature can be effective to form stronger bonds in an area with a small size, although this expected boost does not occur when printing large components.

4.2.4 An analysis of the effects of bead geometry on density

The nozzles in FDM 3D printers extrude circular filaments, which during deposition form a semi-elliptical shape similar to those shown in Fig. 37. The bonding between adjacent filaments expands as time passes, as shown in Fig. 37; however, the process relies on the temperature being above glass transition for a long time to fully-developed contacts, and these ideal conditions often do not satisfy and lead to porosity be formed even in solid infill. Because of this porosity, conductivity in the material cannot be assumed to be equal to those in original filament and requires adjustment. This adjustment should be estimated locally, depending on the porosity and the quality of the bonding between contagious filaments.

The thickness of the deposited layer in FDM is defined by the clearance between the nozzle and the previously deposited material or heated bed, as shown in Fig. 37. This height cannot be more than the diameter of the filament. Although a thinner layer is recommended for better dimensional accuracy and resolution, it does not promote effective and robust bonding between layers and contagious contours, as explained in Chapters 4.2.1 and 4.2.3. Thin layers also increase the time of manufacturing significantly. The width of the laid road (filament) is not smaller than the diameter of the nozzle. This width can be increased above the nozzle diameter

by increasing the flow rate and reducing the extruder speed. However, the width is not recommended to go beyond 1.7 times larger than the diameter.

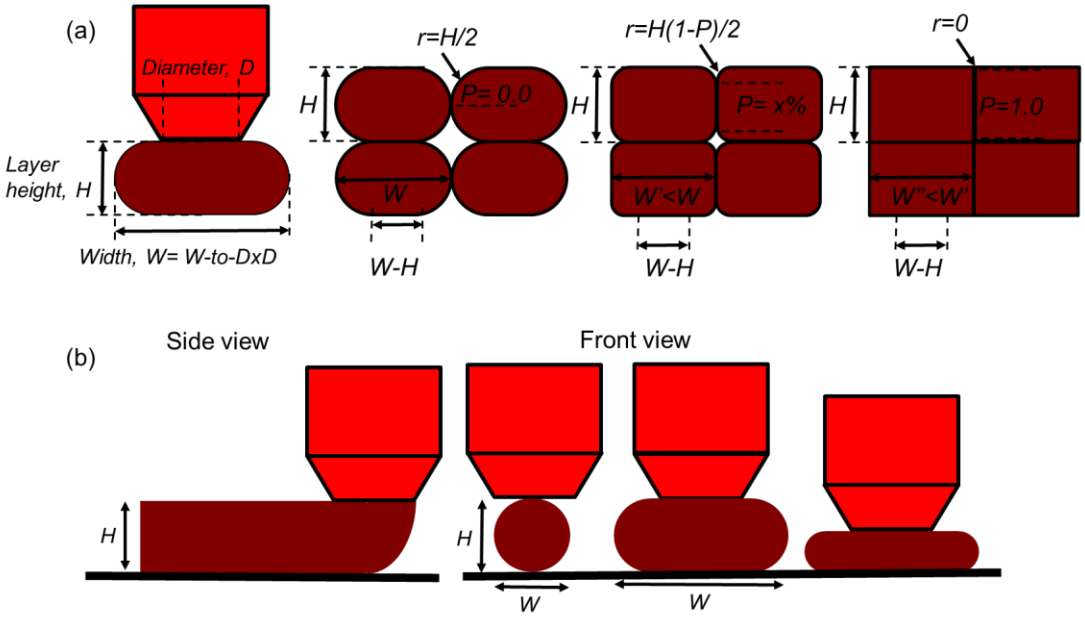

Fig. 37. Schematic of deposition of the filament considering different W-to-D ratio and height(H): (a) As the bonding is developed between to contagious bead (road) while contact quality (P) increases, the initial width (W) of the deposited bead reduces, and (b) front and side view of the filament deposited by extruder.

We defined the shape of the road and its deformed shaped during manufacturing to be a combination of a rectangle with two semicircular on both ends, as shown in Fig. 37. In this framework, this shape can be mathematically reframed based on four parameters: D as the diameter of the nozzle; *H* as the height of the layer; *W-to-D* as the ratio between the width and diameter; and *P* as the contact quality.

The effect of the different ratios between *W-to-D* and *H* is shown in Fig. 38. There are initially void spaces between the filament, as illustrated. The coalescence can take place over time to decrease these void spaces.

The void area between just deposited adjacent bead with zero air gap can be found as:

$$A_{void} = H^2 - \pi H^2/4. \quad (4\text{-}19)$$

This void is when the two beads are separate but barely touch, as shown in Fig. 37-b. We define a parameter *P* as a contact quality between two beads. This contact quality is 0 when the beads begin to touch and can increase to 100% if an amalgamation happens and they become one body as shown in the sequence image in Fig. 37-a and Fig. 38.

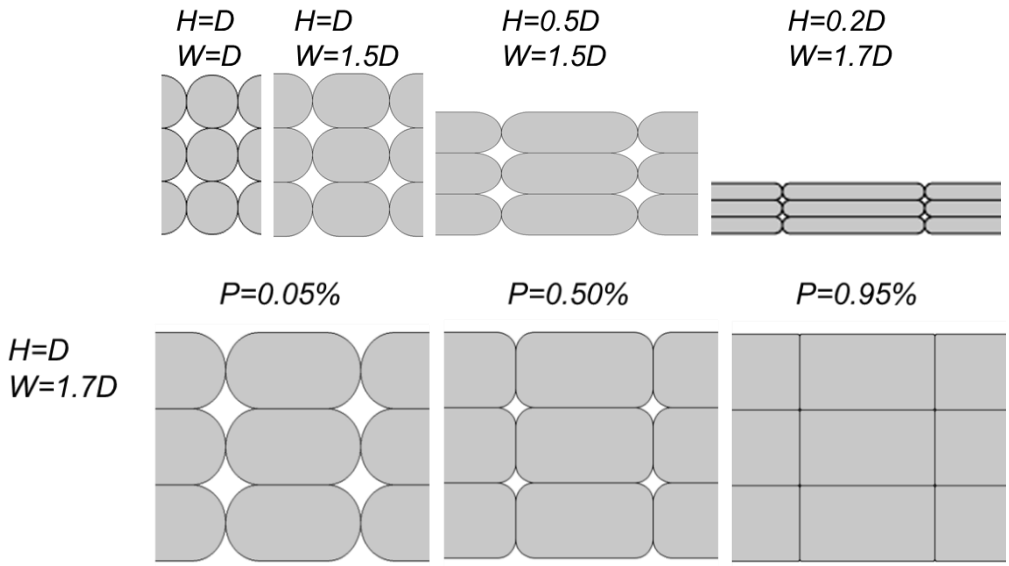

Fig. 38. The different W-to-D and H-to-D ratio cause different SR, in general, lower height with higher width lead to lower RS. In the particular H-to-D and W-to-D ratio, the contact quality can increase by bonding development and lowers the RS ratio.

A factor called solidity ratio, SR, can be defined as the area of the deposited material over the maximum space occupied with the outer dimensions of the part. For example, for a two semi-elliptical bead just in touch and without bonding, the SR is found as:

$$SR = \frac{Deposited\ material\ area}{total\ area} = \frac{WH - \mathrm{H}^2 - \frac{\pi \mathrm{H}^2}{4}}{\mathrm{WH}} = 1 - \frac{H}{W}\left(1 - \frac{\pi}{4}\right). \quad (4\text{-}20)$$

The above equation defines the extreme cases when the beads are laid without any bonding similar to the deposition of racks of pipes on top of each other when their centers are aligned, as shown in Fig. 38. This equation calculates the lower limits of SR with zero air gap in the FDM

process. This values cannot be theoretically less than $\frac{\pi}{4}$% (0.79%) in 100% infill. It also indicates that the higher the H/W ratio contributes to more porosity leading to lower density.

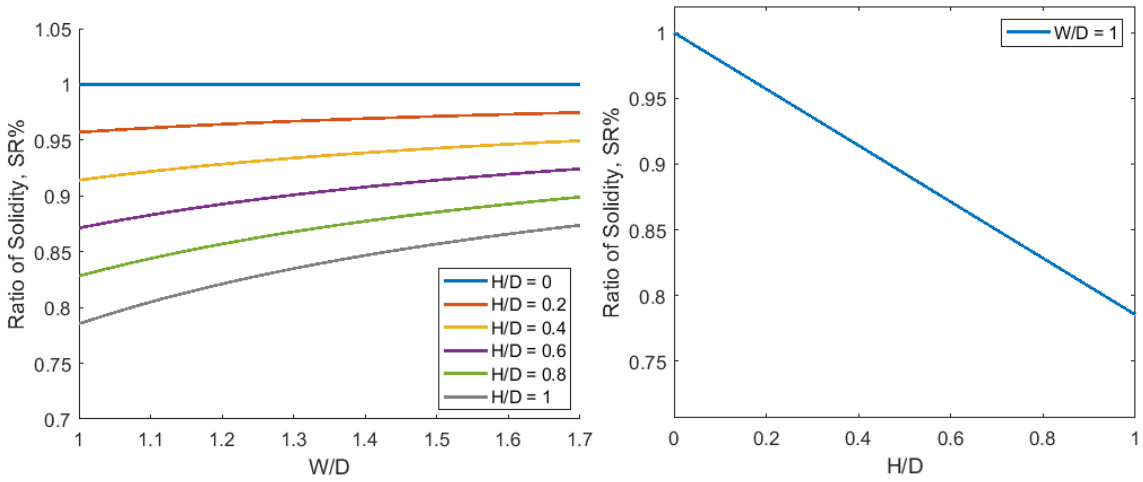

Fig. 39. The theoretical estimation of the solidity ratio (SR) of 3D printed specimens without considering the effect of coalescence after bead depositions only based on the geometry of the bead.

In addition, it suggests that measuring the density of the printed components can be a metric for evaluating the bonding quality by comparing the theoretical and the measured *SR*. In other words, improved bonding increases the *SR* rate; the increased *SR* means lesser porosity and higher density. Thus, if the measured *SR* of the printed components is more than the theoretical *SR*, the bonding quality is higher. On the other hand, the ratio between the density of a watertight printed specimen to the theoretical nominal density of the material is the *SR* of the specimens:

$$SR = \frac{\rho_{printed}}{\rho_{ABS}}. \tag{4-21}$$

We defined *P*, contact quality percentage, based on height, *H*. When the bonding improves, the contact length expands. We also assumed a similar trend of bonding progress for the vertical and horizontal directions. Thus, while the bonding expands, the half-circle shrinks equally in both vertical and horizontal directions, and its radius decreases, as shown in a sequential image

in Fig. 37-a and Fig. 38. In other words, when the radius is *H/2* with *P=0*, the radius becomes *H(1-P)/2* when *P* expands and finally approaches 0 as bonding length covers the total height of the beads.

We applied conservation of mass between the initially deposited bead and the current bead as the contact increased from point contact to the full length equal to the height of the two adjacent beads (0 to 100% of *H*) to calculate the width. The height was unchanged, and the following equation defines the relationship between a new width, W', and *H*, *W-to-D*, *P*, and *D*:

$$\mathrm{A}_{initial} = \mathrm{A}_{\mathrm{coalesced}} \Rightarrow WH - H^2\left(1-\frac{\pi}{4}\right) = W'H - H^2\left(1-\frac{\pi}{4}\right)(1-P)^2, \tag{4-22}$$

$$W' = W - H\left(1-\frac{\pi}{4}\right)[1-(1-P)^2]. \tag{4-23}$$

Since the height of the roads is fixed, Eq. (4-23) also can be an indicator of the initial density to the coalesced density, in other words, theoretical density with zero bonding to the printed part density:

$$\frac{\rho_{printed}}{\rho_{ABS}} = \frac{\mathrm{A}_{\mathrm{coalesced}}}{W' \times H} \;\; and \;\; \frac{\rho_{theoritical}}{\rho_{ABS}} = \frac{\mathrm{A}_{initial}}{W \times H} \xrightarrow{\mathrm{A}_{\mathrm{coalesced}}=\mathrm{A}_{initial}}$$
$$\frac{\rho_{theoritical}}{\rho_{printed}} = \frac{W'}{\mathrm{W}} = 1 - \frac{H}{W}\left(1-\frac{\pi}{4}\right)[1-(1-P)^2]. \tag{4-24-a}$$

With the same analogy, one also can define the SR as follow:

$$SR = \frac{\rho_{printed}}{\rho_{ABS}} = \frac{\mathrm{A}_{\mathrm{coalesced}}}{W' \times H} = 1 - \frac{H\left(1-\frac{\pi}{4}\right)(1-P)^2}{W - H\left(1-\frac{\pi}{4}\right)[1-(1-P)^2]}. \tag{4-24-b}$$

The above equations were used later to estimate the bonding quality. Volumetric contraction is another parameter to be found as a ratio between the difference of the new width and original width divided by original width:

$$\text{Contraction} = \frac{H\left(1-\frac{\pi}{4}\right)[1-(1-P)^2]}{W}. \tag{4-25}$$

This value has been found for different *H-to-D* from 0.2 to 1 and *W-to-D* between 1.0 to 1.7. The maximum shrinkage takes place when *H* and *W* are equal to the nozzle diameter with its maximum being 21.4%. This rate of shrinkage is significant; however, it occurs when the material is soft in temperatures above the glass transition temperature and has minimum effects on deformation and residual stresses. In can be concluded that the higher *H-to-D* and lower *W-to-D* contribute to higher levels of residual stresses because of the higher potential of the contraction and presence of cavities in printed components.

4.2.5 Analyses of spatially varying conductivity due to porosity

We wanted to evaluate the effective thermal conductivity by taking into account the porosity and the development of bonding over time. We defined two configurations consisting of a stack of ten layers vertically or horizontally with three racks of beads to estimate the equivalent conductivity for different levels of bondings.

We solved a steady-state heat transfer with the hot and cold surfaces at the two counter edges and isolation of all the other boundaries. We assumed a negligible effect of the convection and radiation of the air trapped between cavities [107]. The developed FEM model and the boundary conditions for both horizontal and vertical cases are shown in Fig. 40 and Fig. 41, respectively.

The problem solved dimensionlesslly employing COMSOL Multiphysics. The effective conductivity calculated between the internal boundaries, as shown in the figures.

The porous medium dimensionless conductivity was determined similarly to steady-state 1D heat diffusion in a semi-infinite case where the thermal resistance was defined based on material thickness, temperature difference, conductivity, and heat flux as follow:

$$|q_i^*| = \frac{|\theta_1 - \theta_2|}{L_i^*/\kappa_i^*}, \tag{4-26}$$

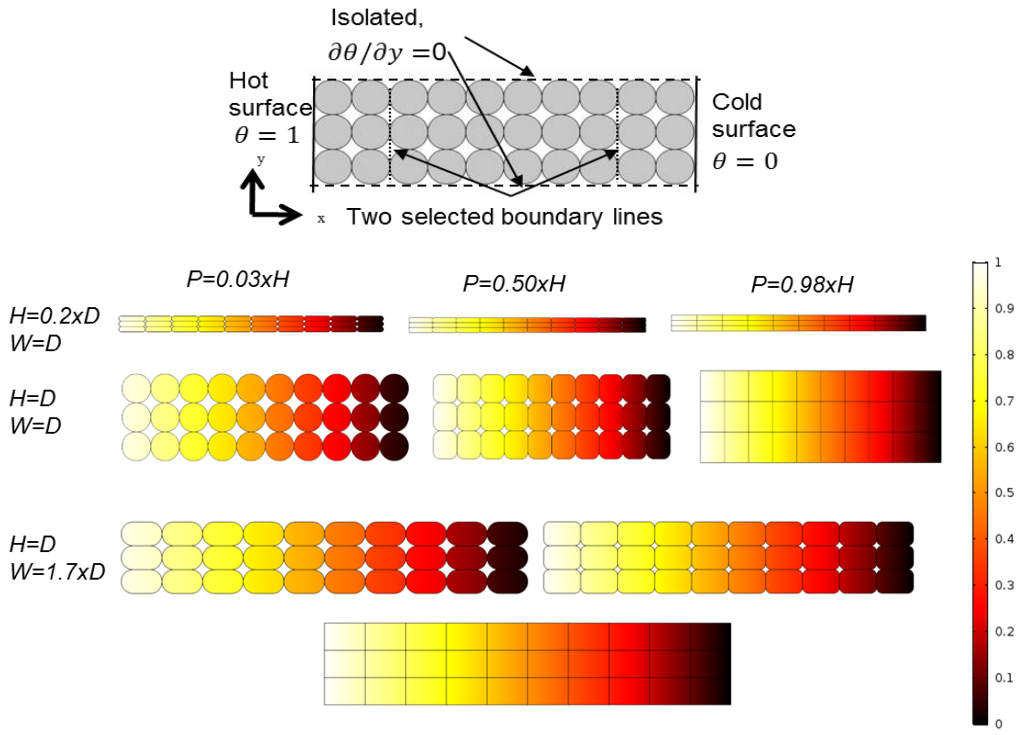

Fig. 40. A FEM model developed for numerical estimation of the effect of bonding and porosity on the local changes of heat conductivity: (a) a FEM model generated using COMSOL Multiphysics ® for estimation of the spatially varying conductivity in x direction; and (b) non-dimensionalized temperature distribution subjected to temperature difference in x-direction for three different sets of *H-to-D* and *W-to-D* ratios at three different levels of bonding quality.

where q_i^* is heat flux, θ_1 and θ_2 are non-dimensionalized temperatures on the selected lines, L^* is the non-dimensionalized length difference between two lines, κ_i^* is the non-dimensionalized conductivity and *i* is the indicator of direction either *x* or *y*.

We employed COMSOL Multiphysics ® to solve the cases parametrically, where the *H/D* changes from 0.2 to 1, and *W-to-D* ratio changes from 1 to 1.7. The boundary conditions for both vertical and horizontal configurations are shown in Fig. 40 and Fig. 41 for estimation of κ_x^* and κ_y^*, respectively.

Thermal distributions for three different configurations on *H*, *W-to-D*, and three different *P* for both vertical and horizontal configurations are shown in Fig. 40 and Fig. 41.

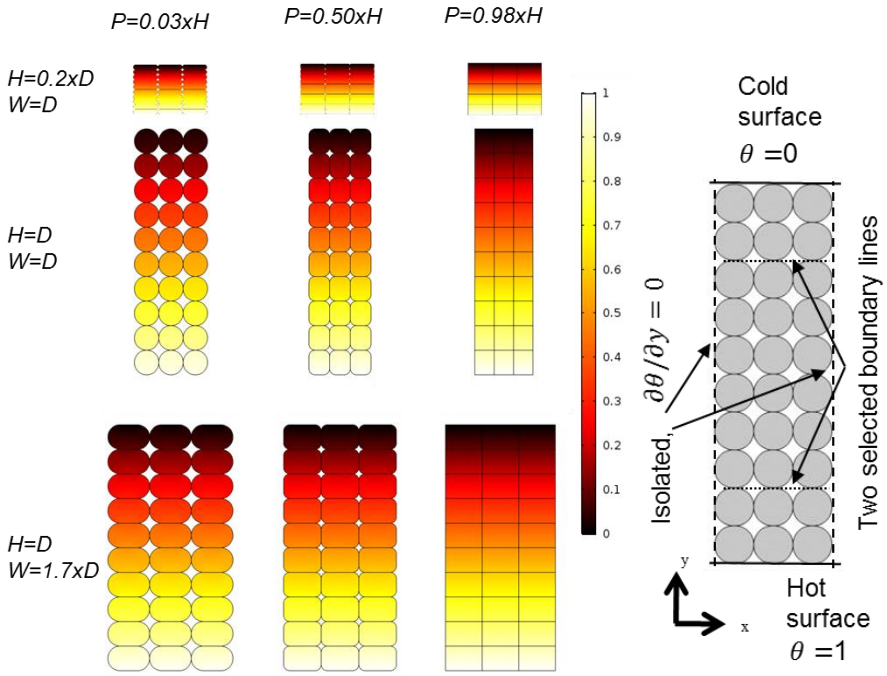

Fig. 41. A FEM model developed for numerical estimation of the effect of bonding and porosity on the local changes of heat conductivity in y-direction: (a) a FEM model generated using COMSOL Multiphysics ® for estimation of the spatially varying conductivity in x direction; and (b) non-dimensionalized temperature distribution subjected to temperature difference in x-direction for a three different set of H-to-D and W-to-D ratios at three different levels of bonding quality.

Non-dimensional conductivity, κ_i^*, is only geometry dependent and is shown in Fig. 42 for vertical and Fig. 44 for horizontal configuration.

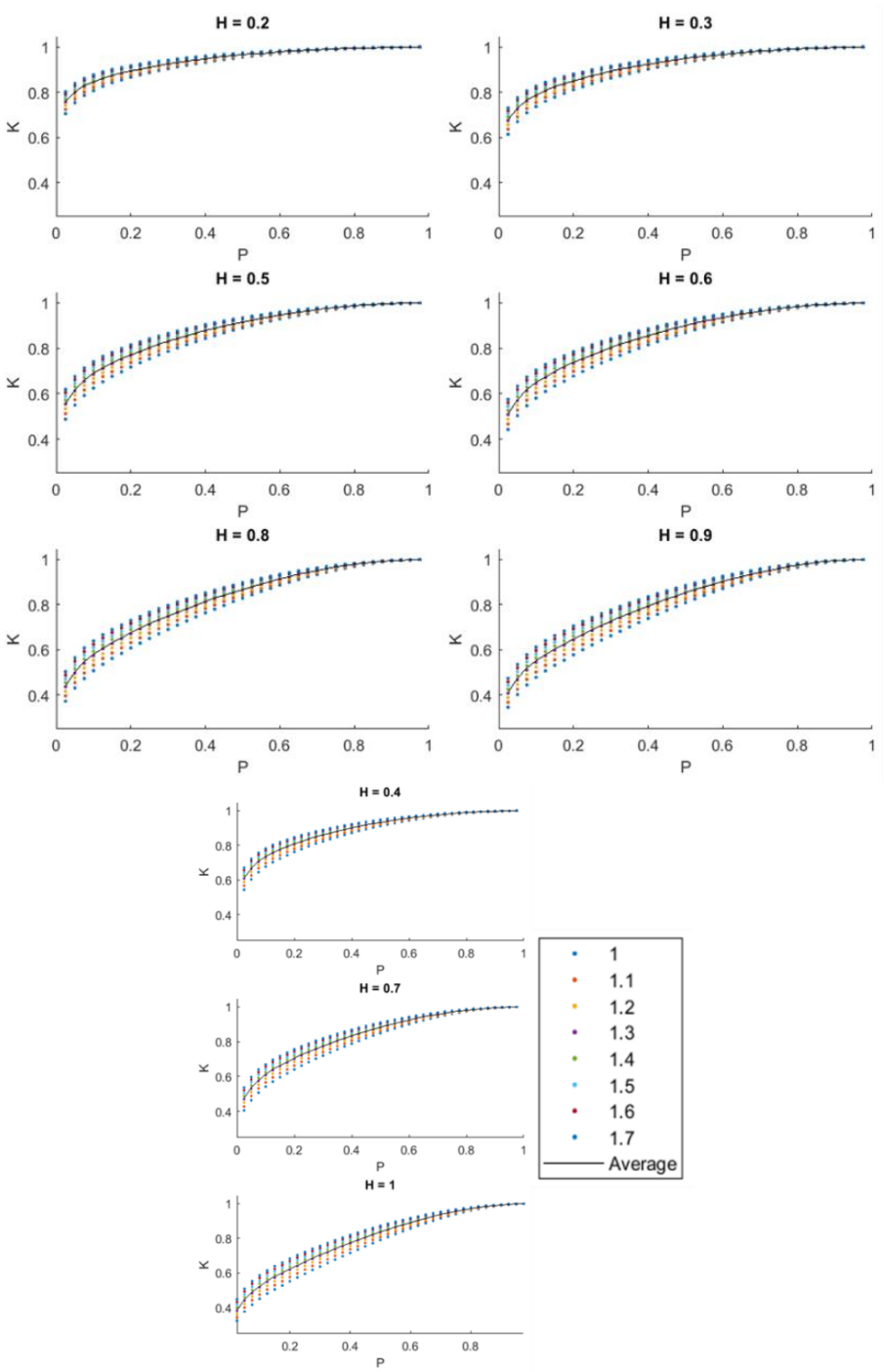

Fig. 42. Estimated heat conductivity in x-direction for the height of the bead changes in 9 levels from 0.2 to 1 *D* for eight different *W-to-D* versus contact quality. The solid line indicates the average of the eight *W-to-D* ratios. The conductivity increases as the contact quality increases and the effect of *P* is more noticeable in higher *H*.

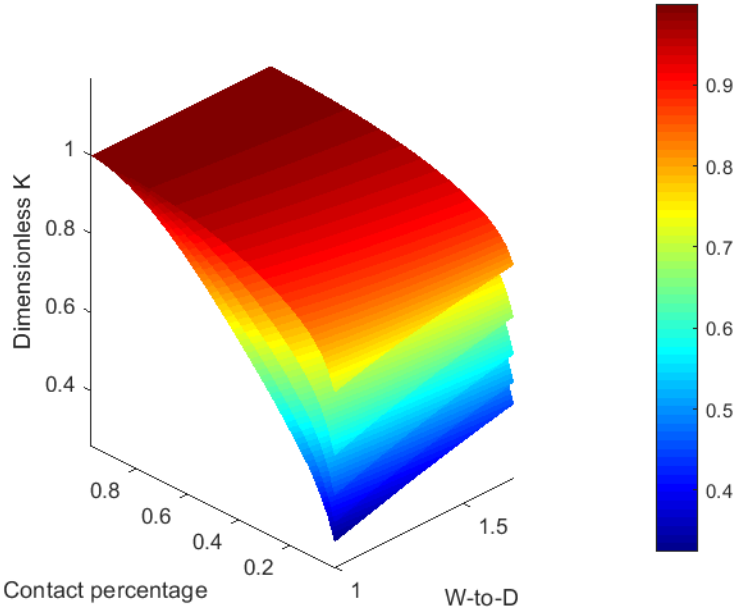

Fig. 43. Surfaces representing the non-dimensionalized conductivity in x-direction for different H-to-D ratio versus contact quality and W-to-D ratio.

Figures 43 and Figure 45 also show the 3D surfaces representing the changes in conductivity due to the changes in contact quality, *H/D*, and *W-to-D* ratio.

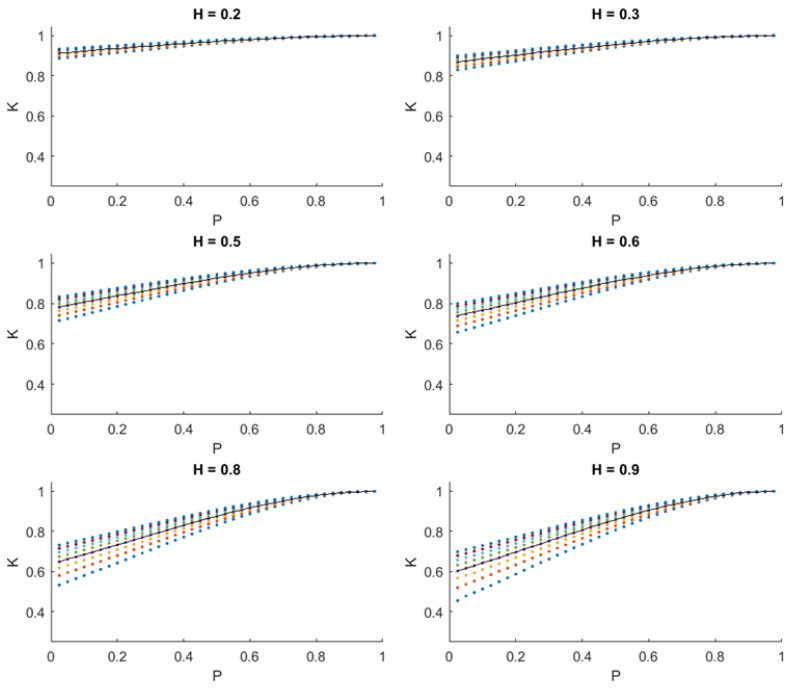

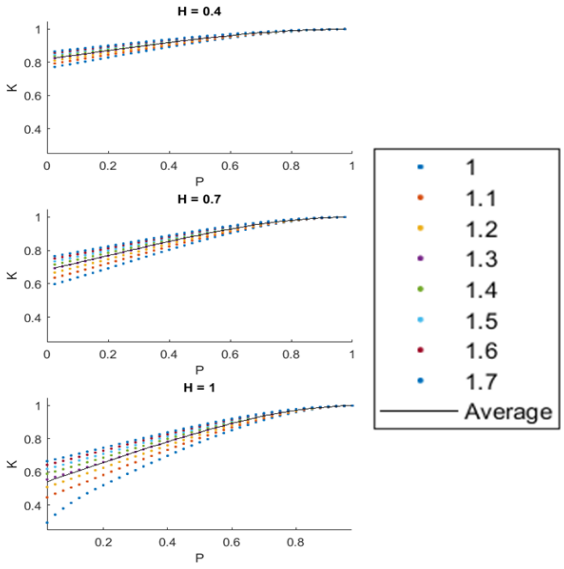

Fig. 44. Estimated heat conductivity in y-direction for the height of the bead changes in 9 levels from 0.2 to 1 D for eight different W-to-D versus contact quality. The solid line indicates the average of the eight W-to-D ratios. The conductivity increases as the contact quality increases, and the effect of *P* is more noticeable in higher *H*.

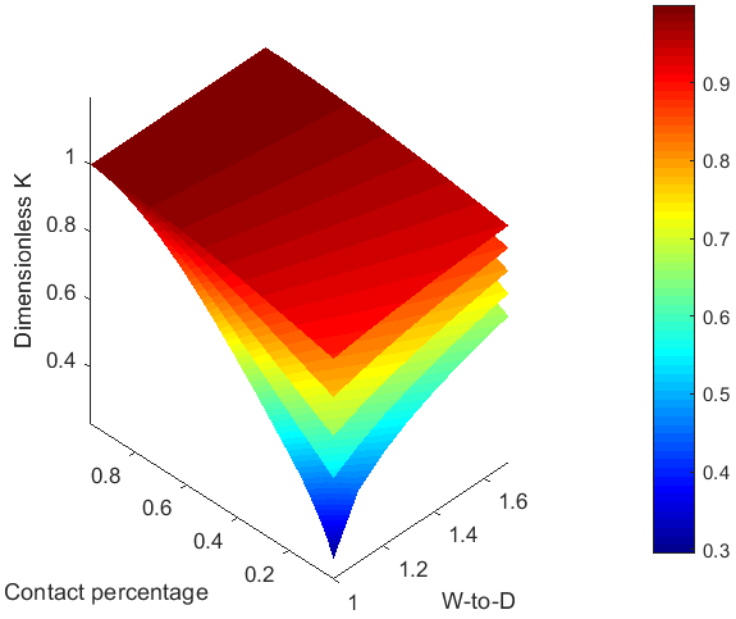

Fig. 45. Surfaces representing the non-dimensionalized conductivity in y-direction for different *H-to-D* ratios versus contact quality and *W-to-D* ratio.

We also calculated the average of the conductivity for each H/D ratio over the *W-to-D*. We then used the curve fitting to this average as a function of contact quality for each H/D ratio, and

used it in our developed numerical model to account for the changes in conductivity as the process progress and the bonding expands. The changes in conductivity for contact quality over 50% for different *W-to-D* ratio is negligible; it allows us to use the average as an acceptable estimation of spatially and temporally varying conductivity for further analyses.

4.2.6 Modal analyses of the testing artifact

We used COMSOL Multiphysics to estimate the dependency and sensitivity of the designed testing artifact to geometrical and material properties. In this process, we altered the nominal values of the parameters shown in Table 20. These changes around the listed nominal values illustrated the sensitivity of the testing artifacts to changes in geometrical and structural properties. Knowing this sensitivity, helped us to find essential parameters to study the characteristics of the artifacts. We swept the selected properties within the specific ranges to provide pools of data required for estimating the mechanical properties. These pools of data were used to evaluate the mechanical properties of testing artifacts knowing their dimensions, density, and natural frequencies.

Table 20: The list of the characteristics and properties of the artifacts changes for modal analyses using COMSOL Multiphysics.

Description	unit	Nominal values
Thickness of internal cantilever, t_c	*mm*	2.0
Thickness of external wings, t_w	*mm*	3.0
Internal length, l_c	*mm*	52.0
Wing length, l_w	*mm*	63.0
Internal width, w_c	*mm*	7.0
Wing width, w_w	*mm*	14.0
End block length, B_c	*mm*	6.0
Top Width, B_w	*mm*	8.0

Module f elasticity, E	MPa	2230.0
Poisson's ratio, ν	–	0.34
Density, ρ	kg/m^3	1040.0

The artifact was designed with two parallel cantilever beams with different thicknesses but on the same plane. Different thicknesses allow us to have a different set of data to characterize the properties of interest. This design provides the basis for comparing the results and also measures the effect of residual stresses and thicknesses. Figure 46 depicts the isometric view of the testing artifact in COMSOL showing the geometrical parameters listed in Table 20.

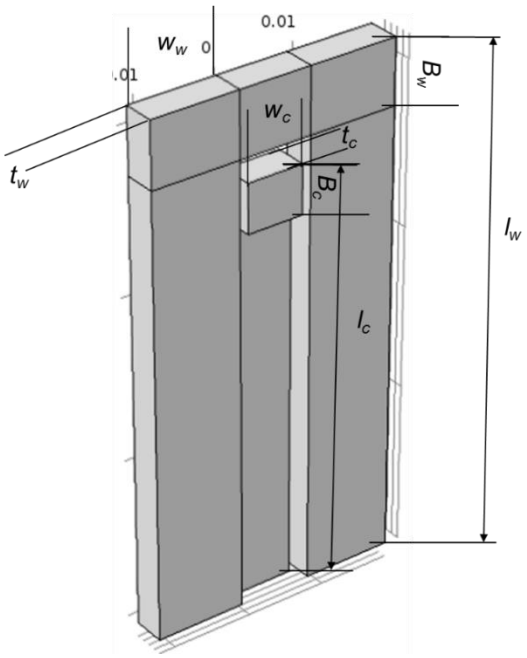

Fig. 46. The isometric view of the artifact in COMSOL Multiphysics with all symbols defining its geometry.

4.2.6.1 Sensitivity analyses to mesh size for modal analyses

One of the essential parameters in a computational analysis is the size of the element. A coarse mesh leads to a faster solution and requires fewer resources, while a fine mesh exponentially increases the runtime. The runtime is essential in our analyses since it significantly affects the data collection processes.

In order to find the best element size, we ran modal analyses in COMSOL Multiphysics ® for seven cases, changing the number of the element from a coarse mesh consisting of 298 elements to an extremely fine mesh of 801,400.

The following graph shows the error of the natural frequencies corresponding to element size with respect to the finest meshes. Increasing the number of elements decreases the error, as shown in Fig. 47. However, the rate of improvement decreases. There is a steep improvement in the accuracy (decrease in error) from the first to the third element sizes, but improvements decrease significantly after. This trend suggests the fourth level mesh provides similar results to the finest mesh with significant lower elements and subsequently lower runtime.

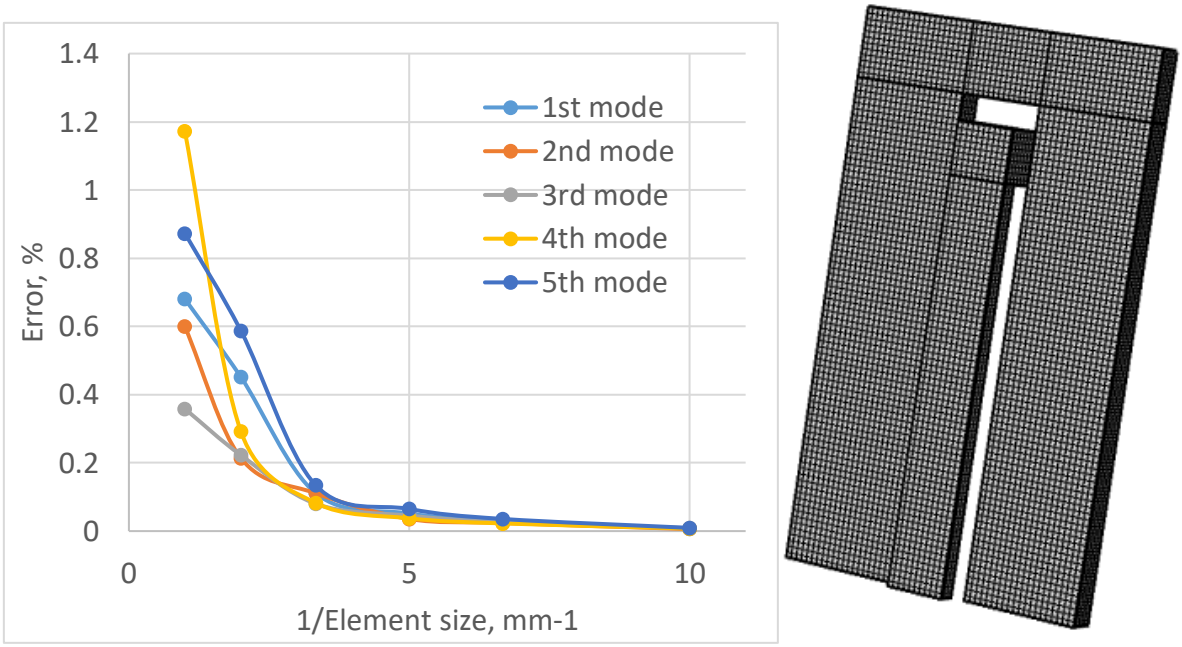

Fig. 47. (a) The error of estimation of the five first natural frequencies decreases as the element size decreases, the graph shows the error concerning the finest mesh versus the inverse of average element size; and (b) the meshed testing artifact for the selected element size.

Considering this graph, case 4 has been selected for further analyses in this dissertation. For this case, the maximum element size is 0.7 mm, and the minimum element size is 0.3 mm, and the number of DOF and elements are 21,800 and 317,949, respectively.

4.2.6.2 Cantilever beam sensitivity analyses for simplified 1D model

In order to understand how the estimation of elasticity is sensitive to parameters, we started by analyzing an analytical model of an anisotropic cantilever beam with fixed area and length.

The analyses of such a simplified model are represented in chapter 3.1.2 above in Eqs (3-13) and (3-14). We altered the parameters based on two strategies. In the first strategy, we applied the known resolution of the machine, for example, the resolution in *x*, *y*, and *z* corresponding to length, width, and thickness, respectively. We also dealt with parameters for which the deviation was not certain, such as density, natural frequency, and Poisson's ratio, and we chose 5% deviation for them. In the second strategy, we blindly considered ±5% changes for all parameters. We analytically determined the deviation in elasticity due to the changes in listed variables and normalized it to elasticity magnitude for each calculation. The nominal values and differentiates are listed in Table 21.

Table 21: The range and the nominal parameter changes for testing artifacts for isotropic material properties.

Description	unit	Range	Nominal values	Nominal or 5% differentiate
Thickness, h	mm	1.5-3.5	2.0	0.25*
Length, L	mm	45.0-70.0	60.0	0.40*
Module f elasticity, E	MPa	1115.0-3345.0	2230.0	111.5
Poisson's ratio, ν	–	0.34	0.34	0.017
Density, ρ	kg/m^3	520.0-1560.0	1040.0	52.0
Natural frequency, ω_n	Hz	Hz	290	3*

*: indicates nominal differentiate.

In this analysis, we only studied the first bending mode since the difference between the other model is only a constant, which does not affect our goal of finding the most effective parameters. Table 22 shows the sensitivity of the module of elasticity to each variable.

Table 22: The sensitivity of the module of elasticity for isotropic material in a cantilever beam due to 5% percent or nominal changes in variables.

Description	Sensitivity at the nominal values for nominal differentiate, %	Sensitivity at the nominal values for 5 percent changes for each variable, %
$\frac{\Delta E/\Delta h}{E} \times \Delta h$	-35.0	-9.3
$\frac{\Delta E/\Delta l}{E} \times \Delta l$	2.7	21.6
$\frac{\Delta E/\Delta \nu}{E} \times \Delta \nu$	-1.3	-1.3
$\frac{\Delta E/\Delta \rho}{E} \times \Delta \rho$	5.0	5.0
$\frac{\Delta E/\Delta \omega}{E} \times \Delta \omega$	3.3	10.3

The analyses of the sensitivity subjected to ±5% changes in each variable reveal the length is the most crucial parameter; natural frequency and thickness come in the second and third places. On the other hand, considering the nominal deviation based on the accuracy of the 3D printing and the measuring tools, the most sensitive component is the thickness. The density and the length also can be measured with relatively good resolution. Thus, the thickness is the most critical parameters to measure with extra attention.

4.2.7 Finding the eigenvalues for isotropic material

We developed FE models in COMSOL Multiphysics® to find the eigenvalues associated with different natural frequencies and mode shapes for thin (center) and thick (wing) sections of the designed testing artifacts. Based on the sensitivity analyses, we knew the critical parameters included length, thickness, Young's modulus (E), density or shear modulus (G), and Poisson's ratio in order. While Young's modulus was critical for bending, both shear modulus and Young's modulus were important in torsion modes. The effect of width was negligible in bending modes. However, width was as important as the module of elasticity in torsion modes

for both center and wing parts. Our sensitivity analyses indicate in the wing part, both Young's and shear moduli have to be incorporated for the correct estimation of eigenvalues associated with natural frequencies. Finally, we ruled out length, assumed the predictable effect of density and thickness, and decided only to study the effect of two parameters—module of elasticity, *E*, and shear modulus, *G*—in order to find the eigenvalues.

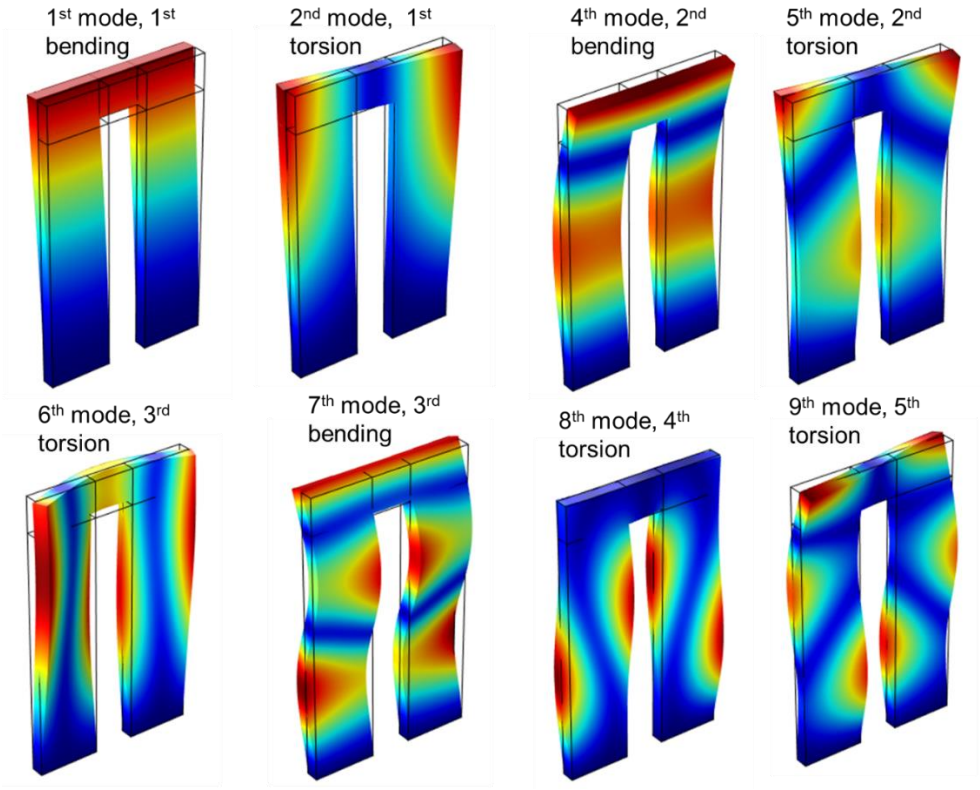

Fig. 48. The mode shapes for the nine first natural frequencies of the wing of the designed testing artifacts.

Table 23 lists the ranges of variables and the steps of changes for sweeping. The solution was solved 165 times for center and wing parts, and we extracted the first ten mode of the center, and first fourteen modes of the wings, and among them gleaned the bending and torsion modes as shown in Fig. 48 and Fig. 49.

We selected five modes of center and six modes of the wing, including bending and torsion modes for further analyses. For each mode, the eigenvalues were found and are listed in Table 24 and Table 25.

Table 23: The selected variables, span, and the increment for obtaining the eigenvalues for isotropic material properties

Description	unit	ranges	increment
Module of elasticity, *E*	MPa	1,115.0- 3,345.0	159.3
Poisson's ratio, ν	-	0.1-0.45	0.035
Shear modulus, *G*		G=*E/2(1+v)*	-
Thickness, *h*	mm	For center: 2.0 For wing: 3.0	N/A
Density, ρ	$Kg/m3$	1040	N/A
Length, *L*	mm	Fixed, 52 for center 63 for wing	N/A

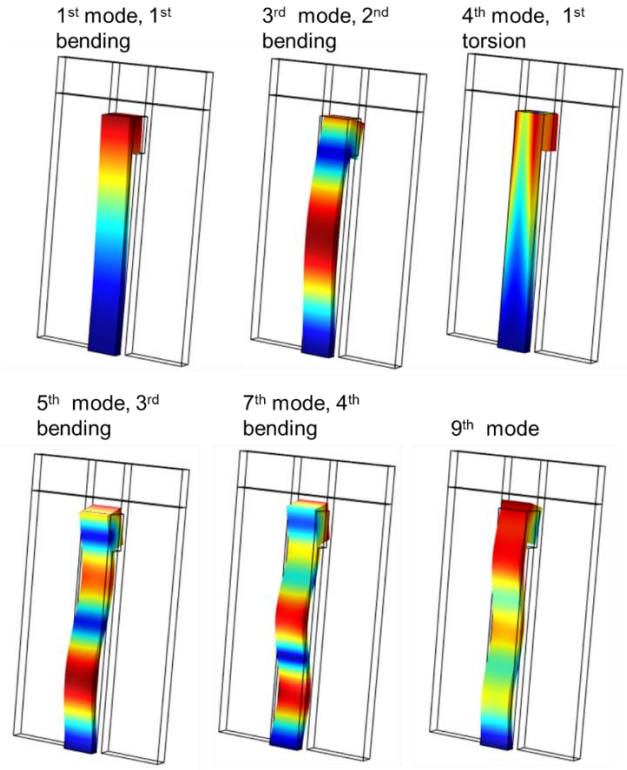

Fig. 49. The mode shapes associated with the first four bending mode and first torsion mode of the beam shape part of the designed testing artifacts.

Figure 48 shows the eight modes, including the three bending modes and five torsional modes of the wings (the peripheral section or thick portion) of the testing artifact.

This analysis also ran for the center part, which, due to its specific design, only had one torsion mode in our range of the first six modes of interest. The five bending and one torsional modes are shown in Fig. 49. Although there were lateral modes, we were not interested in them because the optical sensors are not sensitive to in-plane motion, and the designed excitation unit is optimized for exerting out-of-plane motions.

For each mode, a series of 165 sets of data were produced and used for estimating the eigenvalues. These data were gleaned for the Poisson's ratio between 0.1 and 0.45.

4.2.7.1 Sensitivity analyses for isotropic material properties

The listed parameters in Table 23 changed ±5%, and the natural frequencies found for both wing and center parts of the testing artifacts. The developed modal analyses in Comsol Multiphysics carried out the calculations.

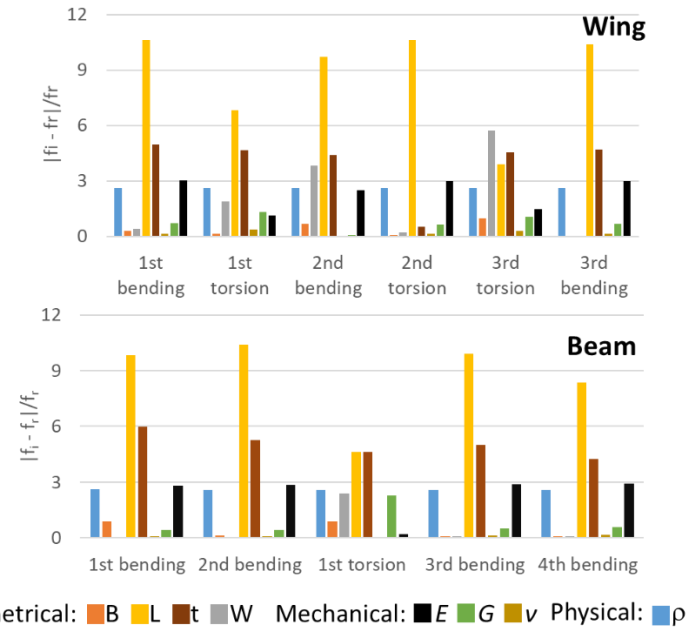

Fig. 50. Sensitivity analyses of the testing artifact to selected geometrical, physical, and structural properties: (a) wing section; and (b) beam (center) section.

For each parameter, the difference between the obtained frequencies, f_i, and reference frequencies, f_r, were found and normalized to the reference values. The results are illustrated in Fig. 50. Results indicate that the most sensitive parameters are length and thickness. The effect of density is similar along different modes, and its significance is interchangeable with the effect of Young's and shear modulus for bending and torsion modes, respectively. The effects of Young's modulus are more significant in bending modes and shear modulus for torsion modes. Width is a critical parameter for torsion and the second bending mode of the wing section.

4.2.7.2 Estimation of isotropic material properties E/G method

The corresponding eigenvalues were obtained by utilizing mean root square minimization for the following equation over the pool of data for each mode of interest.

$$\omega_n = \frac{1}{\sqrt{12 \times \rho}} \times \left[\sqrt{\lambda_{n,1}^4 \frac{E}{(1-\nu^2)} + \lambda_{n,2}^4 \frac{G \times L^2}{b^2}} \right] \times \frac{h}{L^2}, \tag{4-27}$$

All the parameters are defined before, and *n* indicates the mode number. Our evaluation of the eigenvalues determined the following values and with the corresponding R^2 for the wing part:

Table 24: Obtained eigenvalues, $\lambda_{n,i}$, for the wing parts of the artifacts for the three first bending and five first torsion modes.

Description	λ_1	λ_2	R^2
1st bending, mode00	1.5983	0.8271	0.999
1st torsion, mode10	2.2236	1.8145	0.999
2nd bending, mode01	4.0174	2.1100	0.999
2nd torsion, mode11	4.2881	2.6411	0.999
3rd torsion, mode20	4.8757	3.6114	0.999
3rd bending, mode02	6.7451	3.5394	0.999
4th torsion, mode21	5.6946	4.3244	0.999
5th torsion, mode12	6.4648	4.3419	1.000

We also did the same evaluation for the center part. The center part can also be evaluated as a cantilever beam, and the obtained eigenvalues are listed in Table 25. R^2 also defines confidence in the determined values.

Table 25: Obtained eigenvalues, $\lambda_{n,i}$, for the center parts of the artifacts for the four first bending and one torsion modes.

Description	λ_1	λ_2	R^2
1st bending, mode00	1.4240	0.6006	0.999
2nd bending, mode01	3.7849	1.5949	0.999
1st tortion, mode10	2.5775	2.6183	1.000
3rd bending, mode02	6.3847	2.6688-	0.999
4th bending, mode03	8.7441	3.6201	0.999

We applied the least mean square minimization method to find the *E*, *G*, and *v* based on the measured natural frequencies.

4.2.7.3 Estimation of isotropic material properties *E/v* method

We also sought another parallel approach to estimate the isotropic material properties. While the dimensions of the artifact remained unchanged, we found that the eigenvalues were a function of Poisson's ratio, and the ratio between some natural frequencies reflected the dependency on Poisson's ratio known as the Warburton approximation function [215, 235, 320].

The stored data of the FEA analyses were curve fitted to estimate the eigenvalues of the different modes for the beam and wing sections of the testing artifacts. Our investigation revealed the second-order polynomial could adequately define the dependency of eigenvalues to Poisson's ratio. The following approximations were held for all the selected modes.

$$\sqrt[4]{\frac{\omega_{nm}^2 \times L^4 \rho}{D}} = \lambda_{nm}(v) = \sum_{i=0}^{2} a_{nm,i} \times v^i, \qquad (4\text{-}28\text{-a})$$

$$\sqrt[4]{\frac{f_{nm}^2 \times L^4 \rho}{D}} = \frac{\lambda_{nm}(v)}{\sqrt{2\pi}} = \sum_{i=0}^{2} a_{nm,i} \times v^i, \quad \text{(4-28-b)}$$

where, ω_{nm} is the natural angular rotation, f_{nm} is the natural frequencies, and the rest are defined before.

We realized $\frac{\lambda_{nm}^4}{1-\nu^2}$ changes up to 5% throughout the changes in Poisson's ratio for bending modes. We defined new parameters as $\frac{\lambda_{0m}^4}{1-\nu^2} = \gamma_{0m}^4$ and plotted its normalized values with respect to the maximum of the set of data, as shown in Fig. 51 for both wing and beam parts.

These negligible changes suggest the following equation can be used directly for bending modes to estimate the isotropic equivalent Young's modulus while ignoring the Poisson's ratio:

$$\frac{48\pi^2 \times f_{0i}^2 \times L^4 \rho}{\gamma_{ij}^4 h^2} = E_{0i}. \quad \text{(4-29)}$$

The error associated with this equation would be less than 5% for both the wing and beam sections, although the beam section yields better and more accurate results. In addition, the effect of Poisson's ratio is pronounced in shear modulus and contributes to evaluating both Poisson's ratio and shear modulus through an iterative procedure.

For the beam part, $\lambda_{i0}^4 \cong \gamma_{i0}^4$ and the shear modulus can be found directly. However, as it shows in Fig. 51, this assumption is not valid for the wing section. γ_{i0} changes significantly for the torsion modes, although for the bending, its effect may be neglected.

Thus, the wing section torsion modes demonstrate a measurable effect of the Poisson's ratio on the natural frequency, which substantiates our assumption of its contribution to the estimation of the anisotropicity in the printed components. The beam part gives equivalent isotropic material properties, and the wing section can contribute to estimating the anisotropicity. This concurrent entanglement can improve the estimation processes.

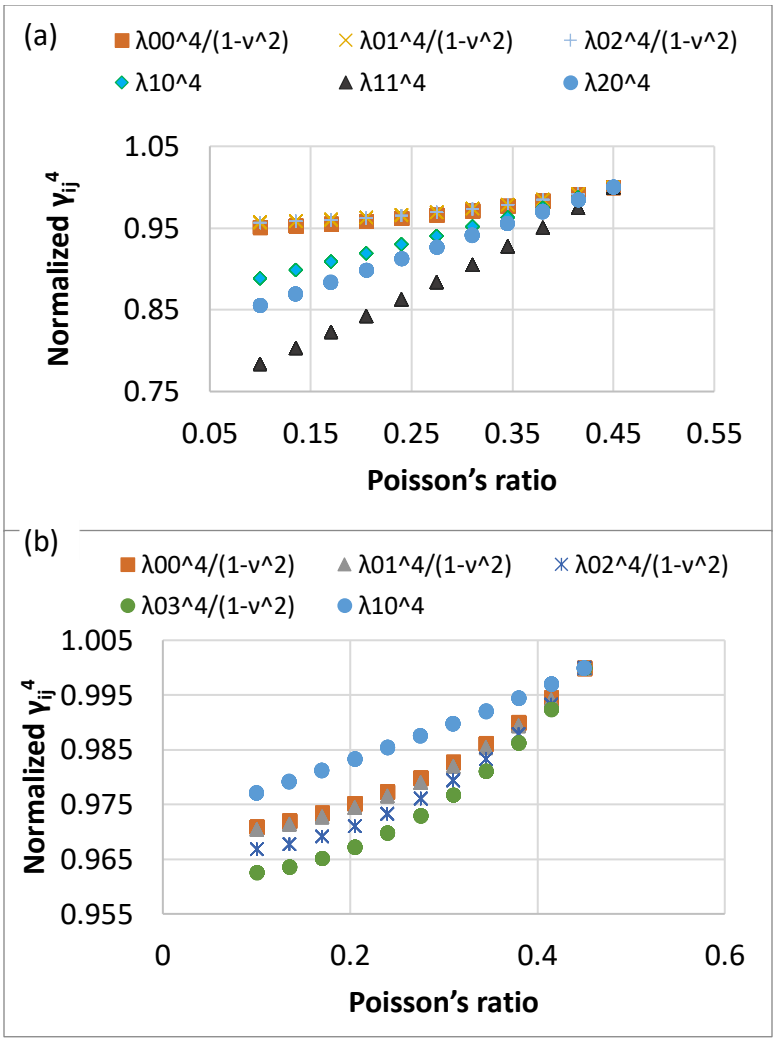

Fig. 51. Graphs show the normalized γ_{ij}^4 versus Poisson's ratios of the testing artifacts: (a) wing section; and (b) beam section.

We determined the average of γ_{ij} ignoring Poisson's effect on the different bending and torsion modes, as listed in Table 26.

Table 26: Obtained corrected eigenvalues, γ_{ij}, for the center and wing sections of the design artifacts.

Description	beam	wing
1st bending, mode$_{00}$	1.648±0.006	1.819±0.011
2nd bending, mode$_{01}$	4.378±0.016	4.595±0.025
1st tortion, mode$_{10}$*	2.6492±0.007	1.972±0.028

2nd torsion, mode$_{11*}$	-	3.127±0.095
3rd torsion, mode$_{20*}$	-	3.972±0.078
3rd bending, mode$_{02}$	7.362±0.031	7.712±0.043
4th bending, mode$_{03}$	10.047±0.048	-

* The γ_{ij} is determined considering the width of the sample as $\frac{48\pi^2 \times f_{ij}^2 \times b^2 L^2 \rho}{\lambda_{ij}^4 h^2} = G_{ij}$

We employed an iterative strategy by using curve fitting for estimating the relationship between Poisson's ratio and eigenvalues and determined the equivalent elastic and shear modulus for the testing artifacts.

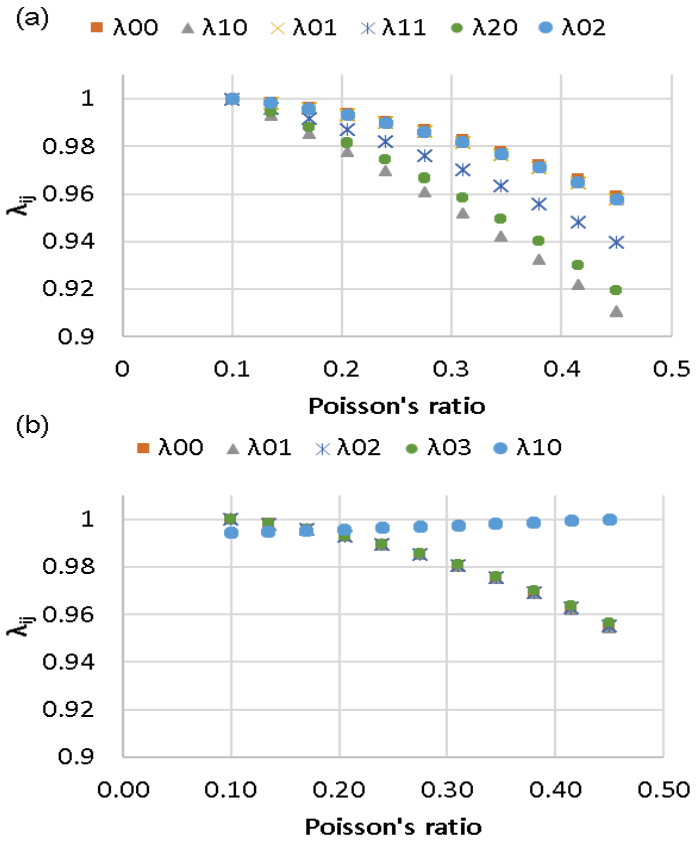

Fig. 52. Graphs show the normalized values of the determined eigenvalues, λ_{nm}, for different modes versus Poisson's ratios of the testing artifacts: (a) wing section; and (b) beam section.

The estimated eigenvalues for bending illustrate strong similarities, and as shown in Fig. 52, their normalized values lay on top of each other. We estimated the dependency of λ_{ij} to

Poisson's ratio and used the polynomial expressed in Eq. (4-28-a) and (4-28-b) to fit curves to collected data.

All the estimated curves revealed a robust correlation for a second-order polynomial as a function of Poisson's ratio with the R^2 determined to be close to 1.0. Although the changes due to the specific design of the testing artifacts were more significant for the wing part compared to the beam, curve fitting was performed for both bending and torsion modes to improve the outcome.

Table 27: The constant for the curve fit of eigenvalues, λ_{nm}, for the wing and beam sections of the designed artifacts.

Description, $mode_{nm}$	$a_{nm,0}$	$a_{nm,1}$	$a_{nm,2}$	R^2
	Wing			
1st bending, $mode_{00}$	1.8064	0.027	-0.4275	0.9999
1st torsion, $mode_{10}$	1.9004	0.1415	0.0396	1.0
2nd bending, $mode_{01}$	4.5701	0.0463	-1.0784	1.0
2nd torsion, $mode_{11}$	2.9845	0.4906	0.0912	1.0
3rd torsion, $mode_{20}$	3.8472	0.466	-0.0438	1.0
3rd bending, $mode_{02}$	7.6708	0.0727	-1.7972	1.0
	Beam			
1st bending, $mode_{00}$	1.6404	0.0251	-0.4315	0.999
2nd bending, $mode_{01}$	4.3596	0.0566	-1.126	1.0
1st tortion, $mode_{10}$	2.6386	0.0322	0.0197	1.0
3rd bending, $mode_{02}$	7.3304	0.079	-1.8301	1.0
4th bending, $mode_{03}$	9.9999	0.0967	-2.4221	1.0

The obtained eigenvalues were functions of Poisson's ratio; thus they can be used to estimate it. We compared the ratio of the different combinations of obtained eigenvalues to find out

which combination could be more sensitive to the changes in Poisson's ration and used it to estimate the Poisson's ratio. The ratio between the eigenvalues directly related to the ratio of their associated square root of natural frequencies is thus:

$$\nu(\lambda_{ij,kl}) = \sum_{z=0}^{2} b_{(ij,kl),z} \times {\lambda_{ij,kl}}^{z}, and\ \lambda_{ij,kl} = \frac{\lambda_{ij}(\nu)}{\lambda_{kl}(\nu)} = \sqrt{\frac{f_{ij}}{f_{kl}}}. \quad (4\text{-}30)$$

When these ratios are measured, it can be used to find the Poisson's ratio, which then can be used for estimating the λ that leads to the estimation of Young's modulus.

Our analyses revealed the following combinations were more sensitive to these changes and could be exploited for estimation of Young's modulus:

- For beam: $\lambda_{02}/\lambda_{10}$, $\lambda_{03}/\lambda_{10}$and $\lambda_{10}/\lambda_{00}$, we also expect to see the similar ratios between $\lambda_{03}/\lambda_{00}$ and $\lambda_{03}/\lambda_{01}$ as well as $\lambda_{02}/\lambda_{01}$ and $\lambda_{02}/\lambda_{00}$.
- For wing: $\lambda_{10}/\lambda_{00}$, $\lambda_{11}/\lambda_{10}$, $\lambda_{20}/\lambda_{01}$ and $\lambda_{02}/\lambda_{20}$, we also expect to see the similar ratio between $\lambda_{02}/\lambda_{01}$ and $\lambda_{02}/\lambda_{00}$ as well as $\lambda_{11}/\lambda_{00}$ and $\lambda_{11}/\lambda_{01}$.

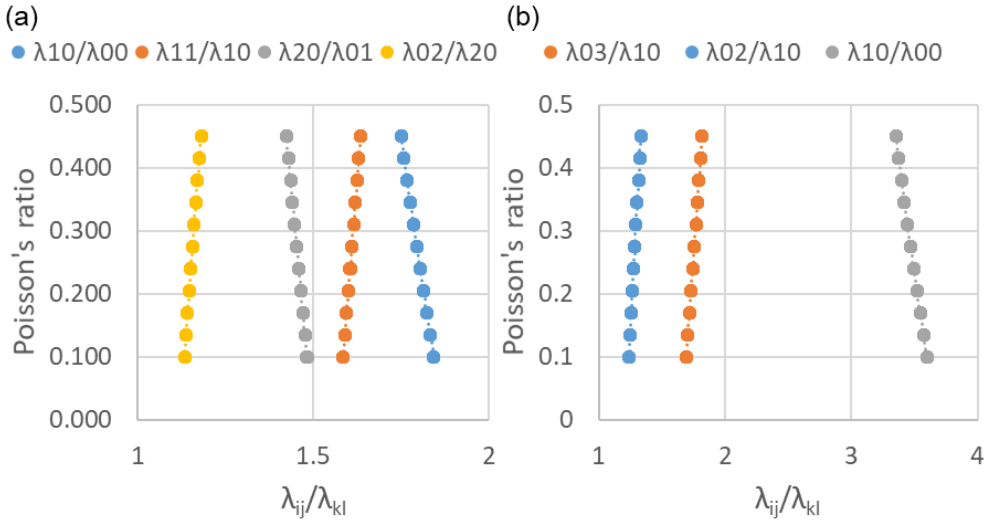

Fig. 53. The graphs show the trends of the selected $\lambda_{ij,kl}$ versus Poisson's ratios of the testing artifacts: (a) wing section; and (b) beam section.

These ratios can be used for the estimation of Young's modulus and Poisson's ratio and for checking the validity and reliability of the measurements. Figure 53 shows two sets of plots and the fitted curve corresponding to the selected eigenvalue ratios versus Poisson's ratios.

We observed that a second-order polynomial regression worked well for demonstration of the dependency, and the determined constants and R^2 are listed in Table 28.

Table 28: The determined curved fit constants for the selected $\lambda_{ij,kl}$ for the testing artifacts corresponding to the graphs shown in Fig. 53.

$\lambda_{ij,kl}$	$b_{(ij,kl),0}$	$b_{(ij,kl),1}$	$b_{(ij,kl),2}$	R^2
	Wing			
$\lambda_{10}/\lambda_{00}$	16.400	-14.209	2.9106	1.0
$\lambda_{11}/\lambda_{10}$	12.757	9.2038	-0.6878	1.0
$\lambda_{20}/\lambda_{01}$	4.1433	0.5949	-2.2431	1.0
$\lambda_{02}/\lambda_{20}$	-22.718	32.365	-10.789	1.0
	Beam			
$\lambda_{02}/\lambda_{10}$	-4.1044	2.9976	0.3134	1.0
$\lambda_{03}/\lambda_{10}$	-5.0507	3.3162	-0.1622	1.0
$\lambda_{10}/\lambda_{00}$	12.558	-5.6449	0.6066	1.0

4.2.8 Modal analyses of the testing artifact to determine the sensitivity to orthotropic material

A model was developed in COMSOL Multiphysics to determine the sensitivity of the testing artifacts to material orthotropicity, including Young's moduli, shear moduli, and Poisson's ratios. We also analyzed the effect of geometrical deviations.

The numerical study of orthotropicity can be extensive and time-consuming as it sweeps a wide range of parameters. Thus, we estimated the upper and lower limits of the magnitude of mentioned mechanical properties, Young's moduli, shear moduli, and Poisson's ratios, and

changed them within the selected ranges listed in Table 29. One can theoretically estimate the properties as expressed in equation (3-24-a) to (3-23-d). Orthotropic structural properties were evaluated as a function of porosity in first principal direction, p_1, between 0 and 20%. These properties are listed in Table 29 and are obtained based on ABS mechanical properties with Young's modulus as E = 2,230.0 MPa, Poisson's ratio as v = 0.34, and shear modulus as G = 831.089 MPa.

Table 29: Changes in the nine independent elasticity constants as the porosity changes between 0 to 20%.

Description	unit	For $p_1 = 0$	For $p_1 = 0.2$
$\overline{E_1}$	MPa	2230.0	1784.0
$\overline{E_2}, \overline{E_3}$	MPa	2230.0	1232.7
$\overline{G_{12}}, \overline{G_{13}}$	MPa	832.1	544.04
$\overline{G_{23}}$	MPa	832.1	459.97
$\overline{v_{12}}\ and \overline{v_{13}}$	-	0.34	0.272
$\overline{v_{23}}, \overline{v_{32}}, \overline{v_{21}}, and \overline{v_{31}}$	-	0.34	0.188
ρ	$Kg/m3$	1040.0	832.0

In the next step, we used finite element software, e.g., COMSOL Multiphysics, to study the effects of the orthotropic properties on the natural frequencies. We did the inverse analyses, meaning we analyzed the artifacts by changing its mechanical and geometrical properties and determined how sensitive each of the properties was to natural frequencies. We altered the variables, listed in Table 30, ±5 percent of the nominal value, found changes in natural frequencies, and normalized them. The obtained values were normalized based on the reference frequencies obtained for the nominal values and listed in Table 30.

We developed analyses for the central beam and the peripheral wings, while assumed orthotropic material properties for both.

Table 30: Changes in the range and the nominal parameters for testing artifacts for orthotropic material properties.

Description	unit	Range	Nominal values	Differentiate, 5 percent of the nominal value
Thickness of internal cantilever, t_c	mm	1.0-4.0	2.0	0.1
Thickness of external wings, t_w	mm	45.0-70.0	3.0	0.15
Internal length, l_c	mm	45-65	52.0	2.6
Wing length, l_w	m	55-70	63.0	3.15
Internal width, w_c	mm	5-10	7.0	0.35
Wing width, w_w	mm	10-20	14.0	0.7
Density, ρ	kg/m^3	832.0-1040.0	1040.0	52.0
Module of elasticity, E_1	MPa	1624.0-2230.0	2230	111.5
Module of elasticity, E_2	MPa	1122.2-2230.0	2230	111.5
Shear modulus, G_{12}	a	272.02-832.1	832.1	41.6
Shear modulus, G_{23}	MPa	459.97-832.1	832.1	41.6
Poisson's ratio, ν_{12}	-	0.272-0.34	0.34	0.017
Poisson's ratio, ν_{23}	-	0.188-0.34	0.34	0.017

The series of COMSOL analyses were performed while changing each parameter of interest, and we extracted the associated bending and torsion modes. We studied the beam and wing part separately by performing backward, forward, and central derivatives based on a 5% deviation around the nominal values listed in Table 30. (The table showing the sensitivity of the measured natural frequency is presented in appendices 9.3.3 and 9.3.4.)

The parameters can be divided into two categories, geometrical and structural. Looking at the geometrical characteristics, one can conclude that the most prominent parameters are the length and thickness; the effect of width for bending modes seems negligible. However, it is

essential for the torsion modes. The effect of the size of the end block compared to the length and thickness is negligible too. Thus the three selected critical parameters are length, thickness, and width. A similar conclusion can be drawn from the sensitivity analyses of the center part, as shown in Fig. 54, including the bending and torsion modes.

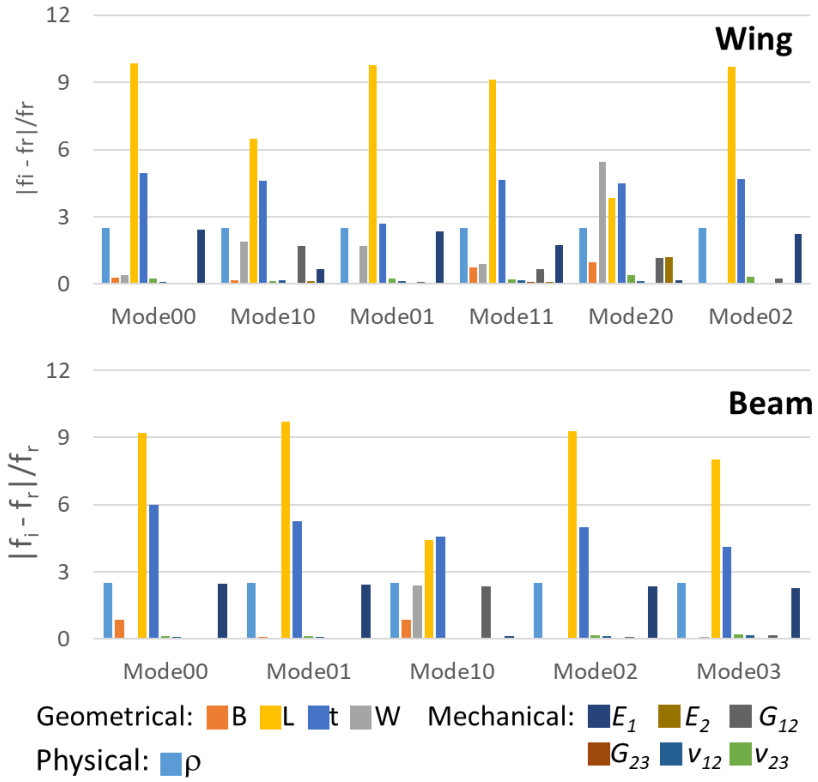

Fig. 54. Sensitivity analyses of the orthotropic testing artifacts to selected geometrical, physical, and structural properties: (a) wing section; and (b) beam (center) section.

Comparing the sensitivity of the orthotropic material properties and density indicates the density is the most critical parameters and shear modulus G_{12} and Young's modulus E_1, are the next essential parameters for torsion and bending modes, respectively. It is also worth mentioning that there is a weak interconnection between these two parameters for different mode shapes. In other words, when the effect of shear modulus for torsion is as high as the effect of density, the sensitivity to Young's modulus is low. A similar pattern is also exhibited for the effects of Young's modulus compared to shear modulus for pure bending modes. The sensitivity

to Poisson's ratio and the G_{21} is negligible, while the effect of E_2 modulus is similarly vital for all modes. Thus, the critical parameters relating to natural frequencies for orthotropic materials in our design are G_{12}, E_1, E_2, and ρ.

Comparing the sensitivity of a lower and upper range of the selected variables, listed in Table 30, indicates that the sensitivity to geometrical attributes does not remarkably change as the material mechanical properties change. This conclusion is also valid for the sensitivity to structural characteristics, although the sensitivity to some parameters such as Poisson's ratio and E_2 moduli are increased in higher bonds. In general, the sensitivity for all variables within the two extremes of these variables seems more and less the same.

We concluded that, in this design, finding the natural frequencies and measuring the critical variables (like thickness, length, and density) accurately can lead to the estimation of the E_2 and E_1 moduli of elasticity from bending modes. Also, from the comparison of different bendings modes, it should be possible to estimate the v_{12}. Our findings also support the idea of the application of torsion modes for estimation of the shear modulus, G_{12}. It is also possible to measure Poisson's ratio by measuring the ratio between different modes.

4.2.9 Finding eigenvalues of the testing artifacts for orthotropic materials

An orthotropic part has nine constants, including the three elastic moduli, shear moduli, and Poisson's ratios for the three principal directions. However, in a thin plate, a transversely isotropic material (in 2-3 plane) can be assumed which reduces the constants to five as follow:

$$E_x = \overline{E_1} > \overline{E_2}\ and\ \overline{E_3}$$
$$E_y = \overline{E_2} = \overline{E_3} \quad (4\text{-}31)$$
$$G_{xy} = \overline{G_{12}} = \overline{G_{13}} = G$$

$$G_{yz} = \overline{G_{23}} = \frac{E_2}{2 \times (1 + v_{23})},$$

$$v_{xy} = \overline{v_{12}} = \overline{v_{13}}$$

$$v_{yx} = \overline{v_{23}} = \overline{v_{32}} = \overline{v_{21}} = \overline{v_{31}} < v_{xy}$$

We demonstrated the five modes of the center and six modes of the wings could allow us to determine these five unknowns for each artifact. It is also known that $\frac{E_x}{v_x} = \frac{E_y}{v_y}$.

We employed finite element models in COMSOL Multiphysics® to find the eigenvalues associated with the different mode shapes for thin (center) and thick (wing) sections of the design testing artifacts for orthotropic material properties. We swept four sets of mechanical properties within the ranges shown in Table 31 by listed increments.

Table 31: The selected variables with ranges for obtaining the eigenvalues for orthotropic material properties

Description	unit	ranges	increment
Elastic modulus, E_1	MPa	1,115.0- 3,345.0	446
Poisson's ratio, v_{12}	-	0.1-0.45	0.070
Poisson's ratio, v_{21}	-	0.1-0.45	0.070
Shear modulus, G_{12}	M	416.045-1248.134	166.418
Thickness, h	mm	For center: 2.0 For wing: 3.0	N/A
Density, ρ	$Kg/m3$	1040	N/A
Length, L	mm	Fixed, 52 for center 63 for wing	N/A

We collected 1,296 sets of data for the beam and wing section separately. These data were checked to satisfy the Poisson's ratio in the following range:

$$-1 < v_{21} < 1 - 2v_{21}^2 \frac{E_1}{E_2}, \tag{4-32}$$

The collected data was analyzed for both center and wing sections of the testing artifact assuming transversely isotropic material. The details of the correlation analyses are presented in Table 32 for the beam and wing section. The table indicates the degree of importance of variables in three levels: very important (VI), important (I), not important (NI). We used Matlab correlation coefficient indicator as well as the FEA analyses to find and sort the importance level. We observed the complex dependency of the frequencies to different material properties, as listed in Table 32. We observed the center section of the testing artifact shows little dependency to Poisson's ratio for both bending and torsion modes. The three first bending modes only depend on the first principal elastic modulus, E_1, and the only torsion mode on shear modulus, G_{12}. Thus the estimation of orthotropic material properties only based on the center part is unattainable.

This observation, for the wing part, is not valid, and we observed more complex dependency to different material properties in different modes. The bending modes and natural frequencies were found related to E_1, and slightly sensitive to v_{12} and v_{21}. The first and third torsion modes were correlated with E_1 and G_{12}, and slightly to v_{21}. The second bending was affected by v_{21}, G_{12}, and slightly v_{12}. Thus, the wing is capable of estimating the E_2, E_1, G_{12}, v_{12}, and v_{21}.

Table 32: The correlation and screening analyses on the bending and torsion modes with respect to the material properties.

Description	Center part								
	E_1	E_2	v_{21}	v_{12}	G_{12}	D_x	D_y	D_1	D_{xy}
$mode_{00}$, 1st bending	VI	I	NI	NI	NI	VI	I	VI	NI
$mode_{01}$, 2nd bending	VI	I	NI	NI	NI	VI	I	VI	NI
$mode_{10}$, 1st torsion	NI	NI	NI	NI	VI	NI	NI	NI	VI
$mode_{02}$, 3rd bending	VI	I	NI	NI	NI	VI	I	VI	NI

$mode_{03}$, 4th bending	VI	I	NI	NI	I	VI	I	I	I
Wing part									
$mode_{00}$, 1st bending	VI	VI	I	I	NI	VI	I	VI	NI
$mode_{10}$, 1st torsion	I	I	NI	NI	VI	I	I	I	VI
$mode_{01}$, 2nd bending	VI	VI	I	I	NI	VI	I	VI	NI
$mode_{11}$, 2nd torsion	VI	VI	NI	NI	I	VI	I	VI	I
$mode_{20}$, 3rd torsion,	I	VI	I	I	VI	I	VI	VI	I
$mode_{02}$, 3rd bending	VI	VI	NI	NI	I	VI	I	VI	I

We first assumed the linear relationship between plate bending stiffness (rigidity) and speculated eigenvalues and presumed no dependency to material properties but only to geometry [229]. We employed Eq. (3-22) after rewriting it in the following forms:

$$\begin{aligned}\omega_{nm}^2\rho h &= \lambda_{1,nm}^4 D_x + \lambda_{2,nm}^4 D_y + \lambda_{3,nm}^4 D_1 + \lambda_{4,nm}^4 D_{xy} \; or \; \omega_{nm}^2\rho h \\ &= \lambda_{1,nm}^4 D_x + \lambda_{2,nm}^4 D_y + \lambda_{3,nm}^4 (D_1 + 2D_{xy}),\end{aligned} \tag{4-33}$$

where, all parameters were defined before, except $\lambda_{i,nm}$, which are the eigenvalues associated with each bending stiffness. The modal analyses eigenvalues α_i^n are determined knowing $\lambda_{1,nm}^4 = \alpha_{1,nm}^4/L^4$, $\lambda_{2,nm}^4 = \alpha_{2,nm}^4/b^4$, and $\lambda_{3\ or\ 4,nm}^4 = \alpha_{3\ or\ 4,nm}^4/L^2 \times b^2$.

Comparing the result of sensitivity analyses between bending stiffness, *D*, and moduli revealed a similar pattern observed in isotropic material properties. This suggested the effects of Poisson's ratios could be incorporated in the definition of eigenvalue, which decoupled the equation from bending stiffness and made natural frequencies functions of moduli:

$$\omega_{n,m}^2 \rho h = \frac{\alpha_{1,nm}^4}{L^4} D_x + \frac{\alpha_{2,nm}^4}{b^4} D_y + \frac{\alpha_{3,nm}^4}{L^2 \times b^2}\left(D_1 + 2D_{xy}\right) =$$

$$\frac{h^3}{12} \times \left[\frac{\alpha_{1,nm}^4}{(1-v_{12}v_{21})\times L^4} \times E_1 + \frac{\alpha_{2,nm}^4}{(1-v_{12}v_{21})\times b^4}\frac{v_{21}}{v_{12}} \times E_1 + \right. \tag{4-34}$$

$$\left.\frac{\alpha_{3,nm}^4}{L^2 \times b^2}\left(\frac{v_{21}\times E_1}{(1-v_{12}v_{21})} + 2G_{12}\right)\right].$$

In this sense, $\frac{\alpha_{1,nm}^4}{(1-v_{12}v_{21})}$ and $\frac{\alpha_{2,nm}^4}{(1-v_{12}v_{21})}$ are for bending and $\alpha_{3,nm}^4$ for flexural rigidity, and all are functions of Poisson's ratios. We defined a new set of parameters as we did for the isotropic material naming them λ, and are defined as:

$$\lambda_{j,nm}^4 = \frac{\alpha_{j,nm}^4}{(1 - v_{12}v_{21})}, j = 1 \; and \; 2$$

$$\lambda_{j,nm}^4 = \alpha_{j,nm}^4, j = 3 \tag{4-35}$$

$$\lambda_{j,nm}^4 = \left[a_{j,nm,0} + a_{j,nm,1} \times v_{12} + a_{j,nm,2} \times v_{21} + a_{j,nm,3} \times v_{12}v_{21}\right.$$

$$\left. + a_{j,nm,4} \times v_{12}^2 + a_{j,nm,5} \times v_{21}^2\right], \mathrm{j} = 1,2, \text{and } 3.$$

We performed stepwise regression, meaning we started by assuming constant λ and then attempted to find the polynomial constants in Eq. (4-35). In this process, we first calculated the center section constants, assuming that the first three bending modes and torsion modes only depended on D_x and D_{xy}, respectively. We directly employed E_1, v_{21}, and G_{12} to estimate eigenvalues.

The relationship seemed linear in terms of bending rigidity, but using mechanical characteristics can transform this linear equation to a non-linear one, specifically for the higher-order mode shapes where all mechanical properties play a role in the estimated values.

The linear relationship can be applied easily to an engineering problem, and it lends itself effectively to the solution of an over-determined system of equations using a least mean square approach. We employed non-linear regression to find the eigenvalues to estimate constants of

Eq. (4-33) accurately [229]. In that sense, the iterative process was applied to correct the eigenvalues based on the FEM analyses on the testing artifact.

Knowing $\nu_{21} \leq \nu_{12} \leq 0.5$ means $\nu_{21} \times \nu_{12}$ is smaller than 0.25 However, $\nu_{21} \times \nu_{12}$ is usually less or equal to 0.15 in orthotropic materials [217]. Therefore, Taylor's series can be used to redefine term $1/(1-\nu_{12}\nu_{21})$ in Eq. (4-35) as follow:

$$\frac{1}{(1-\nu_{12}\nu_{21})} = [1+\nu_{12}\nu_{21}+(\nu_{12}\nu_{21})^2+or(\nu_{12}\nu_{21})^3], n = 1,2,3. \quad (4\text{-}36)$$

Truncating Taylor's series for the third order and above only introduces up to 1.5% error in the maximum possible value of 0.25.

The results of the stepwise regression assuming fixed values are listed in Table 33. The results were obtained for the center and wing part of the testing artifacts, over the previously gathered data of 1,296 natural frequencies for each mode using COMSOL Multiphysics.

Table 33: Obtained eigenvalues, α_i^n, for the center and wing parts of the designed artifacts for bending and torsion modes.

Description	Center part				
	λ_1	λ_2	λ_3	λ_4	R^2
$mode_{00}$, 1st bending	1.6462	0	0	0	0.999
$mode_{01}$, 2nd bending	4.3689	0	0	0	0.998
$mode_{10}$, 1st torsion	0	0	0	2.6406	0.988
$mode_{02}$, 3rd bending	7.3326	0	0	0	0.994
$mode_{03}$, 4th bending*	9.9326	0	0	2.0643	0.998
	Wing part				
$mode_{00}$, 1st bending	1.8160	0	0	0	0.998
$mode_{10}$, 1st torsion	2.0579	0	1.4211	1.6900	0.822
$mode_{01}$, 2nd bending	4.5789	0	0	0	0.996

$mode_{11}$, 2nd torsion	4.7036	0	1.8369	2.1845	0.977
$mode_{20}$, 3rd torsion,	0	1.0160	2.8366	3.3732	0.865
$mode_{02}$, 3rd bending	7.4072	0	2.1362	2.5404	0.989

* E_1 ang G_{12} are used for finding λ_i

The coefficient of determination shows that, although the linear and constant eigenvalues seem to be able to reflect the material properties, they do not provide the high level of confidence needed to estimate this coefficient certainly, and these constants are varying as material properties alter. Results point out that bending modes are less sensitive to Poisson's ratios, and torsion modes such as $mode_{10}$ and $mode_{20}$ are found strongly dependent; we observed a similar pattern for isotropic materials. To improve the estimation, we sought to define the eigenvalues as expressed in Eq. (4-35) and find the polynomial constant for each of them. We also did a stepwise regression and removed the unimportant set of parameters to reach the simplest but the most efficient set of polynomials representing the physics with high confidence.

We did stepwise procedures, explored different combinations, and finally found those that could represent the changes more accurately with a higher coefficient of confidence and fewer constants. In this process, sensitivity analyses were considered to reach the best solution. The summary of the acquired eigenvalues through the above processes are listed in Table 34.

Table 34: Obtained eigenvalues, $\lambda_{j,nm}$, for the center and wing parts of the design artifacts for bending and torsion modes.

Description	Wing part	R^2
1st bending	$\lambda_{1,00} = 1.8095 \times \sqrt[4]{1 - 0.251 \times \nu_{12} - 0.0187 \times \nu_{21} + 0.2552\nu_{12} \times \nu_{21} + 0.0789 \times \nu_{12}^2}$ $\lambda_{2,00} = 0$ $\lambda_{3,00} = 0$ $\lambda_{4,00} = 0$	0.999

1st torsion	$\lambda_{1,10} = 2.4142\sqrt[4]{1 + 0.5178\nu_{12} - 2.7837\nu_{21} - 1.4123\nu_{12}\nu_{21} - 1.2244\nu_{21}^2}$ $\lambda_{2,10} = 0$ $\lambda_{3,10} = 1.4498 \times \sqrt[4]{1.0 - 0.4963\nu_{12} + 0.8888\nu_{21} + 0.7318\nu_{21}\nu_{12} - 1.15368\nu_{21}^2}$ $\lambda_{4,10} = 1.7241 \times \sqrt[4]{1.0 - 0.4963\nu_{12} + 0.8888\nu_{21} + 0.7318\nu_{21}\nu_{12} - 1.15368\nu_{21}^2}$	0.979
2nd bending	$\lambda_{1,01} = 4.5685 \times \sqrt[4]{1 - 0.0710\nu_{12} + 0.3489\nu_{12} \times \nu_{21} + 0.0697\nu_{12}^2 - 0.0443 \times \nu_{21}^2}$ $\lambda_{2,01} = 0$ $\lambda_{3,01} = 0$ $\lambda_{4,01} = 0$	0.997
2nd torsion	$\lambda_{1,11} = 4.7669\sqrt[4]{1 - 0.4391\nu_{12}\nu_{21} - 0.778\nu_{21}^2}$ $\lambda_{2,11} = 0$ $\lambda_{3,11} = 1.8868 \times \sqrt[4]{1.0 - 0.3635\nu_{12} + 1.300\nu_{21}\nu_{12}}$ $\lambda_{4,01} = 2.2438 \times \sqrt[4]{1.0 - 0.3635\nu_{12} + 1.300\nu_{21}\nu_{12}}$	0.991
3rd torsion	$\lambda_{1,20} = 0$ $\lambda_{2,20} = 1.1605 \times \sqrt[4]{1 + 2.7783\nu_{12} - 3.4603\nu_{21} - 6.8609\nu_{12} \times \nu_{21} + 3.6293\nu_{12}^2 + 2.3903 \times \nu_{21}^2}$ $\lambda_{3,20} = 2.9549 \times \sqrt[4]{1 - 3.2337\nu_{12} + 2.4129\nu_{21} - 5.5804\nu_{12} \times \nu_{21} + 4.6574\nu_{12}^2 + 1.3932 \times \nu_{21}^2}$ $\lambda_{4,20} = 3.5139 \times \sqrt[4]{1 - 3.2337\nu_{12} + 2.4129\nu_{21} - 5.5804\nu_{12} \times \nu_{21} + 4.6574\nu_{12}^2 + 1.3932 \times \nu_{21}^2}$	0.979
3rd bending	$\lambda_{1,02} = 7.4542 \times \sqrt[4]{1 - 0.3687\nu_{12} + 0.3621\nu_{21} - 0.2608\nu_{12} \times \nu_{21} + 0.4627\nu_{12}^2 - 0.5744 \times \nu_{21}^2}$ $\lambda_{2,02} = 0$ $\lambda_{3,02} = 2.0294 \times \sqrt[4]{1 + 3.8299\nu_{12} - 3.5404\nu_{21} - 3.3387\nu_{12} \times \nu_{21} - 4.4036\nu_{12}^2 + 3.9589 \times \nu_{21}^2}$ $\lambda_{4,02} = 2.4134 \times \sqrt[4]{1 + 3.8299\nu_{12} - 3.5404\nu_{21} - 3.3387\nu_{12} \times \nu_{21} - 4.4036\nu_{12}^2 + 3.9589 \times \nu_{21}^2}$	0.991

Coefficients of determination (R^2) are significantly improved and are above 0.97. This is an indication of a better correlation and suggests the obtained polynomials reflect the interplayed relationships confidently.

4.2.10 Thermo-structural analyses and verifications

4.2.11 Findings and analyses of the results of the thermo-mechanical models

We employed ANSYS-APDL to simulate the FDM processes thermo-mechanically. The primary assumptions of such an FE model are listed in Table 35, which includes model dimensions, material properties of Acrylonitrile Butadiene Styrene (ABS) filament, and manufacturing parameters of an FDM machine. Material properties except for density (ρ) are assumed based on the information available on the CES EduPack database [99] and those reported by Ziemain et al. [321].

Table 35: Part geometries and manufacturing parameters considered for thermo-mechanical analyses.

Part Geometry and material property		Manufacturing Parameters	
Part length, L	40 ±0.3 mm	Linear deposition velocity for 3D	750 mm/min
Part thickness, w	5±0.35 mm	Layer thickness	0.3 mm
Part height, h	6±0.35 mm	Air gap	0
Specific heat, c_p	1400 J/kg-K	Bulk temperature, T_∞	293.15 K
Density, ρ	940±5 kg/m^3	Extruder temperature, T_{Exd}	393.15 K
Conductivity, κ	0.17 W/m-K	Platform temperature, T_b	343.15 K
Coefficient of expansion, α	70×10-5 m/m-^{o}C	Bead width	0.77 mm
Young's modulus [321]	1486.11 MPa	Stacking Orientation	Longitudinal (0^o)
Yield Stress [321]	24.18 MPa	Ultimate strength [321]	25.15 MPa

The details of the developed computational models and associated assumptions are mentioned in 3.2.2 Thermo-mechanical analysis framework. We did two series of thermomechanical analyses. The first series modeled a cantilever beam freely positioned on the bed; thus, it acted similar to a cantilever beam fully constrained at one end. Representative results(Fig. 55 a-b) show the contours of temperatures and deformations at different times during simulations.

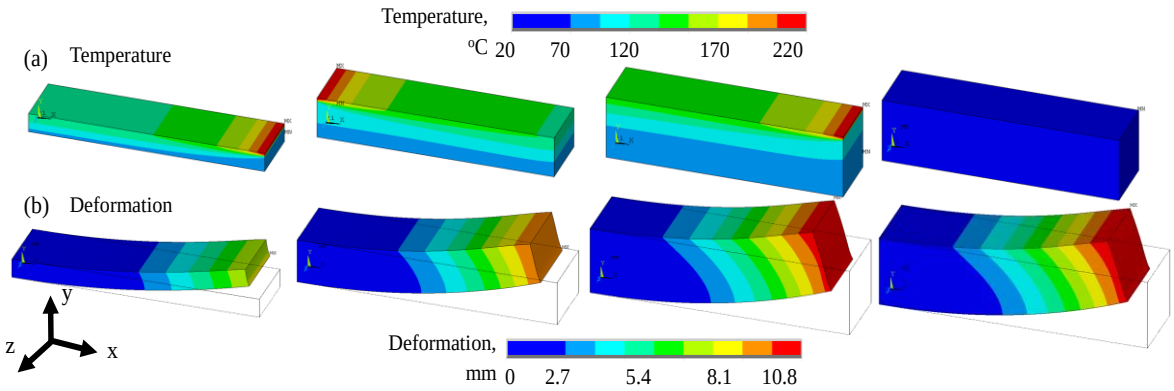

Fig. 55. Representative computational results corresponding to four instances during the manufacturing of a beam including 33% completion, 66% completion, the instance of laying the last set of elements, and the moment part reaches room temperature, respectively from right to left: (a) temperature distributions; and (b) resultant deformations.

The contours of components of stress distributions in all directions and Von Mises stresses corresponding to the temperature and distortion are shown in Fig. 56.

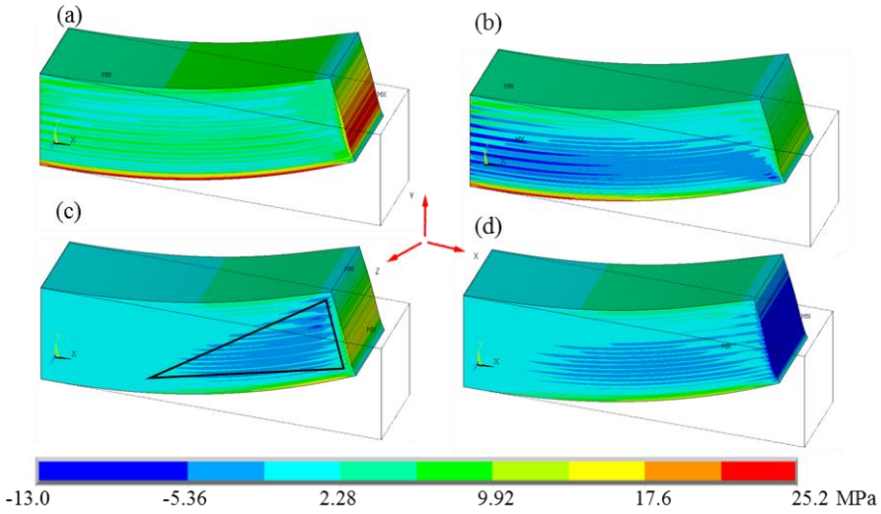

Fig. 56. Contour plot of residual stresses at the end of the simulation for material properties associated with longitudinal orientation: (a) Von Mises stresses, σ_{VM}; (b) x-component, σ_x; (c) y-components, σ_y; (d) shear component, τ_{xy}.

The magnitude of residual stresses corresponding to the status of the model at the end of the simulation shows a relatively high level of stress. For instance, Von Mises stresses vary significantly from 25.2 to 1.0 MPa, from at the bottom heated plate to top edge, respectively.

The FEM analysis suggests the parts are susceptible to failure because of the high level of stresses in some areas close to the boundary.

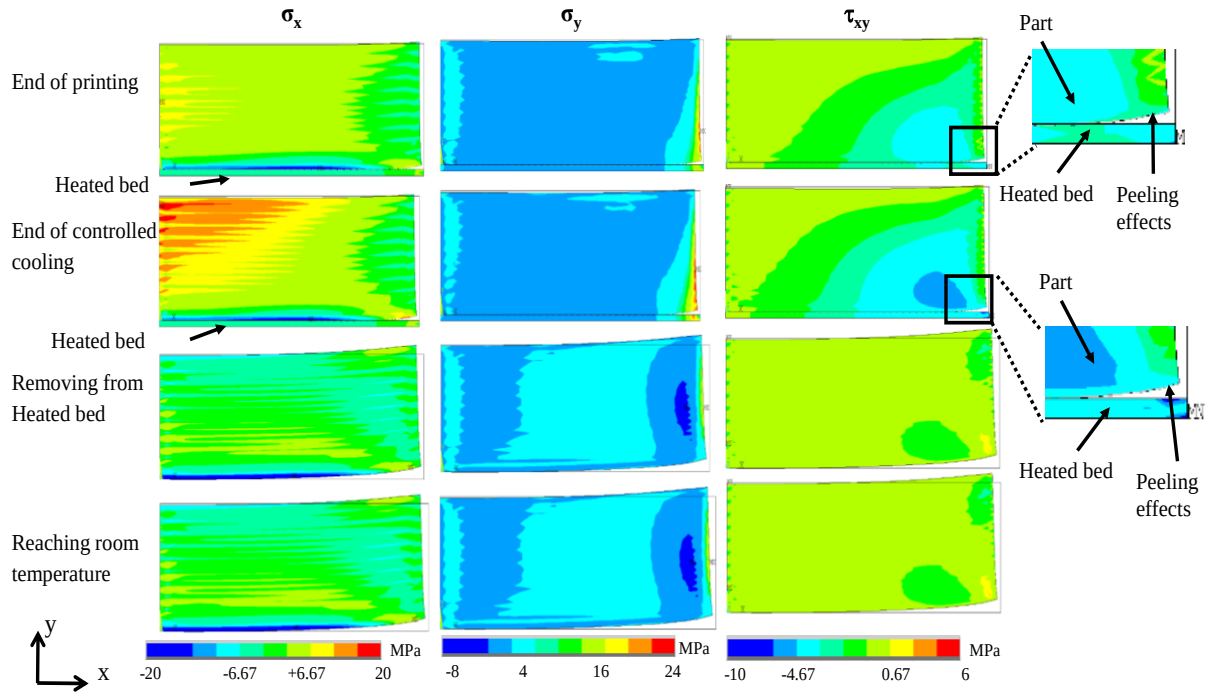

Fig. 57. Computationally predicted contour plots of three principal residual stresses, σ_x, σ_y *and* τ_{xy} at four critical instances, including end of printing, end of controlled cooling attached to the heated bed, removal from the heated-bed, and after reaching room temperature. Simulations can be used to predict peeling of the part from the heated bed.

In the second series, we also included contact elements to simulate bonding between the heated bed and the printed component. Considering this bonding enabled us to simulate the peeling of the part from the heated bed due to the accumulation of residual stresses and distortions. Figure 57 shows representative results illustrating the prediction of distortions and peeling as well as stress distributions in three directions. Besides, the linear distribution of the stresses along the two vertical and horizontal lines corresponds to the center lines of the model are shown in Fig. 58.

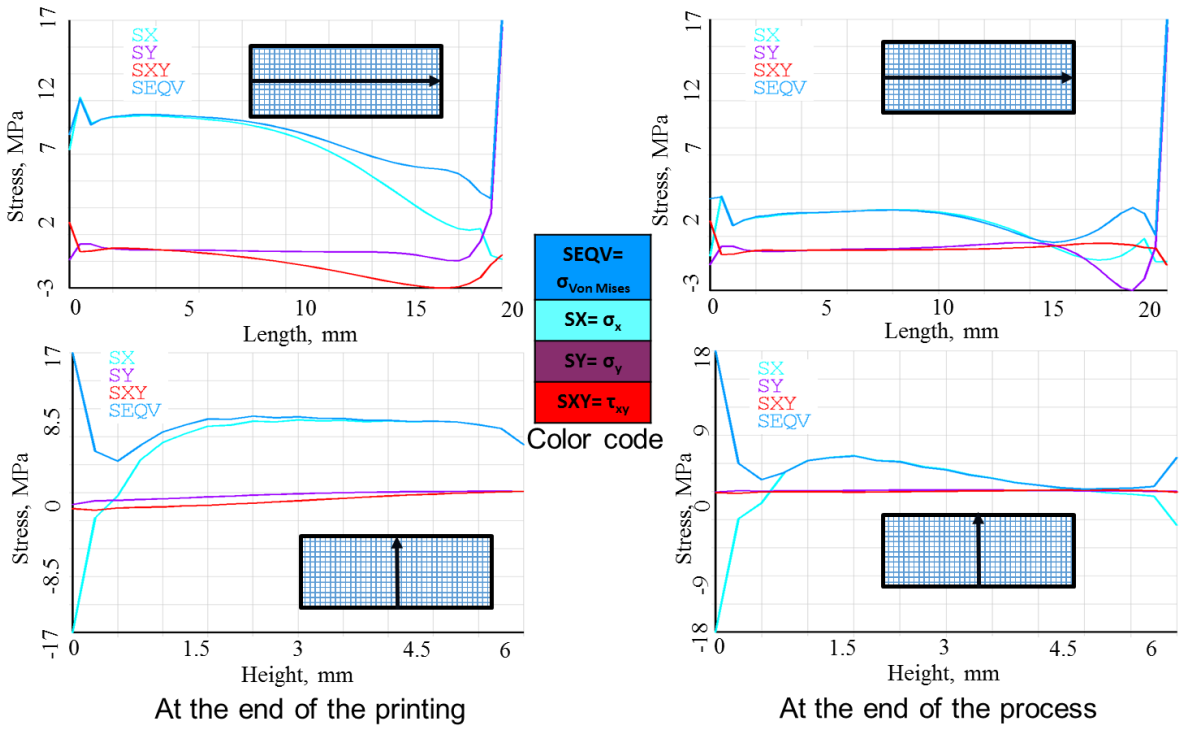

Fig. 58. Plot of Residual stresses, linear distribution plot of three principal components of residual stresses, σ_x, σ_y *and* τ_{xy}, as well as von Mises at the end of part printing and reaching room temperature, along the two vertical and horizontal center lines.

4.3 Experimental results

4.3.1 Tensile test of the filament

ABS is a broadly examined polymeric material in the literature. However, in this study, we decided to perform a tensile test on the filament. The details of the tensile test, including preparation of the specimens and procedures, are described in different standards such as ASTM (ASTM D638), DIN (DIN EN ISO 527-2), and ISO. These well-established procedures establish the correct estimation of the mechanical properties of the material, such as Young's modulus, tensile strength, and tensile elongation. The standard suggests preparing a sample with a dogbone shape, which in FDM technology means to print the sample and test it after. Thus, the

specimens are not pristine ABS, and printing parameters, porosity, bonding quality, and *SR* already affect the specimens.

In order to study the pristine ABS, we either had to print samples or resign ourselves to sample a filament as it is, which does not satisfy standard procedure requirements. We decided to test the filament by using a fixture that has been used previously for performing a micro-test of similar polymers. We cut four different filaments from two different spools, measured their diameters, and performed a tensile test by INSTRON model 5848 MicroTester machine. Figure 59 shows the detail of the testing setup and a picture of the fixture to hold the filament.

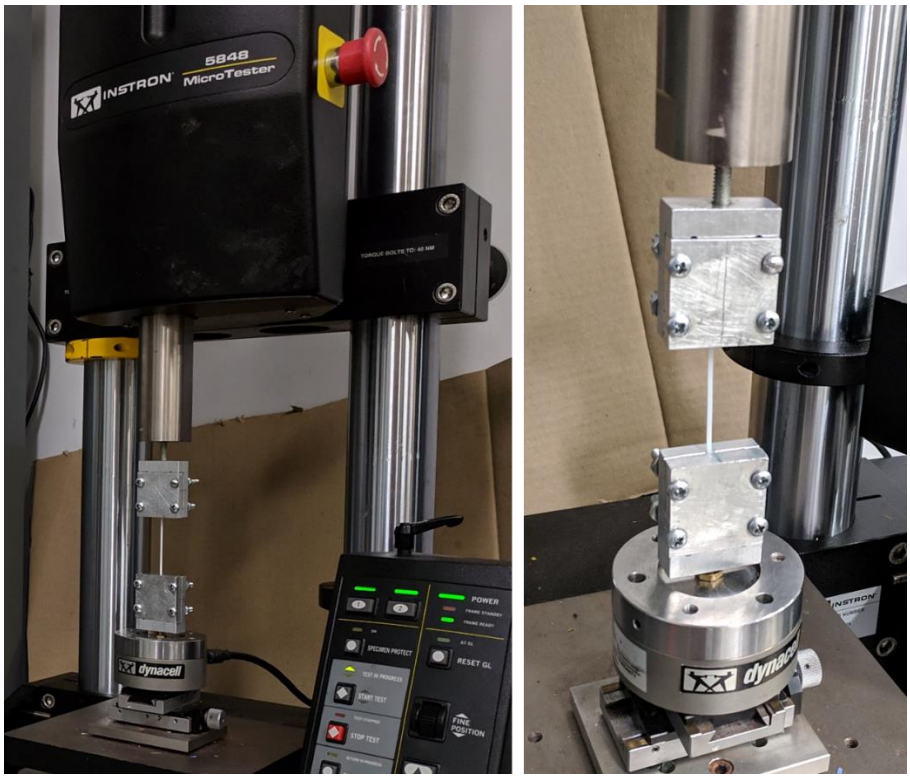

Fig. 59. The setup to execute tensile tests for measuring mechanical testing of the filaments on four different samples: (a) the INSTRON model 5848 MicroTester machine; and (b) the fixture designed for testing polymeric specimens.

The tests were performed similarly with a strain rate of 1.0 mm/min for entire specimens, and the results are shown in Fig. 60. The elastic modulus resonated agreeably with the properties of the ABS, called Z-ABS, reported from the supplier [322]. The average Young's modulus was

obtained as 2,467±14 MPa, which is above 1,800 MPa reported here [173, 322]. However, it measured with 10% deviation compared to the previous measurement on the monofilament reported as 2,230±15 MPa [118]. The tensile strength was found to be 40.92 ±0.97 MPa which is close to reported values by the supplier (38 MPa) but with about 22-25% deviation from the observed values in monofilament tensile test reported by Rodríguez et al. [118] and C. Casavola et al. [173]. We also estimated the yield stresses to be 25.0 MPa. For this study, we assumed the nominal Young's modulus, tensile strength, and yield stress as 2,230, 40.9, and 25.0 MPa, respectively.

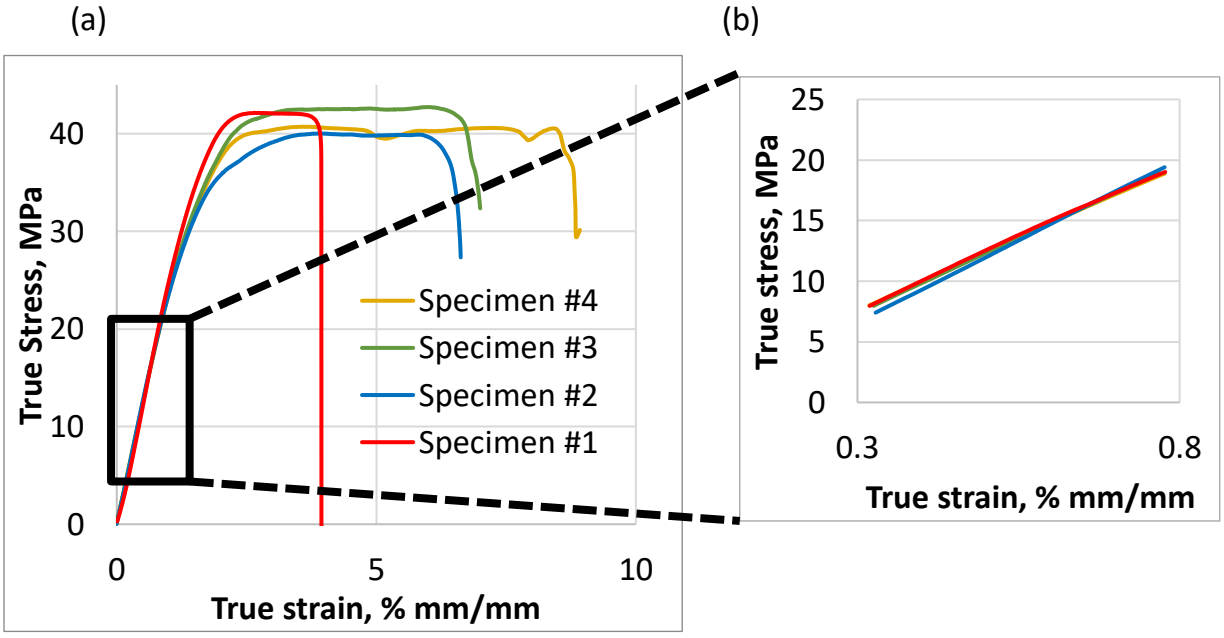

Fig. 60. The tensile test results for the four monofilament tests: (a) the stress-strain curves obtained by INSTRON model 5848 MicroTester machine; and (b) the linear section of the results used for estimation of Young's modulus.

4.3.2 Effects of process parameters on density and porosity

A linear deposition strategy was adopted for printing cubes with size of 15×15×15 mm using an FDM 3D printer. The printing parameters listed in Table 36 altered over the 28 iterations

according to DoE (Table 9). The process was designed to investigate how changes in the selected range affect the quality of bonding and porosity.

Table 36: List and the range of the printing parameters changed for experimental analyses of their effect on density using DoE

Row	Variable	unit	Type	Range (min, mean, max)
1	Extruder Temperature	°C	Continuous	240, 265, 290
2	Heated Bed Temperature	°C	Continuous	40, 70, 100
3	Layer thickness	mm	Continuous	0.09, 0.19, 0.29
4	Extruder Speed	%	Continuous	-50, 0, 50
5	Fan Speed	%	Continuous	0, 50, 100

We followed the DoE tables generated based on the CCD using statistical software explained in chapter 3.5 and 9.2.

Fig. 61. The 28 cubical samples with size of 1.5×1.5×1.5 mm printed under different build parameters to measure the relationship between chosen parameters and density, contact quality, and SR.

28 samples were printed, and their density was measured individually. The 3D printed cubes are shown in Fig. 61. Entire 3D specimens were printed with the same machine, removed, and later cleaned for further measurements. The printing was done arbitrarily upon operator

discretion by choosing a row from the 28 rows listed Table 9 sequentially until the last one. In a few instances, the bonding between the raft layer and the first layer made it challenging to separate the printed part from the raft. However, special attention was given to make sure all samples were kept under the same condition and stored in the same environment.

4.3.2.1 Determination of the density of the filament used for 3D printing

All these 28 samples were printed using the same spool of filament. A buoyancy based experiment was conducted to measure the density. The procedure of this measurement consisted of measuring the weight of each cube with a calibrated precise scale with 0.1 mg resolution and its weight in liquid while it was submerged. The ratio between the original weight and submerged weight multiply by the liquid density gave the density of that particular cube.

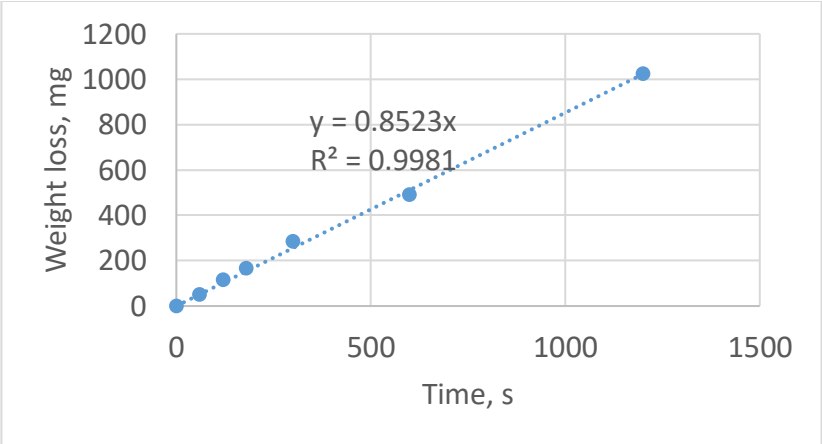

Fig. 62. The evaporation rate of the Methanol in room temperature during consecutive measurements obtained for twenty minutes, including seven instances of weight readouts.

For this study, Methanol (CH3OH) with 99.9% purity product of Fisher Chemical (UN1230) was used. The temperature was measured during and after measurement. The density was estimated based on the pure Methonal density at the measured temperature.

Because of the volatility of the methanol, the weight loss during the measurement was noticeable in scale readout; thus, a separate measurement was done to estimate the weight loss

due to evaporation during the measurement. The weight loss was considered for each set of measurements to compensate for the evaporation loss. Such an expected weight loss for a set of measurements is shown in Fig. 62. Weight loss was measured for up to 20 minutes, and a linear regression was performed to estimate the rate.

Fig. 63. The setup used for measurements of the density using the buoyancy forces: (a) the precise scale capable of measuring weight with 0.1 mg resolution; (b) the thermometer and the glass filled with Methanol to measure the weight of the cubes and their buoyant weights, and (c) the 99.9% Methanol manufactured by Fisher.

Before measuring the density of the cubes, we also tried to measure the density of the filament using the same method to compare it with the manufacturer declared values on the material datasheet and also recheck the validity of the method. A known length of the filaments was cut, and its diameter was measured at different locations. In parallel attempts, the submersion method was also applied to estimate the density. The results of these attempts are

listed in Table 37, where the measured weight on the scale and submerged weight for three iterations along with their averages are recorded.

Table 37: The obtained data of the weight and the submerged weight of the different lengths of the filament for estimating the filament density.

#	Average filament diameter, mm	cut length, cm	Estimated volume by length, cmxmm^2	Filament Weight, g	Submerged filament Weight, g			Average submerged weight, g
				1st	1st	2nd	3rd	
1	1.71±0.01	7.5±0.1	172.244	0.1812	0.130	0.129	0.130	0.130
2	1.71±0.01	7.0±0.1	160.761	0.1702	0.119	0.1209	0.121	0.120
3	1.71±0.01	14.1±0.1	323.818	0.342	0.251	0.2509	0.251	0.251
4	1.71±0.01	10.2±0.1	234.251	0.2476	0.179	0.180	0.180	0.180
5	1.71±0.01	76.3±0.1	1752.293	1.859	1.394	1.407	1.396	1.400

The measurements took between 10 to 20 seconds, and it was hardly possible to precisely record the estimated time for each iteration; therefore, these two extremes were used to measure the evaporation. Table 38 lists the evaluated densities along with standard deviations and averages.

Table 38: The estimated density of the different lengths of the filament based on the data reported in Table 37 corrected considering the evaporation rate.

#	Estimated density by length, kg/m^3	Estimated by buoyancy, kg/m^3	Density considering the effect of evaporation for 10 s, kg/m^3	Density considering the effect of evaporation, for 20 s, kg/m^3
1	1052.00	1106.60	1073.66	1042.61
2	1058.72	1120.35	1084.48	1050.84
3	1056.15	1079.12	1062.28	1045.96
4	1056.98	1091.30	1067.66	1045.01
5	1060.90	1052.26	1049.28	1046.31
Average	1056.95	1089.93	1067.47	1046.15
Std deviation	2.96	23.41	11.71	2.68

It should be noticed that without compensation due to evaporation, the measurements were off. However, after considering the weight losses due to the evaporation, the densities fell into a

reasonable range. Comparing the measured and determined values with the listed properties in the Z-ABS material data sheet as 1,195 kg/m^3 indicated about 13.2% difference. The listed properties in the manufacturer's datasheet seemed greater than the specific gravity of the other filament manufacturers and were above the ranges mentioned in different references [87, 99, 107, 118] and obtained by our measurements. Comparing the different references and our measurements, we concluded that the density measured by our techniques was more reliable. Thus, our measured data was used instead of the manufacture's information for further investigation. Finally, density equal to 1,055 kg/m^3 was selected for further analyses.

4.3.2.2 Measured densities of the printed cubes

Each of the 28 cubes was measured individually according to the protocol, while temperature monitored during all measurements. Due to weight loss, the scale was set to zero prior to each subsequent measurement. The average measured weights of the different cubes are listed in the second and third columns of the following table.

Table 39: The measured weight and submerged weight of the printed cubes used for estimation of the theoretical density, measured density, theoretical *SR*, and measured *SR*.

run	Cube weight, g	Average Submerged weight, g	Theoretical solidity ratio, RS	Theoretical density, kg/m^3	Estimated density, kg/m^3	Measured solidity ration, SR	Difference between estimated and theoretical density, kg/m3	Contact quality, *P*
1	3.391	2.566	0.952	1,004.1	1,046.5	0.992	42.456	60.02
2	3.340	2.594	0.952	1,004.1	1,019.6	0.966	15.560	17.30
3	3.377	2.658	0.844	890.9	1,006.1	0.954	115.235	48.64
4	3.095	2.491	0.844	890.9	983.9	0.933	93.038	37.37
5	3.365	2.642	0.898	947.5	1,008.6	0.956	61.130	36.33
6	3.131	2.377	0.952	1,004.1	1,043.1	0.989	39.016	52.53
7	3.324	2.547	0.952	1,004.1	1,033.5	0.980	29.401	35.91
8	3.413	2.830	0.844	890.9	955.0	0.905	64.161	24.62

Table 39: The measured weight and submerged weight of the printed cubes used for estimation of the theoretical density, measured density, theoretical *SR*, and measured *SR*.

9	2.800	2.212	0.844	890.9	1,002.4	0.950	111.528	46.63
10	3.399	2.640	0.898	947.5	1,019.6	0.966	72.093	44.65
11	3.427	2.643	0.952	1,004.1	1,026.8	0.973	22.724	26.40
12	3.429	2.658	0.898	947.5	1,021.6	0.968	74.126	46.32
13	3.408	2.628	0.898	947.5	1,026.9	0.973	79.460	50.92
14	3.417	2.673	0.898	947.5	1,012.3	0.960	64.839	39.04
15	3.416	2.676	0.898	947.5	1,010.9	0.958	63.408	37.98
16	3.438	2.681	0.898	947.5	1,015.5	0.963	68.021	41.44
17	3.437	2.688	0.898	947.5	1,012.5	0.960	65.082	39.22
18	3.465	2.710	0.844	890.9	1,012.5	0.960	121.645	52.27
19	3.421	2.657	0.898	947.5	1,019.6	0.966	72.127	44.68
20	3.470	2.643	0.952	1,004.1	1,039.7	0.985	35.607	46.08
21	3.469	2.672	0.952	1,004.1	1,028.1	0.974	24.027	28.17
22	3.482	2.688	0.844	890.9	1,025.8	0.972	134.940	60.69
23	3.453	2.749	0.844	890.9	994.7	0.943	103.824	42.63
24	3.470	2.691	0.898	947.5	1,021.1	0.968	73.664	45.94
25	3.478	2.635	0.952	1,004.1	1,045.2	0.991	41.168	57.07
26	3.501	2.722	0.952	1,004.059	1,018.5	0.965	14.452	15.97
27	3.445	2.671	0.844	890.856	1,021.4	0.968	130.499	57.72
28	3.446	2.741	0.844	890.856	995.6	0.944	104.704	43.08

The theoretical solidity ratios were calculated based on the height and width of the deposited filament, as explained in Eq. (4-20). Moreover, the measured solidity ratio listed above is the ratio between the measured density and the nominal density of the perfect solid sample of 1,055.0 kg/m^3. This can be assumed as an indication of the porosity and the average bonding quality in the printed samples.

In addition, the contact quality, *P*, was obtained by considering the height and width of the deposited bead and the measured density, as explained in Eq. (4-24-a). Contact quality potentially indicates the bonding in intra- and inter-layers and directly affects the mechanical

properties. Although the *SR* ratio is an indication too, it does not entirely pertain to bonding and strongly reflects the *H-to-W* ratio.

4.3.2.3 Statistical analyses of density and density difference for cubical samples

In this study, we had five independent and one dependent variables; we assumed the relationships among independent and dependent variables could be defined in a polynomial function. This section is devoted to examine the accuracy of the prediction and to discover the relationships among parameters and properties of interest by investigating statistical parameters, i.e., the coefficient of determination (R^2), ANOVA, P-value, F-ratio, and Coefficient of Variation (CV). The degree of freedom relaxing the three-way interactions is twenty-six; we expected a few of these parameters to be not significant. Therefore, we first did screening analyses and then performed final fitting on the remaining set of parameters.

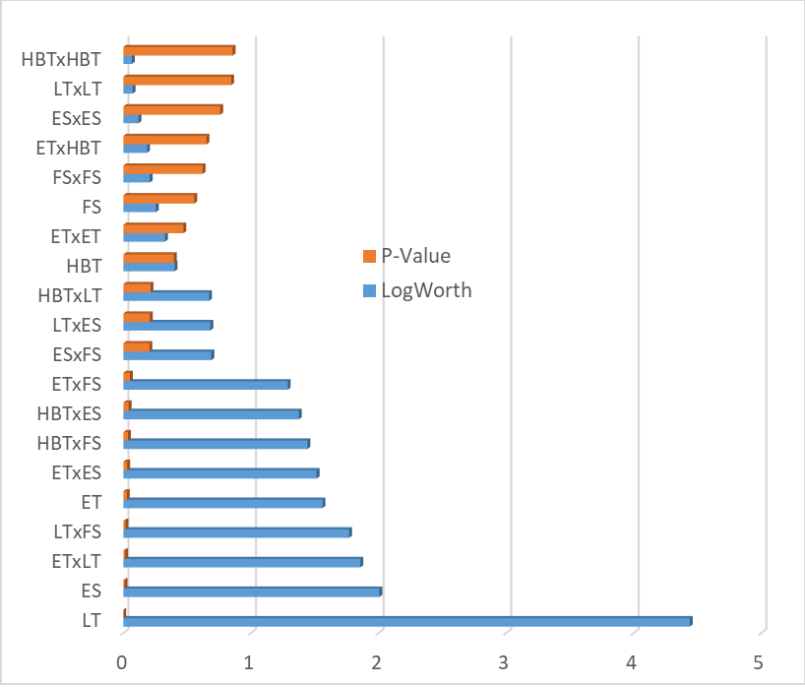

Fig. 64. The screening results of density showing the LogWorth and P-Values of the linear, quadratic, and two-way interaction of the selected sources. Higher LogWorth and lower P-Value suggest higher influences

We did the screening analyses at first to determine the relationship between measured density and the five selected parameters. The LogWorth and the P-Values of the sources and their interactions are listed in Appendix 9.5, and Fig. 64 shows the LogWorths and P-Values side-by-side for the linear, quadratics, and two-way interactions in order of importance.

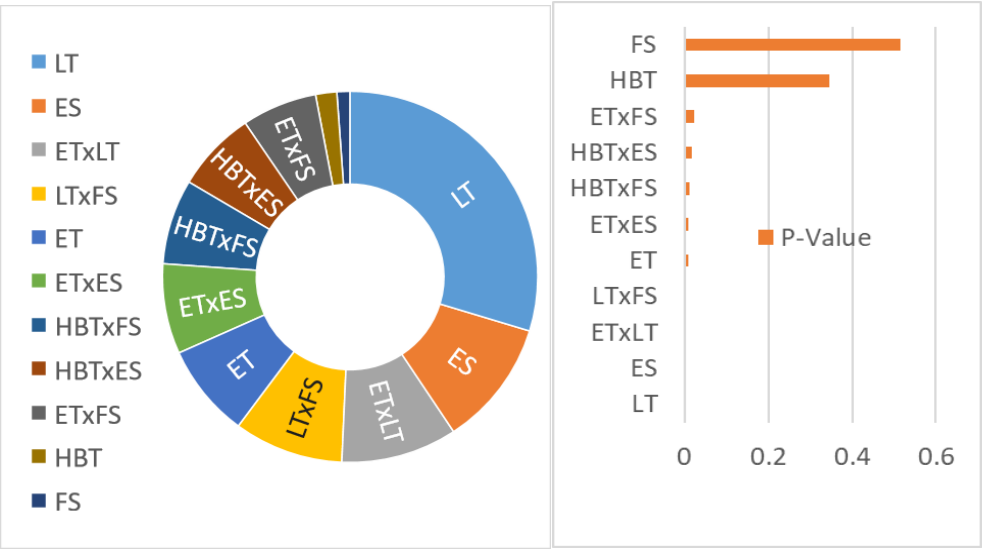

Fig. 65. Result of the updated statistical analyses on density showing the influential sources: (a) Pi diagram showing the LogWorth of the sources; and (b) Bar diagrams showing the P-Values.

One can conclude that a few parameters and their interactions are not significant since their P-Values are above 0.05. The most critical parameters are layer thickness, extruder speed, and the interaction between extruder temperature and layer thickness. The interaction between extruder temperature and layer thickness is an indication of advection; in other words, the volumetric flow rate multiplied by the temperature difference ($dV \times dT$).

Other parameters like heated bed temperature and fan speed were among the least significant. We kept all the first orders and removed those parameters with higher P-Values and examined them to reach the final set of parameters, as shown in Fig. 65 and listed in the appendix section 9.5.1. The summary of the statistical analyses is shown in Table 40.

Table 40: statistical analyses of the screened parameters for the measured density of cubical specimens

Factors	Values
R^2	0.916504
R^2 Adj	0.8591
Root Mean Square Error	7.225692
Mean of Response	1016.67
Observations (or Sum Wgts)	28

The summary of the parameters was estimated for the polynomial along with other statistical data is presented in Appendices chapter 9.5.2.

The graph is shown in Fig. 66 exhibits a good agreement between the calculated values based on estimated polynomial and measured values, with a few values projected outside the confidence bonds.

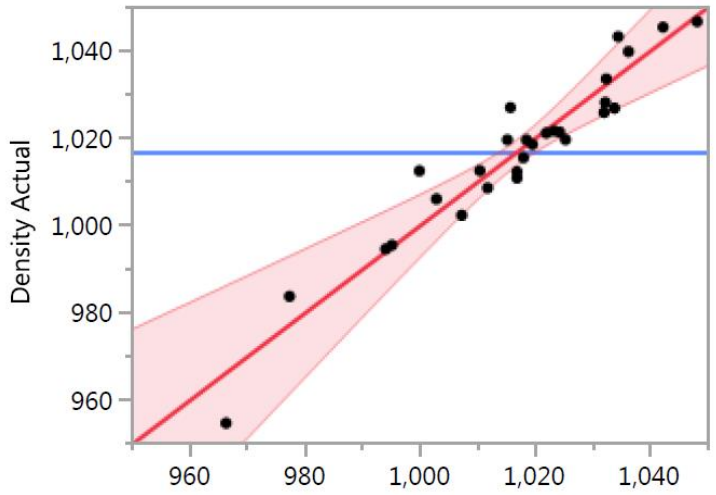

Fig. 66. The graph indicates the actual density compared to the prediction plot of the density for the cubical specimens.

In the next iteration, we tried to improve the estimation. We defined the target to be the difference between theoretical density and measured density instead of the density itself. We

hypothesized that the difference between theoretical density with almost zero weldings and the measured density could be a better indication of the bonding quality.

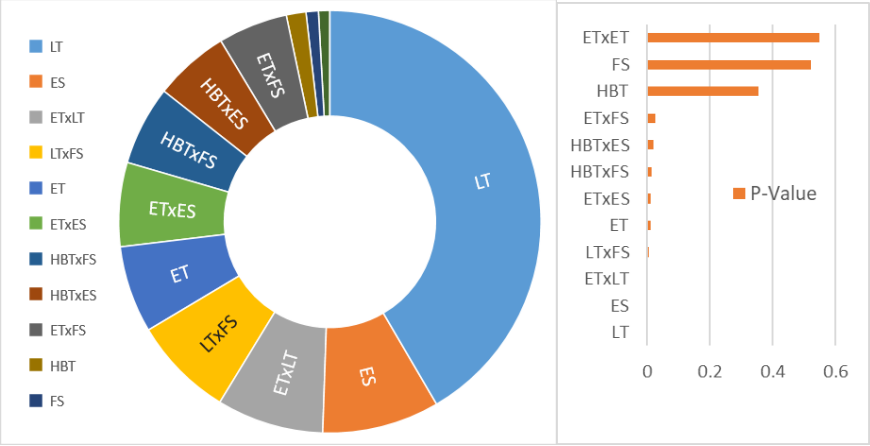

Fig. 67. Result of the updated statistical analyses on density difference showing the influential sources: (a) Pi diagram showing the LogWorth of the sources; and (b) Bar diagrams showing the P-Values.

We analyzed this data accordingly and used the same screening process to find the most significant sources. The result of the screening analyses including a total of 20 sources, is shown in Fig. 68, and the data is presented in 9.5.3 in appendices.

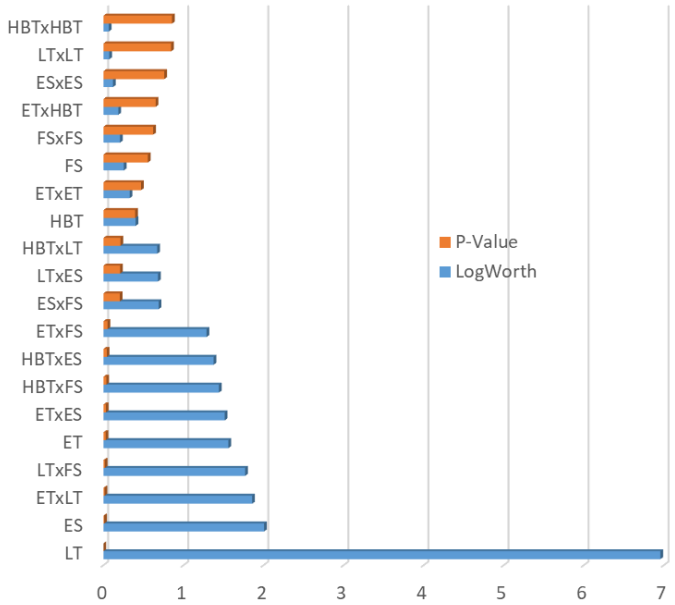

Fig. 68. The screening results on the density difference showing the LogWorth and P-Values of linear, quadratic, and two-way interaction of the selected sources. The higher LogWorth and lower P-Value suggest greater influence.

The prediction accuracy, in this case, improved significantly, and the R^2 approached 0.99. However, there were still some unimportant sources; we removed some insignificant sources and updated the estimation. Such an updated result is shown in Fig. 67.

We analyzed the data statistically, as listed in Table 41. The R^2 of 0.98 percent indicates strong confidence in the results and success in capturing the essential sources that can be used for predicting the density differences reliably.

Table 41: statistical analyses of the screened parameters for the measured density of cubical specimens

Factors	Values
R^2	0.975517
R^2 Adj	0.955931
Root Mean Square Error	7.371903
Mean of Response	69.21196
Observations (or Sum Wgts)	28

All the calculated coefficients for the polynomial estimation are listed in chapter 9.5.4; Fig. 69 shows the general performance of the prediction.

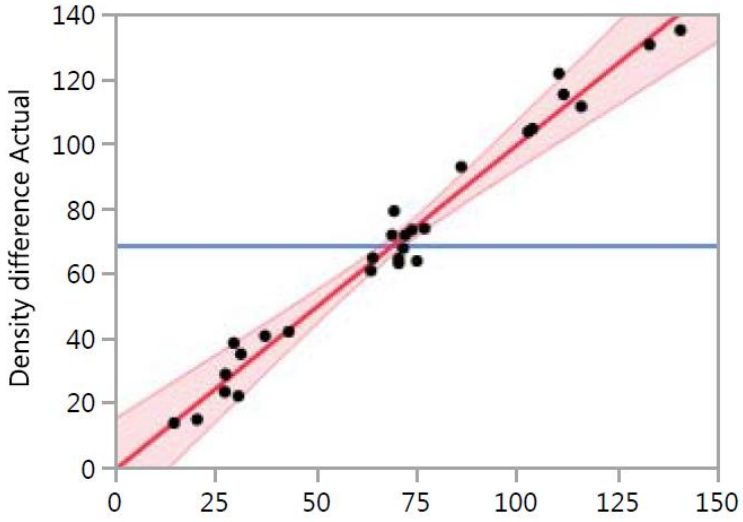

Fig. 69. The graph indicates the actual by prediction plot of the density difference for the cubical specimens.

4.3.2.4 Statistical analyses for contact quality, *P*

The density and density differences were strongly dependent on layer thickness. Although the development of the bonding, which led to increases in density, was observed in the previous analyses, we were interested in examining other factors to evaluate bonding quality. We previously defined the factor named bonding quality, *P*, which could indicate necking development between layers.

Similar to density, we started the analyses by encompassing variables and sources and then by screening more important sources and their combination to proceed with a better understanding of contact quality. Figure 70 illustrates the obtained outcomes based on the results presented in appendix 9.5.5.

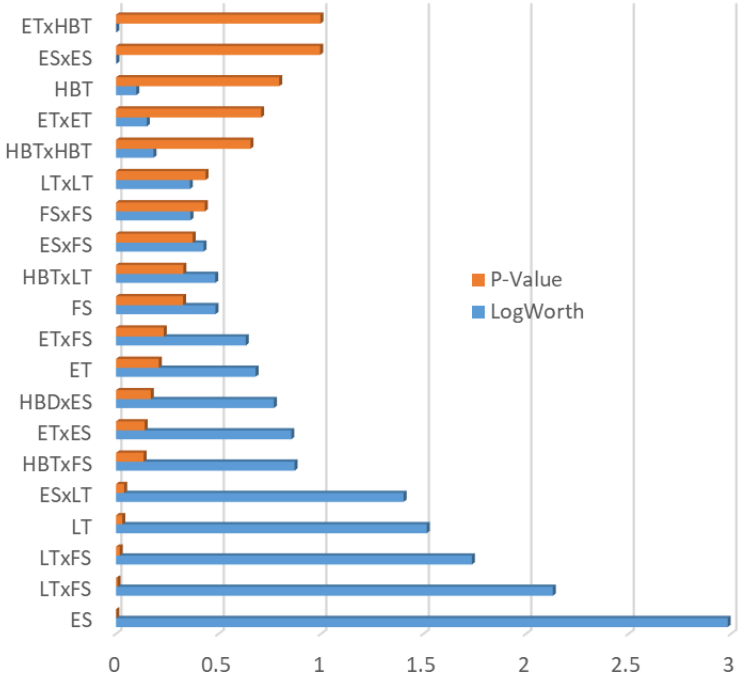

Fig. 70. The screening results on the contact quality, *P*, showing the LogWorth and P-Values of the linear, quadratic, and two-way interaction of the selected sources. The higher LogWorth and lower P-Value suggest greater influences

For bonding quality, the most important parameters are not layer-thickness anymore, and extruder speed turns out to be the most influential parameter. However, the two-way interaction

of layer thickness with extruder speed and fan speed appears in second and third place. This result can be interpreted as the effect of energy deposition in layers helping to improve the bonding quality. Higher velocity and layer thickness mean deposition of higher thermal energy per volume of the cube during printing. We gradually ruled out the parameters with *P-Values* above 12% but kept those with the first order. The final results are presented in Fig. 71 and also 9.5.5 in the appendices section.

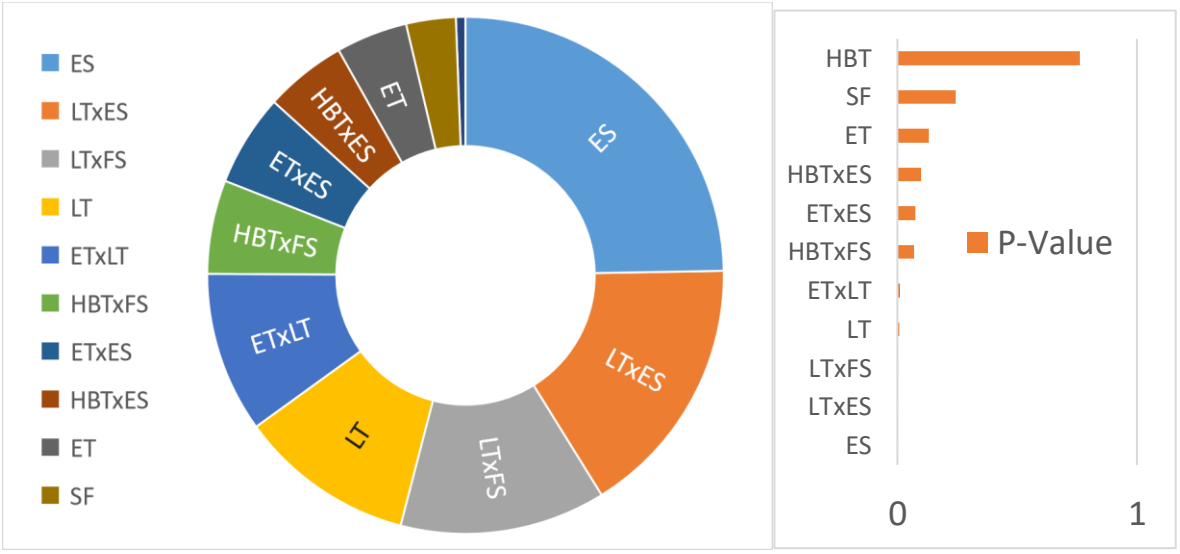

Fig. 71. Result of the updated statistical analyses on contact quality, *P*, showing influential sources: (a) Pi diagram showing the LogWorth of the sources; and (b) Bar diagrams showing the P-Values.

The statistical analyses for contact quality were not found as strong as those for the density, and the R^2 determined 0.87.

Table 42: statistical analyses of the screened sources for the estimated contact quality, *P*, of cubical specimens

Parameters and their interactions	Values
R^2	0.863583
R^2 Adj	0.769796
Root Mean Square Error	5.634819
Mean of Response	42.1286

Table 42: statistical analyses of the screened sources for the estimated contact quality, *P*, of cubical specimens

Observations (or Sum Wgts)	28

Chapter 9.5.6 contains lists of estimated coefficients and further statistical analyses for the polynomial defining the dependency of contact quality to the five selected sources and their critical two-way interactions.

In addition, Fig. 72 shows the predicted versus the actual contact quality. As one can expect, due to lower confidence in prediction, the error range is wider than the two previous graphs shown in Fig. 66 and Fig. 69 and more points appear beyond the confidence bands.

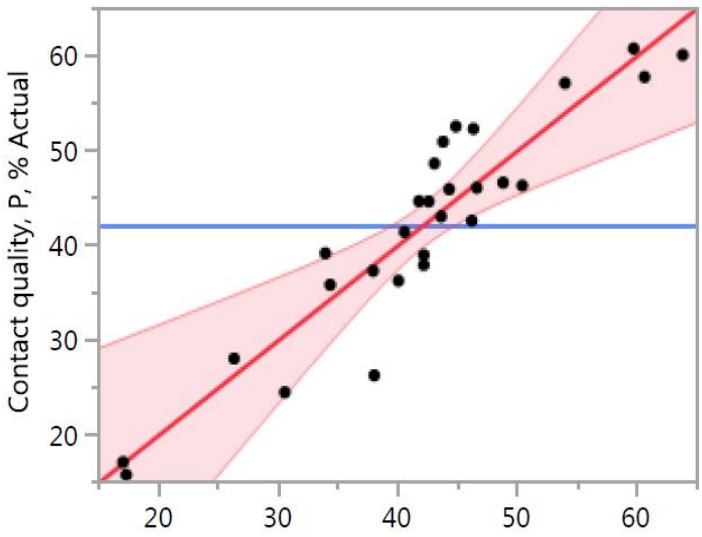

Fig. 72. The graph indicates the actual contact quality by prediction plot for the cubical specimens.

4.3.2.5 Measured densities of the printed cuboids of three different sizes

The above analyses on the density and contact quality of the cubes with 1.5x1.5x1.5 mm exhibited layer thickness as one of the most substantial sources. Thus, in order to assure other parameters were studied adequately and the effect of size was probed in our analyses, we designed another set of experiments as described in chapter 3.5.2.1 with two other significant sources, extruder temperature and extruder speed. Table 10 lists the designed DoE table for this

set of experiments. 16 cuboids were printed with the same 3D printer machine while the width and the height of the deposited filament were fixed as 0.4 and 0.19 mm, respectively. The temperature of the heated bed was maintained at 70°C, with the cooling fans running at 100%. We measured the density of each cuboid with the same procedure described in chapter 4.3.2.1. The results are listed in the following table, Table 43. The theoretical *SR*s and the density were determined as 0.898 and 947.5 kg/m^3, respectively, for entire runs because they were a function of height and width of the beam, which was constant here.

Table 43: The measured and submerged weights of the printed cuboids with three different sizes used for estimation of the density, *SR*.

run	Cuboid weight, g	Average Submerged weight, g	Estimated density, kg/m^3	Measured solidity ration, SR	Difference between estimated and theoretical density, kg/m3	Contact quality, *P*
1	0.1392	0.101	1,027.72	0.97	80.26	51.64
2	0.1364	0.105	967.94	0.92	20.48	10.98
3	0.1373	0.102	1,004.33	0.95	56.87	33.33
4	0.141	0.104	1,009.63	0.96	62.18	37.08
5	0.1364	0.102	1,000.83	0.95	53.37	30.94
6	1.1533	0.877	1,033.60	0.98	86.14	57.29
7	1.1534	0.873	1,038.79	0.98	91.33	62.92
8	1.1475	0.872	1,034.65	0.98	87.19	58.37
9	1.1558	0.879	1,034.28	0.98	86.82	57.99
10	1.149	0.892	1,013.31	0.96	65.85	39.79
11	1.1574	0.885	1,027.97	0.97	80.51	51.87
12	3.1335	2.401	1,030.79	0.98	83.33	54.51
13	3.1422	2.440	1,017.17	0.96	69.71	42.76
14	3.1105	2.399	1,023.93	0.97	76.47	48.30
15	3.146	2.403	1,034.04	0.98	86.58	57.74
16	3.1348	2.442	1,013.81	0.96	66.35	40.17

The theoretical solidity ratios and contact quality were determined for further analyses.

4.3.2.6 Statistical analyses of density difference and contact quality

In this case, there were three independent sources to study. The procedure is the same as described in chapters 4.3.2.3 and 4.3.2.4. We skipped the step of screening and only presented the results of significant parameters.

- **Density difference**

We first studied the density difference and skipped density, as described before. Figure 73 and Figure 74 show the results and some statistical values corresponding to the first six important sources.

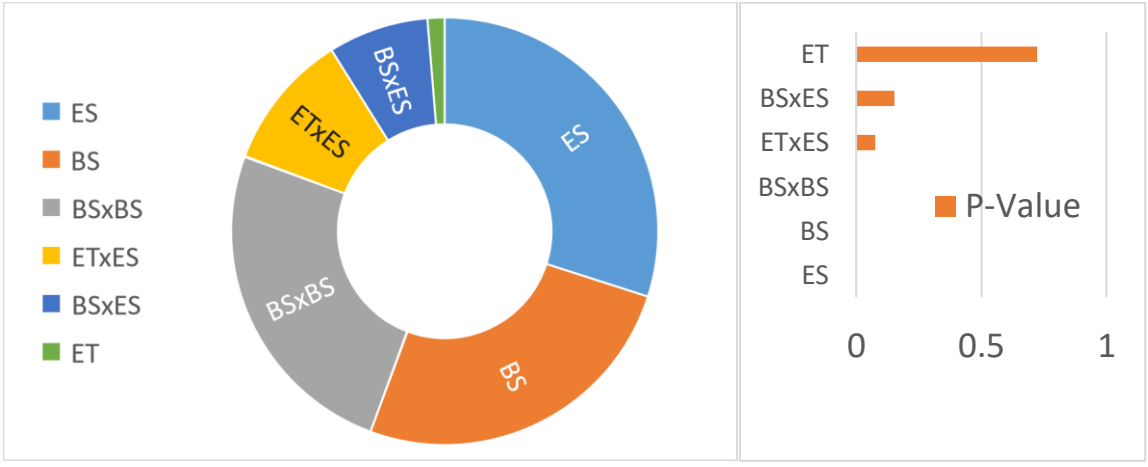

Fig. 73. Result of the updated statistical analyses on density differences for thermal cubes, *P*, showing the influential sources: (a) Pi diagram showing the LogWorth of the sources; and (b) Bar diagrams showing the P-Values.

The trends and effects are found similar to the density difference analyses above, except the quadratic effect of the size appeared in the second place. The selected sources show similarity to the previous experiments, and as we expected, extruder speed appears as the most effective source. The two-way interaction of extruder speed and extruder temperature also appears in the fourth location above "Extruder Temperature" which shows deviation from the previous observation. We expect the effect of size to be less in these analyses; we did not anticipate the quadratic effect of size be more influential than its linear effect. However, this quadratic effect

can be justified knowing the weight of extruder radiation on the samples, which is discussed in 4.3.5 and also reported here [323]. Investigating the prediction profiler for all of these sources indicates the "Extruder temperature" hardly affects the density.

The effect of speed is dominant, and the trend follows a linear proclivity toward increasing the density at higher speed (or decreasing the density difference at higher speed). On the contrary, the effect of size is quadratic like a downward dome, and its maximum happens close to 7 mm. We concluded this interaction might be affected by some other involved physics, such as nozzle radiation in the fabrication of these sixteen cuboids.

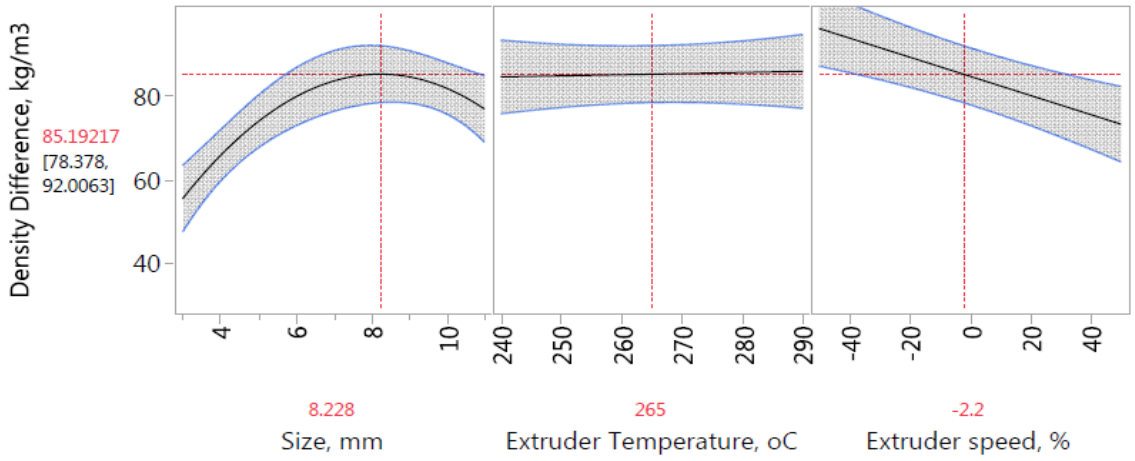

Fig. 74. The prediction profiler shows the dependency of density difference for the three selected sources within the range of boundaries of cuboid specimens.

The statistical analyses on density differences were done, and the results are listed in Table 44 with an $\boldsymbol{R^2}$ of 0.89.

Table 44: statistical analyses of the screened parameters for the estimated contact quality, *P*, of cuboid specimens

Factors	**Values**
R^2	0.887446
R^2 Adj	0.81241
Root Mean Square Error	7.849587

Table 44: statistical analyses of the screened parameters for the estimated contact quality, *P*, of cuboid specimens

Mean of Response	72.09088
Observations (or Sum Wgts)	16

Chapter 9.5.13 lists the estimated coefficients for the corresponding polynomial based on the three selected sources and their most important two-way interactions.

- **Contact quality**

We extended the analyses to the contact quality; Fig. 75 shows the estimated results for the most important parameters. Since we did not include thickness, we expected to see a similar trend between contact quality and density.

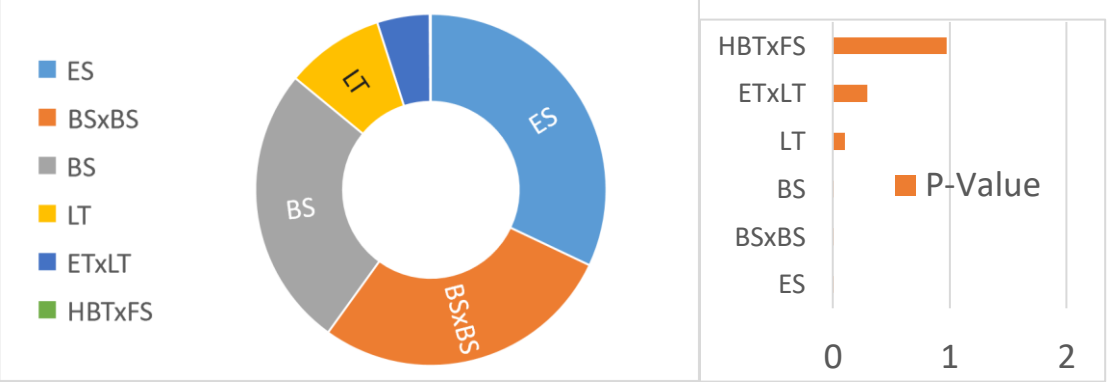

Fig. 75. Result of the updated statistical analyses on contact quality for thermal cubes, *P*, showing the influential sources: (a) Pi diagram showing the LogWorth of the sources; and (b) Bar diagrams showing the P-Values.

The selected parameters show similarity to the analyses of the density difference except that the quadratic effect of speed appears in the second place instead of speed. Analyzing the prediction profiler also shows similar trends and profiles.

The statistical analyses for contact quality were done, and the results listed in Table 45 with R^2 of 0.90.

Table 45: statistical analyses of the screened parameters for the estimated contact quality, *P*, of cuboid specimens

Parameters and their interactions	Values
R^2	0.89904
R^2 Adj	0.831734
Root Mean Square Error	5.572451
Mean of Response	45.98019
Observations (or Sum Wgts)	16

Chapter 9.5.14 includes lists of the estimated coefficients of the corresponding polynomial based on the three selected sources and their most important two-way interactions.

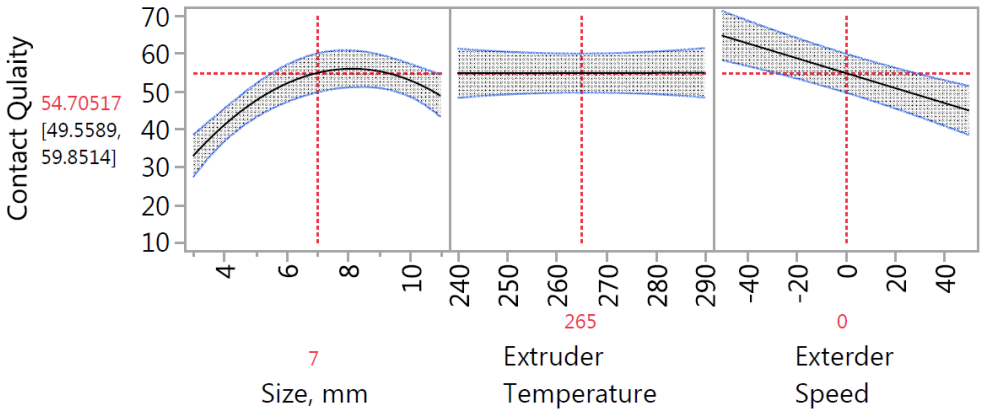

Fig. 76. The prediction profiler shows the dependency of density difference to the three selected sources within the range of boundaries of cuboid specimens.

4.3.3 Estimating the THTC using combined numerical-experimental study

An XYZ Da Vinci 2.0 Duo FDM 3D printer, was utilized for this part of the study. The procedure is explained in Chapter 3.3.3. The part geometries and manufacturing parameters are listed in Table 46 and printed specimens are shown in Fig. 78-a. A calibrated IR FLIR A320 camera was utilized to perform *in-situ* measurements during part fabrication.

Table 46: Part geometries and manufacturing parameters considered for fabrication specimens.

Part and manufacturing geometrical parameters		Manufacturing Parameters	
Sample length, L	50 ±0.3 mm	Deposition velocity in z for D=10 mm, in 1D)	100 mm/min
Part diameters, D	10±0.35 mm, 20±0.35 mm, 30±0.35 mm	Linear deposition velocity for 3D	750 mm/min
Part initial length, Z_0	0.3mm	Ambient temperature T_∞	293.15 K
Emissivity	0.85	Extruder temperature T_{Exd}	393.15 K
Path Width	0.5 mm	Platform temperature T_b	343.15 K
Layer Height	0.1 mm	Nozzle Diameter	0.4
Infill Angle	0°	pattern	rectilinear
Path Width	0.5 mm	Extrusion Factor	1.0
Air gap	0	Number of Layers	As specified

The procedures and methodology described above were applied to estimate values for α and β for Eq. (3-47). The least-square error minimization approach bears the best approximation for the mentioned variables for a 1D computational-experimental problem, which are determined as β=1.61 and α=0.65. Figure 77-b shows computational and experimental profiles while illustrating the effects of different values for parameter α.

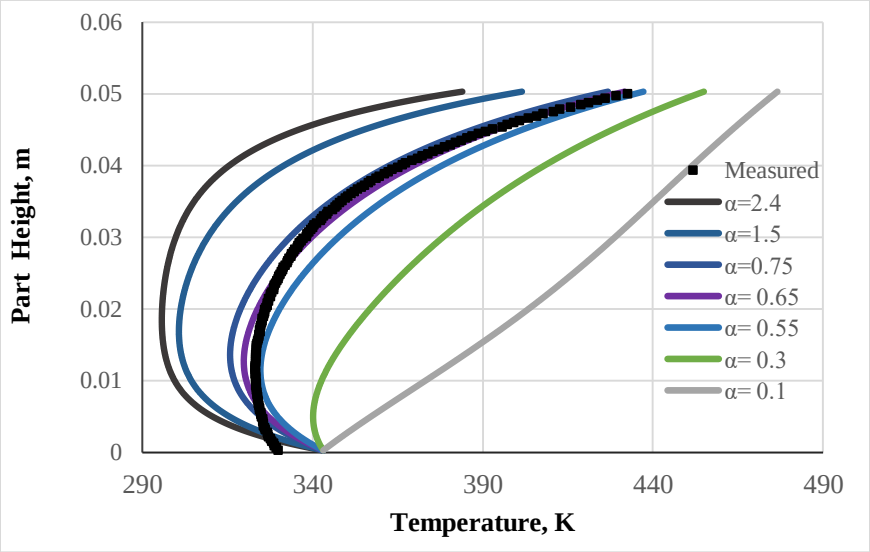

Fig. 77. Computationally and experimentally obtained temperature profiles for a 1D fabrication model showing the effects of parameter α. Profiles correspond to temperatures right after fabrication is completed.

After determining the optimal values for α and β, the investigation continued to compare corresponding temperature profiles for 1D models within different periods. Figure 78-b shows representative computational and experimental temperature profiles obtained throughout the fabrication and cooling of a 1D lumped model. Comparisons show good agreement between simulations and experiments.

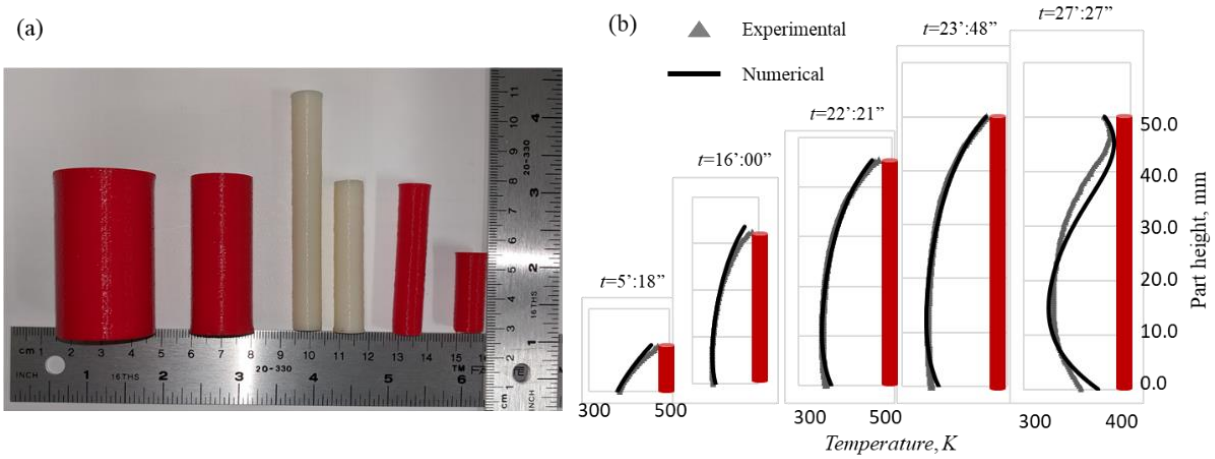

Fig. 78. (a) Different cylindrical specimens printed and monitored in-situ using IR camera; and (b) representative results of the agreement between numerically estimated and experimentally measured temperatures along a vertical line on a cylinder with a diameter of 5.0±0.3 mm and height of 50±0.09 for different instances.

After completing a series of 1D simulations and experiments to define the total heat transfer coefficient (THTC), a 2D investigation was performed. Figure 79 is a comparison between computationally and experimentally obtained results for geometries of D = 20 and 30 mm. Results indicate reasonable agreement, which demonstrates that the proposed combined experimental-computational method is valid for thermal analyses.

(a)

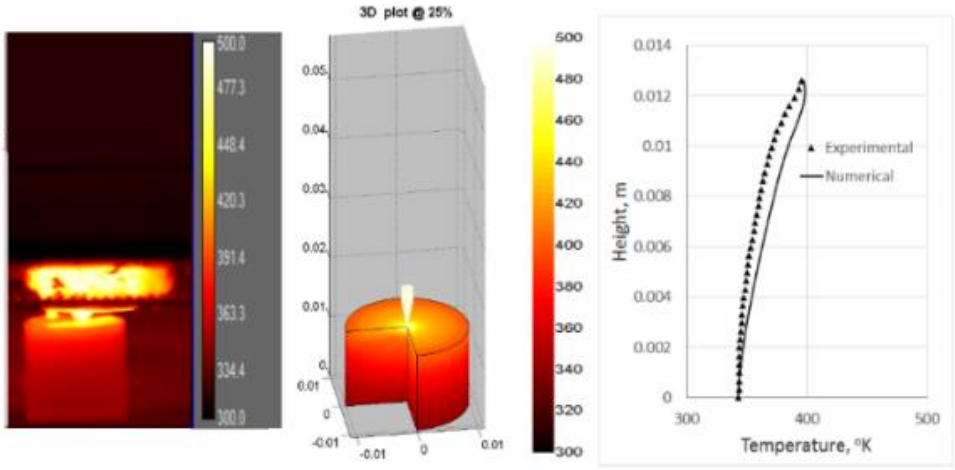
3D plot @ 25%
Experimental
Numerical
Height, m
Temperature, °K

(b)

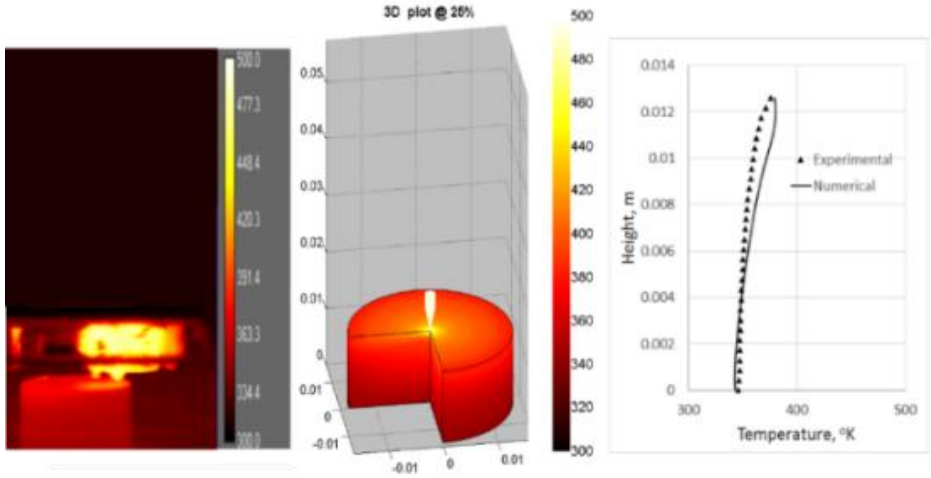
3D plot @ 25%
Experimental
Numerical
Height, m
Temperature, °K

(c)

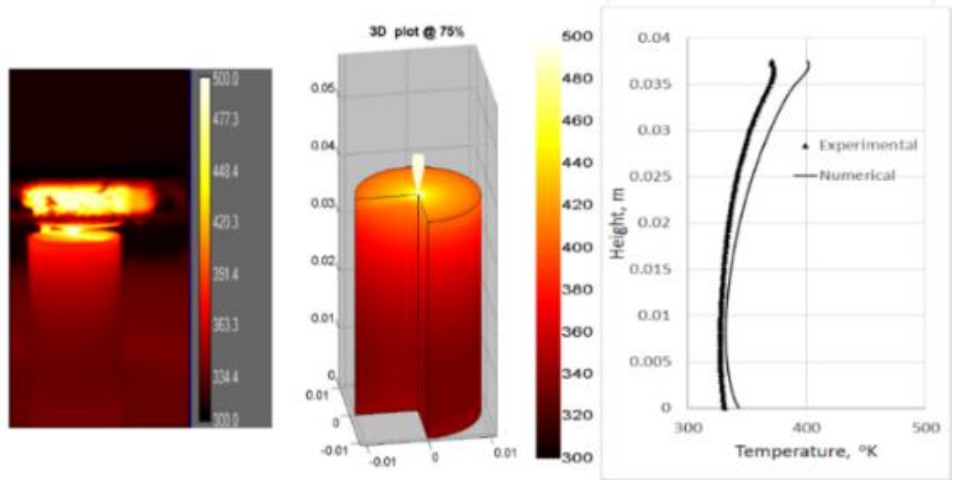
3D plot @ 75%
Experimental
Numerical
Height, m
Temperature, °K

(d)

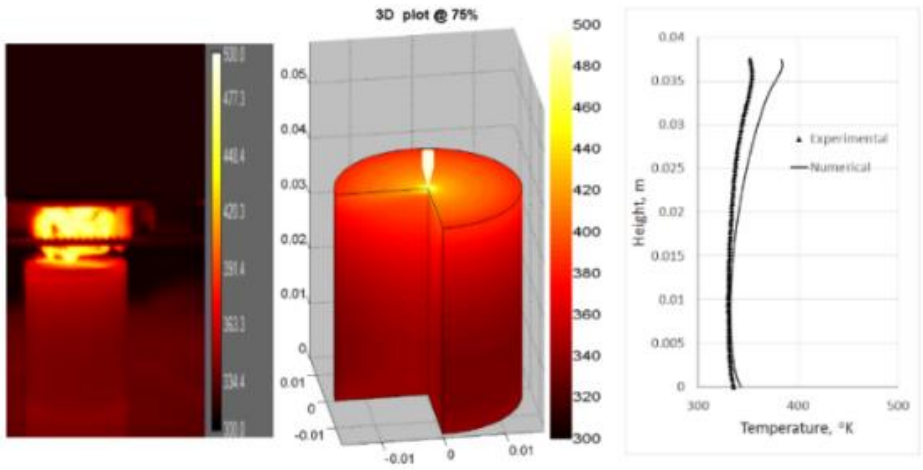

Fig. 79. Comparisons between computational and experimental temperature profiles along the height of the part during fabrication and cooling. Maximum part height is 50 mm, and the temperature varies from 293.15 to 453.15 K, respectively.

4.3.4 Estimation of temperature distributions by corrected emissivity

In addition to the set of experiments we developed on the cylindrical objects explained in Chapter 4.3.3, we also investigated the thermal flow on cubical specimens. We printed three different ABS blocks with square cross-sections of 3, 7, and 11 mm while changing two critical printing parameters: printing speed and extruder temperature.

Table 47: Part physical, geometrical, and manufacturing parameters considered in this study.

Length, *L*	30 ±0.19 mm	Stacking Orientation	Rectilinear, Longitudinal (0º)
Width, *w*	3, 7, and 11 ±0.5 mm	Average ideal time	0.25 s
Material	ABS	Layer thickness	0.19 mm
Color	White	Air gap	0
Specific heat, c_p	1300 J/kg-K	Average bulk temperature T_∞*	35 ºC
Density, ρ	948±5 kg/cm^3**	Raft	Yes
Conductivity, κ	0.16-0.15 W/m-K	Heated-bed temperature T_b	70 ºC
Polymer-Heated bed thermal contact coefficient	4800 W/m^{2}K	Bead width	0.40 mm

h_{conv} for the top layer* **	3 mm: 90 W/m^{2}K 7 mm: 59 W/m^{2}K 11 mm: 47 W/m^{2}K	Linear deposition velocity for 3D	Low (2000), Medium (4000), and High (6000) mm/min
h_{conv} for other layers* **	3 mm: 38 W/m^{2}K 7 mm: 20 W/m^{2}K 11 mm: 7 W/m^{2}K	Extruder temperature T_{Exd}	Low (240), Medium (265), and High (290) ^{o}C
Printing Orientation	Vertical	Cooling	Fan speed 100%

* The bulk or envelope temperature was monitored using an analog thermometer and its average calculated accordingly.
** Density was measured experimentally.
*** The correlation proposed by Churchill [324] is used to estimate the convection coefficient by assuming the velocities of 0.3 and 1.7 m/s for other and top layers, respectively.

The first experiment was performed on a cuboid of 3×3 mm with a speed of 2000mm/min (Low) at a temperature of 290 ^{o}C (High). The second one carried out on a cuboid with 7×7 mm, with a speed of 4000 mm/min (medium), and a temperature of 265 ^{o}C (medium), and the last cuboid with dimensions of 11×11 mm, at a speed of 6000 mm/min (High) and a temperature of 240 ^{o}C (low).

By analyzing the captured thermograms, the average deposition velocities in z-direction were calculated as 15.97, 4.66, and 2.42 mm/min for 3, 7, and 11 mm cuboids, respectively. Table 47 indicates a few parameters, along with other critical information considered for modeling.

The IR camera was installed in front of the FDM machine in a slightly inclined direction but perpendicular to the specimen at the center of the machine. The machine front door was open, and the room temperature and chamber temperature were monitored regularly. The different sizes of the 3D printed cuboids are shown in Fig. 80-a. The printing processes were captured with a frame rate of 2 Hz from the beginning of the process to a few seconds following the completion of the specimens.

The IR camera captured the process of manufacturing three cuboids printed with white ABS filament. The entire process was captured for all three cuboids; however, two critical instances—one at halfway through the process and the other at the completion of the printing process—for the blocks of 7 and 11 mm are demonstrated in Fig. 81.

We wrote an algorithm to correct the IR camera's temperature measurements *in-situ*. The first column of images in Fig. 81-a is the initially reported temperatures, the second column are the corrected temperatures based on emissivity, and the last column shows the temperature difference between the corrected and reported values.

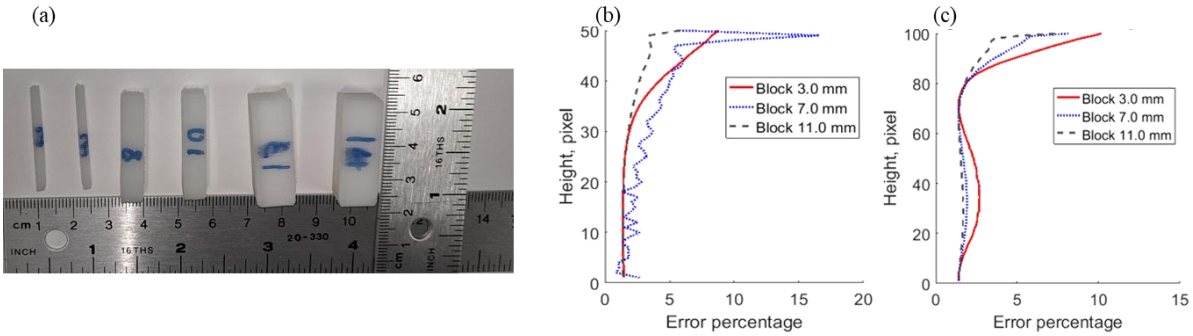

Fig. 80. (a) Different cuboids printed and monitored *in-situ* using IR camera; (b) error percentage in estimation of the temperature along the height of the blocks of 3, 7, and 11 mm at the halfway point of fabrication; and (c) error percentage in estimation of the temperature along the height of the cuboids of 3, 7, and 11 mm upon completion of the fabrication process.

We used the correlation found for the white ABS polymer to account for the effect of emissivity on temperature measurements. These effects were more pronounced at higher temperatures with a maximum error of 15% in areas with temperatures above 240°C.

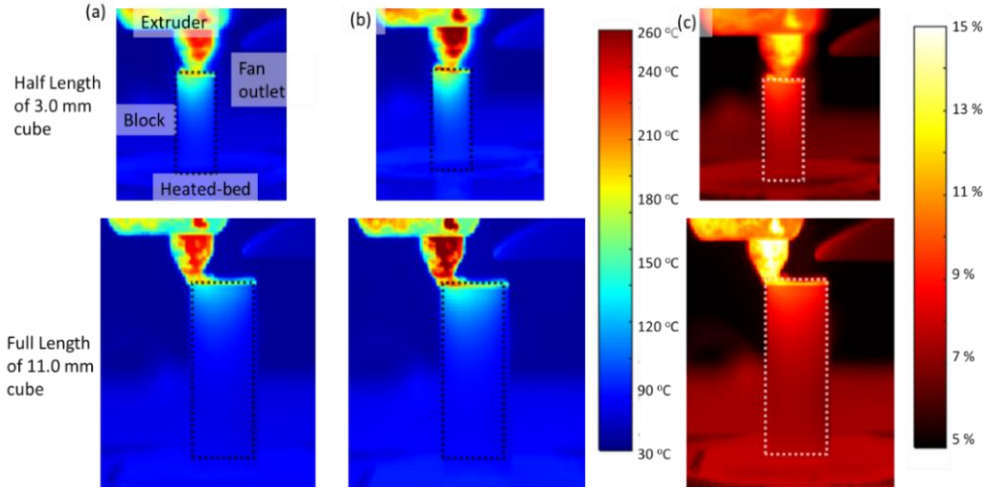

Fig. 81. The first and the second row show the application of the IR camera incorporating the determined emissivity for in-situ temperature measurements at half and full length specimens with 7 and 11 mm, respectively: (a) the original temperature estimated by IR camera; (b) The corrected temperature; and (c) the error percentage.

4.3.5 Comparison between numerical estimation and IR measurements

We developed a simplified 1D simulation to estimate the temperature along the height of three different blocks with the specification mentioned in Table 47. The model is based on assuming the lumped capacity for the cross-sections, even though this assumption could only be satisfied for the cubical section of 3x3 mm. This model contained the corrected emissivity and the adjusted total heat transfer coefficients, which were included as described in chapters 4.1 and 4.2.2, respectively. In addition, polymer-bed thermal resistance also applied as a boundary condition for the contact point between the slender blocks and the heated bed. The concept of discretization of the heat transfer ODE for the numerical solution is also covered in Chapter 3.2.1.2.1 above. The temperature distribution along the height of these three cases for the half and the full length of the blocks are illustrated in Fig. 82-a and b, respectively.

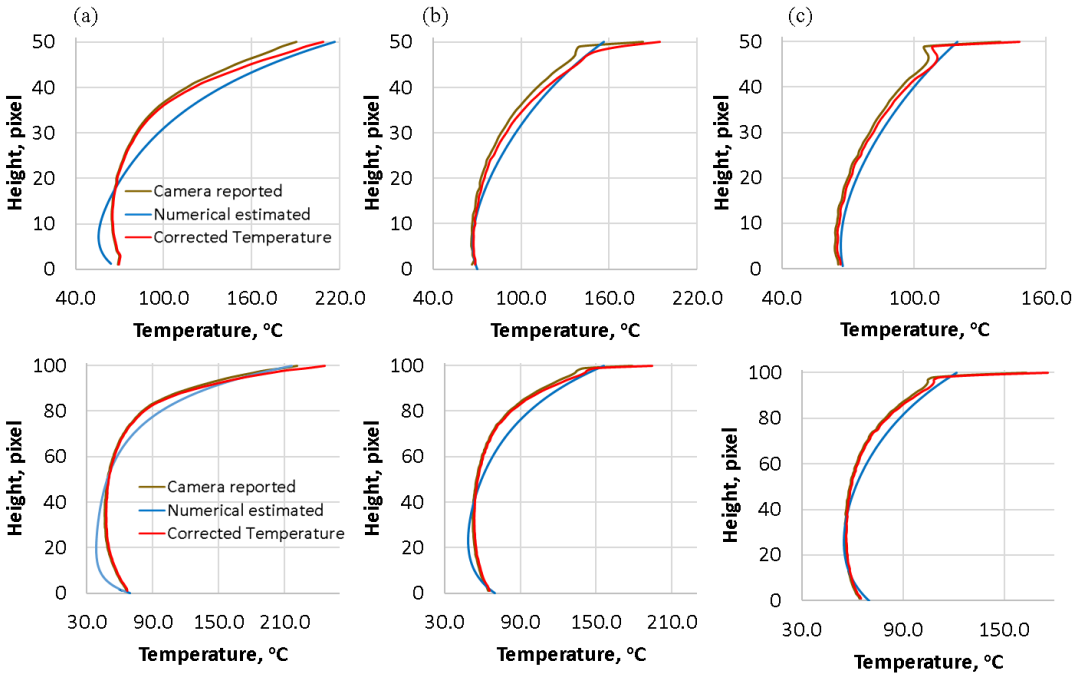

Fig. 82. The comparison between 1D numerical simulations, original, and corrected experimentally measured temperature along the vertical line on the center front-face for the three blocks of sizes 3, 7, and 11 mm at half and full length: (a) 3 mm cuboid; (b) 7 mm cuboid; and (c) 11 mm cuboid.

The results exhibit a strong agreement between the corrected temperature and the estimated temperature for each of the sizes. The maximum difference took place on the top layers of the two larger cuboids. This difference can be attributed to the deficiency of a simplified 1D model to capture the dynamics of the deposition or the radiation and reflection of the extruder with a higher temperature at the top layers. The corrected temperature, except for the few top layers, are in good agreement with numerical estimation.

Looking critically at the numerical model, one can conclude that the lumped capacity model cannot capture the correct temperature distribution and underestimates and overestimates temperature on the lower and top layers, respectively. This conclusion also confirms the finding of 3D analyses using FE, as described in Chapter 3.2.3.2 above and also reported by C. Bellehumuer et al. [38]. Thus, the temperature distribution on the areas right below the top layers where the latest deposited happens needs 3-dimensional analyses to be reliably estimated.

4.3.6 Experimental study of the module of elasticity on the testing artifacts

We printed 28 testing artifacts according to the design experiments. Each of these individual artifacts was printed under different printing settings, while the five selected parameters changed from one to another. We measured several specifications of the printed samples, including their natural frequencies for both center and wing parts, weight, dimensions, and submerged weights, and further analyzed the gathered data. We studied how parameters affected density, contact quality, and natural frequencies. Besides using natural frequencies, dimensions, and densities, we estimated mechanical properties and addressed the effect of process parameters on mechanical properties too.

Moreover, we also compared these data and our previous study on the cubes to present a physics supported perspective. The results hereunder start with density and contact quality and

continue with finding natural frequencies and associated mechanical properties, such as moduli of elasticity and Poisson's ratios for isotropic and orthotropic assumptions. We also did preliminary analyses on the module of elasticity on a cantilever beam.

4.3.6.1 The effect of process parameters on the density of the artifacts

We wanted to find density, solidity ratio, and the contact quality of testing artifacts and compare them with the previous prediction on cubes in order to examine the potential of data extrapolation to more complex geometry.

We used the same strategy mentioned in the section of measuring density to gauge the density of each artifact. The results are listed in appendices 9.6. Then, we applied a similar approach using statistical analyses to predict the linear, two-way, and quadratic interrelationships among parameters and density in a multi-dimensional space.

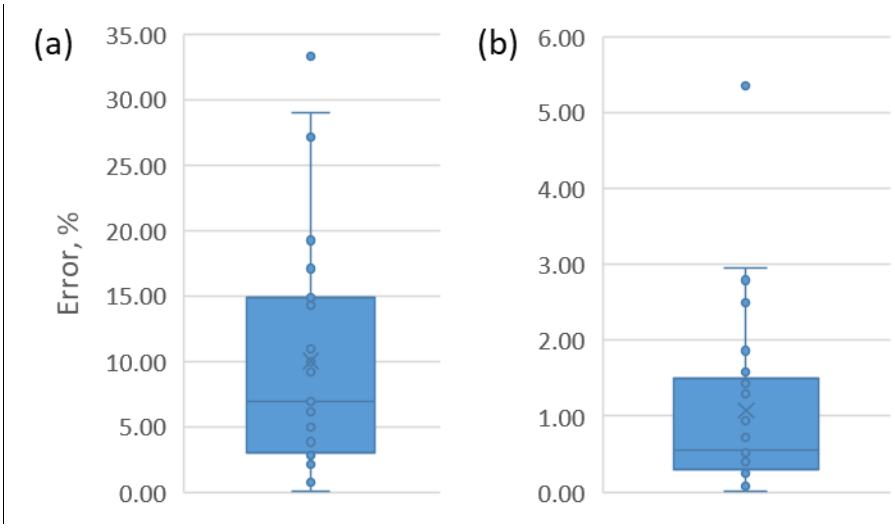

Fig. 83. Box graphs show the distribution of the errors: (a) relative based on the maximum possible deviation, and (b) absolute based on cube predicted.

The results are listed in Table 48 along with the measured density, estimated density (based on cube analysis), and relative errors. In order to have a better understanding of the scale of the error, we measured absolute and relative errors. Absolute errors reflect the differences of density normalized to the measured density. In the relative density error estimation, we obtained error

by finding the potential errors for each specimen and dividing it with the maximum possible error for particular printing parameters. These maximum possible errors were found by estimating the predicted density based on Eqs. (4-20) and (4-21). Knowing the theoretical *SR* and the density of the filament as 1,055 kg/m^3, we estimated the maximum possible error and estimated the deviations of measured density from the estimated densities and listed the errors under the title of "Relative error, %" in Table 48.

Table 48: The measured, estimated, absolute error, and relative error of the measurements of the density of the different testing artifacts.

run	Measure density, kg/m^3	Estimated Density, kg/m^3	Absolute Error %	Relative Error, %
1	1,046.5	1,037.4	0.872	19.23
2	1,019.6	1,039.2	1.922	29.03
3	1,006.1	1,006.1	0.001	2.42
4	983.9	1,004.7	2.120	17.08
5	1,008.6	1,026.3	1.755	14.26
6	1,043.1	1,037.1	0.578	6.92
7	1,033.5	1,032.6	0.086	2.14
8	955.0	1,020.4	6.841	33.27
9	1,002.4	982.0	2.030	14.89
10	1,019.6	990.3	2.873	27.15
11	1,026.8	1,040.0	1.291	10.52
12	1,021.6	1,024.3	0.264	0.04
13	1,026.9	1,027.4	0.047	9.97
14	1,012.3	1,013.6	0.132	3.88
15	1,010.9	1,021.9	1.095	3.83
16	1,015.5	1,022.1	0.656	2.97
17	1,012.5	1,027.6	1.487	15.07
18	1,012.5	1,002.6	0.980	1.00
19	1,019.6	1,023.6	0.391	6.89
20	1,039.7	1,033.9	0.558	2.83
21	1,028.1	1,034.4	0.617	6.13

Table 48: The measured, estimated, absolute error, and relative error of the measurements of the density of the different testing artifacts.

22	1,025.8	1,016.0	0.955	9.19
23	994.7	987.7	0.698	3.42
24	1,021.1	1,021.9	0.076	0.73
25	1,045.2	1,035.7	0.909	10.93
26	1,018.5	1,021.3	0.271	5.00
27	1,021.4	1,004.7	1.627	11.38
28	995.6	1,007.5	1.201	7.98

Figure 83-a shows the error distribution; the average of the estimation ranges between 3 to 15% error; furthermore, the absolute error shown in Fig. 83-a ranges between 0 to 3%, which shows the success of this prediction of the density. The above box graph indicates the effectiveness of employing a simple volume such as a cube and its potential to better understand the physical properties of a 3D printed component on a larger scale.

4.3.6.2 The study on the module of elasticity of cantilever beam

To illustrate the variability of the mechanical properties with respect to process parameters, we printed six cantilever beams similar to one shown in Fig. 19, which is a solid slender flat cantilever beam. Two process parameters were varied, including printing speed as well as printing orientation. Results shown in Table 49 correspond to a cantilever with length, width, and thickness of 70±0.25mm, 30±0.25mm, and 6±0.09mm, respectively. DHI measured the corresponding natural frequencies, and the moduli of elasticity were recovered using Eqs (3-14) and (3-15) for the first bending mode. The obtained results were compared with the experimentally measured properties of pristine ABS filaments.

As illustrated in Table 49, results show that the printing speed significantly affects the elastic modulus of 3D printed specimens. These trends showing the positive effect of printing speed are consistent with findings on the effect of energy deposition reported by others [12, 13, 115].

They confirm the positive effect of printing speed (feed rate) on improving the bonding between layers. Horizontal printing demonstrates elasticity close to the pristine ABS filament because of the alignment of the filament with the axial direction of the beam; but still, the effects of better bonding due to the higher energy deposition associated with higher feed rate are noticeable.

Table 49: Recovered moduli of elasticity of cantilever beams when fabricated at varying printing speeds and orientations. Pristine ABS filament with a reference module of elasticity of 2,230 MPa was used to compute deviations.

Printing speed	Printing direction	1st bending ω_n (Hz)	Module of elasticity (MPa)	Deviation from Ref., %
Fast	Horizontal	299±5	2,148.3	-3.66%
	Vertical	270±5	1,751.8	-21.44%
Normal	Horizontal	294±5	2,077.1	-6.86%
	Vertical	258±5	1,599.53	-28.27%
Slow	Horizontal	291±5	2,034.9	-8.75%
	Vertical	223±5	1,195.0	-46.41%

This experiment illustrated the potential of employing a modal analysis on a flat cantilever beam to recover the relationship among process parameters and mechanical properties and assured us of the effectiveness of our plan. Although the selected set of parameters were only two, and we performed factorial design to illustrate the interplayed complexity, the results meaningfully demonstrated the ability of our approach.

4.3.6.3 Study on moduli of elasticity assuming isotropic material properties

We assumed isotropic material properties to estimate the moduli of elasticity. The testing artifact was examined numerically, as mentioned in Chapter 4.2.9, where we estimated the eigenvalues for the center and wing section of the testing artifact separately. We measured the natural frequencies and mode shapes for both center and wing sections. The first five modes of the center (four bending modes, and one torsion mode) resulting from FEM analyses are shown

with the corresponding hologram side by side in Fig. 84. The holograms were taken using the time-average holographic interferometric described in Chapter 3.3.1.2.

The mode shapes and natural frequencies also measured using the same set-up for each of the 28 printed samples for the wing section as well. Figure 85 illustrates the first six modes, including three bending and three torsions.

The images are shown in Fig. 84 and Fig. 85 were captured using the same setup while the frequency swept from 40 Hz to 5,500 Hz. As explained before, for the isotropic material, we needed at least one bending and one torsion mode, and for the orthotropic material, we needed at least four modes, including bendings and torsions to measure the E_1, E_2, G_{12}, ν_{12}, and ν_{21}.

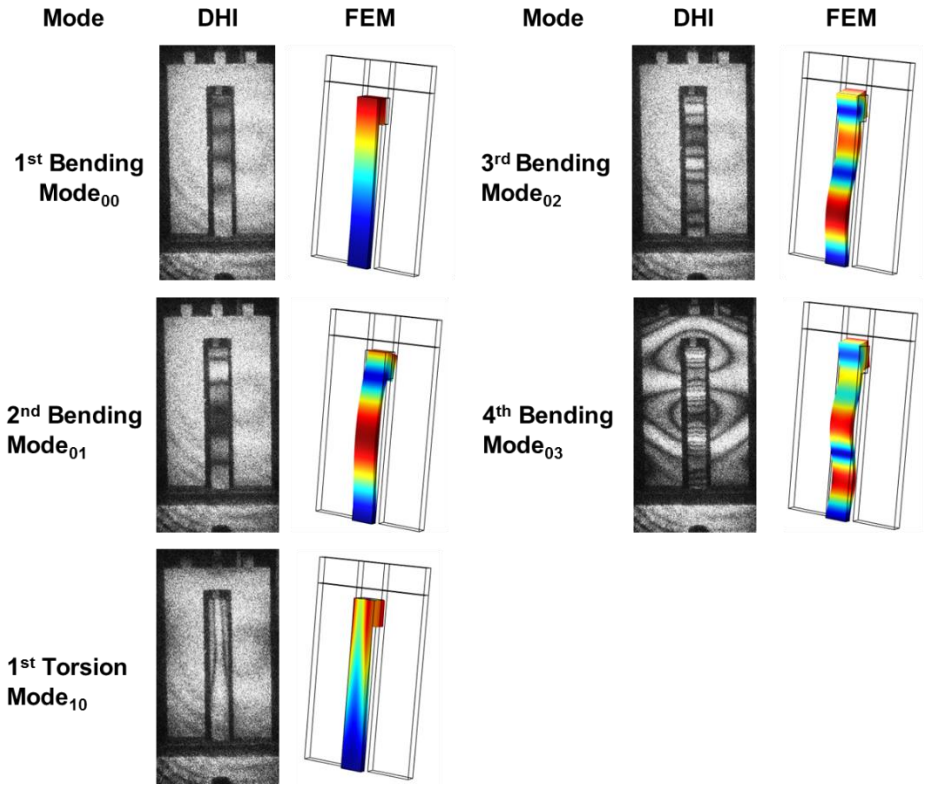

Fig. 84. The first five bending and torsion modes for the center part of the printed testing artifact found using the digital time-average holographic interferometry (DHI).

Presented in appendices, Table 68, Table 69, Table 70, and Table 71 list the measured dimensions and natural frequencies of the center and wing parts, respectively. We found the

moduli of elasticity based on each natural frequencies knowing the eigenvalues, thickness, and density according to Chapter 4.2.7.

We normalized measured natural frequencies with the maximum measured natural frequencies within each mode, and Fig. 86 shows four graphs associated with the bending and torsion modes of the wing and center part, respectively.

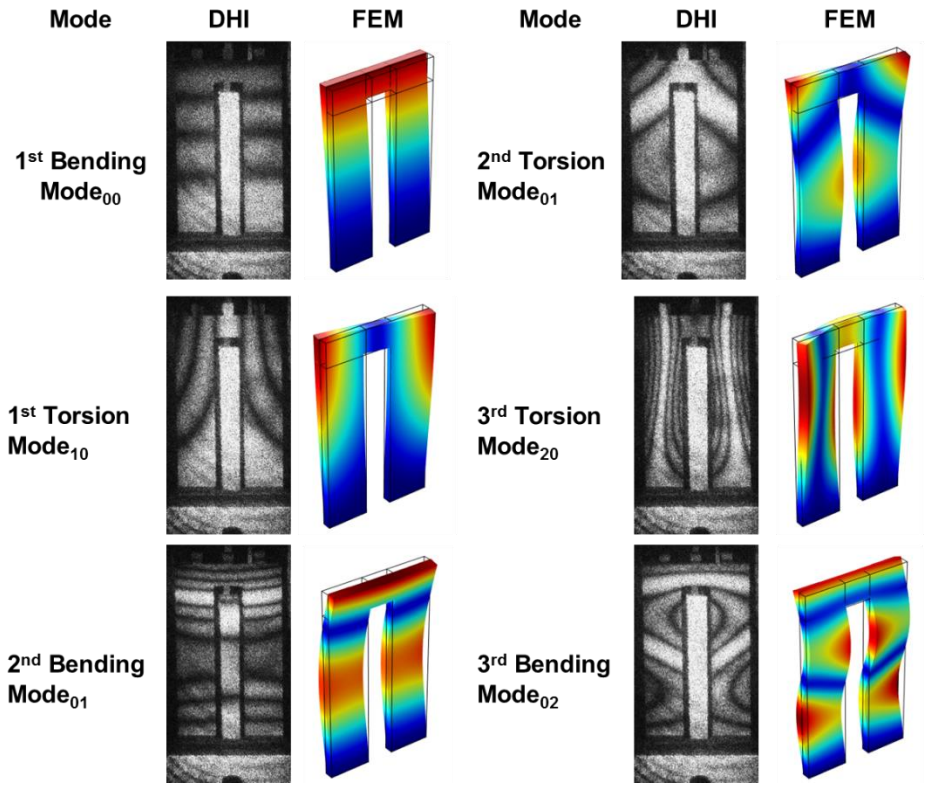

Fig. 85. The first six bending and torsion modes for the wing part of the printed testing artifact measured using the digital time-average holographic interferometry (DHI).

The graphs show significant resemblances in terms of the trends of the natural frequencies, with a proper agreement in hills and the valleys. We explained in Chapter 4.2.7 that the normalized values of eigenvalues had nearly identical trends, which support the observation of similarities in natural frequencies and are a sign of reliable measurements. The artifacts were able to capture the dependencies to parameters and offer a solid ground for comparison. In addition, the center and beam parts exhibit the most robust agreement, while the vicissitudes in

bending and torsion modes for the wing section are more significant than the bending of the center section.

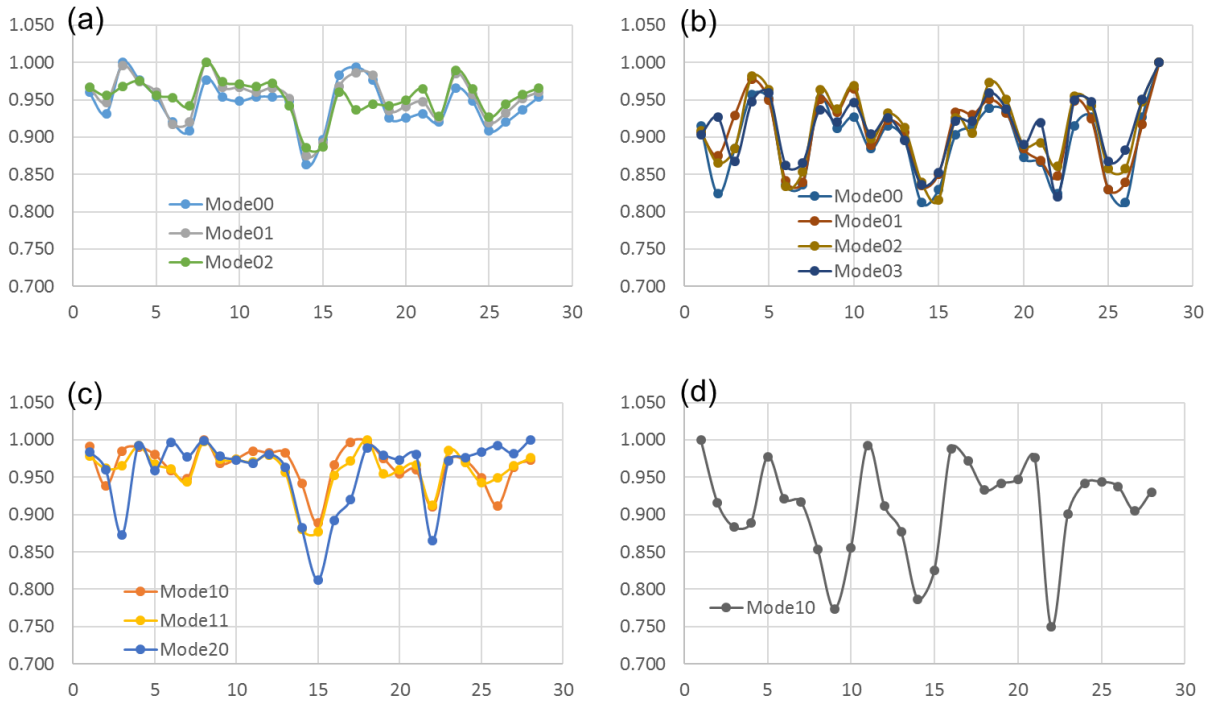

Fig. 86. The normalized to the maximum measured natural frequencies at each mode for the printed testing artifacts: (a) bending modes for the wing sections; (b) bending modes for the center section; (c) torsion modes for the wing section; and (d) torsion mode for the center section.

4.3.6.3.1 Estimation of the isotropic equivalent material properties using the E/G method

We found the elasticity for each artifact and measured the average and standard deviation for both Youngs's and shear moduli based on the E/G method explained before. The calculated results were found using the least-mean square method since we dealt with the overdetermined system of equations where the unknowns were less than the equations.

We expected to observe the same trend for the mechanical properties of the center and wing sections of the testing artifacts. We calculated the difference between the two estimated values for mechanical properties and found the relative differences between them with respect to the nominal values of 2,230, 832.09 MPa, and 0.34, for Young's, shear modulus and Poisson's ratio,

respectively. Although the trends exhibit a striking similarity between the estimated moduli of the center and wing part of the specimens, the differences in some specimens (e.g., numbers 3, 15, 16, and 17) are above 14%.

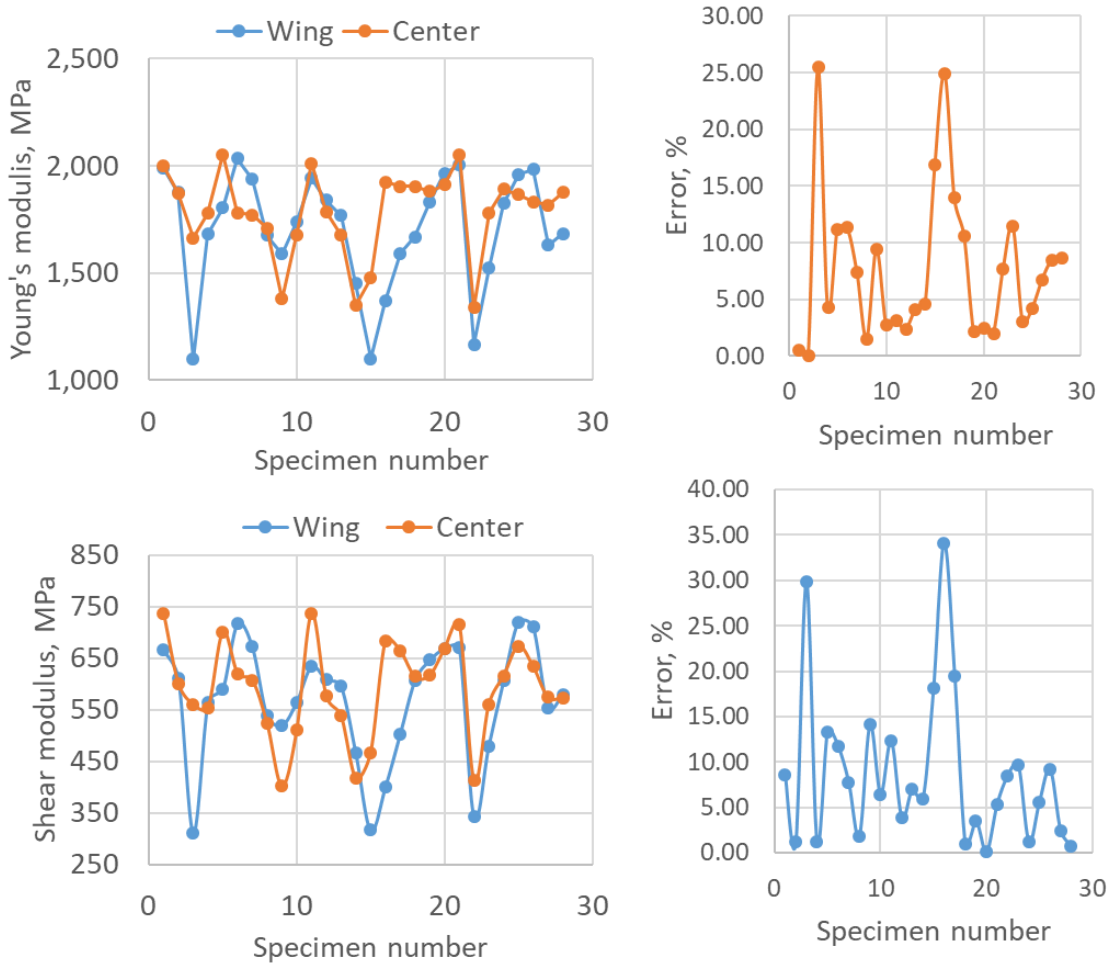

Fig. 87. The estimated moduli of elasticity and relative errors for the beam and wing part of each printed artifacts assuming isotropic material properties: (a) Young's modulus; (b) shear modulus.

We attribute these changes to the anisotropic nature of the specimens, the presence of residual stresses in the wing or center, and the relationship between the geometry (thickness, width, and length) and process parameters on different parts of testing artifacts.

The center section of the specimens acts similarly to a beam, and we expected to have less counter effect of the geometry; thus, the material properties should be close to what was

estimated assuming isotropic material properties along the deposition direction based on composite laminar theory. We explained the estimated elasticity based on the laminate theory in Chapter 3.1.2.2 and Eq. (3-24-a). In this case, the module of elasticity is only related to the porosity, which can be predicted by knowing the density of the specimens. We calculated differences between measured and predicted values, found relative errors, and plotted them in Fig. 88.

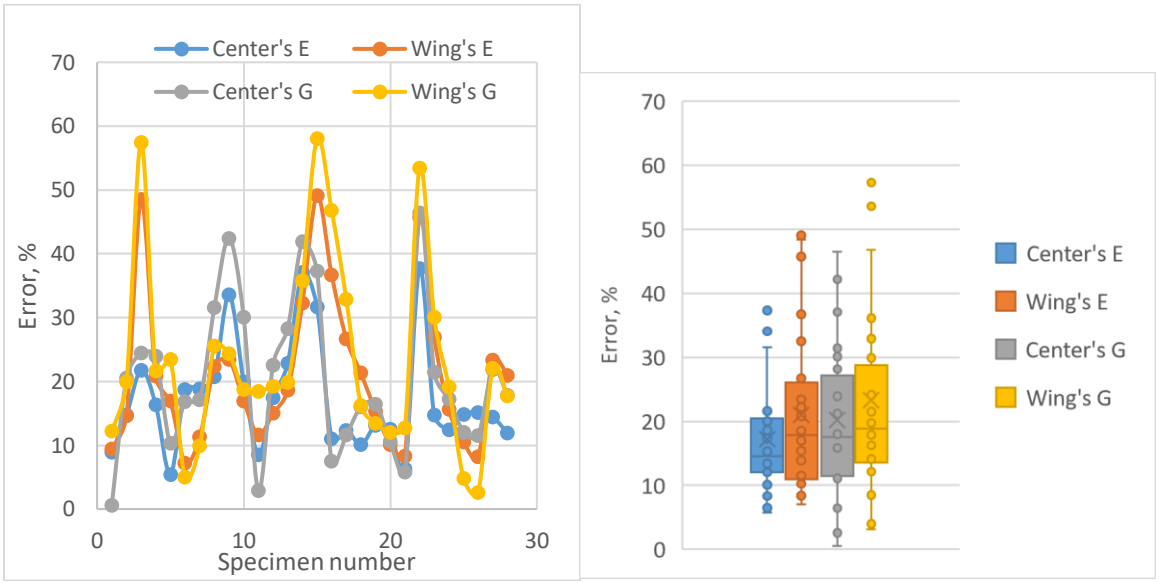

Fig. 88. The estimated error for the moduli of elasticity for the center and wing part with respect to the estimated elasticity based on porosity and the laminate theory.

The average of the measured errors is about 17%, with a minimum of 4% and a maximum of 37% for Young's modulus of the center section. These errors for Young's modulus of the wings reach an average of 22% with 8% and 48% as a minimum and maximum error, respectively. The same comparison on the shear modulus showed an average of error abut 20% and 25% for beam and wing, respectively. The maximum errors are 43% ad 57%, which seemed large.

4.3.6.3.2 Estimation of the isotropic equivalent material properties using the E/v method

We used the methodology defined in Chapter 4.2.7.3 to estimate Young's modulus, *E*; shear modulus, *G*; and Poisson's ratio through the sets of stored frequencies and their ratios. The

method followed the procedure explained before, and we used the correlation for all estimated eigenvalues to account for the effect of Poisson's ratios for both wing and center sections. We ran an iterative procedure, updating the eigenvalues at each iteration, and continued it until reaching a root mean square (RMS) error of 10^{-6} or 1000 iterations. Although we expected to see little (maximum 5%) to no effect of this iterative procedure on the values found for the center section, we applied them for consistency.

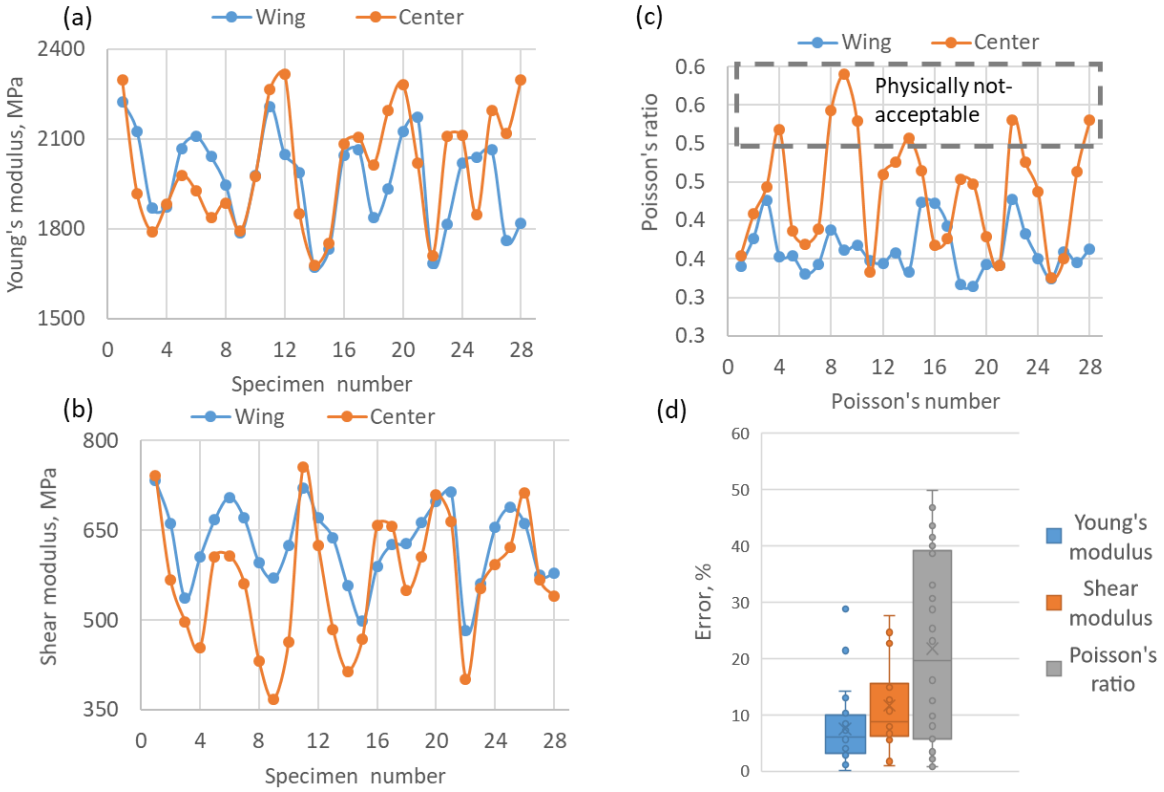

Fig. 89. The estimated moduli of elasticity, shear moduli, Poisson's ration and relative errors for the beam and wing part of each printed artifacts assuming isotropic material properties calculated using E/ν method: (a) Young's modulus; (b) shear moduli, (c) Poisson's ratio, and (d) relative error.

The maximum relative differences were for the Poisson's ratio, shear modulus, and Young's modulus, respectively. The average error for Young's modulus is about 3%, with a maximum of 10%. These values for shear modulus is 8% and 16%. Comparing the estimated Poisson's ratios reveals more consistency in the wing section compared to the beam section. The main issue can

be attributed to the susceptibility of the beam to the estimation of the shear modulus because a single torsion mode was used to assess the shear modulus, and it could introduce higher uncertainties, which might lead to an inaccurate or indeterminate estimation.

On the contrary, the wing par has three natural frequencies of the torsion modes contributing to estimate shear modulus. Therefore, these three sources can minimize the uncertainties using a least-mean square method. The potential source of error for the center part imputes the large error margin for the Poisson's ratios because these uncertainties in calculating *E* and *G* can destructively increase the error in Poisson's ratio.

The method, in general, was able to estimate the modulus. One may conclude that the beam section can be used effectively for the estimation of Young's modulus and the wing for estimation of the shear modulus.

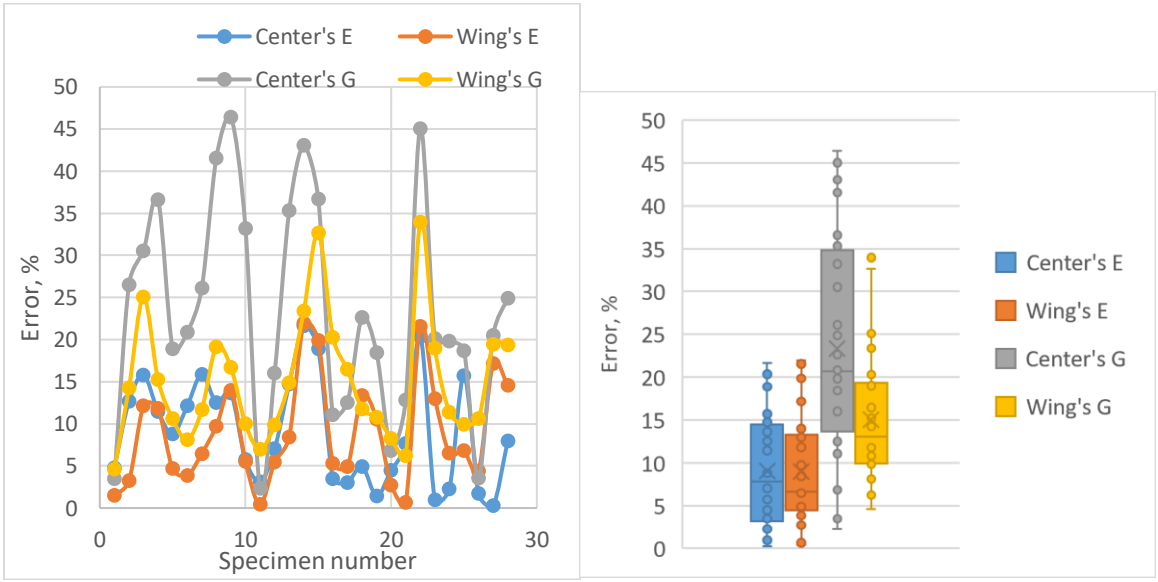

Fig. 90. The estimated error for the moduli of elasticity for the center and wing part with respect to the estimated elasticity based on porosity and the laminate theory.

We calculated error with respect to isotropic materials with known porosity and Fig. 90 shows the relative estimated error between the measured and the predicted values.

The average of the error for Young's modulus of the center part is about 8%, with a minimum error of 0% and a maximum of 20%. These errors for the wings reach an average of 9% with 0% and 22% as a minimum and maximum error, respectively. The same comparison on the shear modulus showed an average of error about 23% and 16% for beam and wing sections, respectively. These errors, as explained before, is more for the center part than the wing part. Although the maximum error reaches as high as 45%, this error for the wing part is about 33%. Comparing these errors with the *E/G* method reveals *E/v* methods showing better and more consistent results.

4.3.6.3.3 Statistical analyses on the effect of process parameters on mechanical characteristics

We studied the effects of process parameters on the measured mechanical characteristics, such as isotropic Young's and shear modulus. The general protocol is similar to our previous statistical analyses, which started by including all parameters and their interaction through DoE and then proceeded by keeping the first order and eliminating the less important parameters in a sequential procedure. We did this for both gathered data based on *E/G* and *E/v* methods. We measured these parameters by knowing the density.

- ***E/G* method**

As seen before, the yield results through the *E/G* method were not as consistent and reliable as the results obtained from *E/v* method, because the ranges and magnitudes of error were seen in *E/G* method. This observation is reflected in the statistical analyses as well; the R^2 turned out to be low for each of the two parts of the testing artifacts for both Young's and shear modulus.

The obtained R-squareds for Young's modulus were 0.39 and 0.58 for the center and wing sections, respectively. These values calculated for shear modulus reached 0.53 and 0.65 for the center and the wing sections, respectively. Thus we did not present the result for *E/G* here.

It is worth mentioning that the trends of shear moduli were generally more dependable and presented better correlation compared to Young's moduli, and the wing part bore better confidence as opposed to the center section. We expected the center part to be less susceptible to error; however, since we only measured one torsion mode, we impute this problem to a potential source of error due to this paucity of data to help predict the shear modulus more accurately. Moreover, the propagation of the effect of this error into Young's modulus through the interrelated set of equations could not be ignored.

- ***E/v* method**

We skipped the screening procedure and jumped into the final results. Statistical analyses revealed similarity to the previous observation, and both Young's and shear modulus were strongly dependent on layer thickness. We graduality ruled out the parameters with *P-Values* above 25% but kept those with the first order. The final results are presented in Fig. 91 and also for Young's modulus in appendices 9.5.15.7 and 9.5.15.10 and for shear modulus in appendices 9.5.15.8 and 9.5.15.11.

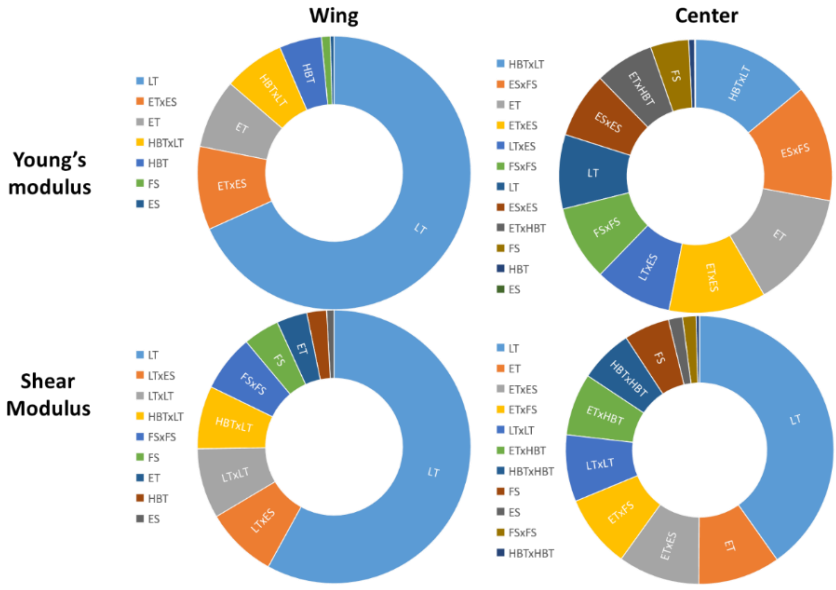

Fig. 91. Results of the statistical analyses on Young's and shear modulus showing influential sources on wing and center sections of the artifacts.

The statistical analyses for Young's moduli were not found as strong as for the density, and the $\boldsymbol{R^2}$ was 0.63 and 0.70 for the center and wing sections, respectively.

Table 50: statistical analyses of the screened sources for the estimated Young's modulus of testing artifacts

Parameters and their interactions	Values
Center	
R^2	0.63
R^2 Adj	0.33
Root Mean Square Error	158.36
Mean of Response	2008.50
Observations (or Sum Wgts)	28
Wing	
R^2	0.70
R^2 Adj	0.59
Root Mean Square Error	100.67
Mean of Response	1966.18
Observations (or Sum Wgts)	28

The same set of analyses was performed on shear modulus to statistically evaluate the effect of process parameters. The results are very similar to Young's modulus but showed some differences. For example, the correlation was more robust than Young's modulus, and the effect of layer thickness was stronger.

The R^2 was 0.71 and 0.75 for the center and wing parts, respectively. These values indicated a relatively better correlation compared to Young's modulus. The details are listed in Table 51.

Table 51: statistical analyses of the screened sources for the estimated shear modulus of testing artifacts

Parameters and their interactions	Values
Center	
R^2	0.72

Table 51: statistical analyses of the screened sources for the estimated shear modulus of testing artifacts

R^2 Adj	0.53
Root Mean Square Error	72.62
Mean of Response	567.28
Observations (or Sum Wgts)	28
Wing	
R^2	0.60
R^2 Adj	0.55
Root Mean Square Error	44.59
Mean of Response	628.06
Observations (or Sum Wgts)	28

Other statistical data, including the estimated coefficient for polynomial, can be found in 9.5.15.8 and 9.5.15.11 of appendices.

Looking into the collected data revealed interesting observations. The most critical parameter is still layer thickness; however, the order differed from density. For Young's modulus, the most important parameters in order were (1) extruder temperature, (2) two-way effect of extruder temperature and fan speed, (3) extruder temperature and extruder speed, and (4) layer thickness and heated bed temperature. This observation corroborated our analytical results on the single filament, where we concluded the extruder speed is not as important as the diameter of the filament, the temperature of the extruder, and the environment, such as fan speed. The most critical parameters are related to advection. These parameters affect the temperature of the filament in the long run; thus, the bonding development, which directly is a result of cyclic temperature history, firmly influenced the Young's and shear modulus. This result can be interpreted as the effect of energy deposition in layers helping to improve the bonding quality. The combination of higher velocity and layer thickness means the deposition of higher thermal energy per volume of the cube during printing.

In addition, Fig. 93 shows the predicted versus the actual Young's and shear moduli. As one can expect, due to the lower confidence in prediction, the error range is broader than that observed in the previous graphs of density and density difference seen in Fig. 66 and Fig. 69 in Chapter 4.3.2.3.

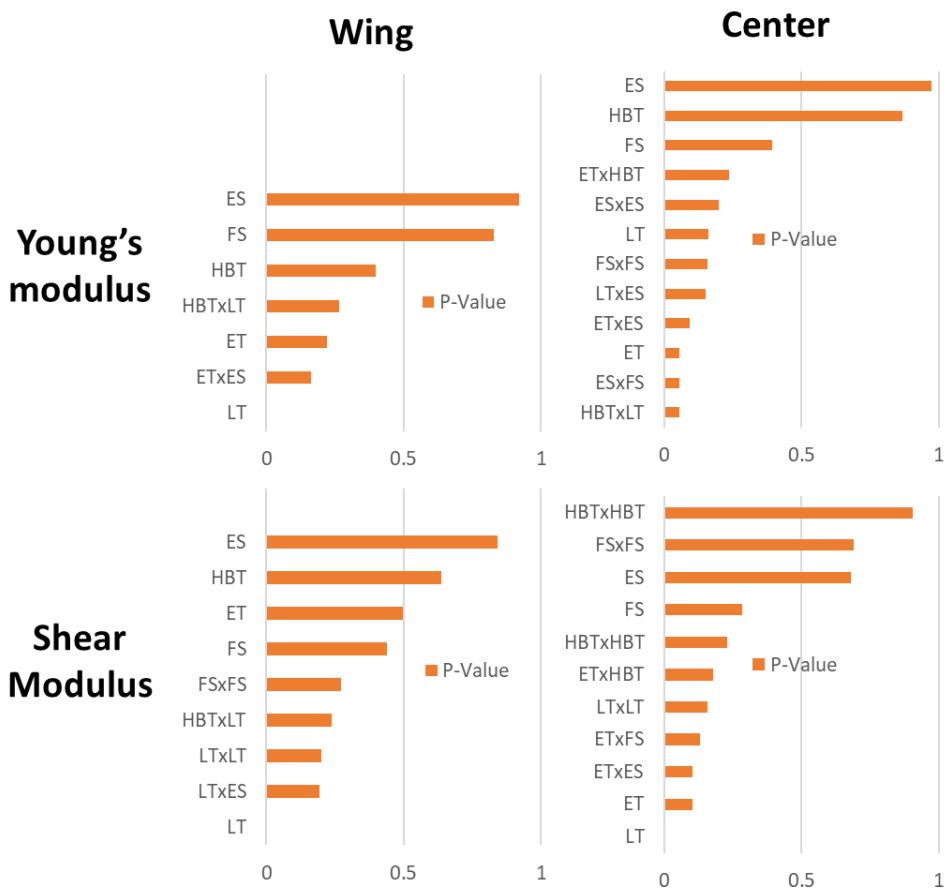

Fig. 92. Result of the statistical analyses on Young's and shear modulus showing the P-value of influential sources.

The collected data indicates a few specimens appeared beyond the confidence level and seemed to be outliers. Rows numbered 11, 12, 14, and 15 of Table 9 were located outsides the expected range. Removing those from the analyses can improve the correlation significantly. The images are shown in Fig. 93 display revised analyses with these points being excluded, and consequently, the correlation improved where the R^2 jumped to above 83 percent for all cases.

Removing these outliers did not change the sequence of important parameters noticeably but changed the LogWorth and its P-values. These outliers are associated with the standard printing speed and temperature, which required further analyses.

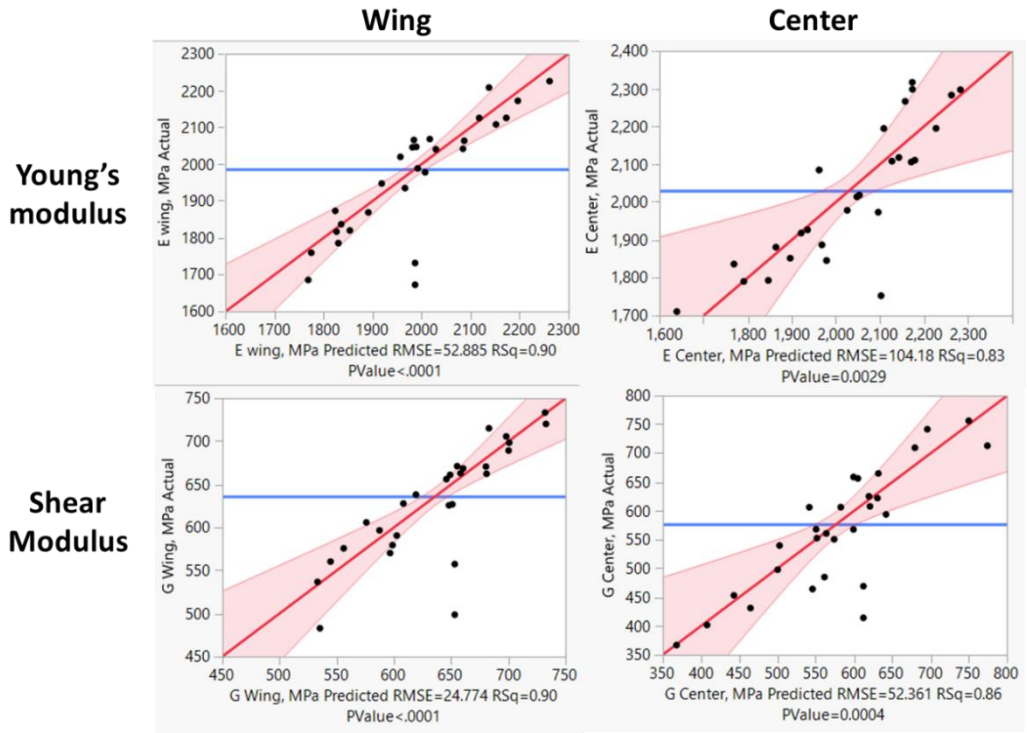

Fig. 93. The graphs indicate the actual by prediction plot of the Young's, *E*, and shear, *G*, moduli for the wing and center sections of the testing artifacts after removing 4 outliers.

4.3.6.4 Study on the module of elasticity assuming orthotropic material

We did the analyses assuming orthotropic material properties. The study on the properties of the beam and wing parts of the testing artifacts exhibited the dissimilarity in the material properties, potentially pointing to orthotropic material properties. This dissimilarity was seen in the wing part more severely; thus, each part had to be analyzed separately. An orthotropic material has nine constants, including the elastic moduli, shear moduli, and Poisson's ratios in the three principal directions. However, in a thin plate, these constants can be reduced to four as mentioned before. We found the five first modes of the center and six modes of the wings that

allowed us to determine these four unknowns for each artifact. As we explained before, the data available for the center part of the testing artifacts does not allow us to measure all the five unknowns of the orthotropic material. Therefore, the analysis was only performed on the wing part of the printed specimen.

We used the method defined in Chapter 4.2.9 to estimate Young's moduli, E_x and E_y, shear modulus, G_{xy}, and Poisson's ratios, ν_{xy} and ν_{yx}. In order to achieve better results, we employed the non-linear equations reflecting the effect of Poisson's ratios with the measured frequencies and through an iterative procedure, corrected the eigenvalues accordingly to reach the convergence criteria. The procedure used the MATLAB least-squares minimization algorithm to solve an over-determinate system of equations while updating the eigenvalues until reaching an RMS of 10^{-6} or 1000 iterations.

Results are presented in three categories: elastic moduli, shear modulus, and Poisson's ratios. We started with elastic moduli in x and y directions and ended up with Poisson's ratios in xy and yx directions.

4.3.6.4.1 Elastic moduli assuming orthotropic material properties for printed artifacts

We obtained the two principal elastic moduli in x and y directions; the z direction is equal to y due to conversely isotropic assumption. We also previously estimated the average porosity or solidity ratio, which also can be used for an estimation of elastic moduli based on laminate theory, as explained in chapter 3.1.2.2. These values are also used for comparison of the estimated moduli. The error was calculated to provide better insight into the accuracy. It also should be noted that we assumed if two deposited beads shared a boundary, the welding along the shared boundary is fully developed. It might not be the case, and they could be located on top of each other with partial bonding along the shared premier.

The specimens were printed with printing direction coincide with x-direction, with zero air gap, and with the same printing map for each layer, from the first to the last layer. Therefore, we defined the first principal direction to coincide with *x*, and the second and third with y and z, respectively.

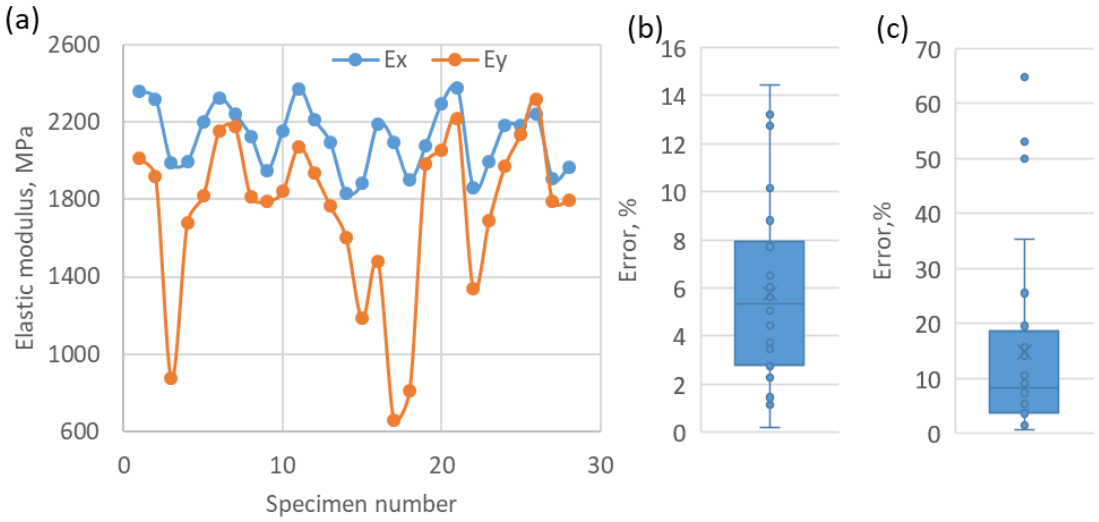

Fig. 94. The estimated moduli of elasticity and errors with respect to the estimated elasticity based on porosity and the laminate theory for the wing part of each printed artifact assuming orthotropic material properties: (a) Elastic moduli; (b) Ex error, and (d) Ey error.

We anticipated the E_y to be less than E_x, and this observation was seen for almost all obtained values except one. We also observed a general trend for E_x and E_y, which confirmed a similar effect of the combination of process parameters in different directions. The E_x errors were found to conform more with estimated E_x based on porosity with an average error of about 5% and with the maximum and minimum error of 14 and 1%, respectively. The calculated error for E_y reached a maximum of 65 percent. We observed errors in rows 3, 15, 17, and 18 to be above 30%, and the estimated modulus were lower than those evaluated through the laminated theory. The bonding has to be developed interlayers to improve the mechanical properties in y-direction, and this development requires time and expands gradually as the bonding quality, *P*, increases. This difference in estimated mechanical properties for some rows can be an indication of low

development of bonding inter-layers and point out to the potential of having low porosity but not developed bonding. In other words, having a high level of compaction but a low level of bonding development. The average error was 17% with the lowest error close to 0%, as shown in Fig. 94. The method, in general, was able to estimate the elastic moduli convincingly, with E_x and E_y showing similar trends, and the magnitudes less than 2,400 MPa.

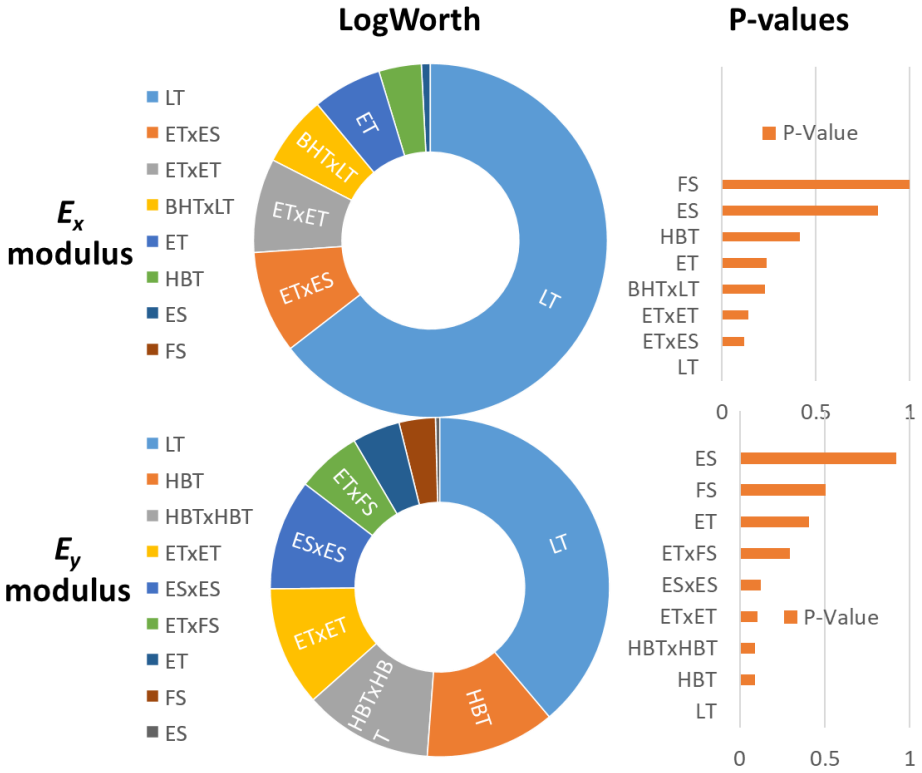

Fig. 95. Result of the statistical analyses on elastic moduli for orthotropic material properties showing the influential sources: (a) Pi diagram showing the LogWorth of the sources; and (b) Bar diagrams showing the P-Values.

- ***Statistical analyses on the measured data***

We studied the effects of process parameters on the measured mechanical characteristics. The general protocol is similar to our previous statistical analyses, which started with including all parameters and their interaction through DoE, and followed by keeping the first order and eliminating the less essential parameters in a sequential procedure. We skipped the screening procedure and jumped into the final results. Statistical analyses were similar to the previous

observation of isotropic material, and both moduli were dependent strongly on layer thickness. We gradually ruled out the parameters with *P-Values* above 25% but kept those with the first order. The final results are presented in Fig. 95.

The statistical analyses for elastic moduli were carried out, and the *R-squares* are determined 0.77 and 0.66 for the center and wing sections, respectively.

Table 52: statistical analyses of the screened sources for the estimated Young's modulus of testing artifacts

Parameters and their interactions	Values
E_x	
R^2	0.77
R^2 Adj	0.68
Root Mean Square Error	95.43
Mean of Response	2119.58
Observations (or Sum Wgts)	28
E_y	
R^2	0.66
R^2 Adj	0.50
Root Mean Square Error	303.00
Mean of Response	1745.94
Observations (or Sum Wgts)	28

The complete statistical analyses and the constants of the two polynomials representing the relationship mathematically are listed in chapters 9.5.16.1 and 9.5.16.2 for E_x and E_y, respectively.

Looking into the collected data revealed interesting observations. The most important parameter was layer thickness; however, the two-way interactions of the extruder temperature with fan speed and quadratic effect of extruder speed were significant for the modulus in x direction. On the other hand, heated bed temperature, the quadratic effect of heated bed

temperature, and the quadratic effect of extruder temperature turned out to be more influential for the y-direction modulus. Here we also observed similar trends to the isotropic assumption for extruder speed, which bore no significant effect on both moduli per se. However, its quadratic effect and the two-way effect with extruder temperatures were influential. The effect of the heated bed was stronger for y direction. The combined effects of the heated bed temperature along with extruder temperature and extruder speed affected the bonding quality in x and y directions.

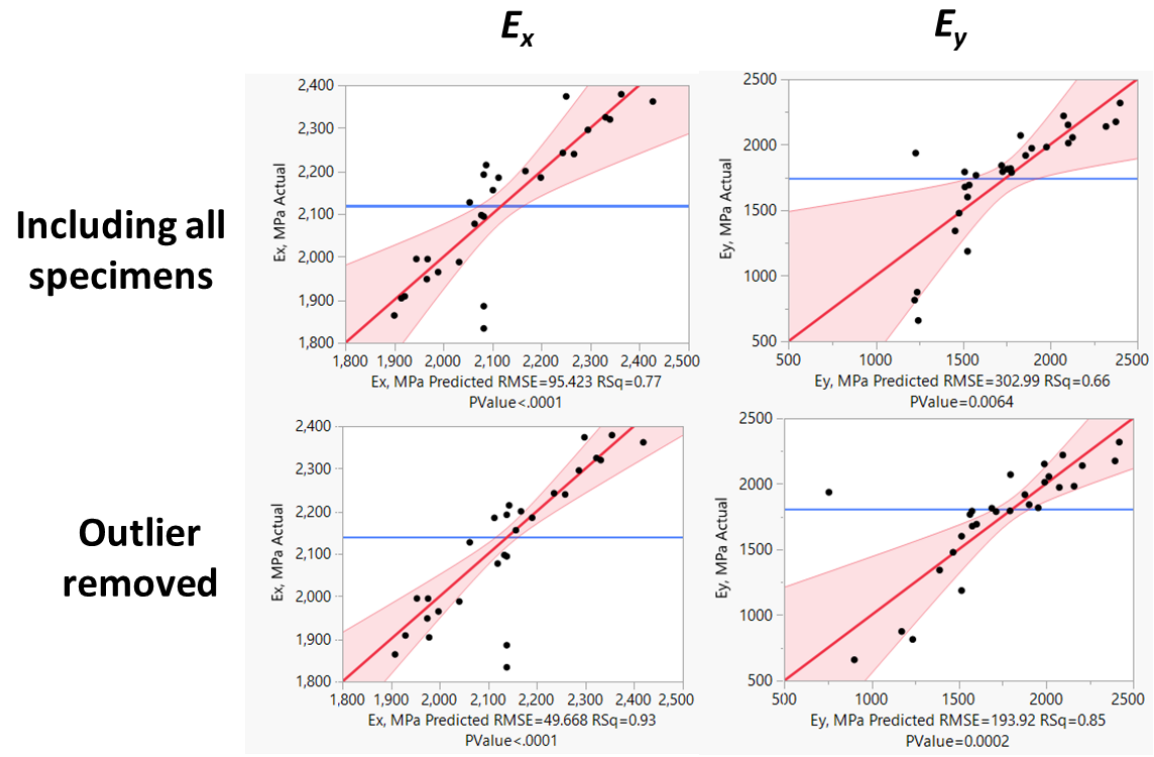

Fig. 96. The graph indicates the actual by prediction plot of the Young's, *E*, and shear, *G*, moduli for the center part of the testing artifacts.

Furthermore, Fig. 96 shows the predicted versus the actual Young's and shear moduli. As one can expect, due to the lower confidence in prediction, the error range is wide.

We examine the possibility of outliers affecting the statistical analyzes and removed four rows of data associated with 12, 14, 15, and 18 of Table 9. Removing those from the analyses

improved the correlation significantly, as shown in the second row of Fig. 96. In these two graphs, R^2 jumped to above 93 and 85 percent for x and y direction, respectively.

4.3.6.4.2 Shear modulus assuming orthotropic material properties for printed artifacts

Assuming a transversely isotropic material means we only had one independent shear modulus G_{xy}. The other shear moduli (G_{yx}, G_{yz}, G_{xz},…) can be estimated knowing the E_x, E_y, ν_{yx}, and ν_{yx}. We found G_{xy} via the iterative procedure described before (4.2.9 and 4.3.6.4), and here we only focus on the summary of results, including statistical analyses after the screening process. In other words, we only included the critical process parameters and their interaction in the following results. The cut-off for the P-value was 25%, and we removed any source with a higher P-value but kept the first order. We also performed a comparison based on laminate theory estimation.

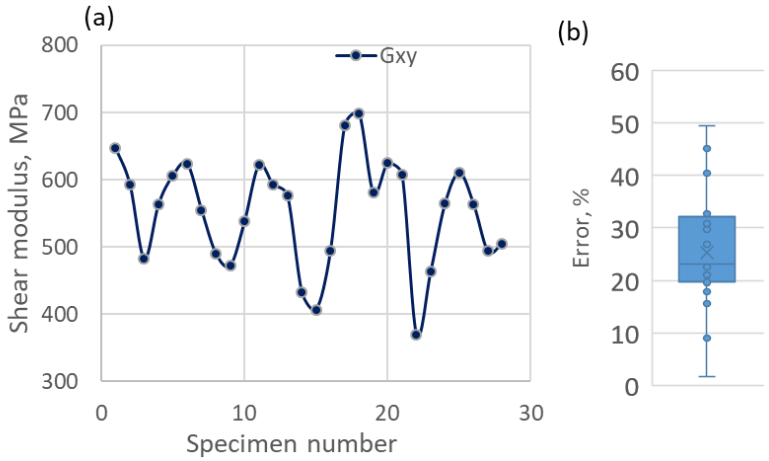

Fig. 97. The estimated shear modulus, and errors with respect to the estimated elasticity based on porosity and the laminate theory for the wing part of each printed artifacts assuming orthotropic material properties: (a) shear moduli; and (b) error.

The errors were distributed within 2 to 45 % compared to the laminate theory estimations. The results are shown in Fig. 97. The average error was about 25%, possibly indicating lower bonding among layers and contiguous beads, and the prospect of lower bonding contradicts the assumption of fully developed weld along the perimeter of the beads. In other words, the shared

boundary among beads was assumed to be fully developed; however, there can be adjacent beads between which necking was still under development and never fully established. We noticed this effect for the E_y in Chapter 4.3.6.4.1, and rows 3 and 15 are seen in both of these cases with differences of more than 30%.

Although the method manifested capability in predicting the shear modulus, further investigation has to be executed to analyze the performance of the bonding based on porosity and the thermal flow to more accurately predict the bonding in intra- and inter-layers.

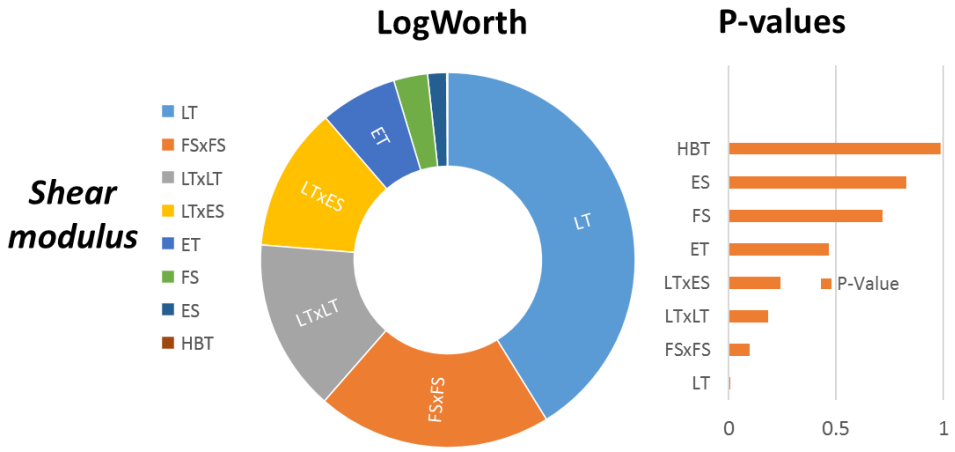

Fig. 98. Result of the statistical analyses on shear modulus for orthotropic material properties showing the influential sources: (a) Pi diagram showing the LogWorth of the sources; and (b) Bar diagrams showing the P-Values.

- ***Statistical analyses on the measured data***

We studied the effects of process parameters on the measured shear modulus. The general protocol is similar to our previous statistical analyses, as explained before. The final results are presented in Fig. 98.

The statistical analyses found $\boldsymbol{R^2}$ equal to 0.42, which does not show a robust correlation on the shear modulus.

Table 53: statistical analyses of the screened sources for the estimated Young's modulus of testing artifacts

Parameters and their interactions	Values
R^2	0.418468
R^2 Adj	0.173613
Root Mean Square Error	73.87078
Mean of Response	552.4312
Observations (or Sum Wgts)	28

The estimated coefficient for the polynomial defining the dependency of moduli to the five selected sources and their critical two-way interactions can be found in chapter 9.5.16.3 in the appendices section.

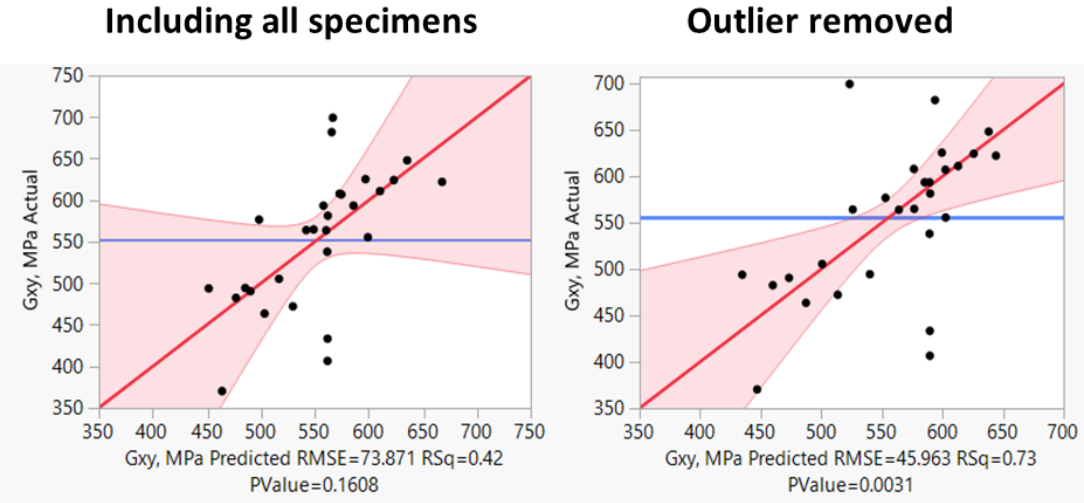

Fig. 99. The graph indicates the actual by prediction plot of the shear modulus, G_{xy}, for the wing part of the orthotopically assumed testing artifacts.

Layer thickness, its quadratic effects, and the combination of layer thickness with extruder speed were among the most critical process parameters. Aside from layer thickness, the rest of the sources does not show a good resemblance to previous observations for elastic moduli.

In addition, Fig. 99 shows the predicted versus the actual shear modulus. As one can expect, due to the lower confidence in prediction, the error range is wide. We removed four outliers

similarly to what we did before and observed significant improvement, as shown in R^2 and P-value are written under the right graph in Fig. 99.

4.3.6.4.3 Poisson's ratios assuming orthotropic material properties for printed artifacts

We obtained the two Poisson's ratios and did the same type of comparison with the prediction as we did before. Poisson's ratios were related to the magnitudes of moduli, and error in their estimation can deteriorate the accuracy of the calculated data. Thus, we expect to observe a feebler correlation for Poisson's ratio. Based on laminate theory prediction, we generally expect to have lower Poisson's ratio of *yx* plane compared to *xy*, and this observation was confirmed for a majority of obtained data.

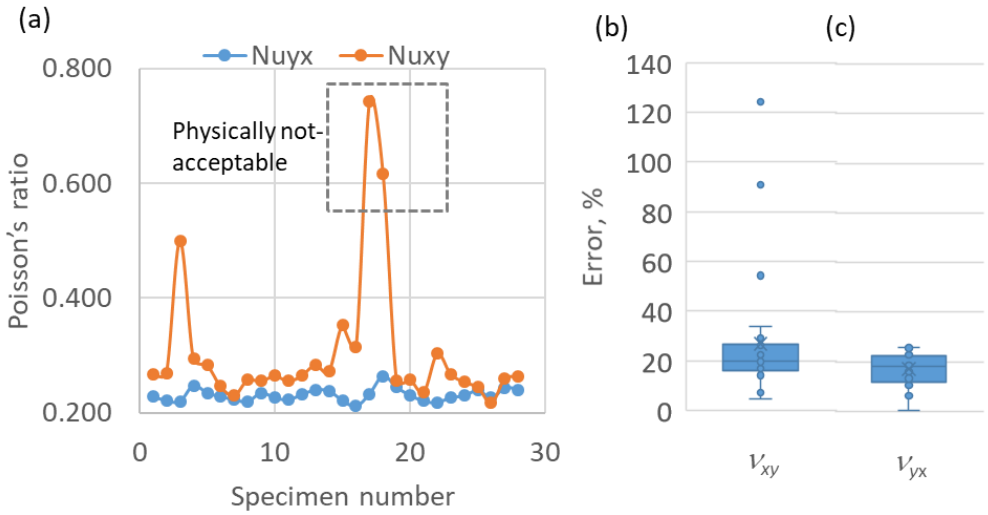

Fig. 100. The estimated Poisson's ratios, and errors with respect to the estimated values based on porosity and the laminate theory for the wing part of each printed artifacts assuming orthotropic material properties: (a) Poisson's ratios; (b) v_{xy} error, and (d) v_{yx} error.

The estimated value for v_{yx} looked more stable compared to v_{xy}, as shown in Fig. 100. Figure 100 suggests that the average error for v_{yx} is about 18%, with error ranges between 6 to 26 %. However, the estimated error for v_{xy} is widely distributed, with a few errors above 50 % and as large as 122%. Those also resulted in Poisson's ratios greater than 0.5, as shown in Fig. 100, which is physically unjustified for polymeric materials. The error average is about 30% in total,

and for the majority of the results exhibited Poisson's ratio less than 0.4 and above 0.2. The Poisson's ratios are directly driven from and related to mechanical properties, and the vicissitudes and uncertainties in the calculation of mechanical priorities can severely affect Poisson's ratios. This reason along with the possibility of not fully developed inter- and Intra-layers bonding impute to these errors in the estimations.

- ***Statistical analyses on the measured data***

We studied the effects of process parameters. Figure 101 shows the LogWorth and P-values for both Poisson's ratios.

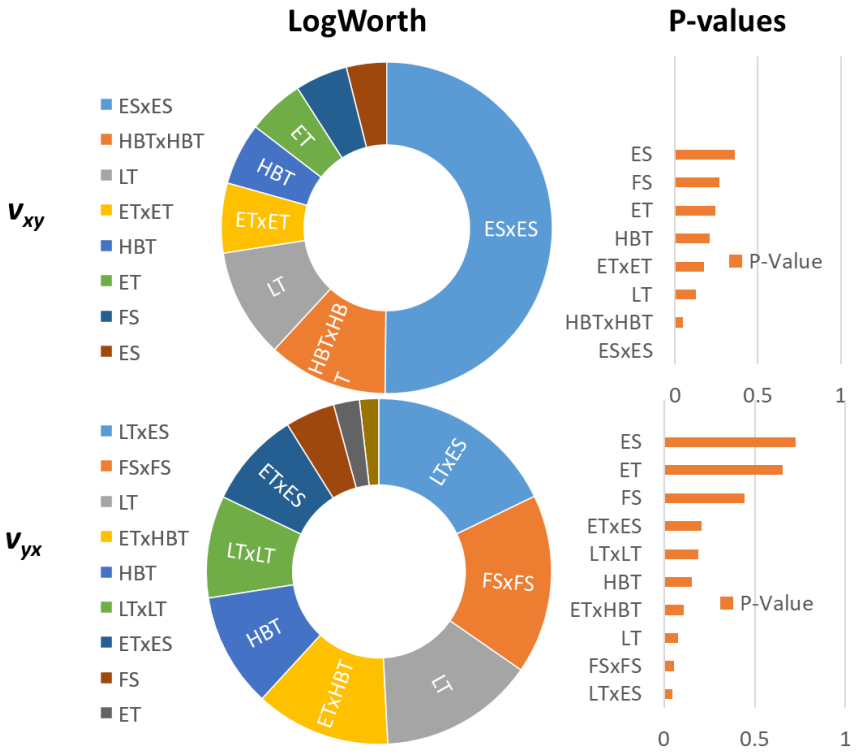

Fig. 101. Result of the statistical analyses on Poisson's ratios for orthotropic material properties showing the influential sources: (a) Pi diagram showing the LogWorth of the sources; and (b) Bar diagrams showing the P-Values.

The statistical analyses were generally not as robust as seen before, and the results listed in Table 54 indicates R^2 were 0.43 and 0.54 for the center and wing sections, respectively.

Table 54: Statistical analyses of the screened sources for the estimated Poisson's ratio for orthotropic assumed testing artifacts

Parameters and their interactions	Values
ν_{xy}	
R^2	0.43
R^2 Adj	0.2
Root Mean Square Error	0.107
Mean of Response	0.305
Observations (or Sum Wgts)	28
ν_{yx}	
R^2	0.54
R^2 Adj	0.28
Root Mean Square Error	0.0093
Mean of Response	0.231
Observations (or Sum Wgts)	28

Chapters 9.5.16.4 and 9.5.16.5 explains the statistical information of the analyses of these Poisson's ratios.

Looking into the collected data revealed interesting observations. The critical parameters are not similar to those seen before, and more variety of parameters seemed important.

In addition, the effect on ν_{xy} and ν_{yx} were not alike. The parameter layer thickness was still important but not in the first place. The two-way interaction of parameters such as extruder speed and extruder temperature seemed more important along with the quadratic effect of speed, heated bed temperature, and extruder speed. The various counter effects along with different order, made it difficult to draw a solid conclusion in terms of the effect of process parameters.

Figure 102 shows the predicted versus the actual Pousson's ratios. As one can expect due to the lower confidence in prediction, the confidence bands are wide. We examined the possibility of outliers and removed four rows of data associated with 12, 14, 15, and 18 of Table 9.

Removing those from the analyses improved the correlation significantly as shown in Fig. 102. In these two graphs, R^2 jumped to above 71 and 62 percent for *xy* and *yx*, respectively.

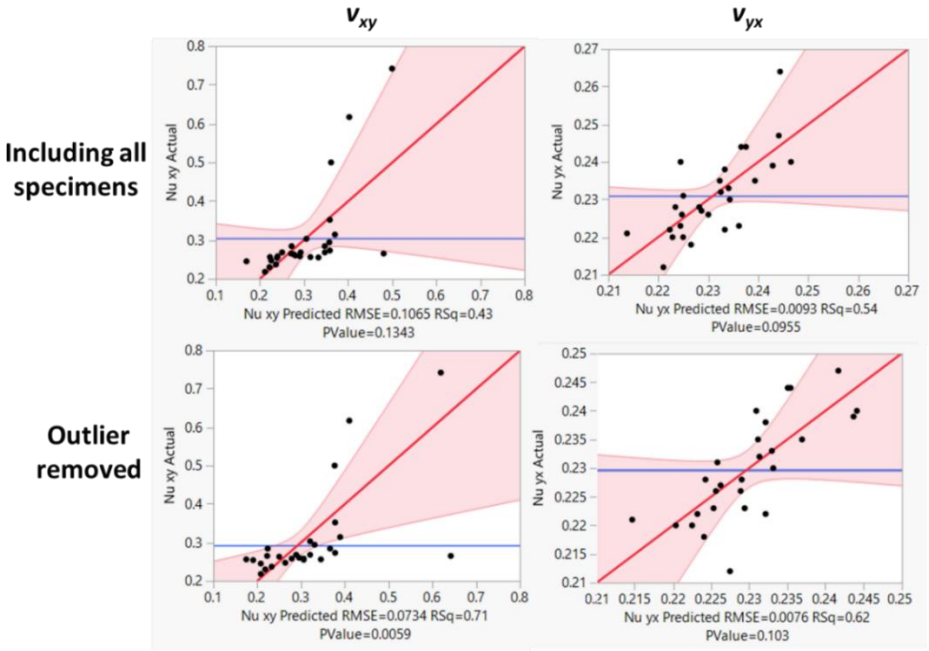

Fig. 102. The graph indicates the actual by prediction plot of the Poisson's ratios for the wing part of orthotopically assumed testing artifacts.

4.3.7 Analyses on the distortions

We performed measurements of distortion of 3D printed components similar to the one shown in Fig. 103-a, we measured the average of magnitudes of total out-of-plane deformation on the front surface of the sample in several instances. The measurement shows that after printing, the part continues to deform due to stress relaxations. Measurements illustrated in Fig. 103-b began immediately after the printing of the object, and distortions were monitored under laboratory conditions for 10 hours using Digital Fringe Projection (DFP). The deformation shows exponential behavior.

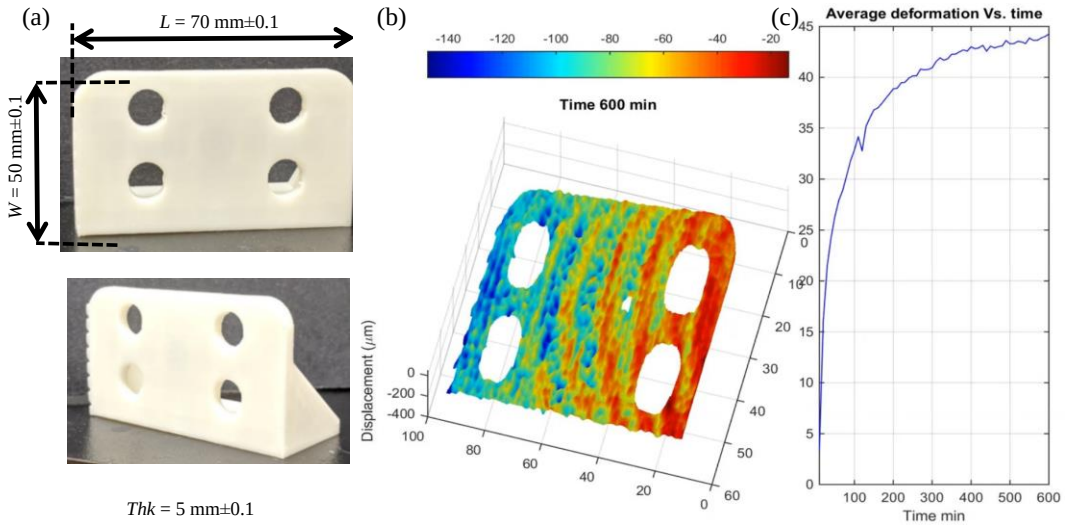

Fig. 103. Monitoring of the out-of-plane deformation on a component for 600 minutes using DFP: (a) the 3D printed component; and (b) measured out-of-plane deformation on the front surface of the sample; and (c) averaged out-of-plane displacement.

4.3.8 Impact analyses

We performed high-speed DIC to study the effect of two process parameters, printing speed and printing directions, on mechanical properties by measuring the group velocity due to impact both for axial and flexural stress waves.

4.3.8.1 Stress wave and impact study

We also conducted impact studies on the same 3D printed part used for the modal study mentioned above in chapter 4.3.6.2 using high-speed DIC (HS-DIC). Representative results presented in Fig. 104 show the corresponding transient response for impact in *x* and *y* directions, respectively. This data was evaluated using Fourier analysis to obtain the natural frequencies and can be used to assess the health and the porosity of the part nondestructively.

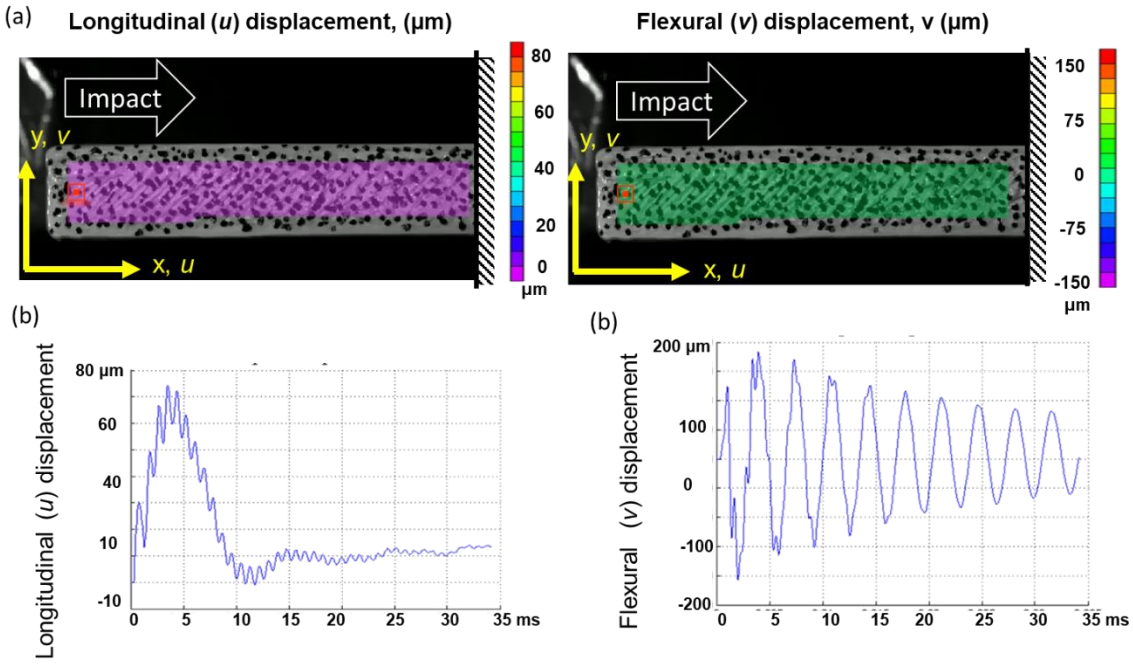

Fig. 104. Representative results of the axial impact on a 3D printed component by HS-DIC: (a) side view of the artifacts prepared for DIC measurements also showing the location of the impactor; (b) displacements in the x-direction, u, for 35 msec; and (c) displacements in the y-direction, v, for 35 msec.

4.3.8.2 Impact analyses

We estimated the elasticity modulus as listed and used Eqs. (3-26) to (3-28) to estimate the wave speeds. Table 55 shows the estimated speed for both longitudinal and flexural directions and its uncertainties. We also plot them in Fig. 105, where one can see the effect of printing speed and orientation better. The results show the same trends seen for the elasticity as expected. This method exhibits a potential for measuring the material properties, and through that, one can be able to find also other critical parameters such as damping and defects.

Table 55: Recovered moduli of elasticity of testing artifacts when fabricated at varying printing speeds and orientations. Experimentally obtained first modes of vibration were utilized. Pristine ABS filament with a reference module of elasticity of 2,030 MPa was used to compute deviations.

Printing Speed	Printing Direction	Longitudinal wave Propagation speed, m/s	Deviation from Ref.	Flexural wave propagation speed, m/s	Deviation from Ref.
	Horizontal	1512± 25	8.2%	73.3± 11.7	9.6%

Fast	Vertical	1365± 23	2.3%	65.5± 10.7	2.1%
Normal	Horizontal	1486± 25	6.4%	71.8± 11.5	7.5%
	Vertical	1304± 22	6.7%	63.7± 10.3	4.8%
Slow	Horizontal	1471± 24	5.3%	71.1± 11.4	6.4%
	Vertical	1127± 19	19.3%	55.9± 9.2	16.3%

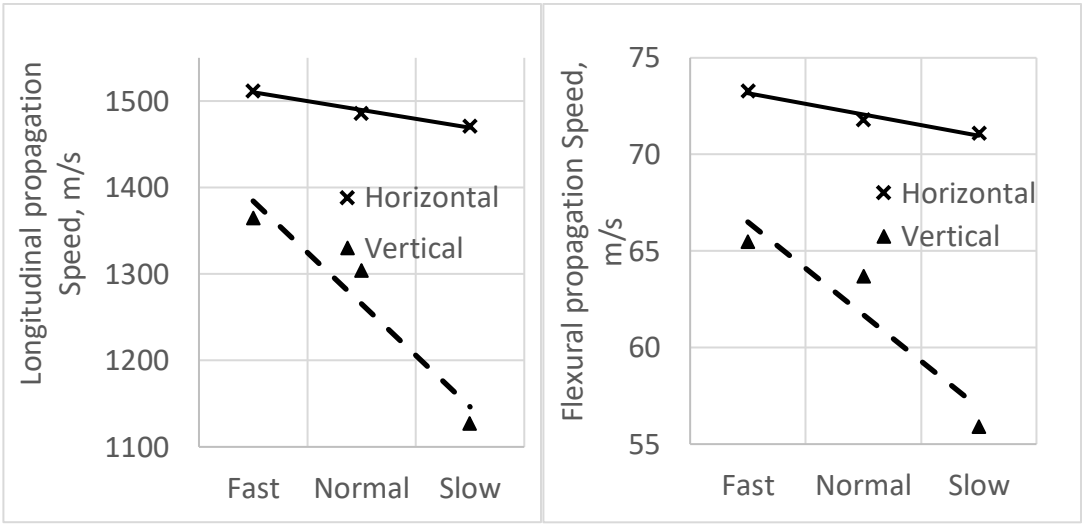

Fig. 105. Group velocities calculated for the six 3D printed cantilever beams under horizontal and vertical orientations with three speed levels speed calculated showing strong effects of speed and orientation: (a) Longitudinal; and (b) Flexural speeds.

4.3.8.3 Stress wave and impact study on a thin plate

We did an investigation on the impact test using 3D HS-DIC to illustrate how a thin plate manufactured using the FDM can respond to an impulse force applied by a pendulum at one end of the plate where the other end is fully constrained, similarly to a cantilever beam. The out-of-plane deformations due to this excitation were captured, and the representative results are shown in Fig. 106. The measurement is quantitative, and the full-field at one instance of the excitation is shown in Fig. 106-a. Figure 106-b demonstrates the transient displacement of four representative points out of all available data for a period of 48 milliseconds. The measurement

was taken using two high-speed cameras in a stereo configuration with a maximum resolution of 1 megapixel at 200,000 Hz.

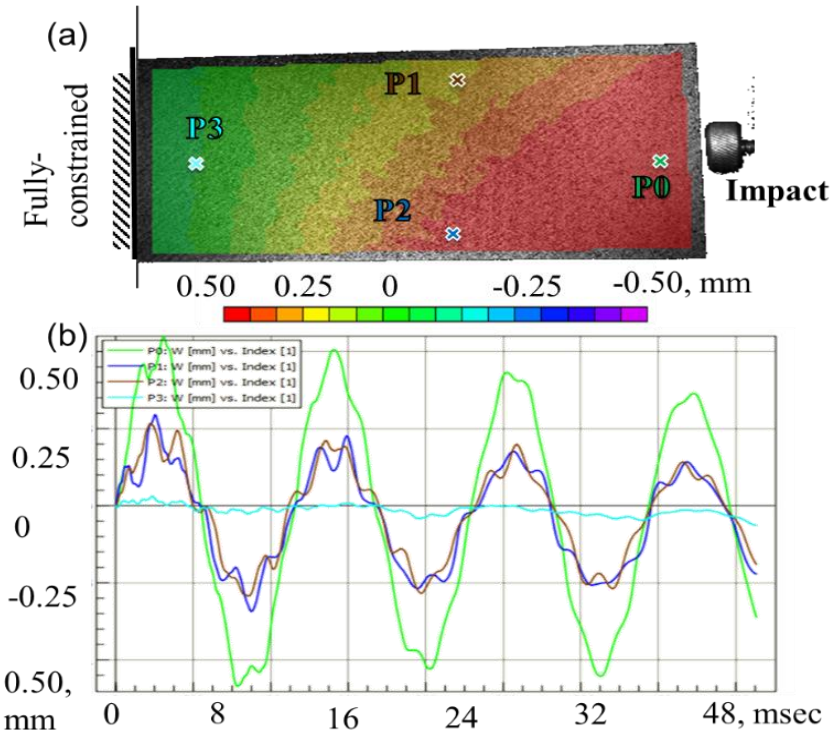

Fig. 106. Representative experimental measurements of out-of-plane deformation in a 3D printed thin plate due to an impact load: (a) one instance of the out-of-plane deformation due to impact load; (b) the transient out-of-plane deformation of four different points.

5. Discussions

In this chapter, we briefly recap our observations regarding (1) the benefit of our approach, (2) our achievement in developing a 1D model, (3) the calibration and application of the thermal imager, and (4) the process by which distortions and residual stresses are engendered in 3D components printed by FDM.

We also discuss the value of using a designed testing artifact to study 3D printed components' characteristics such as density, elastic moduli, shear moduli, and Poisson's ratios. We discussed and explained our findings and reflected on how the five selected process parameters—extruder speed, extruder temperature, fan speed, heated bed temperature, and layer thickness—contributed to changes in the mentioned characteristics.

5.1 Benefits of our approach

We developed a combined approach in our research for a better understanding of the complexity of one of the most widely used 3D printed technology worldwide, FDM.

One of the most essential variables in FDM is thermal flow, and it is crucial to strengthen bonding, change porosity, affect surface finish, form residual stresses, and cause deformations. Thermal flow also defines the bonding quality since FDM depends heavily on the wetting, healing, and diffusion in the contiguous boundaries among laid materials. Applying correct thermal boundary conditions is critical to achieving trustworthy thermal flow, whether one studies meso-scale or macro-scale. Our study indicates that one must find correct values for convection heat transfer and radiation heat transfer coefficient according to the size and environment. We concluded the coefficients calculated for a filament should not be applied to the boundaries of printed components, specifically for large components (larger than 100mm, 4 in) in medium and large FDM 3D printers. In other words, if the convection heat transfer

coefficient, h_{conv}, is estimated based on the size of the filament (usually small compared to the part), it should not be applied after the filament becomes part of the surface. These heat convection coefficients may only be accurate for a hot filament leaving an extruder or at boundaries of the surface close to the extruder and are not valid for other surfaces. We showed the effect of an inaccurate heat transfer coefficient is not a significant issue for a small printer and does not alter the final result meaningfully; nonetheless, for a large component, it is critically important.

A similar analogy can be deduced for the effect of radiation heat transfer, even though the effect of radiation loss on the small 3D printer is negligible compared to the large printer, ignoring radiation loss is not a valid assumption for large 3D printers. In some cases, the value of the radiation is as large as the value of the convection heat transfer coefficient. We found that this effect can be defined mathematically by combining the convection and radiation in a total heat transfer coefficient (THTC). THTC can be found empirically and verified numerically to improve modeling of thermal flow in 3D printed components. The mathematical model of power function was found to be practical.

Another important consideration is the effect of the velocity of the medium. FDM 3D printers usually have a cooling apparatus, such as a fan close to the extruder, to protect thermal overheating. Such an apparatus subsequently cools down the filament and proximate surfaces; however, it is not practical to assume the other surfaces experience the same effect. The assumed speed of the airflow applied to the top surface in the proximity of the extrude is not conceivable for everywhere else. Looking into this effect of medium speed quantitatively revealed that, for small to large 3D printers (as specified in Table 3), h_{conv} can change from 18 to

140 and 3 to 19 W/m^2K for the speed of 0.3 and 1.7 *m/s*, respectively. These considerations should be noted when a numerical model is set up.

We showed a combined numerical-experimental investigation using a thermal imager that could be used for verifying boundary conditions, which latter can be formulated in terms of mathematical functions. These functions can be effortlessly defined for the system-specific numerical model and help to improve the computational solution as we achieved in our combined numerical-experimental approach.

On top of these, a simple numerical model also can provide significant and useful information for a complex 3D geometry. When the interest is a prediction of properties—for example, density and bonding quality, which depend on thermal flow—a simplified model can provide invaluable information. In our study, we developed a 1D model and predicted the thermal flow and measured some indicators such as bonding performance and bonding potential and performed a simplified density measurement on cubes to estimate the bonding quality and predict the density. These simplified thermo-mechanical models, which consider the corrected boundary conditions on the surface, led to an estimator that can forecast the temperature distribution with an average error of less than 10%.

Other critical information to consider is the changes of conductivity within a part as the bonding evolves. We showed that conductivity was strongly geometry and contact dependent, and layer thickness is the most critical parameter to define its value. For example, the conductivity for H/D ratio of 1.0 and W/D ratio of 1.0 changed from 40 to 100% and 65 to 100% of the nominal conductivity as the bonding quality varies from 5% in touch bead to fully solid layer in x and y directions, respectively.

We corrected the thermal resistance between the polymer and heated bed using the data that was reported experimentally. This correction improved the heat transfer prediction and the thermal flow inside 3D printed components. When we included the thickness of the raft layer, the thermal resistance was corrected more precisely to enable improved prediction of the temperature on the contact point and inside the part.

We also concluded that the corresponding heat transfer coefficient had to be commensurate to the size and dimensions of the part and 3D printers. Under forced convection on a cylindrical part with airflow of 1.7 m/s, and for a small 3D printer part with the nominal diameter of 5.5 mm, a calculated value for the heat transfer coefficient is 58 W/m^2K. In contrast, under the same convection but for a large 3D printer surface with a diameter of 500 mm, the heat transfer coefficient is about 8 W/m^2K, which is about 7 times smaller. In this case, the Biot number for ABS component changes from 0.47 to 5.88, which indicates important changes in the physics of thermal flow in the components and shows how internal resistance can significantly overcome the surface resistance. This phenomenon causes heat accumulation inside the body of large components. It also can be interpreted similarly for the extruded filament and supports the supposition that a larger nozzle can improve the bonding between layers because the larger extruded layer tends to lose heat slowly, leading to improved consolidation and higher bonding potential. The ameliorating effect of the larger nozzle on bonding can be construed by rises in Biot number from 0.14 to 0.6 for small extruder diameter of 0.4 and 10 mm, with the heat coefficient of 230 and 42 W/m^2K., respectively.

5.1.1 The simplified 1D numerical model

We developed two distinctive models based on a similar 1D concept to study the filament and slender 3D printed parts. The study for the filament has been developed by others [38, 69,

109]. The size and the conductivity of the filament allow the lumped capacity model to be appropriate for the application. Although the lumped capacity model delivers reliable results for small scales and small diameter filament, this model is not acceptable for large conditions of diameter above 5 mm. However, our analyses show the lumped capacity leads to a conservative model that still can provide beneficial and meaningful information in the filament level for the progress of bonding and temperature distribution in 3D printed components. Through these analyses, we also developed a non-dimensionalized model to look into the effect of density, diameter, specific heat capacity, extruder speed, and convection coefficient. We concluded that the extruder speed itself does not play a role in the cooling time of the recently deposited filament, geometry and environment are more significant; specifically, the diameter of the extruder, the dimension of the deposited filament, enveloped temperature, and coefficient of heat convection. This observation also corroborated and was manifested in our later experimental study, where elastic moduli and bonding quality were weakly affected by speed, compared to other sources such as layer thickness and extruder temperature. A recent study [323] shows that the extruder speed can be critical because of the side effect of the radiation emitted from the extruder. We also concluded that the extruder speed's two-way interaction with extruder temperature and layer thickness is important. In other words, influences of speed apply through the feed rate and energy deposition rate which are compound effects of extruder velocity with other process parameters.

The same development for slender specimens also revealed the potential of a lumped capacity approximation for estimating the bonding quality and the combined radiation-convection heat transfer. Applying them helped us to investigate the THTC and present a mathematical function defining the total heat loss on the boundaries. Besides, this

approximation was found helpful for small objects (diameter or edge of 3 to 11 mm), which may not satisfy the lumped capacity approximation to verify the calibrated IR camera.

5.2 The benefits of thermal imager

Different sensors can be used for thermal measurement, but the IR camera is one of the most convenient and widely used monitoring sensors in 3D printing[145]. We worked on improving the measurement capability of the IR imager by performing a practical procedure to measure the emissivity of ABS. The polymer, in general, showed a descending emissivity trend in higher temperature such that the emissivity reduced from 0.92 to 0.84 for white ABS in temperature as high as 200^{o}C. Data were collected and analyzed to define the relation between temperature and emissivity mathematically.

Correct emissivity is crucial for accurate temperature measurement; thus, the measured value incorporated *in-situ* measurements using Matlab with IR camera. In this process, the internal look-up table was bypassed, and measured radiosity was used iteratively to read the temperature accurately. The process revealed the corrected value in higher temperature could improve the temperature readout by up to 15% in temperature as high as 240^{o}C. Although in lower temperatures, the improvement is not significant, it should not be ignored because the performance of the bonding heavily depends on how long adjacent layers are held above glass transient temperature, which happens in higher temperatures. This correction helps to calibrate IR cameras and other devices relying on correct emissivities, such as a pyrometer, to deliver more accurate measurements. Eventually, having reliable monitoring sensors leads to high quality polymeric functional components.

In the development of large 3D printers such as BAAM, where the deformation and bonding become more important for producing a high-quality product, incorporation of the IR camera

promises improvement and having a corrected and reliable measurement of temperature is an indispensable part of this future development.

5.3 Understand the physics behind distortion and residual stresses in FDM

The distortions and residual stresses are the accumulative effect of transient interactions between part material properties (i.e., CTE, elastic modulus, yield stresses, and thermal conductivity) with process and printing parameters (i.e., thicknesses, laser power, enveloped temperatures and part geometry, scanning strategy, and even part position on the build plate) [37, 106, 179, 242, 325]. During printing, after removal from the platform or even in storage, the part can undergo significant distortions and shape change [34]. This is due to the presence of residual stresses and leads to inaccuracy in final dimensions and failure in functionality. Controlling the printing parameters helps to reduce the residual stresses and distortions in 3D printed components [326-328].

In FDM, the deposited material is hotter than the surrounding material, and the hot-end heats the area that it hovers above; therefore, this local heating causes thermal expansion and generates compressive stresses around the active area. However, the material has a low elasticity at a higher temperature. Thus the magnitude of stresses due to the newly deposited material is negligible. When the hot-end passes, the cooling takes place rapidly, and the material contracts and generates local stresses in the interfaces between filaments. These changes create thermal stresses in the form of tensile and compressive stress for those areas going through shrinkages and expansion, respectively.

On the next layer, when these areas are hit again by the hot-end, temperature increases, the material softens, and stress relaxation can occur. These complex and cyclic phenomena continue

and form the residual stresses and deformations in different locations of the part as the manufacturing proceeds.

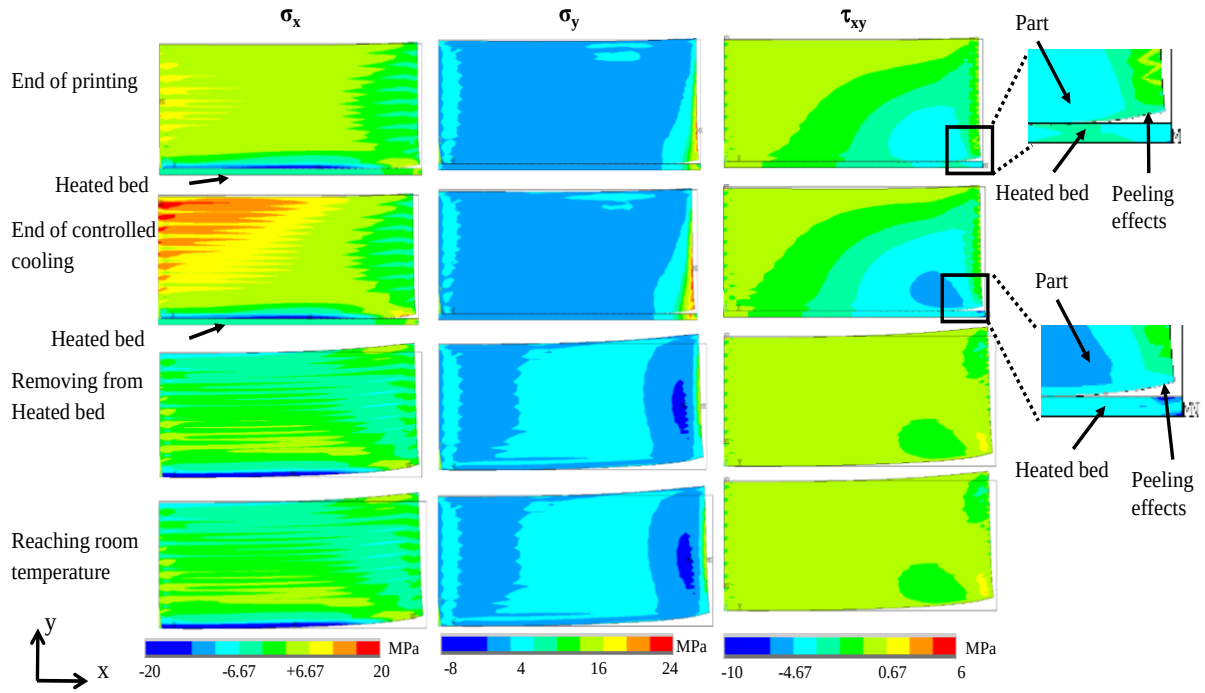

Fig. 107. Computationally predicted contour plots of three principal residual stresses, σ_x, σ_y *and* τ_{xy} in four critical instances, including end of printing, end of controlled cooling attached to the heated bed, removal from the heated-bed, and after reaching room temperature. Simulations can be used to predict peeling of the part from the heated bed.

Furthermore, the central areas of a dense component, i.e., the solid part with the highest infill, lose heat at a lower rate than the boundaries. Thus, in cases of insufficient heat transfer capacity, incorrect cooling mechanism, or low thermal conductivity as in polymers, the central part can remain hotter than the periphery in the course of fabrication. In this sense, when the periphery solidifies, the center still contracts. In other words, the center part wants to become even smaller when the outer section of the part is already solidified. Therefore, the internal section of a part may end up having tensile stresses with boundaries going through compressive stress, as shown in Fig. 107.

The boundary conditions and local strength react with these evolving stresses and cause local warpages or distortions in some critical locations. In the course of manufacturing, the part is welded to a build plate, glued to a platform, or constrained by means of vacuum or other fixtures. As soon as the part is removed, its boundary conditions change, and significant distortion and warpage occur while it reaches a new equilibrium condition. A numerical simulation that predicts the occurrence of a similar event is shown in Fig. 107, where the noticeable deformation was predicted between the second and third row of the set of images showing stress contours due to the removal of the heated bed in the model.

The directional deposition in FDM 3D printers that follows tool paths also considerably affects the creation of distortions and residual stresses. This directional dependency causes stresses to develop along the deposition direction, and the nature of the FDM cannot avoid this occurrence. A filament in this sense acts similar to a stretched spring (i.e., linear spring being preloaded with its length more than its original length) that exerts compressive forces to the surrounding materials along the direction of the deposition when it cools down. In fact, the stresses can be categorized into three main components: longitudinal along the deposition direction, transverse perpendicular to the deposition direction, and normal in the direction of the component thickness. It is expected that the longitudinal stresses are dominant and the normal stresses are the least essential components; however, as explained above the process is complicated, and the development of the welding, necking, diffusion, and polymer entanglement make it even more perplexing to anticipate stresses without physics-based modeling and experimental verification.

Moreover, if the stresses in any location, both compressive or tensile, reach yield stresses, plastic deformation takes place. This process is more probable with material with significant

coefficients of thermal expansion or low yield stress as in polymeric materials. Ignoring these plastic deformations lead to obtaining unrealistic stresses above the yield point, as seen here in reference [106]. However, a satisfactory simulation requires considering the plasticity to achieve accurate stress distributions.

To understand the physics and accurately predict residual stresses and distortions, it is critically important to estimate the thermal flow reliably, apply the material properties correctly, and consider the boundary constraints appositely. Failure to imitate reality in FDM processes can lead to inaccurate simulations and incorrect results.

5.4 Design of testing artifact and DoE

We developed a simplified but efficient testing artifact based on the concept of modal and impact analyses to explore the relationships between process parameters and mechanical characteristics of the 3D printed components. In FDM, it is critical to know how process parameters may affect density, cause distortions, and improve bonding in inter- and intra-layers.

The modal analyses served well to estimate the isotropic and orthotropic material properties, although for orthotropic material, the center section of the testing artifact resembling a beam was not adequate; the plate section of the artifact functioned to estimate material properties. The special design of the testing artifact lets a user find the isotropic material properties and estimate the orthotropic more precisely.

The combined folded beam-plate design not only is useful for modal analyses but also for measuring the residual stresses and distortion. The structure of the testing artifact is simple to be measured using either practical tools like a caliper or non-invasive optical sensors such as light modulators. Finding the curvature of the 3D printed specimen leads to an estimation of the average of the residual stresses inside the beam section.

The modal analyses can be performed either by a full-field-of-view non-invasive optical sensor or other similar approaches, such as acoustic or impact measurement, because the process is merely dependent on the values of the natural frequencies. For more sophisticated measurement to precisely evaluate the mechanical properties, it is beneficial to employ the full-field-of-view optical tools to quantity the mode shape and use the theory explained here [329, 330] to find the anisotropic material properties, but for the FDM machine, where the material properties displayed orthotropic attributes, our method found to be more relevant and feasible.

5.5 Effect of process parameters on 3D printed characteristics

We selected five different process parameters to explore the interaction among them and mechanical properties such as Young's modulus, shear modulus, and Poisson's ratios. We estimated not only the isotropic but also orthotropic material properties to extend the application of our method to the nature of 3D printed components that exhibit strongly direction-dependent material properties. It is crucial to be able to efficiently and effectively find and define the interrelationships and use them for printing optimized and customized components.

We showed it is possible to find the interrelationship through an easy-to-apply procedure and printing only a few specimens, as few as 28 samples. Furthermore, we demonstrated the methods were reliable within error as much as 30% for the mechanical properties.

5.5.1 Density

Density is important because it defines porosity, quality of bonding, and compactness, and also affects natural frequencies. In the process of material deposition similar to FDM, it is possible to estimate the density theoretically, as we explained in Chapter 4.2.4. Since the shape and dimension of the extruded filament are known, we approximate the spaces within the beads and introduce a way to track their changes. This approximation allowed us to reveal the

influences of selected process parameters on characteristics such as density, bonding quality, and mechanical properties. We estimated the theoretical density associated with zero bonding cases and used the difference between measured density and theoretical density to estimate how bonding and void spaces changed under different printing settings.

We analyzed five different process parameters: extruder speed, extruder temperature, fan speed, heated bed temperature, and layer thickness. We found that layer thickness is the most significant parameter among the studied ones. We showed that with the mentioned five variables and their quadratic and two-way interactions (including extruder temperature-later thickness, layer thickness-fan speed, extruder temperature-extruder speed, bed temperature-fan speed, and bed temperature-extruder speed), it was possible to estimate the density with the correlation coefficient of 0.92 with maximum ±5% percent error.

We also learned that it is better to look into the density difference instead of density itself in 3D printed parts by FDM. Therefore, we reached a better correlation with R^2 of 0.98 showing high confidence and error of less than ±3%. This approach can be used for the design of functionally graded materials and pave the ground for the customization of the FDM for manufacturing functional and final products.

We extended the study to mechanical properties and learned that, although the void space might not directly affect the bonding, it could be strong evidence of the quality of bonding between layers when it is combined with the other parameters, such as bonding performance and bonding potential.

We found the layer thickness is one of the most influential parameters for the density difference, with extruder speed and extruder temperature-layer thickness being the second and third important parameters. The effect of layer thickness is two-fold: while a higher layer

thickness causes lower density, it also can lead to better bonding. The extruder temperature, bed temperature, and fan speed were found to be less important in density and density difference.

We also applied a lumped capacity model to slender cuboids to investigate the effect of extruder speed, extruder temperature, and specimen sizes. We did it intentionally because literature suggested extruder temperature and extruder speed were two essential parameters [82, 94, 186, 285, 302, 308, 310, 311], but in our analyses, they were overshadowed by layer thickness. We would be interested to know what would more significantly affect the density and bonding quality beyond layer thickness, and since the significance of layer thickness might overshadow other parameters, we excluded it from analyses and only focused on the three mentioned parameters and their interactions. We found that extruder speed and specimen size are the most important parameters, followed by the quadratic effect of size and extruder temperature-extruder speed. One can perceive this observation by understanding the physics behind the bonding and 3D printing. The effect of size was crucial but at the same time quadratic. This is mostly because of the counter-effect of extruder size and surface dimension due to the thermal effect of the extruder radiation and specimen surface. This effect has been reported here [106, 151, 323] and also was seen in our experimental measurement of the temperature of the top layer. Aside from that, extruder speed and extruder speed-extruder temperature were the most important parameters that pointed out to the thermal flow and energy deposition.

5.5.2 Mechanical properties

Mechanical properties were observed to be more complex than density. The complexity of the bonding, anisotropic nature of the AM component, and the effect of porosity caused intricacy

in observing a strong correlation between selected process parameters and the mechanical properties such as Young's modulus, shear modulus, and Poisson's ratios.

We assumed both isotropic and orthotropic material properties for the testing artifact and accordingly investigated their sensitivity to geometrical and structural properties. We observed that length and thickness are the most effective properties to shift natural frequencies. Density and moduli came after length and thickness. The width of the beam or wing appeared important for torsion modes. This pattern was similarly observed for the orthotropic material as well, but E_2 was found to be important in torsion modes of the wing part as well.

Both beam and wing parts of the testing artifact showed similar trends of the effect of the mentioned parameters for isotropic material. However, for orthotropic material, we observed more interconnected relationships among natural frequencies and mechanical properties such as E_1, E_2, and G_{12} on the wing part compared to the beam part, which allowed us to investigate the orthotropic material properties.

Our method was based on the measurement of natural frequencies and inverse analyses to find the mechanical properties. When the geometry of the object is known, its natural frequencies are only a function of mechanical properties. We observed the Poisson's ratio affected the eigenvalues for some modes and, through the finite element analyses over the many obtained natural frequencies, defined its relationship mathematically.

We also noticed the beam part eigenvalues did not change strongly with Poisson's ratio compared to the wing part, and eigenvalues of the torsion related modes were more pronouncedly altered as the Poisson's ratio changed. We tested the feasibility of two methods *E/G* and *E/v* and concluded the *E/v* methods could work better in estimating the mechanical properties and providing consistent results.

We demonstrated Poisson's ratio did not affect the center part natural frequencies and directly estimated Young's and shear modulus based on the natural frequencies. This estimation also sets the initial guess in the iterative solution for orthotropic material properties to accelerate the process.

We also observed that a polynomial of degree two was sufficient for mathematically defining the effect of Poisson's ratio on eigenvalues and reported the found functions for any other similar problems. We realized that eigenvalue is a function of geometry and Poisson's ratio, indicating the potential of the extension of our method to other AM technology for the investigation of the mechanical properties of 3D printed components as well as machine performance non-destructively.

We also did similar analyses for the orthotropic material and were able to improve the accuracy of inversely estimating mechanical properties by measuring natural frequencies. We performed experimental investigations to provide a better understanding of the effect of the selected parameters on the mechanical properties using the developed DoE method. We printed artifacts and tested them, as explained in the chapter above, and then analyzed the data to reveal the potential relationships among properties and process parameters. The efficacy of these analyses was not seen to be as robust as those for density, but the correlation values between 0.6 to 0.78 were strong enough to gain knowledge on the complexity of interrelationships.

ANOVA analyses on the five selected process parameters and their quadratic and two-way interactions indicated that layer thickness was still the dominant process parameter and that extruder temperature and two-way effect of extruder temperature with extruder speed and layer thickness were among the top influential parameters. The notable conclusion is the extruder speed was found to be at the end of the list of important parameters; although this result was

unexpected, it fulfilled the conclusion drawn from thermal 1D analytical analyses (as described in chapter 4.2.1.1).

Another important finding was the heated bed temperature affected the beam and wing parts differently. Heated bed temperature (HBD) was found influential for the wing section compared to the beam section, an indicator of the sensitivity of the wing section to this parameter. The design of the testing artifact causes a distance between the beam and the heated bed, which can act as a barrier to prevent the effect of the heated bed being projected to the beam section, and consequently, the observation can be expected.

The estimated values for the moduli of elasticity were found within the anticipated range for the ABS polymers, which also corroborated with our tensile test and analytical estimation based on laminated theory. We found the average error of Young's moduli in x and y direction of 6% and 17%. The correlation measured for Poisson's ratio was disappointing; however, the trends showed a similarity between elastic moduli and Poisson's ratios.

Looking into the effect of process parameters on the E_x and E_y also reported the effect of heated bed for in-plane bonding (inter-layer) while the effect of extruder temperature and extruder speed is more important for the out-of-plane bonding (intra-layers).

5.6 Summary of contributions and innovations

We expatiated in the above chapters the significances and benefits of our approach in different areas, and here we summarized them:

- the boundary conditions for the different cases are evaluated and defined mathematically to improve the numerical models and reduce computational costs,

- the developed 1D and 2D numerical simulations (both thermal and thermo-mechanical) are capable of predicting the bonding quality, residual stresses, and distortions,
- applying the proposed corrections helps to advance computational simulations and examine the relationship between process parameters and bonding quality, mechanical properties, residual stresses, and distortions,
- the designed testing artifacts can be employed to estimate physical, and geometrical characteristics, as well as both isotropic and orthotropic mechanical properties of 3D, printed components by FDM,
- the designed testing artifact with the specified shape and geometry can directly help lay and professional users to study density, contact quality, strength, and elastic moduli,
- the FEA in tandem with designed testing artifact can carry on targeted analyses toward the investigation of the complexity of polymeric based 3D printers,
- using DoE helps to methodically reduce the iterations and quantitatively defines the relationships between process parameters and the mechanical, physical, and geometrical characteristics,
- this method can aim process optimization and property customization through the incorporation of the found mathematical functions,
- a combined numerical-computational benefiting from multi-physics computational models and optical full-field methods help to understand the complexity of FDM better,

- the developed method allows us to gather and analyze a large amount of data to further understand AM processes with the help of artificial intelligence (AI).

6. Conclusion and future work

6.1 The benefits of our approach

We presented our efforts on the development of computational-experimental methods to investigate the effects of process parameters in 3D printing by FDM and their relationships with components' performance and mechanical properties. Computational simulations estimate the evolution of distortions and residual stresses in components printed by FDM during and after fabrication. A few boundary conditions and settings are assumed to be tunable and adjustable in the simulations according to feedback from experimental investigations. Optical methodologies were employed for modal and impact analysis and can be extended to distortions analyses of the 3D printed components with unique designs to estimate structural properties and provide feedback for simulations.

Because the phenomena are sensitive to accurate convection and radiation parameters, we propose an approach to defining these parameters in which computational and experimental methods are combined with the hypothesis that the parameters vary following an exponential function. The function is determined through the investigation of 1D models that satisfy lumped conditions. Correlations between 1D and 2D computational and experimental results indicate the validity of the approach, although further investigations are required to verify it for 3D models.

Using the modal analysis, the preliminary study on the build parameters indicates the significant effect of layer thickness, printing speed, and orientation on mechanical properties. The dynamic analysis and impact investigation also illustrate the potential of 3D DIC for further characterization of structural properties such as Poisson's ratio. Also, the preliminary results show the ability of NDT to find defects and abnormalities in structure.

6.2 Summary of findings

An infrared imager is a powerful tool in providing a quantitative metric for the thermal flow and temperature distribution; however, the calibration of the camera and knowing emissivity is crucial to correct readout. We developed a practical procedure to provide enough data for camera calibration and measurement of the emissivity and demonstrated its effectiveness in improving the temperature accuracy where it is required, especially at high temperatures. The emissivity for the polymeric material like ABS showed a descending trend regarding temperature and slight dependency on color. However, the dependency on color was not found to affect the quality of the measurement noticeably. The predicted polynomial expressed dependency of emissivity to temperature can be incorporated in *in-situ* thermal measurement to account for the correction of temperature in an iterative manner. We experienced about 15% percent difference in temperature at 240^{o}C.

A simplified 1D model accounting for the conductivity, contact resistance, and corrected heat transfer boundary condition can be used for estimation of the quality of the bonding. The approach is not as powerful as a 3D model. We also found that 3D modeling is crucial for the early-stage development of the bonding. Thus our recommendation would be to model the current layer 3D for one case then extrapolate the effect through a 1D model to the other layers to be able to predict the quality and potential of the bonding between layers. The total heat transfer coefficient was suggested for ABS polymer and found useful for the 1D and 2D numerical models. In addition, we found the size both for the extruder and part is critical in the magnitude of the thermal loss from the boundary and that the general assumption of the coefficient of heat transfer, about 48 to 82 W/m^2K [13, 69, 87, 106, 107, 109], is not reliable. Knowing that the heat transfer coefficient changes with medium flow speed, we suggested higher values only be used for the current layer where the deposition takes place, and other corrected

values to be used for the boundaries farther from the current layer. We suggested different polynomials for different sizes and conditions to help researchers approximately estimate the heat transfer coefficient and incorporate them seamlessly in their numerical model. We also found that ignoring radiation is not a solid assumption for many cases and can be applied only for extruder size ranging from 0.2 to 1.0, mm; effect of radiation ought to be reflected for larger sizes.

A developed 1D model for the filament suggested the printing speed is not critical compared to the environment and extruder temperature. Although this conclusion was not confidently corroborated with experimental observations, we found printing speed not significant in affecting the moduli of elasticity compared to other parameters and their combinations.

Experimental tools for studying the complexity of 3D printing can be optimized using DoE. We found surface response design to be reliable for defining the effect of process parameters on the moduli of elasticity and density; furthermore, we were able to introduce a polynomial for a multi-dimensional domain of five parameters to estimate properties of interest within acceptable confidence bands of the average of ±30% error.

We found that for density, it is feasible to look into the evolution of the porosity as the filament evolves from no-contact to partially contact. In this process, layer thickness was found to be the most significant parameter, and combining it with extruder speed and extruder temperature can predict destiny with an error of ±5%.

The elastic moduli found to be complex, and the effect of different parameters and their interactions can change the final condition of the 3D printed components. However, our study shows that layer thickness and extruder temperature are the most critical parameters for the moduli of elasticity.

Beyond these detailed observations and conclusion, we established a combined experimental-numerical method for finding the relationships among process parameters and mechanical properties and physical properties, which can be extended for residual stress analyses. A simplified designed testing artifact has been used for the estimation of mechanical properties and density and not only helped to estimate the isotropic but also orthotropic properties. The combined thin-thick structure of a cantilever along with the numerical estimation of the dependency of natural frequency to mechanical properties made it possible to estimate the orthotropic material properties, including Young's and shear moduli and Poisson's ratios. We used full-field-of-view optical non-destructive testing to find the natural frequency, and based on that, through an iterative procedure by correcting the Poisson's ratio, we found the mechanical properties.

A practical and easily measurable method proposed for density measurement and the applied method for relating the porosity and the shape of the filament to the density made it practically convenient in almost all FDM machines to measure the effect of process parameters on the density and potential bonding.

Our proposed methods can be adapted for other 3D printing technology and can be used along with other available methods to non-invasively estimate not only the functionality of the 3D printed component but also to find the performance of the machine and extract process map. Finding a reliable process map is a challenge in the area of functionally relatable 3D printed components, and this methodology can help to accelerate and produce the process map with fewer iterations. Thus, this simplified method not only can contribute to improving quality, predicting density, and estimating mechanical properties but saves time and energy, especially

when 3D printing is expensive, for example, 3D printing with titanium and other expensive materials.

6.3 Contribution and achievements

The combined experimental-computational methodologies benefitting from nondestructive testing by optical methodologies and computational simulations can contribute to extending our understanding beyond the current level to improve the integrity, repeatability, and consistency of 3D printing processes such as FDM. The method intends to elucidate how the process and printing parameters influence the status and functionality of the fabricated components. The results provide a workable and practical guideline for manufacturing components toward better quality with higher fidelity. The result and guidelines could be used directly by the end-user and customer, who may not be familiar with the complexity of polymer 3D printers.

The main significant contributions of this work are listed hereunder:

- the framework takes advantages of the multi-physics computational models and optical full-field methods to understand the complexity of FDM better,
- designed testing artifact can help to quantitatively investigate the relationships between process parameters and distortion, mechanical properties, and physical properties,
- FDM is a complex process, and different effects of process parameters were observed for mechanical and physical characteristics,
- the methodology enables gathering and analyses a large amount of data to further understanding of AM processes.

This study aims to pave the ground to manufacture a part with improved quality, predicted performance, and customized applications while satisfying the consistency and fidelity of final

products. The process will give confidence to industrial sectors and, more importantly, consumers to rely on 3D printed parts manufactured by FDM. This approach will promote the adoption of polymer-based 3D printing in the near future and broaden the acceptance of the system in terms of reliably manufacturing final functional products.

Manipulating this knowledge toward providing the required mechanical properties, characterization, and engineered responses will be another aspect and potential of this study that will lead to functionally graded materials, meta-materials, and customized designs.

6.4 Future work

Future work will include the development of more refined testing artifacts to elucidate the interrelationships between process parameters and part performance. Further, the applicability of specific nondestructive testing methodologies to interrogate parameters such as porosity, defect detections, and residual stresses and distortions can be explored. The model can be expanded to 3D using the improved thermal model, and the estimation will provide better visualization of distortion and residual stresses.

The following list condenses the list of the potential extension of this work in the near future:

- expand analyses to include residual stresses and distortions,
- extend the application of the developed method to other AM technologies,
- examine the achieved regression model to perform optimization and verify its effectiveness through experiments,
- use *in-situ* calibrated camera to understand bonding and controlling the thermal flow,
- apply high-speed impact analyses to test artifacts for defects identification,
- Development of data mining and application of Artificial Intelligence (AI) methods for data analyses as well as for AM process improvements.

7. Social impact of this study

The realization of the components from digital 3D files has become a common fact in our routine life at the beginning of the 21 century. These technologies are categorized under the umbrella of Additive Manufacturing as opposed to subtractive manufacturing. They are claimed to democratize and revolutionize the global parts manufacturing and logistics landscape and to push the shift toward distributed manufacturing and parts-to-demands [24]. AM merits include customization, optimization, sustainability, design freedom, flexibility, energy efficiency, and limitless creation that accelerate the emergence and adaptation of them in industries worldwide [24-26]. Additionally, this growing interest meaningfully provides the potential for a reduction in cost, energy consumption, and carbon footprint [24]. Design freedom, optimization, and the possibility to print functionally graded material give AM incredible advantages over conventional manufacturing to fabricate intricate and complex shapes that are accessible with no or least possible tooling. The product can be designed for manufacturing with less concern about their manufacturability [27]. Complexity is a trade-off in conventional manufacturing, while for AM this is not a major factor as the design paradigm shifts from "design for manufacturing" to "manufacturing for design" [331].

Estimation of the growth rate for AM technology was 27.3% over the past 26 years, and its growth rate kept increasing between 2012-2014, when it hit 33.8% [332, 333]. AM finds its application in a wide range of industries: aerospace, defense, automotive, housing, biomedicine, health, and even food supply and real states. Influential companies like GE, Ford, Toyota, Boing, Airbus, SIEMENS are a few well-known names that have already implemented AM in their design and products. The key impact of AM has been discussed in the area of the supply chain, assembly process, industrial machinery, manufacturing complex geometry, and remote

manufacturing [24, 26, 242, 332]. On the industrial floor, the company can have more independence in manufacturing products directly without the need for third parties and can constantly change and improve upon the product as rapidly as required. Reducing the number of components in manufacturing in complex parts makes it possible to reach the near-net-shape or final-shape with no or minimum post-processing, thus increasing manufacturing speed. Assembly time and processes are significantly reduced by manufacturing the integral components, and overall weight decreases with fewer joints, fasteners, and components [242], while the complexity of assembly lines is reduced. The process of product development (time-to-market) and testing for a new product that is based on the trial-and-error procedures can be made dramatically more efficient as the prototyping can be done in a day or less, by reducing time spent communicating between involved design teams [242, 334]. On the other hand, third-party manufacturers and end-customers have the opportunity to work self-sufficiently, change flexibly from one design to another one, and provide a wide range of complex and different products in their industry's line [26].

Due to the impact of AM in reducing the lead time in manufacturing, its adoption in industries is increasing in the area of design development and prototyping. Also, improvement in new material and technology makes it possible to benefit from manufacturing complex parts in less quantity and provides opportunities for aerospace, defense, luxury, and automobile industries to bring more customization and flexibility to their designs. Hybrid manufacturing [332, 335, 336] to address the shortcomings of AM is a combined solution for companies that want to be hands-on in AM and are not ready, and may not be able to afford to invest in, a total change in their production line. Supply chain for raw material, distribution of the products, and efficiency in managing manufacturing in AM are new fast-growing areas of interest that related

directly to the growth and acceptance of additive manufacturing. Companies like Voodoo[337] and 3D Hubs are businesses that will grow in the near future, and USPS, Amazon, Staples, and Shapeways are starting to manufacture and deliver 3D printed parts. Special post-processing as an inevitable part of several additive manufacturing technologies may be alluring to some keen people to facilitate the processes and making it possible for additive manufacturers to turn profits. Cost-effective mass customization of complex products is another area of opportunities for AM in the near future [30]. Using new technologies and adding integrated functionality like sensors, actuators, and batteries and embedding them in the product during printing opens a new world of customization and functionalization that were not available before. At both luxury and mass production levels, wearable products customizable to specific needs and ergonomics can attract a plethora of individuals that are not satisfied with their in-hand tools. Designing products with functionally graded material (FGM) and mixing different materials is more accessible with AM as opposed to conventional manufacturing and can improve the performance of final products. Flexibility in design and printing complex shapes and structures also expand the application to the programming of the behavior of active materials [30]. This area of design, called inverse engineering, takes advantage of AM merits to program and print the object that serves to predict and manipulate the response of it to excitation. One example of this inverse design is manufacturing prostheses that act similarly to the tissues and bones of replaced limbs.

7.1 Our contributions

AM industries need to achieve a reliable level of certainties and consistencies in the prediction and improvement of mechanical, physical, and microstructural properties of the AM components to convince costumers and clients to rely on their technologies. Such a quantum leap is not far-reaching if our understanding of the scale and direction (positive, negative,

neutral) of the effects of build parameters on AM components is laid effectively. This dissertation takes a small step toward a better understanding of FDM by studying density, contact quality, and moduli of elasticity through introducing a combined computational-experimental study using testing artifacts. We hope our efforts can contribute to the development needed to perform optimization for FDM and achieve a reliable testing procedure for the evaluation of both 3D printed components and 3D printers.

8. References and bibliography

[1] CI, C. I., 2018, "Big Area Additive Manufacturing," HTML, https://www.e-ci.com/baam/.
[2] STRATASYS, 2018, "Additive Manufacturing and Fused Deposition Modeling (FDM)," http://www.stratasys.com/.
[3] THERMWOOD, 2018, "Large Scale Additive Manufacturing (LSAM)," http://thermwood.com/lsam/lsam_main.htm.
[4] MARKFORGED, 2018, "Industrial 3D printing," https://markforged.com/.
[5] STRANGPERESSE, 2018, "Premier Extruders and Accessories for Additive Manufacturing," http://strangpresse.com/.
[6] LEMANTEK, 2016, "FACTORY 2.0 PRODUCTION SYSTEM," https://www.lemantek.com/en/fff/factory.
[7] Migler, K. D., and Ricker, R. E., 2016, "Measurement Science Roadmap for Polymer-Based Additive Manufacturing," Advanced Manufacturing Series (NIST AMS)-100-5.
[8] Sun, Q., Rizvi, G., Bellehumeur, C., and Gu, P., 2008, "Effect of processing conditions on the bonding quality of FDM polymer filaments," Rapid Prototyping Journal, 14(2), pp. 72-80.
[9] Khorram Niaki, M., and Nonino, F., 2017, "Additive manufacturing management: a review and future research agenda," International Journal of Production Research, 55(5), pp. 1419-1439.
[10] Coogan, T. J., and David Owen Kazmer, 2017, "Bond and part strength in fused deposition modeling," Rapid Prototyping Journal, 23(2), pp. 414-422.
[11] Chohan, J. S., Singh, R., Boparai, K. S., Penna, R., and Fraternali, F., 2017, "Dimensional accuracy analysis of coupled fused deposition modeling and vapour smoothing operations for biomedical applications," Composites Part B: Engineering, 117, pp. 138-149.
[12] Zhang, Y., and Chou, K., 2008, "A parametric study of part distortions in fused deposition modelling using three-dimensional finite element analysis," Proceedings of the Institution of Mechanical Engineers, Part B: Journal of Engineering Manufacture, 222(8), pp. 959-968.
[13] Zhang, Y., and Chou, Y., 2006, "Three-dimensional finite element analysis simulations of the fused deposition modelling process," Proceedings of the Institution of Mechanical Engineers, Part B: Journal of Engineering Manufacture, 220(10), pp. 1663-1671.
[14] Favaloro, A., B. Brenken, E. Barocio, N. M. DeNardo and R. B. Pipes, 2016, "Microstructural Modeling of Fiber Filled Polymers in Fused Filament Fabrication," SAMPE conferenceLong Beach, CA.
[15] Brenken, B., A. Favaloro, E. Barocio, N. M. DeNardo and R. B. Pipes, 2017, "Development of a Model to Predict Temperature History and Crystallization Behavior of 3D Printed Parts Made From Fiber-Reinforced Thermoplastic Polymers," SAMPE conferenceLong Beach, CA.
[16] Favaloro, A. J., Brenken, B., Barocio, E., and Pipes, R. B., "Simulation of Polymeric Composites Additive Manufacturing using Abaqus," Proc. Sience in the Age of Experience conference, pp. 15-18.
[17] Pooladvand, K., and Furlong, C., 2015, "Digital Holography and Digital Image Correlation in additive manufacturing," ISEM 2015, 5th International Symposium on Experimental Mechanics, Guanajuato, Mexico.
[18] Digilov, R. M., and Abramovich, H., 2013, "Flexural vibration test of a beam elastically restrained at one end: a new approach for Young's modulus determination," Advances in Materials Science and Engineering, 2013.
[19] Buchaillot, L., Farnault, E., Hoummady, M., and Fujita, H., 1997, "Silicon nitride thin films Young's modulus determination by an optical non destructive method," Japanese journal of applied physics, 36(6B), p. L794.
[20] Roebben, G., Bollen, B., Brebels, A., Van Humbeeck, J., and Van der Biest, O., 1997, "Impulse excitation apparatus to measure resonant frequencies, elastic moduli, and internal friction at room and high temperature," Review of scientific instruments, 68(12), pp. 4511-4515.
[21] Technologies, A. C. F. o. A. M., and Terminology, A. C. F. o. A. M. T. S. F. o., 2012, Standard Terminology for Additive Manufacturing Technologies, ASTM International.
[22] Hannibal, M., and Knight, G., 2018, "Additive manufacturing and the global factory: Disruptive technologies and the location of international business," International Business Review, 27(6), pp. 1116-1127.
[23] Lipson, H., and Kurman, M., 2013, Fabricated: The new world of 3D printing, John Wiley & Sons.
[24] Frazier, W. E., 2014, "Metal Additive Manufacturing: A Review," Journal of Materials Engineering and Performance, 23(6), pp. 1917-1928.
[25] Gibson, I., Rosen, D. W., and Stucker, B., 2010, Additive manufacturing technologies, Springer.
[26] Gao, W., Zhang, Y., Ramanujan, D., Ramani, K., Chen, Y., Williams, C. B., Wang, C. C., Shin, Y. C., Zhang, S., and Zavattieri, P. D., 2015, "The status, challenges, and future of additive manufacturing in engineering," Computer-Aided Design, 69, pp. 65-89.

[27] Mansour, S., and Hague, R., 2003, "Impact of rapid manufacturing on design for manufacture for injection moulding," Proceedings of the Institution of Mechanical Engineers, Part B: Journal of Engineering Manufacture, 217(4), pp. 453-461.
[28] Chu, W.-S., Kim, M.-S., Jang, K.-H., Song, J.-H., Rodrigue, H., Chun, D.-M., Cho, Y. T., Ko, S. H., Cho, K.-J., Cha, S. W., Min, S., Jeong, S. H., Jeong, H., Lee, C.-M., Chu, C. N., and Ahn, S.-H., 2016, "From design for manufacturing (DFM) to manufacturing for design (MFD) via hybrid manufacturing and smart factory: A review and perspective of paradigm shift," International Journal of Precision Engineering and Manufacturing-Green Technology, 3(2), pp. 209-222.
[29] Yang, S., and Zhao, Y. F., 2015, "Additive manufacturing-enabled design theory and methodology: a critical review," The International Journal of Advanced Manufacturing Technology, 80(1), pp. 327-342.
[30] Huang, Y., Leu, M. C., Mazumder, J., and Donmez, A., 2015, "Additive manufacturing: current state, future potential, gaps and needs, and recommendations," Journal of Manufacturing Science and Engineering, 137(1), p. 014001.
[31] Kim, F. H., and Moylan, S. P., 2018, "Literature Review of Metal Additive Manufacturing Defects."
[32] Taheri, H., Shoaib, M. R. B. M., Koester, L., Bigelow, T., Collins, P. C., Bond, L. J. J. I. J. o. A., and Manufacturing, S. M., 2017, "Powder-based additive manufacturing–a review of types of defects, generation mechanisms, detection, property evaluation and metrology," 1(2), p. 172.
[33] Zhang, J., Wang, X. Z., Yu, W. W., and Deng, Y. H., 2017, "Numerical investigation of the influence of process conditions on the temperature variation in fused deposition modeling," Materials & Design, 130, pp. 59-68.
[34] Pooladvand, K., and Furlong, C., 2019, "Computational and Experimental Characterization of 3D Printed Components by Fused Deposition Modeling," Mechanics of Additive and Advanced Manufacturing, Volume 8, Springer, pp. 87-95.
[35] Verma, A., Vishnoi, P., Sukhotskiy, V., and Furlani, E., 2018, "Numerical simulation of extrusion additive manufacturing: fused deposition modeling," Inform. Electron. Microsyst.: TechConnect Briefs, 2018, pp. 118-121.
[36] Talagani, M., DorMohammadi, S., Dutton, R., Godines, C., Baid, H., Abdi, F., Kunc, V., Compton, B., Simunovic, S., and Duty, C., 2015, "Numerical simulation of big area additive manufacturing (3D printing) of a full size car," SAMPE Journal, 51(4), p. 27.
[37] King, W., Anderson, A. T., Ferencz, R. M., Hodge, N. E., Kamath, C., and Khairallah, S. A., 2015, "Overview of modelling and simulation of metal powder bed fusion process at Lawrence Livermore National Laboratory," Mater Sci Tech-Lond, 31(8), pp. 957-968.
[38] Bellehumeur, C., Li, L., Sun, Q., and Gu, P., 2004, "Modeling of bond formation between polymer filaments in the fused deposition modeling process," Journal of Manufacturing Processes, 6(2), pp. 170-178.
[39] Coogan, T. J., 2015, "Fused deposition modeling (FDM) part strength and bond strength simulations based on healing models," University of Massachusetts Lowell.
[40] Gupta, N., Weber, C., and Newsome, S., 2012, "Additive Manufacturing: Status and Opportunities."
[41] Coogan, T. J., and Kazmer, D. O., 2017, "Healing simulation for bond strength prediction of FDM," Rapid Prototyping Journal, 23(3), pp. 551-561.
[42] Anitha, R., Arunachalam, S., and Radhakrishnan, P., 2001, "Critical parameters influencing the quality of prototypes in fused deposition modelling," Journal of Materials Processing Technology, 118(1), pp. 385-388.
[43] Duty, C. E., Vlastimil Kunc, Brett Compton, Brian Post, Donald Erdman, Rachel Smith, Randall Lind, Peter Lloyd, and Lonnie Love, 2017, "Structure and mechanical behavior of Big Area Additive Manufacturing (BAAM) materials," Rapid Prototyping Journal, 23(1), pp. 181-189.
[44] Standard, A., 2012, "F2792. 2012. Standard Terminology for Additive Manufacturing Technologies," ASTM F2792-10e1.
[45] Ding, J., 2012, "Thermo-mechanical analysis of wire and arc additive manufacturing process."
[46] Standardization", G. I. f., 2010, "DIN FL35 - Additive Manufacturing - (Rapid Prototyping) - Fundamentals, terms and definitions, quality parameters, supply agreements," DIN.
[47] Jacobs, P. F., 1995, Stereolithography and other RP&M technologies: from rapid prototyping to rapid tooling, Society of Manufacturing Engineers.
[48] Hull, C. W., 1986, "Apparatus for production of three-dimensional objects by stereolithography," Google Patents.
[49] LITHOZ, 2017, "ADDITIVE MANUFACTURING OF HIGH PERFORMANCE CERAMICS," http://www.lithoz.com/en/.
[50] additively.com, 2016, "Binder Jetting (BJ)," https://www.additively.com/en/learn-about/binder-jetting.
[51] Jim, K., Lee, F., Xin, J., Leung, C., Chan, H., and Chen, Y. J. M. e., 2010, "Fabrication of nano-scaled patterns on ceramic thin films and silicon substrates by soft ultraviolet nanoimprint lithography," 87(5-8), pp. 959-962.
[52] Ning, F., Cong, W., Qiu, J., Wei, J., and Wang, S., 2015, "Additive manufacturing of carbon fiber reinforced

thermoplastic composites using fused deposition modeling," Composites Part B: Engineering, 80, pp. 369-378.
[53] Francis, V., and Jain, P. K., 2016, "Experimental investigations on fused deposition modelling of polymer-layered silicate nanocomposite," Virtual and Physical Prototyping, 11(2), pp. 109-121.
[54] Too, M., Leong, K., Chua, C., Du, Z., Yang, S., Cheah, C., and Ho, S., 2002, "Investigation of 3D non-random porous structures by fused deposition modelling," The International Journal of Advanced Manufacturing Technology, 19(3), pp. 217-223.
[55] Chua, C. K., Leong, K. F., and Lim, C. S., 2010, Rapid prototyping: principles and applications, World Scientific.
[56] Ciocca, L., De Crescenzio, F., Fantini, M., and Scotti, R., 2009, "CAD/CAM and rapid prototyped scaffold construction for bone regenerative medicine and surgical transfer of virtual planning: a pilot study," Computerized Medical Imaging and Graphics, 33(1), pp. 58-62.
[57] Rosenzweig, D. H., Carelli, E., Steffen, T., Jarzem, P., and Haglund, L., 2015, "3D-printed ABS and PLA scaffolds for cartilage and nucleus pulposus tissue regeneration," International journal of molecular sciences, 16(7), pp. 15118-15135.
[58] Masood, S., and Song, W., 2004, "Development of new metal/polymer materials for rapid tooling using fused deposition modelling," Materials & design, 25(7), pp. 587-594.
[59] Nikzad, M., Masood, S., and Sbarski, I., 2011, "Thermo-mechanical properties of a highly filled polymeric composites for fused deposition modeling," Materials & Design, 32(6), pp. 3448-3456.
[60] Singh, R., and Singh, S., 2014, "Development of nylon based FDM filament for rapid tooling application," Journal of The Institution of Engineers (India): Series C, 95(2), pp. 103-108.
[61] Atzeni, E., Iuliano, L., Minetola, P., and Salmi, A., 2010, "Redesign and cost estimation of rapid manufactured plastic parts," Rapid Prototyping Journal, 16(5), pp. 308-317.
[62] Levy, G. N., Schindel, R., and Kruth, J.-P., 2003, "Rapid manufacturing and rapid tooling with layer manufacturing (LM) technologies, state of the art and future perspectives," CIRP Annals-Manufacturing Technology, 52(2), pp. 589-609.
[63] Singh, R., and Garg, H. K., 2016, "Fused Deposition Modeling – A State of Art Review and Future Applications," Reference Module in Materials Science and Materials Engineering, Elsevier.
[64] Kumar, S., and Kruth, J. P., 2010, "Composites by rapid prototyping technology," Materials & Design, 31(2), pp. 850-856.
[65] Rosochowski, A., and Matuszak, A., 2000, "Rapid tooling: the state of the art," Journal of materials processing technology, 106(1), pp. 191-198.
[66] Manufacturingguide, 2018, "Fused Deposition Modeling, FDM," https://www.manufacturingguide.com/en/fused-deposition-modeling-fdm.
[67] Rodríguez, J. F., Thomas, J. P., and Renaud, J. E., 2003, "Mechanical behavior of acrylonitrile butadiene styrene fused deposition materials modeling," Rapid Prototyping Journal, 9(4), pp. 219-230.
[68] Rodriguez, J. F., Thomas, J. P., and Renaud, J. E., 2000, "Characterization of the mesostructure of fused-deposition acrylonitrile-butadiene-styrene materials," Rapid Prototyping Journal, 6(3), pp. 175-186.
[69] Costa, S. F., Duarte, F. M., and Covas, J. A., 2017, "Estimation of filament temperature and adhesion development in fused deposition techniques," Journal of Materials Processing Technology, 245, pp. 167-179.
[70] Srivastava, M., Maheshwari, S., Kundra, T. K., Rathee, S., Yashaswi, R., and Kumar Sharma, S., 2016, "Virtual Design, Modelling and Analysis of Functionally graded materials by Fused Deposition Modeling," Materials Today: Proceedings, 3(10), pp. 3660-3665.
[71] Bellini, A., Shor, L., and Guceri, S. I., 2005, "New developments in fused deposition modeling of ceramics," Rapid Prototyping Journal, 11(4), pp. 214-220.
[72] Wu, G., A. Langrana, N., Sadanji, R., and Danforth, S., 2002, "Solid freeform fabrication of metal components using fused deposition of metals," Materials & Design, 23(1), pp. 97-105.
[73] Hattiangadi, A., and Bandyopadhyay, A., 2000, "Modeling of multiple pore ceramic materials fabricated via fused deposition process," Scripta Materialia, 42(6), pp. 581-588.
[74] Iftikhar, A., Khan, M., Alam, K., Imran Jaffery, S. H., Ali, L., Ayaz, Y., and Khan, A., 2013, "Turbine blade manufacturing through rapid tooling (RT) process and its quality inspection," Materials and Manufacturing Processes, 28(5), pp. 534-538.
[75] Gill, S. S., and Kaplas, M., 2009, "Comparative study of 3D printing technologies for rapid casting of aluminium alloy," Materials and Manufacturing Processes, 24(12), pp. 1405-1411.
[76] Wang, S., Miranda, A., and Shih, C., 2010, "A study of investment casting with plastic patterns," Materials and Manufacturing Processes, 25(12), pp. 1482-1488.
[77] Singh, S., Ramakrishna, S., and Singh, R., 2017, "Material issues in additive manufacturing: A review," Journal of Manufacturing Processes, 25(Supplement C), pp. 185-200.

[78] Alkaios, B. V., 2018, "Introduction to FDM 3D printing," https://www.3dhubs.com/knowledge-base/introduction-fdm-3d-printing.
[79] All3DP, 2018, "20 Best Large 3D Printers of Fall 2018."
[80] INDUSTRIES, B., 2018, "Fused Granular Fabrication (FGF) ".
[81] Antonio, L., Marzio, G., Gabriele, S., and Massimo, M., 2015, "The impact of process parameters on mechanical properties of parts fabricated in PLA with an open-source 3-D printer," Rapid Prototyping Journal, 21(5), pp. 604-617.
[82] Christiyan, K. G. J., Chandrasekhar, U., and Venkateswarlu, K., 2016, "A study on the influence of process parameters on the Mechanical Properties of 3D printed ABS composite," IOP Conference Series: Materials Science and Engineering, 114(1), p. 012109.
[83] Croccolo, D., De Agostinis, M., and Olmi, G., 2013, "Experimental characterization and analytical modelling of the mechanical behaviour of fused deposition processed parts made of ABS-M30," Computational Materials Science, 79, pp. 506-518.
[84] Li, H., 2018, "The effect of process parameters in fused deposition modelling on bonding degree and mechanical properties," Rapid Prototyping Journal, 24(1), pp. 80-92.
[85] Mohamed, O. A., Masood, S. H., and Bhowmik, J. L., 2016, "Optimization of fused deposition modeling process parameters for dimensional accuracy using I-optimality criterion," Measurement, 81, pp. 174-196.
[86] Motaparti, K. P., Taylor, G., Leu, M. C., Chandrashekhara, K., Castle, J., and Matlack, M., 2017, "Experimental investigation of effects of build parameters on flexural properties in fused deposition modelling parts," Virtual and Physical Prototyping, 12(3), pp. 207-220.
[87] Rodriguez, M. J., 2000, "Modeling the mechanical behavior of fused deposition acrylonitrile-butadiene-styrene polymer components."
[88] Li, L., Sun, Q., Bellehumeur, C., and Gu, P., "Composite modeling and analysis of FDM prototypes for design and fabrication of functionally graded parts," Proc. Solid Freegorm Fabrication Symp, pp. 187-194.
[89] Bellini, A., 2002, Fused deposition of ceramics: a comprehensive experimental, analytical and computational study of material behavior, fabrication process and equipment design.
[90] Xu, N., Ye, X., Wei, D., Zhong, J., Chen, Y., Xu, G., and He, D., 2014, "3D artificial bones for bone repair prepared by computed tomography-guided fused deposition modeling for bone repair," ACS applied materials & interfaces, 6(17), pp. 14952-14963.
[91] Agarwala, M., van Weeren, R., Vaidyanathan, R., Bandyopadhyay, A., Carrasquillo, G., Jamalabad, V., Langrana, N., Safari, A., Garofalini, S., and Danforth, S., "Structural ceramics by fused deposition of ceramics," Proc. Proceedings of the Solid Freeform Fabrication Symposium, The University of Texas at Austin Austin, Texas, pp. 1-8.
[92] BRENKEN, B., FAVALORO, A., BAROCIO, E., DENARDO, N., KUNC, V., and PIPES, R. B., "Fused Deposition Modeling of Fiber-Reinforced Thermoplastic Polymers: Past Progress and Future Needs," Proc. Proceedings of the American Society for Composites: Thirty-First Technical Conference.
[93] Shofner, M., Lozano, K., Rodríguez-Macías, F., and Barrera, E., 2003, "Nanofiber-reinforced polymers prepared by fused deposition modeling," Journal of applied polymer science, 89(11), pp. 3081-3090.
[94] Ning, F., Cong, W., Hu, Y., and Wang, H., 2017, "Additive manufacturing of carbon fiber-reinforced plastic composites using fused deposition modeling: Effects of process parameters on tensile properties," Journal of Composite Materials, 51(4), pp. 451-462.
[95] Jiang, D., and Smith, D. E., 2017, "Anisotropic mechanical properties of oriented carbon fiber filled polymer composites produced with fused filament fabrication," Additive Manufacturing, 18(Supplement C), pp. 84-94.
[96] Li, N., Li, Y., and Liu, S., 2016, "Rapid prototyping of continuous carbon fiber reinforced polylactic acid composites by 3D printing," Journal of Materials Processing Technology, 238(Supplement C), pp. 218-225.
[97] Tian, X., Liu, T., Yang, C., Wang, Q., and Li, D., 2016, "Interface and performance of 3D printed continuous carbon fiber reinforced PLA composites," Composites Part A: Applied Science and Manufacturing, 88(Supplement C), pp. 198-205.
[98] Quan, Z., Larimore, Z., Wu, A., Yu, J., Qin, X., Mirotznik, M., Suhr, J., Byun, J.-H., Oh, Y., and Chou, T.-W., 2016, "Microstructural design and additive manufacturing and characterization of 3D orthogonal short carbon fiber/acrylonitrile-butadiene-styrene preform and composite," Composites Science and Technology, 126, pp. 139-148.
[99] M. F. Ashby, J. F., A. Gray, 2016, "The CES EduPack Database for architecture and the built environment," Granta Design.
[100] Mark, J. E., 2007, Physical Properties of Polymers Handbook, Springer New York, New York, NY.
[101] Wypych, G., 2016, Handbook of polymers, ChemTec Publishing, Toronto.
[102] WIKIPEDIA, 2018, "The Free Encycopedia," https://en.wikipedia.org.
[103] Bansal, R., 2011, "Improving dimensional accuracy of fused deposition modelling (FDM) parts using response

surface methodology."
[104] Ali, F., Chowdary, B. V., and Maharaj, J., "Influence of some process parameters on build time, material consumption, and surface roughness of FDM processed parts: inferences based on the Taguchi design of experiments," Proc. Proceedings of The 2014 IACJ/ISAM Joint International Conference.
[105] Zaldivar, R. J., Witkin, D. B., McLouth, T., Patel, D. N., Schmitt, K., and Nokes, J. P., 2017, "Influence of processing and orientation print effects on the mechanical and thermal behavior of 3D-Printed ULTEM® 9085 Material," Additive Manufacturing, 13, pp. 71-80.
[106] Zhou, X., Hsieh, S.-J., and Sun, Y., 2017, "Experimental and numerical investigation of the thermal behaviour of polylactic acid during the fused deposition process," Virtual and Physical Prototyping, 12(3), pp. 221-233.
[107] Costa, S. F., Duarte, F. M., and Covas, J. A., 2015, "Thermal conditions affecting heat transfer in FDM/FFE: a contribution towards the numerical modelling of the process," Virtual and Physical Prototyping, 10(1), pp. 35-46.
[108] Nickel, A. H., Barnett, D. M., and Prinz, F. B., 2001, "Thermal stresses and deposition patterns in layered manufacturing," Materials Science and Engineering: A, 317(1), pp. 59-64.
[109] Atif Yardimci, M., and Güçeri, S., 1996, "Conceptual framework for the thermal process modelling of fused deposition," Rapid Prototyping Journal, 2(2), pp. 26-31.
[110] Pooladvand, K., and Furlong, C., 2017, "Thermo-mechanical Investigation of Fused Deposition Modeling by Computational and Experimental Methods," Mechanics of Composite and Multi-functional Materials, Volume 7, Springer, pp. 45-54.
[111] WIKIPEDIA, 2017, "Fused deposition modeling," HTML, https://en.wikipedia.org/wiki/Fused_deposition_modeling.
[112] Li, L., Sun, Q., Bellehumeur, C., and Gu, P., 2002, "Investigation of bond formation in FDM process," Solid Freeform Fabrication Proceedings,(403), 400407.
[113] Dabiri, S., Schmid, S., and Tryggvason, G., 2014, "Fully Resolved Numerical Simulations of Fused Deposition Modeling," Volume 2: Processing.
[114] Zhou, Y., Nyberg, T., Xiong, G., and Liu, D., "Temperature analysis in the fused deposition modeling process," Proc. Information Science and Control Engineering (ICISCE), 2016 3rd International Conference on, IEEE, pp. 678-682.
[115] Thomas, J., and Rodríguez, J., "Modeling the fracture strength between fused deposition extruded roads," Proc. Proceedings of the 11th Solid Freeform Fabrication Symposium, pp. 16-23.
[116] Kishore, V., Ajinjeru, C., Duty, C. E., Nycz, A., Post, B. K., Lindahl, J. M., and Kunc, V., 2017, "Infrared Preheating to Enhance Interlayer Strength of Components Printed on the Big Area Additive Manufacturing (BAAM) System," Oak Ridge National Laboratory (ORNL), Oak Ridge, TN (United States). Manufacturing Demonstration Facility (MDF).
[117] Fodran, E., Koch, M., and Menon, U., "Mechanical and dimensional characteristics of fused deposition modeling build styles," Proc. Solid Freeform Fabrication Proc, pp. 419-442.
[118] Rodríguez, J. F., Thomas, J. P., and Renaud, J. E., 2001, "Mechanical behavior of acrylonitrile butadiene styrene (ABS) fused deposition materials. Experimental investigation," Rapid Prototyping Journal, 7(3), pp. 148-158.
[119] Bertoldi, M., Yardimci, M., Pistor, C., Guceri, S., and Sala, G., "Mechanical characterization of parts processed via fused deposition," Proc. Proceedings of the 1998 solid freeform fabrication symposium, pp. 557-565.
[120] Bellini, A., and Güçeri, S., 2003, "Mechanical characterization of parts fabricated using fused deposition modeling," Rapid Prototyping Journal, 9(4), pp. 252-264.
[121] Tymrak, B., Kreiger, M., and Pearce, J. M., 2014, "Mechanical properties of components fabricated with open-source 3-D printers under realistic environmental conditions," Materials & Design, 58, pp. 242-246.
[122] Dawoud, M., Taha, I., and Ebeid, S. J., 2016, "Mechanical behaviour of ABS: An experimental study using FDM and injection moulding techniques," Journal of Manufacturing Processes, 21, pp. 39-45.
[123] Chen, F., Brown, G. M., and Song, M., 2000, "Overview of three-dimensional shape measurement using optical methods," OPTICE, 39(1), pp. 10-22.
[124] Huntley, J. M., "Optical shape measurement technology: past, present, and future," pp. 162-173.
[125] Osten, W., 2000, "Application of optical shape measurement for the nondestructive evaluation of complex objects," Optical Engineering, 39(1), pp. 232-243.
[126] Zhang, S., 2010, "Recent progresses on real-time 3D shape measurement using digital fringe projection techniques," Optics and Lasers in Engineering, 48(2), pp. 149-158.
[127] Razavi, P., Tang, H., Pooladvand, K., Ravicz, M., Remenschneider, A., Rosowski, J., Cheng, J., and Furlong, C., 2019, "Application of high-speed DIC to study damage of thin membranes under blast," Dynamic Behavior of Materials, Volume 1, Springer, pp. 361-367.
[128] Tang, H., Razavi, P., Pooladvand, K., Psota, P., Maftoon, N., Rosowski, J. J., Furlong, C., and Cheng, J. T., 2019,

"High-Speed Holographic Shape and Full-Field Displacement Measurements of the Tympanic Membrane in Normal and Experimentally Simulated Pathological Ears," Applied Sciences, 9(14), p. 2809.
[129] Razavi, P., Tang, H., Pooladvand, K., Larson, C., Frank, E. W., Perkoski, J. J., Roberge, J. Y., Walsh, J. C., Rosowski, J. J., and Cheng, J. T., 2020, "3D High-Speed Digital Image Correlation (3D-HSDIC) to Study Damage of Human Eardrum Under High-Pressure Loading," Mechanics of Biological Systems and Materials & Micro-and Nanomechanics, Volume 4, Springer, pp. 57-62.
[130] Sutton, M. A., 2008, "Digital Image Correlation for Shape and Deformation Measurements," Springer Handbook of Experimental Solid Mechanics, W. N. Sharpe, ed., Springer US, Boston, MA, pp. 565-600.
[131] Schajer, G. S., 1981, "Application of Finite Element Calculations to Residual Stress Measurements," Journal of Engineering Materials and Technology, 103(2), pp. 157-163.
[132] Schajer, G. S., 1988, "Measurement of Non-Uniform Residual Stresses Using the Hole-Drilling Method. Part I—Stress Calculation Procedures," Journal of Engineering Materials and Technology, 110(4), pp. 338-343.
[133] Makino, A., and Nelson, D., 1994, "Residual-stress determination by single-axis holographic interferometry and hole drilling—Part I: Theory," Experimental Mechanics, 34(1), pp. 66-78.
[134] Nelson, D., Makino, A., and Fuchs, E., 1997, "The holographic-hole drilling method for residual stress determination," Optics and lasers in engineering, 27(1), pp. 3-23.
[135] Baldi, A., 2005, "A new analytical approach for hole drilling residual stress analysis by full field method," Transactions of the ASME-H-Journal of Engineering Materials and Technology, 127(2), pp. 165-169.
[136] Viotti, M. R., Dolinko, A. E., Galizzi, G. E., and Kaufmann, G. H., 2006, "A portable digital speckle pattern interferometry device to measure residual stresses using the hole drilling technique," Optics and lasers in engineering, 44(10), pp. 1052-1066.
[137] ASTM, 2013, "Standard Test Method for Determining Residual Stresses by the Hole-Drilling Strain-Gage Method," ASTM International.
[138] Casavola, C., Cazzato, A., Moramarco, V., and Pappalettera, G., 2017, "Residual stress measurement in Fused Deposition Modelling parts," Polymer Testing, 58, pp. 249-255.
[139] Burdzik, R., Stanik, Z., and Warczek, J., 2012, "Method of assessing the impact of material properties on the propagation of vibrations excited with a single force impulse," Archives of Metallurgy and Materials, 57(2), pp. 409-416.
[140] Zeng, D.-J., and Zheng, Q.-S., 2007, "Resonant frequency-based method for measuring the Young's moduli of nanowires," Physical Review B, 76(7), p. 075417.
[141] Sandia, N. L., 2018, "Non-Destructive Additive Manufacturing Characterization Coupon," Sandia National Laboratories, S. N. Laboratories, ed.USA, p. 1.
[142] Plagge, D. S., 2016, "Non-Destructive Evaluation of Functional Material Properties Performed on Additively Manufactured Coupons."
[143] Carvalho, P. A., Tang, H., Razavi, P., Pooladvand, K., Castro, W. C., Gandomi, K. Y., Zhao, Z., Nycz, C. J., Furlong, C., and Fischer, G. S., 2020, "Study of MRI Compatible Piezoelectric Motors by Finite Element Modeling and High-Speed Digital Holography," Advancements in Optical Methods & Digital Image Correlation in Experimental Mechanics, Volume 3, Springer, pp. 105-112.
[144] Monzón, M. D., Gibson, I., Benítez, A. N., Lorenzo, L., Hernández, P. M., and Marrero, M. D., 2013, "Process and material behavior modeling for a new design of micro-additive fused deposition," The International Journal of Advanced Manufacturing Technology, 67(9-12), pp. 2717-2726.
[145] Everton, S. K., Hirsch, M., Stravroulakis, P., Leach, R. K., and Clare, A. T., 2016, "Review of in-situ process monitoring and in-situ metrology for metal additive manufacturing," Materials & Design, 95, pp. 431-445.
[146] Dinwiddie, R. B., Love, L. J., and Rowe, J. C., 2013, "Real-time process monitoring and temperature mapping of a 3D polymer printing process," SPIE defense, security, and sensing, International Society for Optics and Photonics, p. 87050L.
[147] Purtonen, T., Kalliosaari, A., and Salminen, A. J. P. P., 2014, "Monitoring and adaptive control of laser processes," 56, pp. 1218-1231.
[148] Krauss, H., Eschey, C., and Zaeh, M., "Thermography for monitoring the selective laser melting process," Proc. Proceedings of the Solid Freeform Fabrication Symposium.
[149] Faye, E., Dangles, O., and Pincebourde, S., 2016, "Distance makes the difference in thermography for ecological studies," Journal of Thermal Biology, 56, pp. 1-9.
[150] FLIR, 2012, The Ultimate Infrared Handbook for R&D Professionals, www.FLIR.com • 1 866.477.3687
©2012 FLIR Systems Inc.
[151] Seppala, J. E., and Migler, K. D., 2016, "Infrared thermography of welding zones produced by polymer extrusion additive manufacturing," Additive Manufacturing, 12, pp. 71-76.

[152] Withers, P. J., and Bhadeshia, H., 2001, "Residual stress. Part 2–Nature and origins," J Materials science technology
17(4), pp. 366-375.
[153] Faghidian, S., Goudar, D., Farrahi, G., and Smith, D. J., 2012, "Measurement, analysis and reconstruction of residual stresses," The Journal of Strain Analysis for Engineering Design, 47(4), pp. 254-264.
[154] Kandil, F., Lord, J., Fry, A., and Grant, P., 2001, "A review of residual stress measurement methods," A Guide to Technique Selection, NPL, Report MATC (A), 4.
[155] !!! INVALID CITATION !!! .
[156] Allen, A., Hutchings, M., Windsor, C., and Andreani, C. J. A. i. P., 1985, "Neutron diffraction methods for the study of residual stress fields," 34(4), pp. 445-473.
[157] Webster, P., Oosterkamp, L. D., Browne, P., Hughes, D., Kang, W., Withers, P., and Vaughan, G. M. J. T. J. o. S. A. f. E. D., 2001, "Synchrotron X-ray residual strain scanning of a friction stir weld," 36(1), pp. 61-70.
[158] Withers, P. J., and Bhadeshia, H., 2001, "Residual stress. Part 1–measurement techniques," J. Materials science Technology, 17(4), pp. 355-365.
[159] Tebedge, N., Alpsten, G., and Tall, L. J. E. M., 1973, "Residual-stress measurement by the sectioning method," 13(2), pp. 88-96.
[160] Prime, M. B. J. J. o. e. m., and technology, 2001, "Cross-sectional mapping of residual stresses by measuring the surface contour after a cut," 123(2), pp. 162-168.
[161] Schajer, G. S., 2010, "Hole-Drilling Residual Stress Measurements at 75: Origins, Advances, Opportunities," Experimental Mechanics, 50(2), pp. 245-253.
[162] Schajer, G. S., 1988, "Measurement of Non-Uniform Residual Stresses Using the Hole-Drilling Method. Part II—Practical Application of the Integral Method," Journal of Engineering Materials and Technology, 110(4), pp. 344-349.
[163] Schajer, G. S., 2010, "Advances in Hole-Drilling Residual Stress Measurements," Experimental Mechanics, 50(2), pp. 159-168.
[164] Viotti, M. R., Gonçalves, A. A., and Kaufmann, G. H., 2005, "Measurement of residual stresses using local heating and a radial in-plane speckle interferometer," Journal Optical Engineering
44(9), p. 093606.
[165] Viotti, M. a. R., Sutério, R., Albertazzi Jr, A., Kaufmann, G. H. J. O., and engineering, l. i., 2004, "Residual stress measurement using a radial in-plane speckle interferometer and laser annealing: preliminary results," 42(1), pp. 71-84.
[166] Pedrini, G., Martínez-García, V., Weidmann, P., Wenzelburger, M., Killinger, A., Weber, U., Schmauder, S., Gadow, R., and Osten, W., 2016, "Residual Stress Analysis of Ceramic Coating by Laser Ablation and Digital Holography," Experimental Mechanics, 56(5), pp. 683-701.
[167] Baldi, A., 2016, "Sensitivity Analysis of i-DIC Approach for Residual Stress Measurement in Orthotropic Materials," Residual Stress, Thermomechanics & Infrared Imaging, Hybrid Techniques and Inverse Problems, Volume 9: Proceedings of the 2015 Annual Conference on Experimental and Applied Mechanics, S. Bossuyt, G. Schajer, and A. Carpinteri, eds., Springer International Publishing, Cham, pp. 355-362.
[168] Schajer, G. S., Winiarski, B., and Withers, P. J., 2013, "Hole-Drilling Residual Stress Measurement with Artifact Correction Using Full-Field DIC," Experimental and Applied Mechanics, Volume 4: Proceedings of the 2012 Annual Conference on Experimental and Applied Mechanics, E. C. Ventura, C. W. Crone, and C. Furlong, eds., Springer New York, New York, NY, pp. 403-414.
[169] Fang, W., Wickert, J. J. J. o. M., and Microengineering, 1996, "Determining mean and gradient residual stresses in thin films using micromachined cantilevers," 6(3), p. 301.
[170] Withers, P., Turski, M., Edwards, L., Bouchard, P., and Buttle, D., 2008, "Recent advances in residual stress measurement," J International Journal of Pressure Vessels Piping, 85(3), pp. 118-127.
[171] Cardinale, G. F., Howitt, D., McCarty, K., Medlin, D., Mirkarimi, P., Moody, N. J. D., and materials, r., 1996, "Analysis of residual stress in cubic boron nitride thin films using micromachined cantilever beams," 5(11), pp. 1295-1302.
[172] Nairn, J. A. J. I. J. o. A., and Adhesives, 2000, "Energy release rate analysis for adhesive and laminate double cantilever beam specimens emphasizing the effect of residual stresses," 20(1), pp. 59-70.
[173] Casavola, C., Cazzato, A., Moramarco, V., and Pappalettere, C., 2016, "Orthotropic mechanical properties of fused deposition modelling parts described by classical laminate theory," Materials & Design, 90, pp. 453-458.
[174] Gurrala, P. K., and Regalla, S. P., 2014, "Part strength evolution with bonding between filaments in fused deposition modelling: This paper studies how coalescence of filaments contributes to the strength of final FDM part," Virtual and Physical Prototyping, 9(3), pp. 141-149.

[175] Wang, T.-M., Xi, J.-T., and Jin, Y., 2007, "A model research for prototype warp deformation in the FDM process," The International Journal of Advanced Manufacturing Technology, 33(11), pp. 1087-1096.
[176] Narang, R., and Chhabra, D., "Analysis of Process Parameters of Fused Deposition Modeling (FDM) Technique."
[177] Luecke, W. E., Slotwinski, J. A. J. J. o. r. o. t. N. I. o. S., and Technology, 2014, "Mechanical properties of austenitic stainless steel made by additive manufacturing," 119, p. 398.
[178] Mertens, A., Reginster, S., Contrepois, Q., Dormal, T., Lemaire, O., and Lecomte-Beckers, J., "Microstructures and mechanical properties of stainless steel AISI 316L processed by selective laser melting," Proc. Mater. Sci. Forum, pp. 898-903.
[179] Shamsaei, N., Yadollahi, A., Bian, L., and Thompson, S. M., 2015, "An overview of Direct Laser Deposition for additive manufacturing; Part II: Mechanical behavior, process parameter optimization and control," Additive Manufacturing, 8, pp. 12-35.
[180] Villalpando, L., Eiliat, H., and Urbanic, R. J., 2014, "An Optimization Approach for Components Built by Fused Deposition Modeling with Parametric Internal Structures," Procedia CIRP, 17, pp. 800-805.
[181] Ahn, S.-H., Montero, M., Odell, D., Roundy, S., and Wright, P. K., 2002, "Anisotropic material properties of fused deposition modeling ABS," Rapid prototyping journal, 8(4), pp. 248-257.
[182] Rayegani, F., and Onwubolu, G., 2014, "Fused deposition modelling (FDM) process parameter prediction and optimization using group method for data handling (GMDH) and differential evolution (DE)," International Journal of Advanced Manufacturing Technology, 73.
[183] Sood, A. K., Ohdar, R. K., and Mahapatra, S. S., 2010, "Parametric appraisal of mechanical property of fused deposition modelling processed parts," Materials & Design, 31(1), pp. 287-295.
[184] Kohad, A., and Dalu, R., "Optimization of Process Parameters in Fused Deposition Modeling: A Review," Proc. International Conference on Recent Trends in Engineering and Science (ICRTES 2017), p. 21st.
[185] Kulkarni, P., and Dutta, D., 1999, "Deposition strategies and resulting part stiffnesses in fused deposition modeling," Journal of manufacturing science and engineering, 121(1), pp. 93-103.
[186] Cunico, M. W. M., 2013, "Study and optimisation of FDM process parameters for support-material-free deposition of filaments and increased layer adherence: This paper investigates control factors and process parameters that allow the fabrication of negative surface features without a support material," Virtual and Physical Prototyping, 8(2), pp. 127-134.
[187] Smith, W. C., and Dean, R. W., 2013, "Structural characteristics of fused deposition modeling polycarbonate material," Polymer Testing, 32(8), pp. 1306-1312.
[188] Torrado, A. R., Shemelya, C. M., English, J. D., Lin, Y., Wicker, R. B., and Roberson, D. A., 2015, "Characterizing the effect of additives to ABS on the mechanical property anisotropy of specimens fabricated by material extrusion 3D printing," Additive Manufacturing, 6, pp. 16-29.
[189] Panda, B. N., Garg, A., and Shankhwar, K., 2016, "Empirical investigation of environmental characteristic of 3-D additive manufacturing process based on slice thickness and part orientation," Measurement, 86, pp. 293-300.
[190] Griffiths, C. A., Howarth, J., Rowbotham, G. d.-A., and Rees, A., 2016, "Effect of Build Parameters on Processing Efficiency and Material Performance in Fused Deposition Modelling," Procedia CIRP, 49, pp. 28-32.
[191] Mohamed, O. A., Masood, S. H., and Bhowmik, J. L., 2015, "Optimization of fused deposition modeling process parameters: a review of current research and future prospects," Advances in Manufacturing, 3(1), pp. 42-53.
[192] Mohamed, O. A., Masood, S. H., and Bhowmik, J. L., 2016, "Mathematical modeling and FDM process parameters optimization using response surface methodology based on Q-optimal design," Applied Mathematical Modelling, 40(23), pp. 10052-10073.
[193] Mohamed, O. A., Masood, S. H., and Bhowmik, J. L., 2017, "Characterization and dynamic mechanical analysis of PC-ABS material processed by fused deposition modelling: An investigation through I-optimal response surface methodology," Measurement, 107, pp. 128-141.
[194] Berretta, S., Davies, R., Shyng, Y. T., Wang, Y., and Ghita, O., 2017, "Fused Deposition Modelling of high temperature polymers: Exploring CNT PEEK composites," Polymer Testing, 63(Supplement C), pp. 251-262.
[195] Yang, C., Tian, X., Li, D., Cao, Y., Zhao, F., and Shi, C., 2017, "Influence of thermal processing conditions in 3D printing on the crystallinity and mechanical properties of PEEK material," Journal of Materials Processing Technology, 248, pp. 1-7.
[196] Sahu, R. K., Mahapatra, S., and Sood, A. K., 2013, "A study on dimensional accuracy of fused deposition modeling (FDM) processed parts using fuzzy logic," Journal for Manufacturing Science & Production, 13(3), pp. 183-197.
[197] Mishra, S., 2016, "A Study On Parametric Appraisal of Fused Deposition Modelling (FDM) Process."
[198] Sood, A. K., Ohdar, R. K., and Mahapatra, S. S., 2009, "Improving dimensional accuracy of Fused Deposition

Modelling processed part using grey Taguchi method," Materials & Design, 30(10), pp. 4243-4252.
[199] Nancharaiah, T., d Ranga Raju, V. R., and Raju, R., 2010, "An experimental investigation on surface quality and dimensional accuracy of FDM components."
[200] Lieneke, T., Denzer, V., Adam, G. A. O., and Zimmer, D., 2016, "Dimensional Tolerances for Additive Manufacturing: Experimental Investigation for Fused Deposition Modeling," Procedia CIRP, 43, pp. 286-291.
[201] Albakri, M., Sturm, L., Williams, C. B., and Tarazaga, P., "Non-destructive evaluation of additively manufactured parts via impedance-based monitoring," Proc. Solid Freeform Fabrication Symposium, pp. 1475-1490.
[202] Waller, J. M., Parker, B. H., Hodges, K. L., Burke, E. R., and Walker, J. L., 2014, "Nondestructive evaluation of additive manufacturing state-of-the-discipline report."
[203] Slotwinski, J., Cooke, A., Moylan, S. J. N. I. o. S., and Technol-ogy, 2012, "Mechanical properties testing for metal parts made via additive manufacturing: a review of the state of the art of mechanical property testing."
[204] Migliori, A., Sarrao, J., Visscher, W. M., Bell, T., Lei, M., Fisk, Z., and Leisure, R. G. J. P. B. C. M., 1993, "Resonant ultrasound spectroscopic techniques for measurement of the elastic moduli of solids," 183(1-2), pp. 1-24.
[205] Kim, J.-T., Ryu, Y.-S., Cho, H.-M., and Stubbs, N. J. E. s., 2003, "Damage identification in beam-type structures: frequency-based method vs mode-shape-based method," 25(1), pp. 57-67.
[206] Nagarajaiah, S., and Basu, B., 2009, "Output only modal identification and structural damage detection using time frequency & wavelet techniques," Earthquake Engineering and Engineering Vibration, 8(4), pp. 583-605.
[207] Alfano, M., and Pagnotta, L., 2006, "An Inverse Procedure for Determining the Material Constants of Isotropic Square Plates by Impulse Excitation of Vibration," Applied Mechanics and Materials, 3-4, p. 287.
[208] Pryputniewicz, R. J., "Time Average Holography In Vibration Analysis," SPIE, p. 6.
[209] Schwarz, J., Saxton, J., and Jauriqui, L., 2005, "Process compensated resonant testing in manufacturing process control," Materials evaluation, 63(7).
[210] Leisure, R. G., and Willis, F. J. J. o. P. C. M., 1997, "Resonant ultrasound spectroscopy," 9(28), p. 6001.
[211] Maynard, J. J. P. T., 1996, "Resonant ultrasound spectroscopy," 49(1), pp. 26-33.
[212] Migliori, A., and Maynard, J. J. R. o. S. I., 2005, "Implementation of a modern resonant ultrasound spectroscopy system for the measurement of the elastic moduli of small solid specimens," 76(12), p. 121301.
[213] Frederiksen, P. S. J. J. o. C. M., 1997, "Experimental procedure and results for the identification of elastic constants of thick orthotropic plates," 31(4), pp. 360-382.
[214] Pedersen, P., and Frederiksen, P., 1992, "Identification of orthotropic material moduli by a combined experimental/numerical method," Measurement, 10(3), pp. 113-118.
[215] Larsson, D., 1997, "Using modal analysis for estimation of anisotropic material constants," Journal of engineering mechanics, 123(3), pp. 222-229.
[216] Lai, T., and Lau, T., 1993, "Determination of elastic constants of a generally orthotropic plate by modal analysis," International Journal of Analytical and Experimental Modal Analysis, 8, pp. 15-33.
[217] Gaul, L., Willner, K., and Hurlebaus, S., "Determination of Material Properties of Plates from Modal ESPI Measurements,# 5," Proc. PROCEEDINGS-SPIE THE INTERNATIONAL SOCIETY FOR OPTICAL ENGINEERING, SPIE INTERNATIONAL SOCIETY FOR OPTICAL, pp. 1756-1762.
[218] ASTM, 2014, "Standard Test Method for Dynamic Young's Modulus, Shear Modulus, and Poisson's Ratio by Sonic Resonance (E1875 − 13)," ASTM Standards, ASTM, p. 9.
[219] ASTM, 2015, "ASTM E1876-15 Standard Test Method for Dynamic Young's Modulus, Shear Modulus, and Poisson's Ratio by Impulse Excitation of Vibration."
[220] Manceau, J.-F., Robert, L., Bastien, F. O., Oytana, C., and Biwersi, S. J. J. o. m. s., 1996, "Measurement of residual stresses in a plate using a vibrational technique-application to electrolytic nickel coatings," 5(4), pp. 243-249.
[221] Berry, B., and Pritchet, W. J. J. o. a. p., 1990, "Internal stress and internal friction in thin-layer microelectronic materials," 67(8), pp. 3661-3668.
[222] Pham, H. T., Bosnyak, C. P., and Sehanobish, K., 1993, "Residual stresses in injection molded polycarbonate rectangular bars," Polymer Engineering & Science, 33(24), pp. 1634-1643.
[223] Stoney, G. G. J. P. R. S. L. A., 1909, "The tension of metallic films deposited by electrolysis," 82(553), pp. 172-175.
[224] Nix, W. D. J. M. t. A., 1989, "Mechanical properties of thin films," 20(11), p. 2217.
[225] Baker, S. P., and Nix, W. D., "Mechanical properties of thin films on substrates," Proc. 34th Annual International Technical Symposium on Optical and Optoelectronic Applied Science and Engineering, SPIE, p. 14.
[226] Saif, M., Hui, C., and Zehnder, A., 1993, "Interface shear stresses induced by non-uniform heating of a film on a substrate," Thin Solid Films, 224(2), pp. 159-167.
[227] Brenner, A., and Senderoff, S. J. J. R. N. B. S., 1949, "Calculation of stress in electrodeposits from the curvature of a plated strip," 42(105), pp. 105-123.

[228] Röll, K. J. J. o. A. P., 1976, "Analysis of stress and strain distribution in thin films and substrates," 47(7), pp. 3224-3229.
[229] Leissa, A. W. J. V. o. p., 1969, "NASA SP-160," pp. 59-60.
[230] Warburton, G., 1954, "The vibration of rectangular plates," Journal Proceedings of the Institution of Mechanical Engineers, 168(1), pp. 371-384.
[231] Young, D. J. J. a. M., 1950, "Vibration of rectangular plates by Ritz method," 17, pp. 448-453.
[232] Barton, M. J. J. O. A. M.-T. O. T. A., 1951, "Vibration of rectangular and skew cantilever plates," 18(2), pp. 129-134.
[233] Bazley, N. W., Fox, D. W., Stadter, J. T. J. Z. J. o. A. M., and Mechanik, M. Z. f. A. M. u., 1967, "Upper and lower bounds for the frequencies of rectangular cantilever plates," 47(4), pp. 251-260.
[234] Lauwagie, T., Sol, H., Roebben, G., Heylen, W., Shi, Y., and Van der Biest, O., 2003, "Mixed numerical–experimental identification of elastic properties of orthotropic metal plates," NDT & E International, 36(7), pp. 487-495.
[235] Alfano, M., and Pagnotta, L., 2006, "Determining the elastic constants of isotropic materials by modal vibration testing of rectangular thin plates," Journal of Sound and Vibration, 293(1), pp. 426-439.
[236] Frederiksen, P. S., 1992, "Identification of temperature dependence for orthotropic material moduli," Mechanics of Materials, 13(1), pp. 79-90.
[237] Li, L., Sun, Q., Bellehumeur, C., and Gu, P., 2002, "Composite modeling and analysis for fabrication of FDM prototypes with locally controlled properties," Journal of manufacturing processes, 4(2), pp. 129-141.
[238] Macaulay, M., 2012, Introduction to impact engineering, Springer Science & Business Media.
[239] Farrell, P., and Ryall, T., 1990, "Vibration of a rectangular cantilever plate," AERONAUTICAL RESEARCH LABS MELBOURNE (AUSTRALIA).
[240] Moylan, S., Cooke, A., Donmez, M. A., Jurrens, K., Moylan, S., and Slotwinski, J., 2012, A review of test artifacts for additive manufacturing, US Department of Commerce, National Institute of Standards and Technology.
[241] Martukanitz, R., Michaleris, P., Palmer, T., DebRoy, T., Liu, Z.-K., Otis, R., Heo, T. W., and Chen, L.-Q., 2014, "Toward an integrated computational system for describing the additive manufacturing process for metallic materials," Additive Manufacturing, 1–4, pp. 52-63.
[242] Thompson, S. M., Bian, L., Shamsaei, N., and Yadollahi, A., 2015, "An overview of Direct Laser Deposition for additive manufacturing; Part I: Transport phenomena, modeling and diagnostics," Additive Manufacturing, 8, pp. 36-62.
[243] Yardimci, M. A., Guceri, S. I., Agarwala, M., and Danforth, S. C., "Part quality prediction tools for fused deposition processing," Proc. Proceedings of Solid Freeform Fabrication Symposium, pp. 539-548.
[244] Ding, J., Colegrove, P., Mehnen, J., Ganguly, S., Almeida, P. M. S., Wang, F., and Williams, S., 2011, "Thermo-mechanical analysis of Wire and Arc Additive Layer Manufacturing process on large multi-layer parts," Computational Materials Science, 50(12), pp. 3315-3322.
[245] Heigel, J. C., Michaleris, P., and Reutzel, E. W., 2015, "Thermo-mechanical model development and validation of directed energy deposition additive manufacturing of Ti–6Al–4V," Additive Manufacturing, 5, pp. 9-19.
[246] Schoinochoritis, B., Chantzis, D., and Salonitis, K., 2017, "Simulation of metallic powder bed additive manufacturing processes with the finite element method: A critical review," Proceedings of the Institution of Mechanical Engineers, Part B: Journal of Engineering Manufacture, 231(1), pp. 96-117.
[247] Gouge, M., Michaleris, P., and ScienceDirect, e., 2017, Thermo-Mechanical Modeling of Additive Manufacturing, Butterworth-Heinemann [Imprint], San Diego.
[248] Majumdar, P., 2005, Computational methods for heat and mass transfer, Taylor & Francis, New York.
[249] Churchill, S. W., and Ozoe, H., 1973, "Correlations for laminar forced convection with uniform heating in flow over a plate and in developing and fully developed flow in a tube," journal of Heat Transfer, 95(1), pp. 78-84.
[250] Dowden, J. M., 2001, The mathematics of thermal modeling : an introduction to the theory of laser material processing, Chapman & Hall/CRC, Boca Raton.
[251] Gkartzou, E., Koumoulos, E. P., and Charitidis, C. A., 2017, "Production and 3D printing processing of bio-based thermoplastic filament," Manufacturing Review, 4, p. 1.
[252] Castro, G., Rodríguez, J., Montealegre, M. A., Arias, J. L., Yañez, A., Panedas, S., and Rey, L., 2015, "Laser Additive Manufacturing of High Added Value Pieces," Procedia Engineering, 132, pp. 102-109.
[253] Li, L., 2002, Analysis and fabrication of FDM prototypes with locally controlled properties, University of Calgary.
[254] Jones, H. R. N., 2000, Radiation heat transfer, Oxford University Press, Oxford ; New York.
[255] Howell, J. R., Siegel, R., and Mengüç, M. P., 2011, Thermal radiation heat transfer, CRC Press, Boca Raton.
[256] Vinokurov, V. A., 1977, Welding stresses and distortion: determination and elimination, British Library Lending

Division.
[257] Frewin, M. R., and Scott, D. A., 1999, "Finite element model of pulsed laser welding," Weld J, 78(1), pp. 15s-22s.
[258] Gibbins, J., 2006, "Thermal contact resistance of polymer interfaces," University of Waterloo.
[259] Ellison, G. N. J. I. T. o. C., and Technologies, P., 2003, "Maximum thermal spreading resistance for rectangular sources and plates with nonunity aspect ratios," 26(2), pp. 439-454.
[260] Song, S., Au, V., and Moran, K. P., "Constriction/spreading resistance model for electronics packaging," Proc. Proceedings of the 4th ASME/JSME thermal engineering joint conference, pp. 199-206.
[261] Pourshaghaghy, A., Pooladvand, K., Kowsary, F., and Karimi-Zand, K., 2006, "An inverse radiation boundary design problem for an enclosure filled with an emitting, absorbing, and scattering media," International Communications in Heat and Mass Transfer, 33(3), pp. 381-390.
[262] Siegel, R., and Howell, J. R., 2002, Thermal radiation heat transfer, Taylor & Francis, New York.
[263] Khairallah, S. A., Anderson, A. T., Rubenchik, A., and King, W. E., 2016, "Laser powder-bed fusion additive manufacturing: Physics of complex melt flow and formation mechanisms of pores, spatter, and denudation zones," Acta Materialia, 108, pp. 36-45.
[264] Francois, M. M., Sun, A., King, W. E., Henson, N. J., Tourret, D., Bronkhorst, C. A., Carlson, N. N., Newman, C. K., Haut, T., Bakosi, J., Gibbs, J. W., Livescu, V., Vander Wiel, S. A., Clarke, A. J., Schraad, M. W., Blacker, T., Lim, H., Rodgers, T., Owen, S., Abdeljawad, F., Madison, J., Anderson, A. T., Fattebert, J. L., Ferencz, R. M., Hodge, N. E., Khairallah, S. A., and Walton, O., 2017, "Modeling of additive manufacturing processes for metals: Challenges and opportunities," Current Opinion in Solid State and Materials Science, 21(4), pp. 198-206.
[265] Kamara, A., Marimuthu, S., and Li, L., 2011, "A numerical investigation into residual stress characteristics in laser deposited multiple layer waspaloy parts," Journal of Manufacturing Science and Engineering, 133(3), p. 031013.
[266] Manual, A. U. s. v., 2019, "ANSYS User's Manual."
[267] Drabousky, D. P., 2009, "Prony series representation and interconversion of viscoelastic material functions of equine cortical bone," Case Western Reserve University.
[268] Wu, W., Geng, P., Li, G., Zhao, D., Zhang, H., and Zhao, J., 2015, "Influence of Layer Thickness and Raster Angle on the Mechanical Properties of 3D-Printed PEEK and a Comparative Mechanical Study between PEEK and ABS," 8(9), p. 5271.
[269] Gilles, P., El-Ahmar, W., Jullien, J.-F. J. I. J. o. P. V., and Piping, 2009, "Robustness analyses of numerical simulation of fusion welding NeT-TG1 application:"Single weld-bead-on-plate"," 86(1), pp. 3-12.
[270] Lindgren, L.-E. J. J. o. t. s., 2001, "Finite element modeling and simulation of welding. Part 2: Improved material modeling," 24(3), pp. 195-231.
[271] Zhang, S., and Huang, P. S., 2006, "High-resolution, real-time three-dimensional shape measurement," Optical Engineering, 45(12), pp. 123601-123601-123608.
[272] Hu, D., and Kovacevic, R., 2003, "Sensing, modeling and control for laser-based additive manufacturing," International Journal of Machine Tools and Manufacture, 43(1), pp. 51-60.
[273] Zhu, X., Chao, Y. J. C., and Structures, 2002, "Effects of temperature-dependent material properties on welding simulation," 80(11), pp. 967-976.
[274] Chu, T., Ranson, W., and Sutton, M. A., 1985, "Applications of digital-image-correlation techniques to experimental mechanics," Experimental mechanics, 25(3), pp. 232-244.
[275] Amiot, F., Bornert, M., Doumalin, P., Dupré, J. C., Fazzini, M., Orteu, J. J., Poilâne, C., Robert, L., Rotinat, R., and Toussaint, E., 2013, "Assessment of digital image correlation measurement accuracy in the ultimate error regime: main results of a collaborative benchmark," Strain, 49(6), pp. 483-496.
[276] Yoneyama, S., 2016, "Basic principle of digital image correlation for in-plane displacement and strain measurement," Advanced Composite Materials, 25(2), pp. 105-123.
[277] Madiouli, J., Sghaier, J., Orteu, J.-J., Robert, L., Lecomte, D., and Sammouda, H., 2011, "Non-contact Measurement of the Shrinkage and Calculation of Porosity During the Drying of Banana," Drying Technology, 29(12), pp. 1358-1364.
[278] Bing, P., Kemao, Q., Huimin, X., and Anand, A., 2009, "Two-dimensional digital image correlation for in-plane displacement and strain measurement: a review," Measurement Science and Technology, 20(6), p. 062001.
[279] Mguil-Touchal, S., Morestin, F., and Brunei, M., 1970, "Various experimental applications of digital image correlation method," WIT Transactions on Modelling and Simulation, 17.
[280] Reich, C., Ritter, R., and Thesing, J., 2000, "3-D shape measurement of complex objects by combining photogrammetry and fringe projection," Optical Engineering, 39(1), pp. 224-231.
[281] Sutton, M., Zhao, W., McNeill, S., Schreier, H., and Chao, Y., 2001, "Development and assessment of a single-image fringe projection method for dynamic applications," Experimental mechanics, 41(3), pp. 205-217.

[282] Babaei, A., and Saadatseresht, M., 2013, "Effect of Digital Fringe Projection Parameters on 3d Reconstruction Accuracy," ISPRS-International Archives of the Photogrammetry, Remote Sensing and Spatial Information Sciences(3), pp. 73-77.
[283] Gorthi, S. S., and Rastogi, P., 2010, "Fringe projection techniques: whither we are?," Optics and lasers in engineering, 48(IMAC-REVIEW-2009-001), pp. 133-140.
[284] Feng, S., Chen, Q., Zuo, C., and Asundi, A., "Practical Considerations for High-Speed Real-Time 3-D Measurements by the Fringe Projection," Proc. Fourth International Conference on Optical and Photonics Engineering, International Society for Optics and Photonics, pp. 1025016-1025016-1025015.
[285] Zhang, J. W., and Peng, A. H., "Process-parameter optimization for fused deposition modeling based on Taguchi method," Proc. Advanced Materials Research, Trans Tech Publ, pp. 444-447.
[286] Hwu, Y., 1991, "Time-average holographic method on the determination of Young's modulus," American Journal of Physics, 59, pp. 287-287.
[287] Powell, R. L., and Stetson, K. A., 1965, "Interferometric vibration analysis by wavefront reconstruction," JOSA, 55(12), pp. 1593-1598.
[288] Celik, H. K., Tan, Y., Seviour, R., and Rennie, A., 2009, "Effect of thermal and mechanical deformation of metamaterial FDM components."
[289] Faes, M., Ferraris, E., and Moens, D., 2016, "Influence of Inter-layer Cooling time on the Quasi-static Properties of ABS Components Produced via Fused Deposition Modelling," Procedia CIRP, 42, pp. 748-753.
[290] Karnati, S., Matta, N., Sparks, T., and Liou, F., "Vision-based process monitoring for laser metal deposition processes," Proc. Proceedings of the 24th Annual International Solid Freeform Fabrication Symposium (SFF 2013), The University of Texas at Austin.
[291] Kousiatza, C., and Karalekas, D., 2016, "In-situ monitoring of strain and temperature distributions during fused deposition modeling process," Materials & Design, 97, pp. 400-406.
[292] Van Weeren, R., Agarwala, M., Jamalabad, V., Bandyophadyay, A., Vaidyanathan, R., Langrana, N., Safari, A., Whalen, P., Danforth, S., and Ballard, C., "Quality of parts processed by fused deposition," Proc. Proceedings of the Solid Freeform Fabrication Symposium, pp. 314-321.
[293] Koch, C., Van Hulle, L., and Rudolph, N., 2017, "Investigation of mechanical anisotropy of the fused filament fabrication process via customized tool path generation," Additive Manufacturing, 16(Supplement C), pp. 138-145.
[294] Chacón, J. M., Caminero, M. A., García-Plaza, E., and Núñez, P. J., 2017, "Additive manufacturing of PLA structures using fused deposition modelling: Effect of process parameters on mechanical properties and their optimal selection," Materials & Design, 124, pp. 143-157.
[295] McLouth, T. D., Severino, J. V., Adams, P. M., Patel, D. N., and Zaldivar, R. J., 2017, "The impact of print orientation and raster pattern on fracture toughness in additively manufactured ABS," Additive Manufacturing, 18(Supplement C), pp. 103-109.
[296] Fatemi, S. A., Ashany, J. Z., Aghchai, A. J., and Abolghasemi, A., 2017, "Experimental investigation of process parameters on layer thickness and density in direct metal laser sintering: a response surface methodology approach," Virtual and Physical Prototyping, 12(2), pp. 133-140.
[297] Sood, A. K., Ohdar, R. K., and Mahapatra, S. S., 2012, "Experimental investigation and empirical modelling of FDM process for compressive strength improvement," Journal of Advanced Research, 3(1), pp. 81-90.
[298] Palanikumar, K., 2008, "Application of Taguchi and response surface methodologies for surface roughness in machining glass fiber reinforced plastics by PCD tooling," The International Journal of Advanced Manufacturing Technology, 36(1-2), pp. 19-27.
[299] Nazan, M., Ramli, F., Alkahari, M., Sudin, M., and Abdullah, M., 2006, "Process parameter optimization of 3D printer using response surface method," METHODOLOGY, 15, p. 17.
[300] Srivastava, M., Maheshwari, S., Kundra, T., and Rathee, S., 2017, "Estimation of the Effect of Process Parameters on Build Time and Model Material Volume for FDM Process Optimization by Response Surface Methodology and Grey Relational Analysis," Advances in 3D Printing & Additive Manufacturing Technologies, Springer, pp. 29-38.
[301] Nidagundi, V. B., Keshavamurthy, R., and Prakash, C. P. S., 2015, "Studies on Parametric Optimization for Fused Deposition Modelling Process," Materials Today: Proceedings, 2(4), pp. 1691-1699.
[302] Peng, A., Xiao, X., and Yue, R., 2014, "Process parameter optimization for fused deposition modeling using response surface methodology combined with fuzzy inference system," The International Journal of Advanced Manufacturing Technology
73(1-4), pp. 87-100.
[303] Motaparti, K. P., 2016, Effect of build parameters on mechanical properties of ultem 9085 parts by fused deposition modeling, Missouri University of Science and Technology.

[304] Nuñez, P., Rivas, A., García-Plaza, E., Beamud, E., and Sanz-Lobera, A., 2015, "Dimensional and surface texture characterization in fused deposition modelling (FDM) with ABS plus," Journal Procedia Engineering, 132, pp. 856-863.
[305] Mohamed, O. A., Masood, S. H., Bhowmik, J. L., Nikzad, M., and Azadmanjiri, J., 2016, "Effect of process parameters on dynamic mechanical performance of fdm PC/ABS printed parts through design of experiment," Journal of Materials Engineering and Performance, 25(7), pp. 2922-2935.
[306] Kumar, S., Kannan, V. N., Sankaranarayanan, G. J. I. J. o. C. E., and Technology, 2014, "Parameter optimization of ABS-M30i parts produced by fused deposition modeling for minimum surface roughness," 3, pp. 93-97.
[307] Lee, B., Abdullah, J., and Khan, Z., 2005, "Optimization of rapid prototyping parameters for production of flexible ABS object," Journal of materials processing technology, 169(1), pp. 54-61.
[308] Abbott, A. C. T., G. P.; Bradford, R. L.; Koerner, H.; Baur, J. W., 2018, "Process-structure-property effects on ABS bond strength in fused filament fabrication," Additive Manufacturing, 19(Supplement C), pp. 29-38.
[309] Górski, F., Kuczko, W., and Wichniarek, R., 2013, "Influence of process parameters on dimensional accuracy of parts manufactured using Fused Deposition Modelling technology," Advances in Science and Technology Research Journal, 7(19), pp. 27--35.
[310] Li, H., Wang, T., and Yu, Z., 2017, "The Quantitative Research of Interaction between Key Parameters and the Effects on Mechanical Property in FDM," Advances in Materials Science and Engineering, 2017.
[311] Ognjan, L., Vera, G., Ivan, R., and Simon, M., 2017, "Investigating impact of five build parameters on the maximum flexural force in FDM specimens – a definitive screening design approach," Rapid Prototyping Journal, 23(6), pp. 1088-1098.
[312] DeCicco, A., and Faust, J., 2013, "Effects of Build Parameters on Additive Materials," MIT Lincoln Laboratory Lexington United States.
[313] Kaveh, M., Badrossamay, M., Foroozmehr, E., and Hemasian Etefagh, A., 2015, "Optimization of the printing parameters affecting dimensional accuracy and internal cavity for HIPS material used in fused deposition modeling processes," Journal of Materials Processing Technology, 226, pp. 280-286.
[314] Fernandez-Vicente, M., Calle, W., Ferrandiz, S., and Conejero, A., 2016, "Effect of Infill Parameters on Tensile Mechanical Behavior in Desktop 3D Printing," 3D Printing and Additive Manufacturing, 3(3), pp. 183-192.
[315] Cantrell, J. T., Rohde, S., Damiani, D., Gurnani, R., DiSandro, L., Anton, J., Young, A., Jerez, A., Steinbach, D., and Kroese, C. J. R. P. J., 2017, "Experimental characterization of the mechanical properties of 3D-printed ABS and polycarbonate parts," Rapid Prototyping Journal, 23(4), pp. 811-824.
[316] Vega, V., Clements, J., Lam, T., Abad, A., Fritz, B., Ula, N., and Es-Said, O. S., 2011, "The effect of layer orientation on the mechanical properties and microstructure of a polymer," Journal of materials engineering and performance, 20(6), pp. 978-988.
[317] Natrella, M., 2010, "NIST/SEMATECH e-handbook of statistical methods."
[318] Morgan, R. V., Reid, R. S., Baker, A. M., Lucero, B., and Bernardin, J. D., 2017, "Emissivity measurements of additively manufactured materials," Los Alamos National Lab.(LANL), Los Alamos, NM (United States).
[319] Yang, F., and Pitchumani, R., 2002, "Healing of Thermoplastic Polymers at an Interface under Nonisothermal Conditions," Macromolecules, 35(8), pp. 3213-3224.
[320] Leissa, A. W., 1973, "The free vibration of rectangular plates," Journal of sound and vibration, 31(3), pp. 257-293.
[321] Ziemian, S., Okwara, M., and Ziemian, C. W., 2015, "Tensile and fatigue behavior of layered acrylonitrile butadiene styrene," Rapid Prototyping Journal, 21(3), pp. 270-278.
[322] Zortrax, 2019, "Professional 3D Printing Solutions for Rapid prototyping," https://zortrax.com/.
[323] Cosson, D. B., and Akué Asséko, A. C., 2019, "Effect of the nozzle radiation on the fused filament fabrication process: 3D numerical simulations and experimental investigation," Journal of Heat Transfer.
[324] Churchill, S. W. J. A. J., 1976, "A comprehensive correlating equation for forced convection from flat plates," 22(2), pp. 264-268.
[325] Zhu, Z., Dhokia, V., Nassehi, A., and Newman, S. T., 2016, "Investigation of part distortions as a result of hybrid manufacturing," Robotics and Computer-Integrated Manufacturing, 37, pp. 23-32.
[326] Rangaswamy, P., Griffith, M. L., Prime, M. B., Holden, T. M., Rogge, R. B., Edwards, J. M., and Sebring, R. J., 2005, "Residual stresses in LENS® components using neutron diffraction and contour method," Materials Science and Engineering: A, 399(1–2), pp. 72-83.
[327] Vasinonta, A., Beuth, J. L., and Griffith, M. L., "Process maps for controlling residual stress and melt pool size in laser-based SFF processes," Proc. Solid Freeform Fabrication Proceedings, Proc. 2000 Solid Freeform Fabrication Symposium, Austin, p. 206.
[328] Klingbeil, N., Beuth, J., Chin, R., and Amon, C., "Measurement and modeling of residual stress-induced warping

in direct metal deposition processes," Proc. Solid Freeform Fabrication Proceedings, Proc. 1998 Solid Freeform Fabrication Symposium, Austin, pp. 367-374.
[329] Grédiac, M., Fournier, N., Paris, P.-A., and Surrel, Y., 1998, "Direct identification of elastic constants of anisotropic plates by modal analysis: experimental results," Journal of sound and vibration, 210(5), pp. 643-659.
[330] Grédiac, M., and Paris, P., 1996, "Direct identification of elastic constants of anisotropic plates by modal analysis: theoretical and numerical aspects," Journal of sound and vibration, 195(3), pp. 401-415.
[331] Campbell, T. A., and Ivanova, O. S., 2013, "Additive manufacturing as a disruptive technology: Implications of three-dimensional printing," Technology & Innovation, 15(1), pp. 67-79.
[332] Strong, D., Danielle Strong, Issariya Sirichakwal, Issariya Sirichakwal, Guha P. Manogharan, Guha P. Manogharan, Thomas Wakefield, and Thomas Wakefield., 2017, "Current state and potential of additive – hybrid manufacturing for metal parts," Rapid Prototyping Journal, 23(3), pp. 577-588.
[333] Wohlers, T., 2014, "Tracking global growth in industrial-scale additive manufacturing," 3D Printing and Additive Manufacturing, 1(1), pp. 2-3.
[334] Robinson, L., and Scott, J., 2014, "Layers of complexity: making the promises possible for additive manufacturing of metals," JOM, 66(11), p. 2194.
[335] Liou, F., Slattery, K., Kinsella, M., Newkirk, J., Chou, H.-N., and Landers, R., 2007, "Applications of a hybrid manufacturing process for fabrication of metallic structures," Rapid Prototyping Journal, 13(4), pp. 236-244.
[336] Matsuura, 2017, "Hybric Manufacturing," http://www.matsuurausa.com/.
[337] VOODOO, 2018, https://voodoomfg.com/.
[338] Bergman, T. L., Incropera, F. P., DeWitt, D. P., and Lavine, A. S., 2011, Fundamentals of heat and mass transfer, John Wiley & Sons.
[339] Churchill, S., and Bernstein, M., 1977, "A correlating equation for forced convection from gases and liquids to a circular cylinder in crossflow," Journal of Heat Transfer, 99(2), pp. 300-306.
[340] Rose, J. J. I. J. o. H., and Transfer, M., 1979, "Boundary-layer flow with transpiration on an isothermal flat plate," 22, p. 1243.
[341] Holman, J. P., 2010, Heat transfer, McGraw Hill Higher Education, Boston.
[342] Popiel, C. O., 2008, "Free convection heat transfer from vertical slender cylinders: A review," Heat Transfer Eng, 29(6), pp. 521-536.
[343] Churchill, S. W., and Chu, H. H., 1975, "Correlating equations for laminar and turbulent free convection from a vertical plate," Int J Heat Mass Tran, 18(11), pp. 1323-1329.
[344] Montgomery, D. C., 2017, Design and analysis of experiments, John wiley & sons.
[345] SOOD, A. K., CHATURVEDI, V., DATTA, S., and MAHAPATRA, S. S., 2011, "Optimization of process parameters in fused deposition modeling using weighted principal component analysis," Journal of Advanced Manufacturing Systems, 10(02), pp. 241-259.
[346] Winer, B. J., 1962, "Statistical principles in experimental design."
[347] Box, G. E., Hunter, W. G., and Hunter, J. S., 1978, "Statistics for experimenters."
[348] Box, G. E., and Draper, N. R., 1987, Empirical model-building and response surfaces, John Wiley & Sons.
[349] Wu, C. J., and Hamada, M. S., 2011, Experiments: planning, analysis, and optimization, John Wiley & Sons.

9. Appendices

9.1 Estimation of boundary condition for convection heat transfer

For estimation of the convection heat transfer, it is necessary to know the effect of the regime of flow, which is defined by calculating associated Reynolds numbers for each case:

$$Re_s = \frac{\rho U_\infty L}{\mu} = \frac{U_\infty L}{\nu}, \tag{9-1}$$

where ρ is fluid density, $U_\infty$is fluid velocity, and L is the characteristic length, and μ is dynamic, and ν is kinematic viscosity. All material dependence parameters were calculated considering the average temperature of the surface and envelope temperature of the fluid. For flow over a flat plate, the critical Reynolds number for transmission from laminar flow to turbulent vary from approximately 10^5 to $3x10^6$ [338].

There are several correlations to estimate the local and average coefficient of thermal convection. A recommended correlation is the one by Churchill and Ozoe [249] that gives the local convection coefficient for laminar flow over an isothermal plate:

$$\overline{Nu_x} = 0.6774 Re_x^{\frac{1}{2}} \frac{Pr^{\frac{1}{3}}}{\left[1 + \left(\frac{0.0468}{Pr}\right)^{\frac{2}{3}}\right]^{\frac{1}{4}}} \; and \; Pe_x \geq 100, \tag{9-2}$$

where Nu_x is local Nusselt number, Pe_x is a Pecklet number ($Pe_x \equiv Re_x Pr$) and Pr is Prandtl number. There is also another correlation for $Pe_x \geq 0.6$ which applies to air flows over an isothermal plate by estimating average Nusselt as:

$$\overline{Nu_x} = \frac{\overline{h_{conv\,x}}x}{\kappa} = 0.664 Re_x^{\frac{1}{2}} Pr^{\frac{1}{3}} \; and \; Pr \geq 0.6. \tag{9-3}$$

Knowing the Prandtl and Reynolds numbers, one can find the Nusselt number for the four different categories mentioned above.

Before estimating the convection heat transfer coefficients, it is worth mentioning that empirical correlations such as mentioned above and below were derived assuming fully-developed thermal and velocity boundary layers; however, those boundary conditions may not be attainable for cases studied hereunder. The estimations were done on two levels: filament level and part level. For the filament level, we estimated h_{conv} for the range of the nozzle diameters listed in Table 3, and for the part level, we assumed the size of the component in three ranges 1-10, 10-50, and 50-500 mm diameters or length.

9.1.1 Estimation of the coefficient of convection for filament

The sizes of cylinders are represented by the four ranges of nozzle size in Table 3. These cylinders were analyzed to determine the coefficient of heat convection.

Churchill and Bernstein [339] suggested the following set of correlations for calculating the heat transfer coefficient for cylindrical objects with different diameters in three ranges of Reynolds number as follows:

- Re_D>400,000

$$\overline{Nu_D} = 0.3 + \frac{0.62\mathrm{Re}_\mathrm{D}^{\frac{1}{2}} Pr^{1/3}}{\left[1+\left(\frac{04}{Pr}\right)^{\frac{2}{3}}\right]^{\frac{1}{4}}}\left[1+\left(\frac{Re_D}{282{,}000}\right)^{\frac{5}{8}}\right]^{4/5}, \tag{9-4}$$

- 10,000<Re_D<= 400,000

$$\overline{Nu_D} = 0.3 + \frac{0.62\mathrm{Re}_\mathrm{D}^{\frac{1}{2}} Pr^{1/3}}{\left[1+\left(\frac{04}{Pr}\right)^{\frac{2}{3}}\right]^{\frac{1}{4}}}\left[1+\left(\frac{Re_D}{282{,}000}\right)^{\frac{1}{2}}\right], \tag{9-5}$$

- Re_D<=10,000

$$\overline{Nu_D} = 0.3 + \frac{0.62\mathrm{Re}_{\mathrm{D}}^{\frac{1}{2}} Pr^{1/3}}{\left[1 + \left(\frac{04}{Pr}\right)^{\frac{2}{3}}\right]^{\frac{1}{4}}}. \tag{9-6}$$

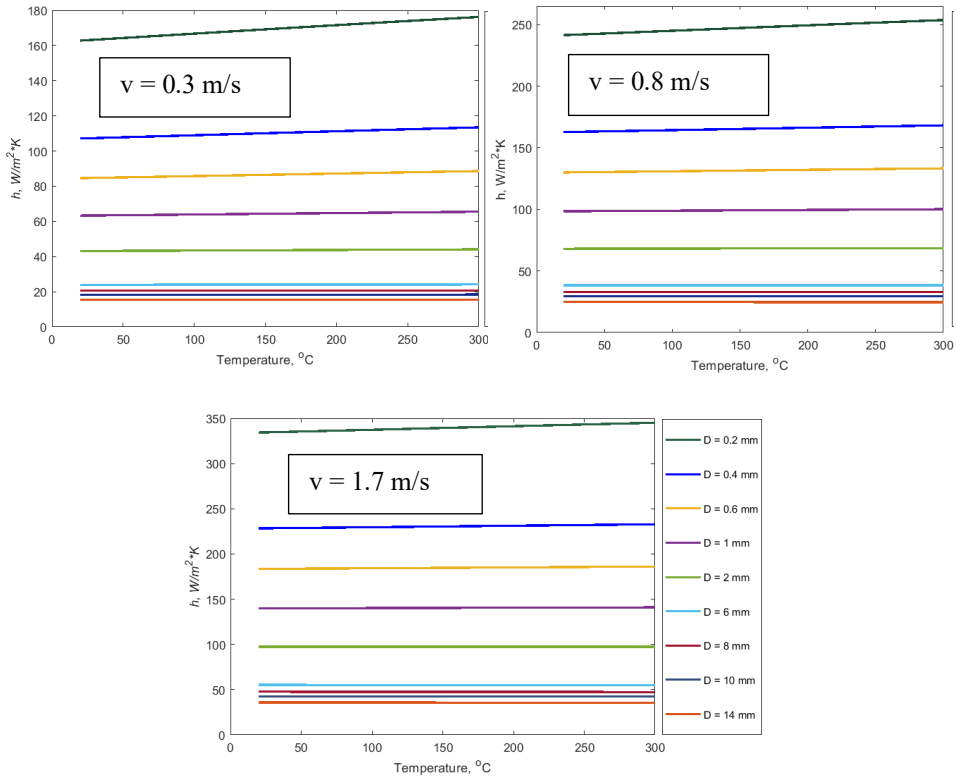

Fig. 108. Coefficient of convection heat transfer calculated for the temperature ranges from 20 to 300 ºC for filament with diameter ranges from 0.2 to 14 mm corresponding to the common nozzle size of the FDM machine.

These coefficients were calculated for three selected velocities of cooling fluid for filament temperatures ranging from 20 to 300 ºC and are shown in Fig. 108. For larger diameters, the changes in coefficient over the temperature were unimportant compared to small diameters. For the smallest diameter (0.2mm) where the changes in convection coefficient are expected to be the largest, these differences between the two extremes of temperature are 7.6%, 4.8%, and 3.1% for the selected velocities of 0.3, 0.8, 1.7 m/s, respectively. One can conclude that these differences are insignificant and neglect the effect of temperature for diameters larger than 0.6

mm. We considered the average values of the h_{conv} as listed in Table 56 for further analyses in this dissertation.

Table 56: The average of the coefficient of convection heat transfer for the four different classes of nozzles over the range of temperature from 20°C to 300 °C, h_{conv} ($W/m^2\,^oC$)

Scale	Nozzle diameter range, mm	Common nozzle diameter, mm	Heat Transfer Coefficients at Different Velocities		
			0.3 (m/s)	0.8 (m/s)	1.7 (m/s)
Micro	0.2-0.6	0.2	169.6	247.59	339.69
		0.4	110.32	165.46	230.59
Meso	0.6-2	0.6	86.60	131.63	184.80
		1.0	64.38	99.25	140.44
Medium	2-8	2	43.60	68.26	97.39
		6	24.04	38.30	55.09
Large	8-14	8	20.64	32.97	47.53
		10	18.35	29.38	42.40
		14	15.38	24.71	35.72

Figure 109 illustrates changes in the average of coefficients of heat convection for different velocities and diameters. It is possible to fit curves to this data, as illustrated in Fig. 109.

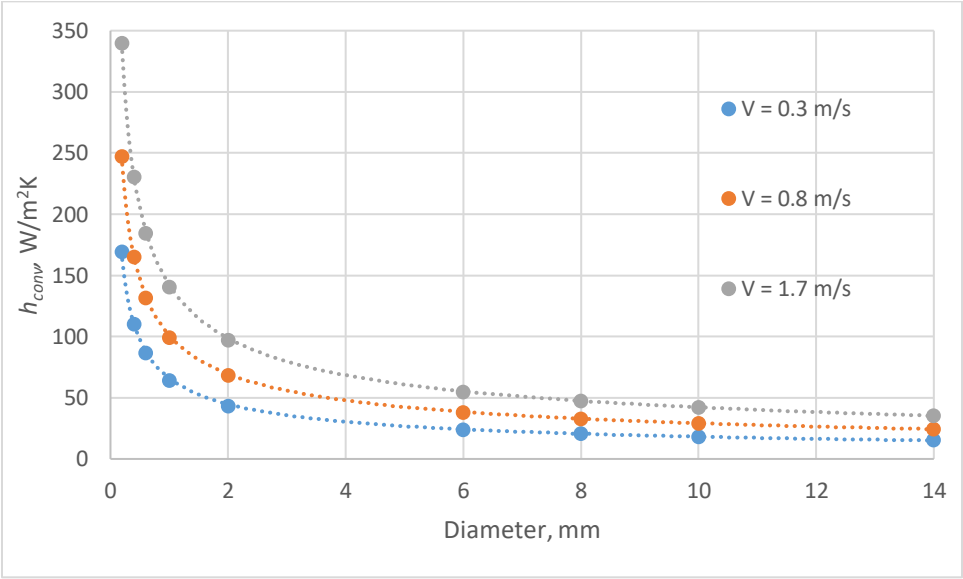

Fig. 109. Curve fitting of the coefficient of convection heat transfer calculated for the temperature ranges from 20 to 300 °C at three different flow velocities for filament with diameter ranges from 0.2 to 14 mm corresponding to different common sizes of the nozzle in FM machines.

Table 48 lists the coefficients of the curve fit along with $\boldsymbol{R^2}$ for the three selected classes of velocity. One may interpolate data to find the h_{conv} for any other values in between.

Table 57: The constants of the fitted curves for convection heat transfer of the four different classes of nozzles, h_{conv} ($W/m^2{}^oC$)

Velocity, m/s	Curve fit equation	R^2
0.3	$66.058 \times d^{-0.561}$	0.9994
0.8	$101.03 \times d^{-0.539}$	0.9997
1.7	$142.27 \times d^{-0.528}$	0.998

9.1.2 Estimation of the coefficient of forced convection for cylindrical 3D printed objects

We also analyzed printed components that had diameters between 1 to 500 mm. We divided diameters into three categories as shown in Table 58.

Table 58: The average of the coefficient of convection heat transfer for three different ranges of cylindrical 3D printed parts, h_{conv} ($W/m^2{}^oC$)

Scale	Printed components Diameters, mm	Selected diameter, mm	Heat Transfer Coefficients at Different Velocities		
			0.3 (m/s)	0.8 (m/s)	1.7 (m/s)
Small	1-10	1	64.38	99.26	140.44
		5.5	25.18	40.05	57.62
Medium	10-50	10	18.35	29.38	42.41
		30	10.37	16.74	24.26
Large	50-500	50	7.98	12.91	18.74
		275	3.36	6.49	10.14
		500	2.48	5.07	8.082

We calculated the h_{conv} for seven different diameters as the upper, lower, and middle values of the three ranges. The results are shown in Fig. 110. Each of these three graphs is associated with one of the selected velocities (i.e., 0.3, 0.7, and 1.3 m/s).

Table 59: The constants of the fitted curves for the average of the coefficient of convection heat transfer for cylindrical objects, h_{conv} ($W/m^2{}^oC$)

Velocity, m/s	Curve fit equation	R^2
0.3	$79.337 \times d^{-1.616}$	0.9424
0.8	$116.14 \times d^{-1.495}$	0.9617

1.7	$161.12 \times d^{-1.443}$	0.9687

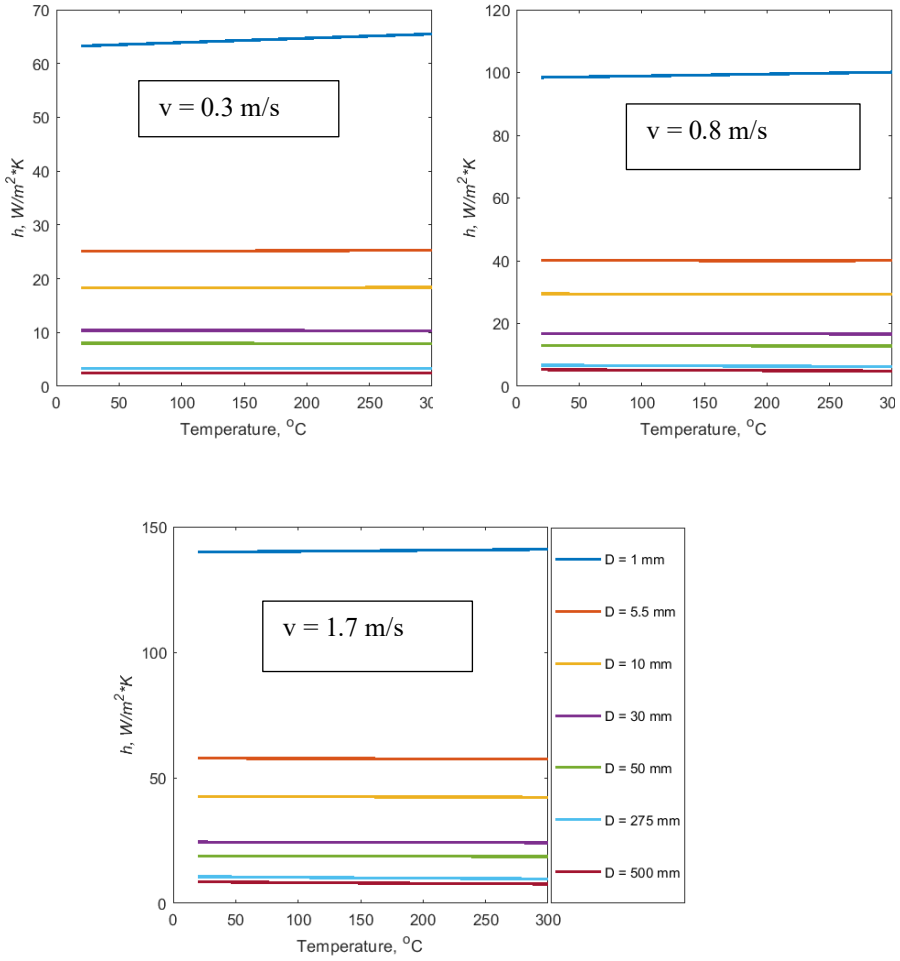

Fig. 110: Coefficient of convection heat transfer calculated for the temperature between 20 to 300 °C for component with diameter ranges from 1-10, 10-50, and 50-500mm.

Because of the significant changes in the diameter, these data were not inclusive; however, we decided to use them to perform curve fittings, and the results are illustrated in Fig. 111.

Table 59 lists the coefficients of curve fitting, and $\boldsymbol{R^2}$s more than 0.94 suggest strong confidence within these wide ranges of changes in diameters. The results of these curve fittings were incorporated into the developed numerical model in this dissertation.

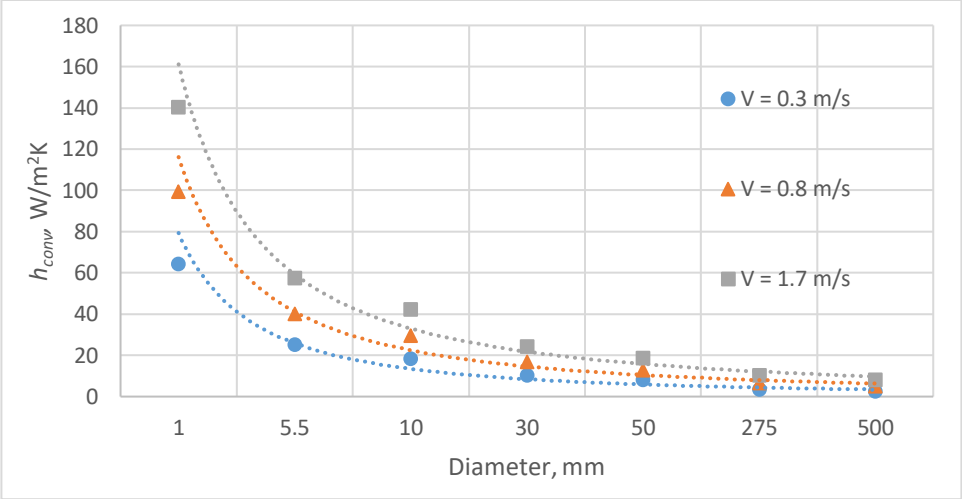

Fig. 111. Coefficient of convection heat transfer calculated for the temperature ranges from 0 to 300 ºC for component with diameter ranges from 1-10, 10-50, and 50-100mm.

9.1.3 Estimation of the coefficient of forced convection for a flat surface

In addition to objects with cylindrical shapes, we also studied flat surfaces by using the same length scale used for cylinders. The correlation proposed by Churchill [324] and Rose [340], which was accurate for all Prandtl numbers was used:

$$\overline{Nu_L} = 0.6774 \frac{Re_L^{1/2} Pr^{\frac{1}{3}}}{\left[1+\left(\frac{0.0468}{Pr}\right)^{\frac{2}{3}}\right]^{\frac{1}{4}}}. \quad (9\text{-}7)$$

The following table lists the average of the coefficient of convection over the temperature range (20 to 300ºC) for the different lengths of a flat plate.

Table 60: The average of convection heat transfer coefficients for flat surfaces, h_{conv} ($W/m^2\,^oC$)

Scale	Flat surface length range, mm	Choice length, mm	Velocity (m/s)		
			0.3	0.8	1.7
Small	1-10	1	66.077	107.904	157.295
		5.5	28.175	46.010	67.071
Medium	10-50	10	20.895	34.122	49.741
		30	12.064	19.700	28.718
Large	50-1000	50	9.345	15.260	22.245
		275	3.985	6.507	9.485
		500	2.955	4.826	7.034

		1000	2.090	3.412	4.974

The following figure, Fig. 112, depicts the changes of h_{conv} over the range of temperature for different size and velocity.

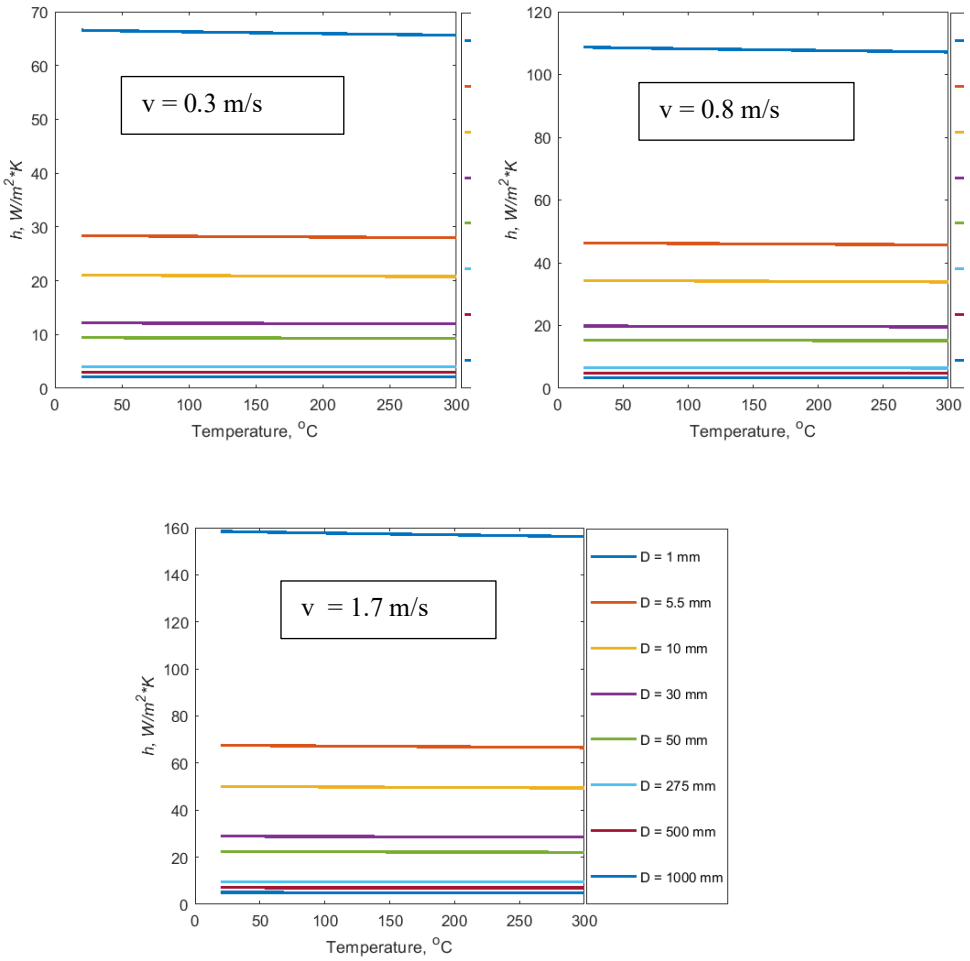

Fig. 112. Coefficient of convection heat transfer calculated for the temperature ranges from 20 to 300 °C in flat surfaces with length ranges from 1-10, 10-50, and 50-1000mm.

The average heat transfer coefficient for the range of the temperature is also shown in Table 60. Comparing the change over the temperature indicated error up to ±3%. This data was used for curve fitting for each velocity, as shown in the following table, Table 61, and Fig. 113.

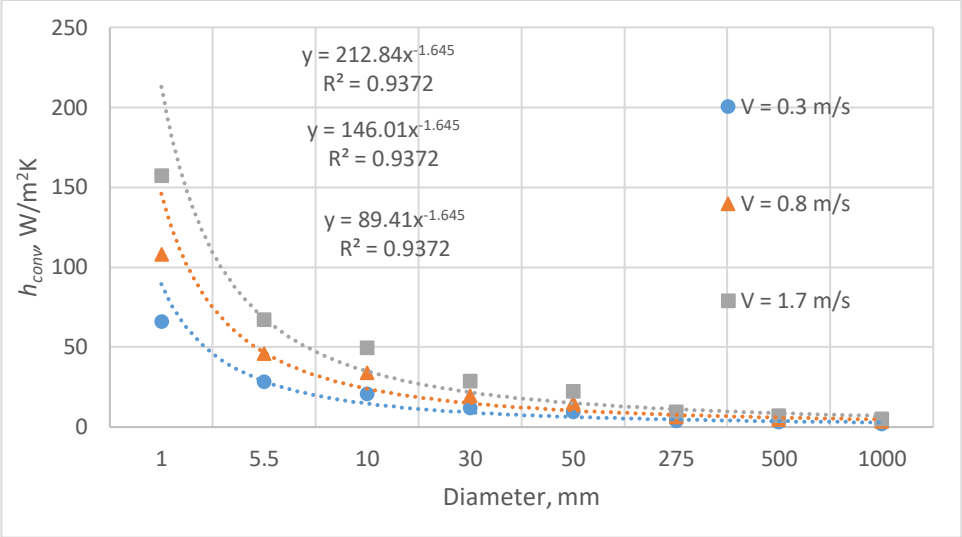

Fig. 113. Curve fitted graphs for the coefficient of convection heat transfer obtained for flat surfaces.

Table 61: The curve fitted coefficient for the average convection heat transfer coefficient for flat surface, h_{conv} ($W/m^2\,^oC$)

Velocity, m/s	Curve fit equation	R^2
0.3	$89.41 \times d^{-1.645}$	0.9372
0.8	$146.01 \times d^{-1.645}$	0.9372
1.7	$212.84 \times d^{-1.645}$	0.9372

9.1.4 Estimation of the coefficient of free convection

Free convection is more perplexing than forced convection because thermal inertia, fluid viscosity, buoyancy forces, and conduction in the fluid are entangled in free convections. Thus, gravity and change in density due to variations in temperature have to be accounted for [341, 342]. For these analyses, following the procedure above, we needed to study cylindrical and flat surfaces separately. Although the correlation for the flat surface could be used for a cylindrical

object, the diameter to height ratio (D/H) might alter this estimation. This variation is because of the transversal curvature effects in a slender cylinder [342].

- **Flat vertical surface**

One of the well-known correlations for flat vertical plates was obtained by Churchill and Chu [343]. This correlation is accurate for all Prandtl numbers within the Rayleigh number of 0.1 to 10^{12}:

$$\overline{Nu_{H-FP}} = \left\{ 0.825 + \frac{0.387 Ra_h^{\frac{1}{6}}}{\left[1 + \left(\frac{0.492}{Pr}\right)^{\frac{9}{16}}\right]^{\frac{8}{27}}} \right\}^2 . \quad (9\text{-}8)$$

The following table lists the average of the coefficient of convection over the temperature range (25 to 300 ^{o}C) for the different lengths of a flat plate.

Table 62: The average of coefficients of free convection heat transfer for flat vertical surfaces with different heights, h_{conv} ($W/m^2\,^oC$)

Scale	Flat Vertical plate category, mm	Choice height of the plate, mm	h_{conv} ($W/m^2\,^oC$)
Small	1-10	1	25.888
		5.5	6.0152
Medium	10-50	10	3.789
		30	1.776
Large	50-1000	50	1.308
		275	0.595
		500	0.490
		1000	0.401

The following figure, Fig. 114, depicts the changes of h_{conv} over the range of temperature for different lengths.

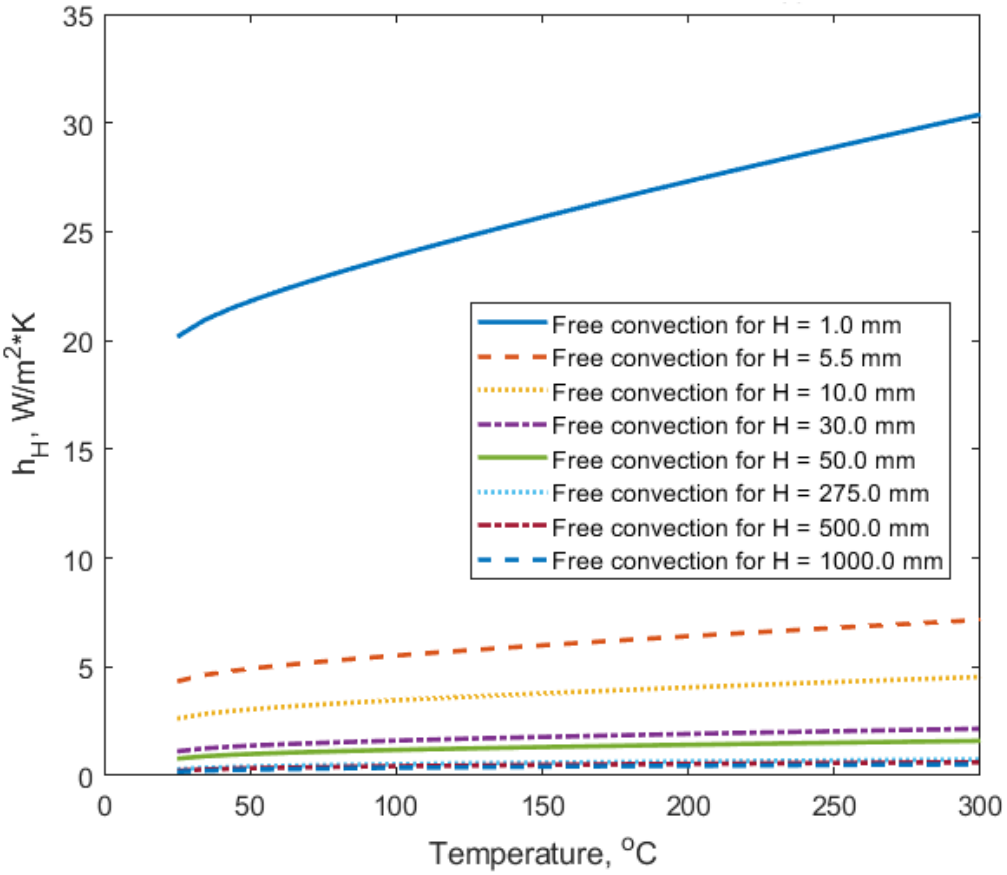

Fig. 114. Coefficient of free convection heat transfer calculated for the temperature ranges from 25 to 300 °C for a flat vertical plate.

The average heat transfer coefficient shown in Table 62 was used for curve fitting over the plate height, and the result is listed in the following table, Table 63; the associated graph is illustrated in Fig. 115.

Table 63: The curve fit for the average coefficient of free convection heat transfer for a vertical flat plate, h_{conv} ($W/m^2\,^oC$)

Height range, m	Curve fit equation	R^2
1.0-1000.0 mm	$17.247\ H^{-0.588}$	0.9677

This curve fitting should be used cautiously for a small height between 1 to 5 mm since the curve fit exhibited large error margins of 35 to 5%; however, above 5.5 mm, the error is significantly lower (<2%).

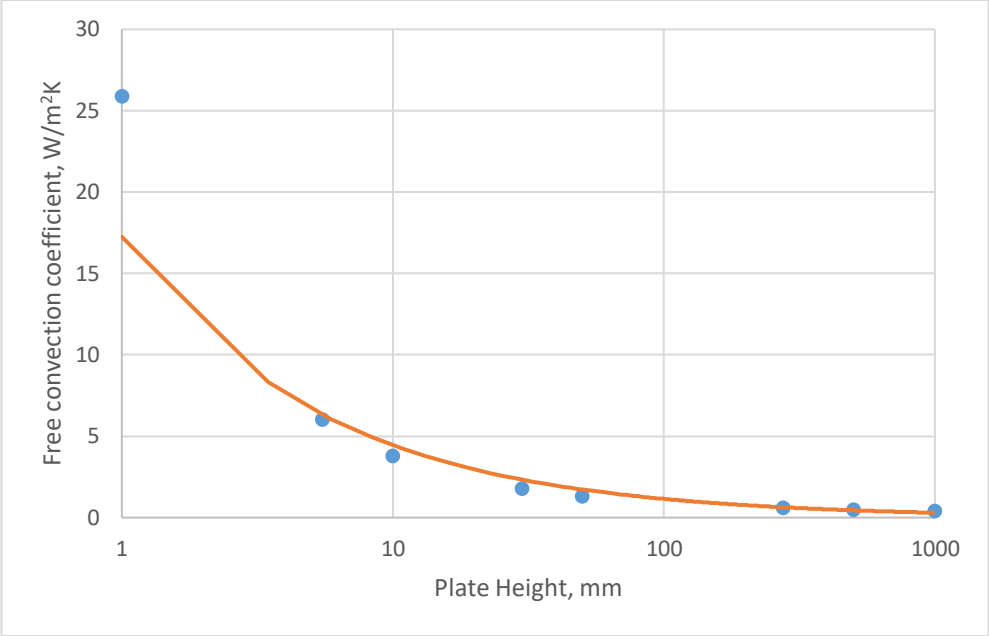

Fig. 115. Curve fitted graph for the coefficient of natural convection heat transfer calculated for the vertical flat surfaces ranges from 1-10, 10-50, and 50-100mm.

- **Vertical cylinder**

If the ratio of height to diameter, H/D, is low, the coefficient of convection is slightly higher than the flat plate [342]. However, if the H/D ratio is smaller than 20, the flat plate approximation can be used to obtain the convection coefficient. Otherwise, the following correlation can be used for laminar flow to correct for the effect of curvature :

$$\overline{Nu_{C-H}} = \overline{Nu_{H-FP}}\left\{1 + 0.3\left[32^{0.5} Gr_H^{-0.25}\left(\frac{H}{D}\right)\right]^{0.909}\right\}, \quad (9\text{-}9)$$

where Nu_{H-FP} is the Nusselt for the flat plate and Nu_{C-H} is the corrected Nusselt for a curved surface. In general, application for 3D printing, fabrication of slender parts is avoided. Thus, it is safe to use the approximation of the flat vertical plate for cylindrical components, except for filament or diameter smaller than 3.0 mm.

9.2 Concept and fundamentals of DoE

Design of Experiments (DoE) is employed to understand cause-and-effect relationships in complex processes. The process begins with defining experiments, knowing variables (causes), and examining their effects to find a correlation between causes and effects. The process may be tedious and endless. However, mathematics and statistics help to comprehend the data efficiently while planing optimized trials and experiments. The Design of Experiment (DoE) is a systematic method to find the possible relationship between factors and outputs based on statistical optimization [317]. Although there may not be an exact way to understand and list all the variables and find whether they are controllable or uncontrollable factors, different DoE techniques help to design the process of data extraction better to reveal the relationship between controllable variables and outputs convincingly.

DoE is generally used for unraveling the root causes of problems and determining their significance and importance on the outputs [344]. The DoE also can be used for optimization processes when the variables are sought to deliver the best and most desirable outputs [85, 192, 285, 299, 302, 306, 345].

The DoE can be used with different purposes in research and industries. In research, it aims to perceive the interactions between factors and outputs, while in industries, it applies to the derivation of desirable outputs without focusing on the interactions per se. Thus, when in research the maximum of the variable is usually limited (e.g., 5 and 6) [346], in industries one may have many more variables (e.g., 16 to 32) [347, 348].

The goal of our study was to understand how build parameters affect distortion, moduli of elasticity, residual stresses, density, and bonding performance in 3D printed components by FDM technology. We aimed to reach an empirical approximation of the outputs as a function of some prominent build parameters.

In our study, we also looked for quadratic effects and interconnections among parameters to define the empirical relationship. In this case, if one assumes there are three variables as $\boldsymbol{X}_1, \boldsymbol{X}_3$ and $\boldsymbol{X}_3$, the empirical relationship is defined as:

$$\boldsymbol{Y} = \boldsymbol{\beta}_0 + \boldsymbol{\beta}_1\boldsymbol{X}_1 + \boldsymbol{\beta}_2\boldsymbol{X}_2 + \boldsymbol{\beta}_3\boldsymbol{X}_3 + \boldsymbol{\beta}_{12}\boldsymbol{X}_1\boldsymbol{X}_2 + \boldsymbol{\beta}_{13}\boldsymbol{X}_1\boldsymbol{X}_3 + \boldsymbol{\beta}_{23}\boldsymbol{X}_2\boldsymbol{X}_3 + \boldsymbol{\beta}_{123}\boldsymbol{X}_1\boldsymbol{X}_2\boldsymbol{X}_3 + \boldsymbol{\beta}_{11}\boldsymbol{X}_1^2 + \boldsymbol{\beta}_{22}\boldsymbol{X}_2^2 + \boldsymbol{\beta}_{33}\boldsymbol{X}_3^2 + \epsilon, \tag{9-10}$$

where Y response (output), X_i are variables, $\boldsymbol{\beta}_{ijk}$ are constants, and ϵ experimental error. Three-way interaction is usually not considered when the quadratic effects are included in the design [317]. The constants of the Eq. (9-10), $\boldsymbol{\beta}_{ijk}$, are determined using the mean square error minimization.

The DoE is applied to vast applications, including comparative experiments, screening experiments, regression modeling, goal achievement (e.g., minimization or maximization of a specific response and multiple goals achievement), and variation reduction [317].

The factorial design is the basic approach to define a DoE in which the level of the factors are defined according to the maximum and minimum permissible values. The classical method is using the full factorial design. A complex engineering problem usually deals with a significant number of parameters, and using full factorial can drastically and exponentially increase iterations while the factors are increasing. Thus, other methods, such as central composite design (CCD) with similar effectiveness but remarkably fewer iterations are applied. CCD fits the second-order model with the minimum possible iterations [344, 349]. For example, if there are K factors and each factor has three levels, which represent the high, medium, and lower, limits of the variables, then the total number of iterations sums up to 3^K. Assuming five variables, the total iterations is 243. However, in this design, instead of using factorial design,

we used cubical CCD known as face-centered central composite design (FCCCD) with three levels for each factor.

9.3 The results of the modal analyses

9.3.1 Modal analyses of the central part of the testing artifacts for isotropic material

Table 64: The sensitivity analyses on the effect of physical and mechanical properties on the natural frequency of the center part (beam section) of the testing artifacts for isotropic material.

Mode	Mode specification	ρ, kg/m^3	ω, Hz	B_C, m	ω, Hz	W_C, m	ω, Hz	L_C, m	ω, Hz	t_C, m	ω, Hz	ν	ω, Hz
1	$Mode_{00}$	988	138.85	0.0057	136.52	0.00665	135.27	0.0494	148.66	0.0019	127.23	0.323	135.15
2			475.59		467.74		441.15		507.95		458.17		463.23
3	$Mode_{01}$		980.17		956.45		954.87		1054.7		905.17		954.09
4	$Mode_{10}$		1629		1601.7		1625.7		1661.4		1514.2		1594.1
5	$Mode_{02}$		2772.6		2704.5		2700.5		2970.1		2567		2698.4
6			3289		3208		3082.4		3515.1		3191.8		3203.5
7	$Mode_{03}$		5164.7		5038.4		5030		5455.1		4819.8		5026.2
8			5888		5730		5929.4		6069.1		5504		5762.1
9			6446.2		6299.7		6281.2		6709.8		6180.9		6276.9
10			8557		8350.4		8059.9		9070.9		8315.9		8333.2
1	$Mode_{00}$	1040	135.33	0.006	135.33	0.007	135.33	0.052	135.33	0.002	135.33	0.34	135.41
2			463.55		463.55		463.55		463.55		463.55		463.66
3	$Mode_{01}$		955.35		955.35		955.35		955.35		955.35		956.02
4	$Mode_{10}$		1587.8		1587.8		1587.8		1587.8		1587.8		1594.5
5	$Mode_{02}$		2702.4		2702.4		2702.4		2702.4		2702.4		2704.8
6			3205.7		3205.7		3205.7		3205.7		3205.7		3206.6
7	$Mode_{03}$		5034		5034		5034		5034		5034		5039.3
8			5739		5739		5739		5739		5739		5764.3
9			6282.9		6282.9		6282.9		6282.9		6282.9		6285.5
10			8340.3		8340.3		8340.3		8340.3		8340.3		8341.9
1	$Mode_{00}$	1092	132.07	0.0063	134.2	0.00735	135.4	0.0546	123.76	0.0021	143.48	0.357	135.52
2			452.38		459.54		485.81		424.76		468.53		463.48
3	$Mode_{01}$		932.32		954.43		955.82		869.3		1005.5		956.94
4	$Mode_{10}$		1549.5		1574.7		1549.9		1520.8		1659.7		1594.9
5	$Mode_{02}$		2637.2		2700.7		2704.2		2467.9		2837		2708.7
6			3128.4		3203.6		3326.7		2935.1		3218.9		3206
7	$Mode_{03}$		4912.6		5032		5037.9		4648.5		5234.2		5048.1
8			5600.6		5749.8		5559.4		5444		5967		5766.3
9			6131.5		6266		6284.6		5919.8		6388.8		6286.7
10			8139.3		8329.6		8608.8		7691.1		8363.5		8342.3

Mode	Mode specification	G Pa	ω, Hz	E, Pa	ω, Hz
1	$Mode_{00}$	79 04	135.9	21 18	135.9

2			464.17		464.17
3	$Mode_{01}$		959.51		959.51
4	$Mode_{10}$		1551.5		1551.5
5	$Mode_{02}$		2715.8		2715.8
6			3201.5		3201.5
7	$Mode_{03}$		5062.4		5062.4
8			5612.8		5612.8
9			6298.3		6298.3
10			8309.6		8309.6
1	$Mode_{00}$	832090000	135.33	2230000000	135.33
2			463.55		463.55
3	$Mode_{01}$		955.35		955.35
4	$Mode_{10}$		1587.8		1587.8
5	$Mode_{02}$		2702.4		2702.4
6			3205.7		3205.7
7	$Mode_{03}$		5034		5034
8			5739		5739
9			6282.9		6282.9
10			8340.3		8340.3
1	$Mode_{00}$	873690000	134.95	2341500000	134.95
2			463.25		463.25
3	$Mode_{01}$		952.56		952.56
4	$Mode_{10}$		1623.7		1623.7
5	$Mode_{02}$		2693.4		2693.4
6			3211.4		3211.4
7	$Mode_{03}$		5015		5015
8			5864.4		5864.4
9			6272.9		6272.9
10			8372.3		8372.3

9.3.2 Modal analyses of the wing part of the testing artifacts for isotropic material

Table 65: The sensitivity analyses on the effect of physical and mechanical properties on the natural frequency of the wing part (plate section) of the testing artifacts for isotropic material.

Mode	Mode specification	ρ, kg/m^3	ω, Hz	B_w, m	ω, Hz	W_w, m	ω, Hz	L_w, m	ω, Hz	t_w, m	ω, Hz	ν	ω, Hz
1	$Mode_{00}$	988	173.11	0.0057	169.18	0.00665	168.01	0.0494	186.65	0.0019	160.34	0.323	168.48
2	$Mode_{10}$		546.97		532.31		543.27		569.52		508.37		534.99
3	$Mode_{01}$		1098.8		1063.9		1030.2		1175.1		1023.9		1071
4	$Mode_{11}$		1104.4		1076.9		1074		1190.7		1070.9		1075
5			1433.4		1387		1410.1		1532.7		1331.7		1397.8
6	$Mode_{20}$		2295		2214.7		2364.7		2324.1		2135.6		2243
7	$Mode_{02}$		3111.2		3031.3		3032.2		3347.9		2889.7		3028.4
8	$Mode_{00}$		3242.1		3128.9		3251.6		3370		3023.7		3170.6
9	$Mode_{30}$		3565.3		3467.5		3532		3789.2		3316.3		3478.7
10			3779.4		3634.2		3592.8		4006.1		3683.4		3687.6
1	$Mode_{00}$	1040	168.72	0.006	168.72	0.007	168.72	0.052	168.72	0.002	168.72	0.34	168.72
2	$Mode_{10}$		533.12		533.12		533.12		533.12		533.12		533.12
3	$Mode_{01}$		1071		1071		1071		1071		1071		1071

4	$Mode_{11}$		1076.4		1076.4		1076.4		1076.4		1076.4
5			1397.1		1397.1		1397.1		1397.1		1397.1
6	$Mode_{20}$		2236.9		2236.9		2236.9		2236.9		2236.9
7	$Mode_{02}$		3032.4		3032.4		3032.4		3032.4		3032.4
8	$Mode_{00}$		3160		3160		3160		3160		3160
9	$Mode_{30}$		3475.1		3475.1		3475.1		3475.1		3475.1
10			3683.7		3683.7		3683.7		3683.7		3683.7
1	$Mode_{00}$	1092	164.66	0.0063	168.27	0.00735	169.39	0.0546	153.37	0.0021	177.09	0.357	168.98
2	$Mode_{10}$		520.28		533.91		523.31		500.55		557.6		531.32
3	$Mode_{01}$		1045.2		1076		1078.6		977.75		1071.1		1071.1
4	$Mode_{11}$		1050.5		1077.6		1110.6		979.93		1128.6		1077.9
5			1363.4		1407.1		1384.8		1277.8		1461.8		1396.5
6	$Mode_{20}$		2183		2258.6		2120.3		2151.8		2336.6		2231.1
7	$Mode_{02}$		2959.3		3033.4		3033.6		2759.6		3173.4		3036.6
8	$Mode_{00}$		3083.9		3190.8		3060.1		2945.2		3293.2		3149.5
9	$Mode_{30}$		3391.3		3482.5		3438.5		3223.3		3631.6		3472.2
10			3594.9		3734.6		3771.3		3388.1		3683.9		3680

Mode	**Mode specification**	***G*, Pa**	***ω*, Hz**	***E*, Pa**	***ω*, Hz**
1	$Mode_{00}$	790480000	169.92	2118500000	163.6
2	$Mode_{10}$		526.08		527.16
3	$Mode_{01}$		1071.7		1044.1
4	$Mode_{11}$		1083.3		1044.4
5			1396		1365.3
6	$Mode_{20}$		2213.7		2204.4
7	$Mode_{02}$		3052.2		2942
8	$Mode_{00}$		3116.5		3120.3
9	$Mode_{30}$		3468.2		3405.6
10			3669.6		3606
1	$Mode_{00}$	832090000	168.72	2230000000	168.72
2	$Mode_{10}$		533.12		533.12
3	$Mode_{01}$		1071		1071
4	$Mode_{11}$		1076.4		1076.4
5			1397.1		1397.1
6	$Mode_{20}$		2236.9		2236.9
7	$Mode_{02}$		3032.4		3032.4
8	$Mode_{00}$		3160		3160
9	$Mode_{30}$		3475.1		3475.1
10			3683.7		3683.7
1	$Mode_{00}$	873690000	167.88	2341500000	174.05
2	$Mode_{10}$		540.47		539.4
3	$Mode_{01}$		1071.2		1098.1
4	$Mode_{11}$		1071.7		1109.7
5			1400.5		1430.4
6	$Mode_{20}$		2260.4		2269.5
7	$Mode_{02}$		3019		3126.4
8	$Mode_{00}$		3199.5		3195.6
9	$Mode_{30}$		3492.9		3553.9
10			3698.9		3760.8

9.3.3 Modal analyses on the central part for Orthotropic material properties

Table 66: The sensitivity analyses on the effect of physical and mechanical properties on the natural frequency of the center part (beam section) of the testing artifacts for orthotropic materials.

Mode	Mode specification	ρ, kg/m^3	ω, Hz	B_C, m	ω, Hz	W_C, m	ω, Hz	L_C, m	ω, Hz	t_C, m	ω, Hz	ν_{23}	ω, Hz
1	$Mode_{00}$	988	138.85	0.0057	136.52	0.00665	135.27	0.0494	148.66	0.0019	127.23	0.323	0.323
2			475.59		467.74		441.15		507.95		458.17		0.323
3	$Mode_{01}$		980.17		956.45		954.87		1054.7		905.17		0.323
4	$Mode_{10}$		1629		1601.7		1625.7		1661.4		1514.2		0.323
5	$Mode_{02}$		2772.6		2704.5		2700.5		2970.1		2567		0.323
6			3289		3208		3082.4		3515.1		3191.8		0.323
7	$Mode_{03}$		5164.7		5038.4		5030		5455.1		4819.8		0.323
8			5888		5730		5929.4		6069.1		5504		0.323
9			6446.2		6299.7		6281.2		6709.8		6180.9		0.323
10			8557		8350.4		8059.9		9070.9		8315.9		0.323
1	$Mode_{00}$	1040	135.33	0.006	135.33	0.007	135.33	0.052	135.33	0.002	135.33	0.34	0.34
2			463.55		463.55		463.55		463.55		463.55		0.34
3	$Mode_{01}$		955.35		955.35		955.35		955.35		955.35		0.34
4	$Mode_{10}$		1587.8		1587.8		1587.8		1587.8		1587.8		0.34
5	$Mode_{02}$		2702.4		2702.4		2702.4		2702.4		2702.4		0.34
6			3205.7		3205.7		3205.7		3205.7		3205.7		0.34
7	$Mode_{03}$		5034		5034		5034		5034		5034		0.34
8			5739		5739		5739		5739		5739		0.34
9			6282.9		6282.9		6282.9		6282.9		6282.9		0.34
10			8340.3		8340.3		8340.3		8340.3		8340.3		0.34
1	$Mode_{00}$	1092	132.07	0.0063	134.2	0.00735	135.4	0.0546	123.76	0.0021	143.48	0.357	0.357
2			452.38		459.54		485.81		424.76		468.53		0.357
3	$Mode_{01}$		932.32		954.43		955.82		869.3		1005.5		0.357
4	$Mode_{10}$		1549.5		1574.7		1549.9		1520.8		1659.7		0.357
5	$Mode_{02}$		2637.2		2700.7		2704.2		2467.9		2837		0.357
6			3128.4		3203.6		3326.7		2935.1		3218.9		0.357
7	$Mode_{03}$		4912.6		5032		5037.9		4648.5		5234.2		0.357
8			5600.6		5749.8		5559.4		5444		5967		0.357
9			6131.5		6266		6284.6		5919.8		6388.8		0.357
10			8139.3		8329.6		8608.8		7691.1		8363.5		0.357

Mode	Mode specification	ν_{12}	ω, Hz	G_{23}, Pa	ω, Hz	G_{12}, Pa	ω, Hz	E_2, Pa	ω, Hz	E_1, Pa	ω, Hz
1	$Mode_{00}$	0.323	135.21	790480000	135.33	790480000	135.31	2118500000	135.29	2118500000	131.98
2			463.34		463.55		463.1		463.46		452.32
3	$Mode_{01}$		954.41		955.34		954.87		955.02		931.97
4	$Mode_{10}$		1587.5		1587.7		1550		1587.5		1585.7
5	$Mode_{02}$		2699		2702.3		2699.5		2701.2		2637.9
6			3204.1		3205.7		3193.6		3205.1		3136.6
7	$Mode_{03}$		5026.4		5033.8		5025.7		5030.8		4917.6
8			5737.3		5737.7		5604.5		5736.5		5730.5

9			6279.1		6282.9		6279.1		6281.6		6128.9
10			8336		8340.1		8289		8338.8		8179.3
1	$Mode_{00}$		135.33		135.33		135.33		135.33		135.33
2			463.55		463.55		463.55		463.55		463.55
3	$Mode_{01}$		955.35		955.35		955.35		955.35		955.35
4	$Mode_{10}$		1587.8		1587.8		1587.8		1587.8		1587.8
5	$Mode_{02}$	0.34	2702.4	832090000	2702.4	832090000	2702.4	2230000000	2702.4	2230000000	2702.4
6			3205.7		3205.7		3205.7		3205.7		3205.7
7	$Mode_{03}$		5034		5034		5034		5034		5034
8			5739		5739		5739		5739		5739
9			6282.9		6282.9		6282.9		6282.9		6282.9
10			8340.3		8340.3		8340.3		8340.3		8340.3
1	$Mode_{00}$		135.46		135.34		135.36		135.38		138.61
2			463.77		463.55		463.95		463.64		474.48
3	$Mode_{01}$		956.35		955.36		955.8		955.69		978.15
4	$Mode_{10}$		1588.1		1587.9		1624.7		1588.1		1589.9
5	$Mode_{02}$	0.357	2705.9	873690000	2702.4	873690000	2705	2341500000	2703.6	2341500000	2765.2
6			3207.4		3205.7		3216.9		3206.3		3272.5
7	$Mode_{03}$		5042		5034.1		5041.6		5037.1		5147.2
8			5740.7		5740.1		5870		5741.3		5747.3
9			6287.1		6283		6286.5		6284.3		6433.1
10			8344.9		8340.6		8387.7		8341.9		8494.8

9.3.4 Modal analyses on the wing part for orthotropic material properties

Table 67: The sensitivity analyses on the effect of physical and mechanical properties on the natural frequency of the wing part (plate section) of the testing artifacts for orthotropic materials.

Mode	Mode specification	ρ, kg/m^3	ω, Hz	B_w, m	ω, Hz	W_w, m	ω, Hz	L_w, m	ω, Hz	t_w, m	ω, Hz	ν_{23}	ω, Hz
1	$Mode_{00}$		173.11		169.18		168.01		186.65		160.34		168.23
2	$Mode_{10}$		546.97		532.31		543.27		569.52		508.37		532.45
3	$Mode_{01}$		1098.8		1063.9		1030.2		1175.1		1023.9		1069.4
4	$Mode_{11}$		1104.4		1076.9		1074		1190.7		1070.9		1073.5
5		988	1433.4	0.0057	1387	0.00665	1410.1	0.0494	1532.7	0.0019	1331.7	0.323	1393.9
6	$Mode_{20}$		2295		2214.7		2364.7		2324.1		2135.6		2244.5
7	$Mode_{02}$		3111.2		3031.3		3032.2		3347.9		2889.7		3022.2
8	$Mode_{00}$		3242.1		3128.9		3251.6		3370		3023.7		3159.9
9	$Mode_{30}$		3565.3		3467.5		3532		3789.2		3316.3		3468
10			3779.4		3634.2		3592.8		4006.1		3683.4		3683.3
1	$Mode_{00}$		168.72		168.72		168.72		168.72		168.72		168.72
2	$Mode_{10}$		533.12		533.12		533.12		533.12		533.12		533.12
3	$Mode_{01}$		1071		1071		1071		1071		1071		1071
4	$Mode_{11}$		1076.4		1076.4		1076.4		1076.4		1076.4		1076.4
5		1040	1397.1	0.006	1397.1	0.007	1397.1	0.052	1397.1	0.002	1397.1	0.34	1397.1
6	$Mode_{20}$		2236.9		2236.9		2236.9		2236.9		2236.9		2236.9
7	$Mode_{02}$		3032.4		3032.4		3032.4		3032.4		3032.4		3032.4
8	$Mode_{00}$		3160		3160		3160		3160		3160		3160
9	$Mode_{30}$		3475.1		3475.1		3475.1		3475.1		3475.1		3475.1
10			3683.7		3683.7		3683.7		3683.7		3683.7		3683.7
1	$Mode_{00}$	1092	164.66	0.0063	168.27	0.00735	169.39	0.0546	153.37	0.0021	177.09	0.357	169.07
2	$Mode_{10}$		520.28		533.9		523.31		500.55		557.6		533.7

3	$Mode_{01}$		1045.2		1076		1078.6		977.75		1071.1		1071.5
4	$Mode_{11}$		1050.5		1077.6		1110.6		979.93		1128.6		1078.4
5			1363.4		1407.1		1384.8		1277.8		1461.8		1399.6
6	$Mode_{20}$		2183		2258.6		2120.3		2151.8		2336.6		2226.6
7	$Mode_{02}$		2959.3		3033.4		3033.6		2759.6		3173.4		3040.7
8	$Mode_{00}$		3083.9		3190.8		3060.1		2945.2		3293.2		3158.7
9	$Mode_{30}$		3391.3		3482.5		3438.5		3223.3		3631.6		3480.7
10			3594.9		3734.6		3771.3		3388.1		3683.9		3680.2

Mode	**Mode specification**	ν_{12}	**ω, Hz**	G_{23}, **P**	**ω, Hz**	G_{12}, **Pa**	**ω, Hz**	E_2, **Pa**	**ω, Hz**	E_1, **Pa**	**ω, Hz**
1	$Mode_{00}$	0.323	168.47	790480000	168.72	790480000	168.67	2118500000	168.63	2118500000	164.6
2	$Mode_{10}$		532.66		533.06		523.83		532.5		529.46
3	$Mode_{01}$		1069.7		1071		1065.8		1068.7		1050.7
4	$Mode_{11}$		1074.8		1076.4		1075.5		1075.7		1051.1
5			1395.4		1396.1		1387.5		1395.6		1372.7
6	$Mode_{20}$		2236.4		2236.4		2210.9		2209.5		2233.3
7	$Mode_{02}$		3026.8		3032.3		3025.4		3030.4		2964.4
8	$Mode_{00}$		3158.5		3158.1		3109.6		3149.7		3136.2
9	$Mode_{30}$		3470.8		3473.6		3445.7		3470.5		3424.7
10			3681.2		3683.7		3657.5		3670.7		3628.4
1	$Mode_{00}$	0.34	168.72	832090000	168.72	832090000	168.72	2230000000	168.72	2230000000	168.72
2	$Mode_{10}$		533.12		533.12		533.12		533.12		533.12
3	$Mode_{01}$		1071		1071		1071		1071		1071
4	$Mode_{11}$		1076.4		1076.4		1076.4		1076.4		1076.4
5			1397.1		1397.1		1397.1		1397.1		1397.1
6	$Mode_{20}$		2236.9		2236.9		2236.9		2236.9		2236.9
7	$Mode_{02}$		3032.4		3032.4		3032.4		3032.4		3032.4
8	$Mode_{00}$		3160		3160		3160		3160		3160
9	$Mode_{30}$		3475.1		3475.1		3475.1		3475.1		3475.1
10			3683.7		3683.7		3683.7		3683.7		3683.7
1	$Mode_{00}$	0.357	169	873690000	168.73	873690000	168.78	2341500000	168.81	2341500000	172.75
2	$Mode_{10}$		533.62		533.19		542.1		533.71		536.65
3	$Mode_{01}$		1072.4		1071		1075.8		1073.1		1090.2
4	$Mode_{11}$		1078.1		1076.4		1077.2		1077.1		1101.5
5			1398.9		1398		1406.4		1398.5		1420.8
6	$Mode_{20}$		2237.5		2237.4		2262		2263.2		2240.4
7	$Mode_{02}$		3038.4		3032.4		3038.9		3034.4		3098.6
8	$Mode_{00}$		3161.7		3161.8		3205.5		3169.5		3179.1
9	$Mode_{30}$		3479.7		3476.4		3506.5		3479.4		3528.3
10			3686.4		3683.7		3707.9		3696.3		3736.7

9.4 Finite Difference Model

For details on the applied methodology for Finite Difference (FD), please refer to the following publication:

- Pooladvand, K., and Furlong, C., 2017, "Thermo-mechanical Investigation of Fused Deposition Modeling by Computational and Experimental Methods," Mechanics of Composite and Multi-functional Materials, Volume 7, Springer, pp. 45-54.

9.5 Statistical analyses of density, density difference, and contact quality

9.5.1 Statistical analyses on the gathered data for density

Source	LogWorth	PValue
Layer thickness (0.09,0.29)	4.440	0.00004
Extruder Speed (-50,50)	2.007	0.00983
Extruder Temperature*Layer thickness	1.858	0.01385
Layer thickness*Fan Speed	1.770	0.01697
Extruder Temperature (240,290)	1.561	0.02747 ^
Extruder Temperature*Extruder Speed	1.515	0.03054
Heated Bed Temperature*Fan Speed	1.443	0.03608
Heated Bed Temperature*Extruder Speed	1.376	0.04211
Extruder Temperature*Fan Speed	1.288	0.05158
Extruder Speed*Fan Speed	0.690	0.20431
Layer thickness*Extruder Speed	0.682	0.20785
Heated Bed Temperature*Layer thickness	0.672	0.21298
Heated Bed Temperature (40,100)	0.402	0.39642 ^
Extruder Temperature*Extruder Temperature	0.327	0.47046
Fan Speed (0,100)	0.255	0.55564 ^
Fan Speed*Fan Speed	0.207	0.62132
Extruder Temperature*Heated Bed Temperature	0.186	0.65191
Extruder Speed*Extruder Speed	0.119	0.75988
Layer thickness*Layer thickness	0.073	0.84546
Heated Bed Temperature*Heated Bed Temperature	0.067	0.85689

Source	DF	Sum of Squares	Mean Square	F Ratio
Lack Of Fit	6	420.38602	70.0643	68.8957
Pure Error	1	1.01696	1.0170	**Prob > F**
Total Error	7	421.40298		0.0920
				Max RSq
				0.9999

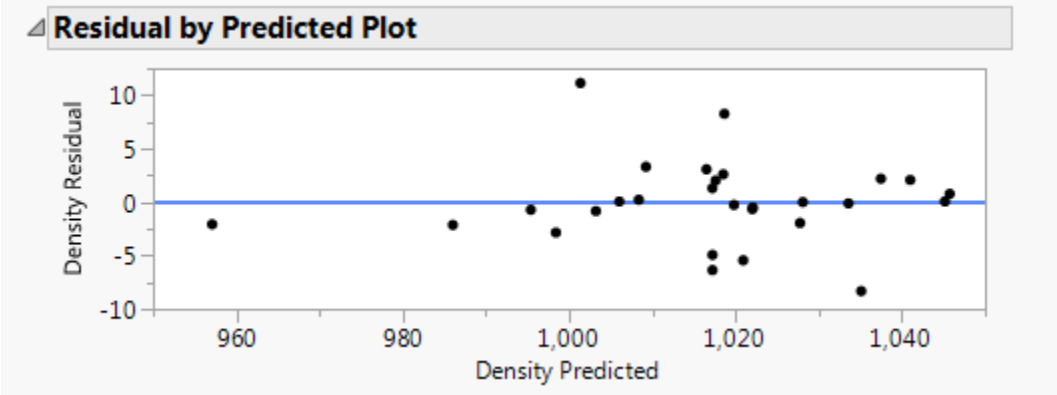

RSquare	0.95788
RSquare Adj	0.837538
Root Mean Square Error	7.758893
Mean of Response	1016.67
Observations (or Sum Wgts)	28

Term	Estimate	Std Error	t Ratio	Prob>|t|	Lower 95%	Upper 95%	F Ratio
Intercept	1017.2268	2.702299	376.43	<.0001*	1010.8369	1023.6167	
Extruder Temperature (240,290)	5.0760433	1.828789	2.78	0.0275*	0.7516452	9.4004414	7.7041
Heated Bed Temperature (40,100)	-1.651817	1.828789	-0.90	0.3964	-5.976215	2.6725814	0.8158
Layer thickness (0.09,0.29)	-16.87059	1.828789	-9.23	<.0001*	-21.19499	-12.54619	85.1008
Extruder Speed (-50,50)	-6.422419	1.828789	-3.51	0.0098*	-10.74682	-2.098021	12.3330
Fan Speed (0,100)	1.1316653	1.828789	0.62	0.5556	-3.192733	5.4560634	0.3829
Extruder Temperature*Heated Bed Temperature	0.9137776	1.939723	0.47	0.6519	-3.672939	5.5004945	0.2219
Extruder Temperature*Layer thickness	6.3245205	1.939723	3.26	0.0139*	1.7378037	10.911237	10.6310
Heated Bed Temperature*Layer thickness	-2.657626	1.939723	-1.37	0.2130	-7.244343	1.9290907	1.8772
Extruder Temperature*Extruder Speed	-5.241378	1.939723	-2.70	0.0305*	-9.828095	-0.654661	7.3015
Heated Bed Temperature*Extruder Speed	4.813591	1.939723	2.48	0.0421*	0.2268742	9.4003079	6.1583
Layer thickness*Extruder Speed	2.6913959	1.939723	1.39	0.2079	-1.895321	7.2781127	1.9252
Extruder Temperature*Fan Speed	-4.545771	1.939723	-2.34	0.0516	-9.132487	0.0409463	5.4921
Heated Bed Temperature*Fan Speed	5.0188762	1.939723	2.59	0.0361*	0.4321593	9.605593	6.6947
Layer thickness*Fan Speed	6.0418776	1.939723	3.11	0.0170*	1.4551607	10.628594	9.7021
Extruder Speed*Fan Speed	-2.715146	1.939723	-1.40	0.2043	-7.301863	1.871571	1.9593
Extruder Temperature*Extruder Temperature	-3.782088	4.957708	-0.76	0.4705	-15.5052	7.9410298	0.5820
Heated Bed Temperature*Heated Bed Temperature	0.927576	4.957708	0.19	0.8569	-10.79554	12.650693	0.0350
Layer thickness*Layer thickness	1.0028155	4.957708	0.20	0.8455	-10.7203	12.725933	0.0409
Extruder Speed*Extruder Speed	-1.575756	4.957708	-0.32	0.7599	-13.29887	10.147361	0.1010
Fan Speed*Fan Speed	2.5613765	4.957708	0.52	0.6213	-9.161741	14.284494	0.2669

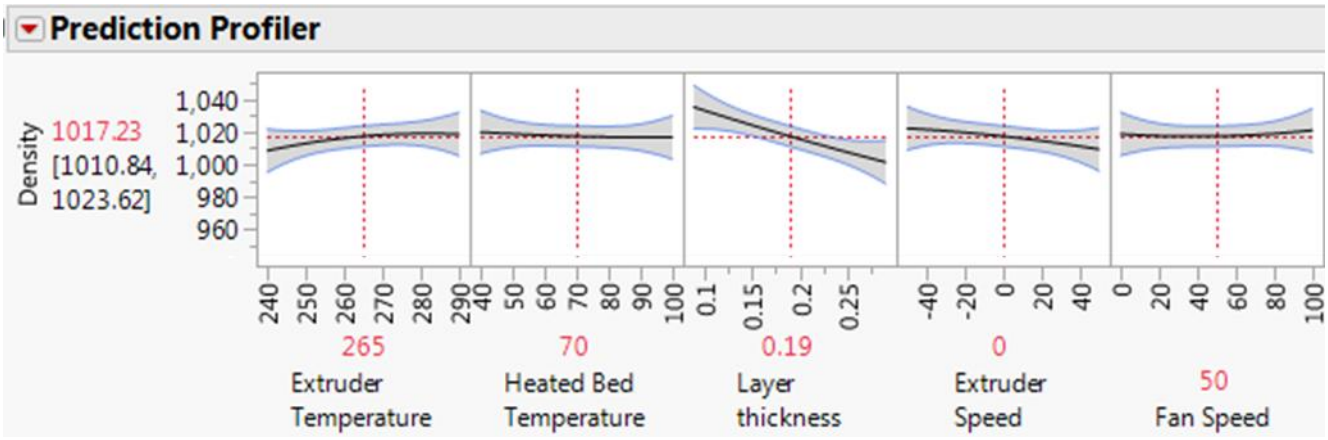

9.5.2 Statistical analyses on the gathered data of reduced variables for density

Source	LogWorth	PValue
Layer thickness (0.09,0.29)	7.538	0.00000
Extruder Speed (-50,50)	3.180	0.00066
Extruder Temperature*Layer thickness	2.924	0.00119
Layer thickness*Fan Speed	2.773	0.00169
Extruder Temperature (240,290)	2.418	0.00382 ^
Extruder Temperature*Extruder Speed	2.341	0.00456
Heated Bed Temperature*Fan Speed	2.220	0.00603
Heated Bed Temperature*Extruder Speed	2.108	0.00781
Extruder Temperature*Fan Speed	1.962	0.01093
Extruder Speed*Fan Speed	1.001	0.09987
Layer thickness*Extruder Speed	0.989	0.10257
Heated Bed Temperature*Layer thickness	0.973	0.10652
Heated Bed Temperature (40,100)	0.563	0.27356 ^
Fan Speed (0,100)	0.349	0.44753 ^

Source	DF	Sum of Squares	Mean Square	F Ratio
Lack Of Fit	12	487.49542	40.6246	39.9470
Pure Error	1	1.01696	1.0170	**Prob > F**
Total Error	13	488.51239		0.1231
				Max RSq
				0.9999

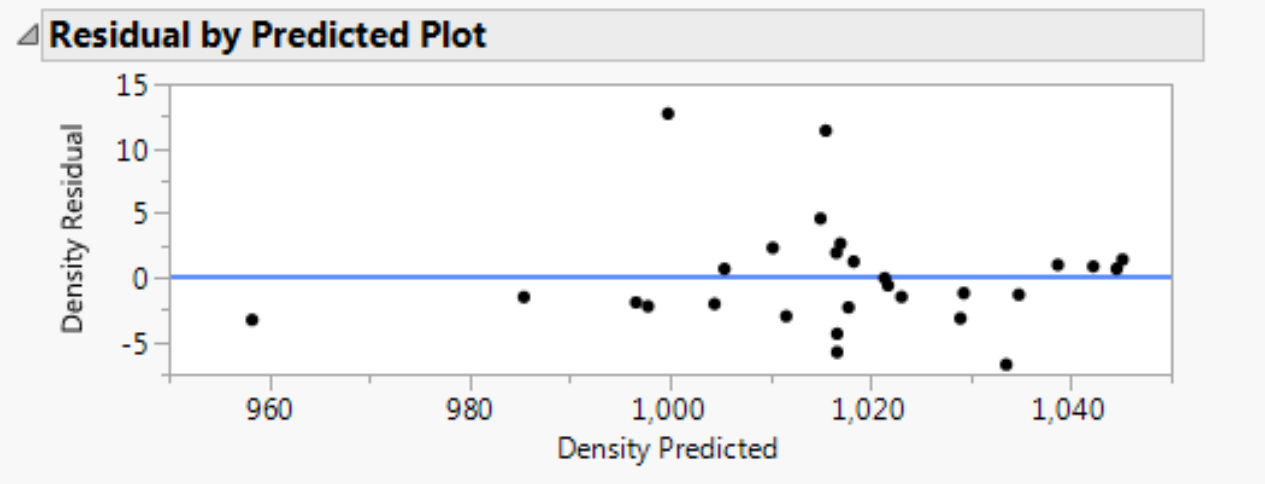

RSquare	0.951173
RSquare Adj	0.898589
Root Mean Square Error	6.13008
Mean of Response	1016.67
Observations (or Sum Wgts)	28

Term	Estimate	Std Error	t Ratio	Prob>|t|	Lower 95%	Upper 95%	F Ratio
Intercept	1016.6701	1.158476	877.59	<.0001*	1014.1673	1019.1728	
Extruder Temperature (240,290)	5.0760433	1.444874	3.51	0.0038*	1.9545836	8.197503	12.3422
Heated Bed Temperature (40,100)	-1.651817	1.444874	-1.14	0.2736	-4.773276	1.469643	1.3070
Layer thickness (0.09,0.29)	-16.87059	1.444874	-11.68	<.0001*	-19.99205	-13.74913	136.3329
Extruder Speed (-50,50)	-6.422419	1.444874	-4.44	0.0007*	-9.543879	-3.300959	19.7578
Fan Speed (0,100)	1.1316653	1.444874	0.78	0.4475	-1.989794	4.253125	0.6134
Extruder Temperature*Layer thickness	6.3245205	1.53252	4.13	0.0012*	3.0137126	9.6353285	17.0311
Heated Bed Temperature*Layer thickness	-2.657626	1.53252	-1.73	0.1065	-5.968434	0.6531818	3.0073
Extruder Temperature*Extruder Speed	-5.241378	1.53252	-3.42	0.0046*	-8.552186	-1.93057	11.6971
Heated Bed Temperature*Extruder Speed	4.813591	1.53252	3.14	0.0078*	1.5027831	8.124399	9.8657
Layer thickness*Extruder Speed	2.6913959	1.53252	1.76	0.1026	-0.619412	6.0022038	3.0842
Extruder Temperature*Fan Speed	-4.545771	1.53252	-2.97	0.0109*	-7.856578	-1.234963	8.7984
Heated Bed Temperature*Fan Speed	5.0188762	1.53252	3.27	0.0060*	1.7080682	8.3296841	10.7251
Layer thickness*Fan Speed	6.0418776	1.53252	3.94	0.0017*	2.7310696	9.3526855	15.5429
Extruder Speed*Fan Speed	-2.715146	1.53252	-1.77	0.0999	-6.025954	0.5956621	3.1389

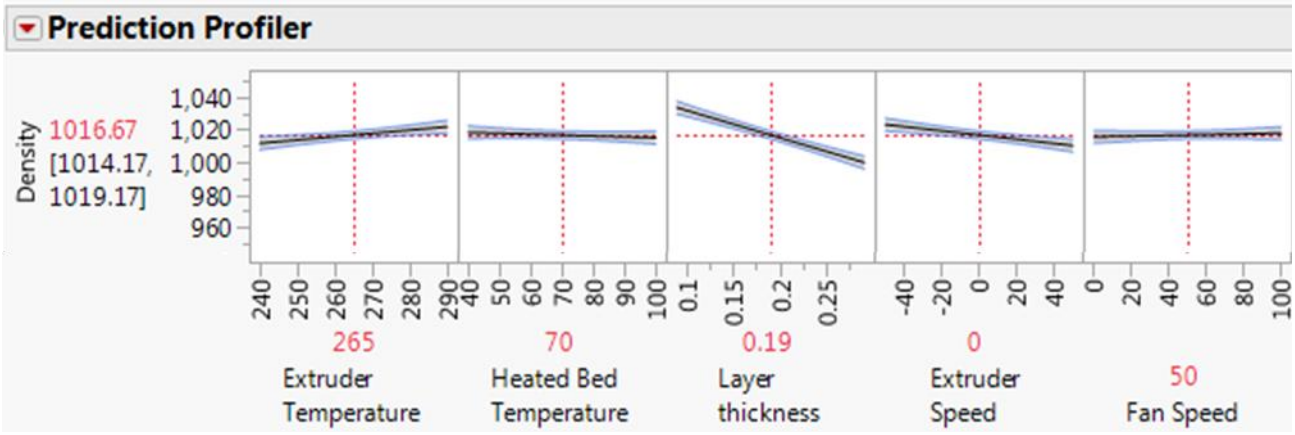

9.5.3 Statistical analyses on the gathered data for density differences

Source	LogWorth	PValue
Layer thickness (0.09,0.29)	6.957	0.00000
Extruder Speed (-50,50)	2.007	0.00984
Extruder Temperature*Layer thickness	1.858	0.01386
Layer thickness*Fan Speed	1.770	0.01697
Extruder Temperature (240,290)	1.561	0.02748
Extruder Temperature*Extruder Speed	1.515	0.03054
Heated Bed Temperature*Fan Speed	1.443	0.03609
Heated Bed Temperature*Extruder Speed	1.376	0.04208
Extruder Temperature*Fan Speed	1.288	0.05156
Extruder Speed*Fan Speed	0.690	0.20434
Layer thickness*Extruder Speed	0.682	0.20781
Heated Bed Temperature*Layer thickness	0.672	0.21287
Heated Bed Temperature (40,100)	0.402	0.39654
Extruder Temperature*Extruder Temperature	0.328	0.47029
Fan Speed (0,100)	0.255	0.55531
Fan Speed*Fan Speed	0.207	0.62150
Extruder Temperature*Heated Bed Temperature	0.186	0.65217
Extruder Speed*Extruder Speed	0.119	0.75976
Layer thickness*Layer thickness	0.073	0.84528
Heated Bed Temperature*Heated Bed Temperature	0.067	0.85660

Source	DF	Sum of Squares	Mean Square	F Ratio
Lack Of Fit	6	420.36285	70.0605	68.4264
Pure Error	1	1.02388	1.0239	**Prob > F**
Total Error	7	421.38673		0.0923
				Max RSq
				1.0000

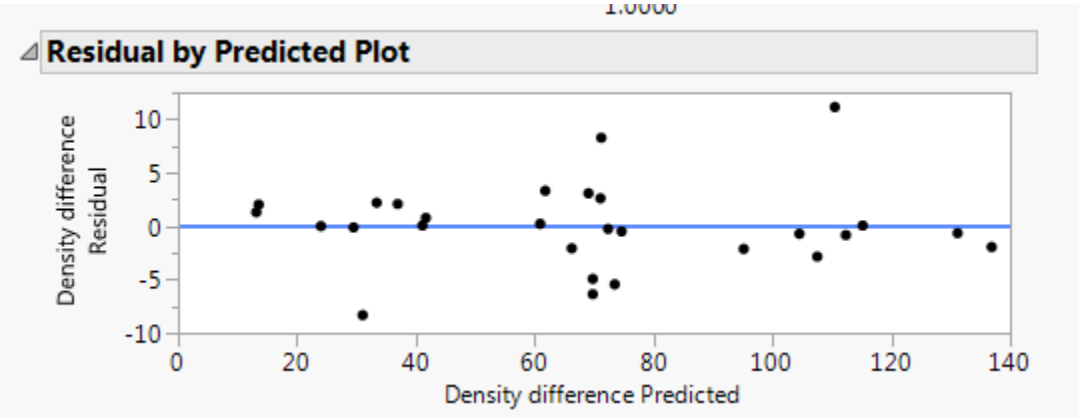

RSquare	0.987344
RSquare Adj	0.951185
Root Mean Square Error	7.758744
Mean of Response	69.21196
Observations (or Sum Wgts)	28

Term	Estimate	Std Error	t Ratio	Prob>|t|	Lower 95%	Upper 95%	F Ratio
Intercept	69.769133	2.702247	25.82	<.0001*	63.379335	76.158931	
Extruder Temperature (240,290)	5.0755556	1.828753	2.78	0.0275*	0.7512408	9.3998703	7.7029
Heated Bed Temperature (40,100)	-1.651333	1.828753	-0.90	0.3965	-5.975648	2.6729814	0.8154
Layer thickness (0.09,0.29)	39.731278	1.828753	21.73	<.0001*	35.406963	44.055593	472.0139
Extruder Speed (-50,50)	-6.421778	1.828753	-3.51	0.0098*	-10.74609	-2.097463	12.3311
Fan Speed (0,100)	1.1326111	1.828753	0.62	0.5553	-3.191704	5.4569258	0.3836
Extruder Temperature*Heated Bed Temperature	0.913	1.939686	0.47	0.6522	-3.673628	5.4996284	0.2216
Extruder Temperature*Layer thickness	6.324	1.939686	3.26	0.0139*	1.7373716	10.910628	10.6297
Heated Bed Temperature*Layer thickness	-2.65825	1.939686	-1.37	0.2129	-7.244878	1.9283784	1.8781
Extruder Temperature*Extruder Speed	-5.241625	1.939686	-2.70	0.0305*	-9.828253	-0.654997	7.3025
Heated Bed Temperature*Extruder Speed	4.814375	1.939686	2.48	0.0421*	0.2277466	9.4010034	6.1605
Layer thickness*Extruder Speed	2.691625	1.939686	1.39	0.2078	-1.895003	7.2782534	1.9256
Extruder Temperature*Fan Speed	-4.54625	1.939686	-2.34	0.0516	-9.132878	0.0403784	5.4934
Heated Bed Temperature*Fan Speed	5.0185	1.939686	2.59	0.0361*	0.4318716	9.6051284	6.6940
Layer thickness*Fan Speed	6.04125	1.939686	3.11	0.0170*	1.4546216	10.627878	9.7004
Extruder Speed*Fan Speed	-2.714875	1.939686	-1.40	0.2043	-7.301503	1.8717534	1.9590
Extruder Temperature*Extruder Temperature	-3.783541	4.957613	-0.76	0.4703	-15.50643	7.93935	0.5824
Heated Bed Temperature*Heated Bed Temperature	0.9294586	4.957613	0.19	0.8566	-10.79343	12.65235	0.0351
Layer thickness*Layer thickness	1.0039586	4.957613	0.20	0.8453	-10.71893	12.72685	0.0410
Extruder Speed*Extruder Speed	-1.576541	4.957613	-0.32	0.7598	-13.29943	10.14635	0.1011
Fan Speed*Fan Speed	2.5599586	4.957613	0.52	0.6215	-9.162933	14.28285	0.2666

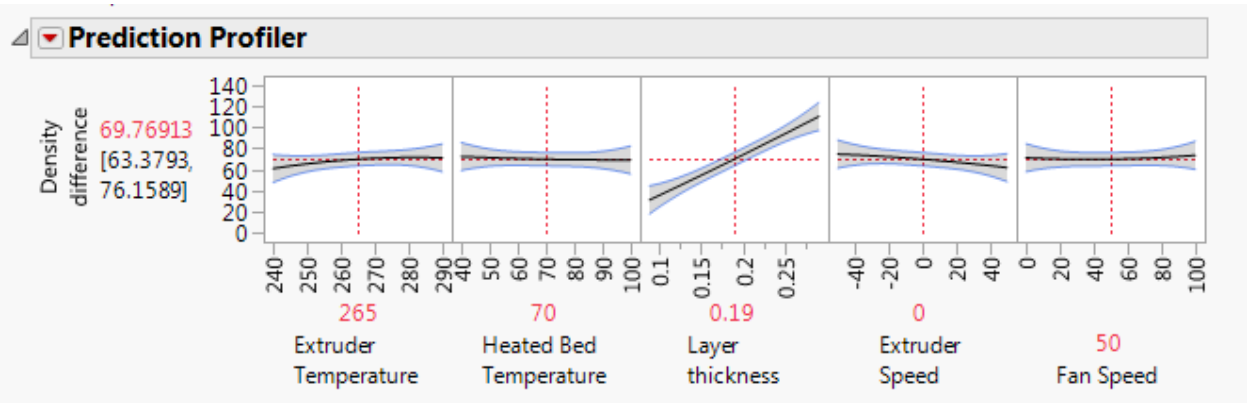

9.5.4 Statistical analyses on the gathered data of reduced variable for density differences

Source	LogWorth	PValue
Layer thickness (0.09,0.29)	12.179	0.00000
Extruder Speed (-50,50)	3.180	0.00066
Extruder Temperature*Layer thickness	2.924	0.00119
Layer thickness*Fan Speed	2.773	0.00169
Extruder Temperature (240,290)	2.418	0.00382
Extruder Temperature*Extruder Speed	2.341	0.00456
Heated Bed Temperature*Fan Speed	2.219	0.00603
Heated Bed Temperature*Extruder Speed	2.108	0.00780
Extruder Temperature*Fan Speed	1.962	0.01092
Extruder Speed*Fan Speed	1.000	0.09990
Layer thickness*Extruder Speed	0.989	0.10254
Heated Bed Temperature*Layer thickness	0.973	0.10645
Heated Bed Temperature (40,100)	0.563	0.27369
Fan Speed (0,100)	0.350	0.44715

Source	DF	Sum of Squares	Mean Square	F Ratio
Lack Of Fit	12	487.47838	40.6232	39.6757
Pure Error	1	1.02388	1.0239	**Prob > F**
Total Error	13	488.50226		0.1235
				Max RSq
				1.0000

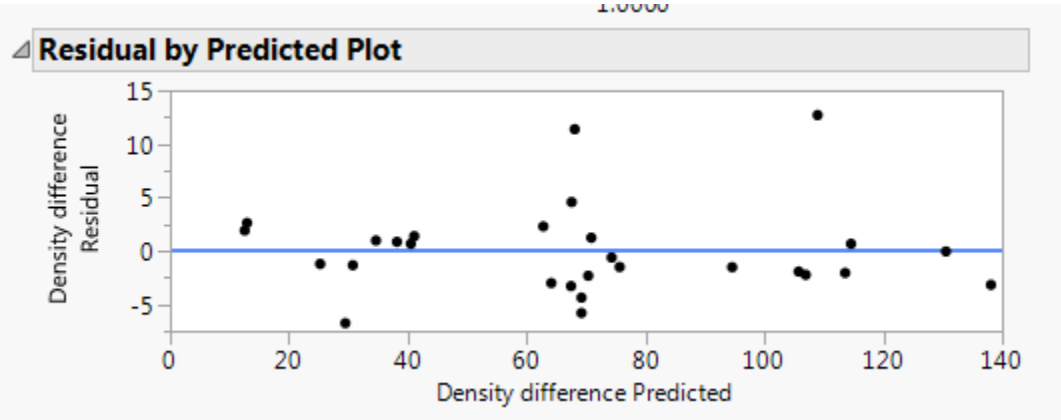

RSquare	0.985328
RSquare Adj	0.969528
Root Mean Square Error	6.130016
Mean of Response	69.21196
Observations (or Sum Wgts)	28

Term	Estimate	Std Error	t Ratio	Prob>|t|	Lower 95%	Upper 95%	F Ratio
Intercept	69.211964	1.158464	59.74	<.0001*	66.709255	71.714674	
Extruder Temperature (240,290)	5.0755556	1.444859	3.51	0.0038*	1.9541282	8.1969829	12.3400
Heated Bed Temperature (40,100)	-1.651333	1.444859	-1.14	0.2737	-4.772761	1.470094	1.3062
Layer thickness (0.09,0.29)	39.731278	1.444859	27.50	<.0001*	36.60985	42.852705	756.1611
Extruder Speed (-50,50)	-6.421778	1.444859	-4.44	0.0007*	-9.543205	-3.30035	19.7542
Fan Speed (0,100)	1.1326111	1.444859	0.78	0.4472	-1.988816	4.2540384	0.6145
Extruder Temperature*Layer thickness	6.324	1.532504	4.13	0.0012*	3.0132264	9.6347736	17.0287
Heated Bed Temperature*Layer thickness	-2.65825	1.532504	-1.73	0.1064	-5.969024	0.6525236	3.0088
Extruder Temperature*Extruder Speed	-5.241625	1.532504	-3.42	0.0046*	-8.552399	-1.930851	11.6985
Heated Bed Temperature*Extruder Speed	4.814375	1.532504	3.14	0.0078*	1.5036014	8.1251486	9.8691
Layer thickness*Extruder Speed	2.691625	1.532504	1.76	0.1025	-0.619149	6.0023986	3.0848
Extruder Temperature*Fan Speed	-4.54625	1.532504	-2.97	0.0109*	-7.857024	-1.235476	8.8004
Heated Bed Temperature*Fan Speed	5.0185	1.532504	3.27	0.0060*	1.7077264	8.3292736	10.7237
Layer thickness*Fan Speed	6.04125	1.532504	3.94	0.0017*	2.7304764	9.3520236	15.5400
Extruder Speed*Fan Speed	-2.714875	1.532504	-1.77	0.0999	-6.025649	0.5958986	3.1383

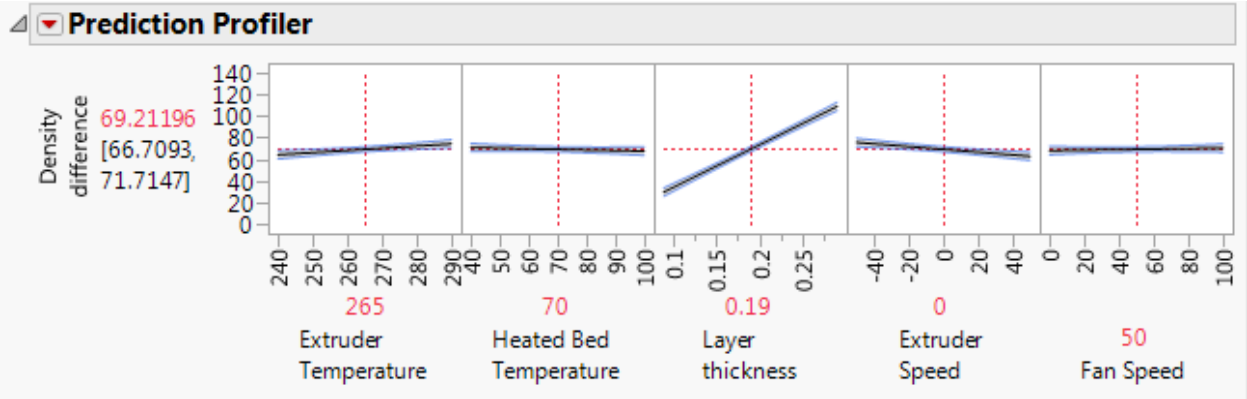

9.5.5 Statistical analyses on the gathered data for contact quality, *P*

Source	LogWorth	PValue
Extruder Speed (-50,50)	2.984	0.00104
Layer thickness*Extruder Speed	2.131	0.00739
Layer thickness*Fan Speed	1.736	0.01836
Layer thickness (0.09,0.29)	1.516	0.03048
Extruder Temperature*Layer thickness	1.403	0.03951
Heated Bed Temperature*Fan Speed	0.871	0.13448
Extruder Temperature*Extruder Speed	0.855	0.13958
Heated Bed Temperature*Extruder Speed	0.770	0.16970
Extruder Temperature (240,290)	0.681	0.20866
Extruder Temperature*Fan Speed	0.633	0.23300
Fan Speed (0,100)	0.485	0.32707
Heated Bed Temperature*Layer thickness	0.484	0.32824
Extruder Speed*Fan Speed	0.427	0.37417
Fan Speed*Fan Speed	0.363	0.43326
Layer thickness*Layer thickness	0.360	0.43677
Heated Bed Temperature*Heated Bed Temperature	0.183	0.65594
Extruder Temperature*Extruder Temperature	0.150	0.70792
Heated Bed Temperature (40,100)	0.099	0.79619
Extruder Speed*Extruder Speed	0.002	0.99572
Extruder Temperature*Heated Bed Temperature	0.001	0.99723

Source	DF	Sum of Squares	Mean Square	F Ratio
Lack Of Fit	6	292.27869	48.7131	87.2490
Pure Error	1	0.55832	0.5583	**Prob > F**
Total Error	7	292.83701		0.0818
				Max RSq
				0.9999

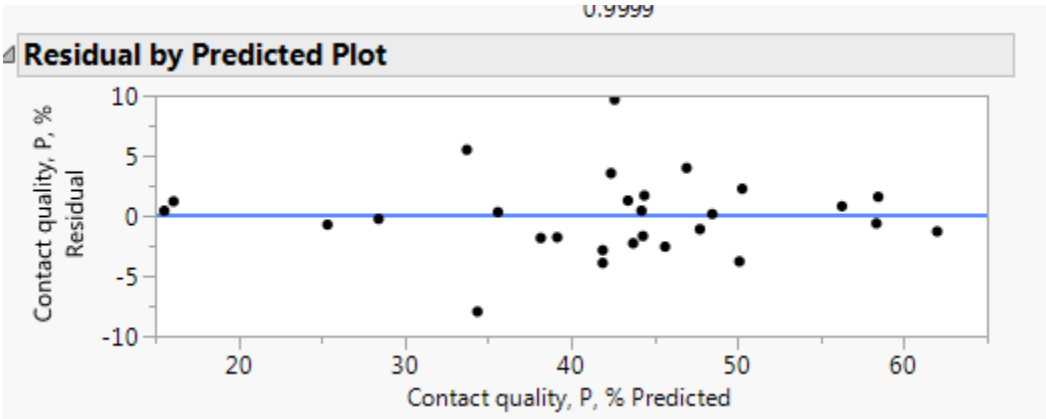

RSquare	0.921365
RSquare Adj	0.696694
Root Mean Square Error	6.46791
Mean of Response	42.1286
Observations (or Sum Wgts)	28

Term	Estimate	Std Error	t Ratio	Prob>|t|	Lower 95%	Upper 95%	F Ratio
Intercept	41.897376	2.25267	18.60	<.0001*	36.570658	47.224093	
Extruder Temperature (240,290)	2.1110223	1.524501	1.38	0.2087	-1.49385	5.7158943	1.9175
Heated Bed Temperature (40,100)	-0.409055	1.524501	-0.27	0.7962	-4.013927	3.1958175	0.0720
Layer thickness (0.09,0.29)	4.1217813	1.524501	2.70	0.0305*	0.5169093	7.7266533	7.3100
Extruder Speed (-50,50)	-8.190541	1.524501	-5.37	0.0010*	-11.79541	-4.585669	28.8649
Fan Speed (0,100)	-1.606229	1.524501	-1.05	0.3271	-5.211101	1.9986434	1.1101
Extruder Temperature*Heated Bed Temperature	-0.005827	1.616977	-0.00	0.9972	-3.829371	3.8177175	0.0000
Extruder Temperature*Layer thickness	4.0832244	1.616977	2.53	0.0395*	0.2596802	7.9067685	6.3767
Heated Bed Temperature*Layer thickness	-1.699222	1.616977	-1.05	0.3282	-5.522766	2.1243223	1.1043
Extruder Temperature*Extruder Speed	-2.694492	1.616977	-1.67	0.1396	-6.518036	1.1290522	2.7768
Heated Bed Temperature*Extruder Speed	2.4751118	1.616977	1.53	0.1697	-1.348432	6.298656	2.3431
Layer thickness*Extruder Speed	6.0253597	1.616977	3.73	0.0074*	2.2018155	9.8489038	13.8854
Extruder Temperature*Fan Speed	-2.110908	1.616977	-1.31	0.2330	-5.934452	1.7126361	1.7042
Heated Bed Temperature*Fan Speed	2.7359641	1.616977	1.69	0.1345	-1.08758	6.5595082	2.8629
Layer thickness*Fan Speed	4.9459649	1.616977	3.06	0.0184*	1.1224207	8.769509	9.3561
Extruder Speed*Fan Speed	-1.534704	1.616977	-0.95	0.3742	-5.358248	2.28884	0.9008
Extruder Temperature*Extruder Temperature	-1.613059	4.132807	-0.39	0.7079	-11.3856	8.1594775	0.1523
Heated Bed Temperature*Heated Bed Temperature	1.9223981	4.132807	0.47	0.6559	-7.850138	11.694934	0.2164
Layer thickness*Layer thickness	-3.408079	4.132807	-0.82	0.4368	-13.18062	6.3644576	0.6800
Extruder Speed*Extruder Speed	0.0229687	4.132807	0.01	0.9957	-9.749568	9.795505	0.0000
Fan Speed*Fan Speed	3.4354517	4.132807	0.83	0.4333	-6.337085	13.207988	0.6910

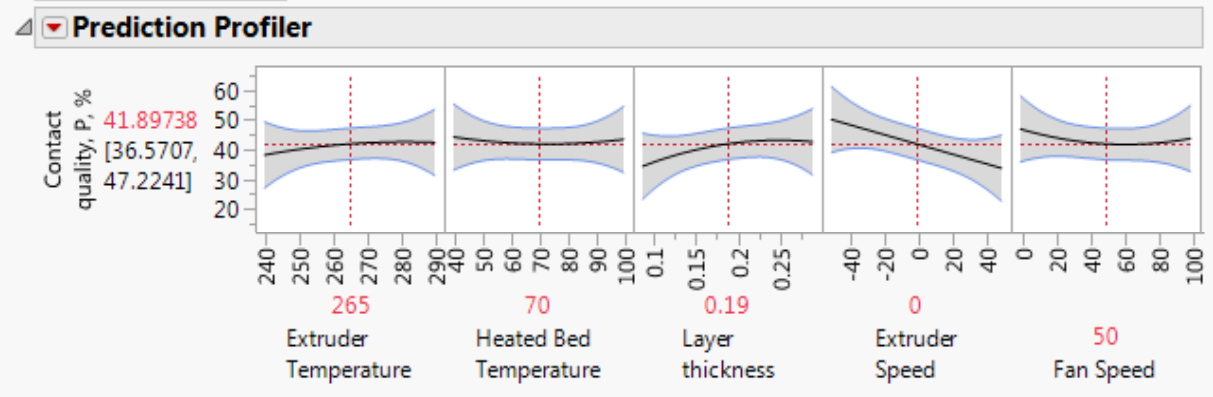

9.5.6 Statistical analyses on the gathered data of reduced sources for contact quality

Source	LogWorth	PValue
Extruder Speed (-50,50)	4.910	0.00001
Layer thickness*Extruder Speed	3.354	0.00044
Layer thickness*Fan Speed	2.663	0.00217
Layer thickness (0.09,0.29)	2.288	0.00515
Extruder Temperature*Layer thickness	2.100	0.00795
Heated Bed Temperature*Fan Speed	1.243	0.05721
Extruder Temperature*Extruder Speed	1.217	0.06061
Heated Bed Temperature*Extruder Speed	1.087	0.08187
Extruder Temperature (240,290)	0.951	0.11204
Extruder Temperature*Fan Speed	0.879	0.13220
Fan Speed (0,100)	0.662	0.21786
Heated Bed Temperature*Layer thickness	0.660	0.21900
Heated Bed Temperature (40,100)	0.126	0.74733

Source	DF	Sum of Squares	Mean Square	F Ratio
Lack Of Fit	13	389.96809	29.9975	53.7279
Pure Error	1	0.55832	0.5583	**Prob > F**
Total Error	14	390.52641		0.1064
				Max RSq
				0.9999

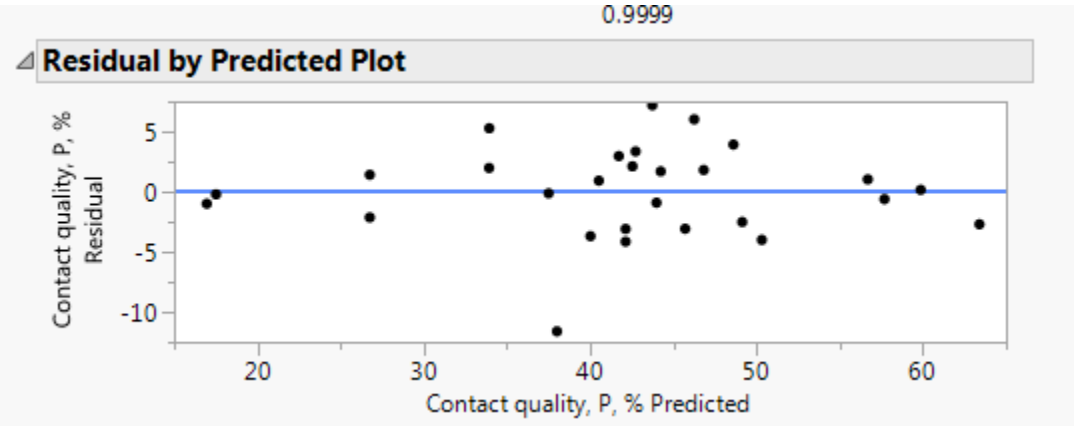

RSquare	0.895133
RSquare Adj	0.797756
Root Mean Square Error	5.281547
Mean of Response	42.1286
Observations (or Sum Wgts)	28

Term	Estimate	Std Error	t Ratio	Prob>|t|	Lower 95%	Upper 95%	F Ratio
Intercept	42.128599	0.998119	42.21	<.0001*	39.987847	44.269351	
Extruder Temperature (240,290)	2.1110223	1.244873	1.70	0.1120	-0.558964	4.7810086	2.8756
Heated Bed Temperature (40,100)	-0.409055	1.244873	-0.33	0.7473	-3.079041	2.2609318	0.1080
Layer thickness (0.09,0.29)	4.1217813	1.244873	3.31	0.0051*	1.4517949	6.7917676	10.9628
Extruder Speed (-50,50)	-8.190541	1.244873	-6.58	<.0001*	-10.86053	-5.520555	43.2888
Fan Speed (0,100)	-1.606229	1.244873	-1.29	0.2179	-4.276215	1.0637577	1.6648
Extruder Temperature*Layer thickness	4.0832244	1.320387	3.09	0.0080*	1.2512762	6.9151725	9.5632
Heated Bed Temperature*Layer thickness	-1.699222	1.320387	-1.29	0.2190	-4.53117	1.1327264	1.6561
Extruder Temperature*Extruder Speed	-2.694492	1.320387	-2.04	0.0606	-5.52644	0.1374563	4.1644
Heated Bed Temperature*Extruder Speed	2.4751118	1.320387	1.87	0.0819	-0.356836	5.30706	3.5139
Layer thickness*Extruder Speed	6.0253597	1.320387	4.56	0.0004*	3.1934115	8.8573079	20.8240
Extruder Temperature*Fan Speed	-2.110908	1.320387	-1.60	0.1322	-4.942856	0.7210401	2.5559
Heated Bed Temperature*Fan Speed	2.7359641	1.320387	2.07	0.0572	-0.095984	5.5679123	4.2936
Layer thickness*Fan Speed	4.9459649	1.320387	3.75	0.0022*	2.1140167	7.777913	14.0314

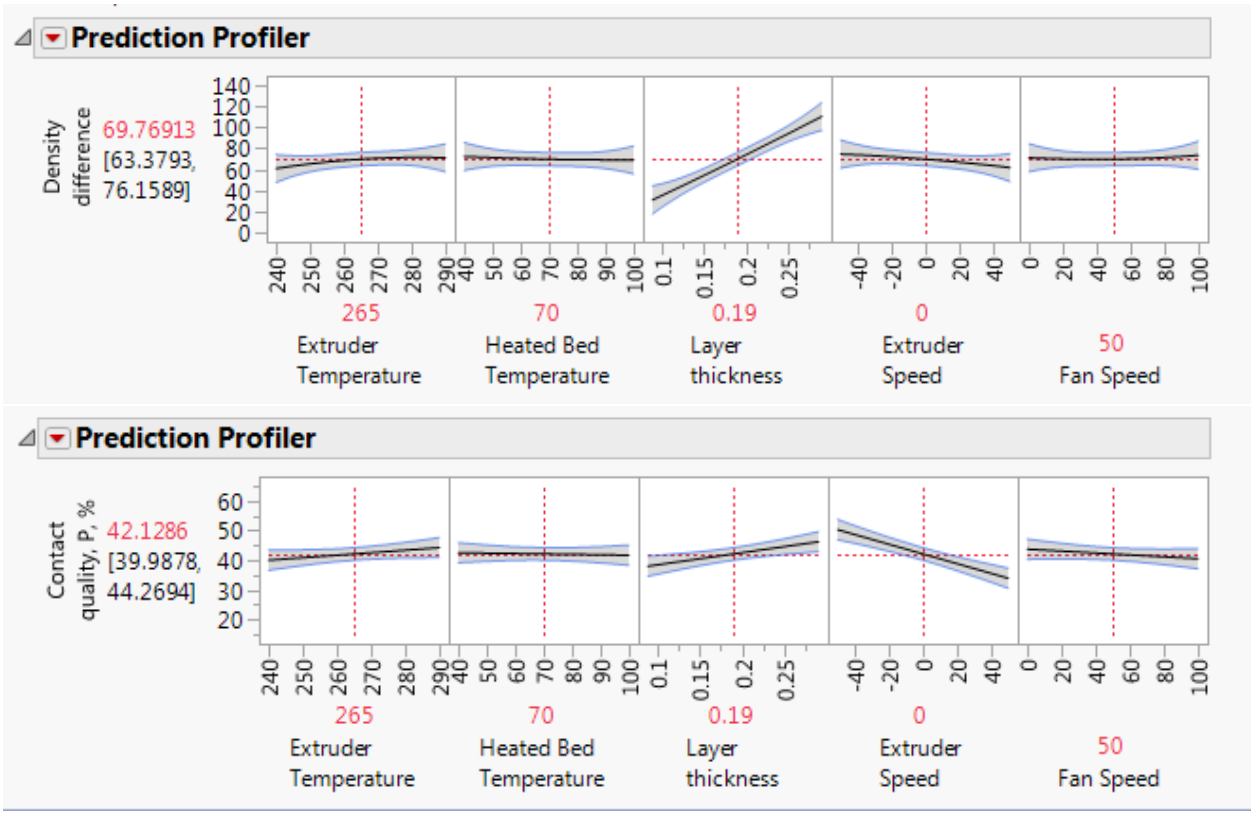

9.5.7 Statistical analyses on the gathered data for density difference of testing artifacts

Source	LogWorth	PValue
Layer thickness(0.09,0.29)	6.534	0.00000
Heated Bed Temperature*Heated Bed Temperature	1.292	0.05099
Layer thickness*Fan Speed	1.179	0.06623
Layer thickness*Extruder Speed	0.998	0.10040
Fan Speed(0,100)	0.718	0.19132
Extruder Speed(-50,50)	0.663	0.21723
Heated Bed Temperature*Extruder Speed	0.649	0.22444
Heated Bed Temperature*Fan Speed	0.620	0.24010
Extruder Speed*Fan Speed	0.556	0.27809
Extruder Temperature*Fan Speed	0.467	0.34111
Heated Bed Temperature(40,100)	0.430	0.37122
Extruder Speed*Extruder Speed	0.333	0.46489
Fan Speed*Fan Speed	0.237	0.57943
Extruder Temperature*Extruder Speed	0.218	0.60498
Extruder Temperature*Extruder Temperature	0.185	0.65264
Extruder Temperature*Heated Bed Temperature	0.106	0.78325
Heated Bed Temperature*Layer thickness	0.048	0.89584
Extruder Temperature(240,290)	0.008	0.98155

Source	LogWorth	PValue
Layer thickness*Layer thickness	0.004	0.99005
Extruder Temperature*Layer thickness	0.002	0.99644

Source	DF	Sum of Squares	Mean Square	F Ratio
Lack Of Fit	6	601.16409	100.194	2.9116
Pure Error	1	34.41181	34.412	**Prob > F**
Total Error	7	635.57590		0.4208
				Max RSq
				0.9990

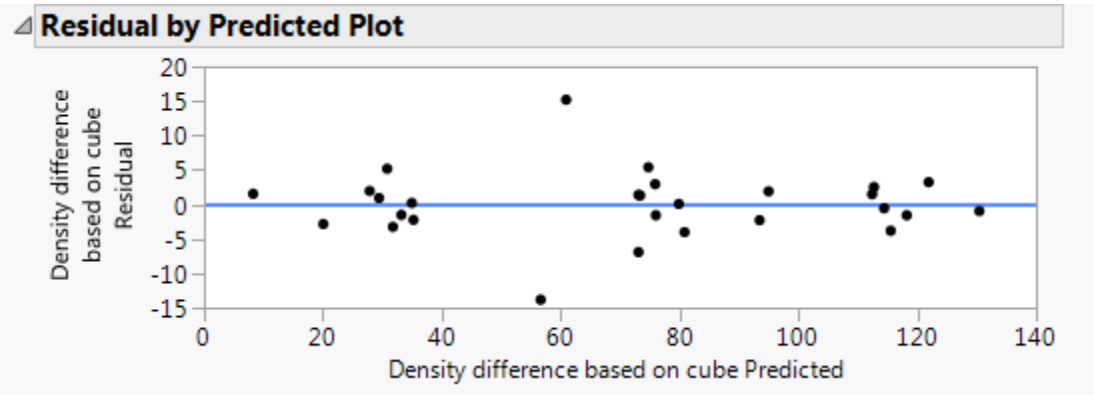

RSquare	0.981966
RSquare Adj	0.930441
Root Mean Square Error	9.528723
Mean of Response	71.07143
Observations (or Sum Wgts)	28

Term	Estimate	Std Error	t Ratio	Prob>|t|	Lower 95%	Upper 95%	F Ratio
Intercept	73.084834	3.318702	22.02	<.0001*	65.237351	80.932318	
Extruder Temperature(240,290)	0.0538333	2.245941	0.02	0.9815	-5.256974	5.364641	0.0006
Heated Bed Temperature(40,100)	2.1456667	2.245941	0.96	0.3712	-3.165141	7.4564744	0.9127
Layer thickness(0.09,0.29)	42.366167	2.245941	18.86	<.0001*	37.055359	47.676974	355.8291
Extruder Speed(-50,50)	-3.045389	2.245941	-1.36	0.2172	-8.356197	2.2654188	1.8386
Fan Speed(0,100)	-3.2485	2.245941	-1.45	0.1913	-8.559308	2.0623077	2.0920
Extruder Temperature*Heated Bed Temperature	-0.681	2.382181	-0.29	0.7833	-6.313962	4.9519622	0.0817
Extruder Temperature*Layer thickness	0.011	2.382181	0.00	0.9964	-5.621962	5.6439622	0.0000
Heated Bed Temperature*Layer thickness	-0.323375	2.382181	-0.14	0.8958	-5.956337	5.3095872	0.0184
Extruder Temperature*Extruder Speed	-1.289875	2.382181	-0.54	0.6050	-6.922837	4.3430872	0.2932
Heated Bed Temperature*Extruder Speed	-3.17425	2.382181	-1.33	0.2244	-8.807212	2.4587122	1.7755
Layer thickness*Extruder Speed	-4.50675	2.382181	-1.89	0.1004	-10.13971	1.1262122	3.5791
Extruder Temperature*Fan Speed	-2.432875	2.382181	-1.02	0.3411	-8.065837	3.2000872	1.0430

Term	Estimate	Std Error	t Ratio	Prob>|t|	Lower 95%	Upper 95%	F Ratio
Heated Bed Temperature*Fan Speed	-3.058	2.382181	-1.28	0.2401	-8.690962	2.5749622	1.6479
Layer thickness*Fan Speed	-5.17875	2.382181	-2.17	0.0662	-10.81171	0.4542122	4.7261
Extruder Speed*Fan Speed	-2.801125	2.382181	-1.18	0.2781	-8.434087	2.8318372	1.3827
Extruder Temperature*Extruder Temperature	2.8617071	6.088578	0.47	0.6526	-11.53549	17.258907	0.2209
Heated Bed Temperature*Heated Bed Temperature	-14.31579	6.088578	-2.35	0.0510	-28.71299	0.0814066	5.5284
Layer thickness*Layer thickness	0.0787071	6.088578	0.01	0.9900	-14.31849	14.475907	0.0002
Extruder Speed*Extruder Speed	4.7057071	6.088578	0.77	0.4649	-9.691492	19.102907	0.5973
Fan Speed*Fan Speed	3.5377071	6.088578	0.58	0.5794	-10.85949	17.934907	0.3376

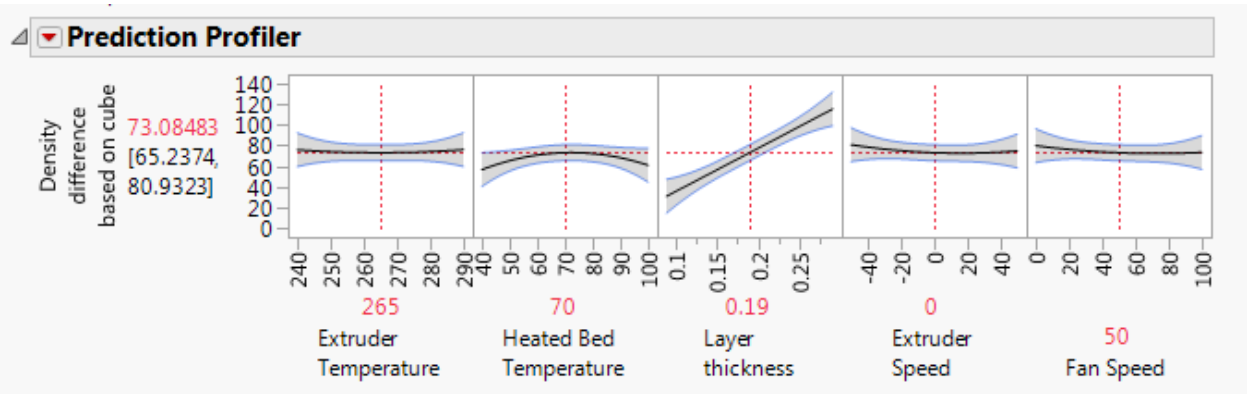

9.5.8 Statistical analyses on the reduced sources for density difference of testing artifacts

Source	LogWorth	PValue
Layer thickness(0.09,0.29)	12.196	0.00000
Heated Bed Temperature*Heated Bed Temperature	1.966	0.01082
Layer thickness*Fan Speed	1.879	0.01321
Layer thickness*Extruder Speed	1.567	0.02709
Fan Speed(0,100)	1.096	0.08009 ^
Extruder Speed*Extruder Speed	1.067	0.08570
Extruder Speed(-50,50)	1.006	0.09869 ^
Heated Bed Temperature*Extruder Speed	0.983	0.10410
Heated Bed Temperature*Fan Speed	0.935	0.11619
Extruder Speed*Fan Speed	0.832	0.14733
Extruder Temperature*Fan Speed	0.690	0.20405
Heated Bed Temperature(40,100)	0.632	0.23311 ^
Extruder Temperature(240,290)	0.011	0.97550 ^

Source	DF	Sum of Squares	Mean Square	F Ratio
Lack Of Fit	13	712.53712	54.8105	1.5928

Source	DF	Sum of Squares	Mean Square	F Ratio
Pure Error	1	34.41181	34.4118	**Prob > F**
Total Error	14	746.94893		0.5576
				Max RSq
				0.9990

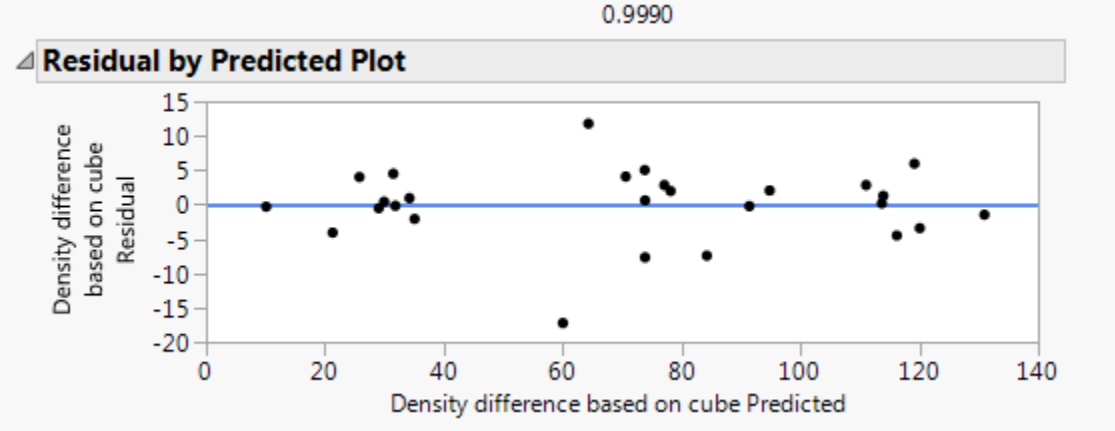

RSquare	0.978806
RSquare Adj	0.959126
Root Mean Square Error	7.304348
Mean of Response	71.07143
Observations (or Sum Wgts)	28

Term	Estimate	Std Error	t Ratio	Prob>|t|	Lower 95%	Upper 95%	F Ratio
Intercept	73.85198	2.442779	30.23	<.0001*	68.612741	79.091219	
Extruder Temperature(240,290)	0.0538333	1.721651	0.03	0.9755	-3.638741	3.746408	0.0010
Heated Bed Temperature(40,100)	2.1456667	1.721651	1.25	0.2331	-1.546908	5.8382414	1.5532
Layer thickness(0.09,0.29)	42.366167	1.721651	24.61	<.0001*	38.673592	46.058741	605.5472
Extruder Speed(-50,50)	-3.045389	1.721651	-1.77	0.0987	-6.737964	0.6471858	3.1289
Fan Speed(0,100)	-3.2485	1.721651	-1.89	0.0801	-6.941075	0.4440747	3.5602
Heated Bed Temperature*Extruder Speed	-3.17425	1.826087	-1.74	0.1041	-7.090817	0.7423169	3.0216
Layer thickness*Extruder Speed	-4.50675	1.826087	-2.47	0.0271*	-8.423317	-0.590183	6.0909
Extruder Temperature*Fan Speed	-2.432875	1.826087	-1.33	0.2040	-6.349442	1.4836919	1.7750
Heated Bed Temperature*Fan Speed	-3.058	1.826087	-1.67	0.1162	-6.974567	0.8585669	2.8043
Layer thickness*Fan Speed	-5.17875	1.826087	-2.84	0.0132*	-9.095317	-1.262183	8.0428
Extruder Speed*Fan Speed	-2.801125	1.826087	-1.53	0.1473	-6.717692	1.1154419	2.3530
Heated Bed Temperature*Heated Bed Temperature	-11.6734	3.974348	-2.94	0.0108*	-20.19753	-3.149272	8.6271
Extruder Speed*Extruder Speed	7.3480987	3.974348	1.85	0.0857	-1.17603	15.872228	3.4184

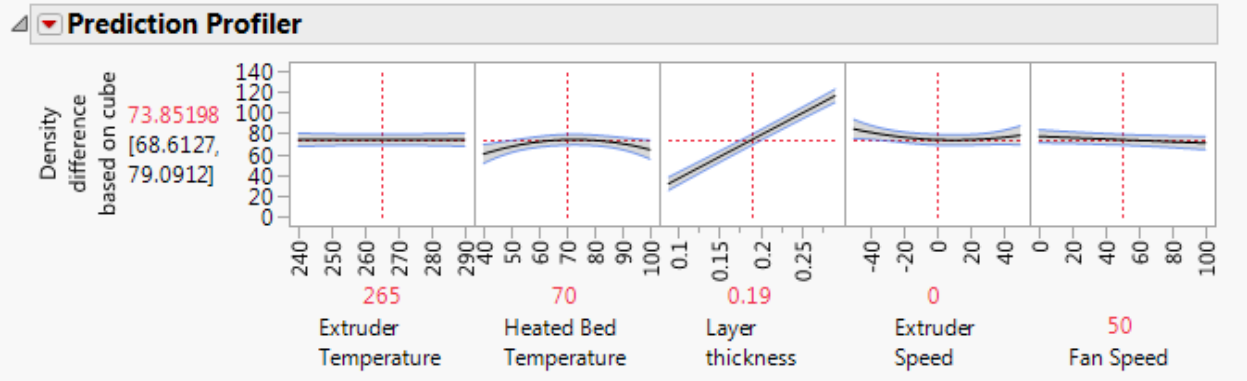

9.5.9 Statistical analyses on the contact quality of testing artifacts

Source	LogWorth	PValue
Layer thickness(0.09,0.29)	1.354	0.04421
Heated Bed Temperature*Heated Bed Temperature	1.111	0.07753
Extruder Speed(-50,50)	0.810	0.15504
Fan Speed(0,100)	0.752	0.17703
Heated Bed Temperature*Extruder Speed	0.484	0.32791
Extruder Temperature(240,290)	0.445	0.35933
Extruder Temperature*Layer thickness	0.440	0.36321
Extruder Temperature*Fan Speed	0.378	0.41921
Heated Bed Temperature*Layer thickness	0.365	0.43110
Layer thickness*Fan Speed	0.341	0.45643
Heated Bed Temperature*Fan Speed	0.299	0.50264
Extruder Speed*Extruder Speed	0.257	0.55316
Fan Speed*Fan Speed	0.168	0.67914
Layer thickness*Extruder Speed	0.137	0.72883
Extruder Speed*Fan Speed	0.122	0.75430
Extruder Temperature*Extruder Temperature	0.119	0.76085
Extruder Temperature*Extruder Speed	0.086	0.82001
Extruder Temperature*Heated Bed Temperature	0.030	0.93355
Heated Bed Temperature(40,100)	0.018	0.96038
Layer thickness*Layer thickness	0.005	0.98891

Source	DF	Sum of Squares	Mean Square	F Ratio
Lack Of Fit	6	443.75253	73.9588	3.4300
Pure Error	1	21.56215	21.5622	**Prob > F**
Total Error	7	465.31468		0.3913
				Max RSq
				0.9887

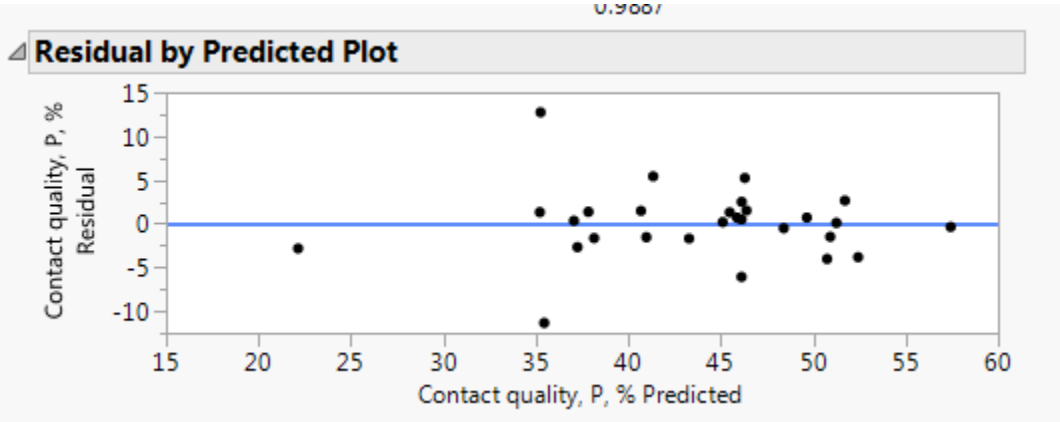

RSquare	0.755351
RSquare Adj	0.056353
Root Mean Square Error	8.15313
Mean of Response	43.73808
Observations (or Sum Wgts)	28

Term	Estimate	Std Error	t Ratio	Prob>|t|	Lower 95%	Upper 95%	F Ratio
Intercept	46.119146	2.839605	16.24	<.0001*	39.404547	52.833745	
Extruder Temperature(240,290)	-1.884949	1.921711	-0.98	0.3593	-6.429074	2.6591756	0.9621
Heated Bed Temperature(40,100)	-0.098921	1.921711	-0.05	0.9604	-4.643046	4.4452038	0.0026
Layer thickness(0.09,0.29)	4.7050025	1.921711	2.45	0.0442*	0.1608778	9.2491273	5.9944
Extruder Speed(-50,50)	-3.062565	1.921711	-1.59	0.1550	-7.60669	1.4815597	2.5398
Fan Speed(0,100)	-2.884629	1.921711	-1.50	0.1770	-7.428753	1.6594962	2.2532
Extruder Temperature*Heated Bed Temperature	0.1761423	2.038282	0.09	0.9336	-4.64363	4.9959144	0.0075
Extruder Temperature*Layer thickness	1.9821831	2.038282	0.97	0.3632	-2.837589	6.8019552	0.9457
Heated Bed Temperature*Layer thickness	1.7026943	2.038282	0.84	0.4311	-3.117078	6.5224664	0.6978
Extruder Temperature*Extruder Speed	-0.48153	2.038282	-0.24	0.8200	-5.301302	4.3382422	0.0558
Heated Bed Temperature*Extruder Speed	-2.14351	2.038282	-1.05	0.3279	-6.963282	2.6762626	1.1059
Layer thickness*Extruder Speed	-0.735585	2.038282	-0.36	0.7288	-5.555358	4.0841866	0.1302
Extruder Temperature*Fan Speed	-1.749173	2.038282	-0.86	0.4192	-6.568945	3.0705992	0.7364
Heated Bed Temperature*Fan Speed	-1.440295	2.038282	-0.71	0.5026	-6.260067	3.3794769	0.4993
Layer thickness*Fan Speed	-1.606591	2.038282	-0.79	0.4564	-6.426363	3.2131808	0.6213
Extruder Speed*Fan Speed	-0.663517	2.038282	-0.33	0.7543	-5.48329	4.1562546	0.1060
Extruder Temperature*Extruder Temperature	1.6488676	5.209614	0.32	0.7608	-10.66991	13.967647	0.1002
Heated Bed Temperature*Heated Bed Temperature	-10.76968	5.209614	-2.07	0.0775	-23.08846	1.5491006	4.2736
Layer thickness*Layer thickness	-0.075065	5.209614	-0.01	0.9889	-12.39384	12.243715	0.0002
Extruder Speed*Extruder Speed	3.2444939	5.209614	0.62	0.5532	-9.074286	15.563274	0.3879

Term	Estimate	Std Error	t Ratio	Prob>|t|	Lower 95%	Upper 95%	F Ratio
Fan Speed*Fan Speed	2.2475014	5.209614	0.43	0.6791	-10.07128	14.566281	0.1861

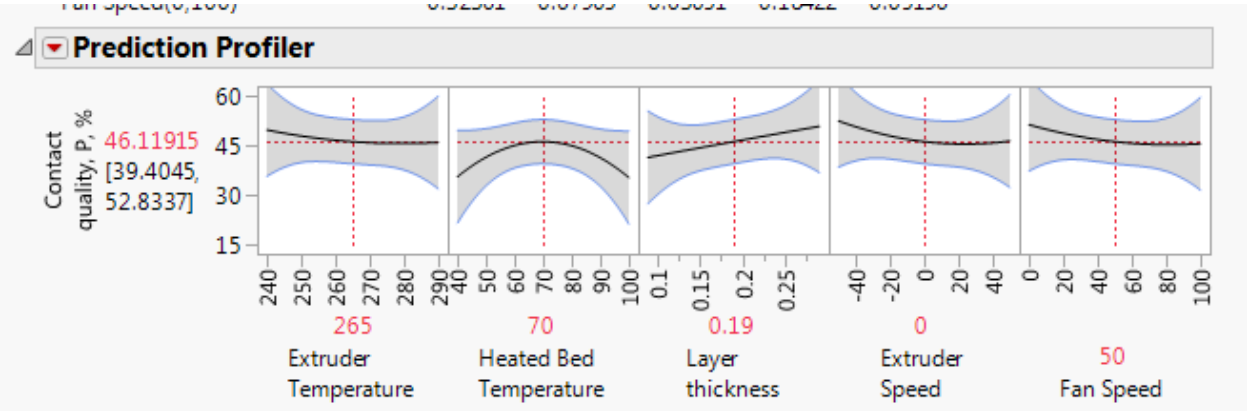

9.5.10 Statistical analyses on the reduced sources for contact quality of testing artifacts

Source	LogWorth	PValue
Layer thickness(0.09,0.29)	2.340	0.00457
Heated Bed Temperature*Heated Bed Temperature	1.886	0.01299
Extruder Speed(-50,50)	1.322	0.04766
Fan Speed(0,100)	1.219	0.06043
Extruder Speed*Extruder Speed	0.784	0.16441
Heated Bed Temperature*Extruder Speed	0.754	0.17614
Extruder Temperature(240,290)	0.687	0.20537
Extruder Temperature*Layer thickness	0.680	0.20908
Extruder Temperature*Fan Speed	0.577	0.26506
Heated Bed Temperature*Layer thickness	0.557	0.27748
Heated Bed Temperature(40,100)	0.024	0.94563 ^

Source	DF	Sum of Squares	Mean Square	F Ratio
Lack Of Fit	15	565.61350	37.7076	1.7488
Pure Error	1	21.56215	21.5622	**Prob > F**
Total Error	16	587.17565		0.5388
				Max RSq
				0.9887

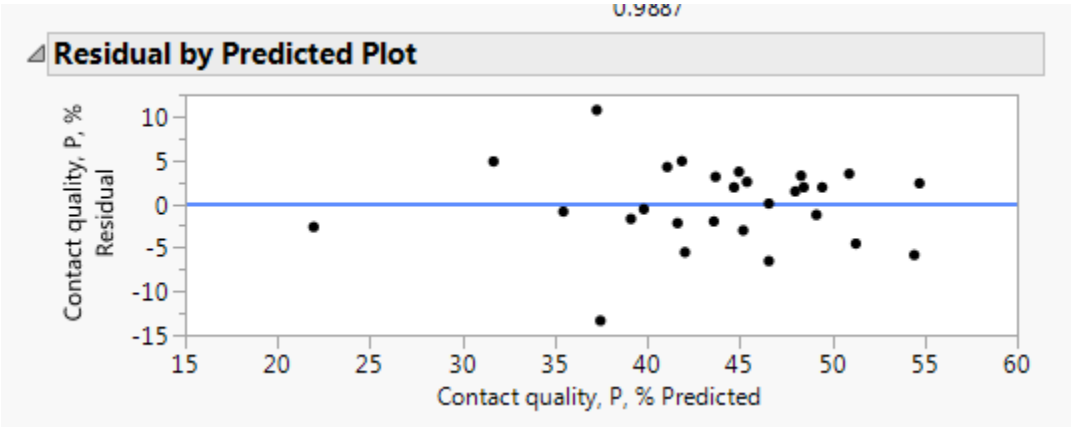

RSquare	0.69128
RSquare Adj	0.479035
Root Mean Square Error	6.057927
Mean of Response	43.73808
Observations (or Sum Wgts)	28

Term	Estimate	Std Error	t Ratio	Prob>|t|	Lower 95%	Upper 95%	F Ratio
Intercept	46.571669	2.025941	22.99	<.0001*	42.276867	50.866471	
Extruder Temperature(240,290)	-1.884949	1.427867	-1.32	0.2054	-4.911892	1.1419938	1.7427
Heated Bed Temperature(40,100)	-0.098921	1.427867	-0.07	0.9456	-3.125864	2.928022	0.0048
Layer thickness(0.09,0.29)	4.7050025	1.427867	3.30	0.0046*	1.6780596	7.7319455	10.8579
Extruder Speed(-50,50)	-3.062565	1.427867	-2.14	0.0477*	-6.089508	-0.035622	4.6004
Fan Speed(0,100)	-2.884629	1.427867	-2.02	0.0604	-5.911571	0.1423144	4.0814
Extruder Temperature*Layer thickness	1.9821831	1.514482	1.31	0.2091	-1.228375	5.1927409	1.7130
Heated Bed Temperature*Layer thickness	1.7026943	1.514482	1.12	0.2775	-1.507864	4.9132521	1.2640
Heated Bed Temperature*Extruder Speed	-2.14351	1.514482	-1.42	0.1761	-5.354067	1.0670483	2.0032
Extruder Temperature*Fan Speed	-1.749173	1.514482	-1.15	0.2651	-4.959731	1.4613849	1.3339
Heated Bed Temperature*Heated Bed Temperature	-9.210989	3.296162	-2.79	0.0130*	-16.19854	-2.223439	7.8090
Extruder Speed*Extruder Speed	4.8031836	3.296162	1.46	0.1644	-2.184367	11.790734	2.1234

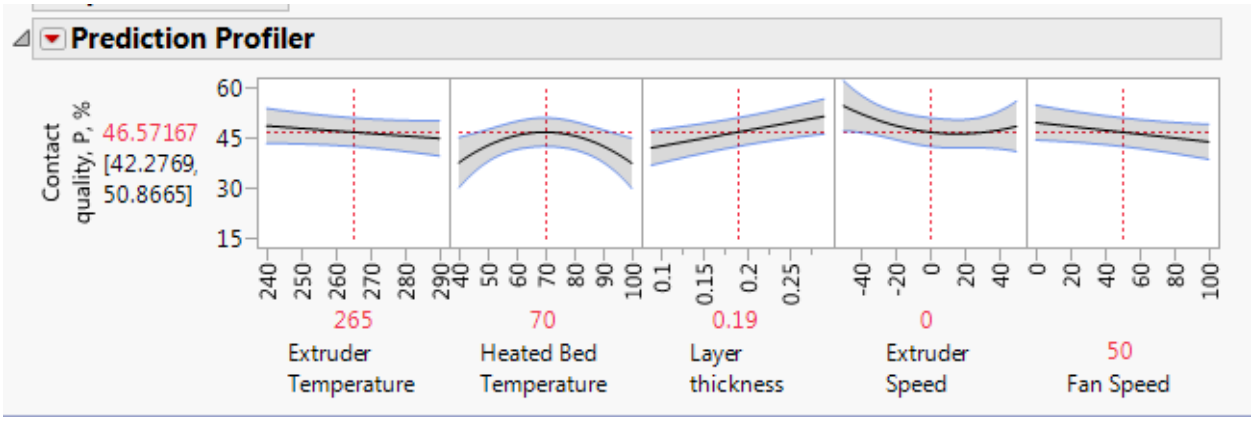

9.5.11 Statistical analyses on the density difference of small cube

Source	LogWorth	PValue
Speed(-50,50)	2.388	0.00409
Size, mm(3,11)	2.071	0.00849
Size, mm*Size, mm	1.549	0.02825
Extruder_T*Speed	0.881	0.13142
Size, mm*Speed	0.656	0.22057
Speed*Speed	0.303	0.49826
Size, mm*Extruder_T	0.238	0.57873
Extruder_T(240,290)	0.119	0.76067
Extruder_T*Extruder_T	0.047	0.89643

Source	DF	Sum of Squares	Mean Square	F Ratio
Lack Of Fit	5	484.01761	96.8035	1437.438
Pure Error	1	0.06734	0.0673	**Prob > F**
Total Error	6	484.08495		0.0200*
				Max RSq
				1.0000

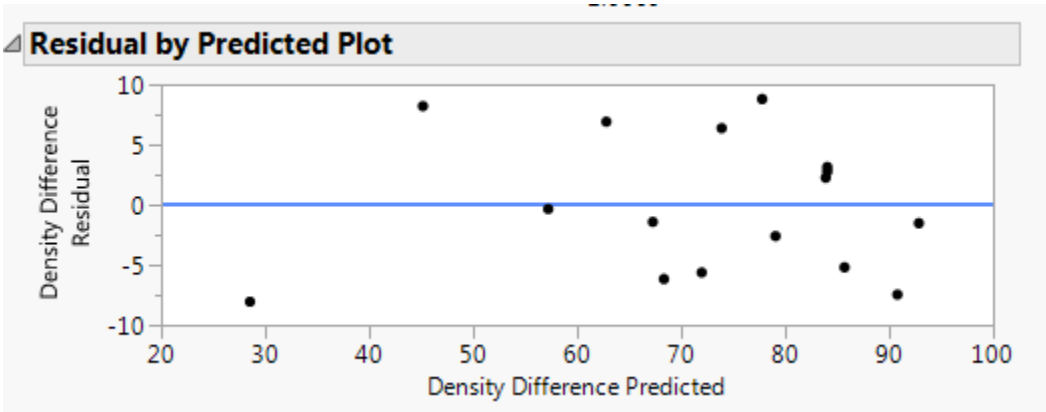

RSquare	0.901747
RSquare Adj	0.754367
Root Mean Square Error	8.982251
Mean of Response	72.09088
Observations (or Sum Wgts)	16

Term	Estimate	Std Error	t Ratio	Prob>|t|	Lower 95%	Upper 95%	F Ratio
Intercept	84.052707	4.252486	19.77	<.0001*	73.64725	94.458164	
Size, mm(3,11)	10.928	2.840437	3.85	0.0085*	3.977701	17.878299	14.8017
Extruder_T(240,290)	0.9056	2.840437	0.32	0.7607	-6.044699	7.855899	0.1016
Speed(-50,50)	-12.7909	2.840437	-4.50	0.0041*	-19.7412	-5.840601	20.2783
Size, mm*Extruder_T	-1.8635	3.175705	-0.59	0.5787	-9.634171	5.9071706	0.3443
Size, mm*Speed	4.34175	3.175705	1.37	0.2206	-3.428921	12.112421	1.8692
Extruder_T*Speed	5.54475	3.175705	1.75	0.1314	-2.225921	13.315421	3.0485
Size, mm*Size, mm	-15.90381	5.532004	-2.87	0.0282*	-29.44014	-2.367483	8.2649
Extruder_T*Extruder_T	0.7511897	5.532004	0.14	0.8964	-12.78514	14.287517	0.0184
Speed*Speed	-3.98631	5.532004	-0.72	0.4983	-17.52264	9.5500166	0.5193

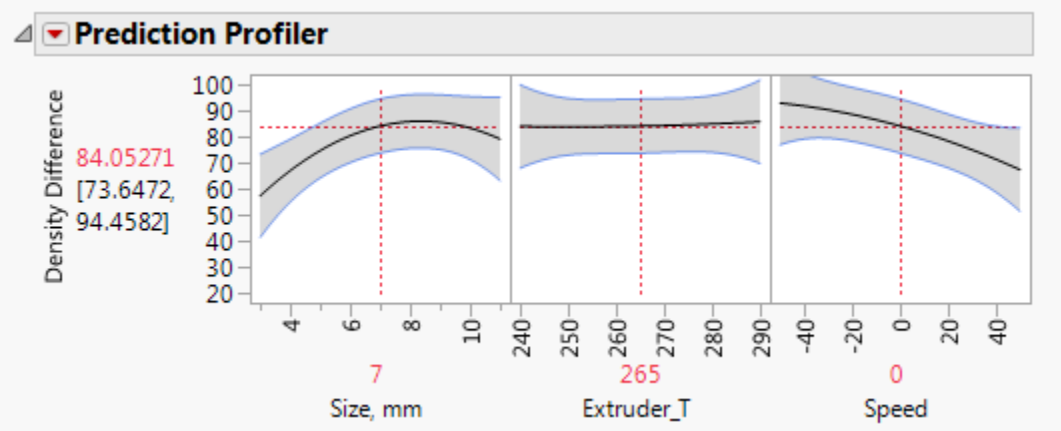

9.5.12 Statistical analyses on the reduced sources for the density difference of small cube

Source	LogWorth	PValue
Speed(-50,50)	3.221	0.00060
Size, mm(3,11)	2.766	0.00171
Size, mm*Size, mm	2.698	0.00200
Extruder_T*Speed	1.115	0.07681
Size, mm*Speed	0.818	0.15215
Extruder_T(240,290)	0.140	0.72366 ^

Source	DF	Sum of Squares	Mean Square	F Ratio
Lack Of Fit	8	554.47685	69.3096	1029.180

Source	DF	Sum of Squares	Mean Square	F Ratio
Pure Error	1	0.06734	0.0673	**Prob > F**
Total Error	9	554.54419		0.0241*
				Max RSq
				1.0000

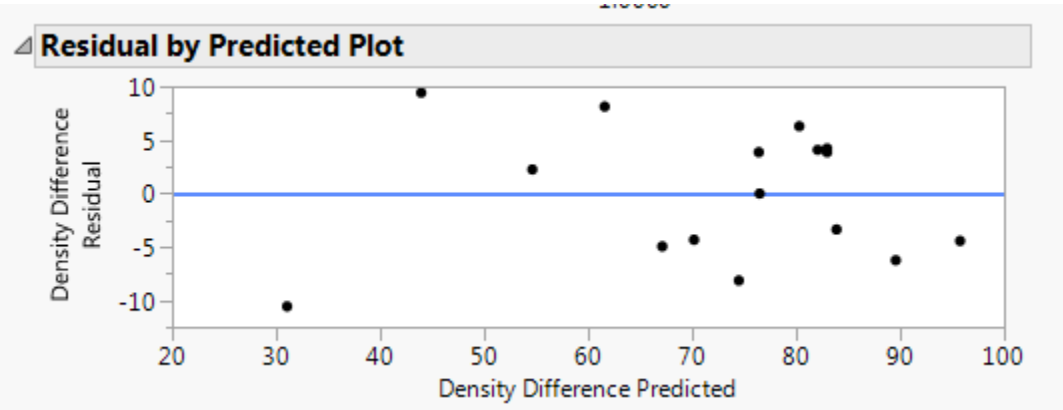

RSquare	0.887446
RSquare Adj	0.81241
Root Mean Square Error	7.849587
Mean of Response	72.09088
Observations (or Sum Wgts)	16

Term	Estimate	Std Error	t Ratio	Prob>|t|	Lower 95%	Upper 95%	F Ratio
Intercept	82.974333	3.204581	25.89	<.0001*	75.725068	90.223598	
Size, mm(3,11)	10.928	2.482257	4.40	0.0017*	5.3127435	16.543257	19.3815
Extruder_T(240,290)	0.9056	2.482257	0.36	0.7237	-4.709657	6.5208565	0.1331
Speed(-50,50)	-12.7909	2.482257	-5.15	0.0006*	-18.40616	-7.175643	26.5527
Size, mm*Speed	4.34175	2.775248	1.56	0.1521	-1.936298	10.619798	2.4475
Extruder_T*Speed	5.54475	2.775248	2.00	0.0768	-0.733298	11.822798	3.9917
Size, mm*Size, mm	-17.41353	4.053509	-4.30	0.0020*	-26.58321	-8.243858	18.4549

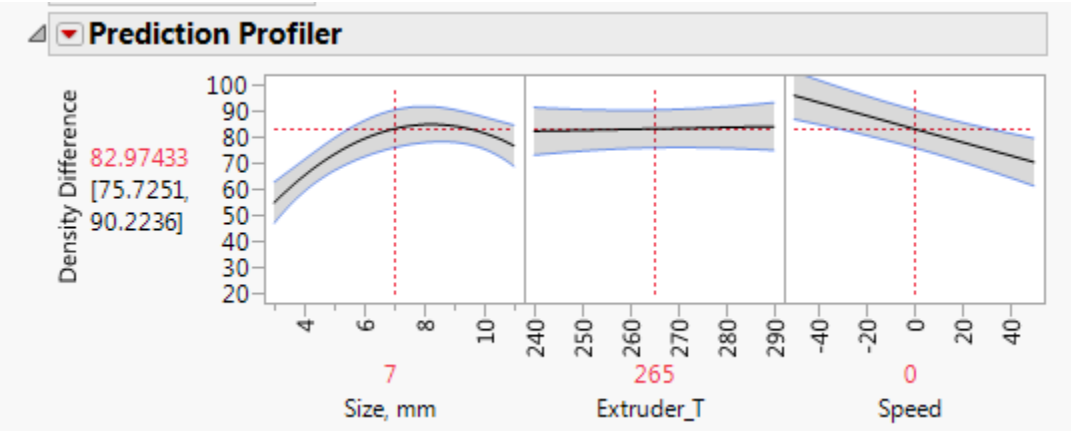

9.5.13 Statistical analyses on the contact quality of the small cubes

Source	LogWorth	PValue
Speed(-50,50)	2.510	0.00309
Size, mm(3,11)	2.059	0.00874
Size, mm*Size, mm	1.748	0.01788
Extruder_T*Speed	0.760	0.17381
Size, mm*Speed	0.416	0.38381
Speed*Speed	0.257	0.55276
Size, mm*Extruder_T	0.093	0.80677
Extruder_T*Extruder_T	0.059	0.87239
Extruder_T(240,290)	0.010	0.97722

Source	DF	Sum of Squares	Mean Square	F Ratio
Lack Of Fit	5	259.42996	51.8860	714.8751
Pure Error	1	0.07258	0.0726	**Prob > F**
Total Error	6	259.50254		0.0284*
				Max RSq
				1.0000

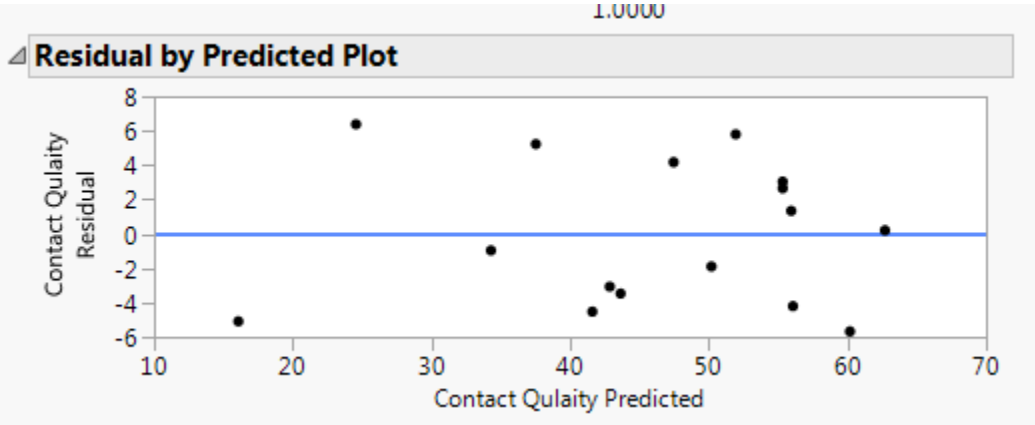

RSquare	0.906254
RSquare Adj	0.765634
Root Mean Square Error	6.576505
Mean of Response	45.98019
Observations (or Sum Wgts)	16

Term	Estimate	Std Error	t Ratio	Prob>|t|	F ratio
Intercept	55.327569	3.113529	17.77	<.0001*	
Size, mm(3,11)	7.949	2.079674	3.82	0.0087*	14.6095
Extruder_T(240,290)	0.0619	2.079674	0.03	0.9772	0.0009
Speed(-50,50)	-9.9239	2.079674	-4.77	0.0031*	22.7706
Size, mm*Extruder_T	-0.594375	2.325146	-0.26	0.8068	0.0653

Term	Estimate	Std Error	t Ratio	Prob>|t|	F ratio
Size, mm*Speed	2.184125	2.325146	0.94	0.3838	0.8824
Extruder_T*Speed	3.587375	2.325146	1.54	0.1738	2.3804
Size, mm*Size, mm	-13.0886	4.05035	-3.23	0.0179*	10.4424
Extruder_T*Extruder_T	0.6788966	4.05035	0.17	0.8724	0.0281
Speed*Speed	-2.546103	4.05035	-0.63	0.5528	0.3952

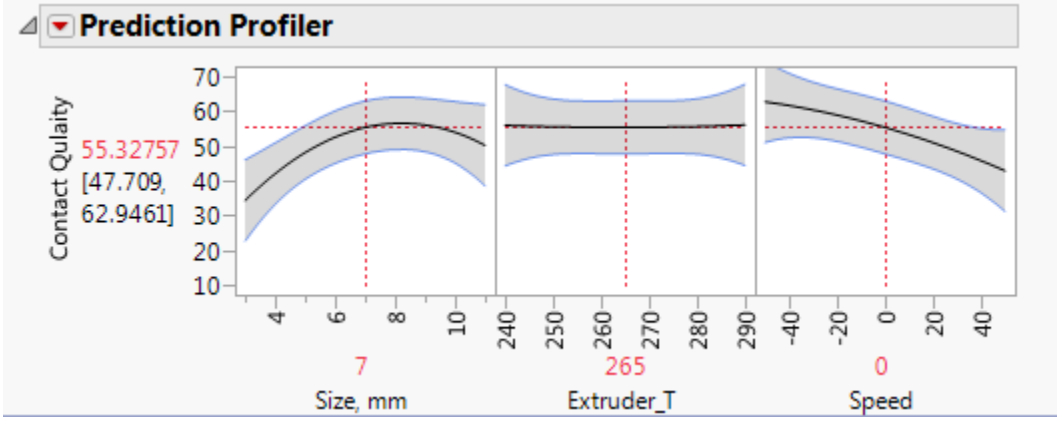

9.5.14 Statistical analyses on the reduced sources for the contact quality of the small cubes

Source	LogWorth	PValue
Speed(-50,50)	3.493	0.00032
Size, mm*Size, mm	3.043	0.00091
Size, mm(3,11)	2.834	0.00147 ^
Extruder_T*Speed	0.992	0.10196
Size, mm*Speed	0.528	0.29635
Extruder_T(240,290)	0.012	0.97275 ^

Source	DF	Sum of Squares	Mean Square	F Ratio
Lack Of Fit	8	279.39733	34.9247	481.1853
Pure Error	1	0.07258	0.0726	**Prob > F**
Total Error	9	279.46991		0.0352*
				Max RSq
				1.0000

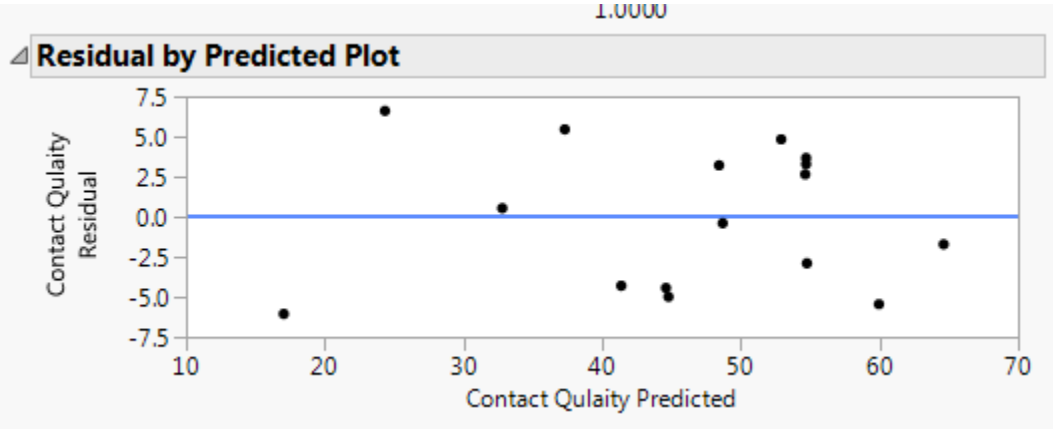

RSquare	0.89904
RSquare Adj	0.831734
Root Mean Square Error	5.572451
Mean of Response	45.98019
Observations (or Sum Wgts)	16

Term	Estimate	Std Error	t Ratio	Prob>|t|	Lower 95%	Upper 95%	F Ratio
Intercept	54.705167	2.274944	24.05	<.0001*	49.558887	59.851447	
Size, mm(3,11)	7.949	1.762164	4.51	0.0015*	3.9627085	11.935291	20.3485
Extruder_T(240,290)	0.0619	1.762164	0.04	0.9727	-3.924391	4.0481915	0.0012
Speed(-50,50)	-9.9239	1.762164	-5.63	0.0003*	-13.91019	-5.937609	31.7155
Size, mm*Speed	2.184125	1.970159	1.11	0.2963	-2.272684	6.6409343	1.2290
Extruder_T*Speed	3.587375	1.970159	1.82	0.1020	-0.869434	8.0441843	3.3155
Size, mm*Size, mm	-13.95997	2.877601	-4.85	0.0009*	-20.46955	-7.45038	23.5346

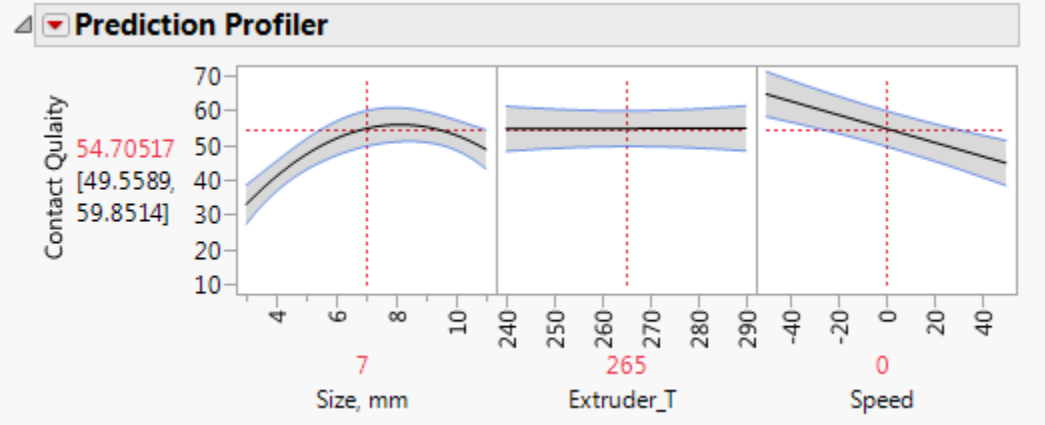

9.5.15 Statistical analyses on the reduced sources for isotropic material property

9.5.15.1 Young's modulus for the center part, E/G method

Source	LogWorth	PValue
Layer thickness(0.09,0.29)	0.879	0.13225
Extruder Temperature*Heated Bed Temperature	0.433	0.36932
Extruder Temperature*Extruder Speed	0.420	0.38008
Heated Bed Temperature*Extruder Speed	0.382	0.41478
Extruder Speed*Fan Speed	0.375	0.42164
Heated Bed Temperature*Layer thickness	0.340	0.45741
Extruder Temperature*Fan Speed	0.323	0.47526
Extruder Temperature*Extruder Temperature	0.261	0.54854
Heated Bed Temperature*Heated Bed Temperature	0.225	0.59619
Layer thickness*Layer thickness	0.223	0.59853
Heated Bed Temperature*Fan Speed	0.183	0.65592
Fan Speed*Fan Speed	0.163	0.68668
Extruder Speed(-50,50)	0.129	0.74347
Extruder Temperature(240,290)	0.123	0.75297
Layer thickness*Extruder Speed	0.114	0.76967
Layer thickness*Fan Speed	0.080	0.83249
Heated Bed Temperature(40,100)	0.051	0.88905
Extruder Speed*Extruder Speed	0.050	0.89218
Fan Speed(0,100)	0.031	0.93151
Extruder Temperature*Layer thickness	0.017	0.96263

Source	DF	Sum of Squares	Mean Square	F Ratio
Lack Of Fit	6	449937.22	74989.5	9.1131
Pure Error	1	8228.78	8228.8	**Prob > F**
Total Error	7	458166.00		0.2483
				Max RSq
				0.9921

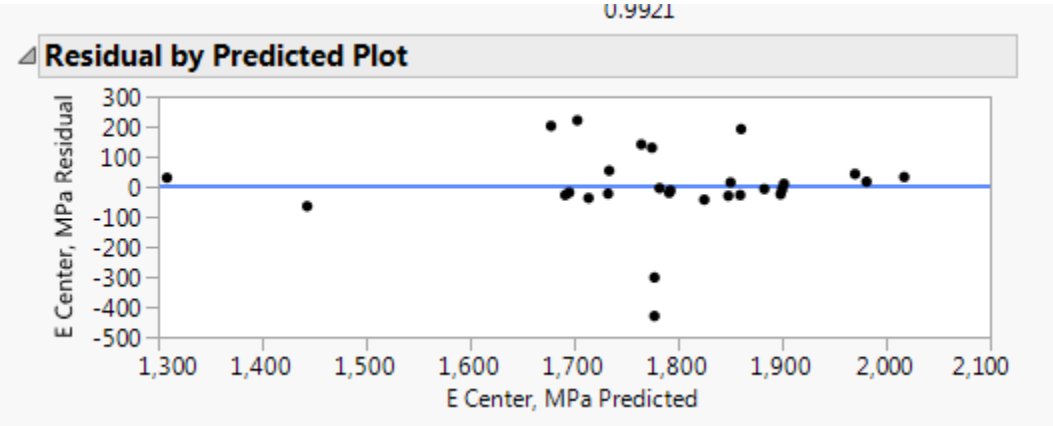

RSquare	0.561708
RSquare Adj	-0.69056
Root Mean Square Error	255.8364
Mean of Response	1784.103
Observations (or Sum Wgts)	28

Term	Estimate	Std Error	t Ratio	Prob>|t|	Lower 95%	Upper 95%	F Ratio
Intercept	1777.2167	89.10375	19.95	<.0001*	1566.5198	1987.9136	
Extruder Temperature(240,290)	19.739778	60.30123	0.33	0.7530	-122.85	162.32952	0.1072
Heated Bed Temperature(40,100)	-8.723278	60.30123	-0.14	0.8891	-151.313	133.86647	0.0209
Layer thickness(0.09,0.29)	-102.7244	60.30123	-1.70	0.1323	-245.3142	39.865301	2.9020
Extruder Speed(-50,50)	20.5325	60.30123	0.34	0.7435	-122.0572	163.12225	0.1159
Fan Speed(0,100)	-5.371944	60.30123	-0.09	0.9315	-147.9617	137.2178	0.0079
Extruder Temperature*Heated Bed Temperature	61.361625	63.95911	0.96	0.3693	-89.87764	212.60089	0.9204
Extruder Temperature*Layer thickness	3.105625	63.95911	0.05	0.9626	-148.1336	154.34489	0.0024
Heated Bed Temperature*Layer thickness	50.2995	63.95911	0.79	0.4574	-100.9398	201.53876	0.6185
Extruder Temperature*Extruder Speed	59.91225	63.95911	0.94	0.3801	-91.32701	211.15151	0.8775
Heated Bed Temperature*Extruder Speed	-55.43838	63.95911	-0.87	0.4148	-206.6776	95.800889	0.7513
Layer thickness*Extruder Speed	19.469875	63.95911	0.30	0.7697	-131.7694	170.70914	0.0927
Extruder Temperature*Fan Speed	48.24575	63.95911	0.75	0.4753	-102.9935	199.48501	0.5690
Heated Bed Temperature*Fan Speed	-29.75288	63.95911	-0.47	0.6559	-180.9921	121.48639	0.2164
Layer thickness*Fan Speed	14.042125	63.95911	0.22	0.8325	-137.1971	165.28139	0.0482
Extruder Speed*Fan Speed	-54.587	63.95911	-0.85	0.4216	-205.8263	96.652264	0.7284
Extruder Temperature*Extruder Temperature	103.02929	163.4721	0.63	0.5485	-283.5208	489.57935	0.3972
Heated Bed Temperature*Heated Bed Temperature	-90.72421	163.4721	-0.55	0.5962	-477.2743	295.82585	0.3080
Layer thickness*Layer thickness	90.133293	163.4721	0.55	0.5985	-296.4168	476.68335	0.3040
Extruder Speed*Extruder Speed	-22.97621	163.4721	-0.14	0.8922	-409.5263	363.57385	0.0198
Fan Speed*Fan Speed	-68.75021	163.4721	-0.42	0.6867	-455.3003	317.79985	0.1769

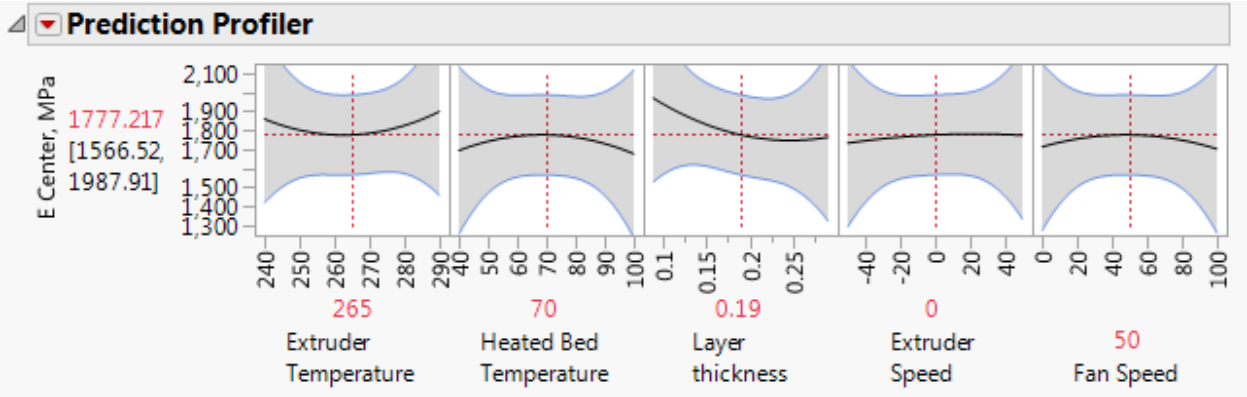

- ***Reduced sources***

Source	LogWorth	PValue
Layer thickness(0.09,0.29)	1.509	0.03100
Extruder Temperature*Heated Bed Temperature	0.690	0.20408
Extruder Temperature*Extruder Speed	0.669	0.21449
Heated Bed Temperature*Extruder Speed	0.603	0.24926
Extruder Speed*Fan Speed	0.591	0.25634
Extruder Speed(-50,50)	0.190	0.64560
Extruder Temperature(240,290)	0.182	0.65832
Heated Bed Temperature(40,100)	0.073	0.84471
Fan Speed(0,100)	0.044	0.90396

Source	DF	Sum of Squares	Mean Square	F Ratio
Lack Of Fit	17	616155.48	36244.4	4.4046
Pure Error	1	8228.78	8228.8	**Prob > F**
Total Error	18	624384.25		0.3602
				Max RSq
				0.9921

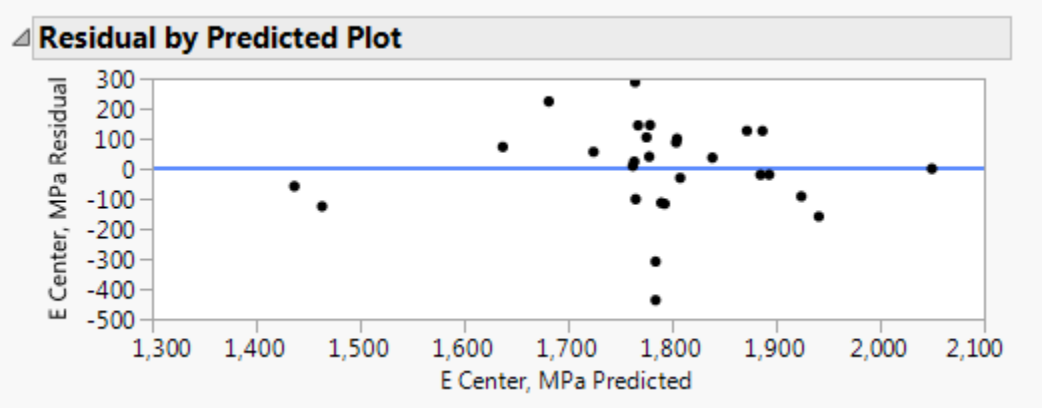

RSquare	0.402699
RSquare Adj	0.104049
Root Mean Square Error	186.2472
Mean of Response	1784.103
Observations (or Sum Wgts)	28

Term	Estimate	Std Error	t Ratio	Prob>|t|	Lower 95%	Upper 95%	F Ratio
Intercept	1784.1029	35.19741	50.69	<.0001*	1710.1559	1858.0499	
Extruder Temperature(240,290)	19.739778	43.89888	0.45	0.6583	-72.48835	111.96791	0.2022
Heated Bed Temperature(40,100)	-8.723278	43.89888	-0.20	0.8447	-100.9514	83.504852	0.0395
Layer thickness(0.09,0.29)	-102.7244	43.89888	-2.34	0.0310*	-194.9526	-10.49631	5.4757
Extruder Speed(-50,50)	20.5325	43.89888	0.47	0.6456	-71.69563	112.76063	0.2188
Fan Speed(0,100)	-5.371944	43.89888	-0.12	0.9040	-97.60007	86.856185	0.0150
Extruder Temperature*Heated Bed Temperature	61.361625	46.5618	1.32	0.2041	-36.46108	159.18433	1.7367

Term	Estimate	Std Error	t Ratio	Prob>|t|	Lower 95%	Upper 95%	F Ratio
Extruder Temperature*Extruder Speed	59.91225	46.5618	1.29	0.2145	-37.91045	157.73495	1.6557
Heated Bed Temperature*Extruder Speed	-55.43838	46.5618	-1.19	0.2493	-153.2611	42.384329	1.4176
Extruder Speed*Fan Speed	-54.587	46.5618	-1.17	0.2563	-152.4097	43.235704	1.3744

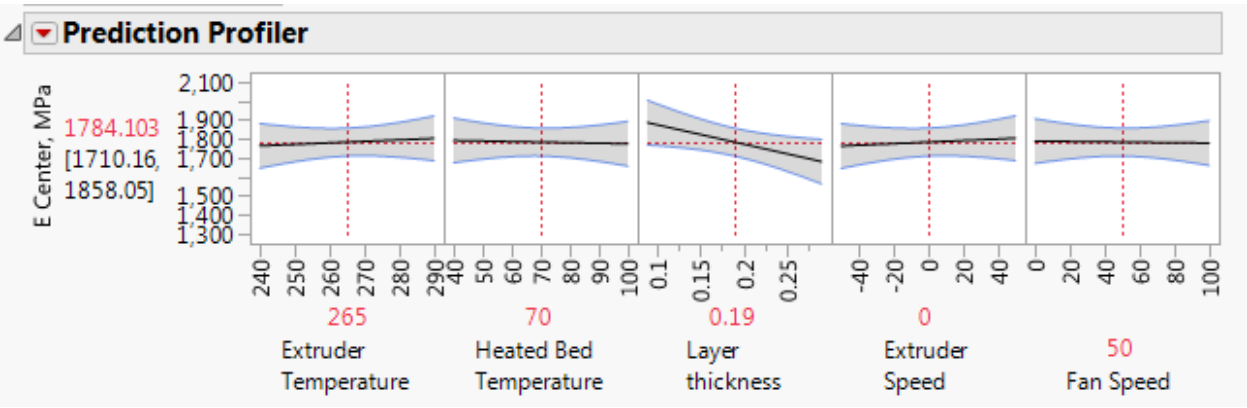

9.5.15.2 Shear modulus for the center part, E/G method

Source	LogWorth	PValue
Layer thickness(0.09,0.29)	2.680	0.00209
Extruder Temperature*Extruder Speed	0.711	0.19475
Layer thickness*Layer thickness	0.681	0.20825
Heated Bed Temperature*Heated Bed Temperature	0.651	0.22344
Extruder Temperature*Heated Bed Temperature	0.639	0.22977
Extruder Temperature(240,290)	0.141	0.72221
Heated Bed Temperature(40,100)	0.106	0.78308
Extruder Speed(-50,50)	0.035	0.92153
Fan Speed(0,100)	0.032	0.92863

Source	DF	Sum of Squares	Mean Square	F Ratio
Lack Of Fit	17	113647.53	6685.15	5.2786
Pure Error	1	1266.45	1266.45	**Prob > F**
Total Error	18	114913.99		0.3311
				Max RSq
				0.9946

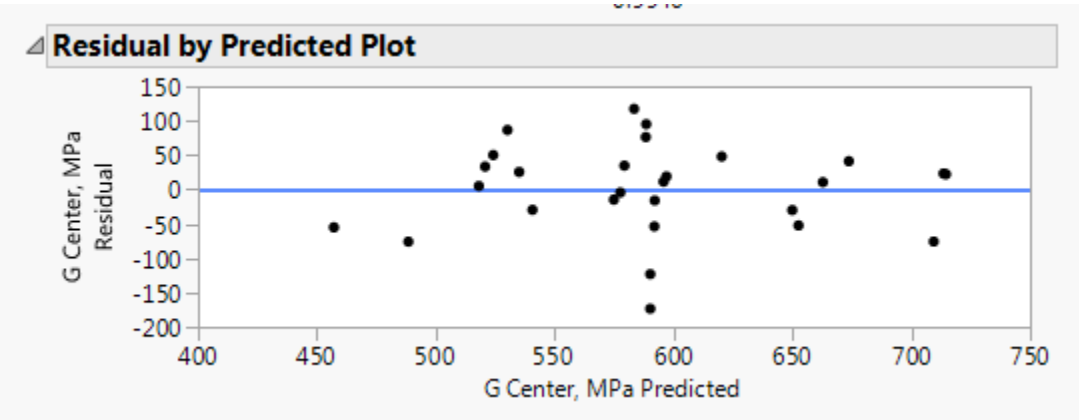

RSquare
RSquare Adj
Root Mean Square Error
Mean of Response
Observations (or Sum Wgts)

Term	Estimate	Std Error	t Ratio	Prob>|t|	Lower 95%	Upper 95%	F Ratio
Intercept	590.1925	26.72101	22.09	<.0001*	534.05374	646.33126	
Extruder Temperature(240,290)	6.801	18.83276	0.36	0.7222	-32.76516	46.367158	0.1304
Heated Bed Temperature(40,100)	-5.263056	18.83276	-0.28	0.7831	-44.82921	34.303102	0.0781
Layer thickness(0.09,0.29)	-67.62983	18.83276	-3.59	0.0021*	-107.196	-28.06368	12.8958
Extruder Speed(-50,50)	-1.881389	18.83276	-0.10	0.9215	-41.44755	37.684769	0.0100
Fan Speed(0,100)	-1.7105	18.83276	-0.09	0.9286	-41.27666	37.855658	0.0082
Extruder Temperature*Heated Bed Temperature	24.831625	19.97516	1.24	0.2298	-17.13462	66.797873	1.5454
Extruder Temperature*Extruder Speed	26.903	19.97516	1.35	0.1948	-15.06325	68.869248	1.8139
Heated Bed Temperature*Heated Bed Temperature	-54.817	43.47451	-1.26	0.2234	-146.1535	36.519548	1.5899
Layer thickness*Layer thickness	56.745	43.47451	1.31	0.2082	-34.59155	148.08155	1.7037

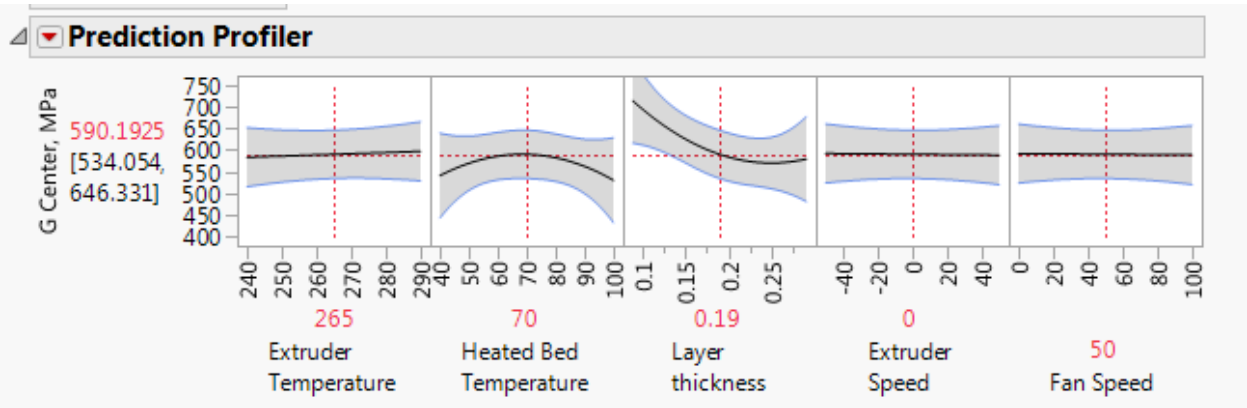

9.5.15.3 Poisson'sration for the center part, E/G method

Source	LogWorth	PValue
Layer thickness(0.09,0.29)	4.625	0.00002
Heated Bed Temperature*Heated Bed Temperature	1.101	0.07931
Layer thickness*Layer thickness	0.978	0.10526
Extruder Speed(-50,50)	0.776	0.16763
Layer thickness*Fan Speed	0.773	0.16852
Extruder Temperature*Extruder Speed	0.706	0.19671
Heated Bed Temperature*Layer thickness	0.657	0.22024
Heated Bed Temperature(40,100)	0.142	0.72029
Extruder Temperature(240,290)	0.074	0.84338
Fan Speed(0,100)	0.044	0.90386

Source	DF	Sum of Squares	Mean Square	F Ratio
Lack Of Fit	16	0.06774541	0.004234	6.1857
Pure Error	1	0.00068450	0.000685	**Prob > F**
Total Error	17	0.06842991		0.3071
				Max RSq
				0.9972

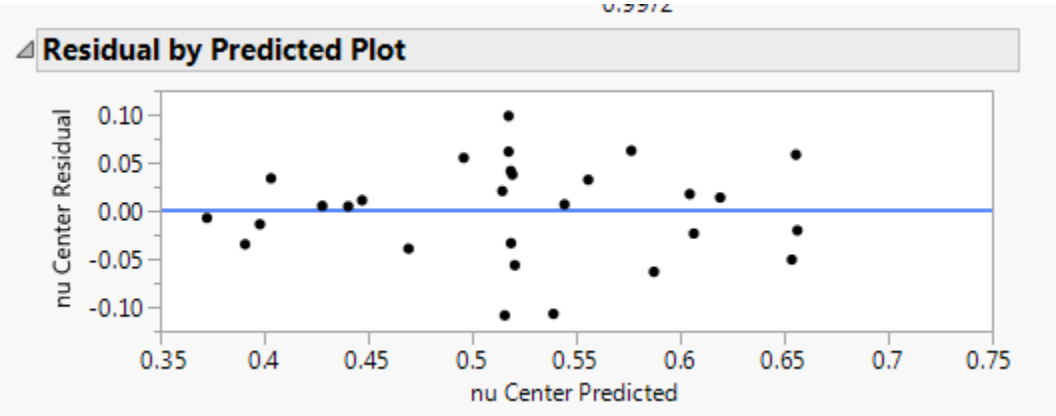

RSquare	0.724105
RSquare Adj	0.561814
Root Mean Square Error	0.063445
Mean of Response	0.520964
Observations (or Sum Wgts)	28

Term	Estimate	Std Error	t Ratio	Prob>|t|	Lower 95%	Upper 95%	F Ratio
Intercept	0.5175132	0.021218	24.39	<.0001*	0.4727474	0.5622789	
Extruder Temperature(240,290)	-0.003	0.014954	-0.20	0.8434	-0.034551	0.0285505	0.0402
Heated Bed Temperature(40,100)	0.0054444	0.014954	0.36	0.7203	-0.026106	0.036995	0.1326

Term	Estimate	Std Error	t Ratio	Prob>|t|	Lower 95%	Upper 95%	F Ratio
Layer thickness(0.09,0.29)	0.0859444	0.014954	5.75	<.0001*	0.0543939	0.117495	33.0302
Extruder Speed(-50,50)	0.0215556	0.014954	1.44	0.1676	-0.009995	0.0531061	2.0778
Fan Speed(0,100)	-0.001833	0.014954	-0.12	0.9039	-0.033384	0.0297172	0.0150
Heated Bed Temperature*Layer thickness	0.0201875	0.015861	1.27	0.2202	-0.013277	0.0536519	1.6199
Extruder Temperature*Extruder Speed	-0.021313	0.015861	-1.34	0.1967	-0.054777	0.0121519	1.8055
Layer thickness*Fan Speed	-0.022813	0.015861	-1.44	0.1685	-0.056277	0.0106519	2.0686
Heated Bed Temperature*Heated Bed Temperature	0.0644342	0.034521	1.87	0.0793	-0.008399	0.1372671	3.4839
Layer thickness*Layer thickness	-0.059066	0.034521	-1.71	0.1053	-0.131899	0.0137671	2.9276

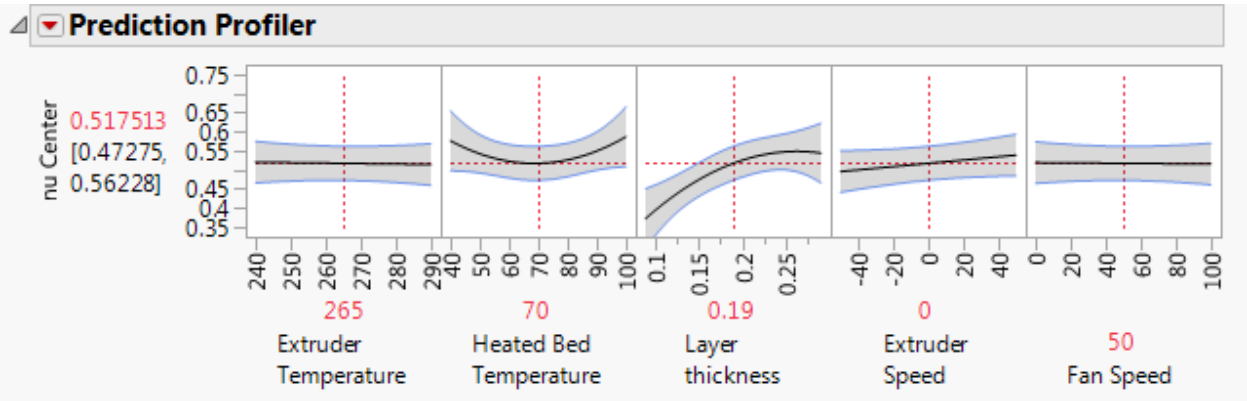

9.5.15.4 Young's modulus for the wing part, E/G method

Source	LogWorth	PValue
Layer thickness(0.09,0.29)	3.801	0.00016
Extruder Temperature*Extruder Temperature	0.905	0.12444
Heated Bed Temperature(40,100)	0.876	0.13320
Layer thickness*Extruder Speed	0.734	0.18433
Heated Bed Temperature*Layer thickness	0.704	0.19770
Heated Bed Temperature*Extruder Speed	0.661	0.21835
Extruder Temperature*Fan Speed	0.658	0.21994
Fan Speed(0,100)	0.472	0.33759 ^
Fan Speed*Fan Speed	0.328	0.46987
Extruder Speed(-50,50)	0.273	0.53309 ^
Extruder Temperature(240,290)	0.026	0.94277 ^

Source	DF	Sum of Squares	Mean Square	F Ratio
Lack Of Fit	15	521579.92	34772.0	0.5660
Pure Error	1	61438.09	61438.1	**Prob > F**
Total Error	16	583018.02		0.7964
				Max RSq

Source	DF	Sum of Squares	Mean Square	F Ratio
				0.9687

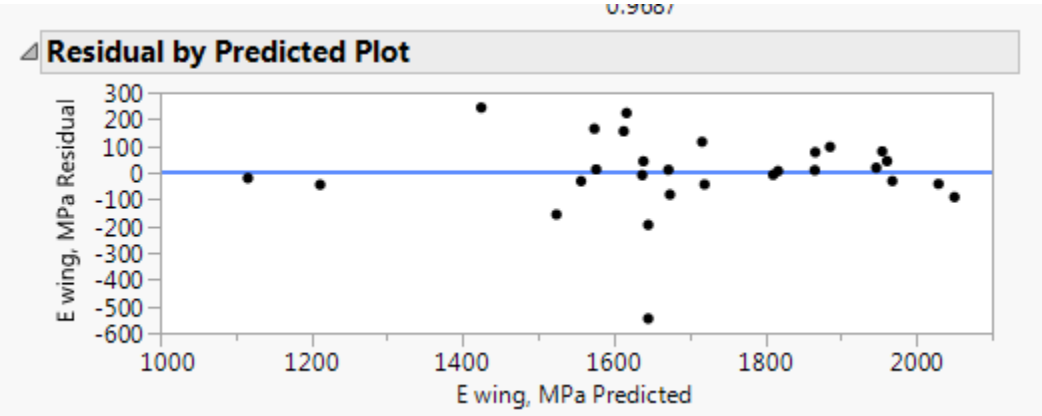

RSquare	0.702991
RSquare Adj	0.498797
Root Mean Square Error	190.889
Mean of Response	1704.149
Observations (or Sum Wgts)	28

Term	Estimate	Std Error	t Ratio	Prob>|t|	Lower 95%	Upper 95%	F Ratio
Intercept	1645.3065	63.83865	25.77	<.0001*	1509.9746	1780.6384	
Extruder Temperature(240,290)	3.2812778	44.99298	0.07	0.9428	-92.09958	98.662131	0.0053
Heated Bed Temperature(40,100)	71.182167	44.99298	1.58	0.1332	-24.19869	166.56302	2.5030
Layer thickness(0.09,0.29)	-220.7709	44.99298	-4.91	0.0002*	-316.1518	-125.3901	24.0766
Extruder Speed(-50,50)	28.663722	44.99298	0.64	0.5331	-66.71713	124.04458	0.4059
Fan Speed(0,100)	-44.47872	44.99298	-0.99	0.3376	-139.8596	50.902131	0.9773
Heated Bed Temperature*Layer thickness	64.138813	47.72226	1.34	0.1977	-37.02786	165.30549	1.8063
Heated Bed Temperature*Extruder Speed	-61.14581	47.72226	-1.28	0.2184	-162.3125	40.02086	1.6417
Layer thickness*Extruder Speed	66.211563	47.72226	1.39	0.1843	-34.95511	167.37824	1.9250
Extruder Temperature*Fan Speed	60.925188	47.72226	1.28	0.2199	-40.24149	162.09186	1.6299
Extruder Temperature*Extruder Temperature	168.41787	103.8641	1.62	0.1244	-51.76419	388.59992	2.6293
Fan Speed*Fan Speed	-76.88513	103.8641	-0.74	0.4699	-297.0672	143.29692	0.5480

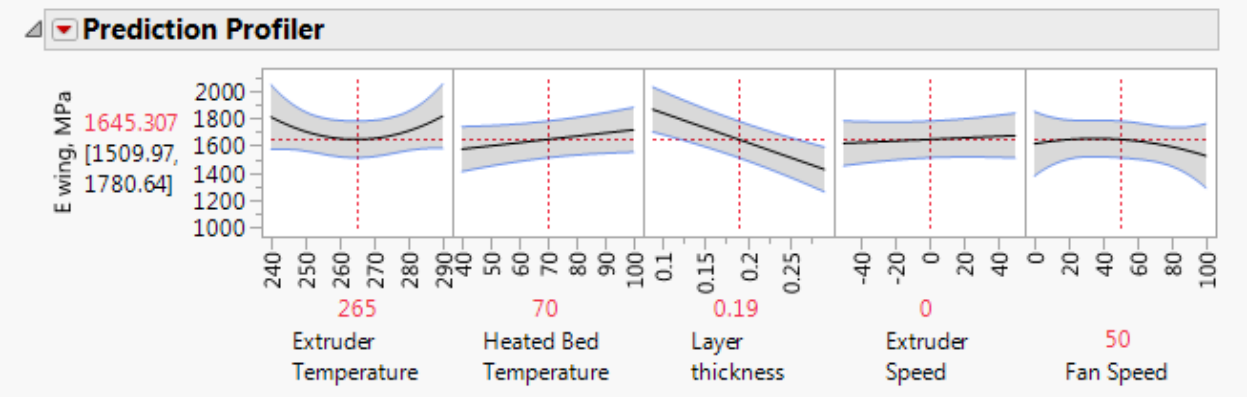

9.5.15.5 Shear modulus for the wing part, E/G method

Source	LogWorth	PValue
Layer thickness(0.09,0.29)	2.680	0.00209
Extruder Temperature*Extruder Speed	0.711	0.19475
Layer thickness*Layer thickness	0.681	0.20825
Heated Bed Temperature*Heated Bed Temperature	0.651	0.22344
Extruder Temperature*Heated Bed Temperature	0.639	0.22977
Extruder Temperature(240,290)	0.141	0.72221 ^
Heated Bed Temperature(40,100)	0.106	0.78308 ^
Extruder Speed(-50,50)	0.035	0.92153 ^
Fan Speed(0,100)	0.032	0.92863

Source	DF	Sum of Squares	Mean Square	F Ratio
Lack Of Fit	17	113647.53	6685.15	5.2786
Pure Error	1	1266.45	1266.45	**Prob > F**
Total Error	18	114913.99		0.3311
				Max RSq
				0.9946

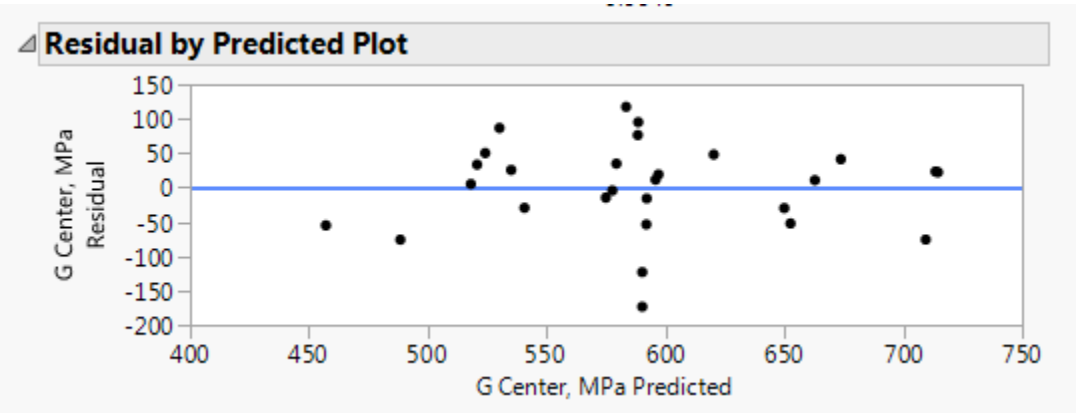

RSquare	0.505963
RSquare Adj	0.258945
Root Mean Square Error	79.90063
Mean of Response	591.4319
Observations (or Sum Wgts)	28

Term	Estimate	Std Error	t Ratio	Prob>|t|	Lower 95%	Upper 95%	F Ratio
Intercept	590.1925	26.72101	22.09	<.0001*	534.05374	646.33126	
Extruder Temperature(240,290)	6.801	18.83276	0.36	0.7222	-32.76516	46.367158	0.1304
Heated Bed Temperature(40,100)	-5.263056	18.83276	-0.28	0.7831	-44.82921	34.303102	0.0781
Layer thickness(0.09,0.29)	-67.62983	18.83276	-3.59	0.0021*	-107.196	-28.06368	12.8958
Extruder Speed(-50,50)	-1.881389	18.83276	-0.10	0.9215	-41.44755	37.684769	0.0100
Fan Speed(0,100)	-1.7105	18.83276	-0.09	0.9286	-41.27666	37.855658	0.0082
Extruder Temperature*Heated Bed Temperature	24.831625	19.97516	1.24	0.2298	-17.13462	66.797873	1.5454
Extruder Temperature*Extruder Speed	26.903	19.97516	1.35	0.1948	-15.06325	68.869248	1.8139
Heated Bed Temperature*Heated Bed Temperature	-54.817	43.47451	-1.26	0.2234	-146.1535	36.519548	1.5899
Layer thickness*Layer thickness	56.745	43.47451	1.31	0.2082	-34.59155	148.08155	1.7037

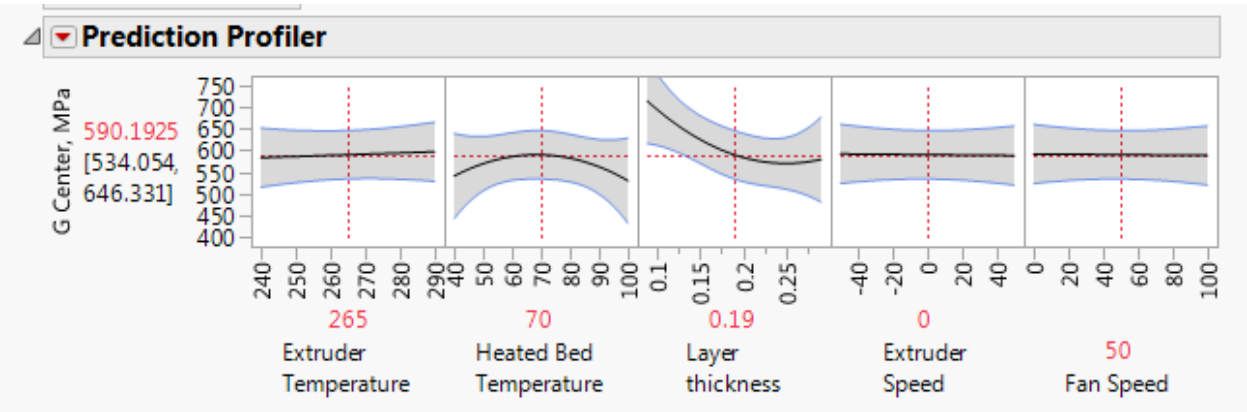

9.5.15.6 Poisson's ration for the wing part, E/G method

Source	LogWorth	PValue
Heated Bed Temperature(40,100)	2.068	0.00855
Layer thickness(0.09,0.29)	1.409	0.03897
Layer thickness*Layer thickness	1.220	0.06021
Layer thickness*Extruder Speed	0.958	0.11024
Fan Speed*Fan Speed	0.594	0.25457
Fan Speed(0,100)	0.558	0.27661
Extruder Temperature(240,290)	0.410	0.38883
Extruder Speed(-50,50)	0.278	0.52744

Source	DF	Sum of Squares	Mean Square	F Ratio
Lack Of Fit	18	0.11505571	0.006392	0.3946
Pure Error	1	0.01620000	0.016200	**Prob > F**
Total Error	19	0.13125571		0.8712
				Max RSq
				0.9440

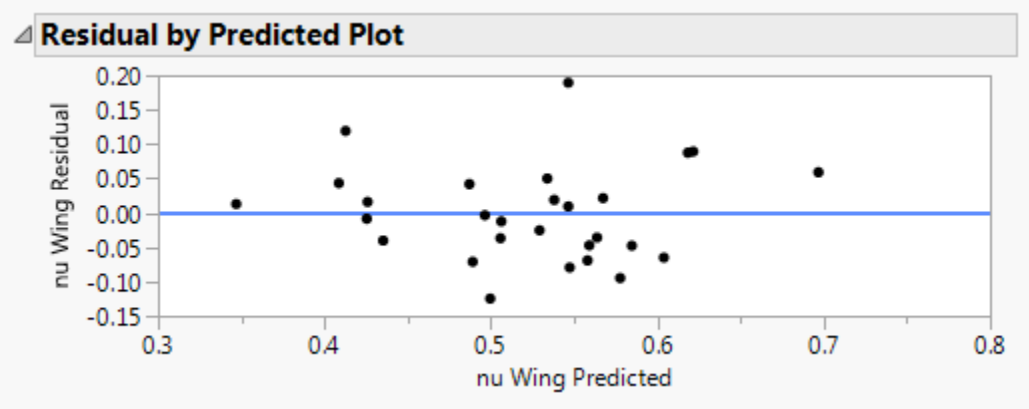

RSquare	0.545892
RSquare Adj	0.354689
Root Mean Square Error	0.083116
Mean of Response	0.522536
Observations (or Sum Wgts)	28

Term	Estimate	Std Error	t Ratio	Prob>|t|	Lower 95%	Upper 95%	F Ratio
Intercept	0.5464737	0.027796	19.66	<.0001*	0.4882956	0.6046517	
Extruder Temperature(240,290)	-0.017278	0.019591	-0.88	0.3888	-0.058281	0.0237257	0.7778
Heated Bed Temperature(40,100)	-0.057444	0.019591	-2.93	0.0085*	-0.098448	-0.016441	8.5981
Layer thickness(0.09,0.29)	0.0434444	0.019591	2.22	0.0390*	0.002441	0.0844479	4.9179
Extruder Speed(-50,50)	-0.012611	0.019591	-0.64	0.5274	-0.053615	0.0283923	0.4144
Fan Speed(0,100)	0.0219444	0.019591	1.12	0.2766	-0.019059	0.0629479	1.2547
Layer thickness*Extruder Speed	-0.034813	0.020779	-1.68	0.1102	-0.078303	0.0086782	2.8069
Layer thickness*Layer thickness	-0.090368	0.045224	-2.00	0.0602	-0.185023	0.004286	3.9930
Fan Speed*Fan Speed	0.0531316	0.045224	1.17	0.2546	-0.041523	0.147786	1.3803

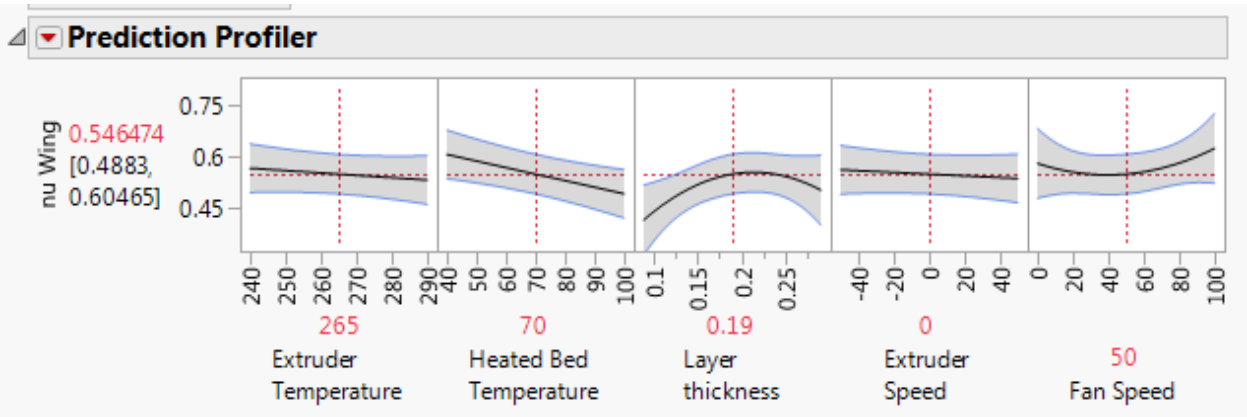

9.5.15.7 Young's modulus for the center part, *E/v* method

Source	LogWorth	PValue
Heated Bed Temperature*Layer thickness	1.262	0.05466
Extruder Temperature*Fan Speed	1.243	0.05721
Extruder Temperature(240,290)	1.239	0.05769
Extruder Temperature*Extruder Speed	1.031	0.09305
Layer thickness*Extruder Speed	0.822	0.15062
Fan Speed*Fan Speed	0.798	0.15935
Layer thickness(0.09,0.29)	0.790	0.16235
Extruder Speed*Extruder Speed	0.700	0.19965
Extruder Temperature*Heated Bed Temperature	0.626	0.23677
Fan Speed(0,100)	0.406	0.39222
Heated Bed Temperature(40,100)	0.062	0.86737
Extruder Speed(-50,50)	0.011	0.97552

Source	DF	Sum of Squares	Mean Square	F Ratio
Lack Of Fit	14	373465.98	26676.1	9.9435
Pure Error	1	2682.78	2682.8	**Prob > F**
Total Error	15	376148.76		0.2442
				Max RSq
				0.9973

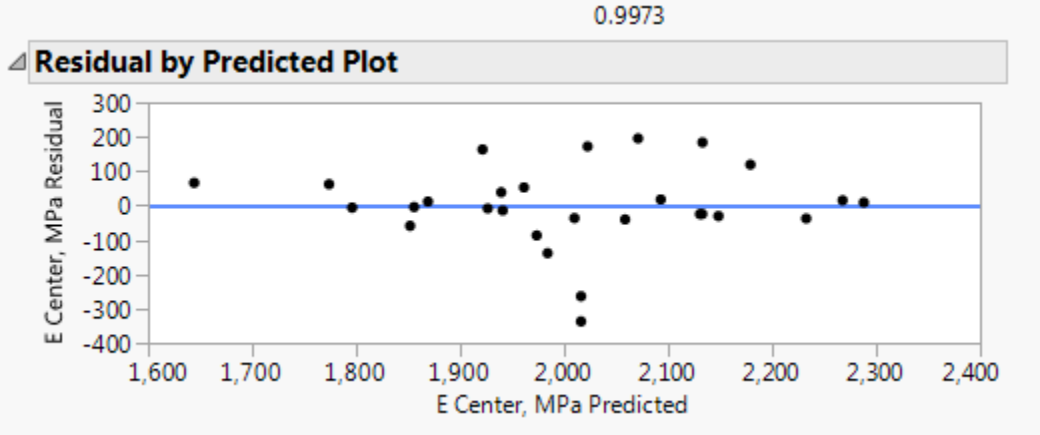

RSquare	0.62683
RSquare Adj	0.328294
Root Mean Square Error	158.3559
Mean of Response	2008.504
Observations (or Sum Wgts)	28

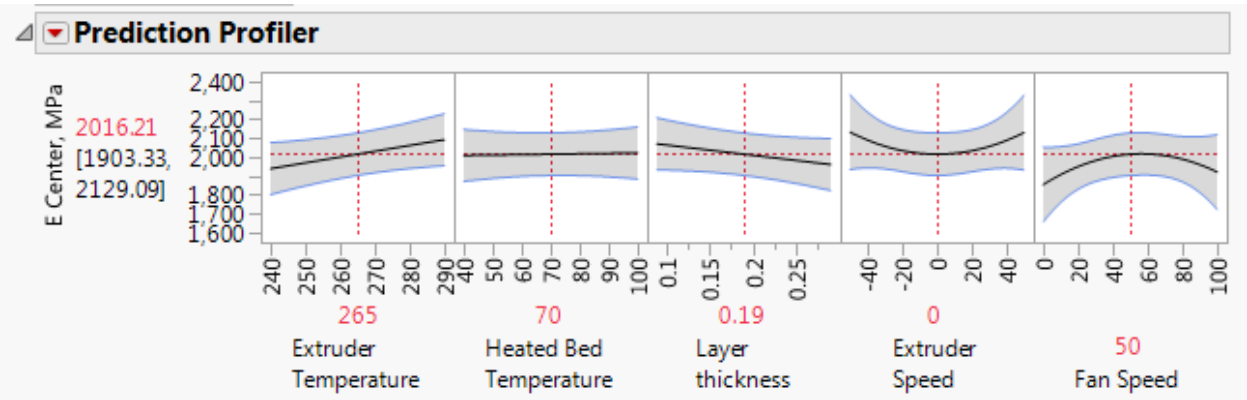

9.5.15.8 Shear modulus for the center part, *E/v* method

Source	LogWorth	PValue
Layer thickness(0.09,0.29)	4.200	0.00006
Extruder Temperature(240,290)	1.024	0.09458
Extruder Temperature*Extruder Speed	1.017	0.09619
Extruder Temperature*Fan Speed	0.914	0.12184
Heated Bed Temperature*Heated Bed Temperature	0.887	0.12964
Layer thickness*Layer thickness	0.801	0.15798
Extruder Temperature*Heated Bed Temperature	0.775	0.16803
Fan Speed(0,100)	0.567	0.27133
Extruder Speed(-50,50)	0.173	0.67077
Heated Bed Temperature(40,100)	0.045	0.90181

Source	DF	Sum of Squares	Mean Square	F Ratio
Lack Of Fit	16	83743.525	5233.97	3.4718
Pure Error	1	1507.581	1507.58	**Prob > F**
Total Error	17	85251.106		0.4011
				Max RSq
				0.9950

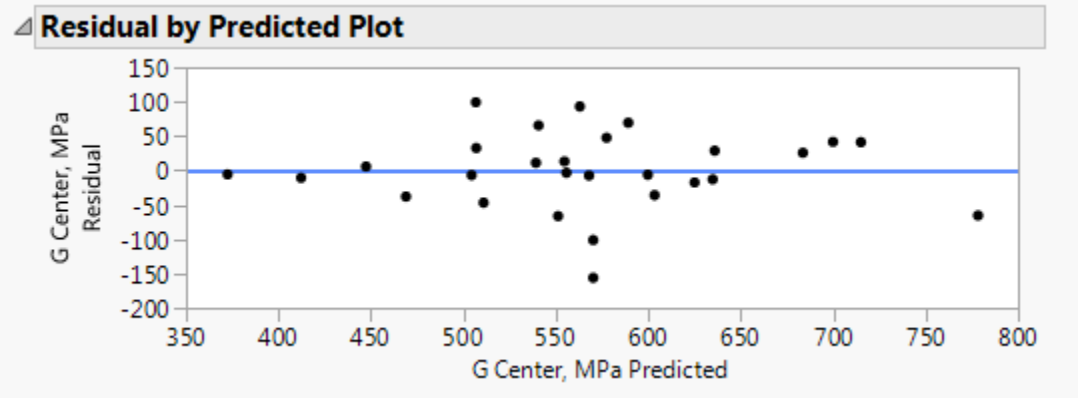

RSquare	0.716659
RSquare Adj	0.549987
Root Mean Square Error	70.81505
Mean of Response	567.2825
Observations (or Sum Wgts)	28

Term	Estimate	Std Error	t Ratio	Prob>|t|	Lower 95%	Upper 95%	F Ratio
Intercept	570.15157	23.68254	24.07	<.0001*	520.18579	620.11736	
Extruder Temperature(240,290)	29.551006	16.69127	1.77	0.0946	-5.664489	64.766501	3.1345
Heated Bed Temperature(40,100)	-2.090281	16.69127	-0.13	0.9018	-37.30578	33.125214	0.0157
Layer thickness(0.09,0.29)	-87.89555	16.69127	-5.27	<.0001*	-123.111	-52.68005	27.7303
Extruder Speed(-50,50)	-7.220112	16.69127	-0.43	0.6708	-42.43561	27.995383	0.1871
Fan Speed(0,100)	18.97732	16.69127	1.14	0.2713	-16.23817	54.192815	1.2927
Extruder Temperature*Heated Bed Temperature	25.493428	17.70376	1.44	0.1680	-11.85824	62.8451	2.0736
Extruder Temperature*Extruder Speed	31.178593	17.70376	1.76	0.0962	-6.173079	68.530266	3.1016
Extruder Temperature*Fan Speed	28.828281	17.70376	1.63	0.1218	-8.523391	66.179954	2.6516
Heated Bed Temperature*Heated Bed Temperature	-61.36994	38.53098	-1.59	0.1296	-142.6632	19.923318	2.5368
Layer thickness*Layer thickness	56.907011	38.53098	1.48	0.1580	-24.38624	138.20027	2.1813

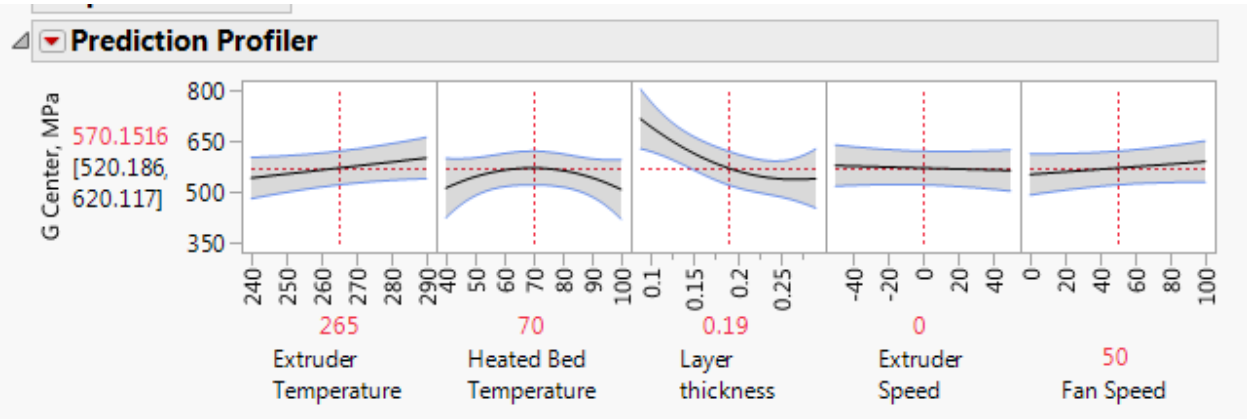

9.5.15.9 Poisson's ratio for the center part, *E/v* method

Source	LogWorth	PValue
Layer thickness(0.09,0.29)	5.786	0.00000
Heated Bed Temperature*Heated Bed Temperature	1.350	0.04470
Layer thickness*Layer thickness	1.233	0.05846
Layer thickness*Fan Speed	0.785	0.16389
Extruder Temperature*Heated Bed Temperature	0.700	0.19945
Heated Bed Temperature*Layer thickness	0.635	0.23164
Extruder Temperature*Extruder Speed	0.592	0.25584
Extruder Temperature(240,290)	0.455	0.35087
Fan Speed(0,100)	0.421	0.37894
Extruder Speed(-50,50)	0.271	0.53633
Heated Bed Temperature(40,100)	0.062	0.86692

Source	DF	Sum of Squares	Mean Square	F Ratio
Lack Of Fit	15	0.02691771	0.001795	2.0301
Pure Error	1	0.00088394	0.000884	**Prob > F**
Total Error	16	0.02780165		0.5065
				Max RSq
				0.9940

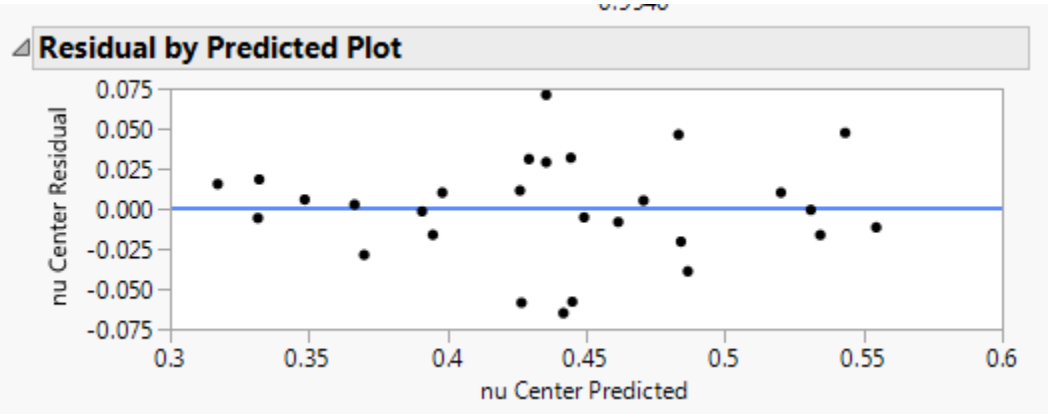

RSquare	0.810275
RSquare Adj	0.679839
Root Mean Square Error	0.041685
Mean of Response	0.437628
Observations (or Sum Wgts)	28

Term	Estimate	Std Error	t Ratio	Prob>|t|	Lower 95%	Upper 95%	F Ratio
Intercept	0.4355813	0.01394	31.25	<.0001*	0.4060288	0.4651338	
Extruder Temperature(240,290)	-0.009442	0.009825	-0.96	0.3509	-0.03027	0.0113867	0.9235
Heated Bed Temperature(40,100)	0.0016731	0.009825	0.17	0.8669	-0.019155	0.0225014	0.0290
Layer thickness(0.09,0.29)	0.0722085	0.009825	7.35	<.0001*	0.0513801	0.0930369	54.0130
Extruder Speed(-50,50)	0.0062093	0.009825	0.63	0.5363	-0.014619	0.0270377	0.3994
Fan Speed(0,100)	-0.008891	0.009825	-0.90	0.3789	-0.029719	0.0119376	0.8188
Extruder Temperature*Heated Bed Temperature	-0.013948	0.010421	-1.34	0.1995	-0.03604	0.0081435	1.7915
Heated Bed Temperature*Layer thickness	0.0129575	0.010421	1.24	0.2316	-0.009134	0.0350494	1.5460
Extruder Temperature*Extruder Speed	-0.012281	0.010421	-1.18	0.2558	-0.034373	0.0098107	1.3888
Layer thickness*Fan Speed	-0.015206	0.010421	-1.46	0.1639	-0.037298	0.0068861	2.1290
Heated Bed Temperature*Heated Bed Temperature	0.0494017	0.022681	2.18	0.0447*	0.0013204	0.097483	4.7442
Layer thickness*Layer thickness	-0.046218	0.022681	-2.04	0.0585	-0.0943	0.0018631	4.1525

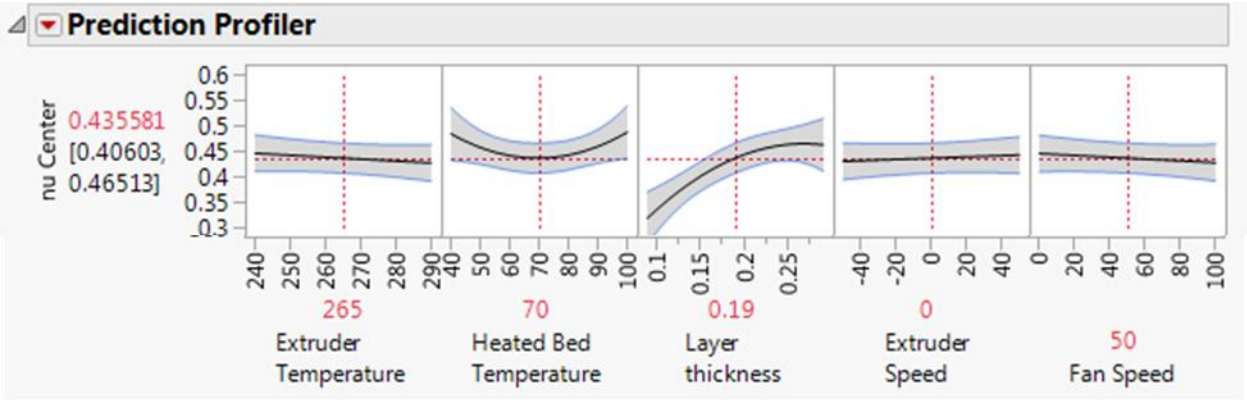

9.5.15.10 Young's modulus for the wing part, *E/v* method

Source	LogWorth	PValue
Layer thickness(0.09,0.29)	5.483	0.00000
Extruder Temperature*Extruder Speed	0.792	0.16143
Extruder Temperature(240,290)	0.658	0.21958
Heated Bed Temperature*Layer thickness	0.579	0.26351
Heated Bed Temperature(40,100)	0.402	0.39664
Fan Speed(0,100)	0.083	0.82644
Extruder Speed(-50,50)	0.036	0.91950

Source	DF	Sum of Squares	Mean Square	F Ratio
Lack Of Fit	14	373465.98	26676.1	9.9435
Pure Error	1	2682.78	2682.8	**Prob > F**
Total Error	15	376148.76		0.2442
				Max RSq
				0.9973

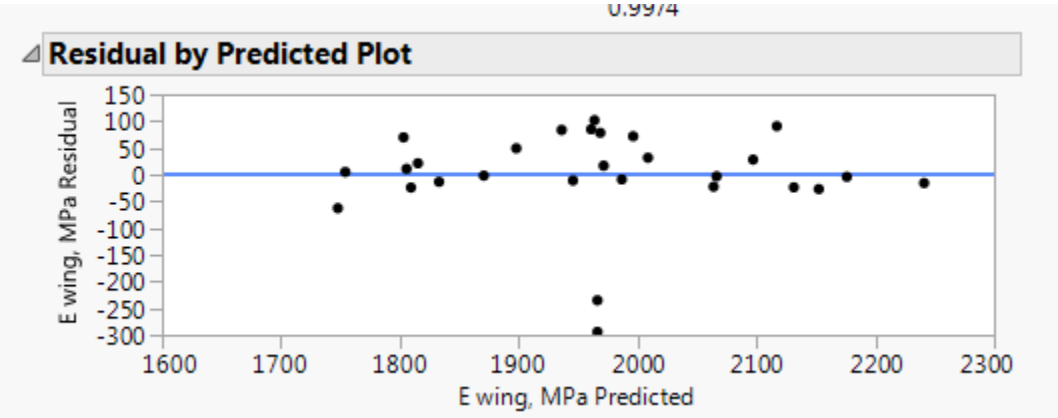

RSquare	0.698545
RSquare Adj	0.593035
Root Mean Square Error	100.6734
Mean of Response	1966.18
Observations (or Sum Wgts)	28

Term	Estimate	Std Error	t Ratio	Prob>|t|	Lower 95%	Upper 95%	F Ratio
Intercept	1966.1799	19.02548	103.34	<.0001*	1926.4934	2005.8663	
Extruder Temperature(240,290)	-30.07378	23.72895	-1.27	0.2196	-79.5715	19.42394	1.6063
Heated Bed Temperature(40,100)	-20.55439	23.72895	-0.87	0.3966	-70.05211	28.943329	0.7503
Layer thickness(0.09,0.29)	-150.9919	23.72895	-6.36	<.0001*	-200.4897	-101.4942	40.4903
Extruder Speed(-50,50)	-2.428556	23.72895	-0.10	0.9195	-51.92627	47.069162	0.0105
Fan Speed(0,100)	-5.271722	23.72895	-0.22	0.8264	-54.76944	44.225996	0.0494
Heated Bed Temperature*Layer thickness	28.956375	25.16835	1.15	0.2635	-23.54388	81.456633	1.3237

Term	Estimate	Std Error	t Ratio	Prob>|t|	Lower 95%	Upper 95%	F Ratio
Extruder Temperature*Extruder Speed	36.5975	25.16835	1.45	0.1614	-15.90276	89.097758	2.1144

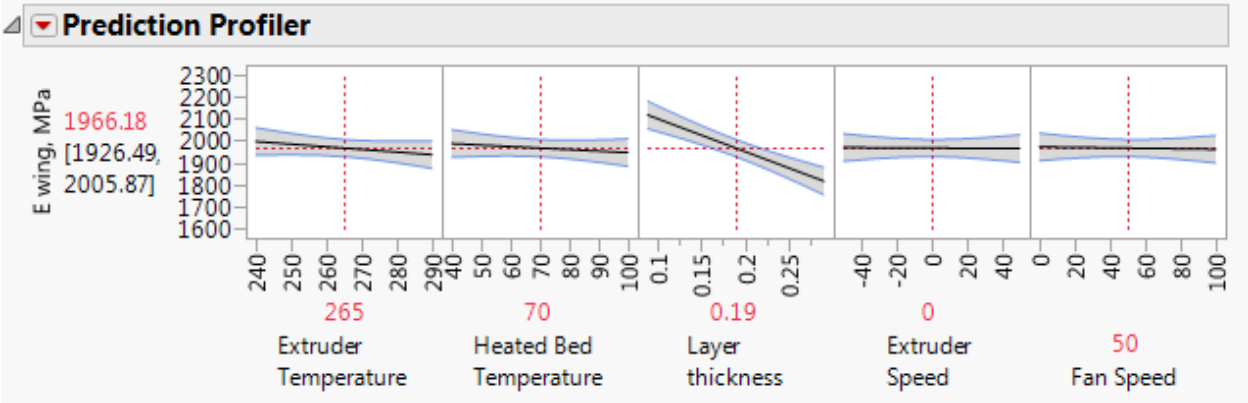

9.5.15.11 Shear modulus for the wing part, *E/v* method

Source	LogWorth	PValue
Layer thickness(0.09,0.29)	4.878	0.00001
Layer thickness*Extruder Speed	0.715	0.19286
Layer thickness*Layer thickness	0.697	0.20090
Heated Bed Temperature*Layer thickness	0.627	0.23614
Fan Speed*Fan Speed	0.564	0.27264
Fan Speed(0,100)	0.359	0.43752
Extruder Temperature(240,290)	0.304	0.49626
Heated Bed Temperature(40,100)	0.196	0.63674
Extruder Speed(-50,50)	0.074	0.84265

Source	DF	Sum of Squares	Mean Square	F Ratio
Lack Of Fit	17	34065.717	2003.87	1.1598
Pure Error	1	1727.779	1727.78	**Prob > F**
Total Error	18	35793.496		0.6339
				Max RSq
				0.9854

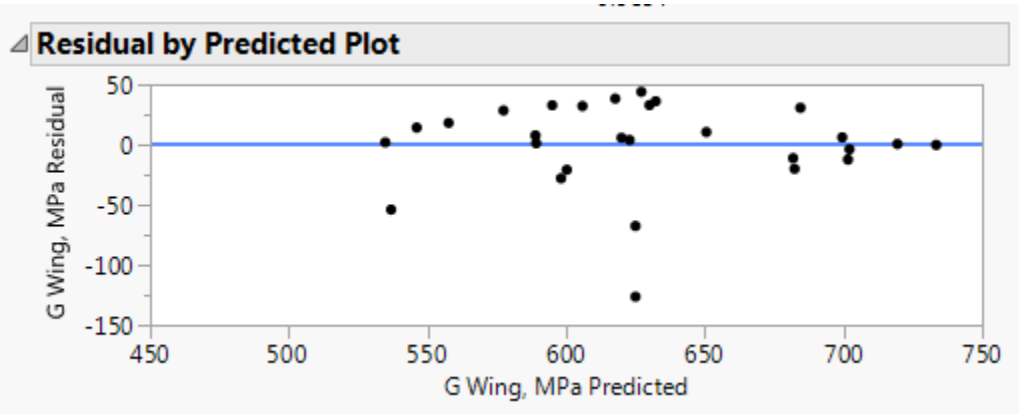

RSquare	0.698173
RSquare Adj	0.54726
Root Mean Square Error	44.59291
Mean of Response	628.0565
Observations (or Sum Wgts)	28

Term	Estimate	Std Error	t Ratio	Prob>|t|	Lower 95%	Upper 95%	F Ratio
Intercept	624.99963	14.91312	41.91	<.0001*	593.66833	656.33093	
Extruder Temperature(240,290)	-7.299278	10.51065	-0.69	0.4963	-29.38133	14.782777	0.4823
Heated Bed Temperature(40,100)	5.0491111	10.51065	0.48	0.6367	-17.03294	27.131166	0.2308
Layer thickness(0.09,0.29)	-62.2425	10.51065	-5.92	<.0001*	-84.32456	-40.16044	35.0683
Extruder Speed(-50,50)	-2.116833	10.51065	-0.20	0.8426	-24.19889	19.965222	0.0406
Fan Speed(0,100)	-8.345778	10.51065	-0.79	0.4375	-30.42783	13.736277	0.6305
Heated Bed Temperature*Layer thickness	13.6635	11.14823	1.23	0.2361	-9.758057	37.085057	1.5021
Layer thickness*Extruder Speed	15.0815	11.14823	1.35	0.1929	-8.340057	38.503057	1.8301
Layer thickness*Layer thickness	32.212342	24.26332	1.33	0.2009	-18.76301	83.187691	1.7626
Fan Speed*Fan Speed	-27.45716	24.26332	-1.13	0.2726	-78.43251	23.518191	1.2806

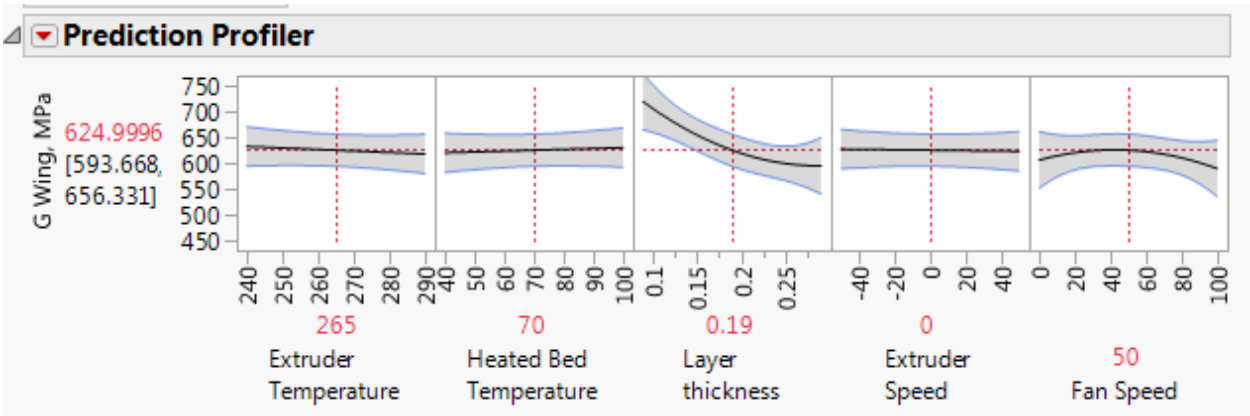

9.5.15.12 Poisson's modulus for the wing part, *E/v* method

Source	LogWorth	PValue
Layer thickness(0.09,0.29)	1.338	0.04597
Fan Speed*Fan Speed	1.232	0.05859
Heated Bed Temperature(40,100)	1.166	0.06821
Layer thickness*Extruder Speed	1.101	0.07923
Layer thickness*Layer thickness	1.075	0.08416
Fan Speed(0,100)	0.441	0.36245 ^
Extruder Temperature(240,290)	0.116	0.76545
Extruder Speed(-50,50)	0.015	0.96691 ^

Source	DF	Sum of Squares	Mean Square	F Ratio
Lack Of Fit	18	0.01079487	0.000600	0.1448
Pure Error	1	0.00414050	0.004140	**Prob > F**
Total Error	19	0.01493537		0.9829
				Max RSq
				0.8541

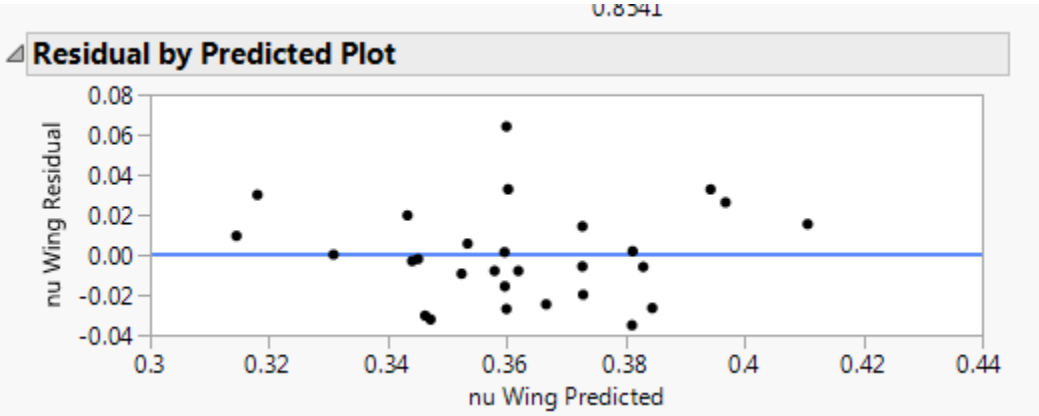

RSquare	0.473886
RSquare Adj	0.252365
Root Mean Square Error	0.028037
Mean of Response	0.361821
Observations (or Sum Wgts)	28

Term	Estimate	Std Error	t Ratio	Prob>|t|	Lower 95%	Upper 95%	F Ratio
Intercept	0.3599605	0.009376	38.39	<.0001*	0.3403356	0.3795855	
Extruder Temperature(240,290)	-0.002	0.006608	-0.30	0.7654	-0.015831	0.0118315	0.0916
Heated Bed Temperature(40,100)	-0.012778	0.006608	-1.93	0.0682	-0.026609	0.0010537	3.7387
Layer thickness(0.09,0.29)	0.0141111	0.006608	2.14	0.0460*	0.0002796	0.0279426	4.5597
Extruder Speed(-50,50)	0.0002778	0.006608	0.04	0.9669	-0.013554	0.0141093	0.0018
Fan Speed(0,100)	0.0061667	0.006608	0.93	0.3624	-0.007665	0.0199982	0.8708
Layer thickness*Extruder Speed	-0.013	0.007009	-1.85	0.0792	-0.027671	0.0016705	3.4399
Layer thickness*Layer thickness	-0.027803	0.015255	-1.82	0.0842	-0.059732	0.0041267	3.3215
Fan Speed*Fan Speed	0.0306974	0.015255	2.01	0.0586	-0.001232	0.0626267	4.0492

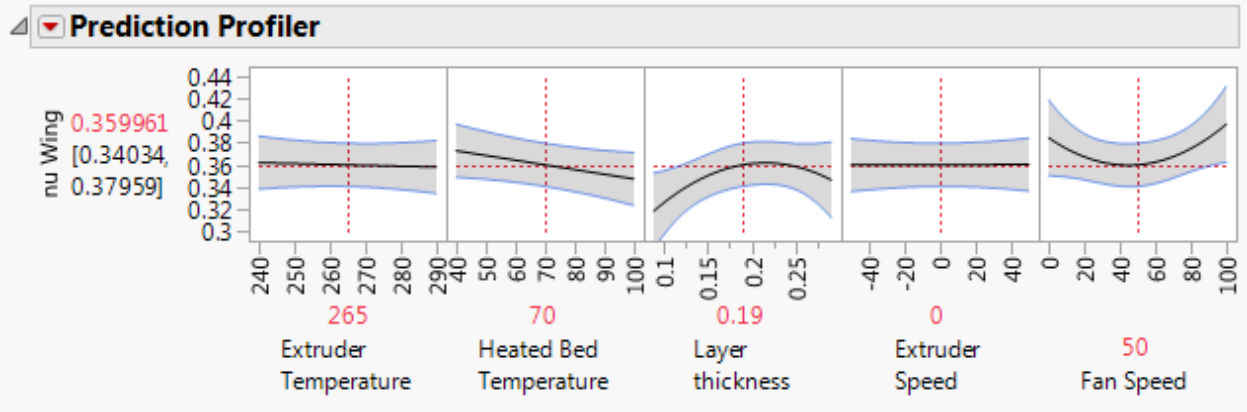
Prediction Profiler
nu Wing
0.359961
[0.34034, 0.37959]
0.44
0.42
0.4
0.38
0.36
0.34
0.32
0.3
240 250 260 270 280 290
40 50 60 70 80 90 100
0.1 0.15 0.2 0.25
-40 -20 0 20 40
0 20 40 60 80 100
265
70
0.19
0
50
Extruder Temperature
Heated Bed Temperature
Layer thickness
Extruder Speed
Fan Speed

9.5.16 Statistical analyses on reduced sources for orthotropic material property

9.5.16.1 E_x modulus for the wing part

Source	LogWorth	PValue
Layer thickness(0.09,0.29)	6.351	0.00000
Extruder Temperature*Extruder Speed	0.922	0.11978
Extruder Temperature*Extruder Temperature	0.846	0.14252
Heated Bed Temperature*Layer thickness	0.635	0.23183
Extruder Temperature(240,290)	0.623	0.23838
Heated Bed Temperature(40,100)	0.382	0.41508
Extruder Speed(-50,50)	0.080	0.83115
Fan Speed(0,100)	0.001	0.99841

Source	DF	Sum of Squares	Mean Square	F Ratio
Lack Of Fit	18	171661.49	9536.75	7.0977
Pure Error	1	1343.64	1343.64	**Prob > F**
Total Error	19	173005.13		0.2882
				Max RSq
				0.9982

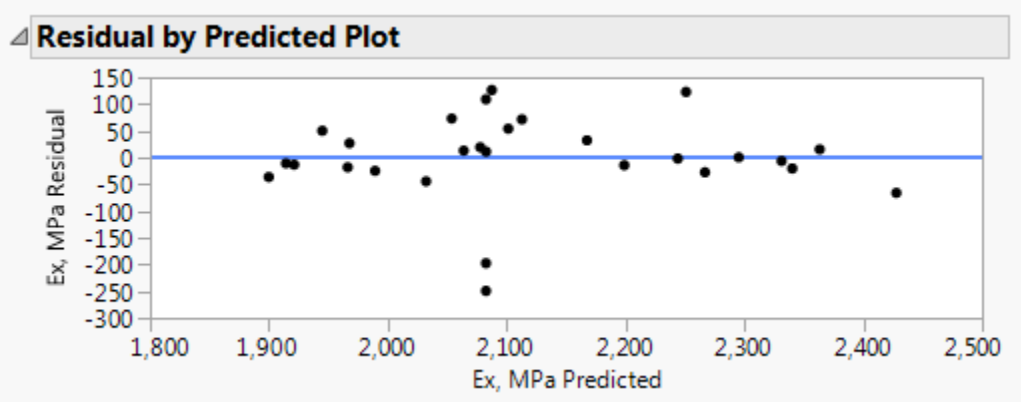

RSquare	0.773081
RSquare Adj	0.677537
Root Mean Square Error	95.42292
Mean of Response	2119.576
Observations (or Sum Wgts)	28

Term	Estimate	Std Error	t Ratio	Prob>|t|	Lower 95%	Upper 95%	F Ratio
Intercept	2082.5616	30.17538	69.02	<.0001*	2019.4038	2145.7194	N/A
Extruder Temperature(240,290)	-27.3795	22.4914	-1.22	0.2384	-74.45454	19.695535	1.4819
Heated Bed Temperature(40,100)	-18.73989	22.4914	-0.83	0.4151	-65.81492	28.335147	0.6942
Layer thickness(0.09,0.29)	-168.2917	22.4914	-7.48	<.0001*	-215.3668	-121.2167	55.9877
Extruder Speed(-50,50)	-4.862278	22.4914	-0.22	0.8311	-51.93731	42.212758	0.0467

Term	Estimate	Std Error	t Ratio	Prob>|t|	Lower 95%	Upper 95%	F Ratio
Fan Speed(0,100)	-0.045278	22.4914	-0.00	0.9984	-47.12031	47.029758	0.0000
Heated Bed Temperature*Layer thickness	29.465375	23.85573	1.24	0.2318	-20.46524	79.39599	1.5256
Extruder Temperature*Extruder Speed	38.86125	23.85573	1.63	0.1198	-11.06937	88.791865	2.6537
Extruder Temperature*Extruder Temperature	57.578233	37.63531	1.53	0.1425	-21.19337	136.34983	2.3406

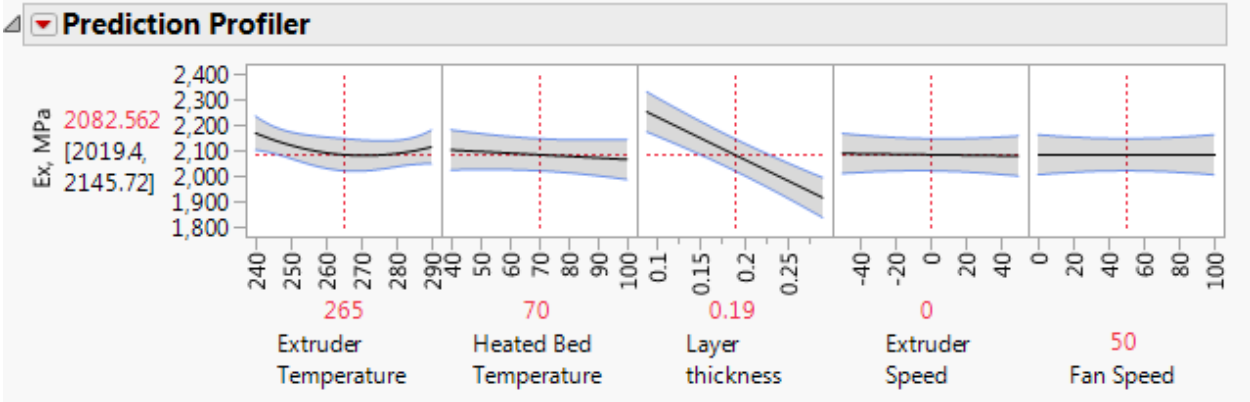

9.5.16.2 E_y modulus for the wing part

Source	LogWorth	PValue
Layer thickness(0.09,0.29)	3.323	0.00048
Heated Bed Temperature(40,100)	1.057	0.08774
Heated Bed Temperature*Heated Bed Temperature	1.048	0.08951
Extruder Temperature*Extruder Temperature	0.976	0.10562
Extruder Speed*Extruder Speed	0.903	0.12511
Extruder Temperature*Fan Speed	0.528	0.29664
Extruder Temperature(240,290)	0.390	0.40782
Fan Speed(0,100)	0.296	0.50611
Extruder Speed(-50,50)	0.036	0.91972

Source	DF	Sum of Squares	Mean Square	F Ratio
Lack Of Fit	17	1566728.6	92160.5	1.0749
Pure Error	1	85736.1	85736.1	**Prob > F**
Total Error	18	1652464.7		0.6517
				Max RSq
				0.9826

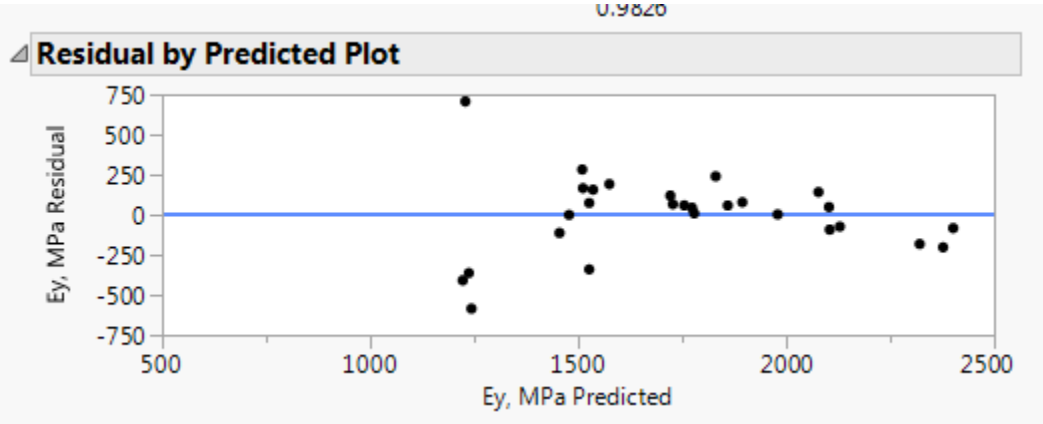

RSquare	0.663686
RSquare Adj	0.495529
Root Mean Square Error	302.9911
Mean of Response	1745.939
Observations (or Sum Wgts)	28

Term	Estimate	Std Error	t Ratio	Prob>|t|	Lower 95%	Upper 95%	F Ratio
Intercept	1526.5576	103.5602	14.74	<.0001*	1308.9856	1744.1295	N/A
Extruder Temperature(240,290)	60.528556	71.41568	0.85	0.4078	-89.51022	210.56734	0.7183
Heated Bed Temperature(40,100)	128.94467	71.41568	1.81	0.0877	-21.09411	278.98345	3.2600
Layer thickness(0.09,0.29)	-303.9282	71.41568	-4.26	0.0005*	-453.967	-153.8894	18.1115
Extruder Speed(-50,50)	7.2990556	71.41568	0.10	0.9197	-142.7397	157.33784	0.0104
Fan Speed(0,100)	-48.45306	71.41568	-0.68	0.5061	-198.4918	101.58572	0.4603
Extruder Temperature*Fan Speed	81.41725	75.74777	1.07	0.2966	-77.72291	240.55741	1.1553
Extruder Temperature*Extruder Temperature	307.64584	180.5634	1.70	0.1056	-71.70381	686.99549	2.9030
Heated Bed Temperature*Heated Bed Temperature	324.06084	180.5634	1.79	0.0895	-55.28881	703.41049	3.2210
Extruder Speed*Extruder Speed	-290.4467	180.5634	-1.61	0.1251	-669.7963	88.902985	2.5875

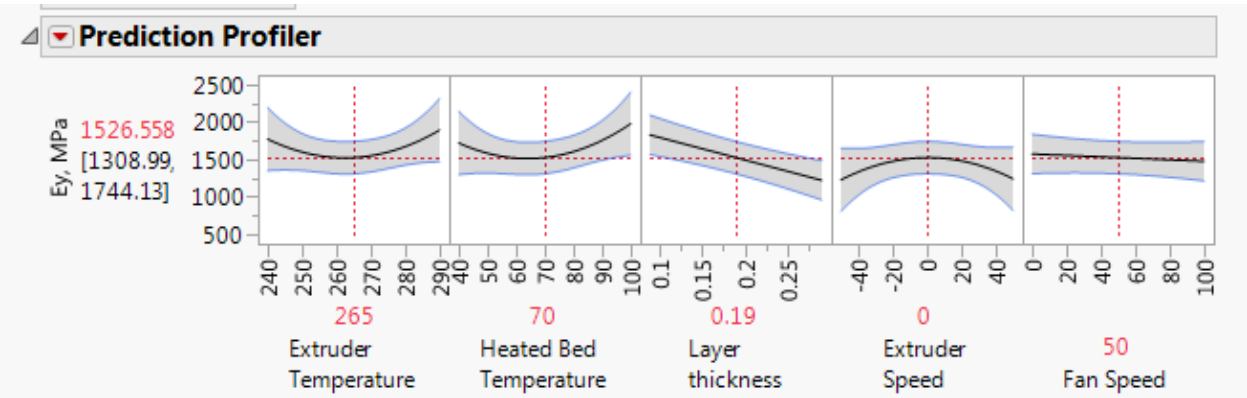

9.5.16.3 G_{xy} modulus for the wing part

Source	LogWorth	PValue
Layer thickness(0.09,0.29)	2.038	0.00915
Fan Speed*Fan Speed	1.004	0.09904
Layer thickness*Layer thickness	0.735	0.18391
Layer thickness*Extruder Speed	0.614	0.24300
Extruder Temperature(240,290)	0.329	0.46904
Fan Speed(0,100)	0.145	0.71633
Extruder Speed(-50,50)	0.081	0.82891
Heated Bed Temperature(40,100)	0.005	0.98850

Source	DF	Sum of Squares	Mean Square	F Ratio
Lack Of Fit	18	103322.55	5740.14	16.0162
Pure Error	1	358.40	358.40	**Prob > F**
Total Error	19	103680.95		0.1945
				Max RSq
				0.9980

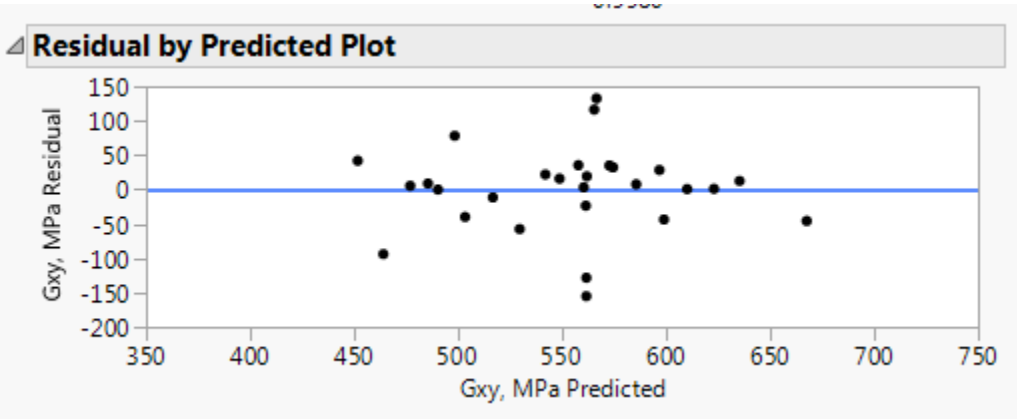

RSquare	0.418468
RSquare Adj	0.173613
Root Mean Square Error	73.87078
Mean of Response	552.4312
Observations (or Sum Wgts)	28

Term	Estimate	Std Error	t Ratio	Prob>|t|	Lower 95%	Upper 95%	F Ratio
Intercept	561.61452	24.70446	22.73	<.0001*	509.90749	613.32155	
Extruder Temperature(240,290)	-12.864	17.41151	-0.74	0.4690	-49.30671	23.578709	0.5459
Heated Bed Temperature(40,100)	0.2543889	17.41151	0.01	0.9885	-36.18832	36.697098	0.0002
Layer thickness(0.09,0.29)	-50.51567	17.41151	-2.90	0.0092*	-86.95838	-14.07296	8.4174
Extruder Speed(-50,50)	3.8147222	17.41151	0.22	0.8289	-32.62799	40.257431	0.0480
Fan Speed(0,100)	-6.422	17.41151	-0.37	0.7163	-42.86471	30.020709	0.1360
Layer thickness*Extruder Speed	22.25325	18.46769	1.20	0.2430	-16.40008	60.90658	1.4520

Term	Estimate	Std Error	t Ratio	Prob>|t|	Lower 95%	Upper 95%	F Ratio
Layer thickness*Layer thickness	55.427901	40.19362	1.38	0.1839	-28.69832	139.55412	1.9017
Fan Speed*Fan Speed	-69.7131	40.19362	-1.73	0.0990	-153.8393	14.413119	3.0083

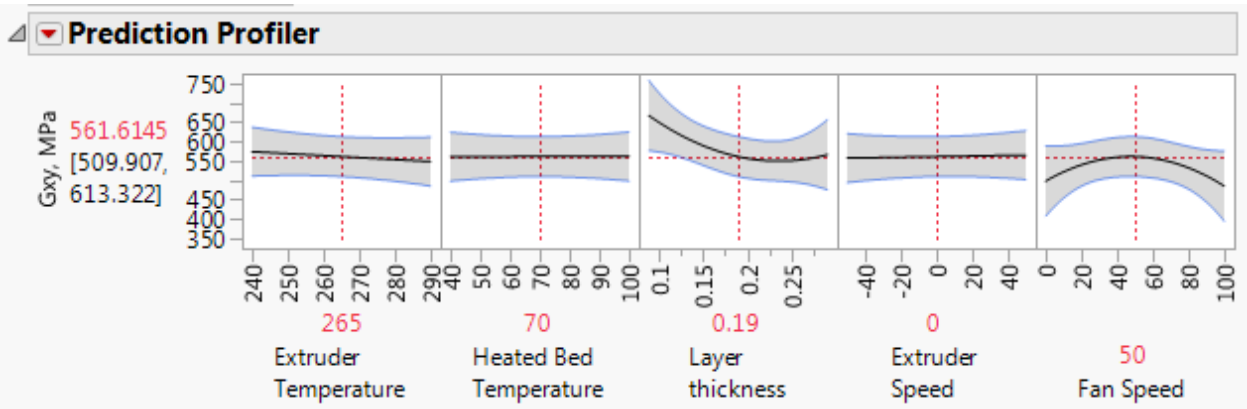

9.5.16.4 v_{xy} modulus for the wing part

Source	LogWorth	PValue
Extruder Speed*Extruder Speed	1.397	0.04007
Layer thickness(0.09,0.29)	1.003	0.09922
Heated Bed Temperature*Heated Bed Temperature	0.767	0.17096
Extruder Temperature*Extruder Temperature	0.677	0.21041
Heated Bed Temperature(40,100)	0.446	0.35827
Fan Speed*Fan Speed	0.391	0.40673
Extruder Temperature(240,290)	0.283	0.52081
Fan Speed(0,100)	0.183	0.65616
Extruder Speed(-50,50)	0.148	0.71146

Source	DF	Sum of Squares	Mean Square	F Ratio
Lack Of Fit	17	0.20393052	0.011996	3.8442
Pure Error	1	0.00312050	0.003120	**Prob > F**
Total Error	18	0.20705102		0.3834
				Max RSq
				0.9918

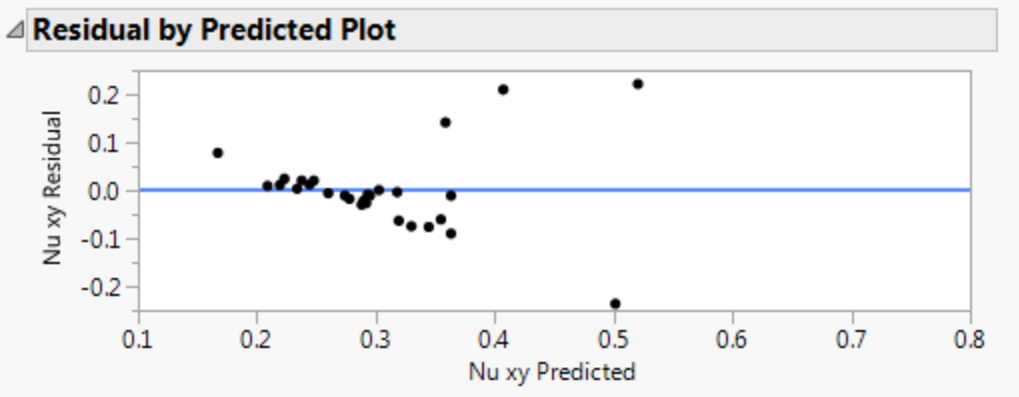

RSquare	0.456355
RSquare Adj	0.184532
Root Mean Square Error	0.107251
Mean of Response	0.304786
Observations (or Sum Wgts)	28

Term	Estimate	Std Error	t Ratio	Prob>|t|	Lower 95%	Upper 95%	F ratio
Intercept	0.3632391	0.037086	9.79	<.0001*	0.2853253	0.441153	N/A
Extruder Temperature(240,290)	-0.016556	0.025279	-0.65	0.5208	-0.069666	0.0365544	0.4289
Heated Bed Temperature(40,100)	-0.023833	0.025279	-0.94	0.3583	-0.076943	0.0292766	0.8889
Layer thickness(0.09,0.29)	0.0439444	0.025279	1.74	0.0992	-0.009166	0.0970544	3.0219
Extruder Speed(-50,50)	0.0095	0.025279	0.38	0.7115	-0.04361	0.06261	0.1412
Fan Speed(0,100)	0.0114444	0.025279	0.45	0.6562	-0.041666	0.0645544	0.2050
Extruder Temperature*Extruder Temperature	-0.086732	0.066779	-1.30	0.2104	-0.227029	0.0535655	1.6869
Heated Bed Temperature*Heated Bed Temperature	-0.095232	0.066779	-1.43	0.1710	-0.235529	0.0450655	2.0337
Extruder Speed*Extruder Speed	0.1477681	0.066779	2.21	0.0401*	0.0074707	0.2880655	4.8965
Fan Speed*Fan Speed	-0.056732	0.066779	-0.85	0.4067	-0.197029	0.0835655	0.7217

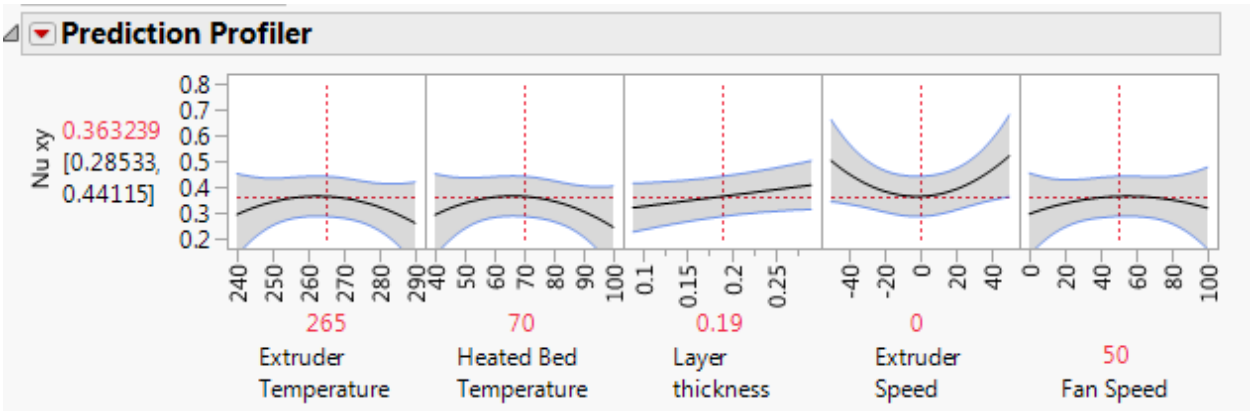

9.5.16.5 v_{yx} modulus for the wing part

Source	LogWorth	PValue
Layer thickness*Extruder Speed	1.354	0.04429
Fan Speed*Fan Speed	1.275	0.05307
Layer thickness(0.09,0.29)	1.104	0.07868
Extruder Temperature*Heated Bed Temperature	0.961	0.10940
Heated Bed Temperature(40,100)	0.812	0.15412
Layer thickness*Layer thickness	0.725	0.18825
Extruder Temperature*Extruder Speed	0.685	0.20632
Fan Speed(0,100)	0.353	0.44398
Extruder Temperature(240,290)	0.184	0.65482
Extruder Speed(-50,50)	0.138	0.72773

Source	DF	Sum of Squares	Mean Square	F Ratio
Lack Of Fit	16	0.00134963	0.000084	0.6590
Pure Error	1	0.00012800	0.000128	**Prob > F**
Total Error	17	0.00147763		0.7642
				Max RSq
				0.9605

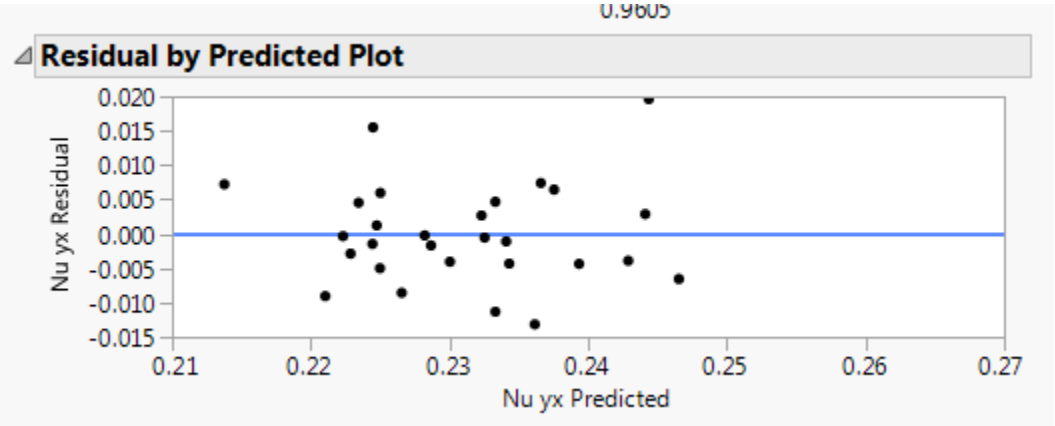

RSquare	0.544223
RSquare Adj	0.27612
Root Mean Square Error	0.009323
Mean of Response	0.231
Observations (or Sum Wgts)	28

Term	Estimate	Std Error	t Ratio	Prob>|t|	Lower 95%	Upper 95%	F-ratio
Intercept	0.2333092	0.003118	74.83	<.0001*	0.226731	0.2398874	N/A
Extruder Temperature(240,290)	0.001	0.002197	0.46	0.6548	-0.003636	0.0056362	0.2071
Heated Bed Temperature(40,100)	0.0032778	0.002197	1.49	0.1541	-0.001358	0.007914	2.2249
Layer thickness(0.09,0.29)	0.0041111	0.002197	1.87	0.0787	-0.000525	0.0087474	3.5001
Extruder Speed(-50,50)	0.0007778	0.002197	0.35	0.7277	-0.003858	0.005414	0.1253

Term	Estimate	Std Error	t Ratio	Prob>|t|	Lower 95%	Upper 95%	F-ratio
Fan Speed(0,100)	-0.001722	0.002197	-0.78	0.4440	-0.006358	0.002914	0.6142
Extruder Temperature*Heated Bed Temperature	0.0039375	0.002331	1.69	0.1094	-0.00098	0.008855	2.8539
Extruder Temperature*Extruder Speed	-0.003062	0.002331	-1.31	0.2063	-0.00798	0.001855	1.7265
Layer thickness*Extruder Speed	0.0050625	0.002331	2.17	0.0443*	0.000145	0.00998	4.7177
Layer thickness*Layer thickness	0.0069539	0.005073	1.37	0.1883	-0.003749	0.0176565	1.8792
Fan Speed*Fan Speed	-0.010546	0.005073	-2.08	0.0531	-0.021249	0.0001565	4.3221

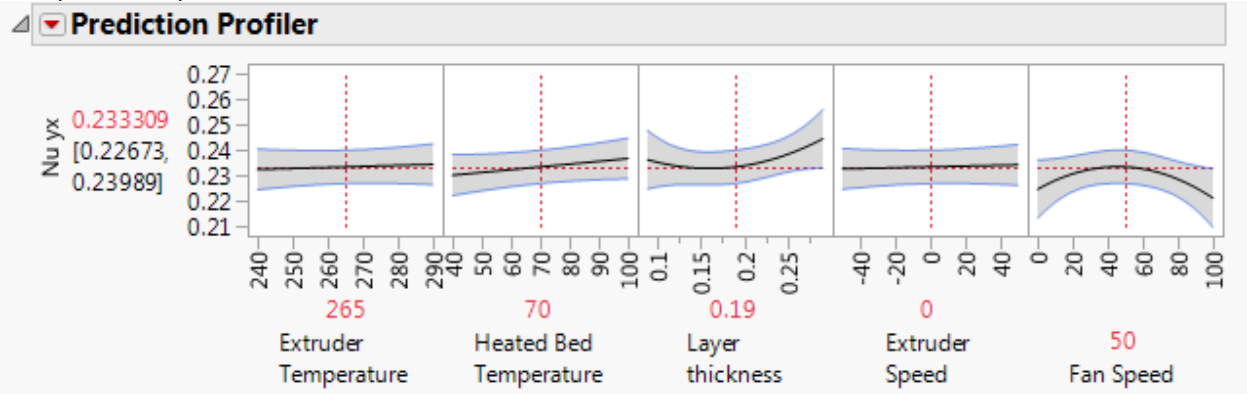

9.6 Dimensional and natural frequencies of the 28 3D printed testing artifacts

- **Central beam (thin part)**

Table 68: Measured dimension and the first two bending and torsion natural frequencies of the center part of the printed testing artifacts

run	Nominal thickness, mm	Measure Thickness, mm	Length, mm	Width of the center, mm	1st bending	2nd bending	1st torsion
1	2.10	2.12	51.75	6.2-6.3	151	1003	1775
2	2.20	2.12	51.85	6.25-6.3	136	993	1626
3	2.30	2.18	51.95	6.35-6.55	146	1058	1568
4	2.40	2.18	51.89	6.36-6.45	158	1070	1580
5	2.35	2.19	51.56	6.40-6.65	157	1081	1735
6	2.14	2.12	51.93	6.15-6.34	137	938	--
7	2.20	2.12	52.02	6.13-6.3	138	955	-
8	2.40	2.18	51.99	6.4-6.5	157	1082	1513
9	2.30	2.18	51.90	6.37-6.45	151	1062	1374
10	2.30	2.19	52.03	6.47-6.50	153	1098	1518

Table 68: Measured dimension and the first two bending and torsion natural frequencies of the center part of the printed testing artifacts

11	2.09	2.12	51.75	6.20-6.4	146	1014	1765
12	2.10	2.19	51.85	6.3-6.4	151	1050	1619
13	2.30	2.19	51.89	6.3-6.4	148	1033	1051
14	2.20	2.19	51.89	6.25-6.35	134	950	1397
15	2.20	2.19	52.02	6.3-6.4	136	958	1439
16	2.22	2.19	51.79	6.29-6.4	156	1062	1754
17	2.20	2.19	51.70	6.35-6.4	162	1059	1726
18	2.30	2.18	51.75	6.4-6.5	155	1082	1657
19	2.20	2.19	51.85	6.25-6.4	154	1065	1672
20	2.05	2.12	51.80	6.25-6.35	144	1007	1682
21	2.20	2.12	51.89	6.26-6.39	142	994	1730
22	2.20	2.18	51.97	6.45-6.55	136	965	1332
23	2.20	2.18	51.85	6.5-6.4	151	1079	1599
24	2.23	2.19	51.85	6.33-6.4	153	1052	1672
25	2.20	2.12	51.97	6.23-6.44	139	943	1667
26	2.00	2.12	51.86	6.2-6.3	134	956	1660
27	2.20	2.18	51.78	6.4-6.5	153	1044	1606
28	2.25	2.18	51.93	6.14-6.35	165	1132	1645

Table 69: The 4th to 5th natural frequencies along with the average and standard deviation of the estimated moduli of elasticity based on these six measurements for the center part of the testing artifacts.

run	3^{rd} bending	4^{th} bending
1	2872	5291
2	2727	4993
3	2812	4933
4	3103	5483
5	3048	5627

Table 69: The 4th to 5th natural frequencies along with the average and standard deviation of the estimated moduli of elasticity based on these six measurements for the center part of the testing artifacts.

6	2639	4932
7	2692	5074
8	3049	-
9	2967	5400
10	3068	5552
11	2849	5316
12	2949	5434
13	2876	5297
14	2657	4905
15	2581	4980
16	2931	5410
17	2866	5410
18	3081	5629
19	3013	5609
20	2814	5223
21	2821	5206
22	2727	4811
23	3021	5574
24	2982	5558
25	2719	5287
26	2708	5147
27	2999	5578
28	3150	5569

- **Wing part (thick plate)**

Table 70: Measured dimension and the first three bending and torsion natural frequencies of the wing part of the printed testing artifacts

run	Nominal thickness, mm	Measure Thickness, mm	Length, mm	Width of the center, mm	1st bending	1st torsion	2nd bending	2nd Torsion
1	2.93	3.10	62.65	13.3-13.45	168	508	1063	1362
2	2.93	2.98	62.80	13.3-13.4	163	481	1040	1339
3	3.19	3.10	62.65	13.55-13.7	175	505	1094	1344
4	3.19	3.28	62.85	13.4-13.55	171	507	1070	1381
5	3.04	3.21	63.10	13.5-13.65	167	502	1056	1347
6	2.93	3.15	62.94	13.30	161	491	1008	1338
7	2.93	3.11	62.83	13.26-13.35	159	486	1012	1313
8	3.19	3.11	62.80	13.25-13.35	171	512	1099	1389
9	3.19	3.25	62.70	13.35-13.60	167	496	1062	1356
10	3.04	3.30	62.88	13.38-13.45	166	499	1062	1356
11	2.93	2.92	62.65	13.44-13.55	167	505	1055	1351
12	3.04	3.15	62.80	13.44-13.6	167	503	1061	1364
13	3.04	3.13	62.85	13.3-13.45	166	503	1046	1332
14	3.04	3.12	62.75	13.35-13.5	151	482	961	1226
15	3.04	2.95	62.88	13.45-13.65	157	455	980	1221
16	3.04	3.13	62.83	13.50-13.55	172	495	1063	1325
17	3.04	3.07	62.70	13.4-13.5	174	511	1084	1353
18	3.19	3.35	62.70	13.5-13.65	171	511	1080	1392
19	3.04	3.15	62.75	13.4-13.55	162	500	1028	1329
20	2.93	3.05	62.80	13.35-13.5	162	489	1034	1336
21	2.93	3.17	62.82	13.42-13.55	163	492	1041	1345
22	3.19	3.35	62.92	13.35-13.55	161	466	1017	1270
23	3.19	3.30	62.60	13.35-13.50	169	498	1082	1372

Table 70: Measured dimension and the first three bending and torsion natural frequencies of the wing part of the printed testing artifacts

24	3.04	3.08	62.88	13.4-13.6	166	498	1052	1349
25	2.93	3.13	62.86	13.3-13.4	159	486	1010	1312
26	2.93	3.08	62.80	13.3-13.4	161	467	1024	1322
27	3.19	3.23	62.70	13.35-13.50	164	493	1045	1343
28	3.19	3.20	62.85	13.2-13.4	167	498	1056	1359

Table 71: The 4th to 6th natural frequencies along with the average and standard deviation of the estimated moduli of elasticity based on these six measurements for the wing part of the testing artifacts.

run	3rd Torsion	3rd bending
1	2119	2959
2	2067	2925
3	1880	2962
4	2136	2984
5	2065	2926
6	2146	2917
7	2105	2883
8	2150	3060
9	2106	2982
10	2096	2972
11	2087	2961
12	2112	2976
13	2074	2883
14	1899	2712
15	1749	2716
16	1920	2940
17	1981	2866

Table 71: The 4th to 6th natural frequencies along with the average and standard deviation of the estimated moduli of elasticity based on these six measurements for the wing part of the testing artifacts.

18	2131	2890
19	2110	2884
20	2096	2905
21	2111	2953
22	1863	2838
23	2092	3027
24	2103	2952
25	2118	2838
26	2136	2889
27	2113	2929
28	2162	2944

9.7 Dimensional and data gathered for the 28 3D printed cubes

Table 72: Gathered data and measured density for 28 3D printed cubes

run	print time, second	material length	Number of path	Number of Layers	weight, scale, g	Weight water, g	Measured density, kg/m^3	Theoretical density, kg/m^3	Measured SR
1	3014.00	1.511	37	173	3.391	2.566	1,046.5	1,004.1	0.992
2	1012	1.511	37	173	3.340	2.594	1,019.6	1,004.1	0.966
3	1045.00	1.519	37	54	3.377	2.658	1,006.1	890.9	0.954
4	356	1.519	37	54	3.095	2.491	983.9	890.9	0.933
5	760.00	1.512	37	82	3.365	2.642	1,008.6	947.5	0.956
6	3014	1.511	37	173	3.131	2.377	1,043.1	1,004.1	0.989
7	1012.00	1.511	37	173	3.324	2.547	1,033.5	1,004.1	0.980
8	1045	1.519	37	54	3.413	2.830	955.0	890.9	0.905
9	356.00	1.519	37	54	2.800	2.212	1,002.4	890.9	0.950
10	760	1.512	37	82	3.399	2.640	1,019.6	947.5	0.966
11	1513.00	1.511	37	173	3.427	2.643	1,026.8	1,004.1	0.973

Table 72: Gathered data and measured density for 28 3D printed cubes

12	1508	1.512	37	82	3.429	2.658	1,021.6	947.5	0.968
13	760.00	1.512	37	82	3.408	2.628	1,026.9	947.5	0.973
14	760	1.512	37	82	3.417	2.673	1,012.3	947.5	0.960
15	760.00	1.512	37	82	3.416	2.676	1,010.9	947.5	0.958
16	760	1.512	37	82	3.438	2.681	1,015.5	947.5	0.963
17	510.00	1.512	37	82	3.437	2.688	1,012.5	947.5	0.960
18	528	1.519	37	54	3.465	2.710	1,012.5	890.9	0.960
19	760.00	1.512	37	82	3.421	2.657	1,019.6	947.5	0.966
20	3014	1.511	37	173	3.470	2.643	1,039.7	1,004.1	0.985
21	1012	1.511	37	82	3.469	2.672	1,028.1	1,004.1	0.974
22	1045	1.519	37	54	3.482	2.688	1,025.8	890.9	0.972
23	356	1.519	37	54	3.453	2.749	994.7	890.9	0.943
24	760	1.512	37	82	3.470	2.691	1,021.1	947.5	0.968
25	3014	1.511	37	173	3.478	2.635	1,045.2	1,004.1	0.991
26	1012	1.511	37	173	3.501	2.722	1,018.5	1,004.1	0.965
27	1045	1.519	37	54	3.445	2.671	1,021.4	890.9	0.968
28	356	1.519	37	54	3.446	2.741	995.6	890.9	0.944

9.8 Dimensional and data gathered for the 16 3D printed slender cuboids

Table 73: Gathered data and measured density for 16 slender printed cubes

run	time, seconds	weight, scale, g	Weight water, g	Measured density, kg/m^3	Difference, kg/m^3	Measured SR	Average deposition velocity, mm/min	51.642
1	112.789	0.1392	0.101	1,027.721	80.263	0.974	15.970	10.984
2	101.80	0.1364	0.105	967.942	20.484	0.917	17.694	33.330
3	102.19	0.1373	0.102	1,004.329	56.872	0.952	17.626	37.081
4	112.79	0.141	0.104	1,009.633	62.175	0.957	15.970	30.944

Table 73: Gathered data and measured density for 16 slender printed cubes

5	101.82	0.1364	0.102	1,000.828	53.370	0.949	17.690	57.292
6	386.73	1.1533	0.877	1,033.601	86.143	0.980	4.658	62.916
7	559.52	1.1534	0.873	1,038.785	91.327	0.985	3.219	58.371
8	386.56	1.1475	0.872	1,034.648	87.190	0.981	4.660	57.990
9	386.52	1.1558	0.879	1,034.281	86.823	0.980	4.660	39.794
10	354.16	1.149	0.892	1,013.310	65.852	0.960	5.086	51.868
11	386.56	1.1574	0.885	1,027.968	80.511	0.974	4.660	54.508
12	1401.39	3.1335	2.401	1,030.787	83.329	0.977	1.285	42.758
13	743.48	3.1422	2.440	1,017.169	69.712	0.964	2.423	48.295
14	877.89	3.1105	2.399	1,023.930	76.472	0.971	2.052	57.741
15	1401	3.146	2.676	1,034.040	86.582	0.980	1.286	40.169
16	743.30	3.1348	2.681	1,013.807	66.349	0.961	2.423	51.642

9.9 Results obtained for printed artifacts assuming isotropic material properties

Table 74: Obtained mechanical properties assuming isotropic material properties for *E/G* method

	Center (beam) part			Wing (plate) part		
run	**Young's modulus, MPa**	**Shear modulus, MPa**	**Poisson's ratio**	**Young's modulus, MPa**	**Shear modulus, MPa**	**Poisson's ratio**
1	1998.034	736.917	0.356	1987.241	665.370	0.493
2	1873.574	600.415	0.560	1874.888	610.003	0.537
3	1663.702	560.281	0.485	1095.812	311.932	0.756
4	1777.201	554.204	0.603	1681.674	564.511	0.489
5	2052.279	700.856	0.464	1802.811	589.809	0.528
6	1782.035	620.075	0.437	2034.677	717.742	0.417
7	1771.081	607.332	0.458	1936.838	671.653	0.442
8	1709.644	523.321	0.633	1676.028	538.176	0.557

Table 74: Obtained mechanical properties assuming isotropic material properties for *E/G* method

	Center (beam) part			Wing (plate) part		
9	1378.467	402.237	0.714	1588.938	519.661	0.529
10	1676.084	511.164	0.639	1738.566	564.797	0.539
11	2012.478	736.968	0.365	1942.709	634.248	0.532
12	1787.127	576.284	0.551	1839.902	608.277	0.512
13	1676.071	538.387	0.557	1768.042	596.270	0.483
14	1347.181	416.896	0.616	1450.282	465.998	0.556
15	1475.468	467.224	0.579	1099.745	316.666	0.736
16	1923.808	683.720	0.407	1367.554	399.736	0.711
17	1904.300	664.783	0.432	1592.234	502.493	0.584
18	1905.168	614.147	0.551	1668.139	606.483	0.375
19	1879.847	616.827	0.524	1832.122	646.139	0.418
20	1911.371	668.329	0.430	1965.349	668.982	0.469
21	2049.825	715.066	0.433	2004.642	670.882	0.494
22	1338.210	412.608	0.622	1166.849	342.040	0.706
23	1780.430	560.723	0.588	1525.021	479.967	0.589
24	1891.159	616.150	0.535	1823.391	606.025	0.504
25	1864.747	673.620	0.384	1959.171	720.289	0.360
26	1832.154	633.848	0.445	1982.185	710.332	0.395
27	1818.007	574.375	0.583	1628.403	554.535	0.468
28	1875.430	573.337	0.636	1682.959	579.662	0.452

Table 75: Obtained mechanical properties assuming isotropic material properties for *E/v* method

	Center (beam) part			Wing (plate) part		
run	**Young's modulus, MPa**	**Shear modulus, MPa**	**Poisson's ratio**	**Young's modulus, MPa**	**Shear modulus, MPa**	**Poisson's ratio**

Table 75: Obtained mechanical properties assuming isotropic material properties for *E/v* method

	Center (beam) part			Wing (plate) part		
1	2,297.48	741.72	0.35	2225.420	733.259	0.34
2	1,918.34	567.61	0.41	2125.604	662.226	0.38
3	1,790.28	497.80	0.44	1868.843	536.710	0.43
4	1,880.78	453.16	0.52	1872.984	605.774	0.35
5	1,978.39	606.30	0.39	2068.149	668.405	0.35
6	1,926.74	607.75	0.37	2107.921	705.582	0.33
7	1,836.26	560.78	0.39	2041.594	670.584	0.34
8	1,886.95	431.14	0.54	1947.371	596.552	0.39
9	1,793.02	366.89	0.59	1785.396	570.151	0.36
10	1,973.45	464.21	0.53	1977.905	625.623	0.37
11	2,266.61	756.33	0.33	2207.984	720.070	0.35
12	2,317.07	625.17	0.46	2047.008	671.045	0.34
13	1,851.71	484.92	0.48	1988.367	637.970	0.36
14	1,679.26	414.21	0.51	1672.177	557.380	0.33
15	1,752.51	469.12	0.46	1731.308	498.596	0.42
16	2,085.05	658.74	0.37	2045.826	590.462	0.42
17	2,106.08	656.27	0.38	2065.688	626.720	0.39
18	2,014.26	550.58	0.45	1836.671	627.701	0.32
19	2,194.78	606.14	0.45	1934.866	662.918	0.31
20	2,283.22	709.49	0.38	2125.421	698.362	0.34
21	2,018.54	664.87	0.34	2172.079	715.091	0.34
22	1,710.60	401.71	0.53	1685.210	482.861	0.43
23	2,108.38	552.55	0.47	1816.565	560.287	0.38
24	2,110.90	593.70	0.44	2019.775	655.964	0.35
25	1,845.67	622.12	0.33	2040.412	689.249	0.32
26	2,195.25	712.97	0.35	2063.476	661.010	0.36

Table 75: Obtained mechanical properties assuming isotropic material properties for *E/v* method

	Center (beam) part			Wing (plate) part		
27	2,118.07	567.94	0.46	1759.255	575.679	0.35
28	2,298.47	539.75	0.53	1819.761	579.353	0.36

9.10 Results obtained for printed artifacts assuming orthotropic material properties

Table 76: Obtained mechanical properties assuming orthotropic material property for wing

run	E_x, MPa	E_y, MPa	G_{xy}, MPa	ν_{xy}	ν_{yx}
1	2,361.99	2,012.47	647.91	0.27	0.23
2	2,320.13	1,917.79	593.39	0.27	0.22
3	1,987.97	874.42	482.45	0.50	0.22
4	1,995.17	1,677.57	563.96	0.29	0.25
5	2,199.91	1,817.41	606.89	0.28	0.23
6	2,325.06	2,151.51	624.12	0.25	0.23
7	2,242.25	2,174.77	555.40	0.23	0.22
8	2,127.02	1,814.01	490.39	0.26	0.22
9	1,948.18	1,792.03	472.18	0.26	0.23
10	2,155.51	1,841.26	537.94	0.27	0.23
11	2,373.86	2,070.46	621.99	0.26	0.22
12	2,213.95	1,935.99	593.34	0.27	0.23
13	2,093.98	1,766.46	576.57	0.28	0.24
14	1,833.38	1,600.43	433.32	0.27	0.24
15	1,885.22	1,186.33	406.54	0.35	0.22
16	2,191.75	1,477.76	494.30	0.31	0.21
17	2,097.26	658.25	681.82	0.74	0.23
18	1,903.63	813.87	699.17	0.62	0.26

Table 76: Obtained mechanical properties assuming orthotropic material property for wing

19	2,077.07	1,982.00	581.25	0.26	0.24
20	2,295.87	2,055.29	625.26	0.26	0.23
21	2,378.89	2,219.60	607.70	0.24	0.22
22	1,863.63	1,342.07	370.25	0.30	0.22
23	1,994.87	1,692.18	463.54	0.27	0.23
24	2,184.48	1,973.01	564.74	0.25	0.23
25	2,184.82	2,138.88	610.85	0.24	0.24
26	2,239.57	2,318.27	563.70	0.22	0.23
27	1,908.12	1,788.31	493.79	0.26	0.24
28	1,964.59	1,793.89	505.31	0.26	0.24